QA: N/A

Civilian Radioactive Waste Management System
Management & Operating Contractor

Natural Analogue Synthesis Report

TDR-NBS-GS-000027 REV00 ICN 02

May 2002

Prepared for:

U.S. Department of Energy
Yucca Mountain Site Characterization Office
P.O. Box 30307
North Las Vegas, Nevada 89036-0307

Prepared by:

Bechtel SAIC Company, LLC
1180 Town Center Drive
Las Vegas, Nevada 89144-6352

Under Contract Number
DE-AC08-91RW00134

DISCLAIMER

This report was prepared as an account of work sponsored by an agency of the United States Government. Neither the United States Government nor any agency thereof, nor any of their employees, nor any of their contractors, subcontractors or their employees, makes any warranty, express or implied, or assumes any legal liability or responsibility for the accuracy, completeness, or any third party's use or the results of such use of any information, apparatus, product, or process disclosed, or represents that its use would not infringe privately owned rights. Reference herein to any specific commercial product, process, or service by trade name, trademark, manufacturer, or otherwise, does not necessarily constitute or imply its endorsement, recommendation, or favoring by the United States Government or any agency thereof or its contractors or subcontractors. The views and opinions of authors expressed herein do not necessarily state or reflect those of the United States Government or any agency thereof.

Civilian Radioactive Waste Management System
Management & Operating Contractor

Natural Analogue Synthesis Report

TDR-NBS-GS-000027 REV00 ICN 02

May 2002

Prepared by:

SIGNATURE ON FILE

A.M. Simmons
Lead Author

05/01/02
Date

Checked by:

SIGNATURE ON FILE

P. Persoff

05/01/02
Date

QA:

SIGNATURE ON FILE

C. Warren

5/1/02
Date

Approved by:

SIGNATURE ON FILE

P. Dixon
Responsible Manager, Natural Barriers Manager

5-1-02
Date

INTENTIONALLY LEFT BLANK

CHANGE HISTORY

Revision Number	Interim Change No.	Effective Date	Description of Change
00		02/15/2002	Initial Issue.
00	01	04/15/2002	Interim change to address comments per AP-7.5Q, Submittal, Review, and Acceptance of Deliverables. Text modified for grammar. Changes indicated by sidebar in margin.
00	02	05/01/2002	Interim change to Table 1-1, KTI Agreements and to correct typographical errors. Text modified on pp. 1T-1, 3-1, 4-1, 6-2, 7-2, 8-1, 10-1, 11-1, 11-5, 11-18, 14-1. Changes indicated by sidebars in margin; on pages modified for ICN 02, only those changes associated with ICN 02 are noted by sidebars.

INTENTIONALLY LEFT BLANK

ACKNOWLEDGMENTS

This work was supported by the Director, Office of Civilian Radioactive Waste Management, U.S. Department of Energy, through Memorandum Purchase Order EA9013MC5X between Bechtel SAIC Company, LLC and the Ernest Orlando Lawrence Berkeley National Laboratory (Berkeley Lab). The support is provided to Berkeley Lab through the U.S. Department of Energy Contract No. DE-AC03-76SF00098. The support of Berkeley Lab Lead, Bo Bodvarsson, is appreciated. Many other individuals lent their support and ideas in development and preparation of this report. The assistance of Swen Magnuson of Bechtel, INEEL is appreciated for helpful discussions and guidance in reviewing the INEEL literature. Jeffrey Hulen of Energy and Geoscience Institute, University of Utah, provided assistance in logging Yellowstone cores. Terry Keith of the USGS provided data used in the Yellowstone natural analogue study. A number of individuals at the National Academy of Sciences Ukraine, International Radioecology Laboratory (Slavutych, Ukraine) and Chernobyl Nuclear Power Plant graciously donated literature for the Chernobyl study.

The report was improved through LBNL technical reviews by Sonia Salah, Gerald Nieder-Westermann, Nicolas Spycher, Timothy Kneafsey, Stefan Finsterle, Joe Wang, and by numerous reviewers during the AP.2-14Q review process. The compliance review of REV 00 ICN 02 was performed by Charlie Warren. Engineering Assurance review of REV 00 ICN 02 was performed by Vivi Fissekidou. A full technical edit was provided by Dan Hawkes.

The following authors contributed to the report. The sections to which they contributed are in parentheses. Ardyth Simmons (1, 3, 4, 7, 8, 9, 10, 11, 12, 14, 15); Gerald Nieder-Westermann (2); John Stuckless (3, 8); Patrick Dobson (5, 6, 7, 11); André Unger (9); Edward Kwicklis (9, 10); Peter Lichtner (9, 10, 11); Bill Carey (11); Giday WoldeGabriel (11); Michael Murrell (10); Timothy Kneafsey (11); Arend Meijer (12); Boris Faybishenko (13).

REV00 ICN 02 was checked by Peter Persoff. Vivi Fissekidou coordinated the AP-2.14Q review process. Production was coordinated by Maryann Villavert, with assistance from Donald Nodora. Carol Valladao was responsible for handling the referencing process, with assistance from June Jackson.

INTENTIONALLY LEFT BLANK

CONTENTS

CONTENTS (Continued)

CONTENTS (Continued)

CONTENTS (Continued)

CONTENTS (Continued)

CONTENTS (Continued)

LIST OF FIGURES

LIST OF FIGURES (Continued)

LIST OF FIGURES (Continued)

LIST OF FIGURES (Continued)

LIST OF FIGURES (Continued)

LIST OF FIGURES (Continued)

LIST OF FIGURES (Continued)

INTENTIONALLY LEFT BLANK

LIST OF TABLES

LIST OF TABLES (Continued)

LIST OF TABLES (Continued)

INTENTIONALLY LEFT BLANK

ACRONYMS AND ABBREVIATIONS

1-D	one-dimensional, one dimension
2-D	two-dimensional, two dimensions
3-D	three-dimensional, three dimensions
ACC	accession number
AMR	Analysis/Model Report
AP	Administrative Procedure
BDCF	Biosphere Dose Conversion Factor
BP	Before Present
BSC	Bechtel SAIC Company, LLC
CEC	Cation Exchange Capacity
CFR	Code of Federal Regulations
ChNNP	Chernobyl Nuclear Power Plant
CRWMS	Civilian Radioactive Waste Management System
DCM	dual-continuum model
DCPT	dual-continuum particle tracker
DIC	dissolved inorganic carbon
DIRS	Document Input Reference System
DOE	U.S. Department of Energy
DST	Drift Scale Test
DTN	Data Tracking Number
EBS	Engineered Barrier System
ECRB	Enhanced Characterization of Repository Block
EHPA	Di (2-Ethylhexyl) Phosphoric Acid
EIS	Environmental Impact Statement
EPA	Environmental Protection Agency
ESF	Exploratory Studies Facility
FEHM	Finite Element Heat and Mass Transfer
FEP	Features, Events, and Processes
FY	Fiscal Year
GMWL	Global Meteoric Water Line
IAEA	International Atomic Energy Agency
IFC	International Formulation Committee
INEEL	Idaho National Engineering and Environmental Laboratory
ISM	Integrated Site Model
ITN	Input Tracking Number
KTI	Key Technical Issue

ACRONYMS AND ABBREVIATIONS (Continued)

LA	License Application
LANL	Los Alamos National Laboratory
LBNL	Lawrence Berkeley National Laboratory
LBT	Large Block Test
LLNL	Lawrence Livermore National Laboratory
LPIT	Large Scale Aquifer Pumping and Infiltration Test (at INEEL)
M&O	Management and Operating Contractor
N/A	not applicable
NARG	Natural Analogue Review Group
NAT	Neutron-Probe Access Tube
NEA	Nuclear Energy Agency
NKC	sodium-potassium-calcium
NRC	U.S. Nuclear Regulatory Commission
NTS	Nevada Test Site
NWTRB	Nuclear Waste Technical Review Board
OCRWM	Office of Civilian Radioactive Waste Management
PA	Performance Assessment
PGA	peak ground acceleration
PMR	Process Model Report
Q	Qualified
QA	Quality Assurance
QAP	Quality Administrative Procedure
QARD	Quality Assurance Requirements and Description
QIP	Quality Implementing Procedure
REE	rare earth elements
RPM	Rock Properties Model
RWMC	Radioactive Waste Management Complex (at INEEL)
SDA	Subsurface Disposal Area (within RWMC, at INEEL)
SEM	scanning electron microscope
S & ER	Yucca Mountain Science and Engineering Report
SHT	Single Heater Test
SN	Scientific Notebook
SNF	spent nuclear fuel
SNL	Sandia National Laboratories
SR	Site Recommendation
SRPA	Snake River Plain Aquifer

ACRONYMS AND ABBREVIATIONS (Continued)

STN	Software Tracking Number
SZ	saturated zone
TBD	to be determined
TBV	to be verified
TDMS	Technical Data Management System
TDS	total dissolved solids
TH	thermal-hydrologic
THC	thermal-hydrologic-chemical
THCM	thermal-hydrologic-chemical-mechanical
THM	thermal-hydrologic-mechanical
TIMS	thermal ionization mass spectrometry
TNT	trinitrotoluene
TOUGH	Transport Of Unsaturated Groundwater and Heat
TRU	transuranic
TSPA	Total System Performance Assessment
TSPA-SR	Total System Performance Assessment Site Recommendation
TWP	Technical Work Plan
UMTRA	Uranium Mill Tailing Remedial Action
UNE	Underground Nuclear Explosion
US	United States
USGS	United States Geological Survey
UZ	unsaturated zone
VA	Viability Assessment
WFD	waste form degradation
WP	waste package
XRD	x-ray diffraction
XRF	x-ray fluorescence
YM	Yucca Mountain
YMP	Yucca Mountain Site Characterization Project
YMSD	Yucca Mountain Site Description

ACRONYMS AND ABBREVIATIONS (Continued)

UNITS

Bq	becquerel
Ci	curie
g	gram
ka	thousand years ago
kg	kilogram
ky	thousand years
m	meter
Ma	million years ago
masl	meters above sea level
mg/L	milligrams per liter
mL/g	milliliters per gram
mm	millimeter
µmho/cm	micro-mho per centimeter
MPa	megapascal
mR/hr	millirads per hour
Mt	megaton
m.y.	million years
Pa	pascal
pCi	picocurie
rem	roentgen equivalent man (i.e., the amount that produces the same damage to humans as 1 roentgen of high-voltage x-rays)
Sv	sievert
t	ton
t/ha	tons per hectare
yr	year

MAJOR HYDROGEOLOGICAL UNITS

CFu	Crater Flat undifferentiated hydrogeologic unit
CHn	Calico Hills nonwelded hydrogeologic unit
PTn	Paintbrush Tuff nonwelded hydrogeologic unit
TCw	Tiva Canyon welded hydrogeologic unit
TSw	Topopah Spring welded hydrogeologic unit

1. INTRODUCTION

1.1 PURPOSE OF REPORT AND LIMITATIONS

The purpose of this report is to present analogue studies and literature reviews designed to provide qualitative and quantitative information to test and provide added confidence in process models abstracted for performance assessment (PA) and model predictions pertinent to PA. This report provides updates to studies presented in the *Yucca Mountain Site Description* (CRWMS M&O 2000 [151945], Section 13) and new examples gleaned from the literature, along with results of quantitative studies conducted specifically for the Yucca Mountain Site Characterization Project (YMP). The intent of the natural analogue studies was to collect corroborative evidence from analogues to demonstrate additional understanding of processes expected to occur during postclosure at a potential Yucca Mountain repository. The report focuses on key processes by providing observations and analyses of natural and anthropogenic (human-induced) systems to improve understanding and confidence in the operation of these processes under conditions similar to those that could occur in a nuclear waste repository. The process models include those that represent both engineered and natural barrier processes. A second purpose of this report is to document the various applications of natural analogues to geologic repository programs, focusing primarily on the way analogues have been used by the YMP. This report is limited to providing support for PA in a confirmatory manner and to providing corroborative inputs for process modeling activities. Section 1.7 discusses additional limitations of this report.

Key topics for this report are analogues to emplacement drift degradation, waste form degradation, waste package degradation, degradation of other materials proposed for the engineered barrier, seepage into drifts, radionuclide flow and transport in the unsaturated zone (UZ), analogues to coupled thermal-hydrologic-mechanical-chemical processes, saturated zone (SZ) transport, impact of radionuclide release on the biosphere, and potentially disruptive events. Results of these studies will be used to corroborate estimates of the magnitude and limitation of operative processes in order to build realism into conceptual and numerical process models used as a foundation for PA in the representative case of postclosure safety.

1.2 DEFINITION OF ANALOGUE

Natural analogues refer to either natural or anthropogenic systems in which processes similar to those expected to occur in a nuclear waste repository are thought to have occurred over long time periods (decades to millenia) and large spatial scales (up to tens of kilometers). Analogues provide an important temporal and spatial dimension to the understanding of processes not accessible to laboratory experiments that may take place in a nuclear waste repository and surrounding area. The use of analogy has been endorsed by the international nuclear waste community as a means of demonstrating confidence in the operation of systems, components, and processes related to nuclear waste disposal (e.g., publications of the International Atomic Energy Agency [IAEA] and the European Community's Natural Analogue Working Group). "The role of a natural analogue should ... be to confirm: (a) that the process is in fact something which can or will occur in practice as well as in theory, and in nature as well as in the laboratory; (b) where, when, and under what conditions it can occur; (c) that the effects of the process are

those envisaged in the model; and (d) that the magnitude of the effects in terms of scale and time are similar to those predicted for a similar set of conditions" (Chapman and Smellie 1986 [124323], p. 167).

1.3 ROLE OF NATURAL ANALOGUES IN PROCESS MODELS AND PERFORMANCE ASSESSMENT

Natural analogues may be applied in a quantitative or a qualitative manner, depending upon the purpose to which they are applied and upon the specific analogue. They can provide descriptive information about the occurrence of various processes, or they may be able to constrain the bounds of those processes. Natural analogues allow testing of the pertinence of individual processes over geologic time and space scales, assessing the relative importance of various processes, and gauging the effects of process coupling. For some processes (e.g., those that are thermally coupled), natural analogues may be the only means of providing the required understanding of long-term and large-scale behavior needed to provide scientific confidence in process models for input to total system performance assessment (TSPA). Analogue investigations may determine the conditions under which the processes occur, the effects of the processes, and the magnitude and duration of the processes.

Analogue information may also provide a body of data for testing codes and for validation of conceptual and numerical models. Natural analogue information may also be used to build confidence in databases themselves. Because natural analogues can be used to evaluate the validity of extrapolating from temporally limited field-scale experiments to longer time scales, or to add confidence when extrapolating from laboratory and intermediate-scale experiments to tests at larger spatial scales, they are uniquely suited to building confidence in process models. In this manner, they are used as a means of model validation, or confidence-building. Each of the Process Model Reports (PMRs) that support Site Recommendation (SR) includes a section on "validation" that in many cases utilizes natural analogue information.

Less commonly, natural analogues may be used to assist and support the selection of scenarios and to establish the probability of occurrence of selected scenarios. Natural analogues do not reduce uncertainty *per se*; that is, the uncertainty bounds on a given parameter value may remain unchanged. However, natural analogues can build confidence that the bounds are set appropriately. Because some uncertainties are greater in natural analogues than at the site being characterized, information from natural analogues should only be used in conjunction with other information to evaluate consistency with laboratory and field data.

Comparison of model predictions with the results of natural analogue investigations will in general only permit confirmation that the model takes into account the relevant processes in appropriate ways. Validation of a predictive model by such comparison provides reasonable assurance that the model reflects future behavior. This is the level of confidence required by 66 FR ([156671], p. 55804), which states, in §63.101(a): "Demonstrating compliance will involve the use of complex predictive models that are supported by limited data from field and laboratory tests, site-specific monitoring, and natural analogue studies that may be supplemented by prevalent expert judgment."

1.4 ROLE OF NATURAL ANALOGUES IN LICENSE APPLICATION

The National Research Council endorsed the use of natural analogues as "natural test cases, geological settings in which naturally occurring radioactive materials have been subjected to environmental forces for millions of years" (National Research Council 1990 [100061], p. 27). The Council's report indicates that natural analogues are essential for validating performance assessment models of geologic repositories over thousands or millions of years, as well as forming the basis for communicating the safety of a deep geologic repository in terms the public can understand. The Nuclear Waste Technical Review Board concurred in these recommendations (NWTRB 1990 [126162], p. xiii).

In 66 FR ([156671], p. 55804, Section 63.101(a)(2)), the Nuclear Regulatory Commission (NRC) has identified natural analogues as one way of demonstrating compliance with the reasonable expectation that postclosure performance objectives will be met. As summarized in Section 1 of this report, the NRC also specifies natural analogues as one method to provide the technical basis for models in (66 FR [156671], p. 55804).

The content requirements for the license application (66 FR [156671], p. 55798, Section 63.21(c)(15)) specify natural analogue studies as one of the measures used to support analyses and models that are used to assess performance of a geologic repository. In addition, the technical criteria for a license application (66 FR [156671], p. 55804) specify the use of natural analogue information as part of the demonstration of compliance with the performance objectives of the disposal regulations. Further, the demonstration of the concept of multiple barriers and the performance of complex engineered structures must include information from natural and archaeologic analogs (66 FR [156671], p. 55805, Section 63.102(h)). The importance of natural analogs in supporting performance assessment models is again included in the requirements for performance assessment (66 FR [156671], p. 55807, Section 63.114(g)).

Ten agreements from the DOE-NRC technical exchanges and management meetings on key technical issues (KTIs) include mention of analogues or information from analogue studies as necessary to address the agreement item. As shown in Table 1-1, two KTI agreement items are at least partially addressed by information in this report. A cross reference to this table is found in the sections of this report that could provide information related to these KTIs.

1.5 CRITERIA FOR SELECTION OF ANALOGUES USED IN MODEL VALIDATION

As pointed out by Pearcy and Murphy (1991 [157563]), the 10,000-year period required for high-level waste isolation is a difficult period to approximate with natural analogues. For instance, most ore deposits are on the order of a million to a billion years in age, whereas anthropogenic sites (i.e., human made) are generally on the order of a few thousand years or less. To be most helpful in terms of long-term processes relevant to a high-level waste repository, it would be useful to find analogues with ages on the order of 1,000 to 1 million years.

Because no single site will be a perfect analogue to all ongoing and anticipated processes at Yucca Mountain, focus is placed on identifying sites having analogous processes rather than total system analogues. Nevertheless, it is still worthwhile to attempt to match as many features and

characteristics as possible when identifying suitable analogue sites. An ideal analogue site to long-term radionuclide transport at Yucca Mountain would have to satisfy the following conditions: (1) a known source term, (2) a similar set of radionuclides, (3) well-characterized with site data, (4) similar geologic conditions, (5) observable long-term conditions, (6) identifiable boundaries of the system, and (7) a clear-cut process that can be decoupled from other processes. It is most useful if the analogue has been in place for at least thousands of years, so that the results of long-term behavior are observable.

In addition to using natural analogues for long-term predictions, models must be able to explain and match the transport times and pathways from contaminated sites that provide anthropogenic analogues, such as Hanford, Washington; the Idaho National Engineering and Environmental Laboratory (INEEL); and the Nevada Test Site (NTS). Anthropogenic analogue sites are a challenge to constrain in models, because they often contain more than one contaminated source, (sometimes with poorly identified source terms), have a complex mixture of radionuclides and other contaminants, and often occur in highly heterogeneneous formations.

With respect to choosing different geochemical transport analogues, Chapman and Smellie (1986 [124323], p. 168) state the following:

> The essentials to bear in mind when selecting analogues are as follows: (1) The process involved should be clear-cut. Other processes which may have been involved in the geochemical system should be identifiable and amenable to quantitative assessment as well, so that their effects can be accountable. (2) The chemical analogy should be good. It is not always possible to study the behavior of a mineral system, chemical element or isotope identical to that whose behaviour requires assessing. The limitations of this should be fully understood. (3) The magnitude of the various physicochemical parameters involved (P, T, Eh, concentration, etc.) should be determinable, preferably by independent means. (4) The boundaries of the system should be identifiable (whether it is open or closed, and consequently how much material has been involved in the process being studied). (5) The time-scale of the process must be measurable, since this factor is of the greatest signficance for a natural analogue.

Care must be taken in selection of an appropriate analogue to represent correctly the process of interest. For example, all uranium deposits are not categorically good analogues for stability of a nuclear waste repository. Uranium deposits indicate the long-term stability of some geologic environments, but some of the same ore deposits could be used to make arguments for massive transport of radioactive materials over large distances by natural processes. Care must also be exercised to exclude those analogues for which initial and/or boundary conditions are poorly known and where important data, such as the source term, are poorly constrained and may not be obtainable. A given site will usually only be analogous to some portion of a repository or to a subset of processes that will occur in a repository. Furthermore, additional processes will have occurred that are not characteristic of the repository. Therefore, choices must be made to select the processes of greatest relevance and the ability to isolate them for study. The long-term nature of analogues introduces some limitations and uncertainties, but analogues can still be used effectively if appropriate selection criteria are determined and applied.

In the early 1990s, the U.S. Department of Energy (DOE)/YMP convened a panel of international experts in natural analogues to provide guidance in selection and use of natural analogues for implementation by the YMP. The Natural Analogue Review Group (NARG) report recommended that natural analogues be process-oriented and "should address the issues resulting from the perturbation of a natural system (the geologic site) by the introduction of a technological system (the repository)" (DOE 1995 [124789], p. 2). The NARG was explicit in stating that "one should clearly discriminate such studies from those which, following the classical approach of earth sciences, are based on the comparative study of geological sites or situations. In particular, all investigations normally part of site characterization, even when considering comparisons with similar remote sites, such as (paleo)hydrology, etc., should not be considered as natural analogue studies" (DOE 1995 [124789], p. 2). The YMP has abandoned that approach and now defines analogues in a more all-encompassing sense in order to avoid the narrower definition.

1.6 SCOPE AND ORGANIZATION OF REPORT

This report considers a broad range of analogues that encompass both the engineered barriers and natural system components of a geological repository at Yucca Mountain. In each section, the conceptual basis for the process model is provided as a framework for discussion of relevant analogue studies and examples. Next, examples of analogue studies relevant to the operative processes in the conceptual models are presented. This is followed by an assessment of the applicability of the information or conclusions derived from the analogue. The current repository design approach (Section 2) and configuration of engineered barriers (Section 5) are provided as the basis against which to identify relevant analogues for those systems. Section 3 presents analogues related to drift stability. Section 4 provides qualitative corroboration of waste form degradation processes. Section 6 presents examples of analogues for waste package corrosion processes. Section 7 addresses analogues for engineered barrier components and processes. Section 8 illustrates seepage into underground openings at sites with varying degrees of analogy. Section 9 addresses unsaturated zone (UZ) flow processes, but is primarily concerned with Part I of a modeling study using INEEL data. Part I of that study describes a flow model that was calibrated using INEEL data and YMP modeling methods. The calibration parameter values were then used in Part II of the study, which is described in Section 10 in a model of radionuclide transport at INEEL. Section 10 also includes results to date of the Peña Blanca field study and literature examples of analogues related to UZ transport. Section 11 presents analogues related to coupled processes, includes an extensive literature search for geothermal analogues, and summarizes experimental work on drillcore from Yellowstone National Park. In addition, Section 11 presents the results of a field and modeling study for the Paiute Ridge coupled processes analogue site and a literature study of thermal-hydrologic-mechanical (THM) processes. Section 12 presents an analysis of uranium mill tailing data relevant to saturated zone (SZ) transport and includes literature examples from selected sites. Section 13 uses parameters measured after the Chernobyl nuclear accident to arrive at Biosphere Dose Conversion Factors (BDCFs) that can be compared to those applied in the Yucca Mountain Biosphere Process Model. Section 14 provides examples of the ways in which analogues have been used to support conceptual models for volcanism and seismic hazard assessments and process models. Finally, Section 15 discusses how the analogue information is applied, both for illustrative purposes and in performance assessments. The ways in which other countries have used analogues in performance assessment are summarized. The specific needs for analogue information requested

by YMP performance assessment are listed, and each of the analogues covered in the report is mapped to its use in either conceptual model development, provision of data, or model validation. In a few cases, topics are identified that could potentially increase confidence with the use of natural analogues.

1.7 QUALITY ASSURANCE

This report provides corroborating information for the modeling of natural and engineered barrier performance at Yucca Mountain. This report was developed in accordance with AP-3.11Q, *Technical Reports*. Other applicable DOE Administrative Procedures (APs) and YMP-LBNL Quality Implementing Procedures (QIPs) are identified in the Technical Work Plan (TWP) *Natural Analogue Studies for License Application* (BSC 2001 [157535]). The Activity Evaluation in the TWP (BSC 2001 [157535], Attachment I) graded the natural analogue work as being non-Q and not subject to control under the DOE Office of Civilian Radioactive Waste Management (OCRWM) Quality Assurance Requirements and Description (QARD) (DOE 2000 [149540]). All procedures followed were current revisions at the time of implementation.

The data collected under this study is corroborative and will not be used directly by Performance Assessment (PA) for licensing. This report will be used to support PA in a confirmatory manner only. The TWP stipulates that all data generated by this work will be unqualified. However, data that have been collected have been submitted to the YMP Technical Data Management System (TDMS) in accordance with AP-SIII.3Q, *Submittal and Incorporation of Data to the Technical Data Management System*. The TWP also exempts the natural analogue work from following AP-SI.1Q, *Software Management*. Procedures that were followed during the course of the work, including AP-SIII.1Q, *Scientific Notebooks*, and AP-12.1Q, *Control of Measuring and Test Equipment and Calibration Standards* are listed on the TWP. Scientific notebooks are used to provide traceability to sample collection, data analysis, calculations, and modeling studies.

Input for this report consisted of a combination of existing information from natural analogue sites reported in the literature and data collected for the YMP. Literature data not developed by the YMP are available for review through the Technical Information Center (TIC); data collected by project personnel are available in TDMS; scientific notebooks (with relevant page numbers) used in preparation of this report are listed in Table 1-2 and are available from the Records Information System (RIS). Software referenced in this report is listed in Table 1-3. More detailed discussion of software usage is provided in relevant scientific notebooks. Finally, this document was developed to meet the deliverable criteria listed in Section 5 of the TWP (BSC 2001 [157535]).

Table 1-1. KTI Agreements Addressed in This Report

Agreement Number	Text of Agreement	Section of This Report
KIA0204	Document that the ASHPLUME model, as used in the DOE performance assessment, has been compared with an analogue igneous system. (Eruptive AC-2). DOE agreed and will deliver calculation CAL-WIS-MD-000011 that will document a comparison of the ASHPLUME code results to observed data from the 1995 Cerro Negro eruption. This will be available to the NRC in January 2001. DOE will consider Cerro Negro as an analogue and document that in Eruptive Processes AMR (ANL-MGR-GS-000002). This will be available to the NRC in FY2002 (Eruptive AC-2).	14.3
KUZ0407 [1]	Provide documentation of the results obtained from the Natural Analogues modeling study. The study was to apply conceptual models and numerical approaches developed from Yucca Mountain to natural analogue sites with observations of seepage into drifts, drift stability, radionuclide transport, geothermal effects, and preservation of artifacts. DOE will provide documentation of the results obtained from the Natural Analogues modeling study. The study was to apply conceptual models and numerical approaches developed from Yucca Mountain to natural analogue sites with observations of seepage into drifts, drift stability, radionuclide transport, geothermal effects, and preservation of artifacts. This will be documented in the Natural Analogues for the Unsaturated Zone AMR (ANL-NBS-HS-000007) expected to be available to NRC FY 2002.	3.2–3.4, 6.2, 8.2–8.4, 10.3–10.5, 11.2–11.5

[1] The Natural Analogue Synthesis Report replaces the AMR in the provision of documentation stated in KUZ 0407

Table 1-2. Scientific Notebooks

LBNL Scientific Notebook ID	YMP M&O Scientific Notebook ID	Responsible Individual	Page Numbers	Citation
YMP-LBNL-AMS-NA-1	SN-LBNL-SCI-108-V1	Simmons, A.	83–87, 124–127, 139–144	Simmons 2002 [157544]
YMP-LBNL-AMS-NA-2	SN-LBNL-SCI-108-V2	Simmons, A.	6–23	Simmons 2002 [157578]
YMP-LBNL-AMS-NA-AU-2	SN-LBNL-SCI-186-V1	Unger, A.	55–63	Simmons 2002 [157578]
YMP-LBNL-DSM-ELS PD-2	SN-LBNL-SCI-190-V2	Dobson, P.	79–80	Simmons 2002 [157578]
YMP-LBNL-AMS-NA PD-1B	SN-LBNL-SCI-185-V1	Dobson, P.	7-1	Simmons 2002 [157578]
YMP-LBNL-AMS-NA PD-photos	SN-LBNL-SCI-185-V1	Dobson, P.	Roll 17 Images 2 and 4	Simmons 2002 [157578]
N/A	SN-LANL-SCI-237-V1	Murrell, M.	16	Simmons 2002 [157578]
N/A	SN-LANL-SCI-215-V1	Lichtner, P.	6–32, 56–59, 63, 69–76, 89–94, 100–104, 107, 110–112, 117–118, 128, 130–131	Simmons 2002 [157578]
N/A	SN-LANL-SCI-234-V1	Lichtner, P.	16, 20, 22–24, 26–33, 61–68, 75–76, 83, 88–90	Simmons 2002 [157578]

Table 1-3. Software Codes Referenced in Text

Software Name	Version Number	Software Tracking Number	Software Reference by Section
ASHPLUME	V 1.4LV	10022-1.4LV-00	14.3
ASHPLUME	V 2.0	10022-2.0-00	14.3
CXTFIT	V 2.1	N/A [2]	10.3.2.1, 11.4.7.1
DRKBA	V 3.3	10071-3.3-00	14.4
EQ3/6	V 7.2b	UCRL-MA-110662	11.2.12.1, 11.3.5
FEHM	2.0	10031-2.00-00	10.3.1, 10.3.6.1, 10.3.6.3, 10.3.6.5
FLOTRAN	1.0	N/A	10.3.1, 10.3.6.1, 10.3.6.3, 10.3.6.4, 11.4.7, 11.4.7.1, 11.4.7.2,
iTOUGH2[1]	V 4.0	N/A	9.3.3, 9.3.5, 9.3.6, 9.3.7, 9.5
Mathematica	V 4.1	N/A	10.3.6.4
TOUGH2	V 1.4	10007-1.4-01	11.3.5
TOUGHREACT	V 2.2	10154-2.2-00	11.3.5
TOUGHREACT	V 2.3	10396-2.3-00	11.3.5
UDEC	V 2.0	B00000000-01717-1200-30004	14.4

NOTE: [1] iTOUGH2 with EOS9 and EOS7r modules

[2] N/A signifies that the code is unqualified and it is currently not tracked by the Software Configuration Management System.

2. REPOSITORY DESIGN SELECTION FOR SITE RECOMMENDATION AND RELATION TO APPLICABLE ANALOGUES

2.1 INTRODUCTION

Studies of natural and anthropogenic systems can improve understanding and confidence in the variables affecting the evaluation and operation of a selected repository design. The selection of appropriate analogues to build confidence in repository design parameters should focus on the variables affecting operational parameters rather than on a specific design for a potential Yucca Mountain repository. The current design approach is flexible in that a wide range of thermal operating modes is being examined. The flexible design approach is presented in Section 2.2. The range of potential thermal operating modes is described on the basis of three evaluated scenarios in Section 2.3, while Section 2.4 presents design methods by which the thermal goals can be achieved. Section 2.5 provides a basis for evaluating analogues to repository materials and processes that are discussed in subsequent chapters.

2.2 FLEXIBLITY IN DESIGN

Refining the design and operating mode of the potential monitored geologic repository at Yucca Mountain has been an ongoing process since inception of the YMP. This iterative design process has been focused on improving the understanding of how design features contribute to the performance of a potential repository and to the uncertainty in that performance.

A primary design aspect has been the thermal load that will be generated by the repository. Previous design concepts have considered higher-temperature operating modes, in which the rock surrounding emplacement drifts exceeds the boiling point of water. More recently, to maintain flexibility in design, the design process has evolved to examine the effects on the repository over a wider range of thermal conditions. A flexible approach to design was introduced in the *Yucca Mountain Science and Engineering Report* (S&ER) (DOE 2001 [153849], Section 2.1.3). The design has flexible operating modes that can be adapted to accommodate a waste stream with potentially evolving thermal characteristics.

2.3 OBJECTIVES OF THERMAL OPERATING MODES

The current design concepts range from a lower-temperature operating mode to a higher-temperature operating mode. For the lower-temperature mode, the objective is to keep the waste package surface temperature below 85°C (DOE 2001 [153849], Section 2.1.2.3). In the higher-temperature mode, the wall rock of the drift is above boiling temperature but the temperature is controlled to prevent boiling fronts from coalescing in the rock pillars between the emplacement drifts. Strategies that have been considered with regard to selecting the operating mode of the repository are presented below.

2.3.1 Manage Boiling Fronts within the Rock Pillars

The higher end of the thermal operating mode, presented in the *Supplemental Science and Performance Analyses* (SSPA) (BSC 2001 [155950], Table 2-1), assumes an average waste package maximum temperature of ~160°C. This mode preserves the capability of the rock mass

to drain percolation flux through the repository horizon by preventing the boiling fronts from coalescing in the rock pillars between the emplacement drifts. In this mode, the close spacing of waste packages with thermally blended spent fuel inventories achieves a relatively uniform distribution of rock temperatures along the drift, limiting potentially complex thermal-mechanical effects resulting from a varying thermal gradient along the drift axis. This operating mode would also meet a design requirement established to maintain the integrity of the waste package cladding by not exceeding a temperature of 350°C, the temperature at which the cladding loses its integrity.

2.3.2 Maintain Drift-Wall Temperatures Below Boiling

One lower-temperature objective is to keep all the rock in the repository below the boiling point of water to reduce uncertainties associated with coupled thermal-hydrologic-chemical-mechanical processes driven by the boiling of water (BSC 2001 [155950], Section 2.3.2). In the higher-temperature operating mode described in the S&ER, the rock temperatures within the first several meters outside the emplacement drifts exceed the boiling point of water for about a thousand years.

2.3.3 Reduce Uncertainty in Corrosion Rates

The lower-temperature end of the range of thermal operating modes was defined by considering the potential for reducing uncertainty in the rate of localized corrosion of Alloy 22 waste package material. At temperatures below about 85°C or relative humidity (RH) below 50 percent, the susceptibility of Alloy 22 to crevice corrosion is very low (DOE 2001 [153849], Section 2.1.5, Figure 2-a). Operating the repository so that the temperature or relative humidity is below this window of crevice corrosion susceptibility may increase confidence that corrosion will not significantly reduce waste package service life.

2.4 MANAGING THERMAL OPERATING MODES

The temperature and relative humidity under which a repository would be operated for any specified underground layout can be managed either singularly or through various combinations of several operational parameters (DOE 2001 [153849], Section 2.1.4) such as by:

- Varying the thermal load resulting from the repository by managing the thermal output of the waste packages
- Managing drift ventilation prior to repository closure
- Varying the distance between waste packages in emplacement drifts.

Figure 2-1 illustrates the variables affecting the thermal performance of the repository, from waste forms to emplacement drifts.

2.5 APPLICATION TO NATURAL ANALOGUES

Because of the flexible design approach, analogues must be considered in terms of repository design variables rather than attempting to match a specific design. The important variables are

temperature of drift walls, presence or absence of a boiling front, dimensions and spacing of drifts, absence of backfill, and ventilation. These variables affect drift stability (addressed in Section 3), waste package and drip shield corrosion (discussed in Sections 5 and 6, respectively), processes operative within the engineered barrier system (addressed in Section 7), and thermally coupled processes affecting the host rock at the drift and mountain scales (covered in Section 11).

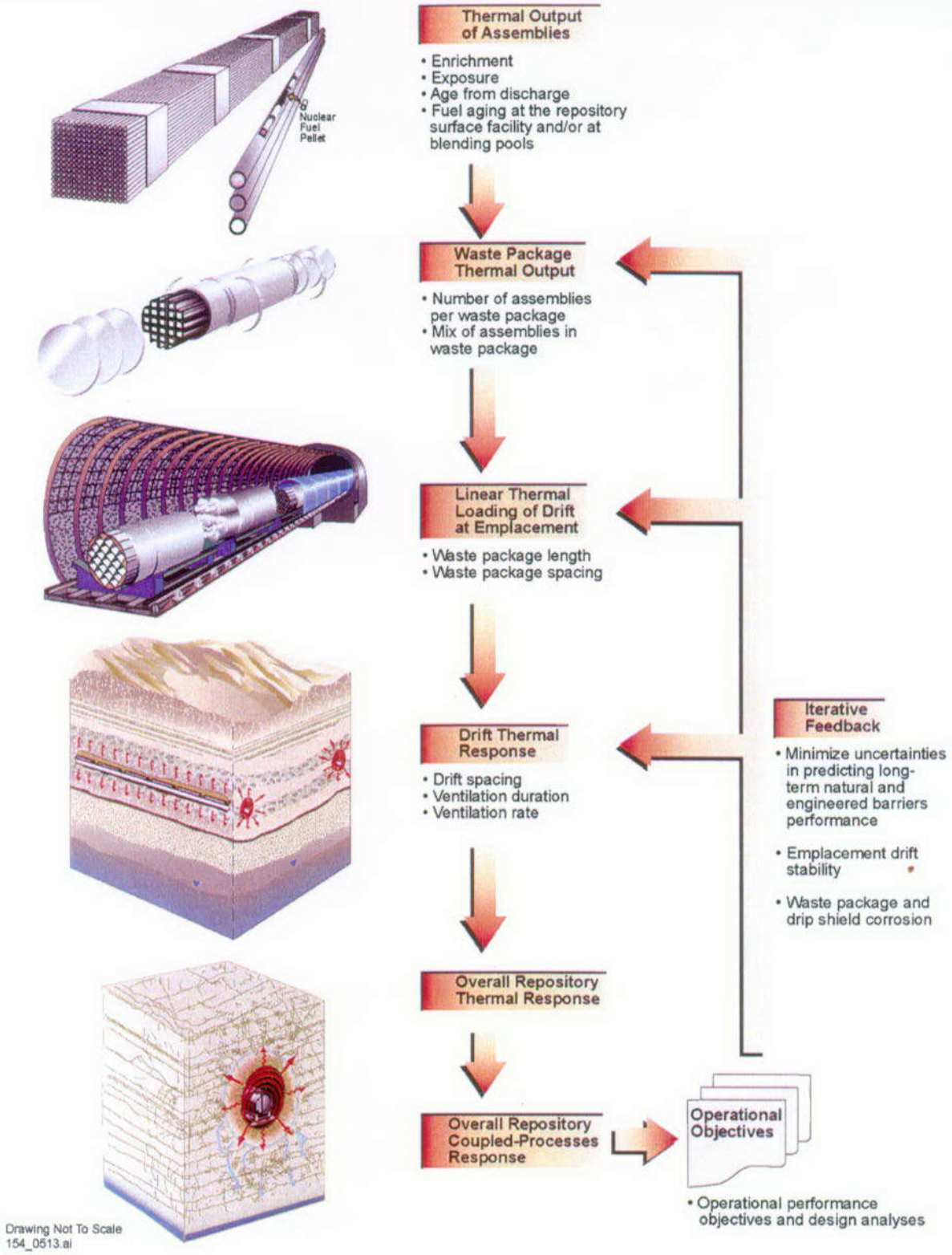

Source: DOE 2001 [153849], Figure 2-8.

Figure 2-1. Variables Affecting the Thermal Performance of the Repository

3. REPOSITORY DRIFT STABILITY ANALOGUES

3.1 INTRODUCTION

Section 2 provided background information on the current flexible design for a potential repository at Yucca Mountain against which to discuss analogues for drift stability. The proposed emplacement drift diameter is 5.5 m (18 ft) (DOE 2001 [153849], Section 2.3.1.1). The ability of underground openings to remain open and stable depends on a number of variables, including: (1) rock strength; (2) the size, shape, and orientation of the opening; (3) orientation, length, and frequency of fracturing; (4) effectiveness of ground support, and (5) loading conditions. There are no exact analogues to the openings that would be created for a potential repository at Yucca Mountain, but numerous examples demonstrate that both natural and man-made underground openings can exist for thousands of years in a wide variety of geologic settings, even with minimal or no engineering. Analogue information is available for natural underground openings (Section 3.2) and man-made excavations (Section 3.3). An analogue demonstrating thermal effects on underground openings is presented in Section 3.4. Effects of ground shaking on underground openings are mentioned in Section 3.4 and discussed in more detail in Section 14. Information found in Section 3.2, 3.3, and 3.4 may help to support arguments associated with Key Technical Issue (KTI) KUZ0407 listed in Table 1-1.

3.2 NATURAL UNDERGROUND OPENINGS

Caves represent examples of natural underground openings. They are abundant, and in many cases, it can be demonstrated that they have remained open for very long spans of time. The oldest documented examples noted in this study are from the limestone formations of the Guadalupe Mountains in New Mexico. Alunite is a mineral that forms on the floor of caves. Undisturbed, uncovered alunite collected from the cave floors has been dated at 4.0–3.9 million years (m.y.) for the Big Room at Carlsbad Caverns and at 6.0 to 5.7 m.y. for the upper level of the nearby Lechuguilla Cave. Alunite from other nearby caves yields ages as old as 11.3 m.y. (Polyak et al. 1998 [156159], p. 1919). Sections of the cave floors have blocks that appear to have fallen from the ceiling; however, none of the dated caves has been closed by rockfall, demonstrating the stability of most of these openings over millions of years. Because these settings are common, they demonstrate stability for most of the openings for millions of years. Many of these openings are as large or larger than those proposed for Yucca Mountain (Figure 3-1).

The San Antonio Mountain Cave in northern New Mexico is an example of a different geologic setting in which an opening has remained open over a long period of time. This cave is a lava tube in basalt from 3.4–3.9 million years ago (Ma) (Rogers et al. 2000 [154320], pp. 89–93). The cave is more than 170 m long and generally several meters wide. In some places, the ceiling is over 12 m high. The large size of the openings combined with abundant cooling fractures has resulted in fallen blocks (generally less than ¾ m in length and width) that cover about 30% of the cave's floor. Several spots preserve a long record (up to 1 m.y.) of sedimentation, more than 400 cm thick, with no collapse (Rogers et al. 2000 [154320], Figure 5). Davis (1990 [144461], p. 338) notes that similar cave sediments in Europe date back 1.5 Ma, which suggests that long-term stability of caves is a common feature.

Most lava tubes are a few thousand to a few hundred thousand years in age. They are commonly ellipsoidal to circular in cross section and several meters in diameter. Some of the most extensive lava tubes are in the Undara region of Australia, where 190,000-year-old tubes reach 100 km in length (Undara Experience 2001 [157515]). Figure 3-2a shows the interior of a lava tube in the Undara region (with a person included in the photo for scale). Lava tubes are also common in Hawaii (Figure 3-2b) and in the Cascade Range of California, Oregon, and Washington, in lava that is modern to a few thousand years in age. Most lava tubes exhibit areas of collapse where the roof is thin, but large sections of open tunnel persist for long periods of time.

The maximum length of time that caves have stood open is usually not known, but the age dates of datable biologic or archeologic materials found in many caves indicate that the caves have remained open for extended periods of habitation without collapse. Some packrat middens found in caves are thousands to tens of thousands of years old, and Davis (1990 [144461], p. 341) reports that over 1,000 middens have been studied in caverns and rock shelters of the western United States. Stuckless (2000 [151957], p. 4-6) reports on several caves in limestone that contain paintings that have been dated at 11,000 to 32,000 years old.

Kebara Cave in Mt. Carmel, Israel, is a very large opening (26 m long and 20 m wide, with a ceiling up to 18 m high), and sediments accumulated on the floor of the cave yield ages as old as 50,000 years (Bar-Yosef et al. 1996 [157419], p. 305). Although the main portion of the cave shows no sign of collapse, a terrace in front of the cave entrance was formed by collapse sometime after 30,000 years ago (Bar-Yosef et al. 1996 [157419], p. 298). However, even this collapsed section must have stood open for more than 20,000 years, because this section was the entrance from before 50,000 until 30,000 years ago.

3.3 ANTHROPOGENIC OPENINGS

Anthropogenic, or man-made, underground openings do not provide as long a history as the natural ones, but they may provide a closer analogy to a mined geologic repository. Here too, there are abundant examples that exhibit considerable stability for hundreds to thousands of years even with minimal engineering. The oldest examples are the Neolithic flint mines of northern Europe and England. These were mined into chalk deposits in 3,000 to 4,000 B.C. At one site in England, shafts that are 6 to 14 m deep access galleries that are 4 to 24 m in length and are still open today (Crawford 1979 [157420], pp. 8–32).

Around 1,500 B.C., Egyptians began excavating tombs on the west bank of the Nile River, across from Luxor. Over 100 tombs were excavated in bedded and jointed limestone (Figure 3-3). The tombs were generally a few meters in length and width and about 2 m in height. Many have pillars that were left for support in the larger rooms. Most of the tombs have incurred some water damage to plaster and paintings on the walls and ceilings, but none seems to have suffered collapse (Simmons 2002 [157578], SN-LBNL-SCI-108-V2, p. 7).

Mining of metallic ores has produced subterranean openings in a variety of rock types and often in intensely altered or fractured rock. Unfortunately, many of the oldest examples have been mined continuously or reopened in more modern times to mine remaining lower-grade ore. The Laurion mines, about 40 km south of Athens, Greece (Figure 3-4), were first mined about 2,000 to 1,500 B.C., but were mined most actively from 600 to 300 B.C. (Shepherd 1993 [157425], p.

75). These silver and lead mines are in a gently dipping sequence of mica schists and marble, with sulfides occurring along the contacts. Shafts 1.25–1.4 m by 1.5–1.9 m were sunk up to 111 m deep (Shepherd 1993 [157425], p. 17). Underground workings were 140 km in length; tunnels averaged 1 m in width and 1.75 m in height (Shepherd 1993 [157425], pp. 17–18). Ore zones were mined out by underhand stoping, which left large cavities a couple of meters high and a few meters in diameter. Pillars of inferior ore-grade rock supported these cavities. Removal of rock from these pillars was punishable by death (Shepherd 1993 [157425], p. 25).

Bronze-age mining of metal also occurred at the Great Orme Copper Mine in Wales. Charcoal recovered from the early workings dates at 1,000 to 2,000 B.C. In 1849, miners broke into a cavern nearly 40 m long, which contained stone hammers, most likely from the Bronze Age. The cavern, mined into limestone, had stood open for nearly 4,000 years (Llandudno Museum 1998 [157526]).

Underground mining was common during the Roman Empire, and the size and state of preservation of the mines not destroyed by subsequent mining are fairly similar. Shepherd (1993 [157425]) and Davies (1935 [157421]) present locations and descriptions for most of these mines. In addition to mining for metals, the Romans created large tunnels to transport water. For instance, the aqueduct at Tresmines, Portugal, is 60 m wide, 80 m high and 480 m long; at Corta das Coras, the tunnel is 100 m wide, 100 m high, and 350 m long (Shepherd 1993 [157425], p. 17).

Buddhist monks carved temples into caves in the fractured Deccan basalts of west-central India, from approximately the second century B.C. until the tenth century A.D., with most excavated in the late fifth or early sixth century A.D. (Behl 1998 [156213], pp. 27, 39). There are 31 caves at Ajanta, India, carved along a 550 m long, horseshoe-shaped gorge of the Waghora River. Each temple originally had steps carved into the rock leading up to it, but only Cave #16 still has a vestige of steps. The monsoonal climate has destroyed the exterior stone structures exposed to the elements, but subterranean openings have been well preserved in spite of the climatic effects. Similar Buddhist caves, from the sixth through the tenth centuries A.D., are preserved at Ellora and from the ninth century A.D. (Jain caves) at Sittanavasal, India (Behl 1998 [156213], p. 39).

The cross-sectional dimensions of most of the temples at Ajanta are larger than those proposed for a mined geologic repository. For example, Cave #10 is 30.5 m × 12.2 m. Cave #2 has a verandah of 14.10 m × 2.36 m, a main hall of 14.73 m × 14.5 m, and a shrine of 4.27 m × 3.35 m. Cave #16 has a verandah of 19.8 m × 3.25 m and a main hall of 22.25 m on a side with a height of 4.6 m. In spite of these large sizes, there is no reported collapse. As in the case of the Egyptian tombs, most of the Ajanta paintings appear to have suffered some water damage and vandalism (Behl 1998 [156213], pp. 234–236).

During the second through eleventh centuries A.D., the Christians of Cappadocia, Turkey, excavated underground cities and churches. One of these cities, Derinkuyu, covered approximately 4 km^2 and had an estimated 15,000 to 20,000 inhabitants (Toprak et al. 1994 [157429], p. 54) during much of the first millennium A.D. As of 1994, eight levels of ancient habitation had been discovered. Access to the underground cities was by way of narrow passageways that could be closed by rolling a 1.5 m diameter millstone across the opening

(Figure 3-5). The excavated rooms were generally several meters across and more than 10 m long.

The geology of Cappadocia (Toprak et al. 1994 [157429], pp. 8–11) is similar to that of southern Nevada (Sawyer et al. 1994 [100075]). In both regions, the late Tertiary section is composed of a thick sequence of silicic volcanic rocks. At Yucca Mountain, the host rock for the potential repository is a densely welded, quartz latite ash-flow tuff that formed about 11.6 Ma, whereas the underground cities of Cappadocia are situated in a partially welded, rhyolite ash-flow tuff that formed about 4 to 9 Ma. The difference in welding at Yucca Mountain and the underground cities of Cappadocia results in markedly different fracture density and engineering properties. Fracture density, which is a major variable contributing to underground collapse, is much lower in the underground cities. Ground support, which would be carefully engineered at Yucca Mountain, was never used in the underground cities. Thus, the fact that there has been no collapse in the underground cities of Cappadocia during the past 1,500 to 1,800 years suggests that excavations in tuff should be stable for long periods of time if undisturbed. Stability of unsupported openings would be favored in tuffs of a low degree of welding and fracturing.

Churches were excavated into the tuff north of the underground cities at Goreme, in Cappadocia, during the ninth to thirteenth centuries A.D. (Toprak et al. 1994 [157429], p. 53). All but one of these show no evidence of collapse. The exception is a collapse of a cliff face that exposes part of the inside of one church. The interior portions of the church are still in excellent condition, and their painted walls and ceilings within are well preserved except for spallation and vandalism (Stuckless 2000 [151957], p. 22).

Some of the underground openings excavated into the tuffs of Cappadocia are still used as dwellings. There are at least two other places where underground excavations are still used as dwellings. In Tunisia, 20 to 40 km south of the city of Gabes, ten underground villages, some of which date back nine centuries, are excavated in limestone (Golany 1983 [157422], pp. 5–6). The limestone is composed of poorly indurated layers approximately 2 m thick, which are easily mined out, along with better indurated layers of similar thickness. Room sizes are typically 2 to 2.5 m on a side, with flat ceilings that may have a supporting column in the center. Similarly, in northern China, thick deposits of slightly indurated loess exist, which could be easily excavated. However, its internal structure is such that loess can form vertical cliffs as much as 30 m in height. The underground dwellings accommodate more than 10 million people, who farm the land above their houses (Golany 1983 [157422], p. 13).

Although all the examples given so far either lack ground support or utilize only unmined pillars, examples do exist of wooden ground support. Around the beginning of the second century A.D., the Roman Emperor Hadrian mandated the use of wooden supports in all mines (Shepherd 1993 [157425], p. 25). Shepherd (1993 [157425], p. 26) provides a discussion of some examples, but does not comment on the stability of openings that were shored up. Tombs in China provide a different kind of example. Sixteen emperors from the Ming Dynasty (1368 to 1644 A.D.) were buried in tombs excavated in rock near Beijing. The earliest of the tombs has 32 sandalwood pillars 1.17 m in diameter; all are still intact and sturdy (Golany 1989 [157423], pp. 21–22).

3.4 UNDERGROUND OPENINGS AFFECTED BY TEMPERATURE

The foregoing descriptions show that both natural and manmade underground openings maintain stability well in an undisturbed setting. In fact, many of the examples given, as well as several mines not discussed, have probably been subjected to significant seismic shaking. Further discussion of seismic effects on underground openings is provided in Section 14.

The stability of underground openings can also be affected by temperature. An example of thermal stresses causing rockfall around rock bolts in a heated area occurred at Linwood Mining Company's limestone excavations (Simmons 2002 [157578], SN-LBNL-SCI-108-V2, pp. 7, 8). Linwood has excavated limestone adjacent to the Mississippi River downstream from Moline, Illinois, since World War I for processing in a kiln. The mine started as a surface quarrying operation, but as excavation progressed, the mine was converted to an underground room and pillar operation. The elevation of the underground workings is lower than the Mississippi River.

The company started venting the kiln exhaust underground in 1971 as part of a solution for controlling dust emissions from the kiln (Simmons 2002 [157578], SN-LBNL-SCI-108-V2, pp. 7, 8). To do this, a 96-acre portion of the mine was nominally mined with 30 ft × 30 ft pillars 21 ft high. This portion was walled off from the active workings. Exhaust from the kiln is vented to these workings at 400°F (204°C), leaving the dust behind for later collection.

The mining company adds bolts and mesh when a karstic depression is encountered, but otherwise the mine is essentially unsupported. Perhaps for this reason, steel-bar rock bolts were placed near the entry of the exhaust. After some period of venting, the rock near the exhaust vent broke out, leaving the bolts that had been emplaced in the rock, with the bottom 5 feet or so of the bolts surrounded by air. It was suggested that the surrounding rock had probably fallen out because heat was transferred up the rock bolt faster than it was transferred through the rock, which resulted in a thermal stress that caused failure for a rock with an unconfined compressive strength of 18,000 psi (~125 MPa) (Simmons 2002 [157578], SN-LBNL-SCI-108-V2, pp. 7, 8).

3.5 SUMMARY

In Section 3, numerous examples are provided of the stability of natural and man-made underground openings for millennia or longer under undisturbed conditions. However, an inherent bias is reflected in the studies because of the difficulty of determining the relative percent of openings that remain versus those that have collapsed. It is more difficult to evaluate the cause of collapse of such openings, whether by human interference or natural causes. The ability of underground openings to remain open and stable under ambient conditions depends on a number of variables, including: (1) rock strength; (2) the size, shape, and orientation of the opening; (3) orientation, length, and frequency of fracturing; and (4) effectiveness of ground support. Radiometric dating of cave floor minerals at Carlsbad Caverns and Lechuguilla Cave indicates that natural openings larger than those proposed for repository drifts at Yucca Mountain have remained open for millions of years. Collapse of the roof of an opening tends to occur where the fracture density is high and the overburden is thin, as is the case with some lava tubes. Factors that contribute to the size of a block falling are fracture spacing, which in turn depends on rock type and texture, and the size and shape of the opening.

The oldest examples of stable man-made openings are Neolithic flint mines dating from 4,000 to 3,000 B.C. However, numerous Roman mines and some aqueducts remain intact that tended to have been constructed of a similar size and now exhibit the same state of preservation. These and other examples demonstrate that both natural and man-made underground openings can exist for thousands of years in a wide variety of geologic settings, even with minimal or no engineering.

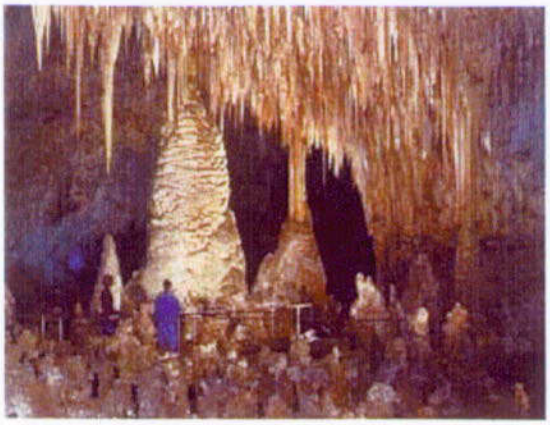

NOTE: Areas such as this have no obvious roof blocks on the floor of the cavern or holes in the ceiling from which blocks might have fallen.

Source: Simmons 2002 [157578], SN-LBNL-SCI-108-V2, p. 6.

Figure 3-1. Photograph of Fairyland in Carlsbad Caverns, New Mexico

(a)

(b)

Source: (a) Undara Experience 2001 [157515] and
(b) USGS 2000 [157517]).

Figure 3-2. Photographs of (a) Lava Tube in Undara, Australia, and (b) Nahuku Lava Tube in Hawaii

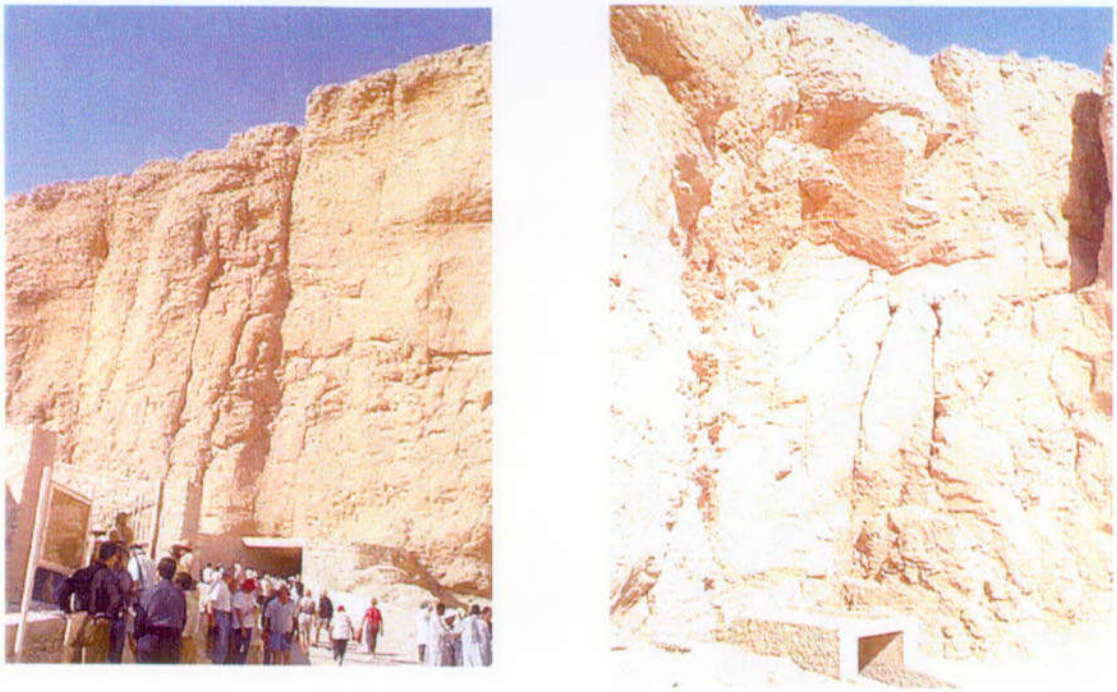

Source: Simmons 2002 [157578], SN-LBNL-SCI-108-V2, p. 6.

Figure 3-3. Photographs of the Nubian Limestone That Hosts the Tombs in the Valley of the Kings, Egypt

NOTE: The roof is formed by mica schist and the floor by marble. Ground support appears to be modern because older reports make no mention of either wood or cement.

Source: Gill 2001 [157516].

Figure 3-4. Mined Out Cavern in the Laurion Mines, Greece

NOTE: The millstone is about 1.5 m in diameter.

Source: Stuckless 2000 [151957], Figure 13.

Figure 3-5. Photograph of a Room in the Underground City of Kaymakli, Turkey

4. ANALOGUES TO WASTE FORM DEGRADATION

4.1 INTRODUCTION

Many variations of waste form types may be emplaced within a potential repository at Yucca Mountain. However, most of the waste will be spent fuel in the form of UO_2, with the remaining 10% or so being encapsulated in borosilicate glass resulting from vitrification of defense high-level nuclear waste. These waste forms are thermodynamically unstable under wet, oxidizing conditions (DOE 2001 [153849], 4.2.6.1). For this reason, quantification of the degradation modes and dissolution rates that determine the source term for performance assessment is extremely important.

Analogue studies may contribute to understanding long-term waste form degradation processes through the record left behind in secondary minerals and groundwater. Many of the published analogue studies of waste form degradation focus on dissolution of uranium under reducing groundwater conditions. This is because most of the geologic waste disposal configurations of other nations involve saturated, reducing conditions. Sketches of the most important and well-studied of these analogue sites were provided in Section 13 of the *Yucca Mountain Site Description* (CRWMS M&O 2000 [151945]). As a whole, the sites with reducing groundwater chemistry have limited applicability to conditions that would be expected to occur at a potential Yucca Mountain repository, which is located in an unsaturated oxidizing environment. However, in some instances, information from these analogue studies can still provide valuable insights into the processes of waste form degradation. Section 4 relies to the extent possible on information derived from oxidizing environments, but relevant information from examples in reducing environments is included to illustrate general principles of waste form dissolution and potential criticality.

Section 4.2 provides a conceptual basis for waste form degradation. Section 4.3 discusses analogues relevant to spent-fuel dissolution rates. Section 4.4 addresses the formation of secondary minerals that may immobilize uranium and fission products. Section 4.5 briefly covers radiolysis and Section 4.6 briefly covers nuclear criticality of the waste form. Section 4.7 summarizes studies of analogues to glass waste forms. Section 4.8 is a summary of the topics discussed.

4.2 WASTE FORM DEGRADATION—CONCEPTUAL BASIS

4.2.1 Overview of Conceptual Basis

Radionuclide release from the waste forms that would be emplaced at Yucca Mountain is a three-step process requiring: (1) degradation of the waste forms, (2) mobilization of the radionuclides from the degraded waste forms, and (3) transport of the radionuclides away from the waste forms (DOE 2001 [153849], 4.2.6.1). Water strongly influences all three processes.

As described in the S&ER (DOE 2001 [153849], 4.2.6.1) radionuclide release begins after breach of the waste package and the ingress of air. If the breach is early, the waste may still be

highly radioactive and physically hot. The thermal output of hot waste packages, particularly from commercial spent fuel, will limit groundwater access at early times. When water enters the package, the rate of water inflow and evaporation will determine when and if water accumulates. During this period, gamma radiolysis (radiation-induced decomposition) of the humid air within the package may cause production of nitric acid, which could condense into any accumulated water. If the breach is late, radiation levels and heat will be much lower, and evaporation and radiolytic acid production will be less important. During either period, water may enter the package either as water vapor or as liquid. The dissolved constituents in the groundwater entering the package may have a significant effect on in-package chemistry only if evaporation has concentrated them by orders of magnitude. This is unlikely to occur unless the waste package is breached only at the top and large amounts of water enter and evaporate within the package. During the latter period, there is no water transport of groundwater species or radionuclides out of the package.

If the package overflows, or if holes in the bottom allow flow-through, fresh water will dilute the groundwater components, and water-based radionuclide releases may begin. The release of radionuclides does not begin until after the breach of the cladding (for spent fuel). Chemistry within the package is important because it influences the rate of degradation of the package and waste forms (including cladding), and it determines the mobility of radionuclides as dissolved or colloidal species. Films of stagnant, concentrated, acidified groundwater are considered the worst possible scenario for degradation, because they do not inhibit oxygen and carbon dioxide transport and may support localized corrosion of the cladding and waste. Such films, however, do not support significant mobilization and transport of radionuclides and are only possible at times when there is an exact balance of water inflow and evaporation.

As stated previously, most of the many waste form types that may be emplaced within a repository are thermodynamically unstable under wet, oxidizing conditions (DOE 2001 [153849], 4.2.6.1). Uranium dioxide fuels will oxidize and hydrate, and glass waste forms will react with water to form clays, zeolites, and oxides. The rate of these reactions, however, will in most cases be quite slow and may be limited by the rate that reactants such as oxygen and water can be transported to the waste form surface. Although a few radionuclides such as cesium and iodine may concentrate between the fuel and cladding during reactor operation, most of the radionuclides will be incorporated within the various waste forms and cannot be released from the waste package until the waste forms degrade.

Once the waste forms degrade, radionuclides as dissolved species and suspended particles may be mobilized by advection or diffusion. Larger particles settle out of solution, or are filtered out by trapping in small openings. Only after gross failure of the package will these larger particles fall or wash out of the package. Particles in the colloid size range, however, can remain suspended and may travel significant distances. The concentration of radionuclides associated with colloids is limited by the colloid concentration and radionuclide carrying capacity of the colloids (DOE 2001 [153849], Section 4.2.6.1). The concentration of dissolved species is limited by the elemental solubility of the radionuclide within the local environment.

4.2.2 Spent Fuel Dissolution in an Oxidizing Environment

Many laboratory studies attempt to measure parameters that can be used to determine the rate of spent fuel dissolution under repository disposal conditions. These studies use either spent fuel itself, uranium dioxide (as an analogue for spent fuel), or uraninite as a natural analogue. Although the uraninite structure can accommodate some degree of oxidation, in highly oxidizing aqueous environments uraninite is unstable and decomposes (Finch and Ewing 1992 [113030], p. 133). Secondary uranyl (U^{+6})-bearing phases precipitate on the surface of the corroding uraninite, and a rind of corrosion products forms. The impurities often contained in uraninite affect its thermodynamic properties, the rate of uraninite alteration, and the composition of the corrosion products (Finch and Ewing 1991 [105591], p. 392). Studies that have examined the dissolution of uraninites under oxidizing conditions found that the dissolution rate was diminished by the presence of thorium, lead, and rare-earth-element impurities in the uraninite (Finch and Ewing 1992 [113030], p. 133). Compared to uraninite, spent fuel has a lower content of these impurities (Finch and Ewing 1992 [127908], p. 466) and on this basis might be considered to dissolve more rapidly.

Most of the uranium released to solution during the dissolution of UO_2 combines with ions in water to form secondary alteration phases. Both natural and experimental uranium systems display a paragenetic sequence of mineral phase formation that is characterized by the following general trend (Stout and Leider 1997 [100419], Section 2.1.3.5):

> UO_2 $\Rightarrow$ uranyl oxide hydrates $\Rightarrow$ alkali and alkaline-earth uranyl oxide hydrates $\Rightarrow$ uranyl silicates $\Rightarrow$ alkali- and alkaline earth uranyl silicates + palygorskite clay.

Specifically, mineralization in the experimentally determined paragenetic sequence of alteration phases is:

> UO_2 $\Rightarrow$ dehydrated schoepite ($UO_3 \cdot 2H_2O$) $\Rightarrow$ compreignacite $K_2(UO_2)_6O_4(OH)_6 \cdot 8H_2O$ + becquerelite ($Ca(UO_2)_6O_4(OH)_6 \cdot 8H_2O$) $\Rightarrow$ soddyite ($(UO_2)_2SiO_4 \cdot 2H_2O$) $\Rightarrow$ boltwoodite ($K(H_3O)(UO_2)\ SiO_4$) + uranophane ($Ca(UO_2)_2Si_2O_7 \cdot 6H_2O$) + palygorskite clay (Wronkiewicz et al. 1996 [102047], p. 94).

Thus, the uranyl oxide hydrates are common initial corrosion products of uraninite during weathering. In the presence of dissolved silica, these early phases alter to uranyl silicates, most commonly soddyite and uranophane. The phases that form depend on the chemical composition of the waters with which the uraninite is in contact, which in turn depends on the mineralogy of the surrounding host rocks and the oxidation potential of the hydrologic environment. The experimentally determined mineral sequence appears to be controlled by precipitation kinetics and is nearly identical to secondary uranium phases observed during the weathering of naturally occurring uraninite under oxidizing conditions, such as that which occurs at the Nopal I uranium deposit, Peña Blanca, Mexico (Wronkiewicz et al. 1996 [102047], Figure 7). In laboratory UO_2 tests and in the natural uranium deposits at Nopal I, the alkali- and alkaline-earth uranyl silicates represent the long-term solubility-limiting phases for uranium (Stout and Leider 1997 [100419], Section 2.1.3.5). Furthermore, at Nopal I, uranium concentrations in groundwater and seepage waters ranged from 170 parts per trillion (ppt) to 6 parts per billion (ppb) (Pickett and Murphy 1999 [110009], Table 2). The upper part of this range is similar to concentrations seen in filtered

samples from spent fuel dissolution experiments (Stout and Leider 1997 [100419], p. 2.1.3.5-4). This added similarity increases confidence that the experiments and the natural analogue reactions may simulate the long-term reaction progress of spent UO_2 fuel following potential disposal at Yucca Mountain.

Uraninite usually contains radiogenic lead that has in-grown through time (Finch and Ewing 1992 [127908], p. 466). As a result, the early-formed Pb-poor uranyl oxide hydrates alter incongruently to uranyl silicates plus radiogenic-Pb-enriched uranyl oxide hydrates, such as curite ($Pb_2U_5O_{17} \cdot 4H_2O$), that may serve to limit the mobility of uranium in nature (Finch and Ewing 1992 [127908], p. 466). Curite may also play an important role in the formation of uranyl phosphates, which are significantly less soluble than the uranyl silicates and control uranium solubility in many groundwaters associated with altered uranium ore (Finch and Ewing 1992 [127908], p. 465). In the absence of lead, schoepite and becquerelite are the common initial corrosion products. The reaction path for the alteration of lead-free uraninite results in the formation of uranyl silicates. Thus, the long-term oxidation behavior for ancient, lead-bearing uraninite is different from that of young, lead-free uraninite, which is more similar to spent fuel. Because the presence of lead effectively reduces the mobility of uranium in oxidizing waters, the concentration of uranium in groundwaters associated with oxidized uranium ore deposits will depend in part on the age of the primary uraninite (Finch and Ewing 1992 [113030], p. 133).

In summary, the paragenesis of uraninite alteration phases depends on the age of the primary uraninite, the mineralogy of surrounding host rocks, and on groundwater composition, pH, and redox potential. In a general oversimplification, the progression of phases of uraninite alteration, in the absence of radiogenic lead in-growth, will be to uranyl silicates, culminating in uranophane in an oxidizing environment. Numerous compositional variations are caused by trace elements present in the system. The composition of schoepite is often used to represent an alteration product in models of spent fuel alteration, but this is an oversimplification, based on observations in nature. As shown by Finch and Ewing (1992 [113030], p. 144), the formation of intermediate-phase schoepite may be favored early during the corrosion of uraninite. Schoepite is not, however, a long-term solubility-limiting phase for oxidized uranium in natural groundwaters containing dissolved silica or carbonate (e.g., the type of groundwaters at Yucca Mountain).

Despite the analogy between uraninite and spent fuel, there are important differences between the two. For one thing, spent fuel is artificially enriched in ^{235}U and contains nuclear fission products that are not present in uraninite; in contrast, uraninite contains a higher proportion of nonradiogenic trace element impurities. Also, the thermal history of spent fuel, unlike that of natural uraninite, may cause lattice and structural crystallization defects in the spent fuel that are not present in the uraninite. In addition, geologically old uraninite contains in-grown radiogenic lead, which would not be found in younger uraninite or in spent fuel. Section 4.3 presents the general dissolution path of uraninite, and by analogy spent fuel, under oxidizing conditions.

4.3 ANALOGUE STUDIES RELATED TO WASTE FORM DISSOLUTION RATES

The remaining issues of most relevance to the behavior of spent fuel in a repository that could be addressed by natural analogues are dissolution and radionuclide release (Section 4.3),

radionuclide retardation by secondary alteration products (Section 4.4), radiolysis (Section 4.5), and criticality (Section 4.6).

4.3.1 Fission-Product Tracer Method

Rates of UO_2 dissolution can be quantified by measuring the amount of fission product released from the uraninite and using this as a tracer. Concentrations of this tracer in the rock or in the groundwater in the vicinity of the uraninite are proportional to the dissolution rate, assuming that the tracer is released from the uraninite only by dissolution (Curtis 1996 [157497]; Curtis et al. 1994 [105270]; 1999 [110987]). The tracers used for this method are ^{99}Tc in rock, or its stable daughter ^{99}Ru, when technetium has decayed to insignificant amounts, and ^{129}I in groundwater. There are several uncertainties in the modeling and assumptions made in this approach, but some consistency is apparent in the results obtained from different uranium orebodies when using the same isotopic system. For example, using the ^{99}Tc tracer at Oklo, Gabon, and at Cigar Lake, Canada, provided average release rates of 1.5×10^{-6} per year and 1.1×10^{-6} per year, respectively (Curtis 1996 [157497], p. 145). However, different rates are obtained when using ^{129}I as a tracer. Applying this tracer at Cigar Lake provided release rates of between 9×10^{-9} and 3×10^{-10} per year, which are 2 to 4 orders of magnitude less than the values obtained using the ^{99}Tc tracer.

Curtis et al. (1994 [105270]) used measurements of ^{99}Tc, ^{129}I, ^{239}Pu, and U concentrations in rock from uranium deposits at Cigar Lake and Koongarra to estimate radionuclide release rates from uranium minerals. At Koongarra, Australia, release rates appear to have been faster (10^{-7} per year; Curtis et al. 1994 [105270], p. 2234) than at Cigar Lake, where model-dependent release constants from the uraninite bearing rocks were $<5 \times 10^{-8}$ per year (Curtis et al. 1994 [105270], p. 2234), producing small deficiencies of ^{99}Tc, and larger ones of ^{129}I. The inferred differences in radionuclide release rates are consistent with expected differences in uranium mineral degradation rates produced by the differing hydrogeochemical environments at the two sites. In the Cigar Lake ore zone, low uraninite solubility in a reducing environment and small water flux through impermeable rock would inhibit the rate of uraninite degradation and thus the rate of radionuclide release. At Koongarra, higher mineral solubilities induced by higher oxidation potentials, higher aqueous concentrations of carbonate and phosphate, and greater water fluxes would be expected to produce higher rates of uranium mineral degradation. Curtis et al. (1999 [110987], p. 284) note that the consistency of $^{239}Pu/U$ and $^{99}Tc/U$ ratios in bulk rock suggests that the redistribution processes observed at Cigar Lake are highly localized and do not result in large-scale losses or gains of these nuclear products from the deposit as a whole. The fission product tracer method could be applied to water samples collected at Peña Blanca (Section 10.4). While this method clearly has potential for quantifying UO_2 dissolution under natural conditions, the method has yet to be refined and differences between results for the two tracers explained. Besides this fission product tracer method, there is no other technique for quantifying directly long-term uraninite dissolution rates in natural analogue studies.

4.3.2 Dissolution of Oklo Uraninite

Application of the fission-product tracer method has not been reported for Oklo, but Oklo provides a unique record of uranium and fission-product retention. Because parts of the Oklo orebody achieved nuclear criticality as a result of highly enriched concentrations of ^{235}U, Oklo

uraninite contains significant quantities of fission products or their stable daughters, directly equivalent to those present in spent fuel. In this regard, Oklo is unlike any other known uranium deposit. A photograph of one of the reactor zones is shown in Figure 4-1.

There are, however, some differences between Oklo uraninite and spent fuel. For one thing, Oklo contains lower concentrations of fission products than does spent fuel. Also the temperature of reaction (400° to 600°C; for a discussion of temperatures, see Zetterström 2000 ([157501], p. 13) and power density were somewhat lower than in a reactor, and the duration of criticality at Oklo (on the order of 0.1 to 0.8 Ma; Louvat and Davies 1998 [125914], p. 140) was much longer than the lifetime of reactor fuel. Recognizing these differences, several large-scale analogue investigations have taken place at Oklo, and much relevant information has been obtained, including semiquantitative information on the fate of radionuclides contained in the orebody.

These analogue investigations (e.g., Louvat and Davies 1998 [125914]; Gauthier-Lafaye et al. 2000 [157499]) have revealed that when the Oklo reactor zones were cooling after periods of criticality, some dissolution of the uraninite and elemental remobilization occurred. However, the limited extent of this remobilization is indicated by the the fact that more than 90% of the uranium "fuel" has remained in the same spatial configuration since criticality (Miller et al. 2000 [156684], p. 81). This implies that uranium has been almost fully retained within the uraninite minerals. The disposition of some performance assessment-relevant elements and other elements in the reactor zones at Oklo is provided in Table 4-1. The transuranic elements neptunium, plutonium, and americium were all formed *in situ* within the uraninite during criticality, and their stable daughters have also been retained due to their compatibility with the crystal chemical structure of their host or in inclusions in the uraninite. Other radiogenic elements, which were less compatible with the uraninite host (e.g., Cs, Rb, Sr, Ba) have been partially or totally lost by diffusion from the uraninite. Some elements (e.g., Tc, Ru, Rh, Pd), however, migrated only short distances and were totally retained within the clay matrix enclosing the reactors. Data for other elements indicate clear deficiencies in the noble gases, halides, and lead (possibly resulting from volatilization) and suggest that some minor loss from the system has occurred for other elements.

Because the reactions ended nearly two billion years ago, the short-lived radionuclides have decayed to more stable daughter nuclides. Analysis of the behavior of these short-lived radionuclides is problematic. According to Brookins (1978 [133930], p. 309), Pu, Np, and Am were likely retained within the reactor, while Bi and Pb would have been redistributed locally without substantial migration (Brookins 1978 [133930], p. 309). Most geochemical observations at Oklo support these predictions to varying degrees. Curtis et al. (1989 [100438], p. 57) conclude that the retention of fission products is related to their partitioning into uraninite or secondary mineral assemblages. Those fission products that partitioned into the secondary mineral assemblages were largely lost over time, pointing to the importance of small uraninite grains in controlling the chemical microenvironment.

It is important to note that most of the observed uraninite alteration at Oklo occurred under hydrothermal conditions. Little uraninite-groundwater interaction has taken place at present-day ambient temperatures, except at the shallow Bangombé reactor zone (Smellie et al. 1993 [126645], p. 144). In summary, the Oklo natural analogue investigations indicate that the kinetics of UO_2 dissolution, either as uraninite or spent fuel, are exceedingly low under reducing conditions expected in the near field of some repositories. While dissolution rates cannot be

quantified readily from natural analogue data, the abundance of naturally occurring uraninite that is nearly 2 billion years old at Oklo indicates its stability in the natural environment.

4.4 ANALOGUE STUDIES RELATED TO IMMOBILIZATION BY SECONDARY MINERALS

Laboratory experiments have shown that UO_2 dissolution is accompanied by the formation of secondary phases on the fuel surface and that these corrosion products can passivate further dissolution (Wronkiewicz et al. 1996 [102047], p. 79). At the temperature and time scales of laboratory experiments, these phases are amorphous. However, natural sites where uraninite accumulations occur and where dissolution has taken place over long time periods could provide insights into the structure and mineralogy of the secondary passivating phases, and indicate whether they have been able to prevent further mobilization of radionuclides.

4.4.1 Shinkolobwe, Zaire

The 1,800 Ma Shinkolobwe uranium orebody in Zaire (at the time of study) was the subject of a comprehensive investigation regarding the corrosion products of uraninite (Finch and Ewing 1991 [105591]). The Shinkolobwe deposit weathers under oxidizing conditions in a monsoonal-type environment where rainfall is above 1 m per year, thus providing more aggressive hydrochemical conditions than might be expected at a repository. At Shinkolobwe, the uraninite is coarsely crystalline and lacks many of the impurities, such as thorium and rare earth elements, found in other uranium deposits. This lack of impurities led Finch and Ewing (1991 [105591], p. 391) to suggest that the thermodynamic stability of the Shinkolobwe uraninite might closely approximate spent fuel.

The deposit has been exposed at the surface since the Tertiary (< 60 million years), and extensive weathering has altered or replaced much of the original uraninite. Uranium (VI) mineralization occurs along fracture zones where meteoric waters have penetrated up to 80 m deep or more. Uraninite crystals at Shinkolobwe are commonly surrounded by dense rinds of alteration minerals, mostly uranyl oxyhydroxides, as well as uranyl silicates and rutherfordine, a uranyl carbonate (UO_2CO_3). Uranyl phosphates are also common within fractures throughout the host rocks, but are rare or absent from corrosion rinds.

Uranyl minerals comprising the corrosion rinds that surround many uraninite crystals undergo continuous alteration. This alteration occurs through repeated interaction with carbonate- and Si-bearing groundwater combined with periodic dehydration of (especially) schoepite and metaschoepite (Finch and Ewing 1991 [105591], p. 396). Such alteration occurs along small (approx. 0.1 to 1 mm) veins within the corrosion rinds. There is a general decrease in grain size as alteration proceeds, most commonly along veins. Schoepite, however, is not observed to re-precipitate where in contact with dehydrated schoepite (Finch and Ewing 1991 [105591], p. 396). Thus, while the formation of schoepite early during the corrosion of uraninite may be favored, schoepite is not a long-term solubility-limiting phase for oxidized uranium in natural groundwaters containing dissolved silica or carbonate (e.g., the type of groundwaters at Yucca Mountain).

Over 50 secondary uranyl phases were identified from the alteration of the uraninite. It was concluded that uraninite transforms to Pb-U oxide hydrates and then to uranyl silicates if sufficient silica is present in the system. Alteration of Proterozoic (~2400 to 700 Ma) uranium deposits such as Shinkolobwe introduce the important Pb-bearing phases, such as curite, which play a role in development of other stable phases in the system. Because of the very young age of repository spent fuel, radiogenic lead would not be present at Yucca Mountain for helping to immobilize spent-fuel elements.

4.4.2 Secondary Phases of Uranium Found at Nopal I, Peña Blanca

See Section 10.4 for a description of the Nopal I site. At Nopal I, uraninite occurs in rhyolite tuff in a semi-arid environment, where it has been exposed to oxidizing groundwater conditions with nearly neutral pH. Uranium was initially deposited as uraninite at Nopal I approximately 8 Ma (Pearcy et al 1994 [100486], p. 729). Geologic, petrographic, and geochemical analyses indicate that primary uraninite at Nopal I has been almost entirely altered to hydrated oxides and silicates containing uranium in the oxidized (uranyl) form. Because of its young geologic age, the deposit is low in radiogenic lead. The sequence of formation of uranyl minerals by alteration of uraninite at Nopal I is shown in Figure 4-2 and is similar in many geologically young uranium deposits located in oxidizing environments.

Leslie et al. (1993 [101714]) and Pearcy et al. (1994 [100486]) compared the alteration of uraninite at Nopal I to laboratory experiments of degradation of spent nuclear fuel potentially to be disposed of at Yucca Mountain, Nevada. They found that uraninite from the Nopal I deposit should be a good natural analogue to spent nuclear fuel because long-term experiments on spent fuel show alteration parageneses, intergrowths, and morphologies that are very similar to those observed at Nopal I (Wronkiewicz et al. 1996 [102047]). Oxidation of the uraninite at Nopal I has produced an ordered suite of minerals, first forming schoepite, a uranyl oxyhydroxide, followed by hydrated uranyl silicates, such as soddyite (Figure 4-2). Consistent with a high calcium abundance in Nopal I groundwater, the dominant secondary uranium phase is uranophane, a hydrated calcium uranyl silicate. Because of the abundance of calcite at Yucca Mountain, uranophane would be a potential secondary phase there as well. In comparison, laboratory experiments find that the general trend is to form mixed uranium oxides, followed by uranyl oxhydroxides, and finally uranium silicates, mostly uranophane with lesser amounts of soddyite (Wronkiewicz et al. 1996 [102047], p. 92). In addition, uraninite at Nopal I has a low trace-element component (average of 3 wt%) that compares well with that of spent nuclear fuel (typically < 5 wt% (Pearcy et al. 1994 [100486], p. 730)). The young age of the Nopal I deposit is another similarity to Yucca Mountain with respect to the absence of Pb-bearing secondary phases.

4.4.3 Secondary Phases at Okélobondo

In the first detailed study of the Okélobondo natural fission reactor in Gabon, which corresponds to the southern extension of the Oklo deposit (Figure 4-3), Jensen and Ewing (2001 [157500]) presented a history of uraninite alteration at that site showing complex mineralogical and textural relationships. The Okélobondo reactor is the deepest of the 16 natural reactors (Figure 4-3). It is situated at the base of a 2.5 m deep synform in the FA sandstone of the Francevillian Series. The Okélobondo reactor zone (RZOKE) developed at the interface between overlying brecciated

high-grade uranium-mineralized FA sandstone and underlying bitumen-rich black shale of the FB Formation. RZOKE is relatively small (2.7 m wide and > 4 m long) and contains a ~ 55 cm thick reactor core (Jensen and Ewing 2001 [157500], p. 32).

Criticality in RZOKE was facilitated by fixation and reduction of oxidized uranium by liquid bitumen and precipitation of uraninite into a dense microfracture network in the FA sandstone. The brecciation of the host rock may have been increased by overpressure created by the accumulation of hydrocarbon gases during diagenetic maturation of oil introduced into the FA sandstone. Chemical analyses and model estimates suggest that the ore grade at criticality at RZOKE was on the order of 20 wt% uranium. Operation of the reactor caused extensive dissolution of the FA sandstone and hydrothermal alteration of the black shale of the FB Formation. The sandstone dissolution was the major process that led to formation of the 2.5 m deep reactor synform and the high uranium concentrations ($\leq$ 90 vol% uraninite) in the core of RZOKE (Jensen and Ewing 2001 [157500], p. 59).

The mineral assemblage of RZOKE is comparable to that reported in the other Oklo reactor zones, in that uraninite and Si-rich illite are the major phases in the reactor core, while chlorite and illite are the major phases in the so-called *argile de pile* (reactor clays forming a halo around the reactor zone). Galena (PbS) is also a major phase in the reactor zone. Minor coffinite ($USiO_4$) and (U,Zr) silicates were also observed in addition to several accessory phases: e.g., titanium oxides, La-bearing monazite, sulfides of Cu, Fe, Co, Ni, and Zn, and ruthenium arsenides. The minor and trace elements include Th, Zr, Al, P, Ce, and Nd that seldom exceed concentrations of 0.1 oxide wt% (Jensen and Ewing 2001 [157500], p. 59). Figure 4-4 shows galena, illite, and zircon embedded in a matrix of (U,Zr)-silicate in the center of the RZOKE reactor core.

The acccessory (U,Zr)-silicate, phosphates, and ruthenium arsenides ($\pm$ Pb, Co, Ni, and S) were of particular importance in secondary retardation of the fissiogenic isotopes (Jensen and Ewing 2001 [157500], p. 59). The (U,Zr)-silicate contains elevated concentrations of ZrO_2, ThO_2, Ce_2O_3, and Nd_2O_3 as compared with the "unaltered" uraninite. This result suggests that the fissiogenic ^{90}Sr, Zr, Ce, and Nd, as well as the Th precursors, were efficiently retarded by the (U,Zr)-silicate during their migration in the reactor zone. Lanthanide element fission products may also have been retained in rare La-bearing monazite observed in the *argile de pile* of RZOKE. Ruthenium arsenides incorporated fissiogenic Ru, probably including ^{99}Ru, the radiogenic daughter of ^{99}Tc.

The presence of lead-uranyl sulfate hydroxide hydrate, anglesite, partial dissolution of uraninite and galena, and the rapid oxidation of pyrite are evidence of a later shift toward oxidative alteration conditions in and around the reactor zone. Hence, the slightly oxidizing deep groundwaters at Okélobondo may have already reacted with the Okélobondo reactor zone.

4.5 RADIOLYSIS

Radiolysis is hydrolysis caused by radiation and results in production of charged species (hydrogen and hydroxide ions) that may react to form more mobile species. Radiolysis can affect both the waste form and the waste package. Because the waste canister is thinner than in previous designs (CRWMS M&O 1999 [107292], Table 5-4), it is not self-shielded, so radiation levels at the outside surface of the canister would be higher. However, it is not certain that

radiolysis will be a problem. The effects of radiolysis in the Oklo ore deposit were discussed by Curtis and Gancarz (1983 [124785]). They calculated the alpha- and beta-particle doses in the critical reaction zones during criticality and the energy provided to the fluid phase by these particles. This energy caused radiolysis of water and the production of reductants (H_2) and oxidants (O_2). The effect of these reductants and oxidants on the transport of radionuclides within and outside the reactors has been difficult to quantify. Iron is most reduced in the samples that show the greatest ^{235}U depletion. Curtis and Gancarz (1983 [124785], p. 36) suggested that the reduction of iron in the reactor zones and oxidation of U (IV) in uraninite was contemporaneous with the nuclear reactions and not a later supergene phenomenon of secondary enrichment. Curtis and Gancarz (1983 [124785], p. 36) suggested that radiolysis of water resulted in the reduction of Fe (III) in the reactor zones and the oxidation of uranium. Furthermore, the authors suggested that the oxidized uranium was transported out of the critical reaction zones and precipitated through reduction processes in the host rocks immediately outside the zones. The reduction processes likely involved organics or sulfides present in the host rocks. However, if the host rocks around the natural reactor cores had not contained species capable of reducing the oxidized uranium transported out of the cores, the uranium could have been transported much further from the critical reaction zones. The important point is that, even with intensive radiolysis, very little (only several percent) of the uranium in the natural reactors was mobilized (Naudet 1978 [126123], p. 590).

Jensen and Ewing (2001 [157500], p. 59) noted a migration of Ce from reactor core to rim at Okélobondo and suggested that this resulted from radiolysis taking place during reactor operation. Cerium, particularly, showed indication of redistribution in the reactor zone, when compared with Nd, in the uraninite rim. Because Ce^{3+} can be oxidized to Ce^{4+}, the difference in the behavior of Ce as compared with Nd, results from oxidative alteration. The different concentration of Ce in the uraninite rims, as compared with their cores across the reactor zone, was produced during reactor operation, perhaps as a result of radiolysis.

4.6 CRITICALITY

The uranium deposit at Oklo, which was the site of naturally occurring neutron-induced fission reactions over 2,000 Ma, was used as a basis for reviewing conditions and scenarios that might lead to nuclear criticality within and outside waste packages in the Swedish waste disposal configuration (Oversby 1996 [100485]). The Swedish concept involves disposal in deep granite with chemically reducing groundwaters, so the specific conditions are not relevant to those of oxidizing environments. Yet in either oxidizing or reducing conditions, the combination of simultaneous factors and probabilities required for criticality to occur seems very unlikely. For criticality to occur, sufficient ^{239}Pu and/or ^{235}U would need to accumulate together with enough water to allow for moderation of neutron energies. This would achieve a state where neutron-induced fission reactions could be sustained at a rate significantly above the natural rate of spontaneous fission. The chemical and physical conditions required to achieve nuclear criticality at Oklo were used by Oversby (1996 [100485]) to estimate the amounts of spent fuel uranium that would need to be assembled in a favorable geometry in order to produce a similar reactive situation in a geologic repository. The amounts of uranium that must be transported and redeposited to reach a critical configuration are extremely large in relation to those that could be transported under any reasonably achievable conditions, even under oxidizing conditions. In addition, transport and redeposition scenarios often require opposite chemical characteristics.

Oversby (1996 [100485], p. vii) concluded that the likelihood of achieving a critical condition caused by accumulation of a critical mass of uranium outside the canisters after disposal is nil, provided that space in the canisters is filled by low solubility materials that prevent entry of sufficient water to mobilize uranium. Criticality caused by plutonium outside the canister could be ruled out because it requires a series of processes, each of which has an increasingly small probability. Criticality caused by uranium outside the canister would require dissolution and transport of uranium under oxidizing conditions and deposition of uranium under reducing conditions. There is no credible mechanism to achieve both oxidizing and reducing conditions in the near-field repository host rock in the long term, after decay of the majority of alpha-active isotopes. Thus, the conditional probabilities required to achieve criticality caused by uranium make the likelihood that criticality would occur vanishingly low.

4.7 NUCLEAR WASTE GLASS ANALOGUES

Among the natural volcanic glasses, basalt glasses are compositionally the most similar to nuclear waste glasses (Lutze et al. 1987 [125923], p. 142). However, there are still substantial compositional differences. Basalt glass and nuclear waste glass are similar in silica content, alteration products, alteration layer morphologies, and alteration rates in laboratory experiments (Grambow et al. 1986 [119228]; Arai et al. 1989 [123814]; Cowan and Ewing 1989 [124396]). Basalt glass alteration has been studied in a number of environments including ocean-floor, subglacial, hydrothermal and surface conditions (Grambow et al. 1986 [119228]; Jercinovic et al. 1986 [125289]; Byers et al. 1987 [121857]; Jercinovic and Ewing 1987 [144605]; Arai et al 1989 [123814]; Cowan and Ewing 1989 [124396]). Inferred alteration rates, as calculated from alteration rinds, range from 0.001 μm (micrometers)/1,000 years to 30 μm/1,000 years (Arai et al. 1989 [123814], p. 73).

Malow and Ewing (1981 [126058]) compared the thermal and chemical stabilities of two borosilicate glasses and one glass ceramic to those of three rhyolitic glasses through a variety of laboratory tests and observations of natural weathering. They concluded that natural glasses are much more stable than waste-form glasses as a result of higher silica contents in the natural glasses (74% versus 28 to 50% in waste-form glasses). Tektites (nonvolcanic glass of extraterrestrial or impact origin) range in age from ~10^5 years to 35 Ma and rarely show signs of alteration, dehydration, or devitrification (Lutze et al. 1987 [125923], p. 148). Their great durability may be a result of their high silica and alumina (~30%) contents and their low (<4%) alkali contents (Lutze et al. 1987 [125923], p. 152).

The compositions of the glasses utilized in natural analogue studies differ somewhat from borosilicate glasses, and this makes a simple analogy dubious for quantitative purposes. High silica and alumina contents, along with low alkali contents and low water contents, are favorable for long-term preservation. The dissolution rates measured on natural glasses are variable, but always very slow. However, natural analogues cannot be used to provide a quantitative estimate for the time at which devitrification will begin, or the rate at which it will proceed in the repository environment. Natural glass studies do suggest that the rate of devitrification is too slow for the process to be significant in the repository. These studies have not, however, considered the effect of radiation. It might be possible to obtain relevant data on the radiation-induced effects on glass durability by examining glasses that contain uranium oxides as colorants, such as the "vaseline glass" produced in Germany and Bohemia in the 1800s (Miller et

al. 2000 [156684], pp. 75–76). In all cases, the differences in chemistry between borosilicate glass and natural and archeological glasses need to be considered when interpreting analogue data. The qualitative evidence from analogues on natural and archeological glasses has added to confidence that the glass degradation processes are well understood and has provided upper bounding limits to the degradation rates.

4.8 SUMMARY AND CONCLUSIONS

The analogue sites located in chemically oxidizing environments are better analogues to conditions expected to occur at Yucca Mountain than the more numerous sites located in reducing environments. However, some examples from reducing environments may be appropriate analogues for processes that would occur under repository conditions in either type of chemical environment. Hence, both types of conditions were considered in studying the processes relevant to waste form degradation. From the evidence presented in this section, the main points are the following:

- The uranium alteration paragenesis sequence at Peña Blanca is a good analogue to alteration of uranium oxide spent fuel. The reaction path of alteration of spent fuel at Yucca Mountain will be similar to that of geologically young, Pb-free uraninite, with schoepite and becquerelite forming as intermediate products followed by uranyl silicates.

- Measurement of the concentration of fission products as tracers in rock and groundwater surrounding uraninite provides a satisfactory approach to estimating natural dissolution rates. This approach was tested at Cigar Lake and Koongarra under reducing and oxidizing conditions, respectively, and the dissolution rate at Koongarra was found to be more rapid. Use of the fission-product tracer method has not been reported for Oklo, but other lines of evidence indicate that dissolution has been slight under reducing conditions at Oklo over the past approximately 2 billion years. Whether deep oxidizing waters at Okélobondo have increased the dissolution of uraninite as well as created an oxidized suite of minerals is something that could be tested.

- Secondary mineral formation was responsible for incorporating uranium at Shinkolobwe, where 50 secondary uranium-bearing phases could be identified. Because of the great age of the Shinkolobwe uranium deposit, radiogenic lead-bearing phases played a role in sequestering uranium. Lead would not play a role in secondary mineralization of younger deposits, nor would it be present in spent fuel at Yucca Mountain. Other secondary phases, particularly (U,Zr) silicates, formed stable phases at Okélobondo. Presumably radiogenic lead was also present at Okélobondo, because of its approximately 2-billion-year age.

- It is uncertain whether radiolysis will be a potential problem around waste packages in the current design scenario (in which waste packages are not self-shielded). Under radiolysis conditions occurring at the time of reactor criticality at Oklo, only several percent of uranium was estimated to have been mobilized for transport from its original site, under far more extreme conditions than those anticipated at Yucca Mountain. Likewise at Okélobondo, radiolysis effects at the time of reactor operation appear to have been confined to rare earth element migration from mineral core to rim. Because liquid water in

contact with spent fuel is required for radiolysis to occur, the problem seems unlikely under either higher- or lower-temperature operating modes for a potential repository at Yucca Mountain.

- Criticality of spent fuel can be triggered by changes in pH as well as by reducing conditions. In the study examined, however, criticality was viewed from the standpoint of redox conditions. Criticality of spent fuel, either within waste packages or by reconcentration of uranium outside of the package, has a very low likelihood, because the probability of certain processes required to achieve critical conditions occurring simultaneously or sequentially renders certain conditions mutually exclusive.

- Although natural glasses are somewhat different in composition from borosilicate nuclear waste glass, studies of natural glass alteration indicate that glass waste forms will be stable in a repository environment at Yucca Mountain. Higher stability is favored by higher silica and alumina content and by lower alkali and water content of the glass. Analogue studies have not considered radiation effects on glass over long time periods to confirm experimental results showing that radiation has little effect on glass waste stability.

NOTE: Vegetable matter in lower center is in foreground. Man standing in lower right-center for scale.

Source: Blanc 1996 [157498], p. III).

Figure 4-1. Photo of a Reactor Zone at the Oklo Natural Fission Reactor, Gabon

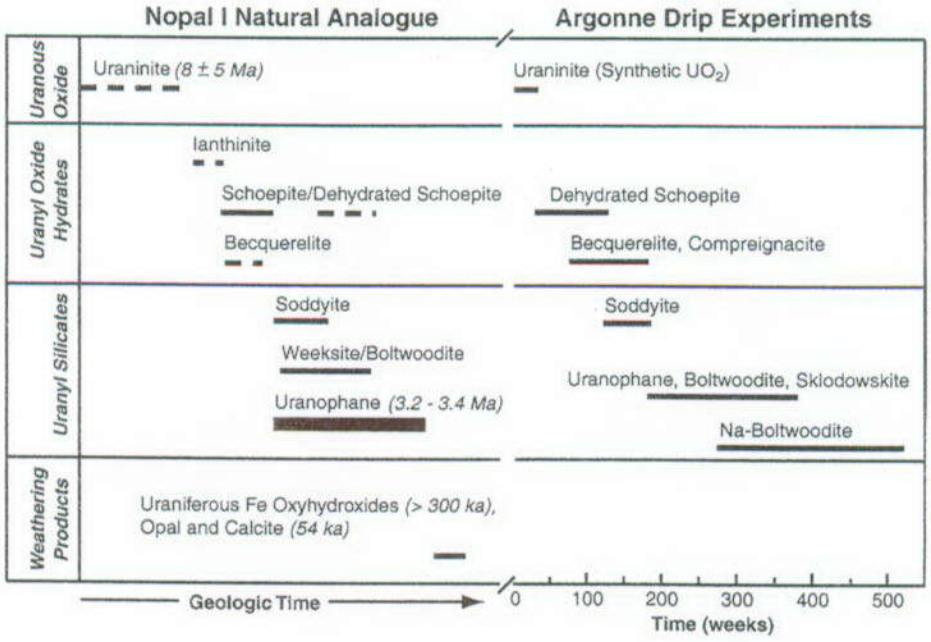

Source: Modified from Murphy 2000 [157487], Figure 1.

Figure 4-2. Sequence of Formation of Uranyl Minerals by Alteration of Uraninite

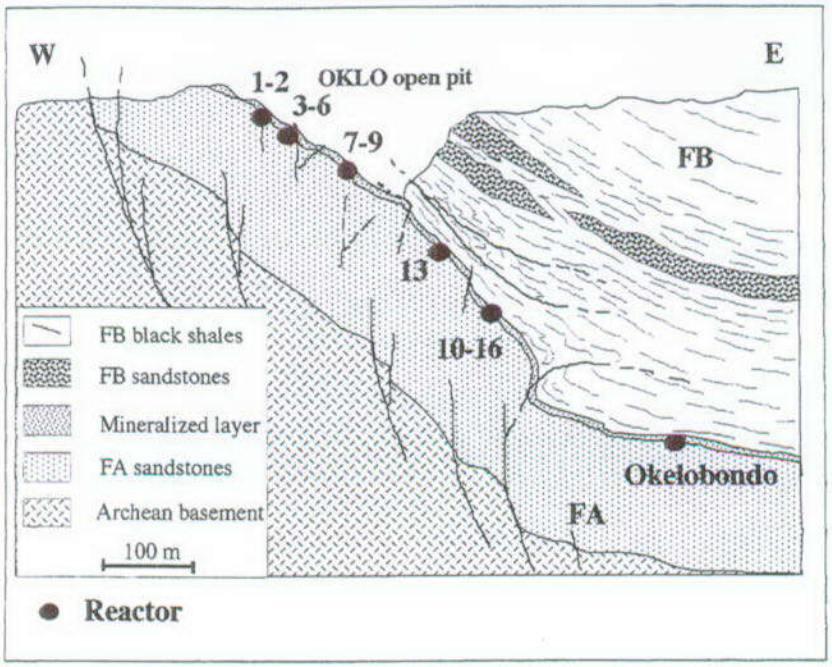

Source: Gauthier-Lafaye 1996 [157542], Figure 4.

Figure 4-3. Schematic Cross Section Showing Depth of Okélobondo Natural Fission Reactor in Relation to other Oklo Reactors

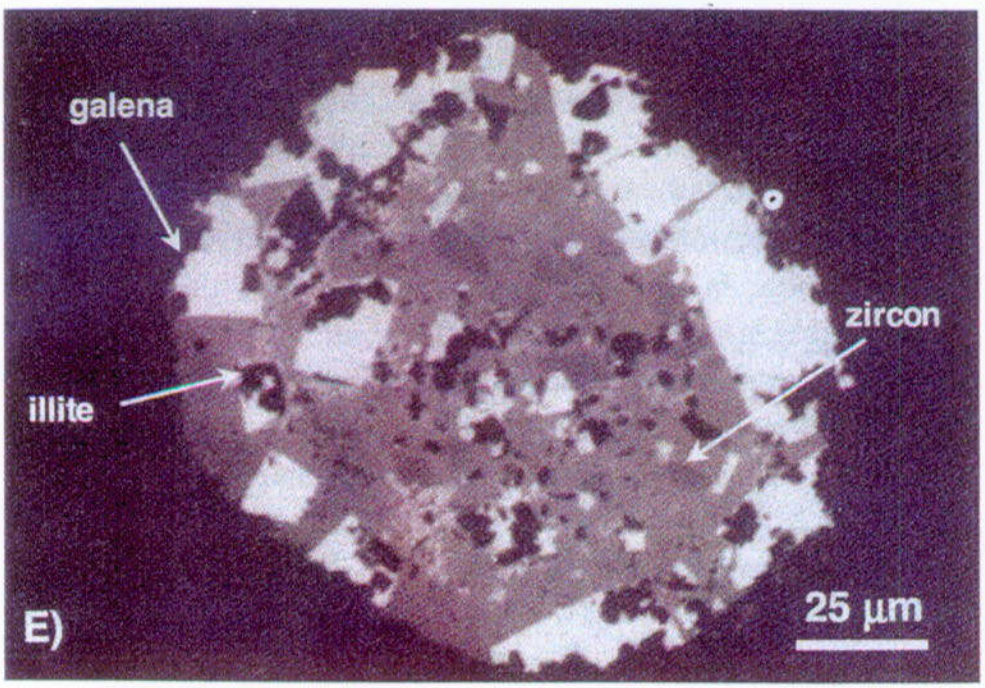

NOTE: The (U,Zr)-Silicate is the medium gray colored matrix mineral in which the other minerals are encased.

Source: Jensen and Ewing 2001 [157500], Figure 11e.

Figure 4-4. Aggregate of (U,Zr)-Silicate, Zircon, Galena, and Illite in the Center of the Okélobondo Reactor Core (RZOKE)

Table 4-1. Elemental Distribution within Uraninite, Inclusions, and Clays for Elements in the Reactor Zones at Oklo

Element	Uraninite	Inclusions	Clays	Migration
Cs				X
Rb				X
Sr				X
Ba				X
Mo		X		X
Tc		X	X	
Ru		X	X	?
Rh		X	X	?
Pd		X	X	?
Y	X		X	
Nb	?	?		
Zr	X	X	X	
Te		X		
REE	X		X	
Ce		X		
Pb	X	X		X
Bi		X		
Th	X		X	
U	X		X	
Np	?	X		
Pu	X		X	

NOTE: REE-rare earth elements

Source: Miller et al. 2000 [156684], Table 4.2 (summarized from Blanc 1996 [157498]).

5. CURRENT ENGINEERED BARRIER SYSTEM DESIGN

5.1 INTRODUCTION

Section 5 provides a context for Engineered Barrier System (EBS) analogues that are discussed in Sections 6 and 7. This section summarizes the key components of the EBS system and describes the materials proposed to be used in the construction of these components. Finally, the key processes that are expected to occur during the operational life span of the EBS are described.

5.2 EBS COMPONENTS

The EBS currently planned for the potential Yucca Mountain repository (Figure 5-1) consists of three main components: (1) drip shield, (2) emplacement drift invert, and (3) waste package (DOE 2001 [153849], Section 2.4). Because they will affect the performance of the EBS, materials included within the waste forms and used in the construction of the emplacement drifts also are considered in the evaluation of the EBS. The following summary of the components of the EBS system is based upon Sections 2.4 and 3 of the *Yucca Mountain Science and Engineering Report* (S&ER) (DOE 2001 [153849]).

5.2.1 Drip Shield

The drip shield is designed to serve as a protective barrier, for the length of emplacement drifts, that will divert water dripping from the drift walls, thus minimizing direct dripping onto the waste packages. The drip shield has the added function of protecting the waste package from rock falls from the drift perimeter. These functions require that the drip shield assembly is both highly resistant to corrosion and has the structural strength to withstand rock falls.

The drip shield consists of three separate elements: the drip shield, supporting structural members, and stands (or "feet") upon which the shield assembly rests (Figure 5-2). Current design plans call for the drip shield to be manufactured from 15 mm (0.6 in.) thick Titanium Grade 7 plates for long-term corrosion resistance. The structural members will be constructed using Titanium Grade 24, which has greater strength than Titanium Grade 7. Alloy 22 (see Table 5.2) will be used for the feet, preventing direct contact between the titanium structural members and the carbon steel beams of the invert.

5.2.2 Drift Invert

The drift invert is designed to form a stable, level platform along the base of the emplacement drift on which the waste package and drip-shield assemblies will be placed. The invert as currently planned (DOE 2001 [153849], Section 2.4.1) consists of two components: a steel invert structure and a crushed-tuff invert ballast.

The steel invert structure needs to provide sufficient support for all expected pre-closure activities for up to 300 years and must also keep the waste packages in a horizontal position for 10,000 years after closure. The steel structure consists of transverse and longitudinal support beams, which serve to transfer the weight of the waste package and drip shield (along with any

needed emplacement and maintenance equipment during the initial phases of operation) to the bedrock (Figure 5-3). Gantry rails, needed to transport the waste packages and drip shields into the tunnel, will be placed along the margins of the support beam structure. Guide beams will be used (if considered necessary to mitigate movement resulting from seismic events) to secure the waste package emplacement pallets and the drip shield assembly. The current design calls for the invert support and guide beams to be manufactured of ASTM A 572/A 572M steel, which was chosen to provide sufficient strength for the emplacement drift environment. The gantry rail will be made of ASTM A 759 carbon steel (DOE 2001 [153849], Section 2.4.1.1).

The invert ballast is designed so that moisture present in the emplacement drift will drain directly into the surrounding rock without flowing along the base of the drift. Crushed tuff, produced by crushing material obtained during the excavation of the emplacement drifts, would be used as the primary ballast material. The ballast will be placed around the steel invert beams, to a level just below the top of the support beams, so that the waste package pallets and drip shields rest on the support beams and not on the ballast. The ballast material will be compacted so that no significant settling will occur over time. The crushed tuff should not be affected by heating related to emplacement of the waste packages. Transport of radionuclides within the crushed tuff is expected to be dominated by diffusive transport, thus serving to retard any potential release of radionuclides into the surrounding host rocks (DOE 2001 [153849], Section 2.4.1.2).

5.2.3 Waste Package

The waste package assembly is designed to securely contain high-level radioactive wastes and serve as the primary element to the EBS. The waste package system consists of two main components: a waste package emplacement pallet and a sealed, corrosion-resistant waste package canister (Figure 5-4).

The waste package emplacement pallets are designed to support the waste package canisters in a horizontal position and facilitate line-loading of the waste packages. Current plans call for the pallets to be manufactured from plates of Alloy 22 (a material highly resistant to corrosion) with support tubes fabricated from Stainless Steel Type 316L (DOE 2001 [153849], Section 2.4.3.1). The V-shaped design will allow the pallets to be used for all waste package canisters.

A number of distinct waste package designs have been developed to accommodate the different waste forms generated from boiling water and pressurized water reactors, excess weapons material, high-level waste, and DOE and naval spent nuclear fuel (Figure 5-5). All of these waste package designs contain a number of important components that are needed to meet performance criteria. The performance criteria (DOE 2001 [153849], Section 3.4.1) are as follows:

- Strength
- Resistance to corrosion and microbial attack
- Predictable materials behavior
- Compatibility with waste package and waste form materials
- Ease of fabrication
- Proven performance record
- Favorable heat transfer properties
- Utility in shielding and preventing criticality.

Table 5-1 lists the major waste package components for commercial spent nuclear fuel waste packages, the composition of each component, and the component function(s).

The different materials chosen for the construction of the waste package system are based on the functional requirements for each component. Key properties include resistance to corrosion and cracking caused by thermal, mechanical, and chemical processes; preservation of the structural integrity of the waste package system; conduction of heat away from the waste forms; and the ability to prevent criticality from occurring. A brief description of each of the main types of materials incorporated in the current design (DOE 2001 [153849], Section 3) is given below.

5.2.3.1 Corrosion-Resistant and Structural Materials

Alloy 22 was selected for the outer barrier of the waste package because of its resistance to corrosion under conditions of high temperatures and low humidity and under all low-temperature conditions, its similar thermal expansion coefficient to stainless steel, and because it can be welded more easily than can titanium. The chemical composition of Alloy 22 is given in Table 5-2. Stainless Steel Type 316NG was chosen for the inner cylinder of the waste package because of its relative strength, compatibility with Alloy 22, and its affordability. The chemical composition of Stainless Steel Type 316NG is given in Table 5-3.

5.2.3.2 Other Waste Package Materials

A variety of other materials will be used in the fabrication of the waste package assembly (DOE 2001 [153849], Section 3.2.2.1). These include Neutronit A 978 (borated 316 stainless steel) or SA 516 Grade 70 carbon steel plates, boron carbide rods with Zircaloy cladding used for control of criticality within the waste package container, and aluminum shunts (SB-209 6061 T4) to assist in heat transport away from the waste form. The waste package will encompass the waste form materials described in Section 5.2.4.

5.2.4 Waste Form Components

The waste forms for disposal at the potential Yucca Mountain repository include spent fuel from commercial power reactors and that owned by the U.S. Department of Energy, solidified high-level radioactive waste, and plutonium waste from excess nuclear weapons. All waste must be in solid form and must not contain flammable or chemically reactive materials. The waste forms will contain fuel rods constructed out of Zircaloy and stainless steel as well as a variety of radioactive waste types, including uranium metal, uranium oxide, uranium dioxide, radioactive borosilicate glass, and plutonium encased in ceramic pellets (DOE 2001 [153849], Section 3). Analogues to waste form materials and their degradation are discussed in Section 4.

5.2.5 Emplacement Drifts

While the emplacement drifts are not considered a component of the engineered barrier system, the materials used in their construction could significantly affect the EBS performance. The emplacement drifts contain a variety of materials that are used to help maintain the integrity of the drift after excavation. The ground support system, designed to stabilize the emplacement drift, includes W6X20 rolled steel ring beams (steel sets), tie rods, welded wire fabric, rock bolts,

and cementitious grout used to secure the rock bolts in place (DOE 2001 [153849], Section 2.3.4.1.2.1). Analogues relevant to emplacement drift components are discussed in Section 7.

5.3 PROCESSES AFFECTING EBS PERFORMANCE

Numerous processes and event scenarios have been identified and considered in designing the EBS (DOE 2001 [153849], Sections 2.4 and 3.1). These can be grouped into four major categories: structural, thermal, chemical, and nuclear criticality. The structural events evaluated involve scenarios (such as mishandling of the packages, seismic events, or rock falls) that would result in the waste package being physically disturbed by an impact that could potentially result in breaching the sealed waste packages. Thermal processes include changes in physical and chemical properties associated with heating caused by radioactive decay of the waste forms, such as thermal expansion and cracking, as well as the effects of heat transfer properties. Chemical processes such as corrosion and chemical reaction of the different materials could also result in breaching of the sealed waste packages and subsequent release of radionuclides into the surrounding environment. Special attention has been placed on the design of the waste packages and composition of the waste forms to prevent the radioactive waste from achieving criticality. The selection of the different materials used in construction of the EBS components has been made to ensure the long-term structural, thermal, and chemical integrity of the waste packages and to prevent the waste forms from going critical.

While the properties of all of the materials selected for the EBS design have been extensively tested and determined in the laboratory, the long-term performance of these materials under the predicted temperature, humidity and chemical environment for the potential Yucca Mountain repository has not been experimentally confirmed. Natural analogues for similar materials found in the natural environment can be used to validate long-term performance models for the EBS. The following sections (6 and 7) provide descriptions of natural analogues for waste package materials and for processes that might take place within the EBS.

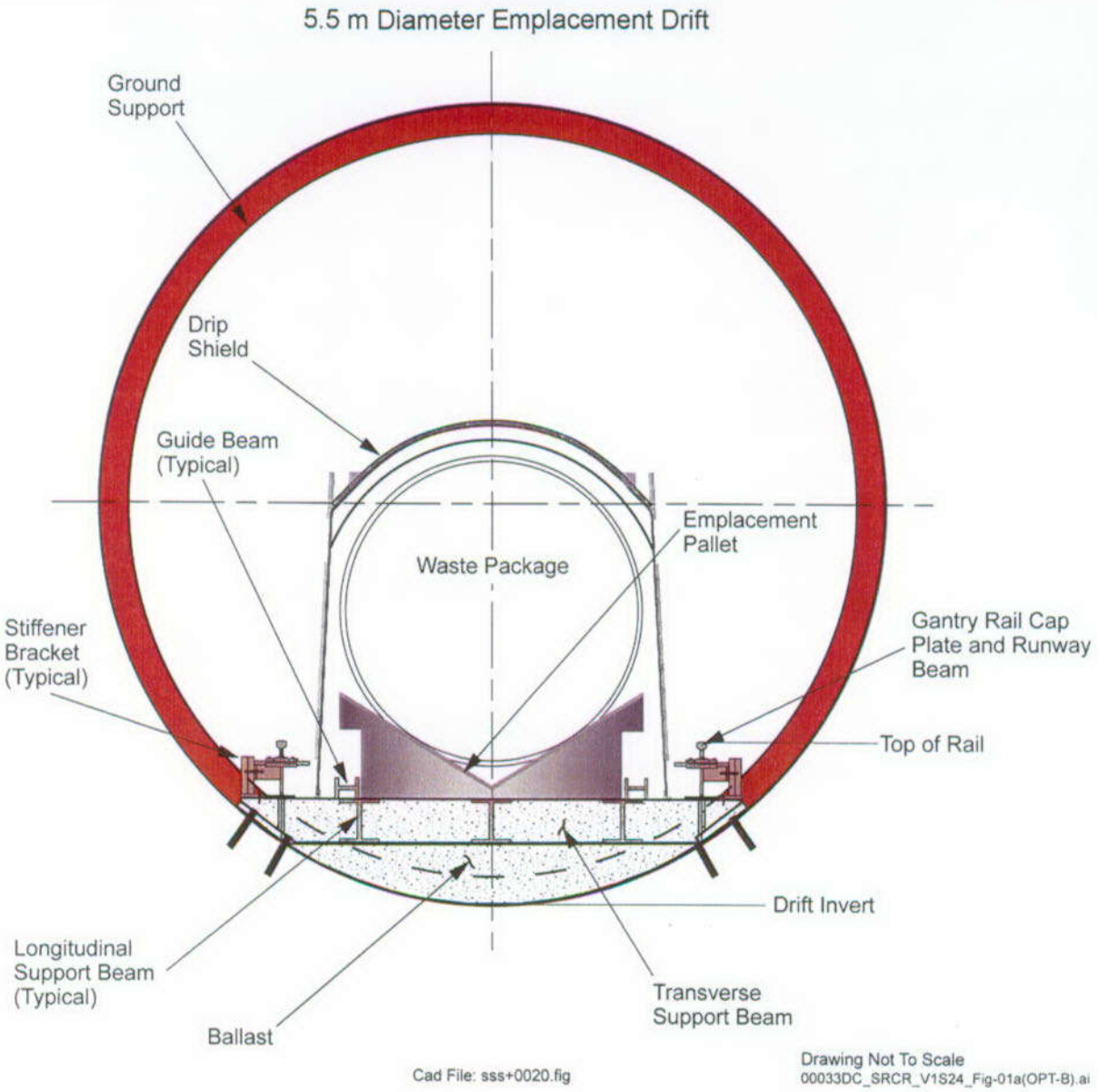

Source: DOE 2001 ([153849], Figure 2-71).

Figure 5-1. Cross Section of Emplacement Drift with EBS Components

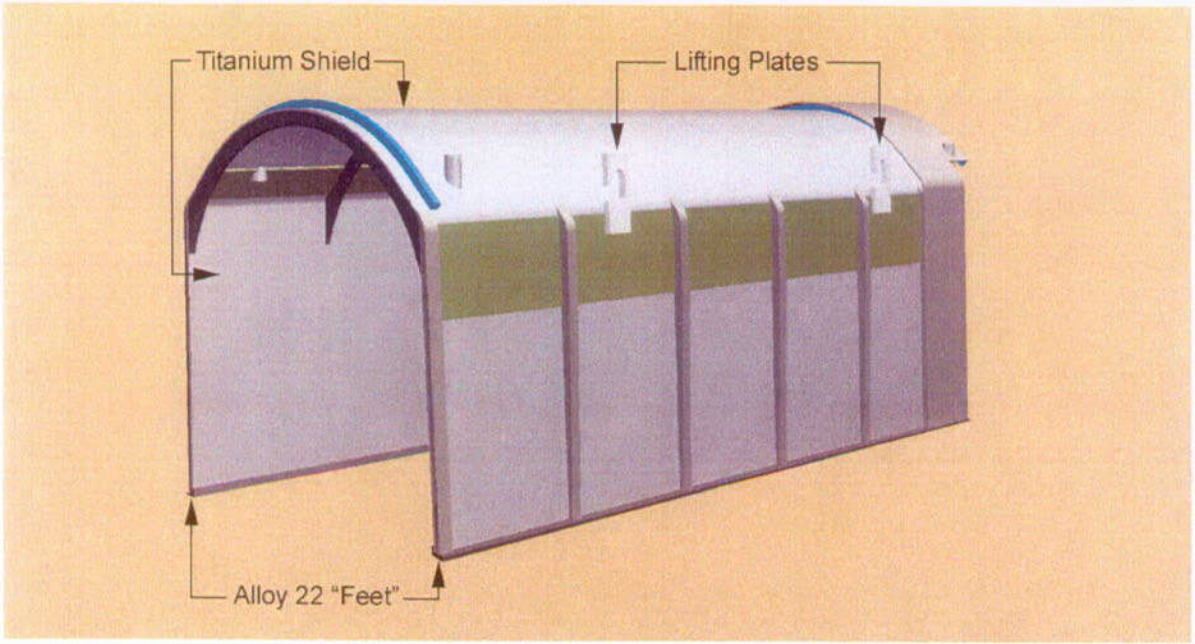

Source: DOE 2001 ([153849], Figure 2-73).

Figure 5-2. Schematic View of Drip Shield Assembly with Drip Shield, Support Members, and Feet

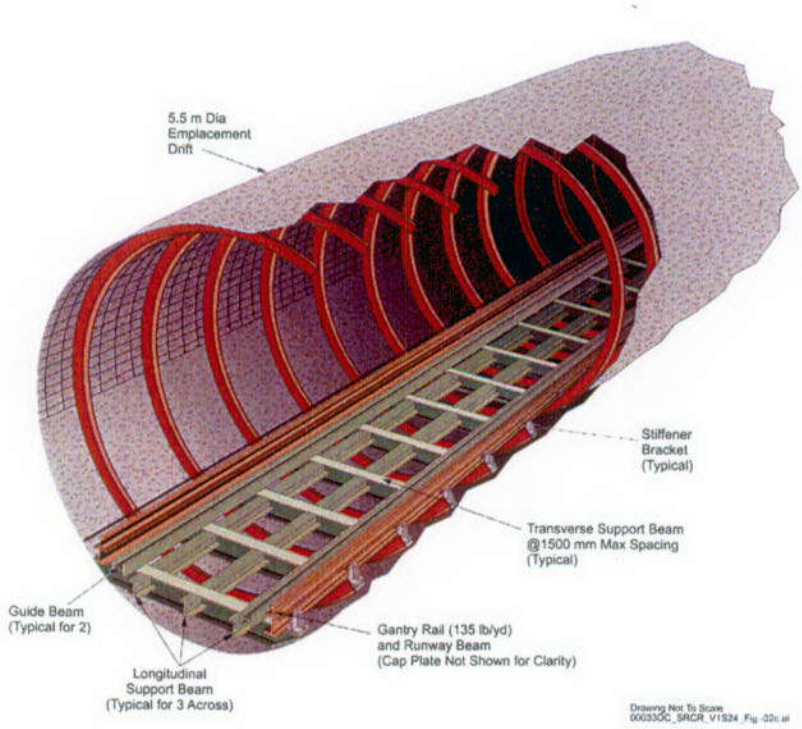

Source: DOE 2001 ([153849], Figure 2-72).

Figure 5-3. Perspective View of Steel Invert Structure in Emplacement Drift

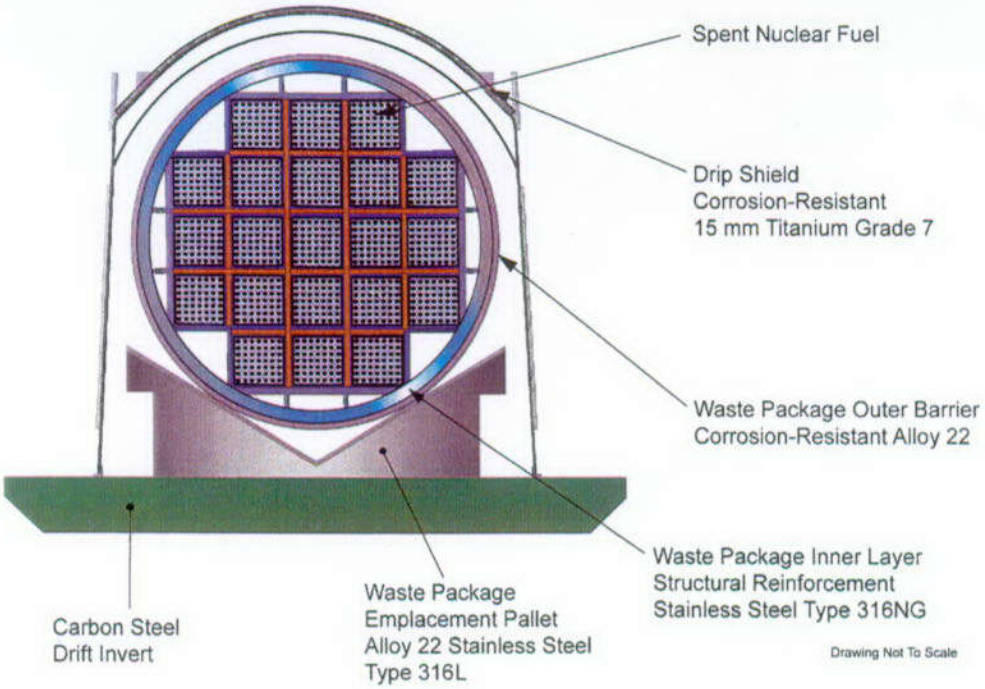

Source: DOE 2001 ([153849], modified from Figure 3-1).

Figure 5-4. Cross Section of Waste Package, Emplacement Pallet, and Drip Shield

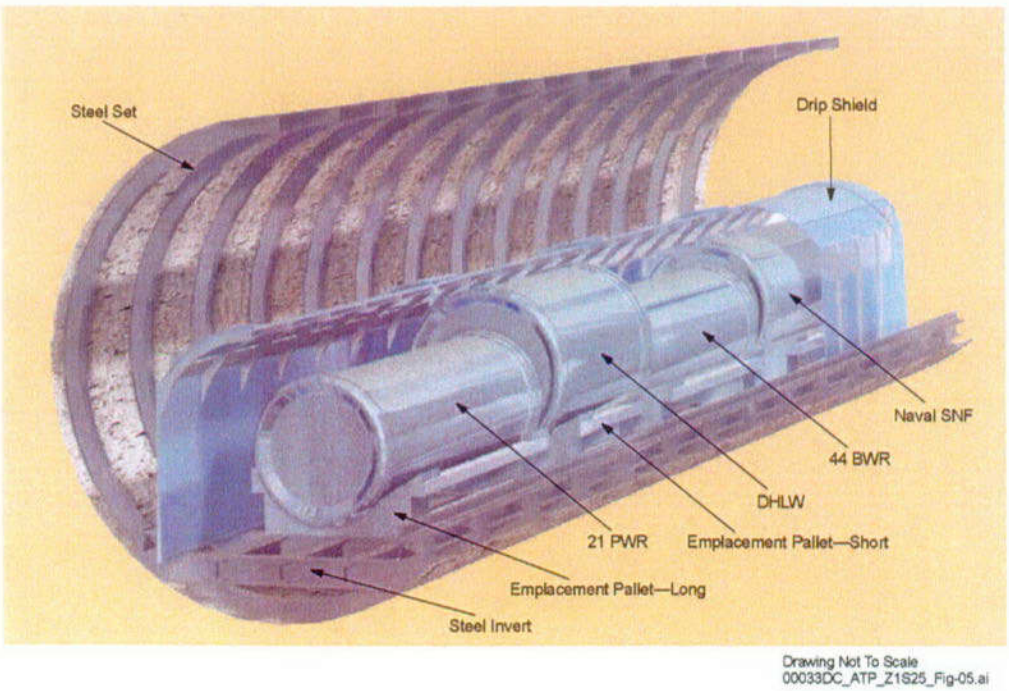

NOTE: PWR = Pressurized Water Reactor; DHLW = Defense High-Level Radioactive Waste; BWR = Boiling Water Reactor; and SNF = Spent Nuclear Fuel. Source: DOE 2001 ([153849], Figure 2-77).

Figure 5-5. Schematic View of Different Waste Packages in Emplacement Drift

Table 5-1. Commercial Spent Nuclear Fuel Waste Package

Component	Composition	Function
Outer barrier and lids	Alloy 22	Protect against corrosion
Support ring	Alloy 22	Hold inner cylinder in place
Inner structural shell and lid	Stainless Steel Type 316NG	Provide structural integrity
Waste package fill gas	Helium	Heat conductor, with need to be compatible with spent fuel
Fuel tubes for internal basket	Carbon steel (SA 516 Grade 70)	Hold fuel assemblies in place and provide structural strength and conduct heat away from cladding
Interlocking plates for internal basket	Carbon steel (SA 516 Grade 70)	Provide structural strength to maintain fuel geometry and prevent criticality
Neutron absorber materials for internal basket	Neutronic A 978 (borated 316 stainless steel)	Prevent criticality, provides structural strength and conduct heat away from waste form to walls of waste package
Thermal shunts for internal basket	Aluminum alloy (SB-209 6061 T4)	Transfer heat from waste form to walls of waste package
Structural guides for internal basket	Carbon steel (SA 516 Grade 70)	Provide structural strength to hold basket structure in place and prevent criticality, conduct heat to walls of waste package
Control rods	Boron carbide with Zircaloy cladding	Provide long-term criticality control

Source: DOE 2001 [153849], modified from Table 3-9, Sections 3.1 and 3.2.2.

Table 5-2. Chemical Composition of Alloy 22

Element	Composition (wt %)
Nickel	50 to 63
Chromium	20.0 to 22.5
Molybdenum	12.5 to 14.5
Iron	2.0 to 6.0
Tungsten	2.5 to 3.5
Cobalt	2.50 (max)
Manganese	0.50 (max)
Vanadium	0.35 (max)
Silicon	0.08 (max)
Phosphorus	0.02 (max)
Sulfur	0.02 (max)
Carbon	0.015 (max)

Source: DOE 2001 [153849], modified from Table 3-12.

Table 5-3. Chemical Composition of Stainless Steel Type 316NG

Element	Composition (wt %)
Iron	61 to 71
Chromium	16.00 to 18.00
Nickel	11.00 to 14.00
Molybdenum	2.00 to 3.00
Manganese	2.00 (max)
Silicon	0.75 (max)
Copper	0.50 (max)
Cobalt	0.10 (max)
Vanadium	0.1 (max)
Nitrogen	0.06 to 0.10
Titanium	0.05 (max)
Tantalum and Niobium	0.05 (max)
Aluminum	0.04 (max)
Phosphorus	0.030 (max)
Carbon	0.020 (max)
Bismuth + Tin + Arsenic + Lead + Antimony + Selenium	0.02 (max)
Sulfur	0.005 (max)
Boron	0.002 (max)

Source: DOE 2001 [153849], modified from Table 3-13.

6. WASTE PACKAGE DEGRADATION ANALOGUES

6.1 INTRODUCTION

This section describes the use of natural analogues to evaluate the long-term performance of metals used in the fabrication of waste packages for storage of high-level radioactive waste. Key concerns for the waste package materials (described in Section 5) include the possible degradation and corrosion of metals caused by mechanical stress, hostile physical and chemical environments, and metallurgical factors. The primary degradation and corrosion issues expected for Yucca Mountain include elevated temperature and humidity, and contact with seepage water that could have corrosive chemistry. A number of different analogues were previously discussed in Chapter 13 of the *Yucca Mountain Site Description* (CRWMS M&O 2000 [151945], Section 13.3.5); those analogues applicable to the waste materials described in Section 5 are briefly summarized below. Additional analogue examples are discussed in more detail in the following subsections.

The long-term stability of the waste package materials is directly related to repository environmental conditions. Preservation of delicate archaeological materials, including metals, appears to be enhanced by their location in an arid or semi-arid unsaturated environment (CRWMS M&O 2000 [151945], Section 13.3.4). Mummified remains 4,000 to 8,000 years in age were recently discovered in shallow burial pits in the high Andes Mountains of Chile. The Dead Sea scrolls were preserved in caves along the shores of the Dead Sea for over 2,000 years. All of these artifacts have survived millennia, and their preservation is attributed in part to being in arid to semiarid unsaturated environments (Winograd 1986 [127015], p. 8).

Metal analogues, involving both naturally occurring and archaeological objects, were also described in the *Yucca Mountain Site Description* (CRWMS M&O 2000 [151945], Section 13.3.5). A cache of Roman iron nails was recovered after almost 1,900 years of burial in Scotland (Miller et al. 1994 [126089], pp. 114–119). Corrosion of the outermost nails formed a protective rust rind, serving to create a more reducing (and thus more stable) environment for the innermost nails. Using a variety of iron archaeological artifacts, Johnson and Francis (1980 [125291], Fig. 3-1) calculated general corrosion rates of 0.1 to 10 μm/yr for most of the artifacts under a range of environmental conditions. Iron meteorites often have poorly constrained exposure histories, but differential corrosion of different mineral phases can be used to estimate relative resistance to corrosion, suggesting that Ni-rich phases (taenite and schreibersite) are more stable than Fe-rich phases (Johnson and Francis 1980 [125291], p. 4.23). Copper-bearing archaeological artifacts, such as sunken and buried bronze cannons, can also be used to estimate general corrosion rates over extended (hundreds to thousands of years) periods of time. These metal analogues, while differing in chemical composition from the waste package films, provide important insights into the way different metals survive corrosion over long time periods, and illustrate the importance of passive films.

Most of the metals being considered for use in the waste packages at a potential Yucca Mountain repository consist of alloys that do not occur naturally and are not present in the archaeological record (see Tables 5-1 to 5-3). However, the long-term behavior of metals with similar compositions that are present either as minerals or as man-made objects can be used to build

confidence in long-term performance models of the waste package materials. Analogues to long-term behavior of metals related to waste package materials are described in Section 6.2.3. Information found in Section 6.2 may help to support arguments associated with Key Technical Issue (KTI) KUZ0407 listed in Table 1-1.

6.2 NATURAL ANALOGUE STUDIES OF CORROSION

This section will discuss new work on some of the natural analogues previously summarized in Chapter 13 of the *Yucca Mountain Site Description* (CRWMS M&O 2000 [151945]), as well as present information on examples not previously discussed in the Site Description.

6.2.1 Environmental Factors Related to Corrosion

Knowledge of the in-drift physical and chemical environment at Yucca Mountain is critical in predicting the long-term performance of waste packages and the EBS. Processes such as the evaporation and condensation of water, precipitation and dissolution of salts, seepage and mass transport of materials into the drift environment, and the abundance, compositions, and reactions between solid, liquid, and gas phases will affect the physical and chemical integrity of waste packages and other EBS components.

One of the key attributes of the potential Yucca Mountain repository is its location within the unsaturated zone, thus reducing the amount of water that can come into contact with waste packages. Previous reviews of natural analogues of caves within the unsaturated zone have demonstrated that very old archaeological artifacts can be preserved in such environments (CRWMS M&O 2000 [151945], Section 13.3.4). Hundreds of wooden and reed fragments of dart and arrow shafts (dated between 3,300 to 9,300 years B.P.) have been recovered from Pintwater Cave in southern Nevada (Buck and DuBarton 1994 [157438], pp. 228, 239). These delicate items were collected from the limestone cave floor and in a test pit excavated within eolian sediments lining the floor of Pintwater Cave (Buck and DuBarton 1994 [157438], p. 226), and their preservation suggests that they were not subjected to prolonged exposure to water. However, as shown in the following example, the maintenance of a stable microclimate is a critical feature in making caves suitable for long-term preservation.

The Altamira cave, located in northern Spain, is the site of Paleolithic cave paintings (Sanchez-Moral et al. 1999 [157382]). Since the discovery of the prehistoric cave art in 1879, significant degradation of the cave paintings has occurred, leading to the cave being closed to the public in 1977. The cave was reopened in 1982 with fixed limits on the number of visitors. Continuous monitoring of the Altamira cave microclimate within Polychromes Hall (a cave chamber with famous polychromatic paintings) during 1997–1998 determined that increases in temperature (Δ = +0.25°C) and CO_2 concentrations (Δ = +500 ppmv) resulted directly from the presence of visitors in the cave (Sanchez-Moral et al. 1999 [157382], p. 78).

Sanchez-Moral et al. (1999 [157382]) used these data to estimate effective calcite corrosion rates for both the baseline and modified (visitor-related case) cave conditions. They predicted that the visitor-induced temperature increase (resulting from radiation of body heat) will greatly increase the amount of water condensation occurring on the cave walls and ceiling. The elevated P_{CO2} (partial pressure of carbon dioxide) conditions caused by human respiration, combined with the

higher amounts of condensation, were predicted to result in visitor-induced corrosion rates (314 mm^3/yr) in Polychromes Hall that are 78 times higher than the baseline (no visitor) case

(Sanchez-Moral et al. 1999 [157382], p. 78). As noted by visual observation and modeling, the relatively minor changes in temperature and P_{CO2} at Altamira had a significant impact on deterioration of the cave art. Thus, the corrosion-resistance properties of waste package materials at Yucca Mountain need to be evaluated for all possible variations in environmental conditions during the postclosure period.

One critical factor affecting the chemical integrity of the waste packages is the potential development of hypersaline fluids within emplacement drifts at Yucca Mountain. Such fluids could be generated by evaporative concentration of dissolved salts in pore waters in the near-drift environment caused by heating, or by dissolution of previously formed salts in the dryout zone around the drift by downward percolating condensate waters and/or surface infiltration. The amount and salinity of water in contact with waste packages depend on a number of factors, including evaporation, condensation, temperature, and fluid flux rates into the emplacement drifts (Figure 6-1). Conceptual and numerical models of these processes suggest that fluid compositions within the emplacement drifts may be highly variable over time (Walton 1994 [127454], pp. 3483–3486).

To constrain models involving the generation of hypersaline fluids at Yucca Mountain, Rosenberg et al. (2001 [154862]) conducted a series of experiments at sub-boiling temperatures (75–85°C) to evaluate the evaporative chemical evolution of pore water from the unsaturated zone and of well water from the saturated zone at Yucca Mountain. Synthetic solutions of these two fluid types were evaporated, with samples collected and analyzed after approximately 100 and 1,000 × evaporative concentration and evaporation to dryness (Table 6-1). A number of different minerals formed from complete evaporation of these waters, including amorphous silica, aragonite, calcite, halite, niter, smectite, thermonatrite, tachyhydrite, and gypsum. The groundwater (obtained from the J-13 well at Yucca Mountain) composition evolved into a high pH, sodium carbonate-bicarbonate brine resulting from the precipitation of calcium-magnesium carbonate, while the UZ pore-water composition evolved into a near-neutral pH, sodium-potassium-calcium-magnesium-chloride-nitrate brine resulting from the precipitation of gypsum. Different fluid chemistry may develop under higher temperature (boiling) conditions as a result of CO_2 degassing, which could have an important impact on the pH of the evolved fluids. These experimental results provide a data set against which to compare brines from analogue sites that have interacted with metals in a natural environment.

Hypersaline fluids, such as those encountered at the Salton Sea geothermal field (Table 6-2), have been observed to aggressively corrode many steel compositions (McCright et al. 1980 [157384], pp. 646–648). Carbon steel drill casings initially used in geothermal production wells at the Salton Sea field experienced general corrosion rates as high as 25.4 mm/yr, with even higher localized corrosion rates observed (Pye et al. 1989 [157385], p. 260). These rates are much higher than the rates of 10–40 μm/yr obtained by Ahn and Soo (1995 [104751], p. 475) for corrosion tests of A216-Grade WCA low-carbon steel in concentrated synthetic groundwater solutions. The differences in corrosion rates likely result from: (1) differences in steel compositions; (2) higher temperatures for the Salton Sea fluids (232–315°C) than that those used for the corrosion experiments (80–150°C); and (3) much higher salinities for the Salton Sea brines (150,000–300,000 ppm TDS) relative to the synthetic experimental brines (7,455 ppm TDS). Corrosion problems at the Salton Sea were successfully mitigated through the use of a corrosion-resistant titanium alloy (see Section 7.2.1). The current drip shield design for Yucca

Mountain (see Section 5.2.1) calls for the use of titanium because of its corrosion-resistant properties.

Another concern for waste package materials is the possible evaporative concentration of minor dissolved constituents, such as arsenic, lead, and mercury, that could enhance corrosion (BSC 2001 [155950], Section 7.3.1.3.4; [157151], Appendix E, Section 3.1.2). The hypersaline Salton Sea brines have significant concentrations of arsenic (8 ppm) and lead (66 ppm). However, groundwaters in the vicinity of Yucca Mountain have only trace amounts of lead, with a median concentration of 9 ppb (Lee 2001 [155241]; Perfect et al. 1995 [101053]). Two samples of J-13 well water from Yucca Mountain were analyzed for lead, with one sample yielding a value of 3 ppb, while the other was below detection (BSC 2001 [155950], Section 7.3.1.3.4; Perfect et al. 1995 [101053]). Lead concentrations in groundwater at Yucca Mountain may be limited by precipitation of lead in the form of carbonate, oxide, or sulfide minerals, or by sorption onto mineral surfaces (BSC 2001 [155950], Section 7.3.1.3.4, [157151], Appendix E, Section 3.1.2). Evaporative concentration of water in the near-drift environment at Yucca Mountain could result in higher lead concentrations. However, even a 1,000-fold increase in lead concentration in J-13 water would still only result in a brine with ~3 ppm lead, over 20 times lower than the concentrations observed in Salton Sea brines. Thus, the very low concentrations of lead in groundwater at Yucca Mountain greatly reduce the risk that lead (and other trace metals) could pose to the chemical integrity of the waste packages.

6.2.2 Passive Film Formation

The formation of passive films has a significant impact on the corrosion-resistant properties of metals and metal alloys (BSC 2001 [155950], Section 7.3.4). Passive films are stratified coatings consisting of an inner oxide layer and an outer layer of hydroxide or oxyhydroxide (Macdonald 1992 [154720], pp. 3434–3437; Marcus and Maurice 2000 [154738], pp. 145–152]. The inner layer forms a corrosion barrier, while exchange occurs within the outer layer of the passive film. These films act as semiconductors or insulators, thus reducing the rate of metal dissolution triggered by an electrochemical potential between a metal and its surrounding electrolyte solution.

The Delhi iron pillar is a 1,600-year old metal artifact (Figure 6-2) that has withstood exposure to the atmosphere with only relatively small amounts of corrosion. Study of the rust layer coating the pillar reveals the presence of crystalline iron hydrogen phosphate hydrate and amorphous iron oxyhydroxides and magnetite (Balasubramaniam 2000 [157383], pp. 2115–2116). The low-porosity crystalline phosphate phase forms a passive film around the pillar, serving to protect it from further corrosion (Figure 6-3). Balasubraminiam (2000 [157383], pp. 2112–2115) interpreted the presence of ~0.25 wt% phosphorous and fine slag particles in the iron to be critical to the development of the corrosion-resistant layer.

6.2.3 Naturally Occurring Metals as Natural Analogues

Josephinite—Josephinite, a naturally occurring Ni-Fe-Co metal-bearing rock consisting of the minerals Ni_3Fe (awaruite), andradite garnet, FeCo (wairuite), and minor to trace amounts of Ni_6Fe_4 and $CaO{\cdot}2FeO$ (calciowüstite), is a possible natural analogue for Ni-Fe alloys (similar to Alloy 22, which is a Ni-Cr-Mo-W alloy) proposed for the Yucca Mountain waste packages. The

type locality of josephinite is the Josephine Ophiolite, a ~150 million-year-old serpentinized ultramafic body in Oregon, where it occurs within serpentine veins and as coarse metallic nuggets in nearby placer deposits (Dick 1974 [154749]). Josephinite was interpreted by Dick (1974 [154749], p. 297) to be a product of hydrothermal alteration and serpentinization of peridotite. Josephinite and awaruite are very stable rock and mineral phases, as evidenced by their survival for millions of years with only minor amounts of oxidation. Because of this long-lived stability, these ordered Ni-Fe-Co metals (Bassett et al. 1980 [157531]) have been proposed as alloys in constructing containers for the storage of high-level radioactive waste (Bird and Ringwood 1980 [157397]; 1982 [157398]; 1984 [157396]).

Relatively unaltered masses of metal that are predominantly Ni_3Fe (with small inclusions of Ni_3As) were discovered in 1999 within harzburgite in the Josephine Ophiolite and as eroded blocks up to ~3 kg (Bird 2001 [157514]). Preliminary Pb and Os isotopic analyses of these new samples suggest that the josephinite metal did not form as an alteration product of the Josephine Ophiolite, but instead may represent xenoliths within the serpentinite body that have a deep-mantle origin (Bird 2001 [157514]).

The josephinite nuggets have alteration rims comprised of Fe_3O_4 (magnetite, with maghemite) and $NiFe_2O_4$ (trevorite). Some samples of josephinite contain the high-temperature phase taenite (a disordered Ni-Fe metal) in addition to awaruite (BSC 2001 [155950], Section 7.3.2.4.2). Phase relation studies of the Fe-Ni system suggest that taenite is not stable below ~350°C, and that α-Fe, pure Ni, and awaruite are the stable phases for this system at ambient temperatures (Botto and Morrison 1976 [154716], p. 264). The persistence of taenite for millions of years suggests that low-temperature phase change rates for taenite are exceedingly slow (BSC 2001 [155950], Section 7.3.2.4.2). X-ray photoelectron spectroscopic analysis of a josephinite placer sample from the Josephine Ophiolite (Figure 6-4) revealed that while both iron and nickel are oxidized on the surface, nickel remains in reduced (metallic) form at depths of 2 nm and greater (analyzed to a depth of 120 nm), indicating that the bulk sample has not undergone significant amounts of oxidation (BSC 2001 [157151], Appendix E, Section 3.3.2, Table 1). Because of its high nickel concentrations, the longevity of josephinite indicates that nickel alloys will have long-term phase stability. While josephinite does not contain the molybdenum and tungsten that serve as stabilizing elements in Alloy 22 passive films, its ability to resist corrosion provides confidence that Alloy 22 will remain passive under potential repository conditions (BSC 2001 [157151], Section 3.3.2, Appendix E).

Chromite—Analogues for chromium are considered because of the chromium content of Alloy 22 (Table 5.2). Chromium occurs in minerals in the form of chromite ($FeCr_2O_4$) and chromium spinel ($Mg(Cr,Al)_2O_4$). These Cr-bearing minerals are typically found in mafic and ultramafic rocks. Elevated concentrations of chromium in groundwaters in the Leon-Guanajuato valley of central Mexico have been attributed to weathering and alteration of chromite from ultramafic rocks of the Sierra de Guanajuato that have been interpreted to be Jurassic in age (Robles-Camacho and Armienta 2000 [157386], pp. 172–173, 178–181). The San Juan de Otates pyroxenite unit consists of pyroxenite and serpentinized peridotite, harzburgite, and wehrlite. Discrete concentrations of ilmenite and chromite occur within these rocks, and form subrounded masses in outcrop. Chromite is typically found as subrounded crystals, often with exsolution borders of magnetite.

A variety of ultramafic rock samples from the Sierra de Guanajuato, with total chromium contents ranging from 55 to 4115 ppm, were leached with acid to evaluate the susceptibility of the rocks to weathering and subsequent release of chromium (Robles-Camacho and Armienta 2000 [157386], pp. 173–181). The laboratory acid treatment was designed to examine (over a much shorter time scale and under much more acidic conditions that found in the field) the effects of weathering resulting from interaction of oxygenated, CO_2-rich groundwater with chromium-bearing minerals (Robles-Camacho and Armienta 2000 [157386], pp. 174–177). The leachate from Cr-rich serpentinite samples yielded the highest concentrations (up to 274 mg Cr/kg rock), suggesting that they have the greatest potential to release chromium. SEM analysis of samples examined after leaching suggests that dissolution occurred along magnetite exsolution borders of chromite grains (Figure 6-5). Total chromium contents of groundwater samples collected from wells, streams, and reservoirs near the ultramafic rocks range up to 0.0149 mg/L. The Ca-Mg-HCO_3 composition of these waters is consistent with interaction with serpentinized ultramafic rocks. The study does not provide information on the rates of chromite weathering, but it does indicate that chromite exsolution borders are susceptible to chemical attack. This observation is analogous to localized corrosion and pitting observed in metals along structural defects.

6.3 SUMMARY

1. The survival of metal archaeological artifacts over prolonged periods of time is related to the corrosion-resistant properties of metals and metal alloys, the development of protective passive film coatings with the onset of corrosion, and the location of artifacts in arid- to semi-arid environments. Such features can be used in the selection of materials and design configuration to enhance the durability of waste packages at Yucca Mountain.

2. Archaeological examples, such as the Altamira cave, illustrate how environmental changes can significantly affect corrosion behavior. A wide variety of environmental conditions is expected to occur in the near-drift environment at Yucca Mountain during the lifespan of the repository. The introduction of heat-generating waste packages and EBS materials into drifts will perturb the existing physical and chemical system at Yucca Mountain. The materials used for the waste packages (and the rest of the EBS) need to withstand the predicted adverse changes in environmental conditions.

3. Small volumes of concentrated brines could develop in the near-drift environment as a result of evaporation and later dissolution of precipitated salts in the dryout zone with rewetting. High-salinity fluids pose a significant corrosion hazard to carbon steel, as seen at the Salton Sea geothermal field, but the use of titanium alloys can effectively minimize this hazard.

4. The survival for millions of years of the naturally occurring ordered Ni-Fe alloy found in josephinite (with only relatively minor amounts of surface oxidation) indicates that this material is highly resistant to oxidation and other forms of corrosion that occur in its geologic environment. While the composition of this metal differs from Alloy 22 (in that it does not contain Cr, Mo, and W), it does provide evidence that a similar alloy can remain passive over prolonged periods of time.

5. The potential instability of chromium-bearing materials is illustrated by the observed natural release (under ambient conditions) of chromium from chromite in the Sierra de Guanajuato ultramafic rocks. Corrosion appears to be concentrated along exsolution rims, analagous to structural defects on metal surfaces. While the chromite has undergone some alteration, it has survived for over 140 m.y. (since Jurassic time). The corrosion behavior of this chromium oxide mineral may differ from that of the chromium-bearing metal alloys (Section 5) that are currently slated for use in the construction of the waste package.

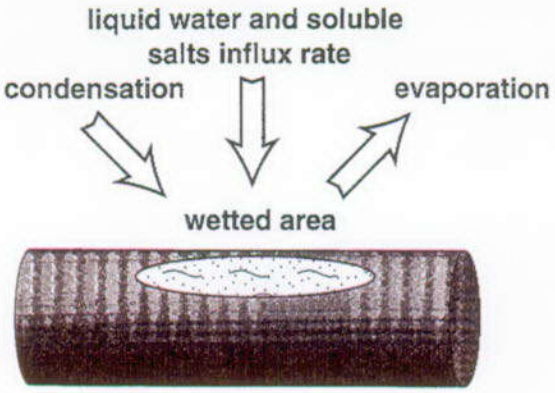

Source: Walton 1994 [127454], Figure 3.

Figure 6-1. Processes Affecting Formation of High-Salinity Fluids on Waste Package Surface

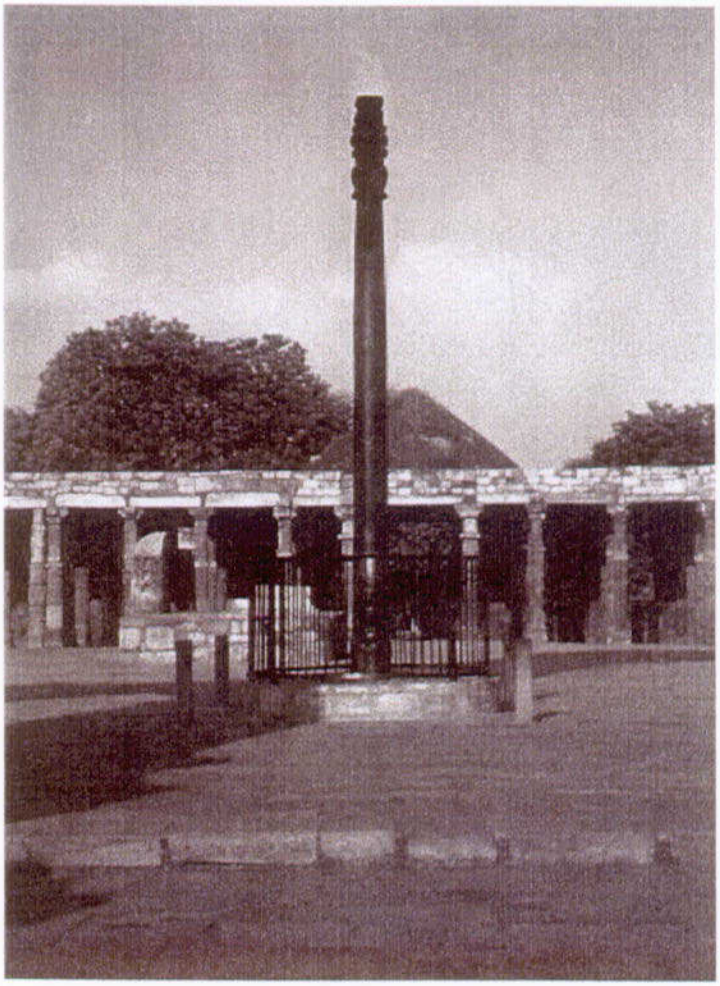

Source: Balasubramaniam 2000 [157383], Figure 1.

Figure 6-2. The Corrosion-Resistant Iron Pillar at Delhi

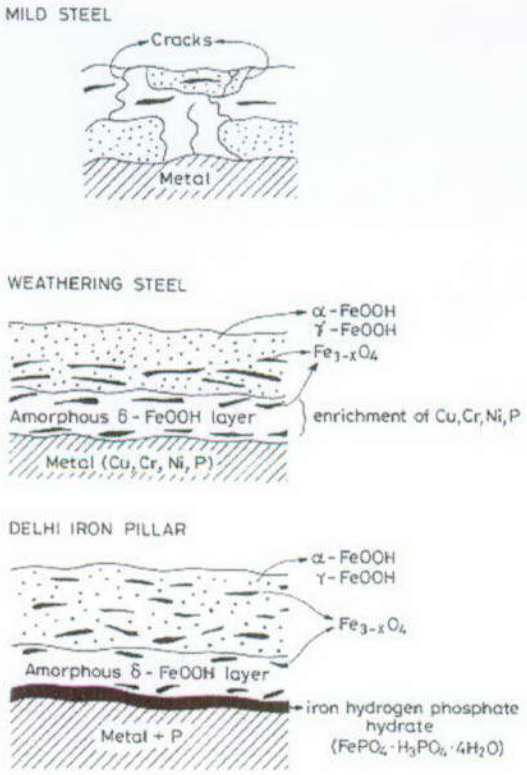

NOTE: Iron hydrogen phosphate hydrate layer on Delhi iron pillar forms a protective, impermeable coating that retards further corrosion.

Source: Balasubramaniam 2000 [157383], Figure 7.

Figure 6-3. Schematic Showing Development of Rust Coating on Mild Steel, Weathering Steel, and Delhi Iron Pillar

NOTE: Metallic-looking areas were analyzed using X-ray photoelectron spectroscopy.

Source: BSC 2001 [157151], Appendix E, Figure 3.

Figure 6-4. Josephinite Sample Used for Surface Analysis Study

(a) 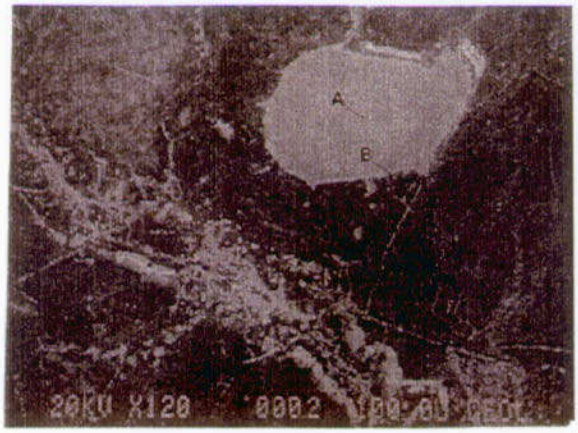

(b) 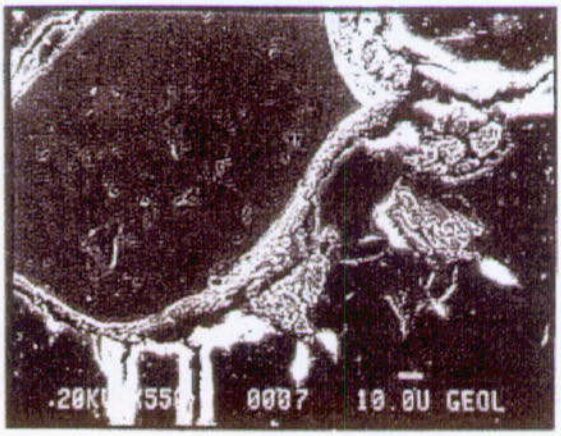

NOTE: White rim around chromite in (b) reflects dissolution of exsolution border around chromite.

Source: Robles-Camacho and Armienta 2000 [157386], Figures 5 and 8.

Figure 6-5. Chromite Grains in Serpentinite Before (a) and After (b) Acid Leaching

Table 6-1. Composition of Synthetic Yucca Mountain Waters (mg/L) from Unsaturated and Saturated Zones and Their Evaporated Compositions

	Synthetic J-13 water	"157 ×" J-13 water	"956 ×" J-13 water	Synthetic UZ water	"62 ×" UZ water	"1243 ×" UZ water
Na	45.2	5,288	43,302	8.56	477	6,223
K	5.2	593	4,701	4.00	268	2,644
Mg	2.1	1.2	0.13	11.8	550	5,546
Ca	5.8	0.06	27.3	57.3	1,713	15,643
SiO_2	10.4	1,040	----	10.4	503	541
HCO_3	105	4,410	24,255	20.3	9.9	<45
SO_4	18.5	2,109	13,209	83.9	1,544	2,098
Cl	7.2	814	5,047	76.6	4,259	52,165
NO_3	7.9	1,035	5,483	10.7	592	----
F	2.3	237	1,622	2.16	38	<542
TDS	209.6	15,527	97,646	285.7	9,954	~85,000
pH	8.07	10.18	----	7.55	7.65	6–6.5

NOTE: TDS calculated as sum of dissolved solids.

Source: Rosenberg et al. 2001 [154862], Tables 2 and 4.

Table 6-2. Typical Salton Sea Geothermal Well Brine Composition

Component	Concentration ppm	Component	Concentration ppm
Na	49,800	Ba	100
K	12,840	B	301
Mg	80	Cu	7
Ca	24,000	Fe	708
SiO_2	658	Pb	66
CO_2	125	Li	177
SO_4	22	Mn	785
Cl	126,700	Rb	62
NH_3	339	Sn	402
As	8	Zn	287
I	5	Br	68
pH	5.8	H_2S	90
		TDS	261,800

Source: Pye et al. 1989 [157385], Table 1.

7. ENGINEERED BARRIER SYSTEM ANALOGUES

7.1 INTRODUCTION

This section describes the use of natural analogues to evaluate the long-term performance of materials used in the construction of the Engineered Barrier System (EBS) and how these materials may affect radionuclide transport. The primary functions of the EBS components are to: (1) protect the waste package from physical and chemical degradation resulting from processes such as seepage, corrosive fluids, and rock fall; and (2) retard any potential transport of radionuclides from the emplacement drift in the event of waste package failure. Key concerns for the EBS materials (described in Section 5) include the possible degradation and corrosion of metals resulting from mechanical stress, hostile physical and chemical environments, and metallurgical factors. Another important performance parameter is the effect of EBS materials on flow and transport of fluids and dissolved solids into and out of the emplacement drifts. Important issues relating to EBS performance include the degradation of materials caused by corrosive fluids, radiation, thermal and physical stresses, and microbial attack, as well as the effects of sorption and colloids on radionuclide transport. A number of analogues were previously discussed in Section 13 of the *Yucca Mountain Site Description* (CRWMS M&O 2000 [151945]); these analogues are briefly summarized below. Additional analogue examples are discussed in more detail in the following subsections.

Three main issues relating to the EBS were discussed in detail in the natural analogues chapter of the *Yucca Mountain Site Description* (CRWMS M&O 2000 [151945], Section 13.3): (1) metal analogues (native metals and archaeological artifacts) in the evaluation of corrosion resistance; (2) cements and alkaline plumes to determine the impact of high pH fluids on EBS materials, surrounding host rock, and radionuclide transport; and (3) the effects of radiolysis on the integrity of waste package materials. A brief summary of earlier work on metal analogues is presented in Section 6 and thus will not be repeated here.

Under the current EBS design, cementitious material is expected to be present in only minor amounts (as grout for rock bolts) in the near-drift environment. The durability of cements over time has been documented by Gallo-Roman cements that are over 1,500 years old (Thomassin and Rassineux 1992 [157439], p. 137). Cementitious mortar from Hadrian's Wall (~1,700 years old) in England (Figure 7-1) has the same calcium silicate hydrate phases found in modern Portland cement, and still possesses excellent strength and stability (Miller et al. 2000 [156684], p. 131). The potential development of hyperalkaline fluids resulting from interaction of water with cementitious material could affect radionuclide transport and reduce the stability of EBS materials. Two areas with hyperalkaline fluids were described in the earlier review of natural analogues (CRWMS M&O 2000 [151945], Section 13.3.6): the Semail ophiolite in Oman, and the Maqarin area in Jordan. Serpentinization reactions in the Semail ultramafic rocks have resulted in the generation of reducing, hyperalkaline (pH = 10–12) Na-Cl-Ca-OH fluids, with associated minerals brucite ($Mg(OH)_2$) and portlandite ($Ca(OH)_2$). The Maqarin analogue site (also discussed in Section 7.3.1) contains a suite of naturally formed cement minerals, including portlandite. High pH (12–13) fluids emanate from these rocks as a result of reaction of groundwater with the cement phases. These analogue sites have been used in the development of

numerical models to predict water-rock reactions and resulting fluid compositions under similar conditions (McKinley et al. 1988 [126077]; Chambers et al. 1998 [157549]).

Chemical decomposition resulting from radiation (radiolysis) was also examined in the *Yucca Mountain Site Description* (CRWMS M&O 2000 [151945], Section 13.3.7). This process was studied at the natural reactor site at Oklo (in Gabon), where high radiation doses were interpreted to have led to radiolysis of water and redox reactions involving the surrounding rocks (Curtis and Gancarz 1983 [124785]). Similar reactions within the waste package assembly could lead to decomposition of the waste packages and release of radionuclides. However, since the waste loads are configured so that they will not approach criticality and the waste package design excludes free water, the amount of radiolysis that might occur at the potential Yucca Mountain repository should be much less than Oklo (see also Section 4 of this report). Section 7.2 describes analogues for EBS materials and Section 7.3 describes analogues for EBS processes.

7.2 ANALOGUES FOR EBS MATERIALS

7.2.1 Analogues for the Titanium Drip Shield

Corrosion caused by saline fluids has been identified as a potential hazard to the integrity of waste packages (see Section 6.2.1 for discussion). The drip shield assembly is designed to protect the waste packages from physical and chemical degradation resulting from events such as rock falls, seepage, and saline fluids. The current drip shield design calls for corrosion-resistant titanium. Titanium metal does not occur in nature, nor in the archaeological record, so other proxies need to be used to assess its long-term resistance to corrosion.

The Salton Sea geothermal field in California is characterized by hypersaline (15-30 wt% TDS) brines that have caused significant corrosion and scaling problems (Pye et al. 1989 [157385], p. 259). A series of corrosion tests led field operators to select Beta-C titanium (Ti-3Al-8V-6Cr-4Mo-4Zr) for the fabrication of corrosion-resistant production casing (Pye et al. 1989 [157385]). Four tests were conducted over a period from 256 to 833 days, involving installation of full-size Beta-C titanium tubulars in geothermal production wells, resulting in no visible pitting corrosion in two of the tests, little or no change in hydrogen content, and no significant degradation in mechanical properties (Pye et al. 1989 [157385], pp. 262–263). In the 833-day test, localized corrosion was observed, occurring at a rate of 7 mils/yr (178 μm/yr); this was interpreted to have occurred in an area where surface contamination had not been completely removed at the start of the test. Local corrosion was observed along 2 of the 48 casing joints in the fourth test; this corrosion was also interpreted to be the result of pre-existing surface contamination.

A longer-term evaluation of the corrosion behavior of titanium-bearing materials can be obtained by examining the stability of naturally occurring titanium minerals. Titanium is present as a major constituent in a number of refractory accessory minerals commonly found as a minor phase in igneous rocks and in heavy mineral concentrates in sediments. These minerals include sphene (titanite) ($CaTiSiO_4(O,OH,F)$), rutile (TiO_2), ulvöspinel (Fe_2TiO_4) and ilmenite ($FeTiO_3$). The Canadian nuclear waste disposal concept includes a metallic titanium container surrounding spent fuel. The corrosion resistance of titanium arises from its passivation in aqueous solutions

by the formation of a protective layer containing rutile (Cramer 1994 [157537], pp. 8–10). At the Cigar Lake uranium deposit in Saskatchewan, Canada, rutile is present within the uranium ore and has persisted unchanged for over a billion years in reducing groundwaters, under hydrothermal conditions, and in a radiation field. While rutile and other titanium-bearing minerals are oxides, and thus do not share the same physical properties as metals, their general resistance to alteration reflects the stable nature of titanium-bearing materials.

7.2.2 Analogues for the Invert Ballast

The nonwelded Calico Hills Formation and portions of the Paintbrush Tuff at Yucca Mountain are possible analogues for processes, such as sorption and ion exchange, that would affect the transport of radionuclides within the crushed tuff invert ballast. The relative lack of fractures in these tuffs results in fluid flow occurring in the tuff matrix, resulting in overall slower fluid flow and transport in these units caused by the lack of fast flow pathways, similar to what is predicted for the crushed tuff invert. Because of the presence of zeolites and/or smectite in the nonwelded tuffs, extensive ion exchange occurs between pore waters and the tuffs (Vaniman et al. 2001 [157427]). The zeolitic tuffs are significantly enriched in cations such as Ca^{2+}, Mg^{2+}, and Sr^{2+}, and depleted in Na^{+} and K^{+} (Figure 7-2); thus, waters are interpreted to have complementary (opposite) enrichments and depletions (Vaniman et al. 2001 [157427], pp. 3420–3423). This ion-exchange process would have a major impact on radionuclide transport, with species such as ^{90}Sr being effectively immobilized by this process. However, the current design for the invert ballast (DOE 2001 [153849], Section 2.4.1.2) uses crushed tuff derived from the repository interval (welded, devitrified Topopah Spring Tuff), which has only minor amounts of zeolites and clays (Vaniman et al. 2001 [157427], Figure 2). As a result, the ion exchange and sorption capacity of the crushed tuff invert ballast should be significantly lower than that observed in the nonwelded tuffs at Yucca Mountain. The crushed tuff invert would have high effective grain surface areas, which would favor sorption of species onto mineral surfaces, thus serving to retard radionuclide transport.

The effects of fluid flow on radionuclide retardation in ash flow tuff can also be evaluated through an anthropogenic analogue. At Los Alamos National Laboratory, radionuclide-bearing liquid wastes were discharged from 1945 to 1967 into gravel- and cobble-filled absorption beds (approximately 6 m × 37 m) built on outcrops of moderately welded rhyolite ash flow tuff (Figure 7-3) (Nyhan et al. 1985 [157447], p. 502). Large amounts (corresponding to a depth of 20.5 m) of tap water and radioactive effluent were added to one of the absorption beds (Bed 1) in 1961 to evaluate radionuclide mobility. The site was revisited in 1978, when profiles of Pu and ^{241}Am were measured in a series of 30.5 m deep boreholes drilled through two of the absorption beds (Bed 1 and Bed 2) and into the underlying ash flow tuff (Nyhan et al. 1985 [157447], p. 502). This study revealed that the bed where water and effluent had been added in 1961 (Bed 1) exhibited higher water saturations, along with significantly more radionuclide migration out of the absorption bed and into the underlying tuff (Figure 7-4), than the bed where no additional fluid had been added during this test (Bed 2). Plutonium and ^{241}Am were not detected beyond 11.28 m below the bottom of Bed 2, whereas 0.3 to 5.1% of the plutonium and 3.0 to 49% of the americium inventory were present within the depth interval of 11.28–27.13 m for Bed 1 (Nyhan et al. 1985 [157447]), p. 506). Elevated concentrations of radionuclides were observed to occur within lower permeability intervals of the tuff. The radionuclide concentrations of fracture fillings were similar to those of adjacent tuff samples, suggesting that fractures did not enhance

radionuclide transport under unsaturated conditions and generally acted as barriers to unsaturated zone (UZ) flow (Nyhan et al. 1985 [157447], pp. 504–505, 508). These results suggest that radionuclide mobility was triggered by flushing of the absorption beds with large volumes of fluids. The volume of the column of fluid used in the Los Alamos test is equivalent to the amount of percolating surface water expected to flow through Yucca Mountain over a timespan of 2,000 to 4,000 years (assuming an infiltration rate of 5 to 10 mm/yr (Flint et al. 2001 [156351], p. 26), and thus represents an illustration of the effects of flushing on radionuclide mobility. However, this example does suggest that the ability of the invert ballast at Yucca Mountain (as well as the underlying welded tuffs) to retard radionuclide migration will depend in part on the amount of water flowing through this interval. Both of the analogue examples described are also relevant to processes controlling radionuclide transport in the UZ at Yucca Mountain (see Section 9).

7.3 NATURAL ANALOGUES FOR EBS PROCESSES

The physical and chemical conditions for the near-field area around the emplacement drifts at Yucca Mountain are predicted to undergo changes over time. These changes would result from coupled thermal-hydrologic-chemical (THC) processes, such as boiling, condensation, fluid flow and transport, and mineral dissolution, alteration, and precipitation (BSC 2001 [154677]). THC processes are also expected to occur within the EBS, and could lead to degradation of the EBS components, resulting in the release and transport of radionuclides away from the EBS. Natural analogue studies for some of the processes expected to impact the EBS system, such as the generation of alkaline plumes resulting from interaction of water with cementitious material and the effects of colloids on radionuclide transport, are described below.

7.3.1 Natural Analogues for Development of Alkaline Plumes from Cement

The presence of naturally occurring cement minerals and associated hyperalkaline groundwaters at Maqarin, Jordan, has been used as a natural analogue for examining the effects of hyperalkaline waters (e.g., Khoury et al. 1992 [125677]; Smellie 1998 [126633]). The Maqarin site consists of interbedded bituminous limestones and marls that have been locally thermally metamorphosed from spontaneous combustion of the bitumen, resulting in the calcination of limestone and formation of cement minerals, including portlandite. Water interacting with portlandite has resulted in the formation of highly alkaline (pH $\approx$ 12.5) groundwaters and the precipitation of minerals such as ettringite and thaumasite at ambient temperatures (Figure 7-5). Initial geochemical modeling efforts resulted in model predictions of dissolved selenium and uranium concentrations that were several orders of magnitude higher than those observed in the field (Linklater et al. 1996 [108896], p. 67). A multicomponent reactive transport model that incorporated mixed equilibrium and kinetic reactions was applied to simulate rock alteration mineralogy and fluid chemistry changes for discrete fractures in the Maqarin system (Steefel and Lichtner 1998 [156714]). These simulations predict the formation of hydrated calcium sulfate and silicate minerals, such as ettringite and tobermorite, which were observed in the field (Khoury et al. 1992 [125677], p. 122), and also reproduced measured fluid pH values. The simulations suggest that mineralization caused by interaction of the hyperalkaline plume with surrounding rocks may result in both reduction of matrix porosity and fracture sealing. Fractures at the Maqarin site have complex mineralogy and textures that suggest that they have undergone repeated sealing and reopening over time. The relative rates of matrix and fracture mineralization

(and associated reduction in permeability) will significantly affect the mobility of the alkaline plume, and thus the transport of associated radionuclides.

The development of large hyperalkaline plumes and associated alteration and transport are not expected to occur at Yucca Mountain. The amount of cementitious material expected to be present in the potential repository (in the form of grout around rock bolts in the emplacement drifts) is much less than what is observed at Maqarin. The fluid pH of the near-field environment thus will be buffered by tuff rather than by portlandite, resulting in less alkaline pH conditions (DOE 2001 [153849], Section 4.2.3.3.3). The Maqarin natural analogue is important to consider in illustrating the effects of alkaline fluids on water-rock processes, and thus constraining EBS design parameters (through minimization of the use of cement) and coupled process models. The ability of the multicomponent reactive transport simulations to reproduce observed water-rock interactions for the alkaline plumes at Maqarin provides confidence that similar THC modeling efforts at Yucca Mountain predict reactive chemistry and transport processes that are expected to occur over time.

7.3.2 Natural Analogues for Colloidal Transport of Radionuclides

Colloids can facilitate radionuclide transport (Figure 7-6) if they are: (1) present in sufficient quantities, (2) mobile, and (3) can bind radionuclides (Wieland and Spieler 2001 [157442], p. 511). Naturally occurring colloids are ubiquitous in groundwaters; sampled by Kingston and Whitbeck (1991 [113930], pp. 26, 57) (mainly from central and southern Nevada) have dilute colloid concentrations ranging from 0.28–1.35 mg/L), and ferric oxide and oxyhydroxide colloids can also be generated through degradation of structural steel present in EBS materials.

Filtration of Fe-bearing colloids has been documented in some environments. For instance, groundwaters in the Poços de Caldas area, Brazil, typically have low concentrations (<1 mg/L) of colloids (Miekeley et al. 1989 [126083], pp. 838, 840–841; 1991 [127199], pp. 35, 49). Most of the colloids there are composed of iron and organic species. Only minor amounts of uranium are associated with colloids, but greater amounts of thorium and rare earth elements are transported in the colloidal fraction. The results of the colloid studies at Poços de Caldas (Miekeley et al. 1989 [126083], p. 841; 1991 [127199], p. 58) suggest that radionuclide and other trace-element transport by colloids does not play a significant role in the geochemical processes of weathering, dissolution, and erosion of these ore deposits. One reason for this could be filtration of material which traps colloids in pore throats and narrow fractures (Smellie et al. 1989 [126636], p. 868). The colloidal material acts as an efficient and largely irreversible sink or trap for many elements (especially if they are immobile), but needs to be taken into account in equilibrium thermodynamic modeling of radionuclide speciation. The point of this example is that the iron-bearing colloids that may form in the Exploratory Studies Facility could be beneficial in complexing with uranium and could be retained effectively in the EBS by filtration.

7.4 SUMMARY

The highly corrosive-resistant nature of titanium has been demonstrated by long-term experiments conducted on a range of metal alloys in wells at the Salton Sea geothermal field. The commercial use of titanium alloys in production casings over the past decade at the Salton Sea has greatly alleviated severe corrosion problems that were previously experienced resulting

from exposure of conventional steel casing to the hot, hypersaline geothermal brines. This anthropogenic example supports the selection of titanium alloys for the construction of a corrosion-resistant drip shield for the EBS.

Mineralogic and geochemical analysis of tuffs in the UZ at Yucca Mountain indicates that the presence of zeolite and clay minerals greatly enhance cation exchange, thus serving to retard the transport of some radionuclides. While the proposed material (devitrified welded tuff) for the invert ballast in the current design does not have high concentrations of these minerals, the high surface area of crushed tuff will retard radionuclide transport through absorption. The Los Alamos example of actinide absorption in a gravel bed provides qualitative evidence of retardation at the contact between an invert-like material and underlying bedrock.

The presence of cementitious materials can potentially lead to the development of alkaline plumes, resulting in corrosion of waste package materials, alteration of surrounding host rocks, and possible enhancement of radionuclide transport. Because the use of cementitious material in the EBS and its environs is restricted to grout for securing rock bolts in the emplacement drifts, hyperalkaline conditions are not expected to develop at Yucca Mountain. However, through reactive transport modeling of the Maqarin site, it has been demonstrated that a model can reproduce the same suite of cement minerals, hyperalkaline water compositions, and pH that were found in the field, thus building confidence in use of such a model for analogous conditions at other sites.

The Poços de Caldas analogue illustrated that iron-bearing colloids may retard the transport of uranium and other spent-fuel components by forming colloids that are then filtrated from suspension at short distances. Degradation of steel structural elements in the EBS could conceivably contribute to this process.

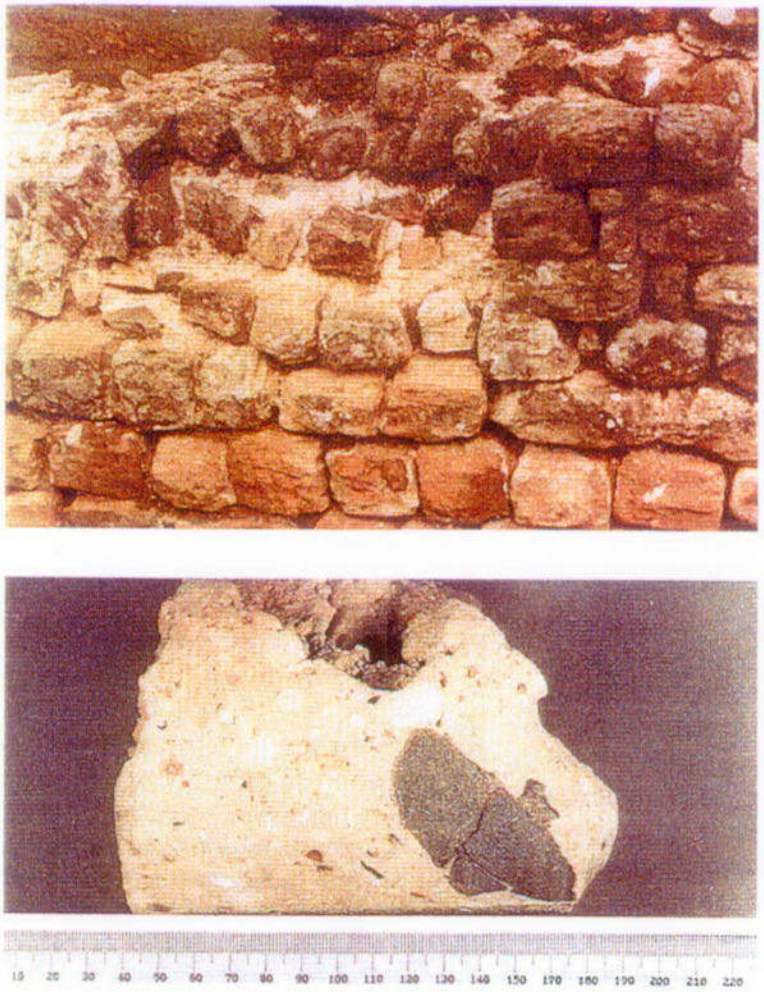

Source: Miller et al. 2000 [156684], Figure B10.2.

Figure 7-1. Portion of Hadrian's Wall in England, Showing Strength and Stability of Roman Mortar after 1,700 Years

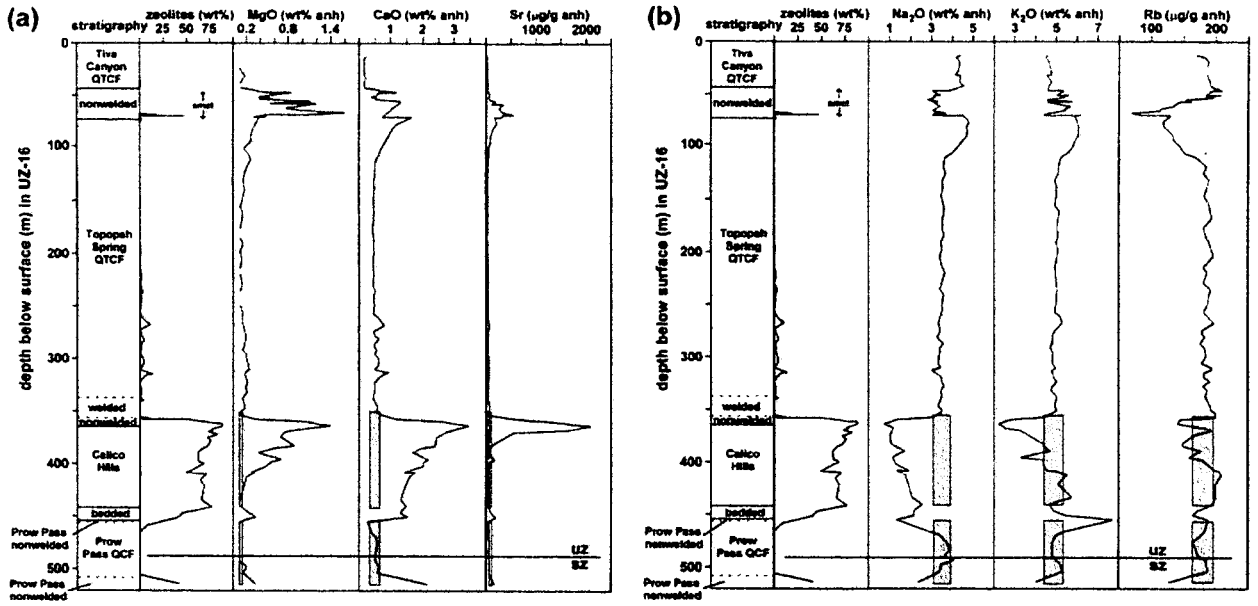

NOTE: Shaded bars represent corresponding compositions of unzeolitized precursor tuffs. Symbols (Q = quartz, T = tridymite, C = cristobalite, F = feldspar) indicate devitrification minerals in welded tuff intervals. UZ-SZ line marks location of water table. Chemical abundances are normalized to anhydrous (anh) compositions.

Source: Vaniman et al. 2000 [157427], Figure 4.

Figure 7-2. Stratigraphic Section of Drill Hole UE-25 UZ#16, with Abundance of Zeolites Plotted versus (a) Alkaline Earth and (b) Alkali Constituents

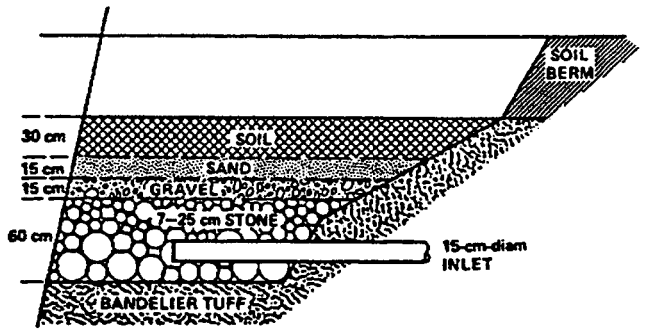

Source: Nyhan et al. 1985 [157447], Figure 1.

Figure 7-3. Cross Section of Absorption Bed for Disposal of Radioactive Liquid Wastes, Area T, DP West Site, Los Alamos National Laboratory

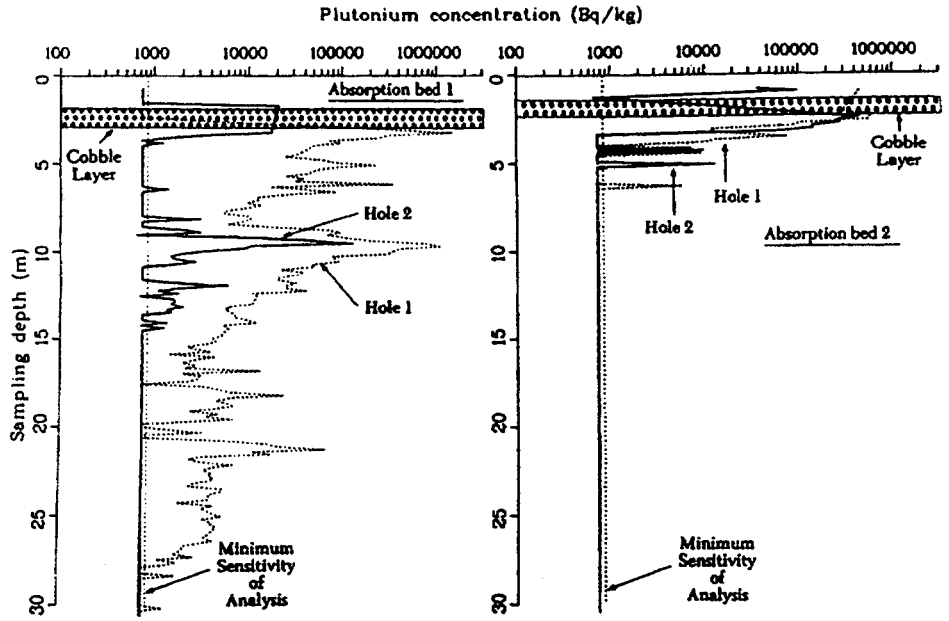

(a)

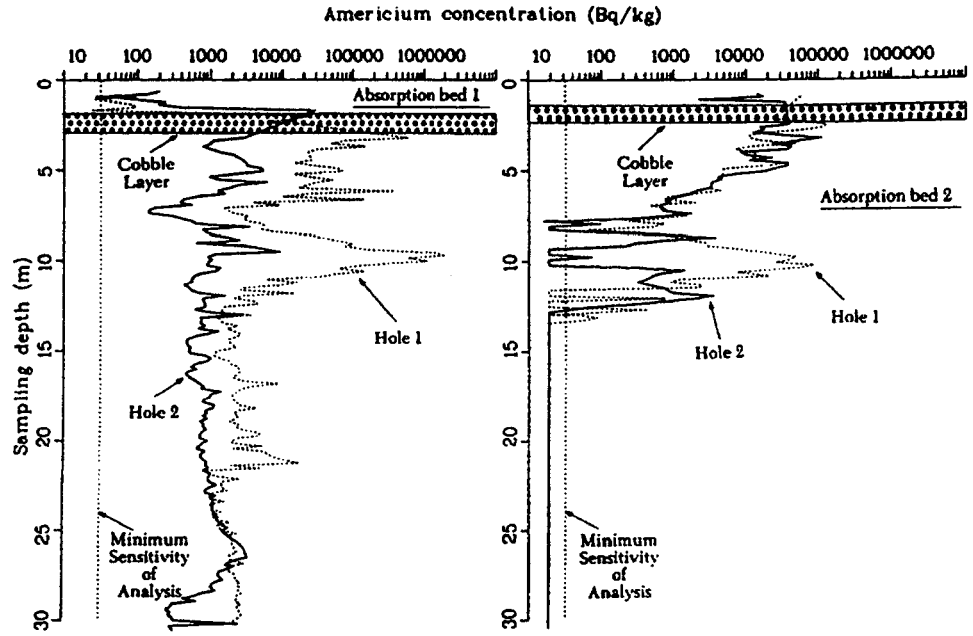

(b)

Source: Nyhan et al. 1985 [157447], Figures 2 and 3.

Figure 7-4. Concentrations of Plutonium (a) and Americium-241 (b) within and beneath Absorption Beds 1 and 2, Area T, DP West Site, Los Alamos National Laboratory (1978)

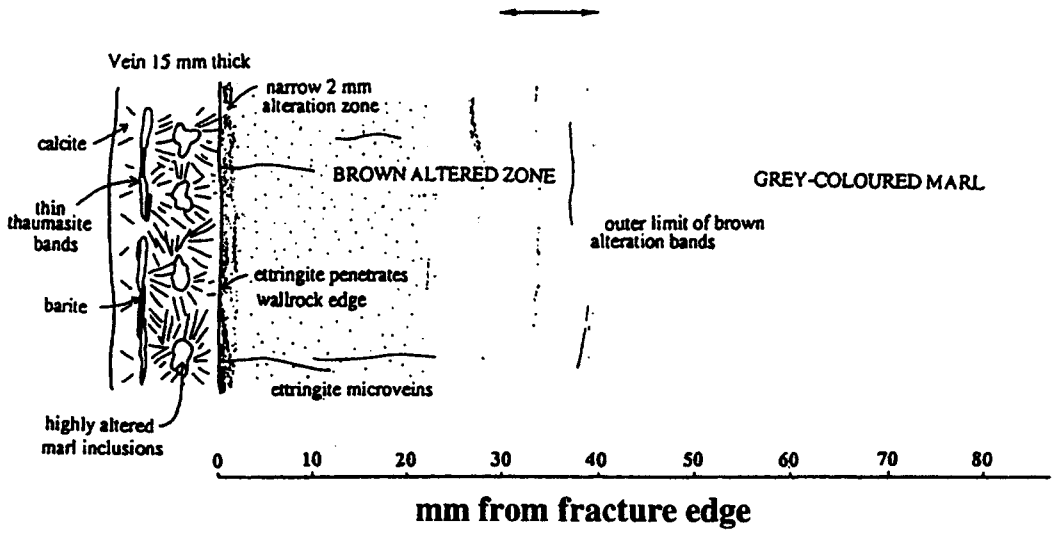

Source: Steefel and Lichtner 1998 [156714], Figure 6.

Figure 7-5. Fracture Mineralization and Wall Rock Alteration at C353 Site, Maqarin, Showing the Presence of Hydrated Calcium Silicate and Sulfate Phases Thaumasite and Ettringite

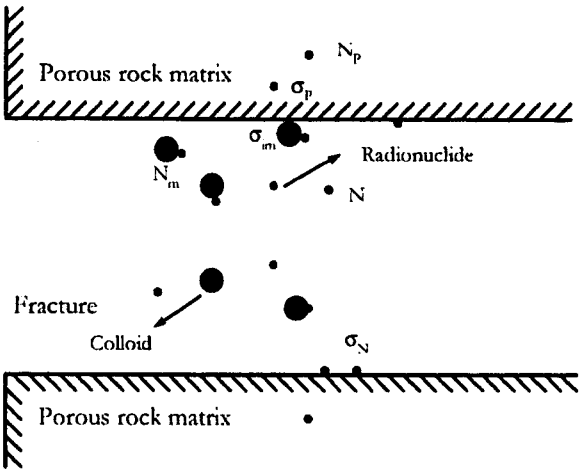

NOTE: N = dissolved radionuclides in fracture,
σ_N = radionuclides on fracture surface,
N_m = radionuclides bound to mobile colloids,
σ_{im} = radionuclides sorbed on immobile colloids,
N_P = dissolved radionuclides in pores of rock matrix,
σ_p = radionuclides sorbed on rock matrix.

Source: modified from Jen and Li 2001 [157463], Figure 1.

Figure 7-6. Schematic Illustration of Radionuclide Transport in a Fractured Rock

8. NATURAL ANALOGUES FOR SEEPAGE

8.1 INTRODUCTION

This section examines several different types of qualitative and quantitative natural analogues for seepage, taken from caves, lava tubes, tombs, rock shelters, and buildings that were investigated since publication of the *FY 01 Supplemental Science and Performance Analyses* [SSPA], *Volume 1: Scientific Bases and Analyses* (BSC 2001 [155950]). It considers the role of the hydrogeologic setting of underground openings on seepage and the effect of relative humidity. It evaluates a number of candidate settings that have been suggested as analogues and demonstrates why they are or are not considered appropriate as seepage analogues. It also examines the question of the preponderance of evidence of preservation of seepage analogues. In this section, the term *infiltration* is used for precipitation that is not lost by runoff, evaporation, or transpiration, and *seepage* is used for that portion of the infiltration within the unsaturated zone (UZ) that enters tunnels or other underground openings. For reference, current precipitation at Yucca Mountain is about 190 mm/yr (DOE 2001 [153849], Section 4.2.1.2.1), with future rates predicted to be 269 to 529 mm/yr (BSC [155950], Table 3.3.1-5). Information found in Sections 8.2, 8.3, and 8.4 may help to support arguments associated with Key Technical Issue (KTI) KUZ0407 found in Table 1-1.

8.2 GEOLOGIC EXAMPLES

Seepage is mainly governed by the capability of individual fractures to hold water by capillary forces, and by the permeability and connectivity of the fracture network, which enables water to be diverted around a drift or underground opening. Both properties determine the effectiveness of the capillary barrier in diverting flow and thus reducing seepage rates below the prevailing percolation flux. Percolation is the downward or lateral flow of water that becomes net infiltration in the UZ. The physical properties of water, together with the hydrologic properties of rock, lead to the prediction that much of the infiltrating water in the UZ will be preferentially diverted around openings, such as tunnels, at the potential mined geologic repository at Yucca Mountain. The percentage of infiltration that can become seepage decreases as infiltration decreases, and at low infiltration rates (<5 mm/yr) and most permeabilities, no seepage occurs (DOE 2001 [153849], Section 4.2.1.4.2). Two natural analogue studies confirm the prediction that most infiltration does not become seepage.

In a two-year study at Kartchner Caverns, Arizona, yearly precipitation ranged from 288 mm to 607 mm, and averaged 448 mm/yr (Buecher 1999 [154295], pp. 108–109). This was similar to the long-term average at two nearby stations. Estimates of seepage into the cave by three methods based on infiltration and precipitation measurements ranged from 4.3 mm/yr to 12.4 mm/yr, with an average of 7.9 mm/yr (Buecher 1999 [154295], p. 110). Thus, less than 2% of the available moisture became seepage. This low seepage occurs even though the cave, which covers an area of approximately 350 m (N-S) by 550 m (E-W), is cut by more than 60 mapped faults (Jagnow 1999 [154296], p. 49 and Figure 3).

The cave at Altamira, Spain, was monitored for 22 months by Villar et al. (1985 [145806]). The volume of water flowing from 9 of 14 "significant drips" was measured, and an average total

seepage of 7 liters/mo was reported. This volume is estimated to represent about 80% of the total seepage (Stuckless 2000 [151957], p. 6), which would bring the total seepage rate up to almost 9 liters/mo. Villar et al. (1985 [145806], Figure 4) also measured the average rainfall. Based on the data from Villar et al. (1985 [145806], Figure 4) the average annual rainfall was calculated to be approximately 1152 mm/yr or 1152 liters/yr/m^2 (Simmons 2002 [157544], p. 144). The average evapotranspiration was calculated as approximately 660 mm/yr (660 liters/yr/m^2), which results in an average net infiltration of about 480 mm/yr (480 liters/yr/m^2). The area of the painted cave studied was reported as 150 m^2, which would result in a monthly volume of infiltration water of about 6,000 liters/mo above the footprint of the area studied in the cave (Simmons 2002 [157544], pp. 143–144). As was the case at Kartchner Caverns, the rock is obviously fractured (Figure 8-1). Nonetheless, less than 1% of the infiltrating water seeped into the cave. The fact that the paintings have not been bleached or dissolved near the fractures suggests that little water has seeped in along fractures during the last 14,000 yrs, which is the age of the paintings (Stuckless 2000 [151957], p. 8).

Both of these examples are from limestone caves in fractured karst terrain. It follows from these examples that UZ flow would be dominated by fracture flow, just as it is at Yucca Mountain. Both caves are much closer to the surface than a potential repository at Yucca Mountain, and therefore, there is a much greater probability for fractures to communicate directly between the underground opening and the surface, thereby facilitating seepage. At the caves, a pulse of water enters at peak saturation, whereas at the potential repository horizon the amplitude of the water pulse is attenuated because of the damping effect of the PTn (BSC 2001 [155950], Section 3.3.3.1). This damping effect yields lower average saturations that are less conducive to seepage. At both Altamira and Kartchner Caverns, precipitation exceeds current rates at Yucca Mountain and those predicted for future climates as well. Thus, the observational data from these natural analogues support the conclusion that seepage into a potential repository at Yucca Mountain would be a very small percentage of the percolation flux, which will therefore result in a very small volume of water entering drifts.

8.3 ARCHEOLOGICAL EXAMPLES

The long-term quantitative hydrologic studies such as those cited above are not common, but there is abundant qualitative evidence that openings in the UZ divert much infiltration, thereby protecting fragile and easily destroyed items. The examples that follow are from both natural and man-made underground openings and include preservation of both anthropogenic and biological materials. The examples chosen are representative and are not meant to constitute an exhaustive listing.

The oldest and perhaps the best known examples of preservation of anthropogenic items within the UZ are the Paleolithic cave paintings of southwestern Europe. The Paleolithic cultural period lasted from 750,000 to 15,000 years ago. There are dozens of caves with paintings (Stuckless 2000 [151957], Figure 1); the oldest of those authenticated is the recently discovered cave of Chauvet, France (Figure 8-2). The cave is located in a subhumid region, with reported precipitation totals within the region ranging from 580 to 780 mm/yr (Stuckless 2000 [151957], p. 3). The Chauvet cave paintings depict animals that are now extinct, such as mammoths, and other species that no longer live in Europe, such as rhinoceroses (Chauvet et al. 1996 [152249]), which attest to a much different paleoclimate from the climate at present. The paintings in the

French caves were made largely with oxides of iron and other minor constituents (Leroi-Gourhan 1982 [156454] p. 105; Ruspoli 1987 [156223], pp. 192–193). Charcoal or manganese oxide was commonly used for black. Neither the iron and manganese oxide nor charcoal would be expected to survive long in the presence of abundant oxidizing water. This is evidenced by a painted block that fell from a painting of a bull at Lascaux, France, and lay painted side down on the damp floor. Although the block fit back into the painting, it had lost all evidence of paint (Breisch 1987 [156456], p. 286).

Well-preserved Paleolithic art is common only in the caves of southern Europe, but examples of late Paleolithic and, more commonly, Neolithic art from the Neolithic cultural period that began about 10,000 B.C. are known throughout the world. Stuckless (2000 [151957]) provides a summary and references for paintings in Africa, South America, North America, and Asia. In most of the world, painted rock shelters are more common than painted caves, which demonstrates that even a few meters of overhang can protect fragile art from infiltration water (Stuckless 2000 [151957], p. 9).

In addition to paintings, caves have preserved fragile artifacts such as the 14,000-year-old clay bison in a cave near Tuc d'Audoubert, France (Stuckless 2000 [151957], Figure 3). Some caves are located in zones of such low percolation flux that they have little, if any, measurable seepage flux. This supports another part of the UZ flow model in which seepage is predicted to decrease with a decrease in infiltration. Caves in Israel provide an example of this, where cloth, ivory, reed mats, and many bronze items have been preserved in a nearly perfect state (Schick 1998 [156641], Color Plates 3.7–3.9; Ozment 1999 [155058], pp. 74–75). These date from about 3,800 B.C., and although the climate is currently drier than that at Yucca Mountain, the preservation demonstrates that the lack of water allows even easily destroyed items to endure for long periods of time and suggests that the predicted zero seepage at low infiltration rates is likely correct.

Relatively dry caves are common throughout the southwestern United States. Because of the dryness, pollen and other delicate plant and animal materials have been preserved for tens of thousands to hundreds of thousands of years (Davis 1990 [144461]; Rogers et al. 2000 [154320]) in caves and lava tubes, respectively. In fact, Davis (1990 [144461], p. 338) notes that dryness in caves is critical to preservation of biotic remains. That such preservation is common is supported by the fact that over 1,000 packrat middens have been studied throughout semi-arid to arid North America, and some of these are older than 40,000 yrs (Davis 1990 [144461], p. 341). The middens are cemented with dried urine, which would dissolve readily in water. Nonetheless, the middens older than about 20,000 yrs (some of these were found near Yucca Mountain) have survived much wetter past climates, similar to those predicted for the future climate at Yucca Mountain, indicating that over a long period of time, little seepage has entered the openings where middens were found.

Underground openings in the UZ have been excavated by early civilizations, but these examples are generally much younger than those from natural systems. Nevertheless, they also provide evidence of the robust protection provided against the effects of water. In addition, these anthropogenic examples broaden the range of geologic settings that can be examined as analogues for a potential repository at Yucca Mountain.

Man-made underground openings include the Egyptian tombs across the Nile River from Luxor. These were excavated in limestone approximately 3,500 to 3,000 years ago. As noted in Section 8.2, this host rock is hydrologically similar in fracturing and low matrix porosity to the welded tuffs of Yucca Mountain. Although the climate is somewhat drier than that at Yucca Mountain, precipitation events have been strong enough to cause mud flows within the Valley of the Kings (Weeks 1998 [154297], pp. 10, 11). Seepage into the tombs is indicated by small areas of spallation of plaster, which can be seen in many tombs for both areas of wall and ceilings (Figure 8-3), but evidence of dripping, such as efflorescence or stalactitic formations, seems to be lacking.

Buddhist monks carved several temples into basalt flows at Ajanta, India, between the second century B.C. and the tenth century A.D. (Behl 1998 [156213], p. 27, 39). Water flow within the basalts would, as at Yucca Mountain, be dominated by fracture flow. The interiors of the temples are painted. The paintings were done on a plaster that consisted of mud, rock dust, and vegetable fiber. The climate at Ajanta is monsoonal, such that the precipitation (800 mm/yr), which is more than four times that at Yucca Mountain (Section 8.1), falls in four months (Stuckless 2000 [151957], p. 19). Nonetheless, many of the paintings are well preserved, except for small areas of spallation (Figure 8-4).

The Christians of Cappadocia, Turkey, excavated underground cities and churches during the second through eleventh centuries A.D. The geology here is similar to that of southern Nevada in that the bedrock is a thick sequence of silicic volcanic rocks. Visits to the underground cities and churches produced no evidence of dripping from the ceiling, but evidence for flow down a wall was found where a fracture intersected the wall (Stuckless 2000 [151957], p. 22). As with the Egyptian tombs and Buddhist temples, some of the church paintings showed evidence of spallation (Figure 8-5).

The caves at Carlsbad Caverns, New Mexico have stood open for as much as 11 m.y. (Polyak et al. 1998 [156159], p. 1919). During that time, seepage occurred as evidenced by stalactites, stalagmites, and flowstone. Today, only a small percentage of the seeps are active in spite of an average precipitation of approximately 500 mm/yr. This is more than twice the amount currently observed at Yucca Mountain and larger than that predicted for likely future climates.

In addition to showing that most infiltration does not become seepage, natural analogues demonstrate that much of the seepage that does occur stays on the walls rather than dripping into the openings. Figures 8-2 and 8-3 show evidence of water flow down walls. Figure 8-6 shows the soot-covered wall and ceiling of a kitchen excavated in the tuffs of Goreme (Cappadocia region), Turkey. The soot deposited along the fracture in the ceiling has been bleached out, presumably because of infiltrating oxygenated water. Stalagtitic deposits that might indicate dripping water do not exist, but the removal of soot below the fracture on the wall would have to be caused by some flow of water down the wall.

Perhaps the best analogue for water that might seep into the tunnels at Yucca Mountain can be seen at Building 810 in the Denver Federal Center, Colorado (Figure 8-7a). The roof of this building is constructed of a series of arches called barrels. Each represents a segment of a cylinder with a diameter of 25 ft, the same diameter as the Exploratory Studies Facility (ESF) at Yucca Mountain. As shown by the white efflorescent salt deposits, water has seeped through the

roof over the loading dock along fractures in the concrete and then flowed on the underside of the roof, until it either evaporates or reaches the vertical sections along the sides of the barrels, where it can drip. The undersurface shown in Figure 8-7b is smoother than much of the ESF tunnel, and thus it may be more effective in diverting seepage to the walls. In contrast, the roughness of the ESF walls may cause asperities that could focus drips. Nonetheless, it demonstrates how seepage could be directed in the tunnels.

8.4 EVALUATING THE ANALOGUES

Although there are many examples of Paleolithic and Neolithic art preserved in caves, questions persist about whether an equal or perhaps even larger number of paintings have been completely destroyed. Null evidence is difficult to evaluate, but a few lines of evidence suggest that paintings have not been totally destroyed in caves where they may have once existed.

First, if paintings had been completely destroyed in some caves, or even parts of caves, one would expect most, if not all, localities to exhibit either a spectrum of preservation from largely destroyed to fully preserved paintings. Alternatively, there should be an explanation for the binary distribution. A variety in the degrees of preservation of cave art was not found in the current literature search, either within individual caves or in the body of literature as a whole. A cave at Palomera in Burgos, Spain, like the cave at Cosquer, has had some paintings removed by water while others are in good condition. This cave, which has paintings dated at 10,950 +/- 100 to 11,540 +/- 100 B.P. (Corchon et al. 1996 [156636], pp. 41–44), has at times had a stream flowing in it that has left organic debris plastered to heights of several meters on the walls. The flooding is younger than the paintings and has apparently destroyed the paintings to the height of the flooding. Lascaux provides another example where one gallery has had over 90% of the paintings removed by wind abrasion (Breisch 1987 [156456], p. 286).

Second, areas where paintings would be least likely to survive, such as drip sites in the ceiling or flow channels on the walls of caves, have probably been the loci of flow for thousands of years. Early man would likely have avoided these areas, because they were too wet to paint. Exceptions to this hypothesis are known. For example, one painting on the ceiling at Chauvet is partly covered by stalactitic calcite (Chauvet et al. 1996 [152249], p. 47). Some paintings have thin coatings of calcite caused by evaporation of thin films of water.

Finally, the shear number of painted caves and the number of paintings in some of the caves argues for a high degree of preservation. In France and Spain alone, there are more than 150 painted caves (Ruspoli 1987 [156223], p. 18). Grand (1967 [156218], p. 28) reports over 2,188 paintings of animals in 110 caves.

In the case of rock shelters, some observational data correlate with preservation or destruction. In sandstone shelters in India, the roots of banyan trees have been noted to provide a preferential path for water across a painting. The part of the painting exposed to water has been encrusted with calcium deposits, "while leaving another part of the same figure—untouched by water—unscathed" (Neumayer 1983 [156221], p. 6).

Not all underground openings provide appropriate analogues. The previous examples of caves and underground openings were all <100 m from the surface. The Mission Tunnel through the

Santa Ynez Mountains near Santa Barbara, California, is closer in depth (200 to 670 m from the surface) to the potential mined geologic repository (300 m depth), as compared to the previous examples. The Mission Tunnel exhibits rapid response to precipitation events and large amounts of seepage flux (1.23 million m^3/yr; Boles 1999 [156635]). Unfortunately, quantitative measurements have not been made, so the percentage of infiltration that becomes seepage is unknown. However, the apparently large amounts of seepage into the Mission Tunnel are caused by flow paths that are within nearly vertical, highly transmissive, fractured sandstone units (Boles 1999 [156635]). Furthermore, at least some part of the flow could be from groundwater seeps below the water table (Boles 1999 [156635]). Thus, the hydrogeology for this potential analogue is drastically different from that for the potential repository at Yucca Mountain, where the hydrologic units are gently dipping and few through-going fractures have a hydrologic connection with the surface.

Mitchell Caverns, located on the eastern slope of the Providence Mountains in the East Mojave National Preserve, California, may also be a potential location for study of seepage. The caverns are found at an elevation of 1,341 m (4,400 ft; Pinto 1989 [156638], p. 6) in a wedge of Permian limestone (approximately 300 Ma; Norris 1999 [156637], p. 10). The limestone layers are upended, folded, and highly fractured by intrusion of younger Jurassic quartz monzonite (approximately 160 Ma; Miller et al. 1991 [156458], Plate 1).

The larger of the caves accessible to the public, Tecopa, exhibits soda straw features, which are hollow stalactites in early stages of development. Tecopa, however, is a drier cave than the other publicly accessible cave, El Pakiva, and is said to be aging. Because Tecopa has two entrances, it is more influenced by the surface environment than El Pakiva cave, which tends to dry out more quickly after a rainfall. Approximately 10 drip locations were observed to begin a few days after a rainfall. All but one of these are in El Pakiva Cave, which is less than 30 m (100 ft) from the surface (Simmons 2002 [157544], pp. 124–125).

The speleothems are nearly inactive under present climate conditions; there are no continuous seeps. The caves respond rapidly after a rainfall. Dripping can be observed to last from a variety of locations up to 28 days after a heavy rainfall (Simmons 2002 [157544], p. 126). Mean annual precipitation measured at the caverns is 18.6 cm (Stein and Warrick 1979 [156642], p. 12).

Because the fractured limestone in which Mitchell Caverns are situated has rapid communication with the ground surface along fracture flow paths after a rainfall, and because there is a considerable bedrock catchment basin above the caves that would enduce seepage, they are not an ideal analogue to the conditions expected at Yucca Mountain. Instead, Mitchell Caverns may provide an intermediate analogue between the cave at Altamira, Spain, where very little water has seeped along fractures, and the Mission Tunnel, California, which experiences heavy flow along numerous surface-intersecting pathways.

8.5 SUMMARY OF SEEPAGE ANALOGUES

One important variable for preservation in underground openings is relative humidity. It is obvious that if relative humidity in the drift is kept below 100% by ventilation, then seepage of liquid water would be reduced or completely suppressed. Most caves are close to but below 100% humidity (e.g., Kartchner RH=99.4 % (Buecher 1999 [154295], p. 111); Altimira RH=98

+/- 2% (Breisch 1987 [156456], p. 290; Quindos 1987 [156640], p. 555)). These caves are naturally ventilated; thus, the amount of seepage in these caves would be expected to be low. This would also be true at Yucca Mountain while ventilation is maintained.

This section has examined several different types of qualitative and quantitative natural analogues. The findings support the hypothesis that most of the infiltrating water in the UZ is diverted around underground openings and does not become seepage. The analogues show that this is true even for areas with much greater precipitation rates than that at Yucca Mountain. Although examples exist where large amounts of seepage can be observed (e.g., the Mission Tunnel and Mitchell Caverns), the hydrogeologic setting is significantly different from that at Yucca Mountain, and thus, these are not appropriate analogues. However, for all of the analogues that show some seepage, at least some of the seepage that enters underground openings does not drip, but rather flows down the walls. In the few instances where dripping has been noted in settings that are analogous to Yucca Mountain, the drips can be attributed to asperities in the surface of the roof and ceiling of the opening. Whether water flows on walls or drips depends on conditions affecting drop formation and drop detachment (e.g., surface tension, roughness angle, saturation). Thus, by analogy at Yucca Mountain, although most water would flow around emplacement drifts, the small amount of seepage that would occur would primarily flow down tunnel walls. In the few instances where dripping may occur, it would be expected to be attributable to asperities in the tunnel ceilings.

NOTE: There is no apparent water damage near fractures through both the iron oxide and charcoal portions of the 14,000-year-old painting.

Source: Stuckless 2000 [151957], p. 8.

Figure 8-1. Painted Bison from the Ceiling of the Cave at Altamira, Spain

NOTE: Although there is evidence of water flow down the wall, in general, there is still good preservation.

Source: Chauvet et al. 1996 [152249], Figure 49 (used with permission of the French Ministry of Antiquity).

Figure 8-2. 32,000-year-old Painted Auroches and Horses from Chauvet Cave

NOTE: The tomb shows no evidence of dripping from the ceiling, but plaster on the wall has been damaged by moisture, and some of the paint shows evidence of water running down the wall. The tomb was excavated in limestone about 1,400 B.C.

Source: Simmons 2002 [157544], p. 141.

Figure 8-3. The Painted Interior of the Tomb of Sennefer

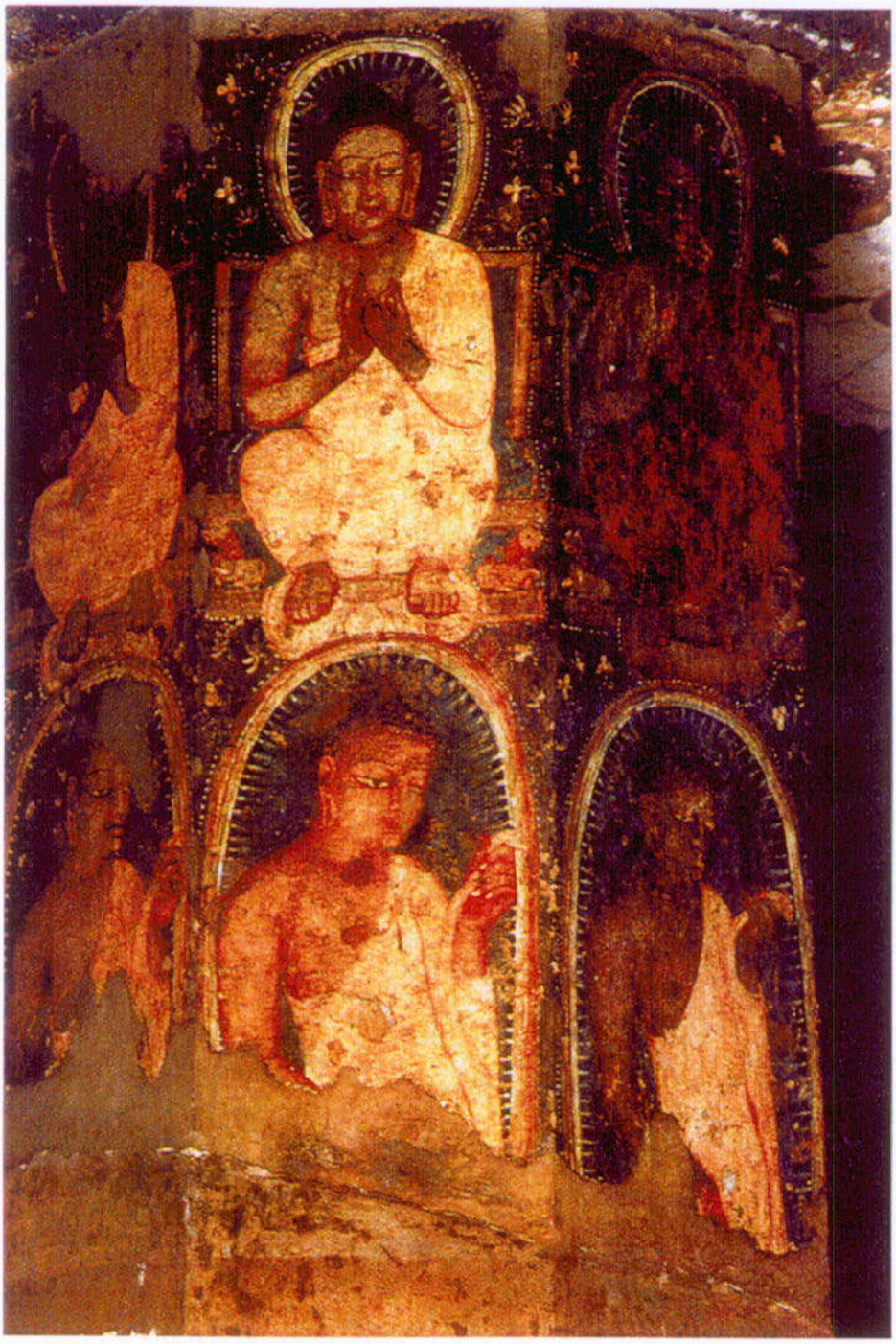

NOTE: The hexagonal column is from the second century B.C.

Source: Behl 1998 [156213], p. 42.

Figure 8-4. Painting from the Underground Ajanta Temple in India Is Fairly Well Preserved in Spite of Its Age and the Wet Climate

NOTE: The perfectly preserved painting on the left was painted in the eleventh century A.D. The painting on the right shows damage from vandals and from spallation of the plaster.

Source: Stuckless 2000 [151957], p. 23.

Figure 8-5. Frescoes on the Ceiling and Walls of the Karanlik Church at Goreme, Turkey, Show Varying Degrees of Preservation, but No Evidence of Dripping from the Ceiling

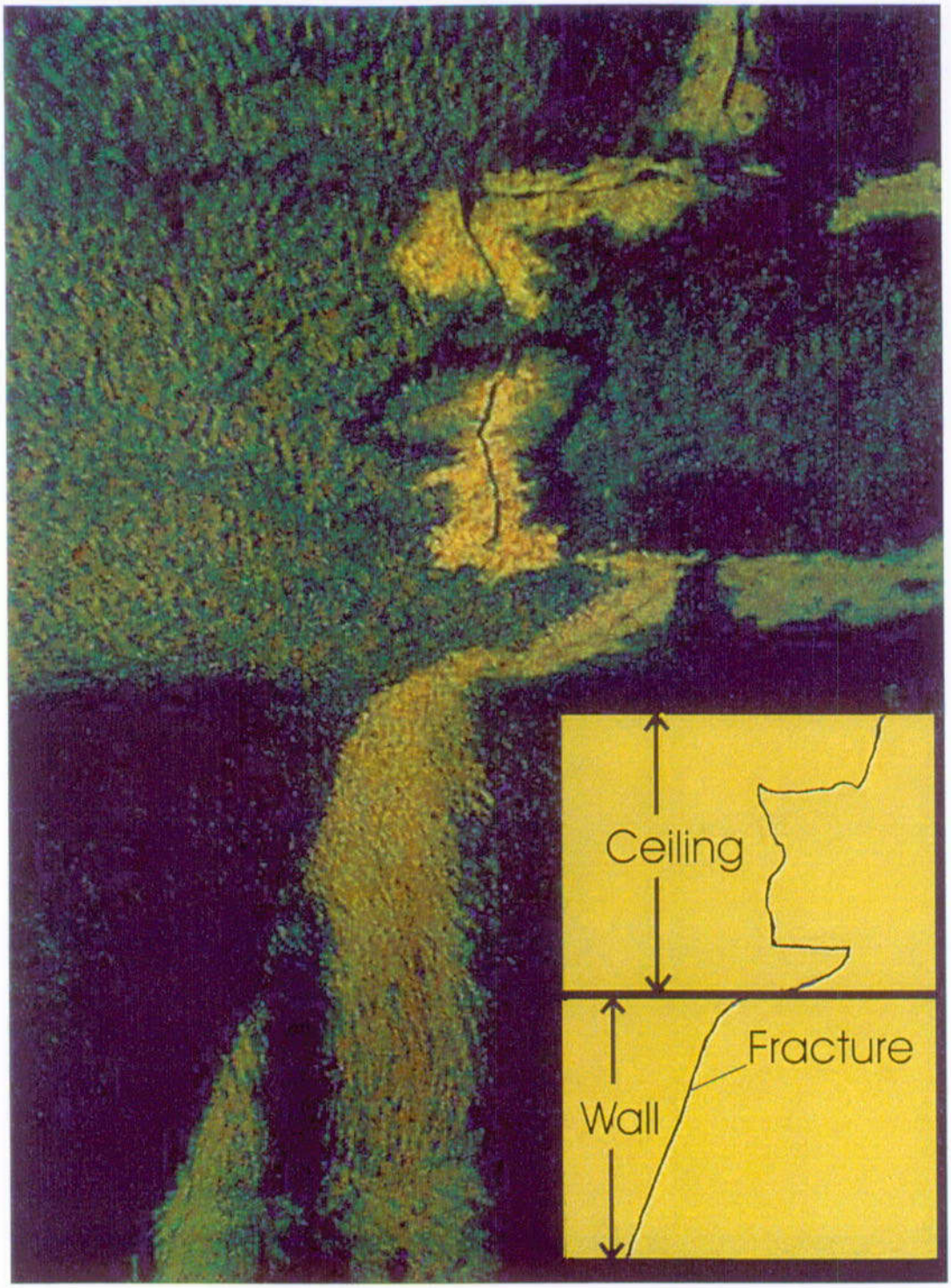

NOTE: The kitchen was excavated into ash flow tuff and was probably in use until the twelfth century A.D. The soot has been removed adjacent to the fracture in the ceiling, possibly by oxidation. Flow has occurred down the wall, as evidenced by removal of some of the soot below the fracture.

Source: Stuckless 2000 [151957], p. 24.

Figure 8-6. Photograph and Drawing of a Fracture in the Blackened Wall and Ceiling of a Kitchen in a Subterranean Monastery at Goreme, Turkey

a)

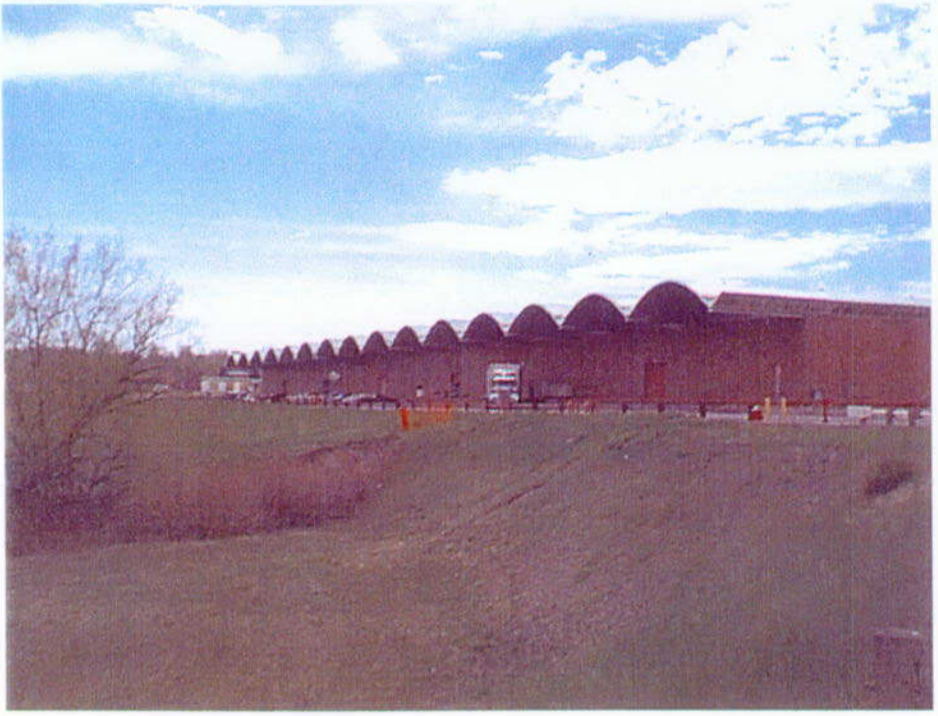

b)

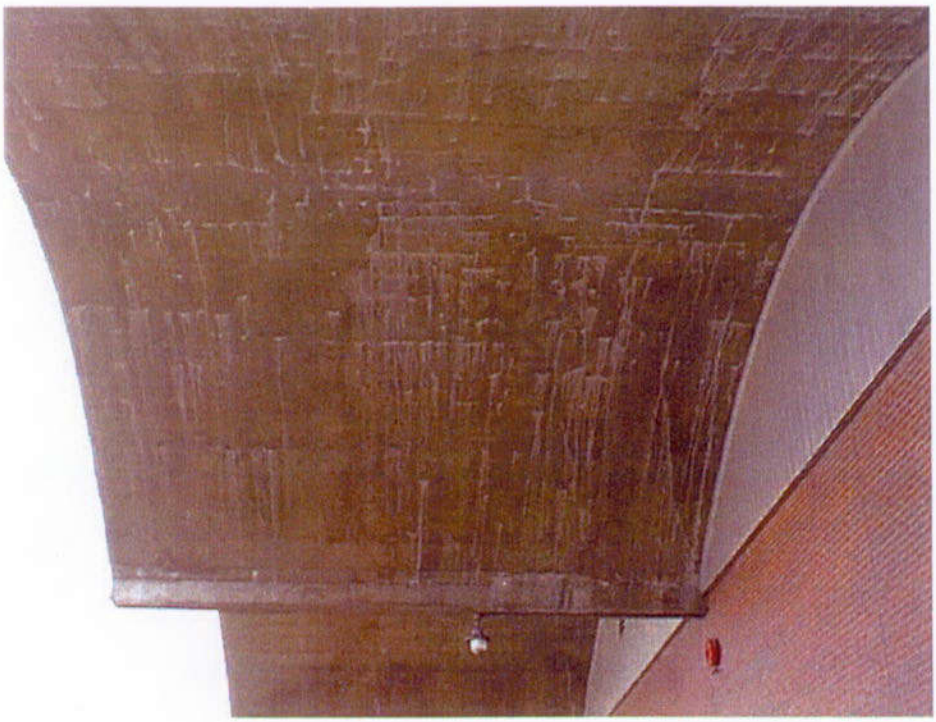

NOTE: Water has seeped along joints in the concrete, but rather than dripping, it has flowed along the curvature of the roof.

Source: Simmons 2002 [157544], p. 142.

Figure 8-7. Photograph of Building 810 in the Denver Federal Center, Colorado (a), and Close-up of the Underside of the Roof over the Loading Dock (b)

9. ANALOGUES FOR UNSATURATED ZONE FLOW

9.1 INTRODUCTION

The conceptual and numerical modeling methodologies for the unsaturated zone (UZ) at Yucca Mountain are applicable to other sites, including Apache Leap (Arizona), Box Canyon (Idaho), Rainier Mesa (Nevada), and other semi-arid sites in fractured rock. These and other examples are presented in *Natural Analogs for the Unsaturated Zone* (CRWMS M&O 2000 [141407]) and in the *Yucca Mountain Site Description* (CRWMS M&O 2000 [151945], Sec. 13). Analogues for climate and infiltration processes are presented in the *Yucca Mountain Science and Engineering Report* (S&ER) (DOE 2001 [153849], Table 4-5). Analogues for UZ flow and seepage processes are listed in the S&ER (DOE 2001 [153849], Table 4-6). In general, these analogues contribute to providing confidence in the understanding of paleoclimatic conditions, the bounds on various climate models, the efficacy of a UZ in isolating nuclear waste, the occurrence of very limited seepage in the UZ, and limited fracture-matrix interactions.

Section 9 presents results of a quantitative analogue investigation that had the objective of utilizing related data sets gathered at the Idaho National Engineering and Environmental Laboratory (INEEL) to test the dual-permeability approach of the Yucca Mountain UZ flow model at another site in an attempt to match results of field tests, thus building confidence in the UZ modeling approach. This section also presents a number of possible locations and configurations for testing the drift shadow zone concept in analogous settings and conditions.

9.2 UZ FLOW MODEL

The UZ flow model is described in *Unsaturated Zone Flow and Transport Model Process Model Report* (UZ PMR) (CRWMS M&O 2000 [151940]) and in the S&ER (DOE 2001 [153849], Section 4.2.1). Available site data are used to provide infiltration and percolation flux distributions and hydrologic properties. The model accounts for the occurrence of perched water and the effects of the PTn unit and fault zones on flow in the UZ.

Upper bound limits on infiltration rates and percolation fluxes at Yucca Mountain are estimated based on multiple approaches, including analyses of chloride and chlorine-36 isotopic ratios, calcite deposition, and the occurrence of perched water. The analysis of chloride data indicates that the average percolation rate over the model domain at Yucca Mountain is about 4.6 mm/yr. Analysis of calcite deposition gives infiltration rates of 2 to 20 mm/yr in the vicinity of borehole USW WT-24. To match perched water occurrences, three-dimensional model calibrations require that the present-day infiltration rate be greater than 1 mm/yr, with an upper limit of about 15 mm/yr (DOE 2001 [153849], Section 4.2.1.3.2). Infiltration and flow patterns at Yucca Mountain are summarized below.

Rainfall for the modern mean climate is about 190 mm/yr (7.5 in/yr) resulting in average steady-state net infiltration of 4.6 mm/yr (0.18 in/yr, DOE 2001 [153849], Table 4-11). The net infiltration is episodic, with a significant amount infiltrating only every few years. There is large spatial variability of infiltration, with most water infiltrating on ridge-tops and in the upper reaches of washes where there is little alluvial cover. Fracture flow dominates in the Tiva Canyon welded hydrogeologic unit (TCw), transmitting water rapidly through the TCw to the

underlying Paintbrush tuff nonwelded hydrogeologic unit (PTn). Flow through the PTn is primarily matrix flow with most of the fast flow occurring via faults, although this represents only a very small fraction of the total flow. Lateral flow occurs in the PTn.

Episodic flow into the Topopah Spring welded hydrogeologic unit (TSw) is damped by the PTn to the extent that flow can be considered steady-state at the boundary to the TSw. However, at or near major faults, episodic flow may still persist through the PTn. Fracture flow dominates in the TSw because this unit is densely welded and highly fractured; additionally, within some subunits of the TSw, the low-permeability matrix is incapable of transmitting the percolation flux estimated to be moving through the unit. Fracture flow in the potential repository horizon, which intersects the Topopah Spring middle nonlithophysal, lower lithophysal and lower nonlithophysal stratigraphic units, is estimated to range from 84 to 94 percent of the total water flow.

Water drainage in the potential repository units is expected to be good, owing to the generally high fracture permeability (~10^{-11} to 10^{-10} m^2 [10^{-10} to 10^{-9} ft^2]) (DOE 2001 [153849], Section 4.2.1.2.5). Evidence for fast or preferential flow is seen at the potential repository horizon, primarily near major faults. It is estimated that the fast component of flow is less than a few percent of the total flow.

9.3 THE SUBSURFACE DISPOSAL AREA AT THE IDAHO NATIONAL ENGINEERING AND ENVIRONMENTAL LABORATORY AS AN ANALOGUE FOR TESTING YUCCA MOUNTAIN MODELING APPROACHES

This section discusses modeling of UZ flow and tracer tests at INEEL. Modeling of UZ transport at this site is discussed in Section 10. Section 9.3.1 provides information on the geologic and hydrologic setting of the Radioactive Waste Management Complex (RWMC) at INEEL as background for a flow modeling study in Section 9.3.2 and a radioactive transport model in Section 10.3. Further discussion comparing similarities and differences between INEEL and Yucca Mountain is found in Section 10.3.5.

9.3.1 Background

Between 1952 and 1986, approximately 180,000 m^3 of transuranic and low-level radioactive mixed wastes, containing about 9.5 million curies of radioactivity, were buried in unlined trenches and pits in shallow sediment above basalt flows at the INEEL in the 144,100 m^2 Subsurface Disposal Area (SDA) of the Radioactive Waste Management Complex (RWMC) (Cecil et al. 1992 [156256], p. 709). Included with these buried wastes were approximately 334,000 liters of transuranic-contaminated mixed-waste sludges that were absorbed on calcium silicate and placed in 55-gallon steel drums (Rawson et al. 1991 [156439]). Since 1970, transuranic wastes have been stored in containers placed above ground on asphalt pads in a part of the RWMC known as the transuranic disposal area. Subsurface disposal of radioactive waste at the SDA is planned to continue until at least 2003 (Lockheed Idaho Technologies Company 1995 [156430]). Environmental monitoring beneath the SDA in both the unsaturated and saturated zones has resulted in positive detections of americium, plutonium, and other waste products that have migrated from the SDA (Dames and Moore 1992 [157409], pp. 73–74; Becker et al. 1998 [157407], pp. 4-36 to 4-37), thereby raising concerns about the long-term

water quality of the Snake River Plain Aquifer (SRPA), the principal source of potable groundwater in the area. Effort is underway to evaluate the long-term risk posed to the aquifer by past waste-disposal practices (Magnuson and Sondrup 1998 [156431]; Becker et al. 1998 [157407]) and to determine the necessity of potentially costly remedial strategies, including exhumation and redisposal of the buried waste.

9.3.1.1 Geologic and Hydrologic Setting

The geologic and hydrologic setting of the RWMC has been described in a series of reports by the U.S. Geological Survey (USGS) and the U.S. Department of Energy (DOE) and its contractors (e.g., Rightmire and Lewis 1987 [156440]; [156441]; Magnuson and Sondrup 1998 [156431]). The top of the surficial sediment in which the wastes are buried is approximately 175 to 180 m above the regional water table. The thick UZ beneath the SDA contains 13 individual basalt flows ranging in thickness from less than 1 m to 17 m and averaging about 5 m in thickness (Knutson et al. 1990 [107839], p. 21). The individual basalt flows can be subdivided into four zones, with varying amounts of rubble, vesicles, and fractures, and grouped on the basis of the presence of three major sedimentary interbeds. Three sedimentary interbeds at 9 m, 34 m, and 73 m have been used to subdivide the basalts into A-, B-, C-, and D-group basalts; correspondingly, the 9 m, 34 m, and 73 m interbeds are alternatively known as the A-B, B-C, and C-D sediment layers (Figure 9.3-1).

Annual precipitation at INEEL ranges from 13 to 36 cm/yr, with an average of 20 cm/yr. About 30 percent of the annual precipitation typically occurs as snow (Barraclough et al. 1976 [156426], p. 45). Chlorine-36, tritium, and neutron-logging data from a series of shallow boreholes drilled just outside the northern boundary of the SDA provided estimates of background infiltration rates for undisturbed soils of 0.36 to 1.1 cm/yr (Cecil et al. 1992 [156256], p. 709). Infiltration rates within the SDA have been estimated to be higher than the background infiltration rates because of the drifting and accumulation of snow within the SDA. Based on neutron-probe measurements of soil moisture changes for the years 1994 to 1995 and weather data extending back to 1952, Martian (1995 [156432], pp. 32–36) estimated that the spatially and temporally variable infiltration rates within the SDA have averaged between 6 and 10 cm/yr since 1952. Only two of the seventeen neutron-probe boreholes were located in the soils within the trenches; therefore, moisture content changes and infiltration rates through the trench fill are not as well characterized as the areas between the trenches. In addition, the SDA has been flooded three times (1962, 1969, and 1982) as a result of the local accumulation of overland flow associated with rapid snowmelt (Vigil 1988 [157416], p. 1, 8). Estimates have been made of the amounts of water that infiltrated (Vigil 1988 [157416]) and which areas of the SDA were flooded (Magnuson and Sondrup 1998 [156431], Figures 2–17). The average depths of the infiltrated water in the flooded areas in the SDA were estimated by Magnuson and Sondrup (1998 [156431], Tables 2–3) to be 0.17 m in 1962, 0.12 m in 1969, and 0.08 m in 1982.

Perched water has been encountered by boreholes within the SDA at depths that correspond roughly to the tops of the sedimentary interbeds (Rightmire and Lewis 1987 [156441], pp. 43–45, Figure 10). Rightmire and Lewis (1987 [156441], p. 45) proposed a hypothesis that the source of at least some of the perched water was actually infiltration from spreading areas, located about 1.7 km to the southwest of the SDA. This infiltration migrated laterally in the UZ along and across the interbeds. Water is diverted from the Big Lost River into these spreading

areas during periods of high flow (>14 m^3/s) to minimize flooding to downstream areas. Support for the hypothesis that the deeper perched water beneath the SDA originated from the spreading areas seemed to Rightmire and Lewis (1987 [156441], p. 65) to be provided by delta-deuterium (δD) and delta oxygen-18 ($\delta^{18}O$) data. The δD and $\delta^{18}O$ values of the deep perched water indicated little evidence for evaporation compared to shallow perched water or to groundwater from the regional aquifer, a relation that Rightmire and Lewis (1987 [156441]) considered to be consistent with their hypothesis that the deep perched water originated from the rapid infiltration (and minimal evaporation) of large amounts of water through the spreading areas. For a comparison of the hydrologic settings of INEEL and Yucca Mountain, see Section 10.3.5.1.

9.3.1.2 Surficial Sediments and Sedimentary Interbeds

The surficial sediments consist of the undisturbed areas between the waste trenches and the trench backfill, which is a mixture of excavated material. In some cases, the trenches and pits were originally excavated down to the top of the uppermost basalt layer; however, in these cases a sediment buffer ranging in thickness from 0.67 to 1.0 m was placed in the trench between the waste and the underlying basalt (Rawson et al. 1991 [156439]).

9.3.1.2.1 Mineralogy

The predominant minerals in surficial sediments and sedimentary interbeds are quartz, plagioclase with the composition of labradorite, pyroxene (probably augite), potassium feldspar, clay, and calcite (Rightmire and Lewis 1987 [156441], p. 11). The percentage of clay is higher and the percentages of plagioclase, potassium feldspar, and pyroxene are lower in the surficial sediments compared to the sedimentary interbeds. Calcite is often 10% or more by weight of the surficial material and sedimentary interbeds (Rightmire and Lewis 1987 [156441], p. 26), with much higher percentages of calcite present locally.

The 9 m interbed (A-B Sediment Layer) contains some organic-rich paleosols, with the organic material possibly introduced by infiltrating water, as well as a red color (due to the oxidation of ferrous iron derived from minerals in the nearby basalts). The 34 m interbed (B-C Sediment Layer) also contains a dark-brown organic-rich soil horizon and caliche, amorphous silica, and Ca-smectite. The 73 m interbed (C-D Sediment Layer) has a red color resulting from iron oxyhydroxides throughout its entire thickness (Rightmire and Lewis 1987 [156441], pp. 24–28).

A study of the clay mineralogy of the surficial sediment, the sedimentary interbeds, and fill material of fractures in the basalt indicated that the dominant clay species are illite, followed by mixed illite/smectite, and finally, kaolinite plus chlorite (Rightmire and Lewis 1987 [156441], Table 8). The smectite that is present is mainly a calcium smectite (Rightmire and Lewis 1987 [156441], p. 40).

9.3.1.2.2 Geochemical Properties

Four measurements of the cation exchange capacity (CEC) of the surficial sediments ranged from 11 to 27 meq/100 g, with an average of 19 meq/100 g (Rightmire and Lewis 1987 [156441], Table 5). There was no apparent correlation between the CEC and the clay content of the sediments. The CEC of the interbed sediments is highly variable (0.9 to 36 meq/100 g) and

appears to be related to the percentage of the expandable layer clays present as either pure smectite or mixed illite/smectite (Rightmire and Lewis 1987 [156441], pp. 33–34).

The distribution coefficient (K_d) values of various radionuclides are given for the surficial sediments, sedimentary interbeds, and basalts in Table 9.3-1 (Dicke 1997 [157410], Table 1). The K_d values were measured using composite samples from the interbed sediments and crushed basalts with the fines removed. The reported values for Am, Cs, Co, Hg, Pu, Sr, Tc, and U were based on site-specific data, with values for other elements estimated from the literature or by analogy with chemically similar elements (Dicke 1997 [157410], pp. 10–11). In cases where literature values were used, the data were screened to remove those values obtained using water compositions very dissimilar to that of water that is present in the UZ beneath the SDA. Data from the literature were also adjusted to reflect differences in the amount and type of clays present in the test material and in the surficial and interbed sediments (Dicke 1997 [157410], p. 5). The data indicate higher K_d values for the sediments, possibly because of a greater amount of reactive minerals, such as smectite, in the sediments. Because the interbed sediments were combined in a single sample, there is no basis for estimating how the sorptive properties vary among the interbeds.

9.3.1.2.3 Unsaturated Zone Matric Potentials

A summary of the matric potentials measured beneath the SDA in the surficial sediments and sedimentary interbeds using tensiometers, heat-dissipation probes, and gypsum blocks was presented by McElroy and Hubbell (1990 [156433]). In the surficial sediments, the shallowest measurements ranged between about -0.2 and -1.3 bars, reflecting seasonal wetting and drying cycles. The deepest measurements taken from near the sediment/basalt interface were near 0 bars, indicating near-saturated conditions. Hydraulic gradients varied over time, ranging between upward and downward flow within the upper 1.2 to 3.3 m of the sediment profile, depending on the location of the borehole, but were consistently downward beneath this range of depths.

The equilibrium matric potentials within the 9 m, 34 m, and 73 m interbeds were between -1.4 and -0.3 bars. In general, wetter conditions existed at the tops of the interbeds compared to the bottoms, and hydraulic gradients across the interbeds were greater than unity.

9.3.1.2.4 Unsaturated Zone Gas Chemistry

Soil gas samples taken from a 0.3 to 0.76 m depth in the surficial sediment at a site approximately 11 miles from the SDA were reported by Rightmire and Lewis (1987 [156441], Table 12). The data from this site may be representative of conditions at the SDA prior to its development as a waste disposal area. The chemistry of the soil gas samples closely resembled the chemistry of air, except for CO_2(g), whose concentration in the soil gas was several times higher than in the atmosphere. The logarithm of carbon dioxide partial pressure (log P_{CO2}) and the delta carbon-13 value ($\delta^{13}C$) of the CO_2(g) were observed to vary seasonally and with depth in the soil zone. Rightmire and Lewis (1987 [156441], p. 59) concluded that log P_{CO2} values (expressed as bar) of -2.84 to -3.04, and $\delta^{13}C$ values of -15.5 to -19.6 per mil were characteristic of shallow soil zone gas in late spring, summer, and early autumn, and that log P_{CO2} values of -2.97 to -3.09, and $\delta^{13}C$ values of -16.4 to -17.2 per mil were characteristic of shallow soil zone gas in early spring. Snow melt in early spring has been hypothesized to be the principal source of

recharge at the SDA (Rightmire and Lewis 1987 [156441], p. 59). A comparison of the geochemical settings of INEEL and Yucca Mountain is presented in Section 10.3.5.2.

9.3.2 Modeling the Large-Scale Aquifer Pumping and Infiltration Test at INEEL

Regional and local-scale Large-Scale Aquifer Pumping and Infiltration Test (LPIT) models were developed as a goal of this work to address issues related to the fate and transport of radionuclides from the RWMC. Modeling activities related to this work were documented in Simmons (2002 [157578], SN-LBNL-SCI-186-V1, pp. 17–21). A companion study that used some of the same data sets to investigate radionuclide retardation is presented in Section 10.3. A location map of the RWMC and SDA sites within INEEL is provided in Figure 9.3-2. Statistically significant radionuclide concentrations have been measured as deep as 43 m (140 ft) and possibly deeper (Becker et al. 1998 [157407], pp. 4-23 to 4-39) beneath the SDA in core samples from a sedimentary interbed. This is thought to be a consequence of the SDA having been flooded in 1962, 1969, and 1982 (Section 9.3.1.1), when infiltrating water may have initiated subsurface migration of the plutonium-contaminated waste. The migration pathway is suspected to be vertically downward through the unsaturated basaltic lava flows and then laterally on the low permeability (silt, clay) interbeds as ponded-water conditions develop. Lateral transport of the radionuclides is suspected to have been enhanced by water infiltrating from the spreading area (Figure 9.3-2), causing ponded-water conditions at a scale significantly larger than the SDA. The fate and transport of radionuclides at the regional scale involves the RWMC, the spreading area, and the inferred saturated zone pathway potential that radionuclides would take from beneath the RWMC to the INEEL boundary (Magnuson and Sondrup 1998 [156431]).

Migration of radionuclides from the RWMC is dependent upon the mechanisms controlling unsaturated flow of infiltrating water. It is also dependent upon the fate and transport of radionuclides within the infiltrating water as it flows through the undulating fractured basaltic lava flows and sedimetary interbeds beneath the SDA. To address these issues, the LPIT was conducted in the summer of 1994 to mimic the intermittent flood events observed at the SDA. The test was located approximately 1.43 km south of the RWMC within the same geological units (Figure 9.3-2). Details concerning the location, design, implementation, and data sets collected during the LPIT are summarized in Dunnivant et al. (1998 [156402]). Magnuson (1995 [156404]) developed a numerical model to simulate the highly transient water infiltration and ponding conditions that existed during the LPIT, as well as transport of the conservative selenium (^{75}Se) tracer introduced in the infiltrating water. The modeling approach involved determining parameters controlling unsaturated and saturated flow and transport in the fractured basalt and sedimentary interbeds. The model was calibrated to ponded water hydrographs and ^{75}Se breakthrough curves within the ponded water measured during the LPIT.

The goal of the new modeling presented in Section 9.3.2 was to build confidence in the modeling approach used for UZ process modeling at Yucca Mountain by comparing simulations to results of the LPIT. To achieve the goals of this work, both regional and local-scale LPIT models were developed. These models were based upon the work of Magnuson (1995 [156404]) and Magnuson and Sondrup (1998 [156431]). The sequence of model development was first to use a local-scale LPIT model (Figure 9.3-2) to determine a set of hydrological parameters by simultaneous calibration to multiple hydrographs, while using a dual-permeability representation

of the basalt fracture and matrix continua. These parameters would represent the large-scale properties of the lithological units affected by the field-scale LPIT test as used in the dual-permeability approach rather than local-scale heterogeneities influencing individual hydrographs. Calibration of the model to the LPIT hydrographs and ^{75}Se breakthrough curves is important from the perspective of the work conducted in support of the potential Yucca Mountain repository. This is because it tests confidence in the dual-permeability approach, which is also used to represent flow and transport processes that are anticipated to occur in the tuff fracture and matrix continua at Yucca Mountain. The next step in the sequence of model development was to use hydrological parameters obtained from the LPIT calibration to simulate the fate and transport of radionuclides from the SDA in the regional model. The dimensions of the regional model are shown in Figure 9.3-2. Results presented here are limited to the LPIT analysis.

9.3.3 Conceptual and Numerical Model

The LPIT consists of a 183 m diameter infiltration pond that was constructed by removing surficial soil to build a 1.5 m high earthen berm. The floor of the infiltration pond was highly uneven, with approximately 80% of the basin floor consisting of a thin layer of soil overlying the basalt, while the remaining 20% consisted of exposed and elevated basalt. The water depth in the infiltration pond ranged from 0.3 m to 2 m (Dunnivant et al. 1998 [156402], p. 950). The area beneath the infiltration pond that was instrumented and influenced by the LPIT test consists of three separate basalt flows (the A, B, and C basalts) with a laterally continuous dense clay sedimentary interbed between the B and C basalts. No sedimentary interbed was found between the A and B basalt flows at the LPIT site.

The three-dimensional model (3–D) made to represent the region influenced by the LPIT used a radial coordinate approach consisting of 20 spokes evenly spaced at 18 degree intervals. The centroids of the elements are shown in plan view in Figure 9.3-3a, which shows contours of the elevation of the top of the B-C interbed. A radial coordinate approach was used because during the LPIT, the infiltrating water was observed to pond on the B-C interbed. It was expected to flow radially away from the perimeter of the infiltration pond, with flow controlled by the topography of the B-C interbed. Lateral flow caused by ponding on the B-C interbed was detected in wells located on the B, C and E rings (Figure 9.3-3a) at several locations (Burgess 1995 [156401]). The perimeter of the LPIT model was located sufficiently far from the E ring to remove any influence of boundary conditions. The surface of the B-C interbed is irregular and is crudely approximated by the plan-view discretization shown in Figure 9.3-3a. Note that this discretization does not place the centroid of a node at the exact position of a well where a specific hydrograph was measured and therefore at the exact elevation of the B-C interbed. This approximation was adopted because of constraints in model size required to achieve reasonable calibration times.

Figure 9.3-3b shows a vertical E-W cross-sectional cut through the center of the model. This figure shows the undulating thickness of the A and B basalts and the B-C interbed. The centroids of the elements are shown in cross section in Figure 9.3-3b, indicating significant mesh refinement at the interface between the B basalt and B-C interbed. Grid refinement exercises necessitated 0.02 m thick elements at this interface to obtain a convergent solution to the physics of water ponding on top of the B-C interbed, while simultaneously imbibing and infiltrating through it. In total, 28 elements were used to discretize the domain in the vertical direction.

Figure 9.3-3b also shows the steady-state water saturations in the fracture continuum calculated using a background infiltration rate of 0.01 m/yr (Cecil et al. 1992 [156256], p. 713). Simulation results indicate that the silt/clay-like nature of the surficial sediments and B-C interbed retain a higher water saturation than the basalt fracture continuum.

Unsaturated flow was simulated using iTOUGH2 with the EOS9 module, which solves Richards' equation, while ^{75}Se transport was simulated using the EOS7r module. The mesh was constructed using a dual-permeability representation for the basalt fracture and matrix continua, while the surficial sediments and B-C interbed were simulated as a single matrix continuum. The dual-permeability grid is used in an analogous manner to that used in simulating site-scale unsaturated flow at Yucca Mountain (Barenblatt et al. 1960 [156255]; Pruess and Narasimhan 1985 [101707]; Bandurraga and Bodvarsson 1999 [103949]). Within the context of the dual-permeability approach, various methods are proposed to reduce the interfacial area between the fracture and matrix continua, and hence the degree to which they interact. They range in complexity from a constant scaling factor (Bandurraga and Bodvarsson 1999 [103949]) to the "active fracture" model of Liu et al. (1998 [105729]). The constant scaling factor approach was adopted for this study to reduce the interfacial area between the basalt fracture and matrix continua. This simplification was adopted given the transient nature of the LPIT test and because the "active fracture" model has only been validated for steady-state flow within the site-scale Yucca Mountain model.

The background infiltration rate prescribed to all surface nodes inside the infiltration pond is shown on Figure 9.3-4. The rate was calculated as part of a water management system and water balance analysis by Starr and Rohe (1995 [156400]). Additional boundary conditions for simulating unsaturated flow within the LPIT model include the sides of the model, which were assigned to be impermeable boundaries, while the bottom of the model is prescribed as a constant-water-pressure condition. For the LPIT transport model, 2 Ci of ^{75}Se was added to the infiltration pond water (approximately 31,650 m^3) and allowed to infiltrate into the fractured basalt from Day 6 to Day 17. The mass fraction of ^{75}Se in the infiltrating water was normalized to 1×10^{-3}, given the linear nature of the advection-dispersion equation describing transport of the conservative ^{75}Se tracer and the lower limits on the convergence tolerance of the Newton and iterative sparse matrix solver schemes (approximately 1×10^{-6}). This scaling is evident in Figure 9.3-8.

9.3.4 Hydrological Parameter and Perched Water Hydrograph Data

Perched water hydrograph data were collected at 17 locations as presented in Burgess (1995 [156401]). These were collected in wells located primarily on the A, B, and C rings (see labeled symbols in Figure 9.3-3a) and with the screen located at the B basalt—B-C interbed interface. Hydrographs were not observed at all locations because of difficulties in completing the well at this interface. Of the 17 hydrographs, six were selected for the calibration effort. Results of numerical tests indicated that inversion using the full 3-D LPIT model containing all 17 hydrographs was too computationally intensive; therefore, a wedge of nodes on radial spokes of 342°–0°–18°–36° was extracted to calibrate simultaneously to hydrographs in wells B04N11, C04C11, B06N11, and C06C11. This set of hydrographs was chosen for calibration because it contained two of the three C–ring hydrographs and matched B– and C–ring wells on the same radial angle. Although well B05O11 contained an observed hydrograph and was within this

wedge, it was not used during the inversion in order to act as a control to test the predictive capability of the calibrated parameter set. The hydrograph at well B08N11 was also independently used as part of a separate calibration to yield a parameter set to test for significant differences between calibrated parameters across the region influenced by the LPIT. The six hydrographs introduced here will be presented in Section 9.3.6, along with calibration results. Selenium-75 breakthrough curves within the ponded water were collected at nine locations, as presented in Burgess (1995 [156401]). Of the nine breakthrough curves, the B04N11 and C04C11 data were selected for calibration because they were within the 342°–0°–18°–36° submodel described above. Furthermore, they have matching B and C ring wells on the same radial angle.

Hydrological parameters relevant to the fractured basalt and sedimentary interbed stratigraphy at the LPIT site were identified in a literature survey to constrain the calibration procedure. These parameters are listed in Table 9.3-2. Because none of the laboratory analysis was done on cores obtained specifically from the LPIT site, only the mean, maximum, and minimum values were used to cover the range over which they may be expected to vary for lithological units in the LPIT area. The relevant parameters include the basalt matrix continuum permeability, k_{BM}; and porosity, ϕ_{BM} (Knutson et al. 1990 [107839], p. 3-93); the B-C interbed matrix continuum permeability, k_{BCM}; porosity, ϕ_{BCM}; residual water saturation, S_{wrBCM}; and van Genuchten capillary pressure parameters α_{BCM} and m_{BCM} (McElroy and Hubbell 1990 [156433]). The properties of the B-C interbed vary significantly because this unit was observed to vary in lithology from a fine silt to clay (McElroy and Hubbell 1990 [156433]). Fracture spacing for the basalt was set to 2.6 m for the entire thickness of the basalt units (Grossenbacher and Faybishenko 1997 [107832]).

All relevant unsaturated flow parameters in the hydrological model are listed in Table 9.3-3. Flow parameters shown in Table 9.3-3 but not discussed in this section were not measured from cores taken at INEEL in the fractured basalt–sedimentary interbed stratigraphy, they were instead based on previous INEEL modeling work conducted by Unger et al. (2000 [156398]). Selenium-75 transport parameters such as the dispersivity and tortuosity of the basalt and B-C interbed were not measured as part of prior laboratory or field investigations. Therefore, it is assumed that ^{75}Se does not undergo either molecular or hydrodynamic dispersion over the 60–day time frame of the LPIT. Hydrodynamic dispersion of the ^{75}Se breakthrough curves will occur instead because of imbibition between the basalt fracture and matrix continua.

9.3.5 Hydrograph Calibration Results

Initial manual calibration indicated that the six most sensitive parameters controlling the calibration of the LPIT model to the hydrographs were the basalt fracture–matrix continua interfacial area constant-scaling factor A_{BFM}, the basalt fracture continuum permability k_{BF}, the basalt matrix continuum permeability k_{BM}, the B-C interbed matrix continuum permeability k_{BCM}, the B-C interbed van Genuchten capillary pressure parameters α_{BCM} and m_{BCM}. The basalt fracture and matrix continua porosities were not sensitive parameters controlling calibration. This is because imbibition of the infiltration front from the basalt fracture continuum to the matrix continuum controlled its downward advection rate rather than the porosity, because of the initial dry conditions present at the site. This is shown on Figure 9.3-5, which depicts the water saturation in the fracture and matrix continua at 35.5 days. At this point, ponding of water is well

developed on the B-C interbed and significant quantities of water have been imbibed into the matrix continua within the migration path of the infiltration front.

Parameter estimation during calibration was performed by iTOUGH2 using a Levenberg-Marquardt algorithm. Five parameters were included for estimation: k_{BF}, k_{BM}, k_{BCM}, α_{BCM} and m_{BCM}. Parameter A_{BFM} was manually adjusted because changes to this parameter required rebuilding the mesh. Initial manual adjustment indicated that a value of $A_{BFM} = 0.01$ provided the best fit to the data when using a Brooks-Corey relative permeability curve, which was also observed by Unger et al. (2000 [156398], p. 14). A van Genuchten relative permeability curve was not used in this study because it caused excessive numerical difficulties when simulating ponding because of its steep gradient at water saturations approaching unity.

Figure 9.3-6 shows simultaneous calibration results to hydrographs B04N11, C04C11, B06N11, and C06C11 using the 342°–0°–18°–36° submodel extracted from the full 3–D LPIT model. This model will be referred to hereafter as the "2–D model," while the entire LPIT model will be referred to as the "3–D model." The symbols in Figure 9.3-6 represent water pressure and indicate ponded-water elevation within the fracture continuum of the B basalt on top of the B-C interbed, where reference atmospheric gas–phase pressure is 85 kPa. Calibration was performed to a subset of the data points shown in Figure 9.3-5 that were chosen to be more evenly spaced in time to prevent biasing the calibration to regions where the data were collected more frequently. Calibration parameters were obtained by setting $A_{BFM} = 0.01$, while the sensitivity of the other five calibration parameters to A_{BFM} was determined by doubling it to $A_{BFM} = 0.02$ and then by halving it to $A_{BFM} = 0.005$. Parameters obtained from the iTOUGH2 calibration are provided in Table 9.3-3.

Comparison of calibrated parameters obtained with $A_{BFM} = 0.01$ indicates that the estimated basalt matrix permeability is almost equal to the mean shown in Table 9.3-2, the B-C interbed permeability is just above the minimum observed value, and the B-C interbed van Genuchten parameters are also near the mean of the values in Table 9.3-2. Although the data in Table 9.3-2 were not obtained from the LPIT site, their close correspondence to the estimated parameters does build confidence in the ability of the LPIT model to yield a spatially averaged set of hydrological parameters to fit the hydrographs. Comparison of calibrated parameters for the three different values of A_{BFM} indicates that the basalt fracture continuum permeability remains constant at $k_{BF} = 3 \times 10^{-10}$ m^2 and is insensitive to A_{BFM} over the range tested. The basalt matrix continuum permeability increases by a factor of 2.51 as A_{BFM} is halved, and decreases by a factor of 2.51 as A_{BFM} is doubled. This indicates that basalt fracture–matrix imbibition is an important process controlling calibration, with A_{BFM} and k_{BM} adjusting themselves proportionately to maintain the same amount of flow into the matrix continuum. Interpreting the response of the B-C interbed parameters to variations in A_{BFM} is considerably more difficult, except that m_{BCM} reaches (and was constrained during calibration by) the maximum observed value for $A_{BFM} = 0.005$, thereby reducing confidence in the physical relevance of the calibration values. In general, given the standard deviation of the estimated parameters, no significant difference exists within two standard deviations between the three parameter sets listed in Table 9.3-4.

The full 3–D LPIT model was used to determine the effect of having reduced the mesh size to the four radial angles of 342°–0°–18°–36° to calibrate to the four hydrographs shown in Figure 9.3-6. The greatest deviation occurs for hydrographs B06N11 and C06C11 because the former is

situated in a local depression, while the latter is situated on a local mound in the elevation of the B-C interbed, as shown on Figure 9.3-3a. Therefore, plan-view grid refinement is necessary to obtain increased numerical convergence for parameters listed in Table 9.3-4. The physical relevance of the converged parameters would still be limited by the sparse distribution of points providing information on the elevation of the B-C interbed.

The full 3–D LPIT model was also used to determine how well the calibrated parameters matched the control hydrograph B05O11 that was located within the 2–D submodel, as well as hydrograph B08N11 that was located outside of the 2–D submodel. Figure 9.3-7a shows that the 3–D model successfully modeled the control hydrograph, thus building confidence in the physical relevance of the estimated parameters. Figure 9.3-7b shows that when the 3–D model is used to simulate the B08N11 hydrograph using parameters from Table 9.3-4, the predictive capacity of the estimated parameters diminishes. B08N11 is the only hydrograph shown because it exhibited the worst fit of the hydrographs located outside of the 2–D submodel. An additional 2–D submodel at a radial angle of 288° was extracted from the 3–D LPIT model to calibrate to the B08N11 data. Calibration was performed with A_{BFM} = 0.01 only; the results are shown on Figure 10.3-7b, with the final calibrated parameters listed in Table 9.3-5. Analysis of the parameters in Tables 9.3-4 and 9.3-5 indicates that for A_{BFM} = 0.01, the mean estimated values for k_{BF} and k_{BM} are significantly different at two standard deviations, while values for k_{BCM}, α_{BCM} and m_{BCM} are not. This implies that at the field scale of the LPIT experiment there is greater heterogeneity in the hydrological properties of the basalt than of the B-C interbed.

9.3.6 Selenium (^{75}Se) Calibration Results

The six parameters identified for the hydrograph calibration were also used to perform a joint calibration on the hydrograph and ^{75}Se data for wells B04N11 and C04C11. The objective of this calibration effort was to determine whether parameters estimated using both flow and transport data are significantly different than those estimated using flow data alone.

Figure 9.3-8 shows joint hydrograph and ^{75}Se results for observation wells B04N11 and C04C11 using parameters estimated from the flow calibration (see Table 4, A_{BFM} = 0.01). Two numerical difficulties were identified during calibration that prevented completion of the iTOUGH2 calibration. First, iTOUGH2 with the EOS7r module did not provide a sufficiently robust flow simulation in comparison with the EOS9 module while simulating water ponding on the B-C interbed. Repeated failure of the Newton iteration caused an excessive number of timesteps, ultimately resulting in an accumulation of numerical mass-balance errors within the ^{75}Se mass conservation equation. This resulted in nonmonotonic behavior of the ^{75}Se mass-fraction curves (as shown on Figure 9.3-8a), making parameter estimation with iTOUGH2 impossible. These mass-accumulation errors are not evident in the water mass-conservation equation, as shown by Figure 9.3-8b.

Transport simulation results show that ^{75}Se mass fractions reached source values of 1×10^{-3}, which are fifteen times greater than peak values observed in the field for B04N11. The tail of the simulated ^{75}Se breakthrough declines much more rapidly than observed in the field. This discrepancy does not result from the omission of molecular diffusion between and within the fracture and matrix continua of the dual-permeability mesh, because upstream-weighting of the advective mass-fraction terms in the discretized mass-balance equations in iTOUGH2 will

introduce significantly more numerical dispersion than would be observed by molecular diffusion alone. Any numerical dispersion would be a product of the coarse grid discretization of the dual-permeability mesh, as well as the highly advective flow fields simulated during the infiltration tests. Given that the general shapes of the simulated breakthrough curves are incorrect, it is suggested that while the dual-permeability conceptual model can be used to simulate unsaturated flow, it may not adequately capture the physics of conservative transport in fractured basalt. Wu et al. (2001 [156399]) suggest that a triple-continuum conceptual model involving an interconnected matrix continuum, large-scale fracture continuum, and a small-scale fracture continuum may provide a better representation of transport. In this case, it is assumed that the small-scale fractures would retain sufficient ^{75}Se to retard its advection, decrease peak breakthrough values, and cause significant tailing of the breakthrough curves. Mass transfer of ^{75}Se from the large-scale fracture continuum into the small-scale fracture continuum would be primarily driven by molecular diffusion, which depends upon the concentration gradient of ^{75}Se (Liu et al. 2000 [154579]). Resolving the concentration gradient would require multiple interconnected nodes to represent the small-scale fracture continuum over a very fine (millimeter) scale. Although testing of the triple-continuum conceptual model would only require rebuilding a new mesh, successful calibration of this conceptual model in iTOUGH2 is contingent upon a more robust flow simulation and removal of the mass-accumulation errors seen in the radionuclide conservation equations.

9.3.7 Conclusions of LPIT Analogue Study

The study of UZ flow at the RWMC was chosen because INEEL is somewhat analogous to Yucca Mountain in hydrogeology. Average precipitation is similar at both sites, although infiltration is higher at INEEL. Perched water occurs in the UZ at both sites. Rock at both sites consists of a fractured porous media – basalt at INEEL and rhyolitic ash-flow tuff at Yucca Mountain. At both sites lateral flow plays a role in diverting flow, whereas the dominant flow paths are along fracture pathways. Fracture-filling minerals consist of clays and calcite at both sites. Although the two sites differ in significant ways (see Section 10.3.5), their similarities made it worthwhile to test modeling approaches of UZ flow (and also radionuclide transport in the UZ, as presented in Section 10) at Yucca Mountain with INEEL data.

Hydrographs of ponded water and ^{75}Se breakthrough curves measured during the LPIT test conducted at INEEL were analyzed to determine parameters controlling unsaturated flow and transport. Analysis of this data involved building a numerical model using iTOUGH2. The numerical model was constructed to conform to the lithological units at the LPIT site, which consisted of surficial clay-like sediments underlain by fractured basalt flows (the A, B, and C basalts) with a clay-like sedimentary interbed (B-C sediment layer) situated between the B and C basalts. The numerical model involved determining parameters controlling unsaturated and saturated flow and transport in fractured basalt, using a dual-permeability modeling approach that has been extensively employed to simulate flow and transport at Yucca Mountain.

Six parameters were identified to be most sensitive in controlling the calibration of the LPIT model to the observed hydrographs. These included the basalt fracture–matrix interfacial area, the basalt fracture and matrix continua permeabilities, the B-C interbed permeability, and van Genuchten capillary pressure α and m values. Simultaneous calibration to hydrographs B04N11, C04C11, B06N11, and C06C11 using iTOUGH2 yielded parameters that were consistent with

the range in values seen in data obtained from cores drilled near the LPIT site. Joint calibration to hydrograph and ^{75}Se data in wells B04N11 and C04C11 was unsuccessful because of numerical difficulties. Preliminary results indicated that while the dual-permeability conceptual model can be used to simulate unsaturated flow, it does not adequately simulate conservative transport in fractured basalt. This is because the matrix continuum needs to be significantly refined relative to the dual-permeability approach to resolve molecular diffusion caused by the concentration gradient between the fracture and matrix continua. This conclusion is especially significant to the site-scale Yucca Mountain model, in which, the dual-permeability approach is used extensively to simulate both unsaturated flow and transport in fractured tuff. The dual-permeability approach provides conservative estimates of peak concentrations and arrival times by underpredicting the mass transfer of conservative (i.e., nonsorbing) tracers from the fracture to the matrix continua.

Parameters estimated by the calibration are inherently spatially averaged over the region sampled by the downward-advecting infiltration front and laterally migrating ponded water. This region starts from directly beneath the infiltration pond and covers the radial area of the four hydrographs. These parameters were able to predict the control hydrograph that was located within the spatially averaged region, but were unable to predict hydrograph B08N11, located outside of this region. Independent calibration to hydrograph B08N11 indicated that the basalt properties showed significantly greater variability than the B-C interbed properties. This implies that the field-scale heterogeneity limits the volume to which the spatially averaged basalt parameters can be assigned relative to the B-C interbed parameters. This may in part result from the fractured–porous dual–continuum nature of the basalt in comparison to the porous single–continuum nature of the B-C interbed.

9.4 DRIFT SHADOW ANALOGUES

The phenomenon of flow diversion around a cavity was investigated for a general homogeneous porous medium by Philip et al. (1989 [105743]). The key feature of this phenomenon with respect to the transport of dissolved or colloidal material from the drift is that flow velocities in a zone beneath the drift are slower than unaffected flow velocities away from the drift (Figure 9.4-1). In particular, the flow velocity at the base of the drift is exactly zero. According to this conceptual model, the zone beneath the drift was also found to have lower water saturation than the undisturbed zone. This region of reduced flow velocity and water saturation beneath the drift is known as the drift shadow.

For a quasi-linear representation of the hydrogeologic properties, Philip et al. (1989 [105743], p. 18) found that the extent of the drift shadow is a function of a characteristic sorptive length scale and the drift radius. The shape of the drift shadow is governed by the ratio of the drift radius to the sorptive length scale. The ratio of the drift radius to the sorptive length scale is a measure of the relative importance of gravitational forces compared with the capillary forces that define flow patterns around the drift.

9.4.1 Caves

The drift shadow phenomenon cannot be accurately tested in the underground facility at Yucca Mountain because the natural system has been greatly perturbed by the heavy use of construction water for dust control and by the large volumes of air exhausted every day. Furthermore, the underground facility probably has not yet come to equilibrium with the undisturbed host rock. Complicating matters is the fact that detection of a drift shadow zone has never been documented for either natural or anthropogenic openings—conceivably ancient underground tombs and features could lie above a drift shadow zone. However, naturally occurring caves provide an opportunity to test for a drift shadow zone beneath an opening in the UZ. Limestone caves are hydrologically similar to the welded tuffs at Yucca Mountain because, in both cases, flow occurs primarily along fractures. Furthermore, caves have had sufficient time to establish hydrologic equilibrium. The Carlsbad, New Mexico, region is ideally suited for such a study because the large number of caves in the region allows for selection of a cave that closely matches the physical characteristics of a potential mined geologic repository. Caves that are known to receive direct surficial runoff should be eliminated from consideration. The cave chosen for study should be as large as or larger than proposed repository emplacement drift cross sections, currently approximately 5 m in diameter. The roof of the cave should be below the zone of surface influence, currently estimated as 6 m. Ideally, the cave should be readily accessible to light drilling equipment and should be sited so as to accommodate a small meteorological data station. The small cave approximately 800 m southeast of Boyd's Waterhole and northwest of Carlsbad, New Mexico (on the Azotea Peak 7½-minute topographic quadrangle map) appears to meet the necessary criteria.

The site should be amenable to standard tracer or infiltration tests. The infiltration tests would push the system out of hydrologic equilibrium by applying enough water to the surface above the cave to establish dripping into the cave. The tracers would be dyes or biodegradable tracers that would be used in an attempt to define flow paths.

9.4.2 Tunnels or Mine

Conceivably, an environmental tracer analysis could be used to demonstrate the presence of a drift shadow. An old mine in an arid region would be an ideal location, especially if its history dated back 100 years or so. Another possibility would be an old railroad tunnel or other tunnel, such as the Never-Sweat Tunnel (for ore haulage) at Apache Leap, Arizona, and the nearby mine. Chlorine-36 could be used as one possible example of an environmental tracer with a pulse input occurring ~50 years ago. If the mine drift is older than 50 years, it is possible that cores collected at present adjacent to the drift would contain the bomb-pulse signal, while cores collected below the drift would not. In a nearby, much younger drift, it would be expected that there would be essentially no difference in ^{36}Cl signal above and below the drift. Chlorine-36 is not the only possible tracer that could be used; the ideal tracer would be without background from the rock, such as an artificial environmental tracer.

9.5 CONCLUSIONS

Hydrographs of ponded water and ^{75}Se breakthrough curves measured during the LPIT test conducted at INEEL were analyzed to determine parameters controlling unsaturated flow and

transport. Analysis of this data involved building a numerical model using iTOUGH2 in a dual-permeability modeling approach, an approach that has been extensively used to simulate flow and transport at Yucca Mountain.

Six parameters were identified to be most sensitive in controlling the calibration of the LPIT model of unsaturated flow in fractured basalt. These included the basalt fracture–matrix interfacial area, the basalt fracture and matrix continua permeabilities, the B-C interbed permeability, and van Genuchten capillary pressure α and m values. Simultaneous calibration to hydrographs using iTOUGH2 yielded parameters that were consistent with the range in values seen in data obtained from cores drilled near the LPIT site. Preliminary results indicated that while the dual-permeability conceptual model can be used to simulate unsaturated flow, it may not adequately capture the physics of conservative transport in fractured basalt. This conclusion is relevant to the site-scale Yucca Mountain model, in which the dual-permeability approach is used extensively to simulate both unsaturated flow and transport in fractured tuff.

Parameters estimated by the calibration are inherently spatially averaged over the region sampled by the downward-advecting infiltration front and laterally migrating ponded water. The region starts from directly beneath the infiltration pond and covers the radial area of the four hydrographs. The basalt properties showed significantly greater variability than the B-C interbed properties. This implies that the field-scale heterogeneity limits the volume to which the spatially averaged basalt parameters can be attributed relative to the B-C interbed parameters. This may in part be due to the fractured-porous dual-continuum nature of the basalt in comparison to the porous single–continuum nature of the B-C interbed.

Finally, natural caves and man-made openings such as mines and tunnels may be suitable locations for testing the drift shadow concept, particularly if those sites have existed long enough to establish hydrologic equilibrium.

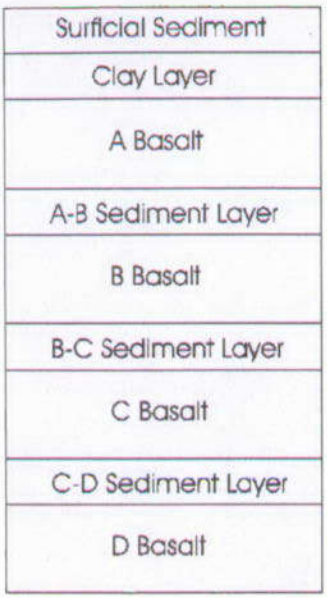

Source: Simmons 2002 [157578], SN-LBNL-SCI-108-V2, p. 8

Figure 9.3-1. Schematic Stratigraphic Sequence Illustrating the Relationship between Basalt Flows and Sediment Layers

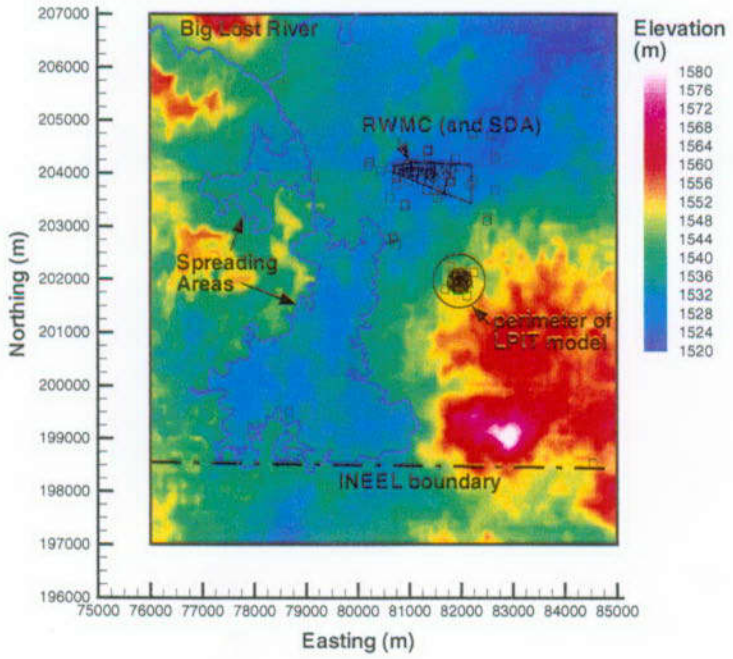

Source: Simmons 2002 [157578], SN-LBNL-SCI-186-V1, p. 58.

Figure 9.3-2. Plan View of Regional Model with Contours of the Ground Surface Elevation

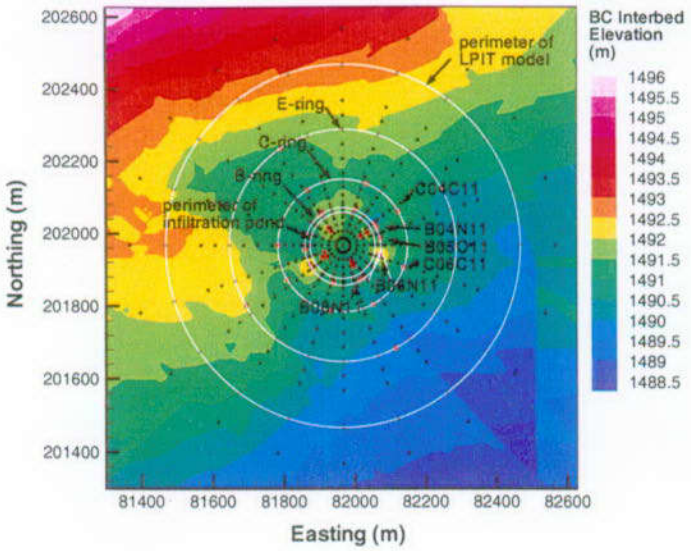

(a)

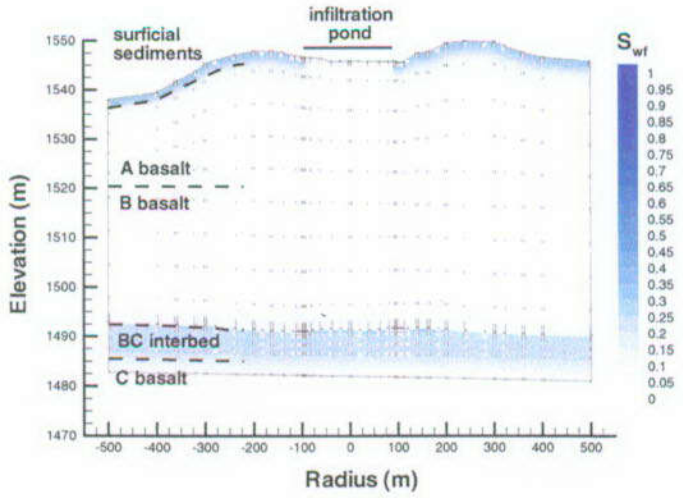

(b)

NOTE: In (a), the centroids of the elements are indicated as black dots and the wells by red dots

Source: Simmons 2002 [157578], SN-LBNL-SCI-186-V1, p. 59

Figure 9.3-3. (a) Top of B-C Interbed Elevation with Centroids of Elements in Plan View As Well As the Location of All Hydrographs Used in this Analysis. (b) East-West Cross-Sectional View Showing the Steady-State Water Saturation in the Fracture Continuum

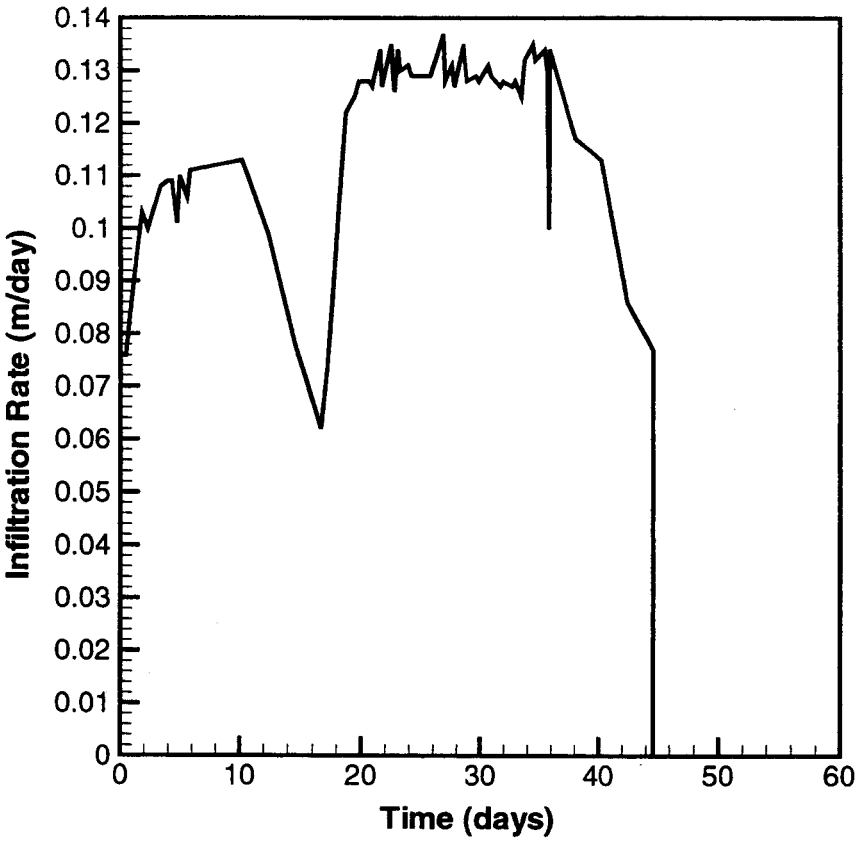

Source: Simmons 2002 [157578], SN-LBNL-SCI-186-V1, p. 60.

Figure 9.3-4. Infiltration Rate Observed by Starr and Rohe (1995 [156400]) during the LPIT Using a Water Balance Analysis

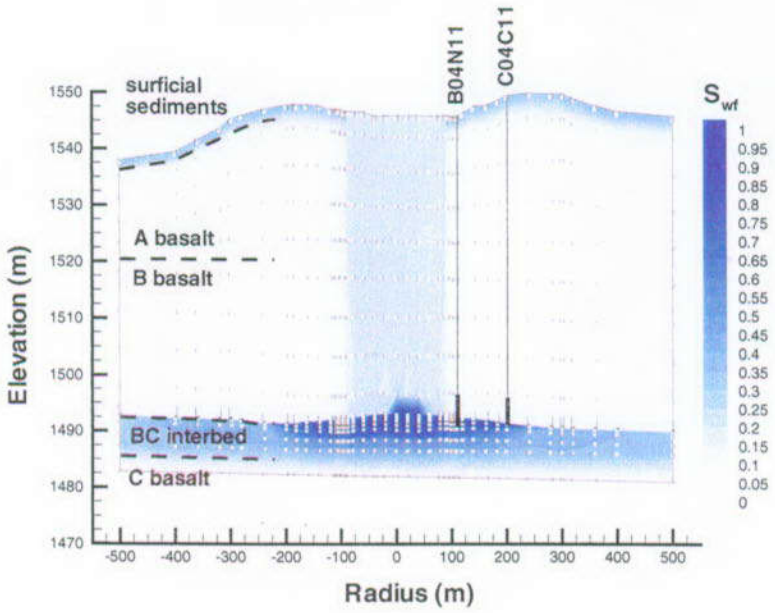

(a)

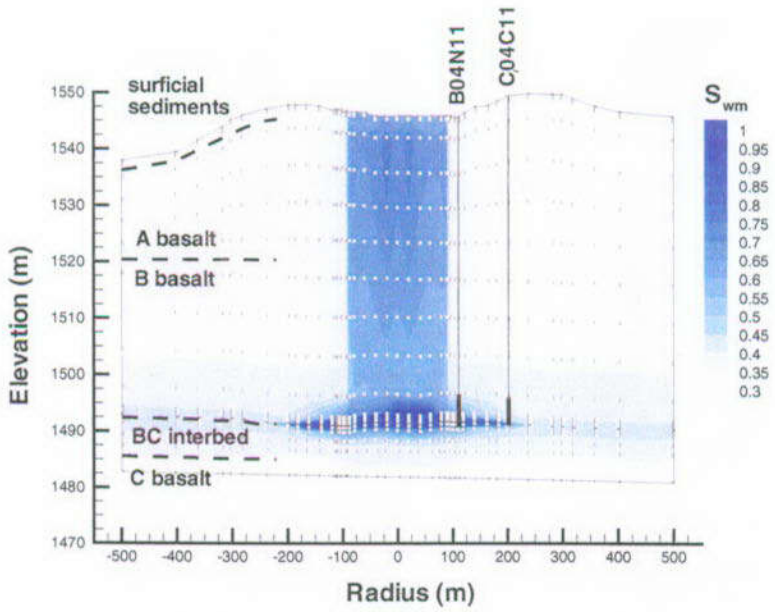

(b)

Source: Simmons 2002 [157578], SN-LBNL-SCI-186-V1, p. 61.

Figure 9.3-5. Water Saturation in the (a) Fracture and (b) Matrix Continua at 35.5 Days after the Start of the LPIT

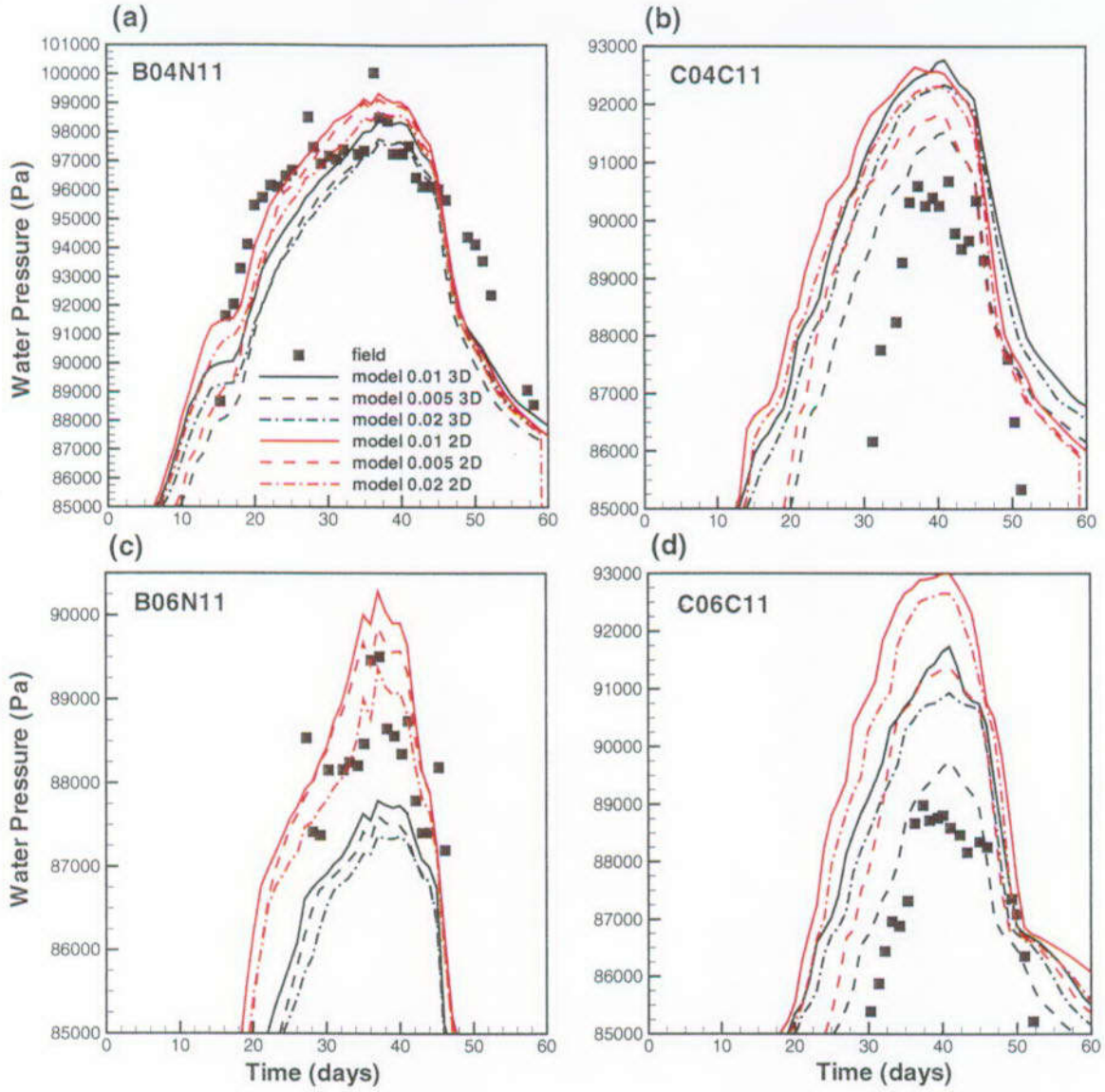

NOTE: Symbols represent field data with reference atmospheric gas phase pressure equal to 85 kPa. Lines represent calibration results using the 2–D submodel and the full 3–D LPIT model with varying A_{BEM} values (0.01, 0.005, 0.02).

Source: Simmons 2002 [157578], SN-LBNL-SCI-186-V1, p. 62.

Figure 9.3-6. Ponded Water Hydrographs in Wells B04N11, C04C11, B06N11 and C06C11

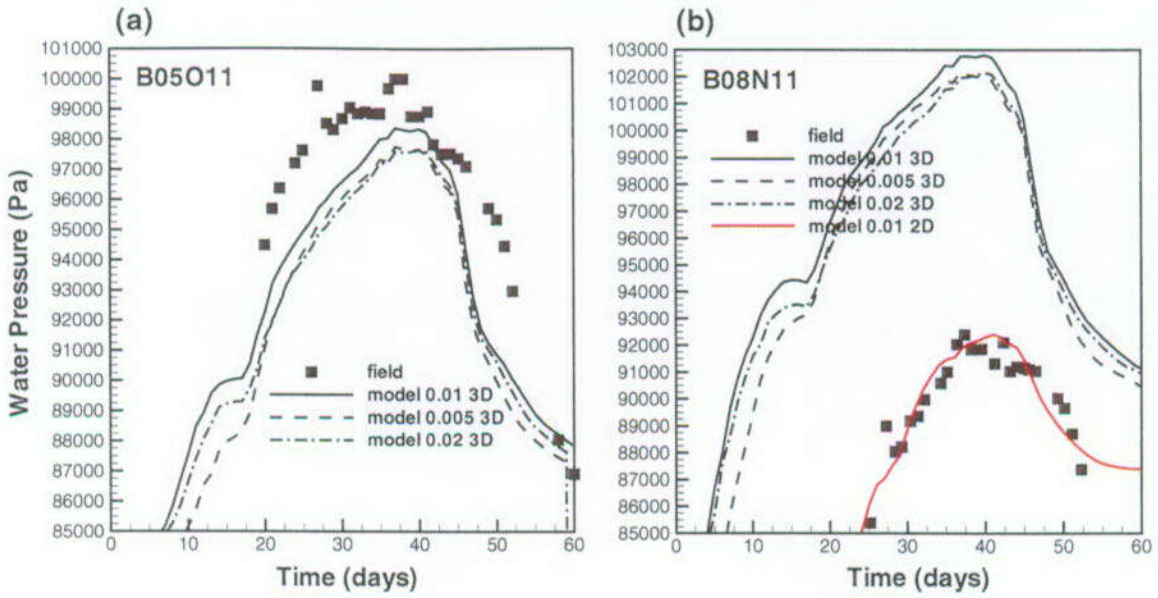

NOTE: Symbols represent hydrograph data while lines represent model results.

Source: Simmons 2002 [157578], SN-LBNL-SCI-186-V1, p. 63.

Figure 9.3-7. (a) Predictive Model Results for Control Hydrograph B05O11 and (b) Calibration Model Results for Hydrograph B08N11

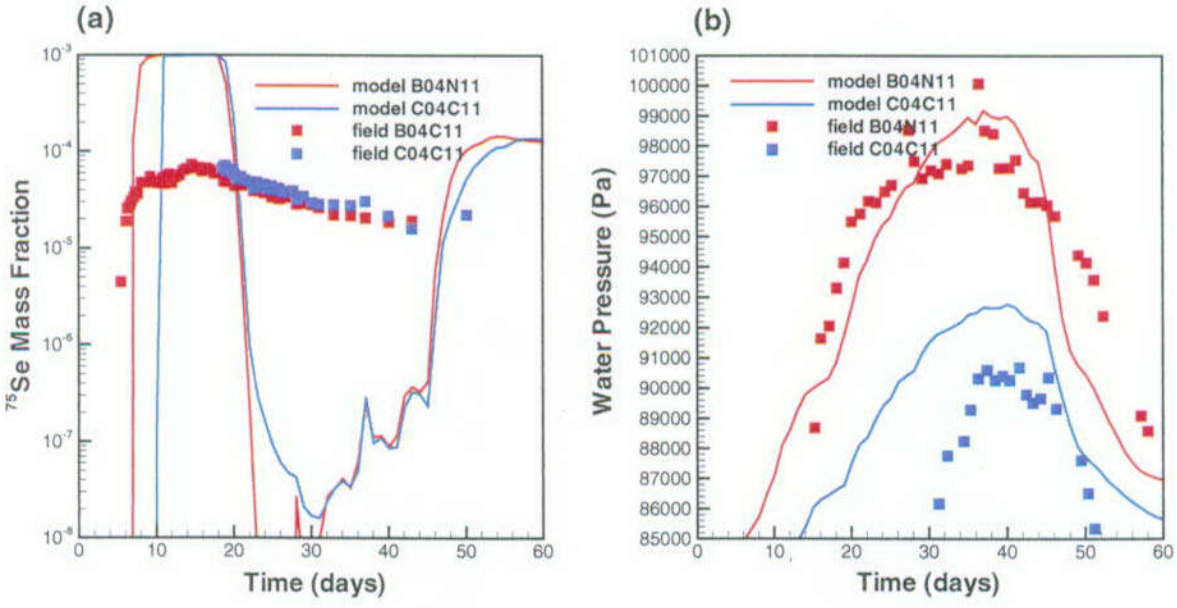

Source: Simmons 2002 [157578], SN-LBNL-SCI-186-V1, p. 63.

Figure 9.3-8. Joint (a) ^{75}Se Breakthrough and (b) Hydrograph Calibration Results for Wells B04N11 and C04C11

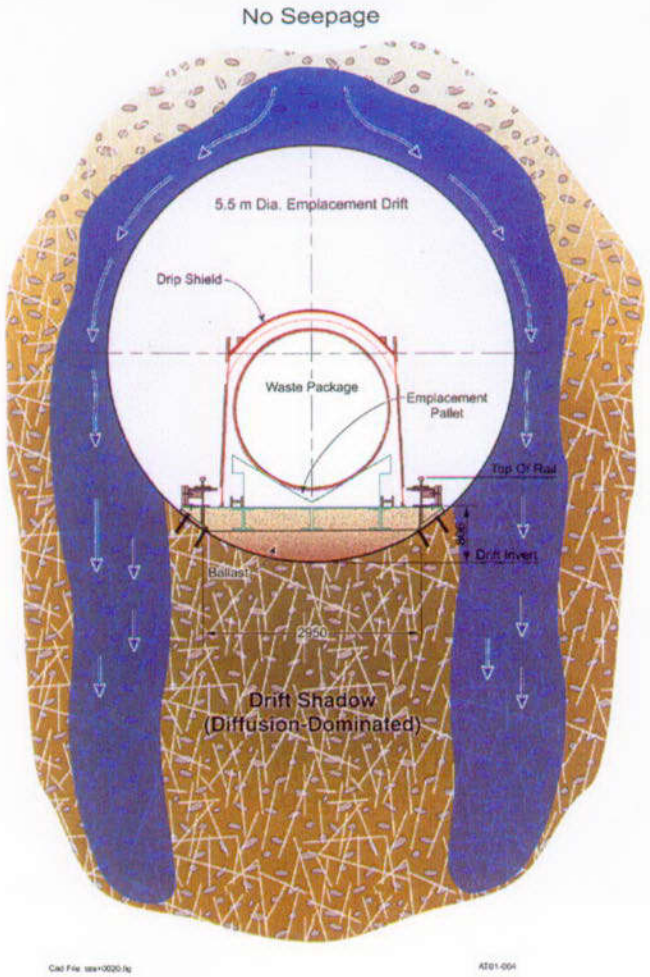

Source: DOE 2001 [153849], Figure 4-116.

Figure 9.4-1. Schematic Diagram of Diffusion Barriers in Invert and Drift Shadow Zone

Table 9.3-1. Distribution Coefficient (K_d) Values for Sorption of Contaminants on INEEL Sediments

Element	K_d Values (mL/g) and Range		
	Surficial Sediments	Interbeds	Basalt
Am	No data	450 (450 to 1,100)	70 (70 to 280)
Co	No data	1,148 (1,148 to 3,912)	11 (11 to 54)
Cs*	950 (589 to 1,253) (75 to 225)	2,228 (2,228 to 3,255)	39 (39 to 44)
Pu	7,800 (7,800 to 22,000)	5,100 (5,100 to 7,900)	70 (70 to 130)
Sr*	24 (23 to 26) (8.3 to 16.6) 50 (35 to 52)	42 (42 to 63) 155 (110 to 186)	6 (6 to 13) (1.1 to 2.7)
Tc	0	0	0
U	No data	3.4 (3.4 to 9)	0.2 (0.2 to 5.2)
Hg	972 (236 to 1,912)	176 (72 to 673)	(9.2 to 87)

NOTE: *Different K_d values for Cs and Sr are from different authors cited by Dicke (1997 [157410], Table 1).

Source: Dicke 1997 [157410], Table 1.

Table 9.3-2. Basalt and B-C Interbed Parameters Collected by Laboratory Analysis of Core Samples

Property	Samples	Mean	Maximum	Minimum
k_{BM} [m^2]	43	†2.24×10^{-15}	9.48×10^{-14}	1×10^{-16}
ϕ_{BM} [–]	50	‡19.2	43.2	5.2
k_{BCM} [m^2]	15	†4.21×10^{-14}	6.86×10^{-12}	1.15×10^{-17}
ϕ_{BM} [–]	15	‡0.530	0.629	0.424
S_{wrBCM} [–]	15	‡0.183	0.376	0.038
α_{BCM} [Pa^{-1}]	15	†7.95×10^{-5}	5.025×10^{-4}	1.938×10^{-6}
m_{BCM} [–]	15	‡0.4	0.86	0.23

†geometric mean

‡arithmetic mean

Source: Simmons 2002 [157578], SN-LBNL-SCI-186-V1, p. 55.

Table 9.3-3. Basalt and B-C Interbed Parameters Used in the LPIT Model

Parameter	Value		
	basalt fracture	basalt matrix	B-C interbed
$k_x = k_y = k_z$ [m^2]	From calibration	From calibration	From calibration
ϕ [–]	0.01	19.2	0.53
S_{wr} [–]	0.01	0.1	0.183
α [Pa^{-1}]	5×10^{-3}	5×10^{-4}	From calibration
m [–]	0.5	0.25	From calibration

Source: Simmons 2002 [157578], SN-LBNL-SCI-186-V1, p. 55.

Table 9.3-4. Parameters Estimated during Calibration to Hydrographs B04N11, C04C11, B06N11 and C06C11

Param.	A_{BFM} = 0.01		A_{BFM} = 0.005		A_{BFM} = 0.02	
	Mean	std. dev.	Mean	std. dev.	Mean	Std. dev.
†k_{BF}	3.27×10^{-10}	0.0701	3.13×10^{-10}	0.0553	3.44×10^{-10}	0.0759
†k_{BM}	2.51×10^{-15}	0.395	6.31×10^{-15}	0.197	1×10^{-15}	0.381
†k_{BCM}	5.01×10^{-17}	1.51	6.31×10^{-17}	0.538	1.26×10^{-16}	0.848
‡α_{BCM}	1×10^{-4}	1.23	4.07×10^{-6}	0.465	1×10^{-4}	0.852
m_{BCM}	0.28	0.341	0.86	0.718	0.67	1.08

†mean permeability values are in [m^2] while standard deviation is in [$\log_{10} m^2$]

‡mean α_{BCM} values are in [Pa^{-1}] while standard deviation is in [$\log_{10} Pa^{-1}$]

Source: Simmons 2002 [157578], SN-LBNL-SCI-186-V1, p. 56.

Table 9.3-5. Parameters Estimated during Calibration to Hydrograph B08N11

Parameter	Mean	std. dev.
k_{BF}	7.05×10^{-10} [m^2]	0.0553 [$\log_{10} m^2$]
k_{BM}	7.94×10^{-14} [m^2]	0.162 [$\log_{10} m^2$]
k_{BCM}	2.51×10^{-16} [m^2]	0.342 [$\log_{10} m^2$]
α_{BCM}	6.31×10^{-5} [Pa^{-1}]	0.690 [$\log_{10} Pa^{-1}$]
m_{BCM}	0.48	0.527

Source: Simmons 2002 [157578], SN-LBNL-SCI-186-V1, p. 56.

10. ANALOGUES TO UNSATURATED ZONE TRANSPORT

10.1 INTRODUCTION

This section presents updates on two recent studies examining transport of radionuclides in unsaturated zone (UZ) conditions. The first is a study of migration of radionuclides at the Idaho National Engineering and Environmental Laboratory (INEEL) with the objective of explaining mechanisms responsible for detection of concentrations of neptunium and uranium in monitoring wells below the water table. The second study presents results of analyses and modeling of uranium systematics at Peña Blanca, Mexico, based on water sampling campaigns in 2000 and 2001. Additional insights derived from natural analogues in Steenkampskraal, South Africa, and Koongarra, Australia, on the significance of colloid transport in the UZ are also presented.

Previous studies have indicated that fractures act as both transport pathways and places of retardation at a number of the analogue sites. This was shown in *Yucca Mountain Site Description* (CRWMS M&O 2000 [151945], Section 13) through analogues from Peña Blanca, Mexico; Akrotiri, Greece; and volcanic tuff-hosted uranium deposits in northern Nevada. At Nopal I (Peña Blanca), uranium has been transported relatively small distances, essentially completely along fractures, and has been sorbed or precipitated onto fracture-coating Fe-oxides and calcites. Colloidal transport of uranium was shown to be minimal at another analogue site in Koongarra, Australia, where filtration of colloids appears to be effective. The YMP total system performance assessment (TSPA) assumes no colloid filtration, an assumption that may be unnecessarily conservative. Data available for the *Yucca Mountain Site Description* also indicated that the geochemical system at Nopal I restricted actinide mobility in the UZ and that by analogy the tuffs at Yucca Mountain should have similar retentive properties and impede the mobility of oxidized uranium. Additionally, clays found in fractures and vitrophyres at Yucca Mountain may also be effective in retarding migration of radionuclides. This conclusion can be drawn from examination of the clay haloes (5–30 cm thick) surrounding ore deposits at Oklo, Gabon, and Cigar Lake, Canada, which have been shown to be effective in retarding the migration of uranium away from the source (CRWMS M&O 2000 [151945], Section 13.5).

Radionuclide migration experiments under unsaturated conditions have also been completed in a 30 cm block of Calico Hills nonwelded tuff from the Busted Butte test facility near Yucca Mountain. This type of study could be thought of as a self-analogue to migration in the Calico Hills nonwelded unit under Yucca Mountain. Elution profiles showed that relative to an ideal conservative tracer (tritiated water), transport of TcO_4^- was approximately 15% faster, but that NpO_2^+ was retarded by a factor of 3 (Vandergraaf et al. 2001 [155042]). These findings fall within the range of retardation coefficients determined from tuff column experiments (Triay et al. 1996 [101024], Appendix A). Retardation of ^{22}Na, ^{60}Co, and ^{137}Cs was higher than for neptunium in the Calico Hills block experiments, and this agreed qualitatively with experimentally determined batch sorption coefficients for these isotopes (BSC 2001 [155950], p. 11-46). The analogues discussed in this section focus primarily on processes occurring at INEEL and Peña Blanca as potential analogues for radionuclide transport in the UZ at Yucca Mountain. Information found in Sections 10.3, 10.4, and 10.5 may help to support arguments associated with Key Technical Issue (KTI) KUZ0407 listed in Table 1-1.

10.2 TRANSPORT IN THE UZ AT YUCCA MOUNTAIN

The evaluation of possible radionuclide transport from the potential repository to the groundwater in the saturated zone (SZ) is key to assessing the performance of the potential repository. In the event of such waste mobilization and migration away from the potential emplacement drifts at Yucca Mountain, the rate of radionuclide transport through the UZ is determined by the percolation flux and by the hydrologic properties and sorptive properties of the tuff units. Water carrying radionuclides may percolate vertically through fractured tuff units, or it may be laterally diverted around low-permeability horizons (particularly where perched water occurs) to fault zones. Diffusion, sorption, and dispersion processes would retard the movement of radionuclides. Each of these processes potentially affects the distribution and concentration of radionuclide particles at the water table.

The transport of aqueous and colloidal radionuclide species can occur in both fracture and matrix continua, with exchange between continua (fracture-matrix interaction) resulting from advective and/or diffusive processes, as well as sorption in the matrix. The flow pathways are determined by the characteristics of hydrogeologic units, faults, and perched water.

These characteristics control the extent of downward versus lateral flow, fracture-matrix interaction, and the partitioning of flow between fractures and the rock matrix. Fractures and faults can be fast flow paths, with diffusion into the matrix and sorption to the rock being the important processes for radionuclide retardation.

The concentration of radionuclides and their daughter products are diminished according to their radioactive decay rates, the extent of sorption onto the solid phase, and dilution as a result of mixing and dispersion. The effects of advective flow processes, sorption of solutes or filtration of colloids, matrix diffusion, hydrodynamic dispersion, and radioactive decay are important factors that play varying roles of significance in slowing the movement of radionuclides through the UZ.

10.3 INEEL AS A POTENTIAL ANALOGUE FOR RADIONUCLIDE TRANSPORT AT YUCCA MOUNTAIN

10.3.1 Background

Section 10.3 presents a preliminary hydrologic and geochemical transport model for americium (Am), cesium (Cs), neptunium (Np), plutonium (Pu), strontium (Sr), and uranium (U) in the UZ beneath the Subsurface Disposal Area (SDA) of the RWMC at INEEL. The geologic, hydrologic, and geochemical bases for the model were summarized in Section 9.3. Section 10.3 uses these bases to develop a conceptual model of flow and transport beneath the SDA. A series of numerical models have been developed that test various aspects of the conceptual model. The computer codes FLOTRAN and FEHM were used to develop models for flow and radionuclide movement in the surficial sediments in and beneath the waste pits. Measurements of radionuclide concentrations made during the drilling of shallow monitoring holes in and near the waste trenches (Humphrey and Tingey 1978 [157491]; Rightmire and Lewis 1988 [156442]) provide a basis for evaluating the model. Flow and radionuclide transport in the UZ beneath the SDA is simulated, and the results are compared to available field data.

10.3.2 Column Experiments

10.3.2.1 Description of Experiment

Column experiments and associated batch tests to measure values of the equilibrium distribution coefficients (K_d) and the reaction-rate coefficients for the sorption of americium-241 (^{241}Am), cesium-137 (^{137}Cs), cobalt-60 (^{60}Co), strontium-90 (^{90}Sr), uranium-233 (^{233}U), and plutonium-239 (^{239}Pu) were carried out at Clemson University and INEEL (Newman 1996 [156434]). The experiments included columns of crushed basalt (> 0.25 mm size fraction), mixed interbed sediments (< 0.25 mm size fraction), and intact basalt cores taken from the same boulder that provided the crushed basalt. In the first phase of the experiments, the steady, saturated flow of synthetic water with a composition (Table 10.3-1, Section 10.3.5.2) similar to groundwater at INEEL was established in the columns. A spiked solution containing tritium (^{3}H) and one or more of the radionuclides of interest was input with the synthetic water for a duration equivalent to about one pore volume and then was flushed with about 200 pore volumes of the unspiked synthetic water. The breakthrough curves of tritium (^{3}H) were fit with the advection-dispersion equation, as implemented in the computer code CXTFIT (Parker and van Genuchten 1984 [126526]), to demonstrate the absence of preferential flow during the experiments and estimate dispersion coefficients for the material in the columns (Newman 1996 [156434], Appendix E). CXTFIT also was used to fit the advection-dispersion equation to the breakthrough curves for each of the radionuclides. These fits provided estimates for the retardation coefficient R_f:

$$R_f = (1 + \frac{\rho_b K_d}{\phi}) \qquad \text{(Eq. 10-1)}$$

where ρ_b is bulk density (g/cm^3) and ϕ is porosity. The K_d values for each combination of radionuclide and column material were then calculated from fitted R values. CXTFIT also includes a variation of the equilibrium advection-dispersion model known as the two-site/two-region model that accounts either for (1) the presence of both equilibrium and nonequilibrium sorption sites or (2) the presence of mobile and immobile water. The advection-dispersion model and the two-site/two-region model were fitted to the radionuclide breakthrough curves, as appropriate, to estimate R and parameters that account for the transfer of radionuclides between the mobile and immobile water.

10.3.2.2 Results of Experiments

Results for the columns containing crushed basalt (Newman 1996 [156434], Table 6, Appendix F) showed that most of the radionuclide mass (except for ^{233}U) was substantially retarded compared to the water. Recovery of the input radionuclide mass was less than 100% for ^{60}Co (~69%), ^{90}Sr (~50%), ^{239}Pu (~33%), and ^{231}Am (~10%), indicating that the unrecovered fraction had a retardation factor greater than 200 (Newman 1996 [156434], p. 28). Two-site/two-region models fit to the breakthrough curves of ^{90}Sr, ^{137}Cs, and ^{233}U generally resulted in better fits to the data than the equilibrium advection-dispersion model; recovery was insufficient to apply the two-site/two-region model to the remaining radionuclides. A fraction of the ^{60}Co (~3%), ^{241}Am (9 to 13%), and ^{239}Pu (10 to 55%) in the column studies exhibited early breakthrough compared with most of the mass of these radionuclides. Fits of the equilibrium advection-dispersion

equation to the breakthrough curves for this so-called enhanced mobility fraction resulted in retardation factors of between 1.5 and 2 (Newman 1996 [156434], Table 6). Possible explanations for the existence of the enhanced mobility fraction included (1) the sorption and transport of these radionuclides on colloids such as SiO_2, (2) the formation of neutral or negatively charged complexes involving these radionuclides and carbonate, and (3) kinetically limited sorption. Related experiments demonstrated that the enhanced mobility fraction of ^{239}Pu increased with total alkalinity and the mobile fraction of ^{241}Am increased with flow rate (Newman 1996 [156434], Figures 15 and 16). However, no definite conclusions regarding the specific causes for the enhanced mobility fraction were made. Batch studies done to evaluate the equilibration time between various radionuclides and crushed basalt showed that the equilibration time for ^{60}Co was not longer than radionuclides lacking an enhanced mobility fraction (such as ^{90}Sr and ^{137}Cs) (Newman et al. 1996 [156434], Table 8). The data from the batch tests for ^{241}Am indicated equilibrium behavior, and data for ^{239}Pu were not reported.

Results from column studies of the interbed material (Newman 1996 [156434], Table 7, Appendix F) indicated much higher sorption of all radionuclides in the interbed material compared to the crushed basalt. The percent recovery for ^{233}U was over 90% but less than 4% for all other radionuclides. Although their retardation factors must be over 200, which is the number of eluted pore volumes following introduction of the spiked solution, exact retardation factors could not be calculated for radionuclides other than ^{233}U. In spite of the large retardation of most of the mass, a small (< 1%), highly mobile fraction of ^{60}Co, ^{241}Am, and ^{239}Pu was observed to break through within the first five displaced pore volumes (Newman 1996 [156434], Section 3.1.2, Figures 11, F-10 to F-13, and F-17 to F-19).

Other experiments conducted as part of the Clemson University and INEEL studies demonstrated that:

(1) 10 to 90% of the water in the intact basalt cores may be immobile, based on the fit of the two-site/two-region model to breakthrough curves of bromide (Newman 1996 [156434], Table 14);

(2) K_d values for ^{90}Sr estimated from column studies of crushed basalt were similar under saturated and unsaturated conditions (Newman 1996 [156434], pp. 68–69); and

(3) K_d values for ^{237}Cs, ^{60}Co, ^{90}Sr, and ^{233}U estimated from batch experiments and column experiments were generally similar, suggesting the applicability of Kd values measured from batch tests to field conditions with much different sediment/water ratios (Newman 1996 [156434], p. 62, Table 13).

10.3.3 Distribution of Radionuclides beneath the Surficial Sediments at the SDA

Several radionuclides, including ^{238}Pu, $^{239,240}Pu$, ^{241}Am, ^{60}Co, ^{137}Cs, and ^{90}Sr, have been found sorbed to rocks and interbed sediments beneath the surficial sediments at the SDA. The locations where radionuclide activities were at least three times greater than the detection limits are noted on maps showing the locations of all deep wells in Figure 10.3-1. These maps are based on a recent data compilation by the USGS (2000 [157415], Tables 3-10a, b, and c), which itself is based on earlier work by Dames and Moore (1992 [157409]). Each map shows the radionuclides

present in different depth intervals, each of which contains either the 9 m, 34 m, or 73 m interbed (see Section 9.3.1.1). Note that not all of the wells shown in Figure 10.3-1 have been sampled, so that well locations with no indicated radionuclides are a mixture of true nondetections and unsampled wells.

The maps in Figure 10.3-1 locally have some lateral and vertical consistency with regard to radionuclide distributions. For instance, closely spaced wells DO-2, 79-2, and TW-1 contain ^{238}Pu, $^{239,240}Pu$, and ^{241}Am at multiple depth intervals. Similarly, well 93 contains ^{241}Am and ^{90}Sr at two different depth intervals (Figures 10.3-2a and 10.3-2b). Elsewhere, however, different radionuclides are present at different depths in a given borehole or different radionuclides are present at the same depths in nearby boreholes, making simple interpretations of these radionuclide distributions difficult. The erratic distribution of these radionuclides may be related to complex flow and transport behavior, including preferential and lateral flow, or to cross contamination during drilling (USGS 2000 [157415]).

Because a complete list of sample locations is not available, it is not known whether the absence of radionuclide detections in Figure 10.3-1 reflects the true absence of radionuclides or simply the absence of samples from those locations. Therefore, although it can be stated confidently that radionuclides are present in the deep subsurface of the SDA, the exact distribution of these radionuclides is uncertain. Qualitatively, however, it is possible to anticipate some of the factors that would be expected to influence the distribution of sorbed radionuclide activities in the subsurface, even if these factors are poorly characterized at present. These factors are (1) the distribution and strength of contaminant sources within the SDA; (2) the distribution of infiltration within the SDA; (3) heterogeneity in fracture properties within the basalt layers; (4) the sorptive properties of the rocks and sediments themselves; (5) the thicknesses of the surficial sediment and sedimentary interbeds; and (6) the orientations of rock/sediment interfaces.

The distribution and strength of the radionuclide sources within the SDA are the subjects of ongoing study at INEEL, and it is likely to be an important control on the observed radionuclide distribution, based on models of nonradiological contaminants at the SDA (Magnuson and Sondrup 1998 [156431]). The models indicated that the observed distribution of these nonradiological contaminants was at least as sensitive to uncertainty in source-term strength as to uncertainty in hydrologic parameters, and a similar sensitivity to source strength could reasonably be expected for the radioactive contaminants as well.

Temporally averaged infiltration rates have been estimated within the SDA (Magnuson and Sondrup 1998 [156431]), based on a study by Martian (1995 [156432]) that used neutron probe moisture logs from 17 boreholes within the SDA and historic data on the nature of the spring thaw to calibrate surficial sediment properties and estimate time-varying drainage from the surficial sediments into the underlying basalts over a 42 yr period. Although there is uncertainty associated with these estimates, the analyses that generated the estimates were as complete as can be expected, and it is unlikely that future analyses will be able to reduce this uncertainty.

Heterogeneities within individual basalt flows are known to exist (Knutson et al. 1990 [107839]) and indicate that the brecciated upper and lower margins may be the most porous and permeable parts of the basalt flows. This conceptual model has suggested to some (Rightmire and Lewis 1987 [156441]) that the basalt permeability is highly anisotropic, with higher permeability in the

subhorizontal direction. Beyond this general conceptual model, however, very little is known about the details of the permeability distribution in the basalts beneath the SDA. It is unlikely that the permeability variations resulting from fractures in the basalts would ever be known in sufficient detail to be able to explain the contaminant distribution, if indeed these permeability variations are the controlling factor.

The thickness of the surficial sediments and the sedimentary interbeds is a possible control on the distribution of radionuclides, because flow through the sediments is through the porous matrix rather than the fractures and the sediments have a much higher porosity and water content than the basalts. Therefore, assuming that flow is primarily vertical, effective porosity between the land surface and any depth largely depends on the thickness of the sediments within that depth interval. Radionuclide migration is expected to be most rapid where the surficial sediments and sedimentary interbeds are thin or absent.

If contrasts in the hydrologic properties of rocks and sediments beneath the SDA cause water to flow laterally along the interfaces between these layers, the orientation of these interfaces may indicate the areas toward which water and contaminants are moving. Lateral flow is possible both when the vertical flux greatly exceeds the vertical hydraulic conductivity of the least permeable layers, and at lower fluxes, when capillary barriers delay or prevent the entry of water moving through fine-grained layers into underlying coarse-grained layers (Montazer and Wilson 1984 [100161]). As discussed below, contour maps of these interfaces exist and can be used to infer flow directions if lateral flow along these interfaces were to occur.

Of all the factors cited above that are likely to influence radionuclide transport at the SDA, perhaps the best known are the thickness and orientations of the major hydrostratigraphic units. Contour maps of the thickness of the sedimentary units and the orientations of the upper surfaces of each hydrostratigraphic layer, including the basalt groups, were created using SURFER (V. 7.0) and data from Magnuson and Sondrup (1998 [156431], Table 2-1) as shown in Figures 10.3-2 to 10.3-11. Unfortunately, the possible relation between the radionuclide distributions shown in Figure 10.3-1 and the layer thicknesses and orientations shown in Figures 10.3-2 to 10.3-11 have been difficult to identify because of uncertainty in the actual extent of the contamination and in other factors likely to influence transport.

10.3.4 Perched Water

The distribution of perched water within the SDA was examined to determine if it could provide some indication of flow paths and evidence for the possible stratigraphic and topographic controls on its occurrence. Perched water has been observed at many locations within the SDA along the surficial sediment/basalt interface, where seasonal water levels have been monitored in several wells and boreholes (Hubbell 1993 [157412], p. 2-6; 1995 [157413], p. 2). Hydrographs of this shallow perched water showed strong seasonal effects, with the highest perched water levels occurring after the spring snow melt. Perched water at the surficial sediment/basalt interface has been found in topographically low areas (MS-03, MS-04, pit 9 wells 1, 2, 3, and 6, and possibly W-06 and NAT-06; see Hubbell 1993 [157412], Figure 1; 1995 [157413], Figure 1 for well locations), but higher elevation areas were not monitored, so the role of topography is unclear. Perched water at the surficial-sediment/basalt interface has also been found in structurally low areas at the surficial sediment/basalt contact (Acid pit well 4 and NAT-16).

However, most of SDA is in a structurally low area along surficial sediment/basalt contact (Figure 10.3-4), so the SDA as a whole may be receiving subsurface lateral flow from the adjacent areas.

Deep perched water has been found consistently in a number of wells within the SDA (Hubbell 1993 [157412]; 1995 [157413]). The wells that contain perched water, the average depth to the top of the perched water, and the perched water elevations are shown in Figure 10.3-12. Wells in which perched water is found at or above the B-C interbed are listed in blue, whereas wells with deeper perched water are listed in red. A comparison of perched water locations shown in Figure 10.3-12 with the contour maps shown in Figures 10.3-2 to 10.3-11 indicates the following: (1) wells D-10, 92, 93-02D, and 8802D are in topographically low areas (Figure 10.3-2); (2) wells 92, 93-02D, and 78-1 are at structurally low areas in the surface of the uppermost (A) basalt (Figure 10.3-4); (3) wells with perched water at the B-C interbed (77-2 and 78-1) are at locations where the A-B interbed is absent (Figure 10.3-5); (4) only well 93-02D is at a structurally low point in the top of the B-C interbed (Figure 10.3-8); and (5) only well 93-02D is at a structurally low point in the top of the C-D interbed. These observations, summarized in Figure 10.3-12, suggest that the topography, the orientation of the surficial sediment/basalt interface, and, possibly, the absence of the A-B interbed may determine where perched water is found at the SDA.

10.3.5 On the Use of INEEL as a Potential Analogue for Radionuclide Transport at Yucca Mountain

The following sections discuss the similarities and differences between various facets of the hydrogeology and geochemistry at Yucca Mountain and the SDA of INEEL. The motivation for this comparison is to evaluate the potential use of the SDA as an analogue for radionuclide migration from a potential repository at Yucca Mountain through the UZ at some time in the distant future.

10.3.5.1 Comparison of Hydrogeologic Settings

There are several similarities in the general hydrogeologic settings that recommend the use of the SDA as an analogue for Yucca Mountain. First, both sites are presently relatively arid. Average annual precipitation is approximately 200 mm/yr at INEEL (Rawson et al. 1991 [156439], p. 478) and 190 mm/yr at Yucca Mountain (DOE 2001 [153849], Table 4.11). The relatively low precipitation rates and high evaporative demand result in estimated net infiltration rates of approximately 10 mm/yr for undisturbed soils near the SDA (Cecil et al. 1992 [156256], p. 711), whereas steady-state deep infiltration rates at Yucca Mountain are estimated to be between 1 and 12 mm/yr (Flint et al. 2002 [157411]), averaging 4.6 mm/yr (DOE 2001 [153849], Table 4.11), depending on the local topographic setting.

The second similarity exists in the hydrostratigraphic settings of the sites and their anticipated effect on water movement through fractures. In the UZ at INEEL, fractured basalts alternate with relatively thin, unconsolidated sedimentary layers (Rightmire and Lewis 1987 [156441]). At Yucca Mountain, relatively unfractured, nonwelded tuffs alternate with fractured, welded tuffs (Scott et al. 1983 [101156]). At both sites, water is expected to move from fractures into the porous matrix and back into fractures as it percolates downward through the fractured layers,

into the unconsolidated sedimentary material or nonwelded tuffs, and back into fractured layers (Montazer and Wilson 1984 [100161]; USGS 2000 [157415]). The details of water movement across the boundaries between these layers may have implications for the formation of perched water, lateral flow, fingering through the porous material, and flow focusing in fractures underlying the porous layers.

The third similarity is the presence of perched water at both sites, some of which may have migrated laterally beneath the present or proposed waste-disposal areas from adjacent areas. Perched water beneath the SDA may have resulted from the diversion of water from the Big Lost River during periods of high flow into spreading areas located 1 to 2 km southwest of the SDA (Rightmire and Lewis 1987 [156441], pp. 40–41, 60–65). At Yucca Mountain, perched water beneath the northern part of the proposed repository area may have originated, in part, from water that had infiltrated in the northern part of Yucca Mountain and moved southward along low-permeability layers at depth (Wu et al. 1999 [117167], pp. 163, 176). At both sites, an understanding of the source and cause of the perched water is important for what it may imply about the magnitude of recharge at the disposal areas and for predicting the pathways that waste may take to the SZ.

Finally, both sites have potential flow-focusing mechanisms. According to one possible conceptual model (USGS 2000 [157415], pp. 2.8–2.10), perched water flowing laterally above or through the sedimentary interbeds at the SDA may be funneled into areas where the interbeds are absent, resulting in the accelerated movement of water and waste compared to areas where the interbeds are present. Additionally, there is the potential for water in the interbeds to flow toward low points along the irregular lower contacts between the sedimentary interbeds and underlying basalts, thereby focusing flow into the basalts in these areas. At Yucca Mountain, lateral flow along stratigraphic contacts may divert water laterally until it is redirected downward by faults or by other discontinuities in the interface between the diverting layers (Montazer and Wilson 1984 [100161], pp. 47–52). Additionally, fault zones mapped at the surface narrow with depth through the PTn (Day et al. 1998 [101557], Plate 2), a factor that could tend to focus water flow through the PTn. In the deep subsurface at Yucca Mountain, most recharge may reach the water table along faults or by moving laterally along perched layers (Flint et al. 2002 [157411]). Both potential recharge mechanisms at Yucca Mountain would tend to concentrate flow and mix water that has flowed through different areas.

Certain dissimilarities that exist between the hydrogeologic settings at the SDA and Yucca Mountain must be taken into account when radionuclide migration in the UZ at the SDA is used as an analogue for how radionuclides could migrate in the UZ at Yucca Mountain. First, in spite of the similarity in precipitation rates and long-term recharge rates of the sites, recharge rates at the SDA site have increased considerably since the SDA was constructed. The drifting of snow within the SDA and its melting during subsequent spring thaws are estimated to cause a net infiltration at the SDA of between 60 and 100 mm/yr, with an estimated long-term spatial average of 85 mm/yr (Martian 1995 [156432], pp. 31–36). Additionally, the SDA has been flooded three times because of the collection of surface runoff in the topographically low areas formed, in part, by the compaction of backfill in the waste pits and trenches. The three flood events of 1962, 1969, and 1982 are estimated to have resulted in the infiltration of 365 mm of water, or the equivalent of about 36 yr of natural infiltration, over the site (Magnuson and Sondrup 1998 [156431], Table 2-3). Thus, a great deal more water has actually been available to

mobilize waste at the SDA than is estimated to be available at Yucca Mountain under present climate conditions or at the SDA under undisturbed conditions.

A second dissimilarity between the two sites is in the fracture patterns in the basalts at the SDA and the welded tuffs at Yucca Mountain. At the SDA, fracture densities are greatest along the brecciated margins and least in the dense interiors of the individual basalt flows (Knutson et al. 1990 [107839], p. 119; Rightmire and Lewis 1987 [156441], p. 41), suggesting that horizontal permeability may be much larger than the vertical permeability in the basalts. Anisotropy of this type in the basalts, like the presence of the sedimentary interbeds, would enhance lateral flow in the UZ. At Yucca Mountain, the generally steep dips of fractures in the Topopah Spring Tuff are likely to favor a high vertical to horizontal permeability ratio in that unit, a hypothesis supported by air-injection and pneumatic pressure-wave analysis (Rousseau et al. 1999 [102097], p. 76). High vertical to horizontal anisotropy in the Topopah Spring Tuff would tend to promote more vertical drainage than might be expected at INEEL. However, beneath the densely welded part of the Topopah Spring Tuff, welding changes and stratified mineral alteration zones also effectively create a high horizontal-to-vertical permeability ratio in the deeper units, so conditions at Yucca Mountain become more similar to those at the INEEL site at depth.

A third distinction between the hydrogeologic settings at Yucca Mountain and INEEL is that fractures in the basalts are often filled with sediments, including authigenic calcite and clay, and detrital clay, silt, and sand that probably washed into the fractures when individual flows were exposed at the land surface (Rightmire and Lewis 1987 [156441], pp. 22–24). Besides providing additional surface area for radionuclide sorption within fractures, the presence of sediment in the fractures at INEEL reduces the likelihood of sheet or film flow within the fractures. Sheet and film flow could be inferred to take place in some fractures at Yucca Mountain, based on the observation that mineral coatings have been deposited preferentially on the footwall of dipping fractures (Paces et al. 1998 [107408], p. 37)

10.3.5.2 Comparison of Geochemical Settings

This section compares the overall geochemical settings of Yucca Mountain and the SDA at INEEL, including mineralogy and water and gas compositions.

The rocks beneath the SDA are tholeiitic and alkali olivine basalts. The dominant minerals in the basalts are olivine (Fo_{50} to Fo_{90}), plagioclase (average An_{65}), clinopyroxene, minor magnetite, and illmenite (Rightmire and Lewis 1987 [156441], p. 10). The interbedded sedimentary material was deposited by rivers and streams draining the surrounding mountains, as well as in lakes that formed when lava flows dammed these streams (Rightmire and Lewis 1987 [156441], p. 11). Eolian deposits are also present. Mineralogically, the interbedded sedimentary material consists of quartz, plagioclase, potassium feldspar, clinopyroxene, olivine, chlorite, clays (illite, illite/smectite, and kaolinite, in order of abundance), and amorphous silica. Calcite-rich and iron-oxide coated horizons exist in the interbeds (Rightmire and Lewis 1987 [156441], pp. 11, 20–24). As mentioned previously, fractures are often filled with sediment and have deposits of calcareous clay.

In terms of their bulk composition, the rocks at Yucca Mountain are classified as rhyolitic and quartz-latitic tuffs. The vitric nonwelded tuffs are composed of sodium- and potassium-rich glass

(Broxton et al. 1987 [102004], Table 3; Vaniman et al. 1996 [105946], Table 1-7). The interiors of thick welded tuffs have devitrified to quartz and feldspar. Phenocrysts include plagioclase (An_{10} to An_{30}), potassium feldspar, biotite [Mg/(Mg+Fe) = 35 to 70%] (Vaniman et al. 1996 [105946], Figure 1.22), and quartz, with trace amounts of hornblende, pyroxene, and magnetite. Major alteration products include smectite, zeolites, silica, and calcite in the rock matrix (Vaniman et al. 1996 [105946], Section 4), and opal, calcite, smectite, zeolites, manganese oxide, and hematite deposited along fracture walls (Vaniman et al. 1996 [105946], Section 5.5).

One factor likely to influence the transport of actinides at the SDA, and potentially at Yucca Mountain, is the dissolved inorganic carbon (DIC) concentration of the groundwater. The DIC of the groundwater is a function of the carbon dioxide partial pressure of the gas in the recharge environment and of the extent to which calcite or other carbon-bearing minerals have been dissolved along the flow path. The DIC of groundwater affects the migration of radionuclides because of the tendency for U, Pu, and other actinides to form aqueous complexes with carbonate (CO_3^{2-}) ions (Langmuir 1997 [100051], pp. 495–530). The formation of neutral or negatively charged aqueous complexes reduces the proportion of the actinides that are present in solution (as positively charged ions that tend to sorb to the rock as a result of ion exchange or surface complexation reactions), thus enhancing the mobility of the radionuclide in groundwater (Langmuir 1997 [100051], pp. 537–538).

Calcite is present in the soils and along fractures in the UZ at Yucca Mountain (Paces et al. 1998 [107408]), and in the surficial sediments, sedimentary interbeds, and fractures in the basalts at INEEL (Rightmire and Lewis 1987 [156441], pp. 21, 31, 33). The natural background carbon dioxide partial pressures of gases in the UZ at Yucca Mountain (Yang et al. 1996 [100194], Figure 18) and at INEEL (Rightmire and Lewis 1987 [156441], p. 55) are similar (log $P_{CO_2\,(bar)}$ = –3.0), and the natural background oxygen partial pressures at the two sites are approximately at atmospheric levels (log $P_{O_2\,(bar)}$ = –0.7). However, the decomposition of buried organic wastes at the SDA may have caused local, and presumably temporary, increases in the carbon dioxide partial pressure, as indicated by calculated log P_{CO_2} for soil water that are much greater than –3.0 (see below). The same processes may have locally reduced log P_{O_2} at the SDA, but no measurements are presently available. In summary, although the background compositions of gases in the UZ at INEEL and Yucca Mountain are similar, the oxidation of buried organic matter at the SDA may have caused local unsaturated zone gas compositions to be substantially different than the gas compositions that exist at Yucca Mountain today.

The chemistry of selected unsaturated zone pore and perched water, and regional groundwater from Yucca Mountain and the SDA, is given in Table 10.3-1. The data for these wells show that the groundwater from the SDA has higher concentrations of most major species except for dissolved silica. Speciation calculations show that the water samples from Yucca Mountain are at or slightly below saturation with calcite and have values of log $P_{CO_2\,(bar)}$ between –3.17 (UZ-14 CHn) and –2.41 (WT-3); water samples from the SDA are all slightly supersaturated with calcite and have values of log $P_{CO_2\,(bar)}$ between –3.03 (well 92) and –2.52 (W02).

At Yucca Mountain, clays, zeolites, and iron- and manganese-oxide coatings that exist in rock pores and fracture walls could sorb radionuclides and slow their migration (Vaniman et al. 1996 [105946], Section 4). Clays and iron-oxide coatings are ubiquitous in the surficial sediments, sedimentary interbeds, and sediment-filled fractures in the basalts at INEEL (Rightmire and

Lewis 1987 [156441]). At both Yucca Mountain and INEEL, the dominant clays are smectites (Vaniman et al. 1996 [105946], Section 5.5.6) or mixed illite/smectite (Rightmire and Lewis 1987 [156441], Table 5); generally, the cation exchange capacity of the clays increases with the percentage of expandable smectitic clay layers. In terms of sorbing substrates, zeolites are more prevalent at Yucca Mountain (Bish and Chipera 1989 [101195]), and iron oxides more prevalent at INEEL, because of the presence of abundant iron in the basalts.

There appears to be more organic matter at the SDA than at Yucca Mountain. In addition to the organic matter mixed with the radioactive waste (Rawson et al. 1991 [156439], p. 478; Magnuson and Sondrup 1998 [156431], p. 4-48), the sedimentary interbeds at the SDA contain organic-rich paleosols (Rightmire and Lewis 1987 [156441], p. 27). Organic matter has the potential to facilitate the movement of radionuclides by forming anionic organic complexes with little tendency to sorb on rock surfaces (Langmuir 1997 [100051], pp. 523–524).

10.3.5.3 Other Challenges and Benefits of Using INEEL as an Analogue for Radionuclide Transport

Several challenges exist if the SDA is used as an analogue for radionuclide transport. The first challenge is that the source terms for various radionuclides are uncertain. The source term reflects the mass of the radionuclide buried in the SDA, its solubility in the existing hydrochemical environment, and its rate of release from any encapsulating medium. Recent attempts to model the observed movement of nonradioactive contaminants beneath the SDA have shown that model results are as sensitive to the assumptions about the poorly known source terms as they are to the expected uncertainty in subsurface transport parameters (Magnuson and Sondrup 1998 [156431], p. 6-2).

The second challenge that the SDA poses as an analogue site is that there has been a lack of consensus on the significance of low-level concentrations of radionuclides in pore and perched water and groundwater beneath the SDA. Many suspected detections of radionuclides have been either near the detection limit, found to be less than the detection limit when resampled, were irreproducible in samples that were split and analyzed by different laboratories, or deemed unlikely to be true detections because of the absence of other radionuclides that should have been present along with the "detected" radionuclide (USGS 2000 [157415], Chapter 4). Even when there has been agreement that the radionuclide is present at statistically nonzero concentrations in the subsurface, there have been questions as to whether or not the contamination was brought into the deeper subsurface during drilling. In summary, there is no well-defined distribution or plume of radionuclides in the deep subsurface that can be used to calibrate geochemical transport models of radionuclides at the field scale.

A third challenge for the potential use of the SDA as an analogue site is that it is hydrogeologically complex. As discussed above, flow through the basalts may depend on local fracture patterns or on details of the configuration of the basalt/interbed interface that may never be known in detail sufficient to make deterministic predictions with confidence. Also, there is uncertainty in the UZ percolation flux because of past flooding events at the SDA and possible lateral migration of water in the deep UZ from nearby water-spreading areas (Magnuson and Sondrup 1998 [156431], pp. 6-3, 6-4). Predictions of radionuclide transport are therefore subject not only to uncertainty in geochemical processes and parameters but also to a great deal of

complexity in hydrologic processes. Ideally, a site chosen as an analogue for geochemical processes at Yucca Mountain would exist in a very simple, well-understood hydrologic environment, so that the geochemical processes and parameters could be clearly identified.

In spite of these limitations as an analogue site, the SDA has produced a great deal of site data, and many analyses have been done of both the hydrologic and geochemical environment at the site. Moreover, INEEL as an institution is highly motivated to collect additional data and perform additional analyses, so that some of the uncertainty discussed in the preceding sections will undoubtedly be reduced at some time in the future. The SDA does not serve as a typical analogue in the sense that it can provide clear, unambiguous, and widely accepted explanations for radionuclide migration that indicate the expected behavior of radionuclides at Yucca Mountain. However, examination of the SDA site by the Yucca Mountain Site Characterization Project (YMP) is useful in that it provides additional opportunities to test models similar to those that have been or will be developed for Yucca Mountain. To better understand which lessons the scientific community (including regulatory agencies and oversight groups) have learned from the SDA is truly relevant to the YMP.

10.3.6 The SDA Modeling Study

The overall purpose of the models developed as part of this study is twofold. First, it is important for INEEL to understand the processes that resulted in the apparent migration of radionuclides to the deep UZ. Only then can they determine if the causes for mobilization and transport of radionuclides continue to exist, or if recent improvements at the site have eliminated the conditions that led to the earlier mobilization of the waste. In particular, if the radionuclides present in the deep subsurface could have been transported there only because of past flooding (and the potential for future flooding has been eliminated by berm construction, drains, or other mechanisms), then the likelihood for continued or renewed mobilization of radionuclides at the SDA may be small. Conversely, if radionuclide migration has resulted from flow-focusing processes that are caused by permanent geologic features of the site, or from geochemical conditions that are likely to persist for a long time, the continued or renewed transport of radionuclides becomes more likely.

For the YMP, it is important to understand if the processes that resulted in the apparent migration of radionuclides at the SDA are present or will be present at Yucca Mountain in the future. If radionuclide transport at the SDA has been facilitated by flooding events or geochemical conditions at the SDA (such as the co-burial of radionuclides and chelate-forming organic chemicals) that are unlikely to exist at Yucca Mountain, then radionuclide migration at the SDA becomes no more than a cautionary warning to "do no harm" to Yucca Mountain by inadvertently altering its natural hydrologic or geochemical state. Alternatively, if radionuclide migration at the SDA is the result of hydrologic or geochemical processes that are or will be common to both sites, numerical transport models of the SDA may have substantial transfer value to the YMP in terms of experience and understanding gained. In any case, modeling radionuclide transport at the SDA provides the possibility to actually test model predictions against reality, a possibility that is lacking at Yucca Mountain.

10.3.6.1 General Strategy for the Calibration of Radionuclide Transport Models at the SDA

In view of the uncertainties in the hydrologic system, the radionuclide source term, and even in the distribution of radionuclides in the field environment at the SDA, two radionuclide transport models were developed: (1) a shallow one-dimensional model extending a few meters from the waste burial pits to the top of the underlying basalt and (2) a deep two-dimensional model extending from the ground surface to the water table beneath the SDA. The purpose of the shallow model is to identify the transport parameters of the sediments through trial-and-error matches of the model to the measured radionuclide concentrations beneath the waste burial pits. This model requires assumptions about the local infiltration rate as well as other transport parameters, but because the measured profile does not extend into the fractured basalts, it is relatively simple hydrologically. The first model was used to simulate the transport of radionuclides in the surficial sediments beneath the waste-disposal pits. Field studies (Humphrey and Tingey 1978 [157491]; Rightmire and Lewis 1988 [156442]; Rawson et al. 1991 [156439]), provided measurements of radionuclide concentrations in a relatively simple hydrologic setting that did not directly involve flow in the fractured basalts. The effects of assumptions regarding source-term inventory and of hydrologic property contrasts were explored in this group of simulations.

The deeper two-dimensional model is restricted to transport of a single tracer. The results of the model were qualitatively compared to measurements of matric potential, observations of perched water, and the distributions of radionuclides and other contaminants in the interbed sediments, perched water, and the Snake River Plain Aquifer. The overall purpose of the two-dimensional model is to identify combinations of rock hydrologic and geochemical properties that could have allowed the deep migration of radionuclides through the basalt layers and interbedded sediments. The fully coupled, nonisothermal, two-phase flow and reactive transport computer codes FLOTRAN (Lichtner 2001 [156429]) and FEHM (Zyvoloski et al. 1997 [100615]) were used for the modeling studies.

10.3.6.2 Numerical Simulations of Water Flow and Conservative Tracer Transport

Single- and dual-permeability models of water flow and conservative tracer transport were based on a highly schematic representation of the UZ beneath the SDA. The purpose of these schematic models was to investigate the conditions under which radionuclides might have reached the B-C and C-D interbeds at depths of approximately 34 and 73 m, respectively. The flow domain for these models extends 60 m in the horizontal direction and from land surface to slightly below the water table at a depth of approximately 180 m. A background infiltration rate of 1 cm/yr (Cecil et al. 1992 [156256], p. 711) was used to establish steady flow conditions in these models and was maintained at land surface outside the waste-disposal area throughout the transient period, assumed to span the last 50 years. Within the 12 m wide waste disposal area, the flux was increased to 8 cm/yr at the start of the transient part of the simulations, reflecting the increase in infiltration rates that are estimated to have occurred at the SDA because of disturbances to the natural conditions following construction of the SDA in 1952 (Magnuson and Sondrup 1998 [156431], pp. 1-5, 1-7). Additional amounts of water (Table 10.3-2) were applied over ten-day periods 10, 17, and 30 yr into the transient part to represent flood events that occurred at the SDA in 1962, 1969, and 1982 (Magnuson and Sondrup 1998 [156431], Table 2-3).

10.3.6.3 Results of Single-Continuum Models

In the single-continuum models, only the fracture-continuum properties of the basalts and the matrix-continuum properties of the surficial sediments and sedimentary interbeds are represented (Table 10.3-3). Shown in Figure 10.3-13 is a comparison of the saturation profile for the single continuum obtained using the computer codes FLOTRAN and FEHM with a numerical solution of Richards equation obtained from Mathematica (Wolfram 1991 [157417]). As can be seen from the figure, excellent agreement is obtained for the two codes, as well as good agreement with the Mathematica solution. The slight offset between FEHM and FLOTRAN can be attributed to differences in the discretization approach used in the codes.

The saturation calculated using the single-continuum model at the end of the 50 yr transient period (2002) is shown in Figure 10.3-14. No significant lateral changes in simulated saturation are present resulting from the higher infiltration rates associated with the waste disposal area in the central part of the model domain. McElroy and Hubbell (1990 [156433], p. 362) reported capillary pressures of 0.2–1.3 bars in the surficial sediments and 0.3–1.3 bars in the 9 m, 34 m, and 73 m interbeds. McElroy and Hubbell (1990 [156433], p. 363) also reported that conditions were wetter at the tops of the sedimentary interbeds than at the bottoms, a condition that is also present across the interbeds in the simulation results (see also Figure 10.3-13).

The relative tracer concentrations (concentration relative to input concentration) at the end of the 50 yr transient period are shown for the upper 80 m of the model domain in Figures 10.3-15a and b for constant and pulse infiltration, the latter representing the flooding events listed in Table 10.3-2. Shown in Figure 10.3-16 is the tracer concentration for both FLOTRAN and FEHM for constant infiltration and pulsed infiltration using FLOTRAN along the centerline of the computation domain. The tracer is applied with unit concentration within the waste-disposal area in the central part of the model domain. Outside this region, a concentration of 10^{-3} is applied. An initial concentration of 10^{-8} is assumed. The model results indicate that a small fraction of a conservative solute could migrate from shallow waste-disposal pits to the 73 m interbed within 50 years, given the infiltration rates and rock properties assumed in this model. The pulse release leads to a somewhat greater penetration depth.

10.3.6.4 Results of Dual-Permeability Models

In the dual-permeability models, the basalt fracture-continuum properties and the sediment matrix-continuum properties are the same as in the single-continuum models and, additionally, the basalt matrix-continuum properties and sediment fracture-continuum properties are included. The FLOTRAN code requires that dual-permeability models have a fracture continuum throughout the model domain, but it is unlikely that the unconsolidated sedimentary layers actually contain fractures. Ideally, then, the fracture continuum in the sedimentary layers would be defined in such a way that it transmits negligibly small amounts of water and does not affect the saturations or capillary pressures in the matrix continuum of the same sedimentary layer or in the fracture continuum of the adjacent basalts. Therefore, the fracture-continuum properties and fracture-matrix interaction terms in the sedimentary layers (see note to Table 10.3-3) were chosen to ensure that the water flow rates, saturations, and capillary pressures of the sedimentary layers in the dual-permeability models were nearly identical to the flow rates, saturations, and capillary pressures of the sedimentary layers in the single-continuum models. This was done by

assigning a low volume to the fracture continuum in the sedimentary layers and making the fracture-matrix interaction term large enough to result in the equivalent continuum limit of the dual-continuum model. Hydrodynamic equilibrium between the fracture and matrix continua in the sedimentary layers is maintained and dominated by the properties of the matrix continuum. The approach was verified by comparing the saturation of the matrix continuum in the dual-permeability model with the saturation of the sedimentary layers of the single-continuum model, in a one-dimensional steady-state model with infiltration rate of 1 cm/yr (Figure 10.3-17). Also shown is the numerical solution to Richards equation obtained using the software code Mathematica (Wolfram 1991 [157417]) for the single-continuum case. Saturation of the sedimentary layers in the two models is nearly identical. As expected, saturation of the fracture continuum of the basalt layers in the dual-permeability model is slightly less than that of the basalt layers in the single-continuum model, because a small part of the flux in the dual-permeability model moves through the basalt matrix. In the upper parts of the individual basalt flow units, the fracture continuum and matrix continuum are not in capillary-pressure equilibrium, probably because the large reduction in the fracture-matrix surface area (0.01) limits water flow from the fractures into the matrix. However, capillary-pressure equilibrium is re-established with depth within the flow unit as water flows from the fractures into the matrix.

The simulated saturation profiles for the fracture and matrix continua of the dual-permeability model are shown in Figure 10.3-18 after an elapsed time of 50 years for constant infiltration. Matrix saturations in the basalts are much higher than fracture saturations throughout the model domain because the assumed moisture retention characteristics allow the matrix to retain more water at high capillary pressures than the fractures. The fracture and matrix continua are in approximate capillary-pressure equilibrium above the 73 m interbed, but, similar to the results of the one-dimensional steady-state dual-permeability model (Figure 10.3-17), the matrix capillary pressures just below the 73 m interbed correspond to drier conditions (have higher capillary pressures) than in the adjacent fractures. Gradually, as water flows from the fractures into the matrix, capillary-pressure equilibrium between the two continua is re-established with increasing depth below the 73 m interbed.

The relative tracer concentrations at the end of the 50 yr transient period are shown for the upper 80 m of the fracture and matrix continua in Figure 10.3-19 for the case of constant infiltration. The fracture-continuum relative concentrations (Figure 10.3-19a) are slightly less than the concentrations of the single-continuum model at the same location (Figure 10.3-15a) because some of the tracer has moved into the basalt matrix in the dual-permeability model. The additional storage provided by the basalt matrix prevents the tracer from arriving at the 73 m interbed in the dual-permeability model. However, tracer is present in the 9 m interbed at a relative concentration of 0.06 and in the 34 m interbed at a relative concentration of 0.03, despite the much lower concentrations or absence of the tracer in the overlying basalt matrix (Figure 10.3-19b). Clearly, the tracer distribution in the matrix continuum of the A-B and B-C interbeds reflects the transport of tracer almost exclusively through the fractures of the basalt units.

It should be noted that in the single-continuum models, the basalt layers used the properties listed for the A-, B-, C-, and D-basalts. In the dual-permeability models, these property values were used for the fracture continuum in the appropriate layer, and "basalt matrix" properties were used for the matrix in all basalt layers. All layers (including sedimentary layers) in the dual-permeability model were assumed to have cubic matrix blocks 1 m on a side and a bulk fracture

porosity of 0.01. Fracture-continuum properties of the sedimentary layers were assumed to be the same as those given for the matrix in Table 10.3-2. In the basalt layers, the effective fracture-matrix area calculated from the block dimensions was reduced by a factor of 0.01 based on model calibration results of the large-scale infiltration test (Section 9.3). In the sedimentary layer, the fracture-matrix area was increased by a factor of 100 to ensure hydrodynamic equilibrium between the fracture and matrix continua. The equivalent continuum permeability was twice that given for the interbed matrix permeability.

10.3.6.5 Flow and Transport Simulations with Dipping, Discontinuous Layers

The previous simulations in Sections 10.3.6.3 and 10.3.6.4 have considered an idealized hydrostratigraphy for the SDA in which layers are horizontal and of uniform thickness. In contrast, structural contour and isopach maps (see Section 10.3.3) indicate that the SDA is located in an area where the surficial-sediment/basalt interface is relatively low and where the interbeds have variable thicknesses and dips. To examine the effect that departures from the idealized stratigraphy of the previous case might have on flow and transport beneath the SDA, investigators created a model with the computer code FEHM that considers the structural depression in the A-basalt beneath the SDA and treats the 9 m and 34 m interbeds as dipping discontinuous layers (Figure 10.3-20). The C-D interbed is horizontal with uniform thickness, as in the previous calculations.

The FEHM model is based on a single-continuum representation with the same hydrologic properties as used in the previous single-continuum models (Table 10.3-3). The FEHM model has a constant vertical node spacing of 0.5 m and horizontal node spacing of 1.0 m. In this model, the pulses of water associated with flooding events are not used; instead, the flux in the central 12 m of the model domain was increased to 10 cm/yr during the 50 yr transient period to implicitly account for these events. This led to slightly more water being introduced into the UZ than in the previous models for the last 50 yrs (5 m for this model compared with the 4.61 m of water introduced for the cases with flood events).

For a steady-state uniform infiltration rate of 1 cm/yr, flow-lines calculated by particle tracking in FEHM indicate that the clay layer at the base of the surficical sediment strongly focuses flow toward low areas in this layer beneath the hypothetical SDA, at the center of the model domain (Figure 10.3-21). The interbeds also divert water laterally along their upper surface, but the amount of offset for the flow lines is less than 5 m at any interbed. Because water flow is focused by the slope of these layers, wetter conditions exist at low points in the clay layers and where the interbeds terminate, even when infiltration rates are uniform. (Note that water potentials were calculated by subtracting a uniform air pressure of 1 bar from the calculated water pressure; a water potential of 0 bars indicates saturated conditions.)

Saturations calculated at the end of the 50 yr transient period, in which 10 cm/yr of infiltration was applied in the central 12 m of the flow domain, indicate that the basalts are wettest below the ends of the overlying interbeds (Figure 10.3-22). Tracer concentrations near the water table at the end of the 50 yr transient period are highest where the 34 m interbed has focused water flow (Figure 10.3-3). Peak tracer concentrations at the water table are about 0.12 compared to peak concentrations of about 0.05 for the case with uniform, horizontal layers. Although slightly more water was applied in the case with discontinuous layers, the pattern of saturation (Figure 10.3-

22) and tracer concentrations (Figure 10.3-23) suggests that part of the early breakthrough is caused by some water flowing around rather than through the high-porosity interbeds. Also, flow rates are relatively high where flow is focused by the dipping, discontinuous layers.

10.3.6.6 Reactive Transport Calculations

In this section, vertical radionuclide transport through the surficial sediment zone in the SDA is investigated. Using representative soil-zone water and P_{CO2}, along with surface site density, cation exchange capacity, and mineralogy of the soil zone, sorption profiles for ^{241}Am, ^{238}Pu, ^{137}Cs, and ^{90}Sr were calculated and compared with field observations. The resulting model calibration predicts a high retardation factor for Np and essentially no retardation for U.

10.3.6.6.1 Sorption Reactions: Surface Complexation and Ion Exchange

Both surface complexation reactions and ion exchange are included in the description of sorption. The radionuclides americium and plutonium take part in surface complexation reactions, and cesium takes part in ion exchange. Strontium is involved in both sorption processes. The generic form of surface complexation reactions can be written as

$$X_m^{\alpha} + \sum_j \nu_{jk}^{m\alpha} A_j \Leftrightarrow A_k^{m\alpha} \qquad \text{(Eq. 10-2)}$$

where X_m^{α} denotes the surface site of type α, A_j an aqueous primary species, $A_k^{m\alpha}$ the sorbed surface complex, and $\nu_{jk}^{m\alpha}$ the stoichiometric coefficient matrix. This description neglects the role played by the counter ion and therefore does not conserve charge separately within the aqueous and solid phases whenever the surface complex is charged. It is presently unknown what effect this inconsistency may have on predicting retardation and changes in solution chemistry, such as pH (Lichtner 1996 [101409], pp. 57–59). Ion exchange reactions have the form

$$z_j X_{z_i} A_i + z_i A_j \Leftrightarrow z_i X_{z_j} A_j + z_j A_i, \qquad \text{(Eq. 10-3)}$$

where $X_{z_i} A_i$ refers to the sorbed cation. These reactions conserve charge rigorously in both aqueous and solid phases, unlike the representation used for surface complexation reactions. Sorption reactions for surface complexation included in the model calculations are listed in Table 10.3-4 along with corresponding selectivity coefficients. The data were taken from Zavarin and Bruton (2000 [156443] and 2000 [156444]). Cations taking part in ion exchange reactions are listed in Table 10.3-5, along with their selectivity coefficients. The data were adapted from generic values given in Appelo (1996 [156425]).

Generally, sorption reactions involve multiple sorption sites associated with different mineral surfaces. Two distinct philosophies have been articulated in the literature (Davis et al. 1998 [154436]) for modeling sorption reactions. One approach is to develop a detailed model based on the specific minerals present in the sorbing medium. This approach has the advantage of being more mechanistically based and having the potential capability of incorporating changes in mineral abundances on sorption. Its primary disadvantage is the extensive amount of data required as input parameters to the sorption model. An alternative approach is based on the bulk properties of the porous medium. This approach is more phenomenological, but has fewer data

requirements. It is based on direct measurements of bulk properties such as cation exchange capacity (CEC) and surface site densities. In this report, the bulk approach is used, employing a multisite description of surface complexation reactions and a single-site representation of ion exchange reactions.

For a dilute aqueous solution, retardation of a particular primary species is derived from the distribution coefficient K_j^D, defined as the ratio of total sorbed to total aqueous concentration of that species

$$R_j = 1 + K_j^D \qquad \text{(Eq. 10-4)}$$

The distribution coefficient is given by the expression

$$K_j^D = \frac{1}{\phi \Psi_j}\left[\sum_{km\alpha} \nu_{jk}^{m\alpha} \Xi_k^{m\alpha} + \Xi_j^{ex}\right] \qquad \text{(Eq. 10-5)}$$

involving a sum over surface complexation and ion exchange isotherms, where $\Xi_k^{m\alpha}$ refers to the sorbed concentration of surface complex $A_k^{m\alpha}$, and Ξ_j^{ex} refers to the ion exchange isotherm. The quantity Ψ_j represents the total aqueous concentration of the subscripted species.

Sorption reactions used for surface complexation include the surface sites: >FeOH, >SiOH, >AlOH, and $>Ca^{2+}$. Unknown is the appropriate site density to use in the calculations. The site concentration associated with the *m*th mineral, denoted by n_α^m [mol/dm^3], can be expressed as a product of a number of factors involving the intrinsic mineral site density (η_α^m [# sites/nm^2]), mineral concentration ($\rho_m \phi_m$ [kg/dm^3]), and mineral specific surface area (A_m [m^2/kg]). Thus, the site concentration can be calculated from

$$n_\alpha^m = \frac{1}{N_A} \eta_\alpha^m A_m \rho_m \phi_m \qquad \text{(Eq. 10-6)}$$

where N_A denotes Avogradro's number, the intrinsic site density is denoted by η_α^m, and the specific surface area is represented by A_m.

Retardation caused by ion exchange is proportional to the CEC of the exchanging medium and the bulk rock density. The conventional definition of the CEC is in units of meq/100 g solid. A more useful quantity is mole equivalents of exchange sites per bulk volume of porous medium, denoted by the symbol ω. The two quantities are related by the porosity and grain density of the porous medium

$$\omega = (1 - \phi)\rho_s \mathrm{CEC} \qquad \text{(Eq. 10-7)}$$

where ρ_s denotes the grain density and ϕ the porosity. Retardation is proportional to ω and, thus, to the product of the bulk density and the CEC.

10.3.6.6.2 Model Simulations

Calculations were performed in one dimension with a constant infiltration Darcy flow rate of 10 cm/yr, a porosity of 50%, and an average saturation of 0.58 (Magnuson and Sondrup 1998 [156431], p. 4-8, Table 4-2). Radioactive decay was not included in the simulations. An aqueous diffusion coefficient of 10^{-5} cm^2/s with a tortuosity of 0.294 taken from Magnuson and Sondrup (1998 [156431], Table 4-2, p. 4-8) for the surficial sediment layer was used in the simulations.

The injection fluid composition is listed in Table 10.3-6. The fluid composition is taken from Well 99 corresponding to perched water as listed in Table 10.3-1. The pH was adjusted to give equilibrium with calcite, which otherwise would have been supersaturated by one log unit. This adjustment resulted in a reduction in the reported pH of 8.4 to 7.59. The redox state of the fluid is not given in Table 10.3-1. As discussed below, to obtain a simultaneous fit to the concentration profiles for plutonium and americium, it was necessary to invoke reducing conditions. The initial fluid composition was set to be the same as the injection fluid, with the exception of the radionuclide concentrations: plutonium, americium, cesium, uranium, and neptunium, which were set to small values (10^{-20} mol/L) and strontium, which was given the value of 5×10^{-16} mol/L to fit the minimum observed strontium value. It was not determined how much of the strontium profile resulted from nonradioactive strontium that was naturally occurring. The calculated $log\ P_{CO_2}$ = -2.18, which is quite high, presumably resulted from decomposition of organic matter in the waste and soil zones. As can be seen by inspection of Table 10.3-6, carbonate complexes play an important role in speciation of americium and uranium and less so for neptunium. Plutonium exists primarily in the IV oxidation state in the form of the complex $Pu(OH)_4$.

The observed sorbed concentration profiles were fit by adjusting the surface site densities and the injected radionuclide concentrations. Site densities >FeOH, >AlOH, and >SiOH were adjusted to fit the observed profiles. The $>Ca^{2+}$ site density was arbitrarily set to 10^{-4} mol/L. The resulting site densities used in the simulations are listed in Table 10.3-7.

Speciation results of the injection fluid for the amount sorbed for different radionuclides participating in surface complexation are presented in Table 10.3-8, in which the contribution to the distribution coefficient is listed for each surface site. It can be seen that plutonium contains contributions from sorption sites >FeOH and >AlOH, whereas americium is primarily sensitive to site >AlOH and to a lesser extent site >Ca. There were no data available for uranium and neptunium. The distribution coefficients are much smaller than those reported by Dicke (1997 [157410]) as listed in Table 9.3-1.

An entirely different result is obtained under oxidizing conditions. In this case, both plutonium and americium are strongly sorbed to >FeOH, with americium several orders of magnitude greater compared to plutonium. Because under oxidizing conditions plutonium is not sorbed to any other sites, it is not possible to fit the plutonium and americium profiles simultaneously under these conditions.

Generic values for the ion exchange selectivity coefficients (see Table 10.3-5) were taken from Appelo (1996 [156425]). The CEC was varied to fit the cesium profile. A value of 0.02 mol/kg was obtained. This value is at the lower limit of the reported CEC range for the surficial

sediments of 0.27 to 0.02 mol/kg (Rightmire and Lewis 1987 [156441], Table 5). The strontium profile was predicted by the model without any additional fitting.

The resulting fit to the data is shown in Figure 10.3-24, corresponding to advection and diffusion. The obtained fit does not capture the observed decrease in plutonium concentration at depth of approximately 1 m. This discrepancy could be a result of several factors, including heterogeneity, lateral flow, and the possibility of the presence of the contact between the clay and basalt layer that occurs at this depth. Other species also indicate a slight increase in concentration at this depth.

10.3.7 Discussion

Several interpretations of radionuclide transport in the surficial sediment zone are possible. One is that lateral flow occurred, sweeping out part of the radionuclide plume. The thickness of the stratigraphic layers is highly irregular, and the possibility exists that flow occurred along the interface between the clay layer and the surficial sediment layer. Another possibility is that a catastrophic or sudden release of a pulse of fluid, caused by a flooding event, released a pulse of radionuclides that propagated downward with reduced retardation, due to kinetic effects caused by fast flow rates. For this situation, the data are interpreted as background flow (or diffusion) producing the upper monotonically decreasing profile with depth. The lower portion of the profile, where the concentration is increasing was the result of a sudden flow event. Presumably, according to this interpretation, the peak lies at a still greater depth below that at which the data were collected.

The model calculations predict retardation factors for neptunium and uranium that are seen to be orders of magnitude higher compared to the other radionuclides. This result would indicate that very little movement of neptunium and uranium should be observed. No values for these radionuclides were reported that could be taken as consistent with their predicted high retardation.

Finally, although it was necessary to assume reducing conditions for fluid coming from the SDA, it is not expected that such conditions would persist at greater depths because of the partially saturated conditions that are present there, leading to oxidizing water.

10.3.8 Conclusion

The main conclusion to be drawn from this study is that INEEL presents a far wetter environment than that of Yucca Mountain. This increase in infiltration is manifested in higher infiltration at the SDA and flooding events that could have resulted in enhanced radionuclide migration beneath the SDA. Focused flow resulting from the undulating topography of the basalt flows and sedimentary interbeds would be expected to exacerbate the situation, leading to even greater distances of radionuclide migration, as demonstrated in the modeling exercises.

It was found that to fit observed radionuclide concentrations in the surficial sediment layer, reducing conditions were required. Otherwise, it was not possible to fit the observed profiles of both americium and plutonium simultaneously. Note that although detailed waste compositions are not currently known, there is significant organic matter in the waste that is not inconsistent with the assumption of reducing conditions. However, as noted above, such conditions are not

expected to prevail at greater depths, where the system would be expected to be oxidizing. The calculated profiles did not capture the increase in concentration observed at greater depth near the base of the surficial sediment layer. To further test and validate model predictions, continuity of data at greater depths beneath the SDA would be needed along with site-specific data for surface complexation site densities.

10.4 RADIONUCLIDE FLOW AND TRANSPORT STUDIES AT PEÑA BLANCA, MEXICO

10.4.1 Objectives

The goal of these studies is to construct a three-dimensional conceptual model of the transport of uranium and radiogenic daughter products at Peña Blanca, Mexico (*Technical Work Plan for Natural Analogue Studies for License Application* (BSC 2001 [157535], p. 4)). A three-dimensional model will extend the previous work at Peña Blanca that was limited to collection of data for exposed planar surfaces. The model will also address whether there has been preferential flow/drainage downward through fractures or if there has been a net flux of uranium off-site. To accomplish this, three wells will be drilled at the site to obtain core samples from within and beneath the uranium ore body and to collect water samples from beneath the ore body. The core and water samples will be analyzed using a variety of techniques to support development of the conceptual model of transport at Peña Blanca. The conceptual model will then be tested using numerical methods employed by the UZ Flow and Transport Model to build confidence in understanding UZ transport at a potential Yucca Mountain repository.

10.4.2 Background

In the 1970s, the Peña Blanca region, approximately 50 km north of Chihuahua City, was a major target of uranium exploration and mining by the Mexican government. Since that time the Nopal I uranium deposit has been studied extensively because it is a good analogue for evaluating the fate of spent fuel, associated actinides, and fission products at a geologic repository in unsaturated volcanic tuff. Previous studies associated with Peña Blanca as well as a geologic description of the site were reviewed in *Natural Analogs for the Unsaturated Zone* (CRWMS M&O 2000 [141407]). Briefly, the Nopal I uranium deposit at Peña Blanca represents an environment that closely approximates that of the potential high-level radioactive waste repository at Yucca Mountain, Nevada, in the following ways:

- Climatologically: both are located in semi-arid to arid regions
- Structurally: both are parts of a basin-and-range horst structure composed of Tertiary rhyolitic tuffs overlying carbonate rocks
- Hydrologically: both are located in a chemically oxidizing, UZ 100 m or more above the water table
- Chemically: the alteration of uraninite to secondary uranium minerals at Nopal I may be similar to the eventual fate of uranium fuel rods in a potential geologic repository like Yucca Mountain.

10.4.3 Previous Radionuclide Transport Studies at Peña Blanca

Studies of uranium-series disequilibria within and around uranium deposits can provide valuable information on the timing of actinide mobility and hence the undisturbed stability of a potential repository over the geologic time scales associated with the required lifetime of the facility. Previous studies at Peña Blanca dealing with bulk samples and fractures have focused on the extent and timing of uranium-series mobility or transport at this site, and have been summarized in *Natural Analogs for the Unsaturated Zone* (CRWMS M&O 2000 [141407]). Some of these studies reported open-system behavior, suggesting mobility of uranium and its daughter products. In contrast, previous uranium-series thermal ionization mass spectrometry (TIMS) work at Nopal I (CRWMS M&O 2000 [141407], pp. 89–90) found closed-system behavior, suggesting very limited mobility in fracture-filling material for uranium. Briefly, the TIMS results indicated that the uranium (235, 238), thorium, and protactinium in the fracture-filling minerals have remained stable for more than 300 ka at Nopal I.

Pickett and Murphy (1999 [110009]) presented measurements of U-Th isotopic composition and concentration in various water samples collected near the Nopal I uranium deposit during relatively wet conditions (see 1995 collections in Table 10.4-1). The observed uranium and thorium concentrations generally correlate with concentrations of major cations and anions and total conductivity, which may reflect evaporation-dilution or rock dissolution effects on all of these species. Thorium and uranium concentrations also correlate strongly with each other, which is surprising given the expected differences in solution chemistry and potential solubility controls for these two elements. Pickett and Murphy (1999 [110009], p. 812) interpreted these concentrations in the context of solubility control by various uranium silicate minerals (haiweeite, soddyite) and thorianite. They found that the perched water is close to solubility for haiweeite, a calcium uranyl silicate mineral. All of the other waters are undersaturated with respect to uranium mineral phases. However, all of the waters are supersaturated with respect to thorianite, which is attributed to the presence of colloidal thorium in the <0.2 μm fraction of these samples. The occurrence of undersaturation for uranium and supersaturation for thorium indicates that radionuclide transport in the UZ may be controlled by kinetic factors such as evaporation, rock dissolution, and colloid formation, which complicate the interpretations based on thermodynamic (solubility) considerations. The incorporation of kinetic factors will be discussed below with respect to the generalized radioisotope transport model of Ku et al. (1992 [109939]).

10.4.4 Ongoing Work at Nopal I

As previously summarized, prior work at Peña Blanca contrasts the long-term stability of uranium and thorium in fractures against the ongoing dissolution of uranium by surface waters, as evidenced by elevated uranium concentrations and $^{234}U/^{238}U$ in adit seepage waters. The net flux off-site is not well constrained other than by the 8 ± 5 m.y. age of the primary uranium mineralization at Nopal 1 (Pearcy et al. 1994 [100486], p. 729). Current (2002) work is discussed in the following subsections.

10.4.4.1 Drilling

The goal of current work (BSC 2001 [157535], p. 4) is to extend geochemical studies to the third dimension by drilling wells at Nopal I. Work is now underway to drill one borehole through the uranium ore deposit to a depth of approximately 200 m. The borehole is planned to penetrate the SZ to at least 20 m, and core will be collected during drilling. In addition, two additional wells will be drilled at approximately +50 m and –50 m from the borehole. Monitoring wells will be installed to sample ground water on a quarterly basis.

10.4.4.2 Surface Water Sampling

The work of Pickett and Murphy (1999 [110009]) has been extended to include water samples collected at Nopal I during the dry season. Samples were collected in February 2000 and March 2001 (Simmons 2002 [157544], pp. 86–87). These data provide new information on temporal and seasonal variations at the site (see Section 10.4.4.4). As with the previous work, samples are of three different types: (1) perched water trapped in an old borehole about 20 m outside the deposit, (2) seep water obtained from an old adit approximately 8 m below the +10 m surface (see Figure 10.4-1), and (3) a groundwater sample located in the regional carbonate aquifer 1.3 km southeast of the deposit. In addition, data has been collected from an old mining camp well located about 0.6 km southeast of the deposit.

These new data, along with the 1995 data from Pickett and Murphy (1999 [110009]), are detailed in Table 10.4-1. In many cases, the new data show higher uranium concentrations ratios than the results from Pickett and Murphy for samples collected during the wet season. This could result from longer fluid/rock interaction times or from greater evaporation. A portion of the collection system is shown in Figure 10.4-2. The water is collected in plastic sheets, in which it remains until sampled. Although the adit is comparatively cool and damp, evaporation could greatly influence the uranium concentrations.

Stable isotope data were obtained for some of these adit samples to evaluate the effects of evaporation on the uranium concentrations. These data are shown in Figure 10.4-3. When water evaporates, the isotopic composition of the resulting vapor will be shifted to lower values of $\delta^{18}O$, and the residual water will be shifted to higher values on a plot of δD versus $\delta^{18}O$. The stable isotope data for AS-5 (from a water well) and AS-6 (from a drill hole into a perched water horizon) have significantly lower values than other samples. They fall on the Global Meteoric Water Line (GMWL) and probably represent the average composition for the precipitation at the site. The adit samples all lie much higher on this plot. Of these, AS-2, AS-3, and AS-4 all fall significantly to the left of the GWML and may represent atmospheric water vapor that has diffused into the adit and condensed in the cooler, underground environment, followed by some period of evaporation in the collection system. AS-1 lies on the GMWL, but probably does not represent a rainwater sample, because it is relatively high for meteoric water at this latitude; it is closer to the opening of the adit and may represent a more evaporated version of cluster AS-2, AS-3, and AS-4. The evolution of stable isotopes for the adit samples appears to have at least three components: (1) evolution of vapor from GMWL, (2) modification by water/rock interaction, and (3) evaporation in the adit collection system. A simpler approach planned for evaluation is to normalize the uranium data to chloride or bromide concentrations.

10.4.4.3 Radioisotope Transport Modeling

A model based on naturally occurring uranium- and thorium-series disequilibria is being tested for characterization of the *in situ* migration of actinide nuclides in and around the Nopal I uranium deposit. Estimates can then be made of the rates of sorption-desorption, hence retardation factors, and dissolution-precipitation of the isotopes over a range of time scales, in both the SZ and UZ. Such information is vital to testing or validating performance assessment models for geologic nuclear waste disposal.

Current models utilizing uranium- and thorium-series disequilibria for radioisotope transport in geologic systems are primarily based on the steady-state flow assumption (Ku et al. 1992 [109939], pp. 639,640). These models, while elucidating the behavior of radioisotopes in the phreatic zone, may not sufficiently constrain the isotope transport in unsaturated vadose layers where the concentration and transport behavior of radioisotopes are often governed by nonsteady conditions. During the past year, the uranium-series transport model of Ku et al. (1992 [109939]) has been extended to include the nonsteady-state situations. Free of the steady-state assumption, this new, generalized radioisotope transport model has the two important features of being applicable to both the SZ and UZ, and providing simultaneous constraints on the behavior of radioisotopes in dissolved, colloidal, sorbed, and solid pools of a groundwater system.

The model makes the following assumptions: (1) in natural water-rock systems, radionuclides reside in four "pools"—dissolved, colloidal, sorbed, and solid—with the colloidal pool being treated as a mobile particle pool; (2) radionuclides in the sorbed and colloidal pools are in first-order sorption equilibrium with those in the dissolved pool; (3) radionuclides in the solid pool are transferred to the dissolved pool through dissolution and α-recoil, whereas those in the dissolved pool are incorporated into the solid pool through precipitation.

The data in Table 10.4-1 have been analyzed using this model. In contrast to the thermodynamic modeling of Pickett and Murphy (1999 [110009]), this model provides a means to characterize kinetically controlled radionuclide transport at Peña Blanca. The uranium data from the 1995 wet-period measurements are shown in Figure 10.4-4.

As predicted by the model, a linear relationship exists between $^{234}U/^{238}U$ and $1/^{238}U$ in waters collected from the vadose zone near the Nopal I uranium deposit (Figure 10.4-4a), due to α-recoil-induced ^{234}U enrichment in the water. The one sample from the carbonate aquifer (SZ) shows a much lower $^{234}U/^{238}U$ ratio, perhaps caused by prolonged interaction with old calcites in the aquifer, allowing uranium exchange between rock and solution to mask the effect of ^{234}U enrichment in the water. Using the model as well as the slope and intercept from Figure 10.4-4a, the relative input rates of uranium from solids to the solution through dissolution and α-recoil can be derived. The ^{234}U α-recoil rate for the adit fluids is calculated to be ~9 dpm/L/yr. The dissolution rates are ~8.3 dpm/L/yr for ^{238}U and ^{234}U (or 47×10^{-9} mol/L/yr for ^{238}U and 2.6×10^{-12} mol/L/yr for ^{234}U).

The model also allows determination of the fluid transit time (τ_w) in the UZ. Because of the short transit time of water in the UZ, ^{238}U concentrations increase linearly with increasing τ_w (Fig. 10.4-4b). Meanwhile, the $^{234}U/^{238}U$ ratio decreases rapidly with increasing τ_w and very high $^{234}U/^{238}U$ ratios can occur when the water has a very short transit time in the UZ. It is estimated

that the transit time for the seep water that infiltrated into the Level +00 adit 8 m below the surface is about 6–29 days; for the perched water at 10.7 m depth in an old borehole, the transit time is about 0.4–0.5 years. The large values of τ_w for the perched water may reflect the long residence time of water in the borehole. Note that because water at different sites may have different pathways, the value of τ_w itself does not provide information on possible connections between the perched and seep waters sampled. In conclusion, although the water transit time in the UZ is quite short, significant dissolution of uranium may have occurred in a low-water flux, high-uranium concentration setting near the Nopal I uranium deposit.

10.4.4.4 Seasonal Variability of Uranium Dissolution Rate in UZ

To assess temporal variations in the transport of uranium in the UZ, samples of perched and adit seep waters were collected during the dry winter season in late February 2000 and again in early March 2001. The results are plotted in Figure 10.4-5a. Compared with samples collected during the September wet season of 1995, many of these new measurements show much higher ^{238}U concentration and lower $^{234}U/^{238}U$, suggesting increased uranium dissolution and/or lower α-recoil associated ^{234}U enrichment rates during the dry season. The low humidity during the dry season may have also enhanced evaporation, causing higher uranium concentrations in the waters sampled.

The data collected during the winter dry season depart considerably from the linear relationship between $^{234}U/^{238}U$ and $1/^{238}U$ predicted by the model for the wet season of 1995 (Figure 10.4-5a). Such a departure could result from: (1) high and variable evaporation under low humidity conditions and (2) incomplete flushing associated with low rainfall during the dry season. Linear regressions on data for the perched and adit seep waters collected during March 2001 give a ^{234}U α-recoil rate (λP_r) of ~5.7 dpm/L/yr. Compared to the ~9 dpm/L/yr for the wet season, this lower α-recoil rate estimate may reflect incomplete flushing of waters through the vadose layers during the dry season. Dissolution rates of uranium are estimated to be about 24 dpm/L/yr for ^{238}U and ^{234}U (or 136×10^{-9} mol/L/yr for ^{238}U and 7.5×10^{-12} mol/L/yr for ^{234}U). These rates are about three times higher than those in the wet season, possibly suggesting a favorable physiochemical condition (e.g., increased oxygenation) for uranium dissolution during dry periods. In this context, it should be noted that the samples collected 15 m from the adit entrance show $^{234}U/^{238}U$ values lower than secular equilibrium, which suggests dissolution of material previously preferentially depleted in ^{234}U by α-recoil effects.

Note in addition that large variations in the ^{238}U concentration and $^{234}U/^{238}U$ ratio were also found in samples collected from the SZ during the dry season (Figure 10.4-5b). While no clear correlation between ^{238}U and $^{234}U/^{238}U$ is seen, the plots suggest that both the decreased water infiltration flux and the increased uranium dissolution rates in the vadose zone may contribute to the higher dry-season uranium concentrations in the SZ. Observations such at these may have important implications for the effects of climate change on the long-term stability of uranium in the environment.

10.4.5 Work in FY02

Although the data and modeling discussed above provide useful preliminary data for uranium transport at Peña Blanca, spatial dependence and the net flux of uranium transport from the

deposit via groundwater cannot be thoroughly evaluated without higher resolution sampling of any potential groundwater uranium plume in the vicinity of the deposit. This will be accomplished through the drilling program at Nopal I (BSC 2001 [157535], pp. 4–5).

In addition to the core and fluid samples from the borehole and wells, the perched, seep, and aquifer waters from the sites previously sampled will be resampled (see above). Where adequate samples can be obtained, isotopes will be measured of uranium (^{234}U and ^{238}U), thorium (^{232}Th, ^{230}Th, ^{228}Th, and ^{234}Th), radium (^{226}Ra, ^{228}Ra), polonium (^{210}Po) and lead (^{210}Pb) in the fluid samples. Radioactive disequilibria in sorbed phases will also be studied, using leaching methods on the core samples. Since it may be difficult to collect enough fluids from the UZ for all of the proposed measurements, data on the sorbed phases should provide an alternative way to assess the radionuclide transport in the UZ.

The U-series modeling effort will be extended to the thorium and radium isotopes. Measurements of polonium and lead isotopes will be applied to the Th model to further evaluate the role of colloids in the transport of these nuclides. Modeled results on uranium transport may be affected by the evaporative concentration in UZ fluids. To correct for this possible effect, the chloride or stable isotope measurements made on water samples from the UZ will be compared with those on rainwater. Model sensitivity and validity will be tested, and ways to evaluate the uncertainties of model parameters will be sought. Results from the Peña Blanca analogue study will be provided for testing the UZ process model.

10.5 OTHER TRANSPORT ANALOGUES

10.5.1 Steenkampskraal

The Steenkampskraal monazite mine, located about 100 km south of Vaalputs, South Africa, provides an example of colloidal transport of radionuclides in the UZ (Figure 10.5-1). Steenkampskraal is a licensed low-level waste radioactive-waste disposal site in South Africa that is being considered as a potential high-level waste disposal site. Steenkampskraal is the richest monazite ore body in the world. From 1952 to 1963 it was the world's leading producer of thorium and rare earth elements (REE), with total production estimated at 50,000 metric tons of monazite concentrate, containing 45 wt % REE oxides, 4% thorium oxide, and 600 ppm uranium oxide (Jarvis et al. 1997 [157489], p. 12). Monazite and fluorapatite together constitute approximately 80% of the ore mass, along with minor sulfides, oxides, and silicates. Locally, the ore shows enrichment of Fe/Ti oxides. The mine is situated within the granulite facies high-temperature zone of the Namaqualand Metamorphic Complex, where model U-Pb ages of the mineralization are given as 1180 $\pm$40 Ma (Jarvis et al 1997 [157489], p. 12).

A characterization study was undertaken to investigate the degradation of monazite and apatite and to assess the extent of uranium, thorium, and REE transport away from the primary ore body under *in situ* conditions. One of the main objectives of the study was to evaluate the role of colloids in promoting the mobilization and retardation of trace metals. The average rainfall in the area is 70 mm/yr (Jarvis et al. 1997 [157489], p. 15). Upper sections of the mine experience permanently unsaturated conditions. The steady-state level of the water table is 50 m below the surface when pumping is stopped. The pH of the waters ranges from 7.3 to 8.4 (Jarvis et al. 1997

[157489], p. 21). Analyses of waters collected from boreholes indicate supersaturation by 2 to 3 orders of magnitude with respect to amorphous uranium (UO_2) and thorium (ThO_2) phases.

There is a marked fractionation between light and heavy REEs, with the heavier elements strongly enriched in the aqueous phase (Figure 10.5-2). The heavy REEs show a greater tendency for complexation and a greater affinity for mineral surfaces (Jarvis et al. 1997 [157489]), suggesting association with colloidal particles. Given the degree of fractionation exhibited by the lanthanide series elements (REEs), finely comminuted monazite cannot represent the dominant colloidal phase. Extensive leaching and alteration of the original mineralogy must have occurred and has resulted in a phase or phases containing proportionally more uranium, thorium, and REE than the parent. A similar phenomenon has been observed at other localities where monazite weathering is accompanied by preferential loss of uranium and thorium (Jarvis et al. 1997 [157489], p. 16).

Results of the study indicate that the monazite deposit behaves as a partly open system, especially where monazite disseminated in its silicate matrix is exposed to oxidizing surface and groundwaters along fractures and stratigraphic discontinuities, such as the contact between overburden and bedrock. Under these conditions, there is evidence that colloids in the infiltrating water act as vectors for the transport of thorium, uranium, and REE. This evidence includes very high concentrations of uranium and thorium and fractionation between the heavy and light REE in samples taken from boreholes. Final results of this study are not yet available, but the information to date indicates that both the Steenskampskraal and Nopal I sites are open systems with respect to thorium, with colloidal transport being the main transport mechanism. Both sites are similar to Yucca Mountain with respect to unsaturated, oxidizing conditions. This suggests that should thorium escape waste packages emplaced at Yucca Mountain, it would likely be transported by colloids, unless attenuated by filtration.

10.5.2 Koongarra

The Koongarra uranium deposit at Alligator Rivers, Australia is found at the steeply tilted contact between Proterozoic sandstone and schist (CRWMS M&O 2000 [151945], Section 13). The ore body is located in a shallow unsaturated environment that is subject to seasonal fluctuations of monsoons. Payne et al. (1992 [124812]) investigated the role of colloids in transport of uranium in the dispersion fan of the weathered zone above the ore body. The colloids and particles included clay minerals, particularly kaolinite, and chlorite, along with fine quartz grains. Iron was present as particle coatings, and in a separate colloidal form. The amount of ^{238}U associated with colloids ranged up to 6.5%, whereas the amount of ^{230}Th associated with colloids ranged from 10% to 85%. However, ^{230}Th was associated to a much greater extent with larger particles, which are unlikely to be mobile in natural groundwaters. The high $^{227}Th/^{230}Th$ ratio was high in some fractions, indicating that ^{227}Ac could be present as colloids. Overall, however, there was little colloidal material in these groundwaters, with only iron, uranium, thorium, and actinium showing a significant association with colloids (Payne et al. 1992 [124812], p. 481).

10.6 CONCLUSIONS

The hydrogeologic and geochemical setting at Peña Blanca is closely analogous to that at Yucca Mountain, as described in Section 10.4.2 and in CRWMS M&O 2000 [141407]. While the

hydrogeologic and geochemical features at INEEL are less similar to Yucca Mountain, of the contaminated anthropogenic sites initially considered for study, INEEL provided the closest similarity in that it occurs in a fractured porous medium with perched water zones and units of varying permeability. It provided the additional advantage of data sets that included radionuclides, which strengthen model testing aspects of the analogue study. Radionuclide transport in the surficial sediment zone at the RWMC can be interpreted in a number of ways. One is that lateral flow occurred, sweeping out part of the radionuclide plume. The thickness of the stratigraphic layers is highly irregular, and the possibility exists that flow occurred along the interface between the clay layer and the surficial sediment layer. This would be in keeping with the hypothesis of Nimmo et al. 2001 [154458]). Another possibility is that a catastrophic or sudden release of a pulse of fluid caused by a flooding event released a pulse of radionuclides that propagated downward with reduced retardation, owing to kinetic effects in turn caused by fast flow rates. Presumably, according to this interpretation, the concentration peak lies at a still greater depth below that at which the data were collected.

The model calculations predict retardation factors for neptunium and uranium that are seen to be orders of magnitude higher compared to the other radionuclides. This result would indicate that very little movement of neptunium and uranium should be observed. No values for these radionuclides were reported that could be taken as consistent with their predicted high retardation.

In comparison to Yucca Mountain, the wetter environment at INEEL is manifested in higher infiltration at the SDA and flooding events that could have resulted in enhanced radionuclide migration beneath the SDA. Focused flow, resulting from the undulating topography of the basalt flows and sedimentary interbeds, would be expected to exacerbate the situation, leading to even greater distances of radionuclide migration, as demonstrated in the modeling exercises. The UZ Flow and Transport Model at Yucca Mountain considers a range of infiltration rates that are then used to bound the range of percolation flux. Because the PTn has a damping effect on flow to the TSw, it is unlikely that the enhanced transport scenario proposed in the INEEL modeling study would occur at Yucca Mountain.

At Nopal I, the evolution of stable isotopes for the adit samples appears to have at least three components: (1) evolution of vapor from the GMWL, (2) modification by water/rock interaction, and (3) evaporation in the adit collection system. A simpler approach planned for evaluation shortly is to normalize the uranium data to chloride or bromide concentrations. It is estimated that the transit time for the seep water that infiltrated into the Nopal I Level +00 adit 8 m below surface is about 6–29 days, and for the perched water at 10.7 m depth in an old borehole, the transit time is about 0.4–0.5 years. The large values of τ_W for the perched water may reflect the long residence time of water in the borehole. It should be noted that as water at different sites may have different pathways, the value of τ_W itself does not provide information on possible connections between the perched and seep waters sampled. In conclusion, although the water transit time in the UZ is quite short, significant dissolution of uranium may have occurred in a low-water flux, high-uranium concentration setting near the Nopal I uranium deposit. If analyses from future sampling campaigns confirm that transit time is short in the UZ at Nopal I, then the implications would need to be considered for the similar low-water flux environment at Yucca Mountain.

Compared with samples collected during the September wet season of 1995, many of the new measurements in late February 2000, and again in early March 2001, show much higher ^{238}U concentration and lower $^{234}U/^{238}U$, suggesting increased uranium dissolution and/or lower α-recoil-associated ^{234}U enrichment rates during the dry seasons. The low humidity during dry seasons may have also enhanced evaporation, causing higher uranium concentrations in the waters sampled.

The data collected during the winter dry seasons of 2000 and 2001 depart considerably from the linear relationship between $^{234}U/^{238}U$ and $1/^{238}U$ predicted by the model for the wet season of 1995 (Figure 10.4-5a). Such a departure could be caused by: (1) high and variable evaporation under low humidity conditions, and (2) incomplete flushing associated with low rainfall during the dry season. The uranium dissolution rates are about three times higher than those in the wet season, possibly suggesting a favorable physiochemical condition (e.g., increased oxygenation) for uranium dissolution during dry periods.

Large variations in the ^{238}U concentration and $^{234}U/^{238}U$ ratio were also found in samples collected from the SZ during the dry season. Both the decreased water infiltration flux and the increased uranium dissolution rates in the vadose zone may contribute to the higher dry-season uranium concentrations in the SZ. Observations such at these may have important implications for the effects of climate change on the long-term stability of uranium in the environment.

As a final point, colloid transport appears to be an important factor for migration of thorium in one open unsaturated system, Steenkampskraal, but not in another, Nopal I. Both systems have similar hydrologic conditions to those at Yucca Mountain, although the rock type is different at Steenkampskraal. At Koongarra, another unsaturated but seasonally fluctuating system, colloid transport takes place but is a minor mechanism of uranium transport. Because seasonal fluctuations in uranium dissolution have been discovered at Nopal I, it would be useful to investigate the possibility of colloid transport in that system. A more informed understanding of the implication for colloid transport in the UZ at Yucca Mountain could then be had and could be used to evaluate whether TSPA assumptions that disregard colloid filtration are appropriately conservative.

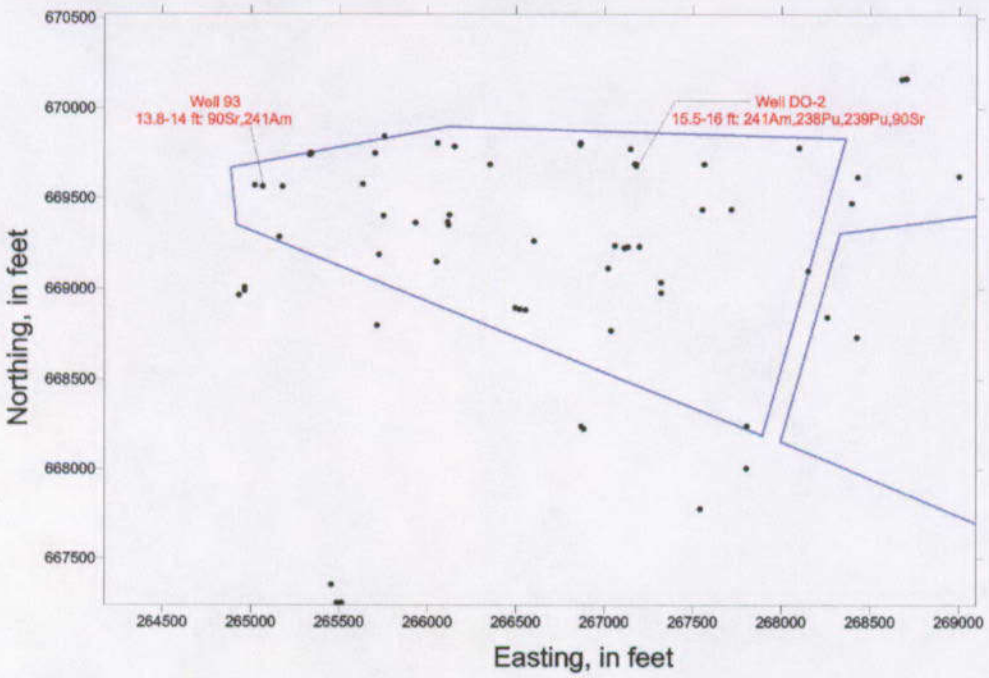

Source: Simmons 2002 [157578], SN-LANL-SCI-234-V1, p. 61.

Figure 10.3-1a. Map of SDA and Deep Wells Showing Location of Radionuclide Concentrations Greater Than Three Times Detection for Depth Intervals to the 9 m Interbed

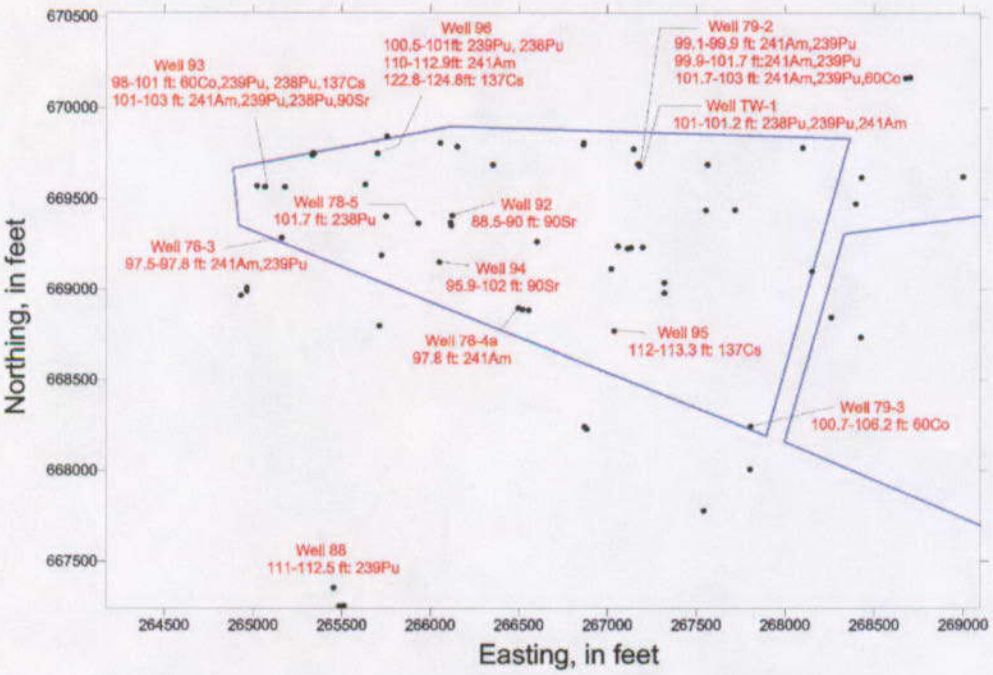

Source: Simmons 2002 [157578], SN-LANL-SCI-234-V1, p. 61.

Figure 10.3-1b. Map of SDA and Deep Wells Showing Location of Radionuclide Concentrations Greater Than Three Times Detection for Depth Intervals to the 34 m Interbed

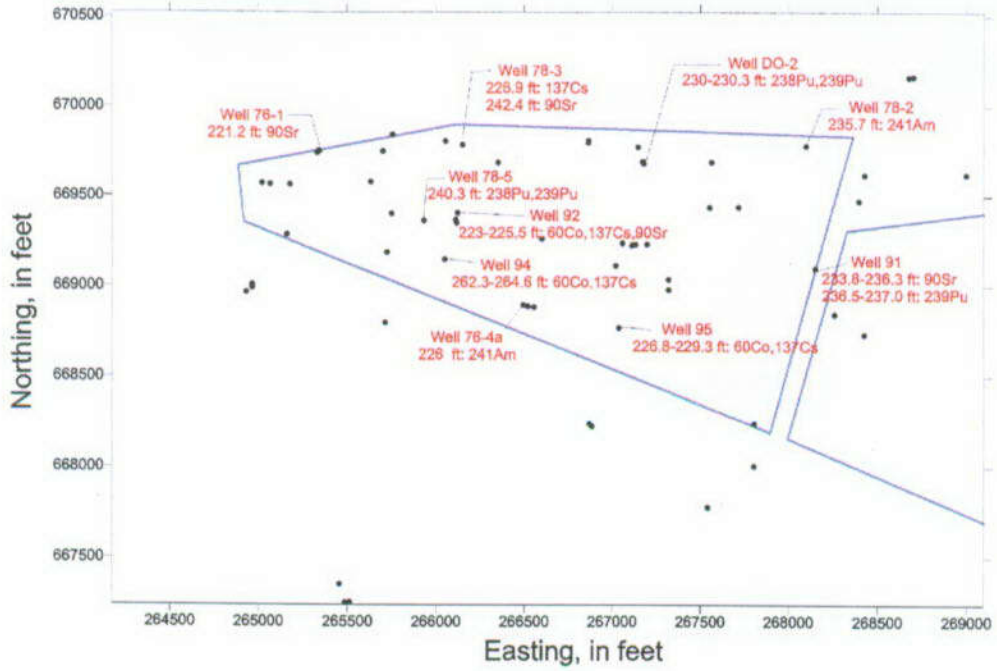

Source: Simmons 2002 [157578], SN-LANL-SCI-234-V1, p. 62.

Figure 10.3-1c. Map of SDA and Deep Wells Showing Location of Radionuclide Concentrations Greater Than Three Times Detection for Depth Intervals to the 73 m Interbed

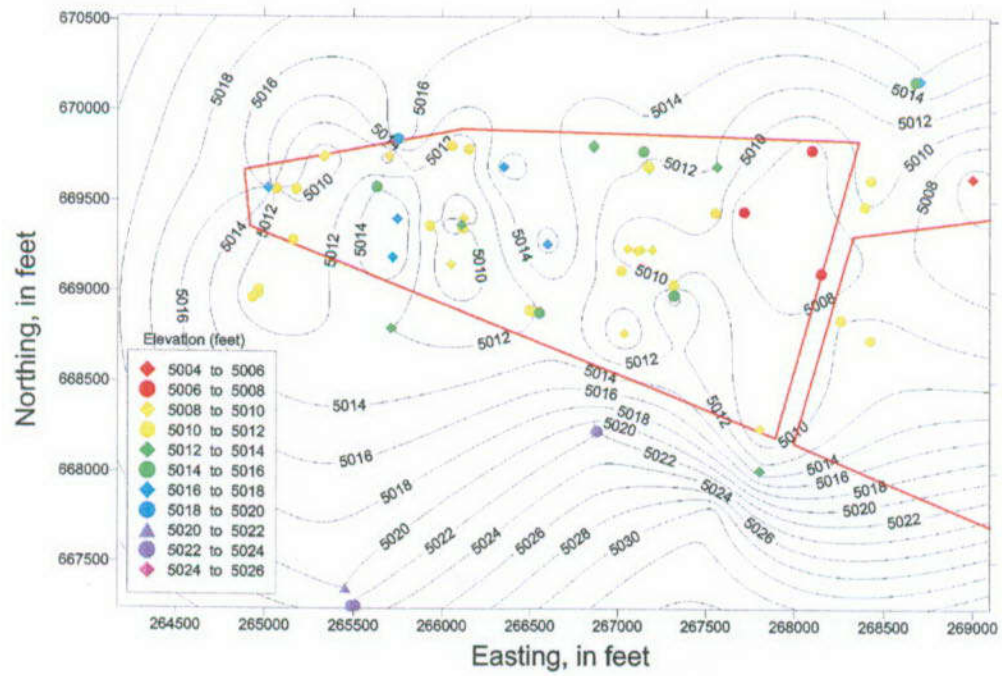

Source: Simmons 2002 [157578], SN-LANL-SCI-234-V1, p. 63.

Figure 10.3-2. Ground Surface Elevation in the Vicinity of the SDA

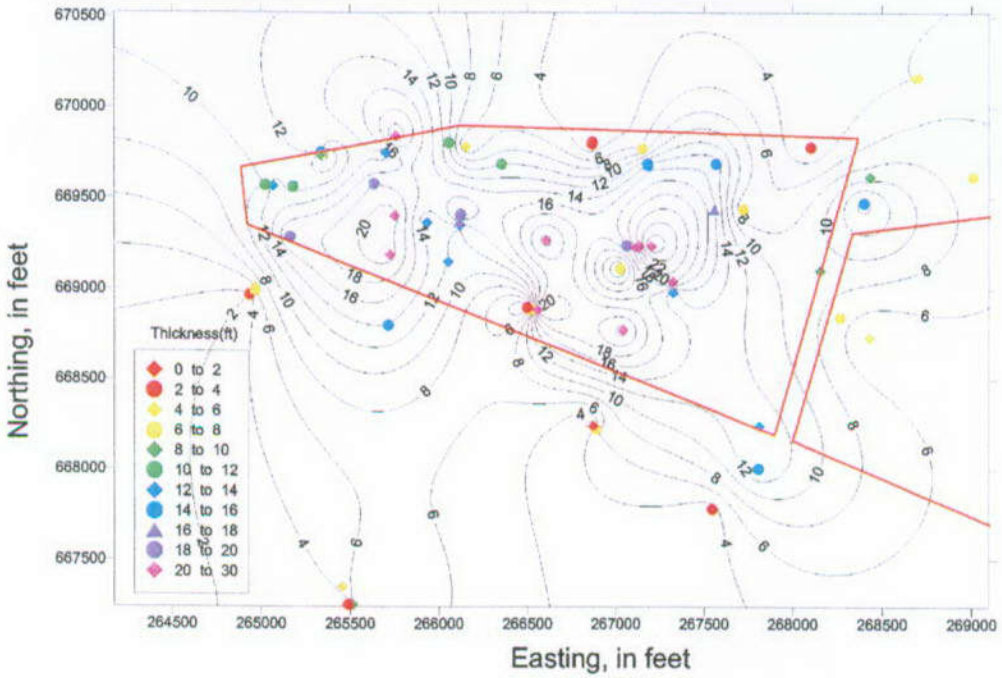

Source: Simmons 2002 [157578], SN-LANL-SCI-234-V1, p. 64.

Figure 10.3-3. Surficial Sediment Thickness in the Vicinity of the SDA

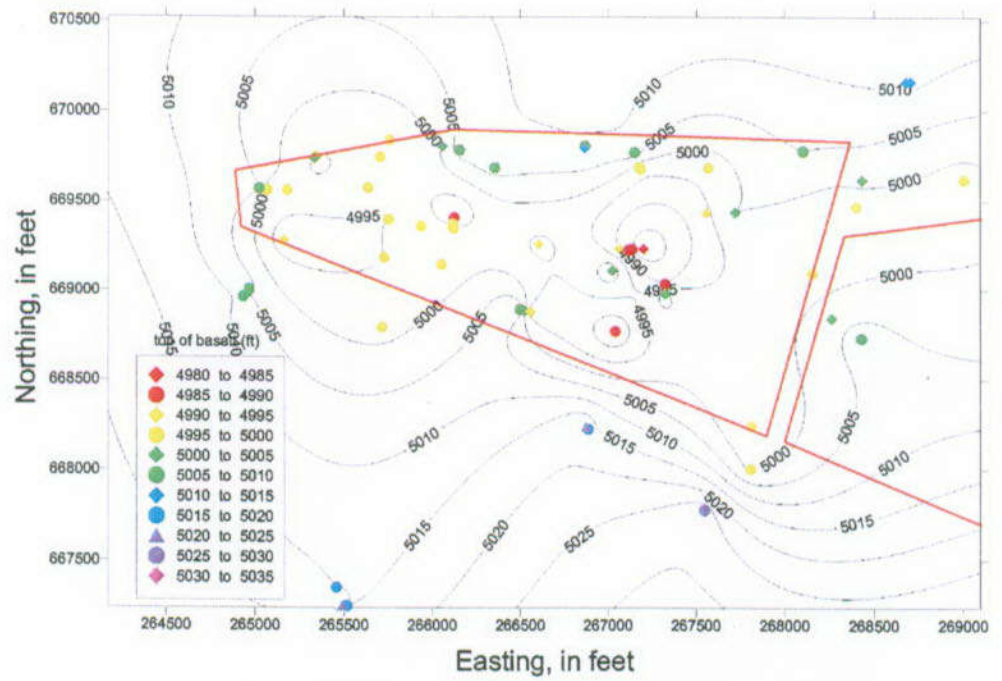

Source: Simmons 2002 [157578], SN-LANL-SCI-234-V1, p. 64.

Figure 10.3-4. Elevation of Top of Basalt Flow A in the Vicinity of the SDA

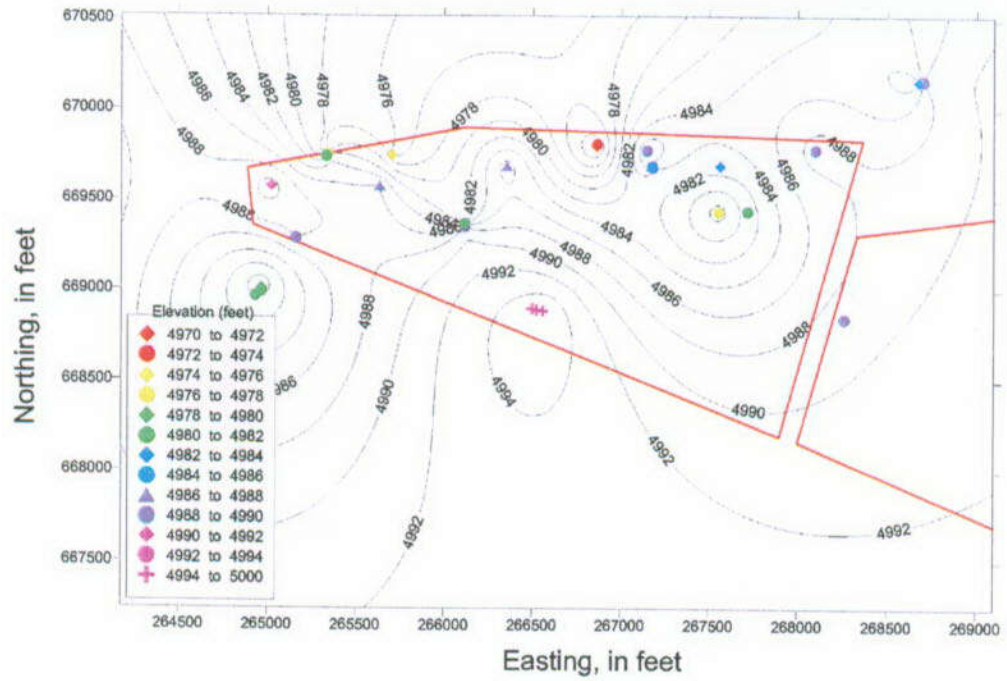

Source: Simmons 2002 [157578], SN-LANL-SCI-234-V1, p. 65.

Figure 10.3-5. Elevation of Top of AB Interbed in the Vicinity of the SDA

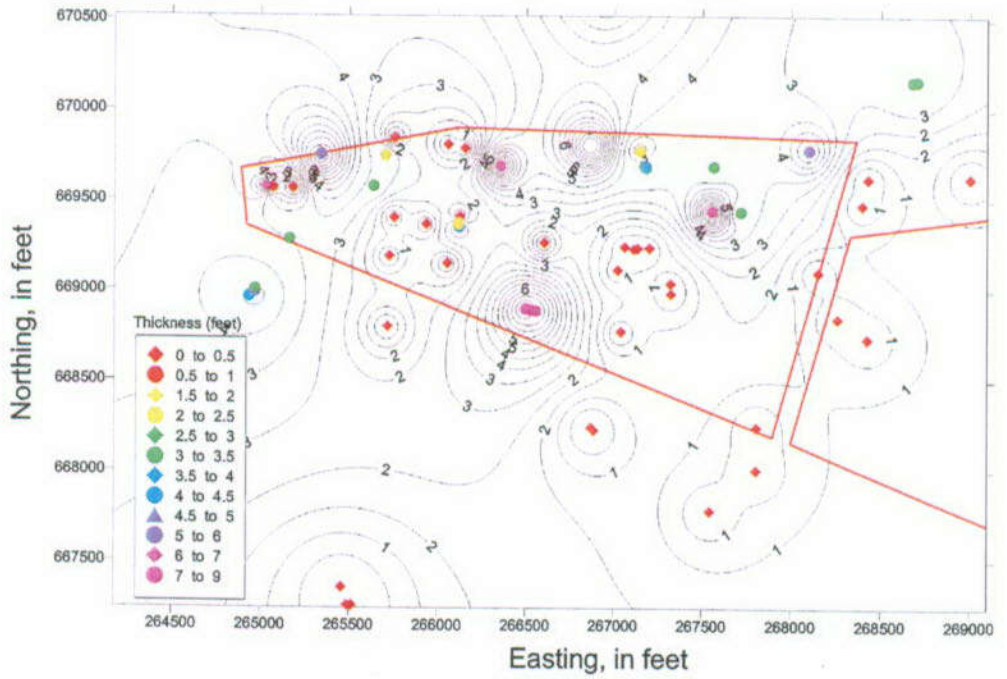

Source: Simmons 2002 [157578], SN-LANL-SCI-234-V1, p. 65.

Figure 10.3-6. Thickness of AB Interbed in the Vicinity of the SDA

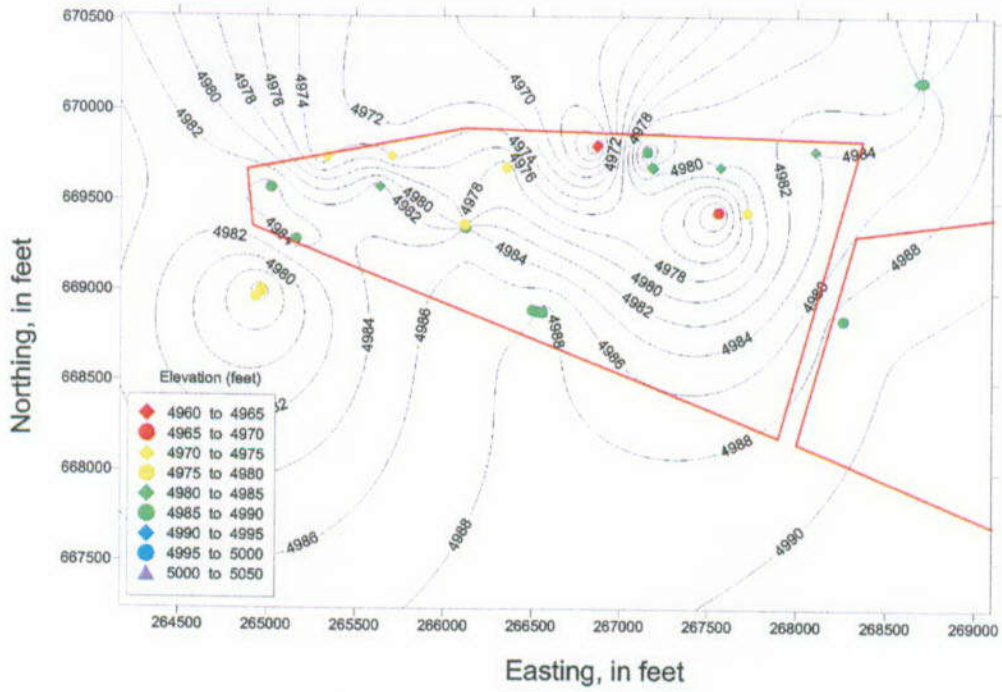

Source: Simmons 2002 [157578], SN-LANL-SCI-234-V1, p. 66.

Figure 10.3-7. Elevation of Top of B Basalt in the Vicinity of the SDA

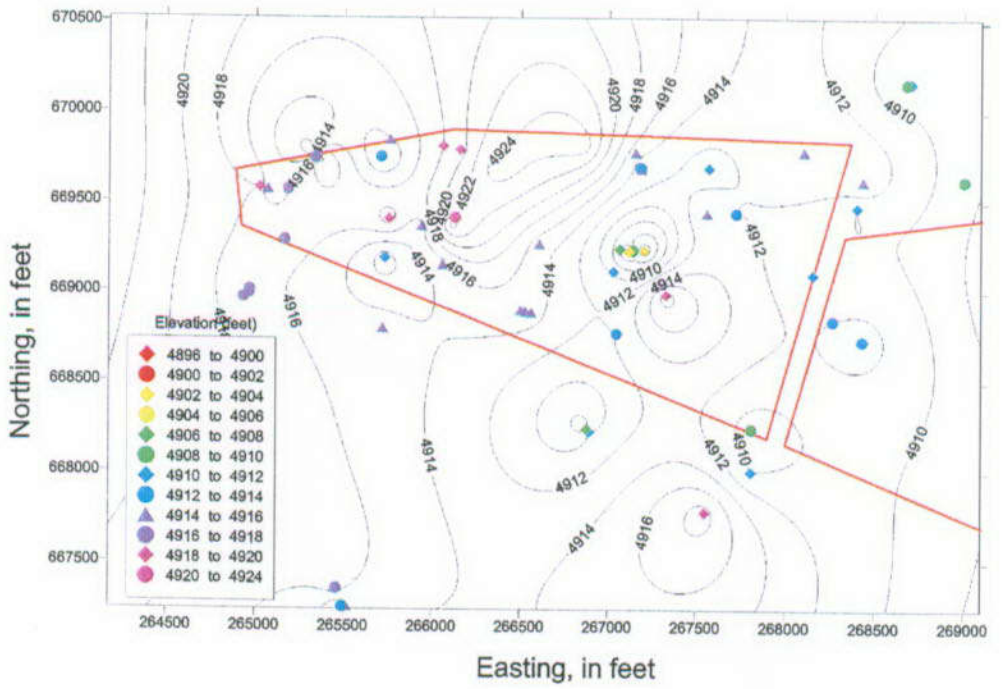

Source: Simmons 2002 [157578], SN-LANL-SCI-234-V1, p. 66.

Figure 10.3-8. Elevation of Top of BC Interbed in the Vicinity of the SDA

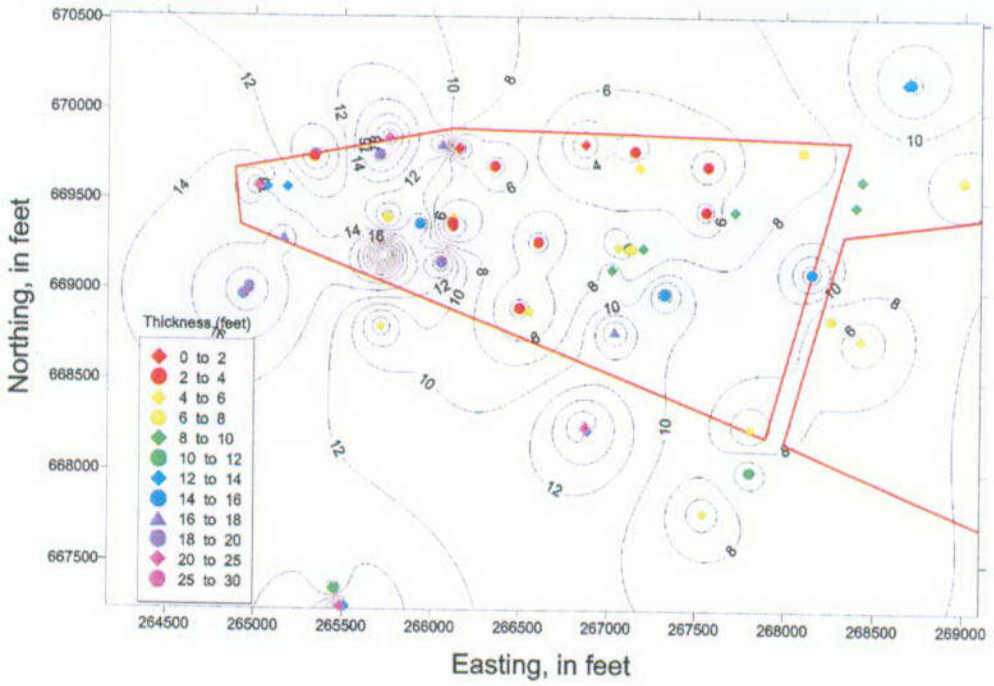

Source: Simmons 2002 [157578], SN-LANL-SCI-234-V1, p. 67.

Figure 10.3-9. Thickness of BC Interbed in the Vicinity of the SDA

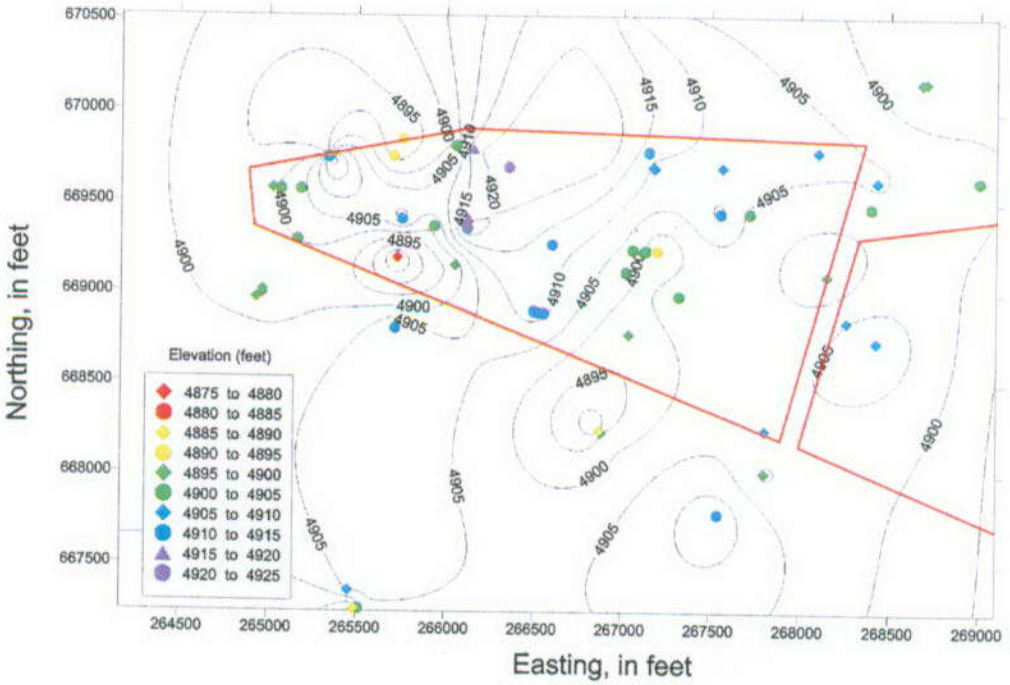

Source: Simmons 2002 [157578], SN-LANL-SCI-234-V1, p. 67.

Figure 10.3-10. Elevation of Top of C Basalt in the Vicinity of the SDA

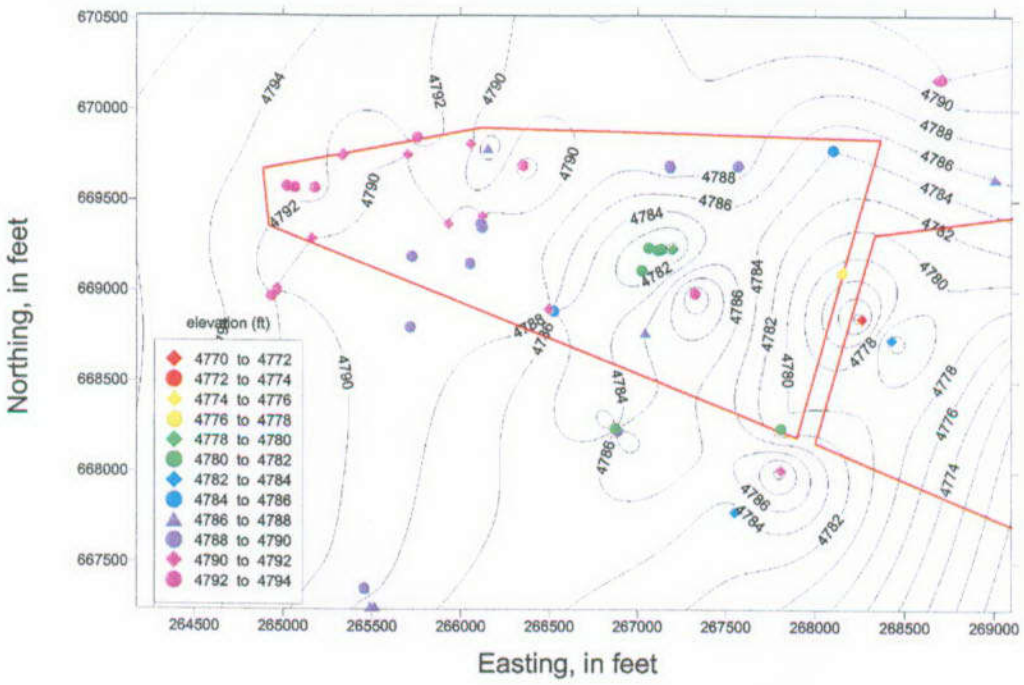

Source: Simmons 2002 [157578], SN-LANL-SCI-234-V1, p. 68.

Figure 10.3-11. Elevation of Top of CD Interbed in the Vicinity of the SDA

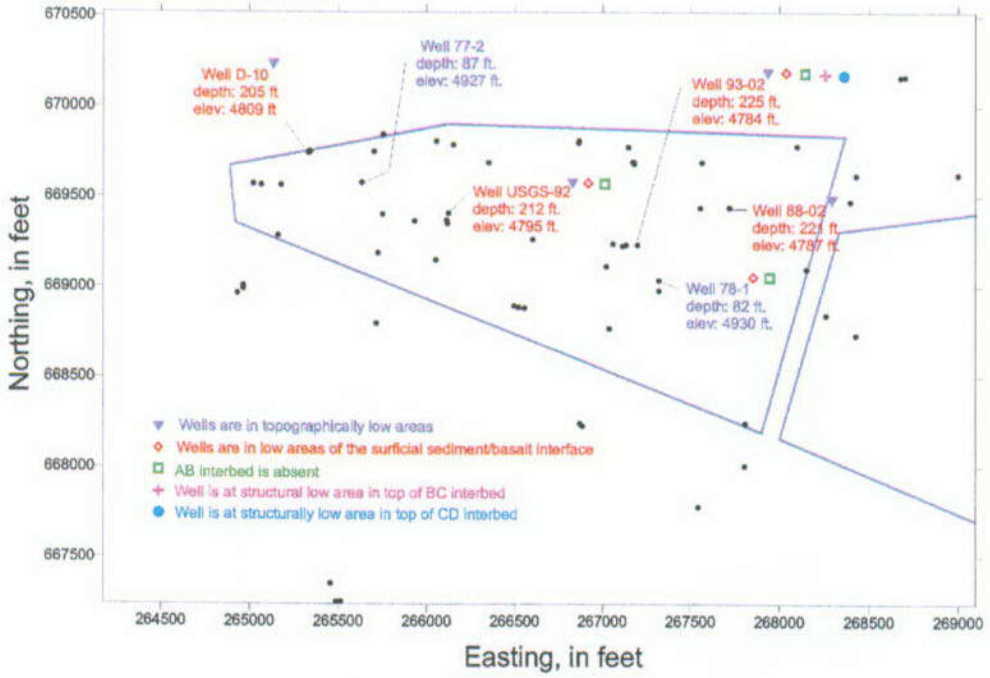

Source: Simmons 2002 [157578], SN-LANL-SCI-234-V1, p. 75.

Figure 10.3-12. Depths and Elevations of Perched Water in the Vicinity of the SDA

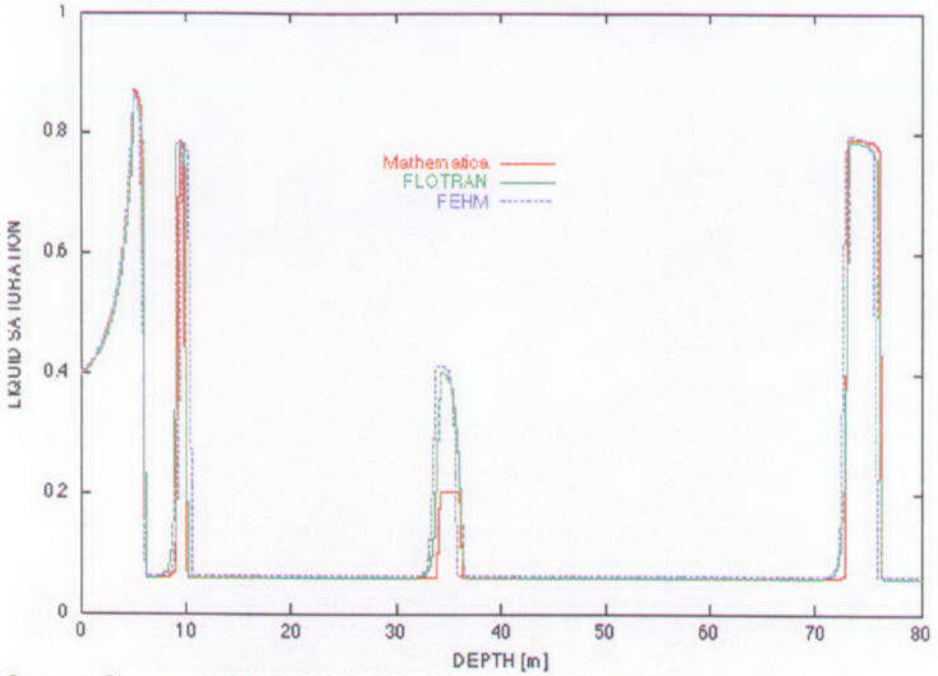

Source: Simmons 2002 [157578], SN-LANL-SCI-234-V1, p. 16.

Figure 10.3-13. Comparison of Steady-State Saturation Profiles for FEHM and FLOTRAN for Single-Continuum Simulation

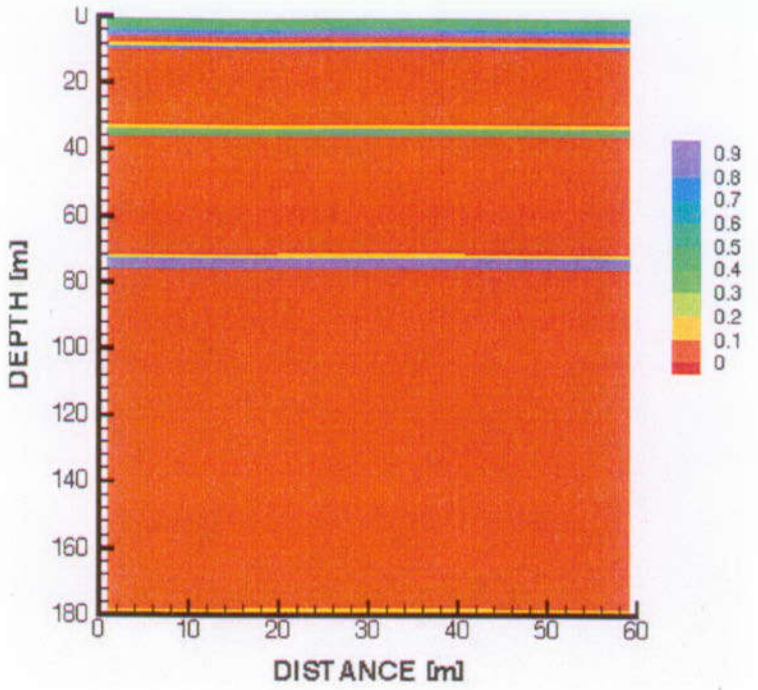

Source: Simmons 2002 [157578], SN-LANL-SCI-234-V1, p. 20.

Figure 10.3-14. Liquid Saturation for the Single-Continuum Simulation

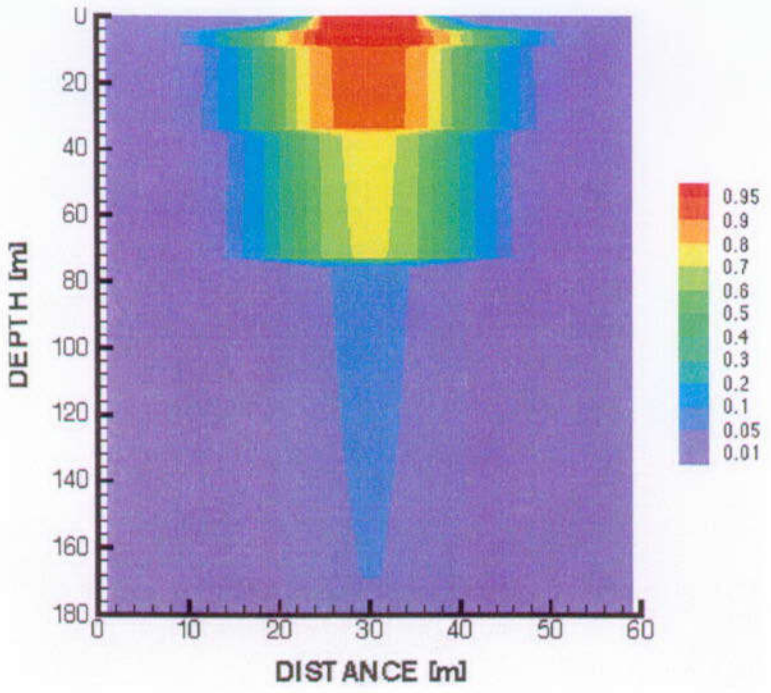

Source: Simmons 2002 [157578], SN-LANL-SCI-234-V1, p. 23.

Figure 10.3-15a. Normalized Tracer Concentration after 50 Years for the Single-Continuum Model with Constant Release

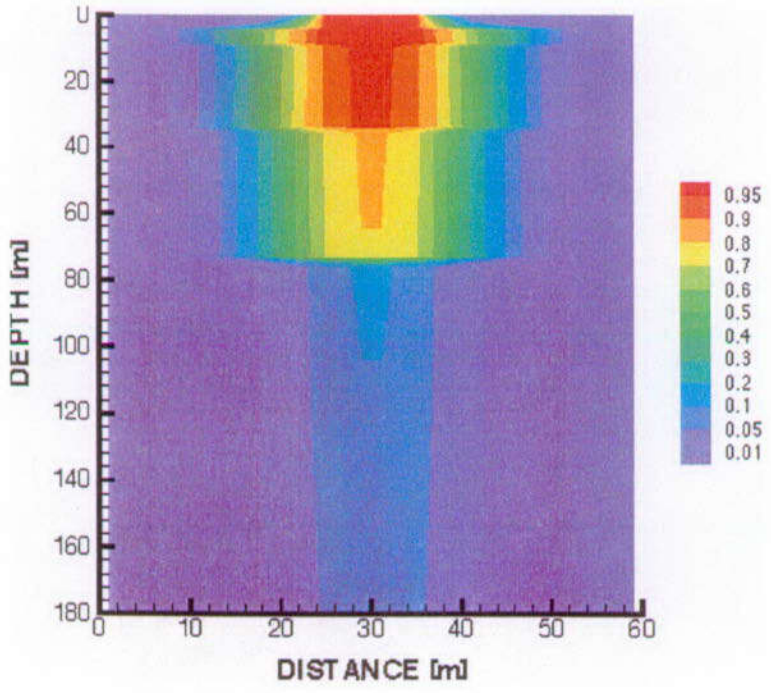

Source: Simmons 2002 [157578], SN-LANL-SCI-234-V1, p. 23.

Figure 10.3-15b. Normalized Tracer Concentration after 50 years for the Single-Continuum Model with Pulse Release

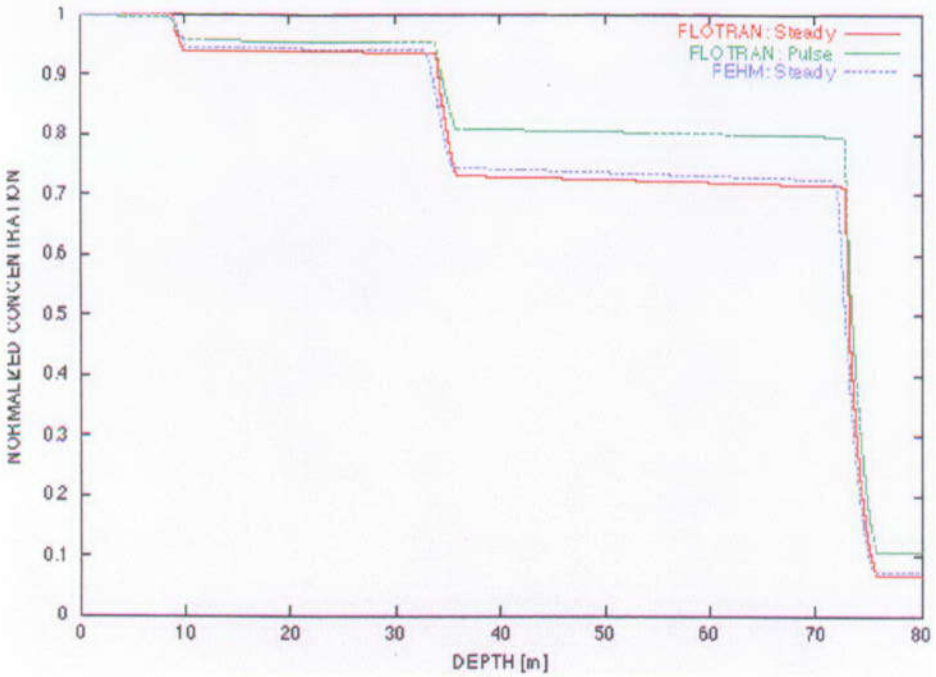

NOTE: Also Shown is the Pulse Release using FLOTRAN.

Source: Simmons 2002 [157578], SN-LANL-SCI-234-V1, p. 24.

Figure 10.3-16. Comparison of FEHM and FLOTRAN for Normalized Tracer Concentration after 50 Years for the Single-Continuum Model with Steady Release at the Center of the Injection Region

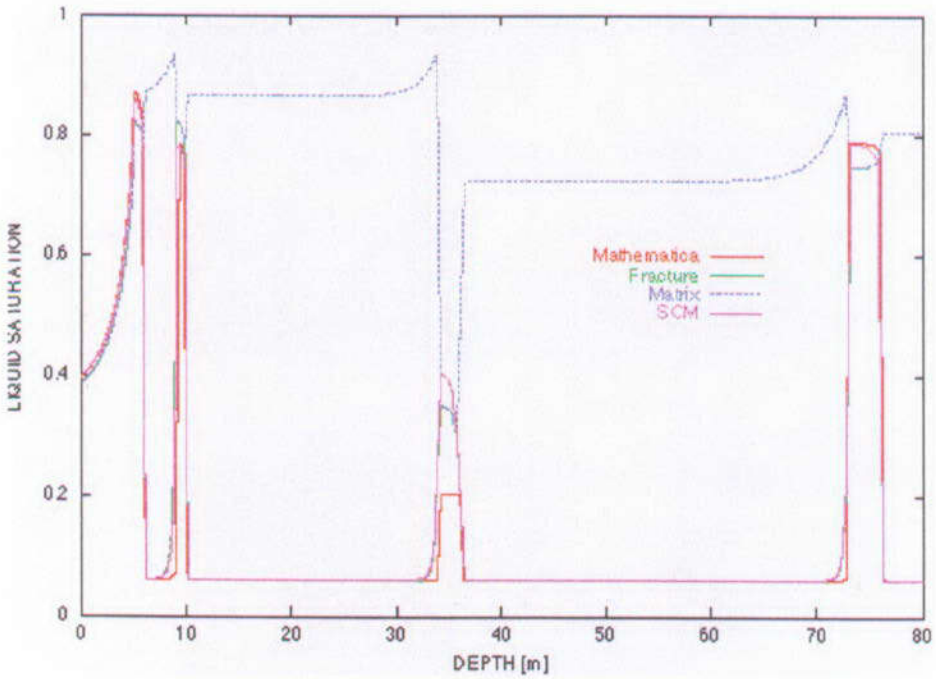

Source: Simmons 2002 [157578], SN-LANL-SCI-234-V1, p. 24.

Figure 10.3-17. Comparison of Steady-State Saturation Profiles for Single- and Dual-Continuum Simulations

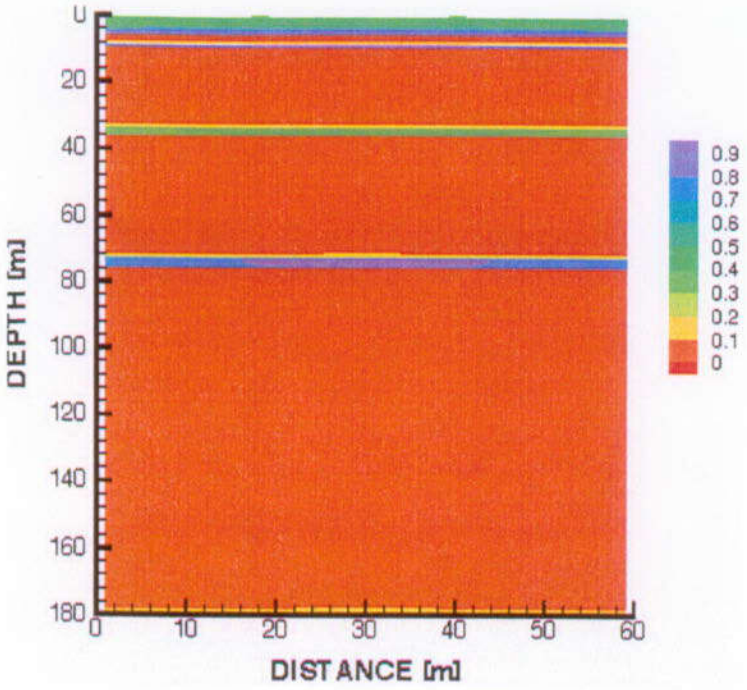

Source: Simmons 2002 [157578], SN-LANL-SCI-234-V1, p. 26.

Figure 10.3-18a. Liquid Saturation for Fracture Continuum

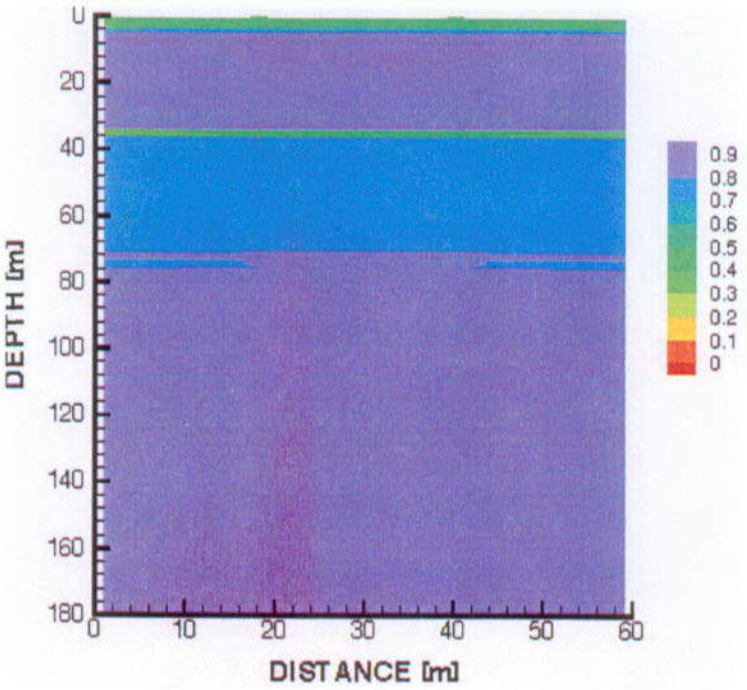

Source: Simmons 2002 [157578], SN-LANL-SCI-234-V1, p. 26.

Figure 10.3-18b. Liquid Saturation for Matrix Continuum

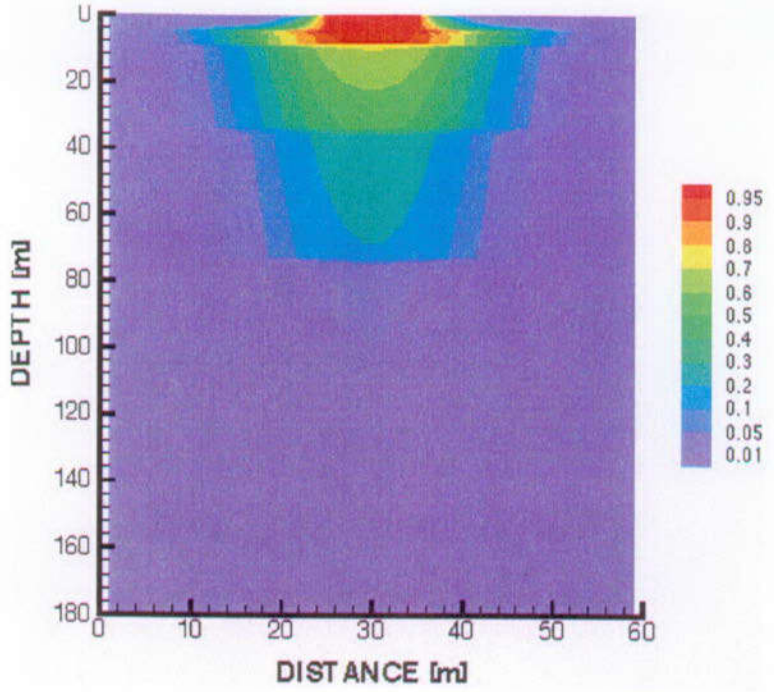

Source: Simmons 2002 [157578], SN-LANL-SCI-234-V1, p. 27.

Figure 10.3-19a. Normalized Tracer Concentration for Fracture Continuum

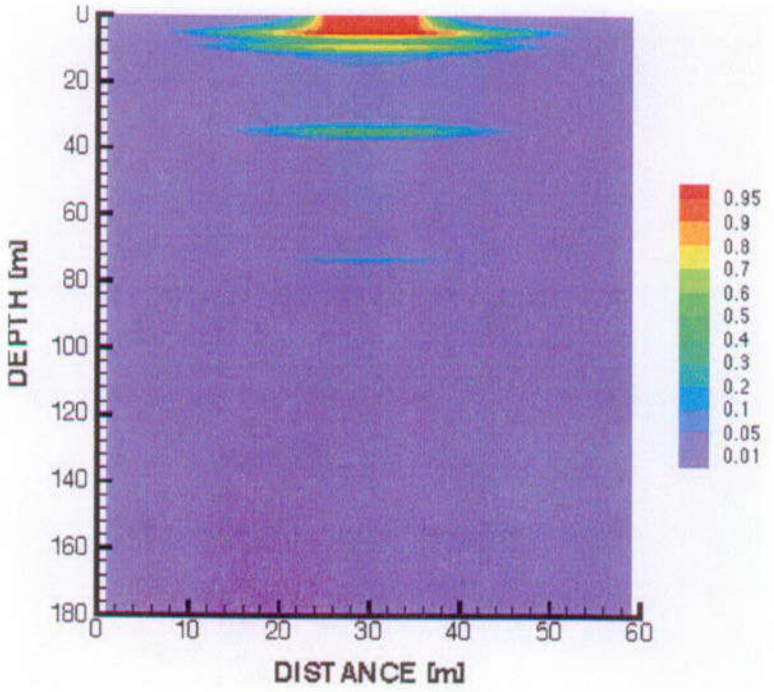

Source: Simmons 2002 [157578], SN-LANL-SCI-234-V1, p. 27.

Figure 10.3-19b. Normalized Tracer Concentration for Matrix Continuum

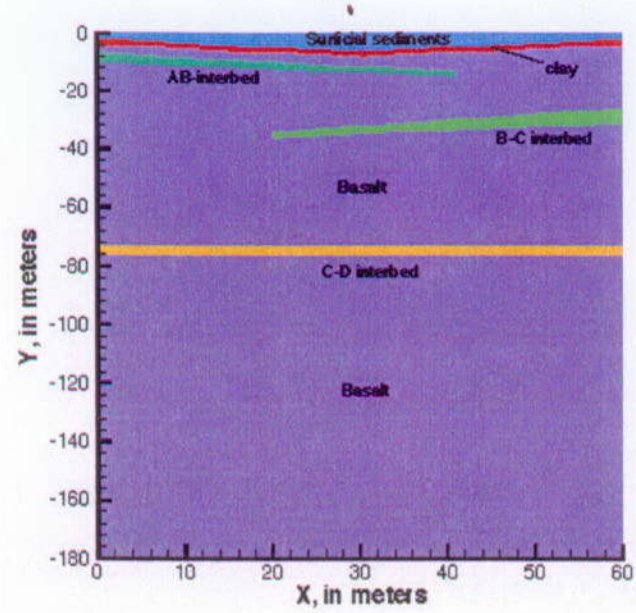

Source: Simmons 2002 [157578], SN-LANL-SCI-234-V1, p. 76.

Figure 10.3-20. Hydrostratigraphy

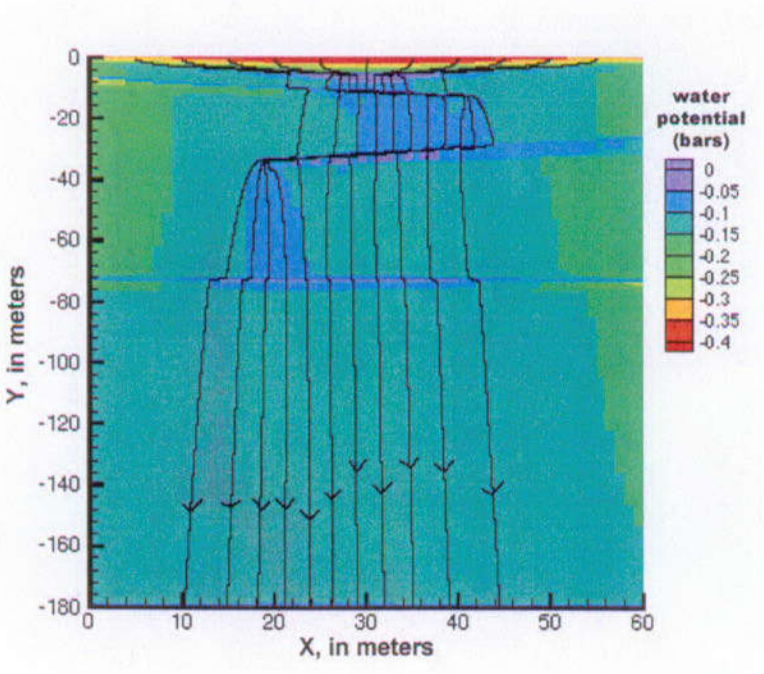

NOTE: Arrows indicate particle-tracking flow lines.

Source: Simmons 2002 [157578], SN-LANL-SCI-234-V1, p. 83.

Figure 10.3-21. Steady-State Water Potentials

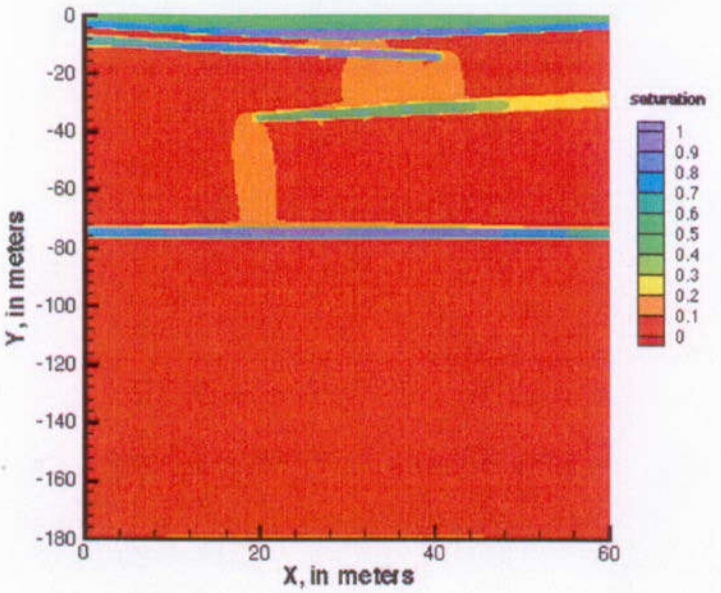

Source: Simmons 2002 [157578], SN-LANL-SCI-234-V1, p. 88.

Figure 10.3-22. Liquid Saturation at 50 Years

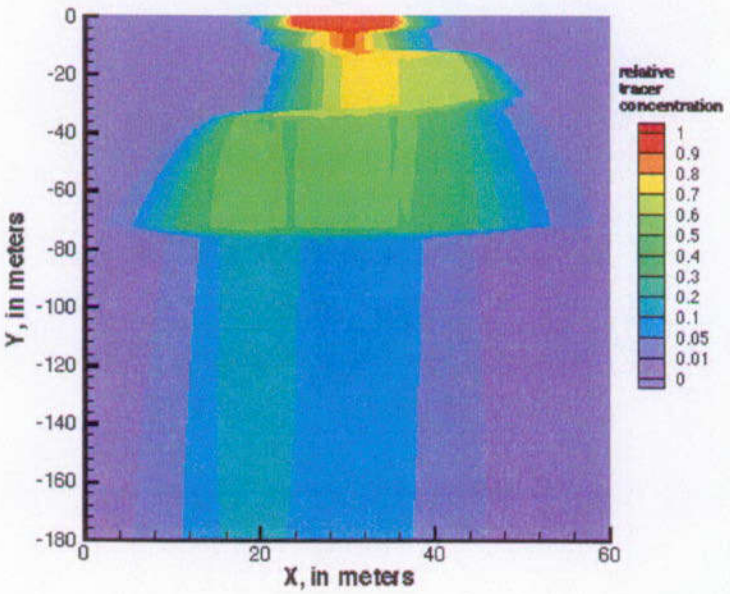

Source: Simmons 2002 [157578], SN-LANL-SCI-234-V1, p. 89.

Figure 10.3-23. Normalized Tracer Concentration at 50 Years

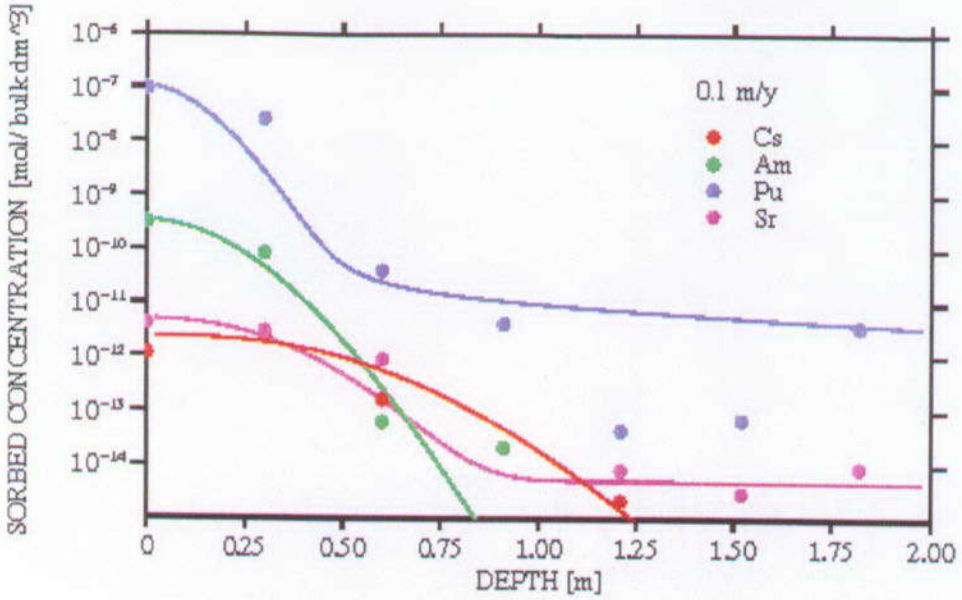

Source: Simmons 2002 [157578], SN-LANL-SCI-234-V1, p. 30.

Figure 10.3-24. Comparison of Field Data for Sorption of Cs, Pu, Am, and Sr for a Flow Velocity of 0.1 m/yr through the Surficial Sediment

DTN: LB0202PBANALOG.001 [157610]

Figure 10.4-1. Schematic of Level +00 Adit Sampling Locations

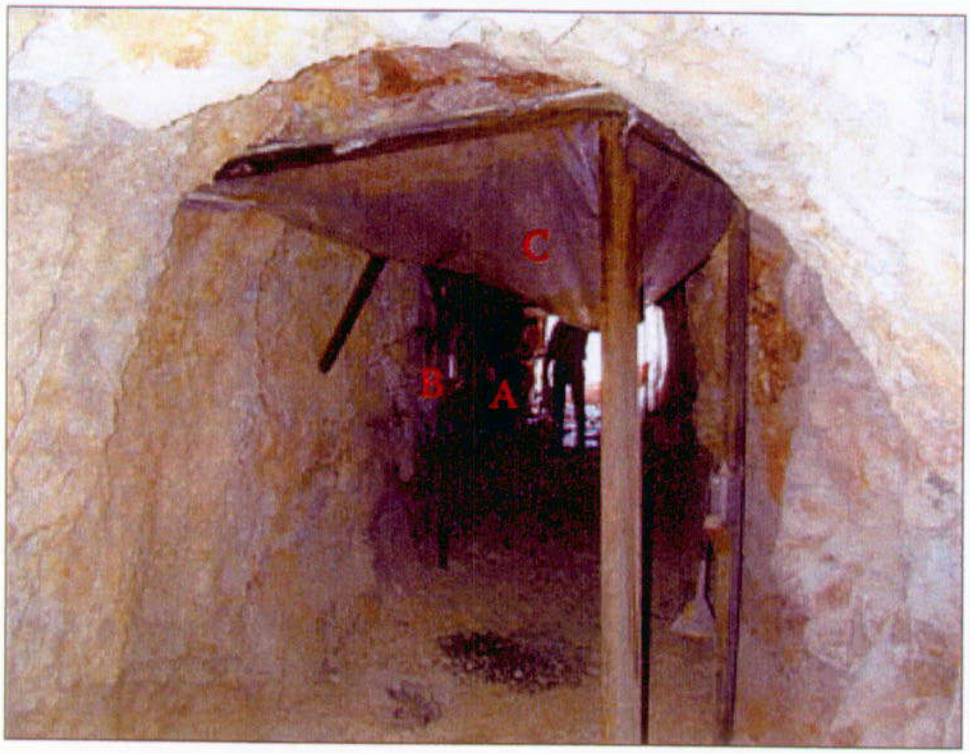

DTN: LB0202PBANALOG.001 [157610]

Figure 10.4-2. Photo of Sampling Locations A, B, and C in the Nopal I +00 Adit

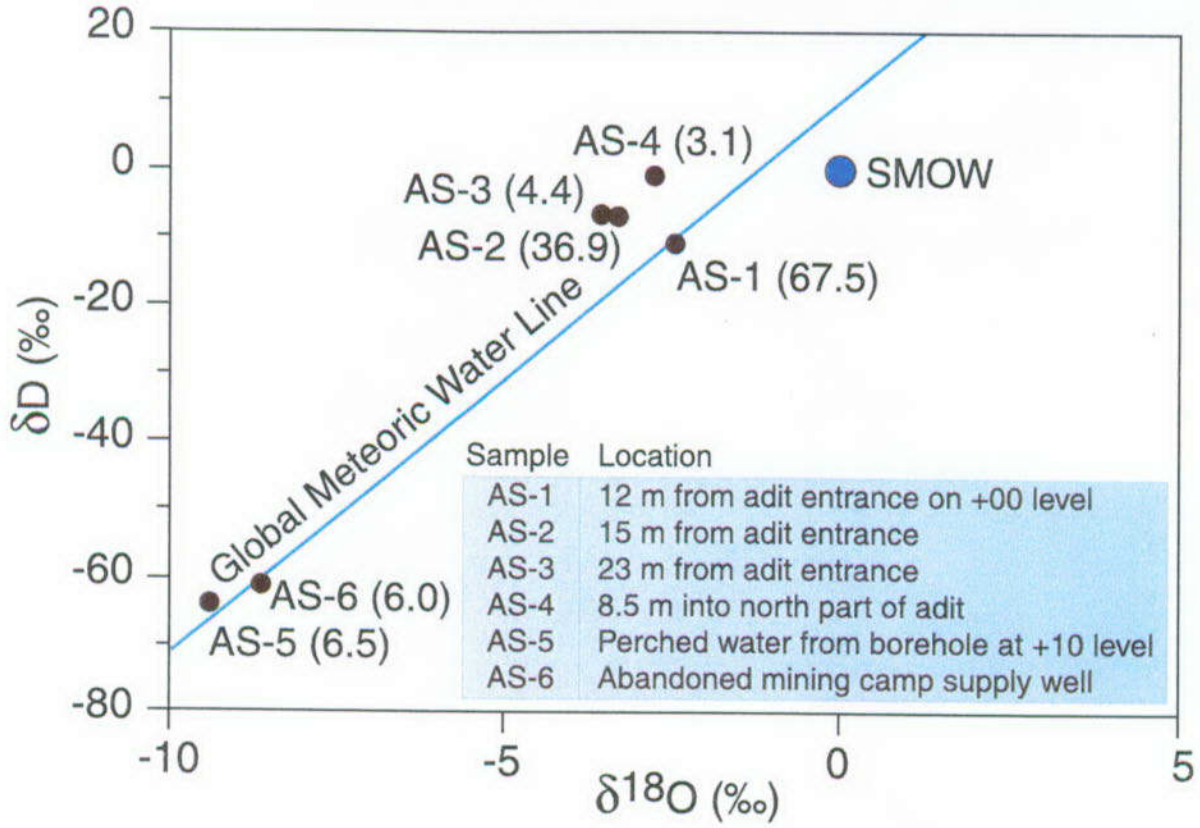

DTN: LB0202PBANALOG.001 [157610]

NOTE: Also shown is the position of the global meteoric water line and SMOW (Standard Mean Ocean Water).

Figure 10.4-3. Plot of δD versus $\delta^{18}O$ for water samples collected (black circles) from Peña Blanca during February 2000

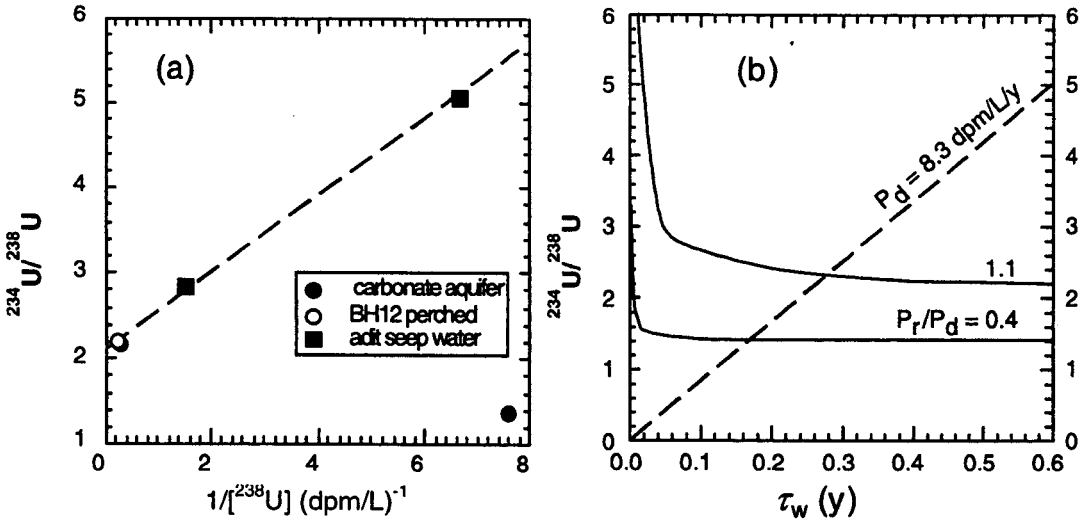

NOTE: The dashed line in (a) delineates the positive linear correlation for waters sampled from the UZ. Its slope and intercept can be used to derive P_r (input from recoil) and P_d (input from dissolution) by the model. (b) shows a rapid decrease of $^{234}U/^{238}U$ to a relatively constant level within a couple of weeks after the water enters the UZ. The low $^{234}U/^{238}U$ activity ratio of 1.39 in the carbonate aquifer as shown in (a) requires a P_r/P_d ratio of about 0.4, about three times smaller than that in the UZ.

$(dpm/L)^{-1}$ values calculated from data in Table 10.4-1, using half-lives of ^{234}U and ^{238}U.

Source: Modified from Pickett and Murphy 1999 [110009], Figure 15.

Figure 10.4-4. (a) $^{234}U/^{238}U$ Activity Ratio vs. Reciprocal ^{238}U Activity in Nopal I Waters and (b) $^{234}U/^{238}U$ Activity Ratio (solid lines) and ^{238}U Concentration (dashed line) as a Function of Water Transit Time (τ_w) in the UZ

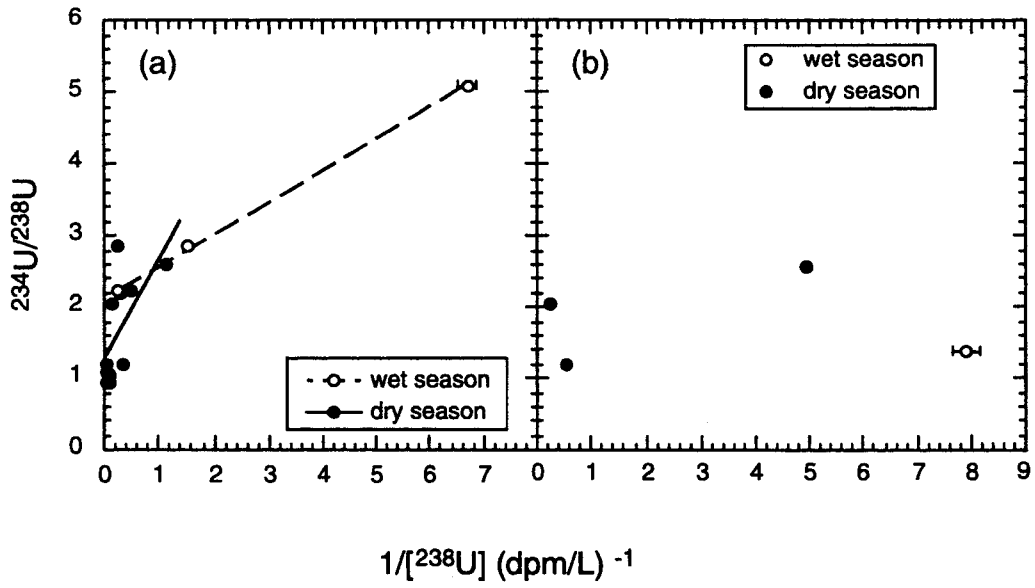

NOTE: Solid and dashed lines in (a) are linear regressions for samples collected during the dry (February 2000 and March 2001 collections) and wet (August - September of 1995) seasons, respectively. Dissolution of uranium is higher during the dry periods.

Source: Data values calculated from data in Table 10.4-1, using half-lives of ^{234}U and ^{238}U.

Figure 10.4-5. $^{234}U/^{238}U$ Activity Ratio vs. Reciprocal ^{238}U Activity in Nopal I Waters from (a) UZ and (b) SZ

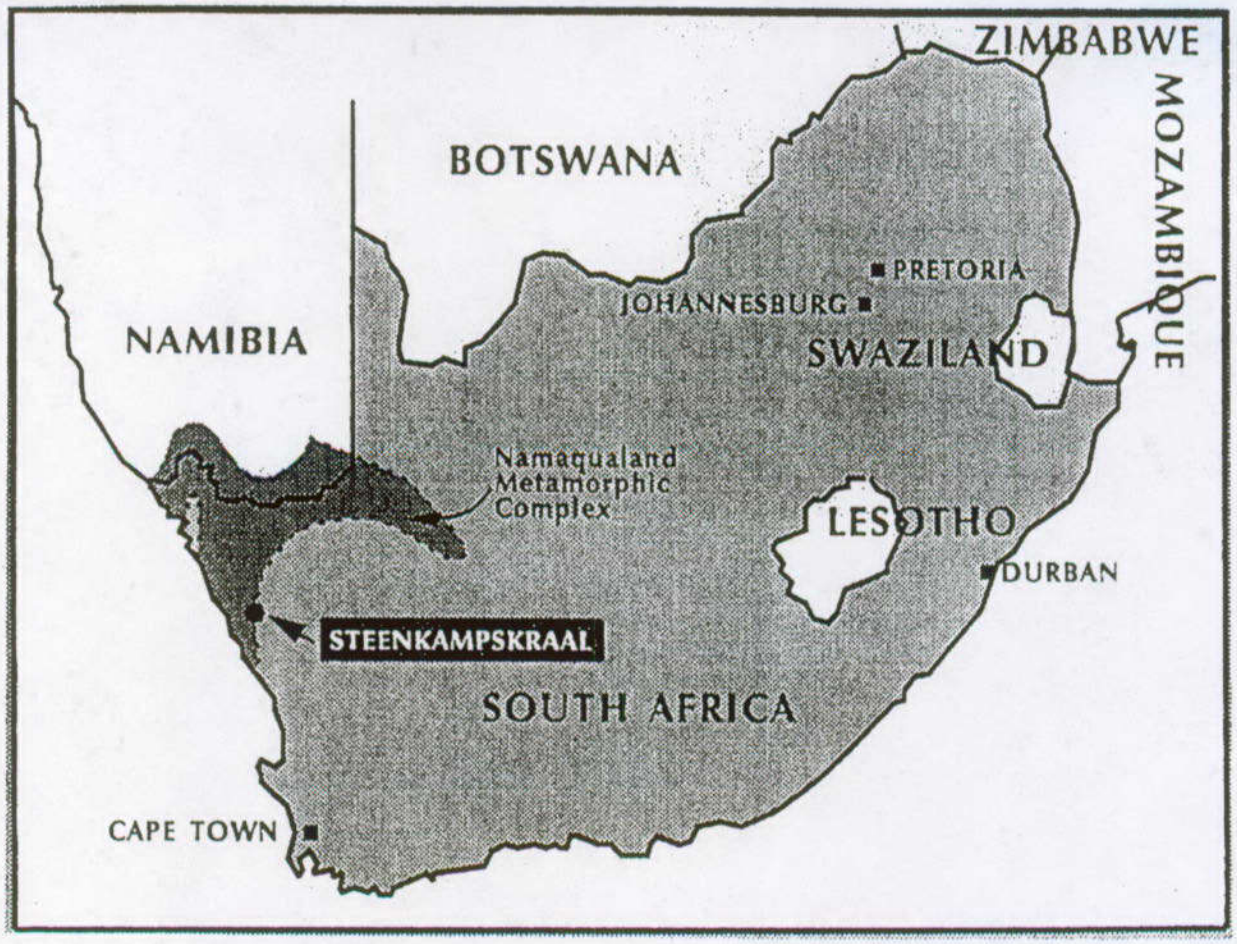

Source: Jarvis et al. 1997 [157489], Figure 1.

Figure 10.5-1. Location of Steenkampskraal, South Africa

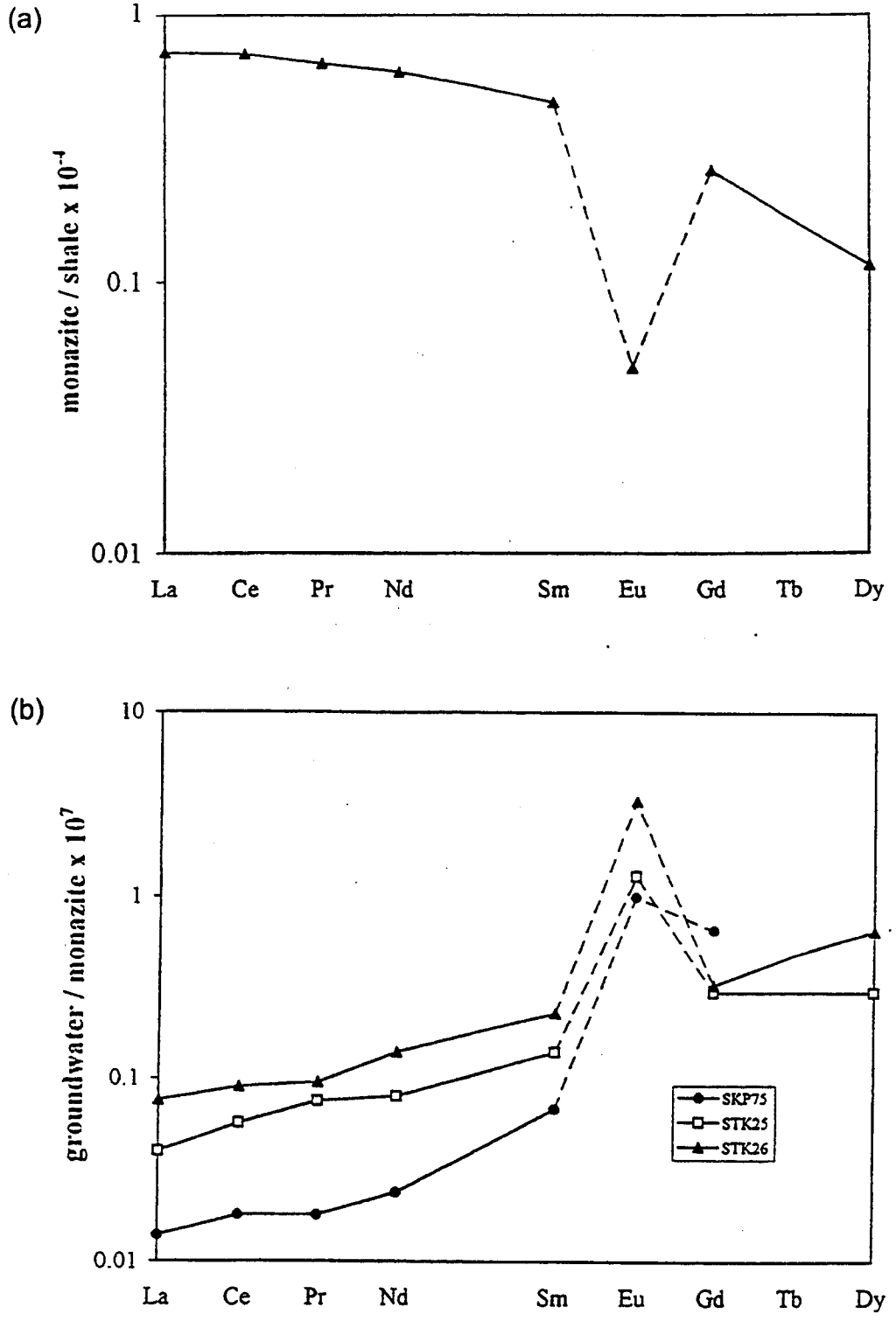

Source: Jarvis et al. 1997 [157489], Figures 3 and 4.

Figure 10.5-2. (a) Shale-normalized REE Pattern for Steenkampskraal Monazites and (b) REE Distribution for Groundwater Samples Normalized to Average Steenkampskraal Monazite

Table 10.3-1. Chemical Characteristics of Selected Samples of Pore Water, Perched Water, and Groundwater from Yucca Mountain and the Subsurface Disposal Area of INEEL

Location		Temp. (°C)	pH	Ca (mg/L)	Mg (mg/L)	Na (mg/L)	K (mg/L)	Cl (mg/L)	SO_4 (mg/L)	HCO_3 (mg/L)	SiO_2 (mg/L)	F (mg/L)	NO_3 (mg/L)	Data Source
Yucca Mountain	UZ-14 pore water (CHn)	28*	8.7	1.2	0.2	155	—	16	14	160	72.0	—	4	A
	UZ-14 perched water	25*	7.8	31	2.5	35	4.1	7.0	24.2	146.4	40.7	—	17.1	B
	WT-3 saturated zone	31.8	7.6	11.2	1.0	49.0	3.9	6.0	18.3	138.5	56.0	2.3	5.7	C
INEEL	Borehole W02 Lysimeter W0L01	5 to 10*	8.1	46.1	15	188	1.5	27	133	508	—	0.2	—	D
	Well 92 perched water (10/29/76)	13.5	8.4	29	17	120	12	81	64	290	22	0.4	—	E
	RWMC production well saturated zone	13	8.1	45	15	9.0	2.8	13	27	180.4	28	0.2	3.0	F

NOTE: *estimated temperature

Sources: A = Yang et al. 1996 [100194], Table 3, sample UZ-14/1563.6-1563.8/up1,2,3.
B = Yang et al. 1996 [100194], Table 6, sample UZ-14D.
C = DTN: GS980908312322.008 [145412].
D = Dicke 1997 [157410], Table 5.
E = Rightmire and Lewis 1987 [156441], Table 13, sample of 10/29/1976.
F = USGS 2000 [157415], Table 4-2.

Table 10.3-2. Additional Water Inputs to the Waste-Disposal Area Due to Flooding

Year	Infiltration Rate (m/day)	Total Equivalent Depth of Infiltrating Water (m)
1962	1.66×10^{-2}	0.166
1969	1.24×10^{-2}	0.124
1982	7.49×10^{-3}	0.075

Source: Magnuson and Sondrup 1998 [156431], Table 2-3.

Table 10.3-3. Hydrologic Properties Used in the One- and Two-Dimensional Single-Continuum and Dual-Permeability Models

Layer	Depth (m)	Porosity	Permeability (m^2)	Residual Saturation, S_{wr}	Pore-size Distribution, λ	Air Entry Parameter, α (Pa^{-1})
Surficial sediments	0-5	0.50	6.8×10^{-13}	0.194	0.401	1.642×10^{-4}
Clay layer	5-6	0.05	1.0×10^{-15}	0.246	0.273	1.817×10^{-4}
A-basalt	6-9	0.01	2.5×10^{-12}	0.010	0.500	4.094×10^{-4}
AB (9 m) interbed	9-10	0.57	1.0×10^{-15}	0.246	0.273	1.817×10^{-4}
B-basalt	10-34	0.01	2.5×10^{-12}	0.010	0.500	4.094×10^{-4}
BC (34 m) interbed	34-36	0.48	4.0×10^{-15}	0.083	0.273	3.270×10^{-4}
C-basalt	36-73	0.01	2.5×10^{-12}	0.010	0.500	4.094×10^{-4}
CD (73 m) interbed	73-76	0.57	4.0×10^{-15}	0.246	0.273	1.817×10^{-4}
D-basalt	76-180	0.01	2.5×10^{-12}	0.010	0.500	4.094×10^{-4}
Basalt matrix		0.14	5.0×10^{-17}	0.066	0.322	3.917×10^{-5}

NOTE: λ and α are pore-size distribution and air-entry parameters in the van Genuchten (1980 [100610]) moisture characteristic functions (see Lichtner 2001 [156429]).

Source: Simmons 2002 [157578], SN-LANL-SCI-234-V1, p. 22.

Table 10.3-4. Sorption Reaction Stoichiometry and Parameter Values for a Nonelectrostatic Description of Surface Complexation Reactions

Surface Complex Reaction						log *K*	*z*
Iron oxide							
$>FeO^-$	1 >FeOH	$-1\ H^+$				8.930	−1
$>FeOH_2^+$	1 >FeOH	$1\ H^+$				−7.290	1
$>FeOAm^{++}$	1 >FeOH	$-1\ H^+$	$1\ Am^{+++}$			−1.240	2
$>FeOAm(OH)_2$	1 >FeOH	$-3\ H^+$	$1\ Am^{+++}$	$2\ H_2O$		15.29	0
$>FeOHPuO^{++}$	1 >FeOH	$1\ H^+$	$1\ PuO_2^+$	$-0.25\ O_2(aq)$	$-0.5\ H_2O$	−2.010	2
$>FeOHPuO_2$	1 >FeOH	$-1\ H^+$	$1\ PuO_2^+$	$-0.25\ O_2(aq)$	$0.5\ H_2O$	6.210	0
$>FeOHPuO_2^+$	1 >FeOH	$1\ PuO_2^+$				−4.790	1
$>FeOHPuO_3^-$	1 >FeOH	$-2\ H^+$	$1\ PuO_2^+$	$1\ H_2O$		10.66	−1
$>FeOHUO_3$	1 >FeOH	$-2\ H^+$	$1\ UO_2^{++}$	$1\ H_2O$		3.050	0
$>FeOHUO_2^{++}$	1 >FeOH	$1\ UO_2$++				−6.630	2
$>FeOHNpO_2^+$	1 >FeOH	$1\ NpO_2^+$				−4.320	1
$>FeOHNpO_3^-$	1 >FeOH	$-2\ H^+$	$1\ NpO_2^+$	$1\ H_2O$		11.26	−1
$>FeOSr^+$	1 >FeOH	$-1\ H^+$	$1\ Sr^{++}$			5.3	−1
>FeOSrOH	1 >FeOH	$-2\ H^+$	$1\ Sr^{++}$	$1\ H_2O$		14.14	−1
Aluminosilicate							
$>SiO^-$	1 >SiOH	$-1\ H^+$				7.200	−1
$>SiOPuO^+$	1 >SiOH	$2\ H^+$	$1\ PuO_2^+$	$-0.25\ O_2(aq)$	$-0.5\ H_2O$	2.600	1
$>SiOPuO_2$	1 >SiOH	$-1\ H^+$	$1\ PuO_2^+$			6.430	0
$>SiOPuO_3H^-$	1 >SiOH	$-2\ H^+$	$1\ PuO_2^+$	$1\ H_2O$		14.80	−1
$>SiOUO_3H$	1 >SiOH	$-2\ H^+$	$1\ UO_2^{++}$	$1\ H_2O$		5.180	0
$>SiOUO_3^-$	1 >SiOH	$-3\ H^+$	$1\ UO_2^{++}$			12.35	−1
$>SiONpO_2$	1 >SiOH	$-1\ H^+$	$1\ NpO_2^+$			3.720	0
$>SiONpO_3H^-$	1 >SiOH	$-2\ H^+$	$1\ NpO_2^+$	$1\ H_2O$		12.16	−1
$>SiOAm^{++}$	1 >SiOH	$-1\ H^+$	$1\ Am^{+++}$			−0.7	2
>SiOAmO	1 >SiOH	$-3\ H^+$	$1\ Am^{+++}$	$1\ H_2O$		14.20	0
$>AlO^-$	1 >AlOH	$-1\ H^+$				9.730	−1
$>AlOH^+$	1 >AlOH	$1\ H^+$				−8.330	1
$>AlOPuO^+$	1 >AlOH	$1\ PuO_2^+$	$-0.25\ O_2(aq)$	$-0.5\ H_2O$		−1.03	1
$>AlOPuO_2^-$	1 >AlOH	$-2\ H^+$	$1\ PuO_2^+$	$-0.25\ O_2(aq)$	$0.5\ H_2O$	16.85	−1
$>AlOPuO_2$	1 >AlOH	$1\ PuO_2^+$				3.090	0
$>AlOUO_2^+$	1 >AlOH	$-1\ H^+$	$1\ UO_2^{++}$			−3.130	1
$>AlONpO_2$	1 >AlOH	$-1\ H^+$	$1\ NpO_2^+$			4.670	0
$>AlONpO_3H^-$	1 >AlOH	$-2\ H^+$	$1\ NpO_2^+$	$1\ H_2O$		14.26	−1
$>AlOAm^{++}$	1 >AlOH	$-1\ H^+$	$1\ Am^{+++}$			−2.490	2
Calcite							
$>PuO_2^+$	1 $>Ca^{++}$	$-1\ Ca^{++}$	$1\ PuO_2^+$			−1.850	1
$>UO_2^{++}$	1 $>Ca^{++}$	$-1\ Ca^{++}$	$1\ UO_2^{++}$			−5.120	2
$>NpO_2^+$	1 $>Ca^{++}$	$-1\ Ca^{++}$	$1\ NpO_2^+$			−2.350	1
$>AmCO_3^+$	1 $>Ca^{++}$	$-1\ Ca^{++}$	$1\ HCO_3^-$	$-1\ H^+$	$1\ Am^{+++}$	−1.587	1
$>Sr^{++}$	1 $>Ca^{++}$	$-1\ Ca^{++}$	$1\ Sr^{++}$			1.750	1

Source: Simmons 2002 [157578], SN-LANL-SCI-234-VI, p.29.

Table 10.3-5. Ion Exchange Selectivity Coefficients and Fitted Cation Exchange Capacity (CEC)

Cation	Selectivity Coefficient
Na^+	1.
Cs^+	12.5
Sr^{++}	2.857
K^+	5.
Mg^{++}	2.
Ca^{++}	2.5
	CEC (mol/kg solid)
	0.02

NOTE: Selectivity coefficients modified from Appelo 1996 [156425], pp. 197.

Source: Simmons 2002 [157578], SN-LANL-SCI-234-V1, p. 28.

Table 10.3-6. Composition of Injected Fluid

Table 10.3-6a. Primary Species Properties					
Species	**Molality**	**Total Concentration**	**Activity Coeff.**	**Species Activity Ratio/H^+**	**Constraint**
Ca^{++}	6.7143×10^{-4}	7.2355×10^{-4}	6.7444×10^{-1}	1.1936×10^{1}	1 total
K^+	3.0692×10^{-4}	3.0692×10^{-4}	8.9884×10^{-1}	4.0415	1 total
Mg^{++}	6.3025×10^{-4}	6.9944×10^{-4}	6.8849×10^{-1}	1.1908×10^{1}	1 total
Na^+	5.2197×10^{-3}	5.2197×10^{-3}	9.0166×10^{-1}	5.2721	1 total
Cl^-	2.4696×10^{-3}	2.4706×10^{-3}	8.9884×10^{-1}	-1.0162×10^{1}	–1 charge
SO_4^{-2}	5.9941×10^{-4}	6.6627×10^{-4}	6.5908×10^{-1}	-1.8331×10^{1}	1 total
HCO_3^-	4.4631×10^{-3}	4.7528×10^{-3}	9.0166×10^{-1}	–9.9048	1 total
F^-	1.9919×10^{-5}	2.0154×10^{-5}	9.0027×10^{-1}	-1.2255×10^{1}	1 total
SiO_2(aq)	3.6615×10^{-4}	3.6615×10^{-4}	1.0000	–3.4363	1 total
H^+	2.7897×10^{-8}	2.0345×10^{-4}	9.1373×10^{-1}	0.0000	3 calcite
Al^{+++}	3.5938×10^{-17}	5.5068×10^{-10}	4.4062×10^{-1}	6.2189	3 K-feldspar
Fe^{++}	1.0078×10^{-11}	1.6446×10^{-11}	6.7444×10^{-1}	4.1123	3 goethite
Sr^{++}	4.7300×10^{-13}	5.0000×10^{-13}	6.6693×10^{-1}	2.7837	1 total
PuO_2^+	9.9671×10^{-15}	4.0000×10^{-9}	9.0166×10^{-1}	–6.4470	1 total
UO_2^{++}	1.1940×10^{-17}	1.1110×10^{-10}	6.6305×10^{-1}	–1.8141	1 total
NpO_2^+	7.1760×10^{-11}	1.1150×10^{-10}	9.0166×10^{-1}	–2.5897	1 total
Am^{+++}	7.5783×10^{-14}	2.0000×10^{-11}	4.0148×10^{-1}	9.5429	1 total
Cs^+	4.0000×10^{-13}	4.0000×10^{-13}	8.9736×10^{-1}	–4.8435	1 total
O_2(aq)	1.2611×10^{-48}	-1.0030×10^{-9}	1.0000	-4.7899×10^{1}	4 O_2(g)
Solution conditions:					
Temperature: 25.0°C		Ionic strength: 1.0087×10^{-2}		Solution density: 0.99780 g/cm^3	
pH: 7.5936		pe: 1.931		Eh: 1.1430×10^{-1} V	
Charge balance: $-q = -6.3071 \times 10^{-16}$					
Computational parameters:					
Boundary condition: type 1		Iterations: 5			

Source: Simmons 2002 [157578], SN-LANL-SCI-234-V1, p. 31.

Table 10.3-6 continued. Composition of Injected Fluid

Table 10.3-6b. Properties of Complexes				
Complex	**Molality**	**Activity Coeff.**	**Species Activity/H^+**	**log *K***
$CO_2(aq)$	2.25165×10^{-4}	1.0000	–3.6475	6.3414
$MgSO_4(aq)$	4.43159×10^{-5}	1.0000	–4.3534	2.4125
$CaSO_4(aq)$	2.25424×10^{-5}	1.0000	–4.6470	2.1004
$CaHCO_3^+$	2.23075×10^{-5}	0.90166	2.9029	1.0429
$MgHCO_3^+$	2.08899×10^{-5}	0.90166	2.8744	1.0329
CO_3^{-2}	1.12691×10^{-5}	0.66305	–20.057	–10.325
$CaCO_3(aq)$	7.00620×10^{-6}	1.0000	–5.1545	–7.0088
$MgCO_3(aq)$	3.01655×10^{-6}	1.0000	–5.5205	–7.3562
$MgCl^+$	7.76285×10^{-7}	0.90166	1.4445	–0.13865
OH^-	4.44777×10^{-7}	0.90027	–13.906	–13.991
$CaCl^+$	2.22229×10^{-7}	0.90166	0.90124	–0.70039
MgF^+	1.92570×10^{-7}	0.90166	0.83903	1.3486
CaF^+	4.28435×10^{-8}	0.90166	0.18632	0.67736
$Pu(OH)_4(aq)$	3.99990×10^{-9}	1.0000	–8.3980	–13.920
$CaOH^+$	2.78300×10^{-9}	0.90166	–1.0010	–12.850
AlO_2^-	5.49982×10^{-10}	0.90166	–16.814	–22.879
$CaCl_2(aq)$	4.95545×10^{-10}	1.0000	–9.3049	–0.65346
$UO_2(CO_3)_3^{-4}$	5.83351×10^{-11}	0.18815	–40.452	–9.4530
$UO_2(CO_3)_2^{-2}$	5.18682×10^{-11}	0.65908	–25.394	–3.7613

Source: Simmons 2002 [157578], SN-LANL-SCI-234-V1, p. 90.

Table 10.3-6c. Mineral Saturation Indices		
Mineral	Saturation Index	log *K*
Dolomite	1.16594	–2.52402
Hematite	9.59704×10^{-1}	1.68702×10^{1}
Quartz	5.69305×10^{-1}	4.00565
Chalcedony	2.98104×10^{-1}	3.73444
Goethite	0.00000	7.95526
Calcite	0.00000	–1.85424
K-feldspar	0.00000	2.94216×10^{-1}
$Pu(OH)_4$	-1.57462×10^{-1}	–5.67951
Magnesite	-4.62767×10^{-1}	–2.29848
SiO_2(am)	-7.16385×10^{-1}	2.71996
Kaolinite	–1.70898	–6.79726
Gibbsite	–1.77543	–7.75591
Muscovite	–1.90002	-1.35668×10^{1}
Gypsum	–2.27448	4.47292
Beidellite-Ca	–2.29087	–5.56815
Sepiolite	–3.72692	-3.04075×10^{1}
Brucite	–4.47379	-1.62984×10^{1}
Magnetite	–5.38525	6.50570

Source: Simmons 2002 [157578], SN-LANL-SCI-234-V1, p. 32.

Table 10.3-6d. Gas Compositions			
Gas	log Partial Pressure	Pressure (bars)	log *K*
O_2(g)	–45.00	1.0000×10^{-45}	2.8993
CO_2(g)	–2.180	6.6104×10^{-3}	7.8092

Source: Simmons 2002 [157578], SN-LANL-SCI-234-V1, p. 32.

Table 10.3-7. Fitted Surface Complexation Site Densities

Site	Concentration (mol/bulk dm^3)
>FeOH	4.0×10^{-7}
>AlOH, >SiOH	5.0×10^{-6}
>Ca++	1.0×10^{-7}

Source: Simmons 2002 [157578], SN-LANL-SCI-234-V1, p. 28.

Table 10.3-8. Contribution of Radionuclides to Surface Complexation Sites

Component	Site	Mineral K_d (dm^3/dm^3)	Retardation: $1 + K_d$	% Adsorbed
Sr^{++}	>FeOH	5.9996×10^{-5}		
	>SiOH	0.0000		
	>AlOH	0.0000		
	$>Ca^{++}$	4.9530×10^{-6}		
Total of all sites:		6.4949×10^{-5}	1.0001	6.4945×10^{-3}
PuO_2^+	>FeOH	2.3473×10^{1}		
	>SiOH	1.7024×10^{-11}		
	>AlOH	3.4754×10^{1}		
	$>Ca^{++}$	7.0217×10^{-8}		
Total of all sites:		5.8227×10^{1}	5.9227×10^{1}	9.8312×10^{1}
UO_2^{++}	>FeOH	4.4734×10^{-2}		
	>SiOH	1.1785×10^{-3}		
	>AlOH	5.7571×10^{-3}		
	$>Ca^{++}$	4.1468×10^{-6}		
Total of all sites:		5.1674×10^{-2}	1.0517	4.9135
NpO_2^+	>FeOH	7.7954×10^{-3}		
	>SiOH	7.5785×10^{4}		
	>AlOH	7.5055×10^{-4}		
	$>Ca^{++}$	5.7351×10^{-2}		
Total of all sites:		7.5785×10^{4}	7.5786×10^{4}	9.9999×10^{1}
Am^{+++}	>FeOH	4.9624×10^{-1}		
	>SiOH	3.9129×10^{-1}		
	>AlOH	2.8157×10^{1}		
	$>Ca^{++}$	4.0926		
Total of all sites:		3.3137×10^{1}	3.4137×10^{1}	9.7071×10^{1}

Source: Simmons 2002 [157578], SN-LANL-SCI-234-V1, p. 33.

Table 10.4-1. Measurements of U-Th Isotopic Composition and Concentration in Various Water Samples Collected near the Nopal I Uranium Deposit

Sampling Location	Sample ID	Collection Date	U (ppb)	(+/-) (%)	$^{234}U/^{238}U$ atom ratio ($\times 10^{-6}$)	(+/-) (%)	δD (‰)	$\delta^{18}O$ (‰)	Notes
Perched water from borehole at +10 level	BH12W95-5	August 1995	4.79	0.20	119.66	0.18			
	BH12W95-11	September 1995	5.77	0.25	120.86	0.14			
	AS-5	25 February 2000	5.73	0.19	156.75	0.10	-64	-9.3	
	030701 2001	7 March 2001	10.40	0.19	112.59	0.11			
8.5 m into north part of adit at +00 level	ADIT95-6	September 1995	0.20	2.4	278.40	0.16			
	AS-4	25 February 2000	2.87	0.30	121.15	0.25	-1	-2.8	
	030701-02	7 March 2001	1.20	0.24	142.05	0.20			E in Figure 10.4-1
23 m from adit entrance	ADIT95-9	September 1995	0.89	0.54	156.16	0.11			
	AS-3	February 2000	4.03	0.19	64.61	0.18	-7	-3.6	
	030701-03	7 March 2001	26.96	0.18	64.36	0.10			D in Figure 10.4-1
15 m from adit entrance	AS-2	25 February 2000	36.92	0.19	51.53	0.16	-7	-3.4	
	030701-04	7 March 2001	16.49	0.28	50.51	0.40			C in Figures 10.4-1, 10.4-2
12 m from adit entrance	AS-1	25 February 2000	68.46	0.19	58.21	0.14	-11	-2.5	B in Figures 10.4-1, 10.4-2
5 m from adit entrance	030701-05	7 March 2001	13.01	0.23	56.14	0.20			A in Figures 10.4-1, 10.4-2
Abandoned mining camp supply well	AS-6	25 February 2000	2.53	0.25	64.93	0.30			
Poços Ranch	WW95-03	September 1995	0.17	2.8	76.02	0.22			Well
	AS-7	25 February 2000	0.27	1.0	140.00	1.0	-61	-8.7	Holding Tank
	030701-06	7 March 2001	5.71	0.19	111.69	0.10			Holding Tank

Source: 1995 samples from Pickett and Murphy 1999 [110009], Table II.
2000 and 2001 samples from Simmons 2002 [157578], SN-LANL-SCI-237-V1, p. 16; SN-LBNL-SCI-108-V1, pp. 86, 87.

11. ANALOGUES TO THERMALLY COUPLED PROCESSES

11.1 INTRODUCTION

Numerous igneous-intrusion contact zones have been examined with the objective of understanding chemical reactions and migration of elements away from the heated contact zone, as well as understanding thermal-hydrologic-chemical (THC) effects. A number of these studies are described in CRWMS M&O (2000 [141407]; 2000 [151945], Section 13), as summarized by the following.

The effects of shallow (<500 m) magmatic intrusions into unsaturated host rocks can be quite different from effects associated with deeper hydrothermal systems. Deeper, saturated hydrothermal systems may display evidence that a large-scale hydrothermal cell was established (Brookins 1986 [109877], p. 337). In contrast, both the Banco Bonito study (Stockman et al. 1994 [117820], p. 88) and the Grants Ridge basalt intrusion study (WoldeGabriel et al. 1999 [110071], p. 409) indicate that the effects of high-temperature (~850°C; Stockman et al. 1994 [117820], p. 88) intrusions into these unsaturated environments appear to have been slight, to have been limited to within 10 m or so of the contacts, and to show no evidence of fluid-driven convective heat transfer or pervasive hydrothermal alteration of the country rock. These field studies, along with the Paiute Ridge field studies (see Section 11.4), provide limiting high-temperature-case natural analogues for evaluating THC processes resulting from the heat released by the decay of radioactive waste in an unsaturated environment.

A good analogy for understanding future water-rock interactions at the mountain scale is the fossil hydrothermal system at Yucca Mountain itself. Most zeolitic alteration occurred 13 to 11.6 Ma, at about the same time as tuff emplacement (Bish and Aronson 1993 [100006], p. 148). After formation of the major zeolitic horizons, deep-seated hydrothermal activity persisted until about 10 Ma. This activity was evidently limited to temperatures of 90–100°C, because at prolonged exposure to temperatures greater than 90°C, the sorptive zeolites clinoptilolite and mordenite are altered to the nonsorptive minerals analcime plus quartz and/or calcite, and this transformation did not occur.

Section 11 reports analyses conducted since CRWMS M&O 2000 [141407] of THC and thermal-hydrologic-mechanical (THM) natural analogue studies. Section 11.2 presents the results of an extensive survey of geothermal literature for the purpose of obtaining insights from coupled processes operating in geothermal fields. Section 11.3 then provides a detailed examination of THC processes relevant to the Yucca Mountain drift-scale system, observed at the Yellowstone, Wyoming, geothermal field. Section 11.4 presents results of a field investigation and modeling study of evidence left in a fossil hydrothermal system at Paiute Ridge, Nevada. Next, examples are given in Section 11.5 of evidence for THC effects on transport. Section 11.6 reports THM effects to a potential repository from a number of settings with analogous conditions. Finally, Section 11.7 summarizes what can be learned about THC and THM coupled processes relevant to a potential high-level waste repository at Yucca Mountain. Information found in Sections 11.2 through 11.5 may help to support arguments associated with KTI KUZ 0407 listed in Table 1-1.

11.2 GEOTHERMAL ANALOGUES TO YUCCA MOUNTAIN THERMAL-HYDROLOGIC-CHEMICAL PROCESSES

11.2.1 Objectives

The goal of Section 11.2 is to demonstrate the utility of geothermal systems as natural analogues for processes that are expected to occur in the potential Yucca Mountain repository. The primary objective of Section 11.2 is to use geothermal systems as natural analogues for illustrating coupled processes that impact permeability, fluid flow, and chemical transport. The introduction to this section notes some of the key THC processes observed in geothermal systems, and how these processes might impact the potential Yucca Mountain repository. A summary of key components of geothermal systems is then presented, followed by a description of the potential Yucca Mountain repository and a discussion of limitations of geothermal analogues for the Yucca Mountain system. The main body of this report consists of descriptions of geothermal analogues for each of the key THC processes identified. This is followed by a discussion of how these processes could impact the total site performance. Finally, suggestions are made for additional work that would further extend the use of geothermal systems in the validation and confirmation of Yucca Mountain models. The initial stages of a literature survey identified the Yellowstone geothermal system as particularly relevant for the Yucca Mountain system. Detailed analysis of core samples from Yellowstone was conducted to supplement previous studies of the Yellowstone geothermal system. The results of this work are described in detail in Section 11.3 of this report.

11.2.2 Introduction

Geothermal systems can be used as a natural laboratory for examining many of the coupled THC processes expected for the potential nuclear waste repository at Yucca Mountain, Nevada (Simmons and Bodvarsson 1997 [126511]; CRWMS M&O 2000 [141407]). Key processes that are expected to occur in the potential high-level nuclear waste repository at Yucca Mountain, such as boiling and condensation and mineral dissolution and precipitation, and their effects on permeability, fluid flow, and radionuclide transport, can be observed in many geothermal systems. Prior use of geothermal systems as natural analogues has focused on the verification of geochemical models (e.g., Meijer 1987 [101345]; Apps 1995 [154615]; Bruton et al. 1995 [117033]). However, active and fossil geothermal systems can also yield important insights into the consequences of processes such as boiling, condensation, fluid mixing, and water-rock interaction associated with fluid flow in matrix and fractures (Figure 11.2-1). These systems allow observation of the effects of processes over much longer time scales than are possible in laboratory or field testing, and provide a benchmark for coupled process modeling. Characterization of the effects of water-rock interaction (such as mineral precipitation and dissolution) on matrix and fracture permeability in geothermal systems can then be used to estimate potential changes in fluid flow resulting from the thermal impact of storing high-level nuclear wastes in fractured ash flow tuffs.

This study builds upon an earlier review of geothermal systems as natural analogues (Simmons and Bodvarsson 1997 [126511]; CRWMS M&O 2000 [141407]). This study expands the scope of the earlier review by including additional THC processes that are observed in geothermal systems and incorporates the results of new geothermal studies as part of a literature review.

Because no single geothermal analogue is suitable for all elements of Yucca Mountain, the geothermal analogues are used to evaluate the effects of individual THC processes, with multiple geothermal examples examined for each process of interest.

11.2.3 Similarities between Geothermal Systems and Yucca Mountain

There are many similarities between geothermal systems and an anthropogenic (man-made) hydrothermal system that would be created by the emplacement of high-level nuclear waste. For most geothermal systems, intrusion of magma at shallow crustal levels results in high heat flow and the formation of a convective hydrothermal system with associated water-rock interaction. In the anthropogenic system, heat-generating nuclear waste would induce changes in the ambient system. Both types of systems are subjected to coupled THC processes (Table 11.2-1) such as conductive and advective heating, fluid flow and chemical transport through matrix and fractures, boiling and condensation, and mineral dissolution and precipitation. These processes can result in important changes in the fluid flow properties of the rocks surrounding the heat source over time.

The use of geothermal systems as natural analogues for THC processes is most applicable for the higher temperature (above boiling) operating mode, because many of the processes mentioned in Table 11.2-1 would have little effect on a cooler, sub-boiling repository. These processes will have a greater impact in the near-field area, where the effects of heating (and associated THC processes) are expected to be most pronounced. For all cases, the magnitude of the effects of many THC processes (such as boiling, condensation, mineral dissolution, and precipitation) is envisioned to be significantly reduced at Yucca Mountain as a result of the much lower anticipated fluid and thermal flux rates than those observed in active geothermal systems. Key differences between geothermal systems and Yucca Mountain are described in Section 11.2.7. However, geothermal systems provide well-constrained examples of how THC processes can modify important hydrogeologic properties (such as porosity, permeability, and sorptive capacity) that would affect the total system performance of a geologic high-level radioactive waste repository.

11.2.4 Key Physical Components of Geothermal Systems

Prior to providing detailed evaluation of geothermal systems of natural analogues, it is worthwhile to examine the key components of these systems. While geothermal systems are found in a variety of geologic and tectonic environments and have many different characteristics, they all share a number of common traits. These include: (1) heat source, (2) fluids, (3), permeable flow paths, and (4) impermeable boundaries. Another important feature present in many vapor-dominated geothermal systems is a heat pipe, consisting of a boiling zone and condensation zone. Each of these features is discussed below.

11.2.4.1 Heat Source

Most active geothermal systems have magmatic heat sources, consisting of shallow intrusions that provide a high-level heat source for periods ranging from 100,000 to over 1,000,000 years. These intrusive bodies also supply magmatic components (such as water, CO_2, SO_2, and HCl) that often control the chemistry of the reservoir fluids. For example, the granitic pluton

underlying The Geysers geothermal field in California was emplaced around 1.2 Ma (Dalrymple et al. 1999 [156374], pp. 293–297), serving as a long-lived heat source for the still-active geothermal field. The Krafla and Námafjall geothermal fields, located along the Mid-Atlantic Rift Zone in Iceland, are much younger systems, where recent ongoing volcanic activity (1975–1984) led to the injection of magma into an existing geothermal well bore (Larsen et al. 1979 [155885]).

11.2.4.2 Fluids

Geothermal energy is extracted from local thermal anomalies in the earth's crust through the withdrawal of heated fluids. These fluids have a number of origins: connate (formation) waters, surface (meteoric) waters, juvenile (magmatic) waters, and seawater. The relative amounts of these fluids depend greatly on the geology and tectonic environment, the groundwater hydrology, the local climate, and the size and composition of the cooling and degassing intrusive heat source. The origin and abundance of these fluid types in geothermal systems can be determined through isotopic and geochemical study of fluid compositions (e.g., Giggenbach 1997 [156338]; Kennedy and Truesdell 1996 [156339]; Arnórsson 1995 [156321]).

11.2.4.3 Permeable Flow Paths

The development of a convecting geothermal reservoir (and the successful exploitation of such a resource) depends on the presence of high-permeability pathways. Many geothermal reservoirs are hosted by rocks with low matrix permeabilities, resulting from either intrinsically low permeabilities (i.e., intrusive igneous rocks and welded ash flow tuffs) or from hydrothermal alteration. The presence of a high-permeability fracture network in many geothermal systems allows for the heated fluids to flow convectively within the reservoir. Such permeable fracture networks may be generated by faulting occurring within tectonically active areas (Moore et al. 2001 [156320]; Forster et al. 1997 [156355]).

11.2.4.4. Impermeable Seals

The longevity of a geothermal resource depends on the presence of an impermeable cap above the reservoir. Without such a cap, heated fluids would buoyantly rise to the surface, rapidly dissipating the heat of the source. This impermeable barrier may result from a pre-existing low-permeability formation, but often develops as a result of extensive argillic alteration occurring at temperatures of 100–200°C. Lateral permeability barriers along the margins of geothermal systems can form by precipitation of retrograde solubility minerals, such as anhydrite and calcite, from descending (and heating) fluids along the margins of a geothermal system (Allis and Moore 2000 [156316], p. 215).

11.2.4.5 Heat Pipes

Geothermal heat pipes have been described for a number of vapor-dominated geothermal systems (Ingebritsen and Sorey 1988 [137537]; Allis and Moore 2000 [156316]). In a geothermal heat pipe (Figure 11.2-1), water boils at the heated (lower) end, and water vapor migrates to the cooler region where it condenses and the heat of vaporization is released. The condensed water then flows back to the heated end by gravity or capillary forces. The region within the heat pipe will be at a nearly uniform temperature near the boiling point of water. The

condensate water will be undersaturated with respect to the host rock minerals and will begin to dissolve constituents from the rock and gases locally present. Some of the water containing the dissolved constituents will flow through the fractures back down towards the heat source. Water flowing back towards the heat source will boil again, precipitating the formerly dissolved solids. The repeated dissolution and precipitation will affect fracture permeability by locally widening apertures where dissolution takes place, or narrowing apertures where precipitation occurs.

The heat-pipe features observed in geothermal systems have also been demonstrated in smaller-scale laboratory experiments. A heat-pipe reactor was built using tuff chips from Yucca Mountain and operated for 30 days (Rimstidt et al. 1989 [142190]). In the top region (condensation zone), etching and dissolution were observed. In the center region, few indications of dissolution or precipitation were observed. In the bottom region, extensive precipitation was observed with silica, iron oxyhydroxides, stilbite, and possibly clays forming. A layer of rock grains tightly cemented with amorphous silica formed at the face of the heater; this mineralization would result in reduced permeability. Similar heat-pipe features were also observed in the column tests reported in Lowry (2001 [157900]).

11.2.5 Characteristics of the Potential Yucca Mountain Repository

The potential nuclear waste repository is sited within a section of crystal-poor, devitrified, moderately to densely welded Topopah Spring tuff that forms part of a 1,000 m (3,300 ft) thick section of 11–14 Ma ash flow tuffs at Yucca Mountain (CRWMS M&O 1997 [100223], Figure 35). The repository horizon is overlain by 300 m (980 ft) of nonwelded to densely welded tuff, and underlain by a sequence of nonwelded to densely welded Miocene ash flow tuffs, older Tertiary volcanic and sedimentary rocks, and Paleozoic dolomites. The repository would be located within the unsaturated zone (UZ), 350 m (1,150 ft) above the regional water table (Figure 11.2-2). The potential repository is located in fractured unsaturated host rock with very low matrix permeability. The combination of low matrix permeability and unsaturated rock helps keep water from waste packages, thus retarding unwanted processes such as corrosion of the waste packages, dissolution of the waste materials, and transport of radionuclides to local aquifers. Fluid flow along high-permeability fractures may, however, result in seepage.

The higher-temperature operating mode (BSC 2001 [155950], Section 2.3) consists of a drift spacing of 81 m (266 ft), with drip shields, line load waste packaging, and 50 years of drift ventilation after the waste has been emplaced. These design attributes (see also Section 2 of this report) are used to minimize seepage onto the waste containers, limit peak temperatures in the drifts, and reduce the likelihood of the development of coalescing boiling zones, thus permitting drainage to occur in the pillar regions between the drifts. For the higher-temperature operating mode, maximum temperatures of around 120°C are predicted for the drift wall (BSC 2001 [155950], Section 4.3.5.3.3), with temperatures greater than 100°C predicted to persist in the waste package and near-field for 1,000–2,000 years. Other design possibilities also under consideration include a lower-temperature operating mode in which the maximum temperature at the drift wall will never exceed 85°C (BSC 2001 [155950], Section 3.2.5).

The near-field repository environment is predicted to undergo two distinct phases resulting from the thermal loading: dryout and rewetting. Dryout is predicted to occur as the waste packages transfer their heat to the surrounding environment. The size of the dryout zone will vary with

time and may extend up to 13 m (43 ft) away from the drift walls, depending on waste package configuration (BSC 2001 [154677], Section 6.4.5.1). During the dryout phase, liquid water will be converted to water vapor, which will effectively displace air from this zone. This is important because the oxygen necessary for many corrosion reactions will be present only in low concentrations. As the heat output from the waste package diminishes with time, dryout zones are predicted to gradually undergo rewetting from reflux of CO_2-replenished condensate and ambient percolation. The rewetting will be accompanied by an influx of air back into the near-drift environment as temperatures drop below the local boiling point and slowly approach ambient (pre-repository) thermal conditions (BSC 2001 [154677], Section 6.6.5).

Subsurface fluid flow for the Yucca Mountain area is controlled by the permeability and unsaturated hydraulic properties of the Miocene ash flow tuff sequence. Densely welded sections of the tuff have very low matrix permeabilities, and fluid flow through these sections is controlled by faults and fractures. Nonwelded tuffs have significantly higher matrix permeabilities and fewer fractures, and thus matrix flow appears to be the dominant process in these sections. These differences in matrix and fracture permeability as a function of welding (Figure 11.2-3) are characteristic of ash flow tuff deposits (Winograd 1971 [156254]). The potential repository is located within a densely welded devitrified tuff (Figure 11.2-2), and thus bulk permeability for this horizon is controlled by fractures.

Fracture permeability depends on a variety of fracture characteristics, including fracture orientations relative to the regional stress field, fracture density and spacing, fracture apertures, and the presence or absence of mineralization within the fractures. Field permeability measurements have been made at the Yucca Mountain Exploratory Studies Facility (ESF) to evaluate the variability of permeability and identify controlling factors. The matrix permeability of the welded Topopah Spring tuff (TSw) is 3 to 6 orders of magnitude lower than the fracture permeability (LeCain 1997 [100153], pp. 28–29), so fluid flow within this formation should be highly focused along fractures.

11.2.6 Time Scales of Geothermal Processes

Time scales of processes expected to occur in a geologic nuclear waste repository are compared with processes that occur in geothermal systems shown in Table 11.2-2. Because of these very long and variable time scales, it is not possible to create a scale model of a potential nuclear waste repository, study all of these processes for a short while, and then extend this knowledge to real repository future behavior. Laboratory and field-scale studies have been conducted and others are currently underway to study some of these processes for the purpose of model validation. Computer-based numerical modeling is being used to interpret and extend these results within a framework of well-understood physical laws and data. The same processes expected to occur at a geologic high-level nuclear waste repository at Yucca Mountain have been occurring over the long-term in geothermal systems, making the study of geothermal systems highly relevant to the long-term understanding of possible repository behavior.

11.2.7 Limitations of Geothermal Analogues

It is important to note several important differences between most geothermal analogues and the potential Yucca Mountain repository:

- The potential Yucca Mountain repository is located within unsaturated rocks, while most geothermal systems have saturated conditions. While the repository may develop locally saturated areas (such as the condensation zone), this difference should result in reduced water-rock interaction for the thermally loaded repository system. Convective liquid flow will not develop under unsaturated conditions, and thus thermal and fluid fluxes for the Yucca Mountain system will be significantly lower than those found in high-temperature geothermal systems. Advective transport will still occur within the fracture network, and thus chemical transport rates could be fairly rapid along the fast flow paths within the UZ at Yucca Mountain. Several natural analogues that have experienced elevated temperatures under unsaturated conditions (Banco Bonito, New Mexico, and Paiute Ridge intrusive complex, Nevada) exhibit very little hydrothermal alteration resulting from the heat pulse event (Stockman et al. 1994 [117820]; Lichtner et al. 1999 [121006]; and Section 11.4 of this report).

- Liquid-dominated geothermal systems have increasing hydrostatic pressures with depth, reflecting the presence of a hydrostatic column. Boiling within a geothermal system at depth thus occurs at progressively higher temperatures (following the boiling point-depth curve). Because Yucca Mountain is an unsaturated system, fluid pressures will typically not exceed atmospheric pressure, and thus boiling should occur at temperatures around 96°C throughout the system.

- The higher-temperature operating mode for the potential Yucca Mountain repository is predicted to have an areally restricted and short-lived (1,000–2,000 yrs) higher temperature (>100°C) pulse, thus limiting the time when boiling and condensation processes could occur. In addition, because of the unsaturated nature of the Yucca Mountain system, dryout zones should develop around the high-temperature repository drift areas, also serving to reduce the potential impact of water-rock interaction.

- For the lower-temperature operating mode, drift-wall temperatures will never exceed boiling point values, and thus precipitation of dissolved species resulting from boiling will not occur. Some increase in the concentration of dissolved species may result from evaporation in this case. The lower predicted temperatures in this operating mode will also result in less extensive water-rock interaction, with reduced amounts of mineral alteration, dissolution, and precipitation.

- Speciation and transport of dissolved species may be affected by the redox state of the system. Geothermal systems are typically somewhat reducing in nature (as evidenced by the presence of H_2S rather than SO_2 in most geothermal fumarolic gases), whereas the Yucca Mountain system is expected to be more oxidizing (owing to the presence of atmospheric oxygen in the gas phase). This difference in oxidation state could affect the transport and precipitation of chemical components with multiple oxidation states (such as Fe^{2+}/Fe^{3+} and U^{4+}/U^{6+}), but should not significantly impact the behavior of important sealing species such as silica.

- Gas compositions of geothermal systems differ significantly from that predicted for Yucca Mountain, which lacks a magmatic fluid component. While both systems will contain CO_2 and air, most geothermal systems also contain significant amounts of sulfur-

bearing gases (typically H_2S) that can lead to the development of acidic fluid compositions when oxidized.

11.2.8 Geothermal Examples of Heat and Fluid Flow

Many geothermal systems worldwide have been the subject of heat and fluid flow studies. Fluid flow in geothermal systems is controlled in part by thermal buoyancy effects, chemically controlled density contrasts, and channelized flow resulting from permeability barriers. Drilling of exploration and production wells in developed geothermal fields facilitates the collection of downhole temperature and pressure data. Production flow and tracer tests also permit the determination of formation permeability and fluid flow paths and rates. Reservoir simulation models have been widely used along with such data to predict future heat and fluid flow behavior in commercial geothermal reservoirs under production (e.g., Bodvarsson et al. 1993 [138618]; Steingrimsson et al. 2000 [156686]; also see Section 11.2.8.2). The ability of these models to accurately forecast changes in reservoir behavior provides confidence that similar models developed for Yucca Mountain will reasonably simulate future repository performance. Two aspects of heat and fluid flow in geothermal systems are discussed in detail below. The first topic is the role of faults and fractures in providing high-permeability pathways for fluid flow within the convecting geothermal reservoir. The second topic is the use of numerical models to create natural-state models and to simulate the effects of production and reinjection on geothermal reservoirs.

11.2.8.1 Fracture-Dominated Fluid Flow

Many geothermal systems have reservoir rocks with relatively low matrix permeabilities, but high overall formation permeability caused by the presence of a high-permeability fracture network (Bodvarsson and Witherspoon 1989 [156337], p. 3). For some systems, this network is dominated by a few large-scale faults that control both the location of surface thermal features as well as fluid flow in the subsurface. Several examples of these geothermal systems are described below.

Dixie Valley, Nevada

The Dixie Valley geothermal field is located along the active Stillwater normal fault, in an area of high regional heat flow in the Basin and Range province of Nevada. The production wells are targeted to intersect strands of this fault at depth. Interference and tracer tests conducted in this field demonstrate that the high-permeability wells are well connected by a high-permeability fracture network. In a tracer test at Dixie Valley, three tracer combinations were introduced into three wells (Adams et al. 1989 [156348], pp. 215–217). Pre-test modeling based on the porous medium approximation identified seven well pairs that were expected to show tracer breakthrough. Only one well produced tracer, identifying a connected fracture network between the injection site and the producing well. The minimum velocity (based on a straight line between injection and the producing well) for the tracer front was 5 m/hr, and the minimum velocity for the tracer peak was 1.4 m/hr. As part of another investigation at Dixie Valley, a series of four tracer tests was performed (Rose et al. 1998 [156341]). Tracers were introduced in pulses in target injection wells located in the southern and central portions of the field. The tracers were detected only in a cluster of seven wells located between the injection wells. The

amount of short-circuiting between the wells differed for each injection well, with one of the wells having a much shorter residence time than the others, indicating heterogeneity in the fracture network. Breakthrough curves presented by Rose et al. (1998 [156341], Figure 2) can be used to calculate tracer-front minimum velocities ranging from about 0.7 to 3 m/hr (average = 1.6 m/hr) and peak minimum velocities ranging from about 0.4 to 0.8 m/hr (average = 0.6 m/hr).

Silangkitang, Indonesia

The Silangkitang geothermal field is one of several geothermal systems located along the Great Sumatran fault zone. The main thermal features are located along surface traces of this major strike-slip fault (Gunderson et al. 1995 [156361], p. 691). Exploration wells drilled directionally to penetrate the main trace of the fault encountered extremely high fluid flow rates within the fault zone (Gunderson et al. 2000 [156310], Figure 4, pp. 1184–1185). In contrast, nearby vertical wells that do not intersect the fault have very low formational permeabilities, thus underscoring the importance of the fault in providing high-permeability flow paths. Higher temperatures and increased alteration were encountered near the fault, which serves as an upflow zone for this geothermal system (Moore et al. 2001 [156320], pp. 1190–1191).

Wairakei, New Zealand

The Wairakei geothermal field is located in the Taupo Volcanic Zone, a tectonically active area that has been the site of voluminous Quaternary volcanism. Normal faults cutting the area appear to be the primary conduits for high-volume fluid flow. Grindley (1965 [154663]) identified three groups of wells based on their relative deliverabilities. Wells intersecting faults have very high permeabilities (>1 darcy) that cannot be precisely quantified because of a lack of pressure drawdown during production tests. Wells drawing on reservoir storage have pronounced drawdown, with calculated permeabilities ranging from 5–30 millidarcies. Nonproductive wells typically intersect hydrothermally cemented rocks with intrinsically low (<1 millidarcy) permeabilities. The intensely altered, impermable rocks serve to protect the producing reservoir from cold water encroachment. Tracer tests conducted at Wairakei (Jensen and Horne 1983 [156643], Table 1) suggest minimum flow velocities along fractures that are as high as 38 m/hr. These flow velocities result from high-pressure gradients within the system; similar gradients are not expected for Yucca Mountain.

Relevance to Yucca Mountain

These geothermal examples show the importance of high-permeability fractures in the circulation of geothermal fluids. Numerous normal faults (i.e., Solitario Canyon, Bow Ridge, Dune Wash, Drill Hole Wash, Pagany Wash, Sever Wash, Sundance, Ghost Dance) have been identified at Yucca Mountain, but little is currently known about their permeability (BSC 2001 [155950], Section 3.3.4.5.1). If these faults are permeable, then they could serve as fast fluid flow paths for infiltrating surface waters reaching the repository level, as well as pathways for dissolved radionuclide transport from the waste packages down to the water table.

The presence of bomb-pulse tritium and ^{36}Cl in water samples collected from core samples from the potential repository horizon within Yucca Mountain suggests that fault and fracture pathways have experienced relatively fast rates of fluid flow (Fabryka-Martin et al. 1997 [100145]). Based

on these results, minimum fluid-flow velocities calculated using a distance of 300 m (distance from the surface to the sampled areas) and a maximum time of 50 years (first generation of bomb-pulse tritium and ^{36}Cl) are on the order of 0.0007 m/hr; these rates are much slower than those observed in geothermal fields. Because the bomb-pulse tracer flow rate estimate is poorly constrained, a number of fluid flow experiments have been conducted along faults within the ESF at Yucca Mountain with the goal of obtaining better estimates of flow velocities. A series of *in situ* flow tests was conducted in Alcove 4 between two boreholes 1.07 m apart that intersected a minor normal fault (Salve and Oldenburg 2001 [157316], Figure 8, p. 3049). Measured flow velocities along the fault ranged from 0.08–0.58 m/hr. In another test between Alcove 8 and Niche 3, the time (~840 hr) between water release and the onset of seepage along a fault that intersects both the main drift and cross-drift tunnels (Figure 11.2-4) and the distance between these two areas (~25 m) can be used to calculate a flow velocity of about 0.03 m/hr (Salve et al. 2001 [156848]). The measured fluid velocities from these field experiments are significantly higher than those obtained from the bomb-pulse data and may reflect the need for surface infiltration rates to be high enough to initiate and sustain fracture flow (Flint et al. 2001 [156351], pp. 19–21, 24, 25).

The percolation flux at Yucca Mountain is much lower than the fracture flow rates described above. The percolation flux depends on the magnitude and spatial distribution of surface infiltration rates, as well as other factors, such as the presence of fast flow paths and lateral diversion within low-permeability intervals. Present-day infiltration rates are estimated to vary from 0–80 mm/yr, with an average value of about 5–10 mm/yr, for the potential Yucca Mountain repository block area (Flint et al. 2001 [156351], pp. 22–23). Thus, it is critical to understand the role of faults and fractures at Yucca Mountain and how these features could serve to accelerate and/or focus fluid flow within the potential repository.

11.2.8.2 Heat and Fluid Flow Simulations for Geothermal Systems

Numerical simulation of geothermal fields has been performed successfully for more than three decades. The Code Comparison Study (Molloy 1981 [156407]) evaluated several geothermal simulators with six test problems. The codes tested all performed reasonably well, indicating that the physics of the test problems were correctly represented. Numerical simulation of geothermal fields has proved to be of great economic importance in aiding geothermal companies to understand where to drill and to predict production capacity (Simmons and Bodvarsson 1997 [126511]). In a recent examination of geothermal simulations, more than 100 field simulations have been carried out worldwide since 1990 using a variety of simulators (O'Sullivan et al. 2001 [156353]).

Over the decades of geothermal reservoir simulation, a robust modeling process has been developed. The process includes data collection and evaluation, conceptual model development, numerical model design, natural-state modeling, history matching, prediction, and postauditing. Each step is dependent on the preceding steps, and thus changes in any preceding step require modifications in all subsequent steps.

In the first step, all available data are evaluated. The data may be from several sources, including flow tests, well logs (temperature, lithology, electrical resistivity), fluid chemistry, self-potential surveys, measurements on core samples, topography, location and flow rates from hot springs

and fumaroles, seismic data, precision gravity surveys, and other techniques. The data evaluation may be performed by individuals from many disciplines, yielding a conceptual model that is typically distilled into a few plan- and cross-sectional schematics providing an understanding of how the reservoir works.

The numerical model is constructed to resemble the conceptual model. Region size, gridblock sizes, boundary conditions, fluid chemistry, and equations of state are selected and parameters are assigned for each gridblock. The first step in model calibration is natural-state modeling. In natural-state modeling, the numerical model is tested by placing a heat source into the system at some time in the past (usually thousands to millions of years ago) and running the model forward to obtain a match with current measurements. If an adequate match is not obtained, parameters are altered within reason and the process is repeated. Many iterations are often required, and this procedure may be partially automated (White et al. 1997 [156340]; Bullivant and O'Sullivan 1998 [144410]; Finsterle 1999 [104367]). The importance of field features may be identified in this step, often leading to inferences of fluid inflows and faults.

The second step in model calibration is history matching, which can be performed when fluids have been produced from the geothermal system. In history matching, the field perturbation (caused by fluid extraction) is modeled, with the results compared to field measurements (temperature, pressure, enthalpy, brine composition). Again, parameters are adjusted until a reasonable match is obtained. Since natural-state modeling is performed for long time frames and history matching over significantly shorter time frames (years to decades), different types of parameters can be inferred. In natural-state modeling, parameters such as permeability are inferred. In history matching, storage-type parameters like porosity are inferred. Changes in parameters at any stage require verification in earlier stages. Calibration of a model using both natural-state modeling and history matching is a significant milestone in the creation of a viable reservoir model and becomes increasingly difficult as the amount of data increases.

Upon completion of successful natural-state modeling and history matching, the model is used for predictive purposes. Geothermal fields are modeled for a variety of reasons, but generally to devise a strategy for energy extraction. These models are generally evaluated and updated when development is planned. Few postaudits of geothermal field models have been published (post audits of two fields were found in the literature), although model performance is often monitored and demonstrated. The postaudit of Olkaria East Geothermal Field, Kenya (Bodvarsson et al. 1990 [136384], pp. 399–407) showed that the field-wide decline in steam rate agreed very well with predictions. A well-by-well comparison identified adequate predictions for 75% of the wells. Many of the wells for which prediction was inadequate had limited production when the initial model was constructed, and thus there was insufficient history on which to base the predictions for these wells. In a postaudit of the Nesjavellir Field, Iceland, Bodvarsson et al. (1993 [138618]) evaluated predictions made with a 1986 model for pressure decline and enthalpy changes. Acceptable agreement was reported between modeled and measured data (Figure 11.2-5), particularly considering that the prediction time (6 years) was longer that the 1–3 yr calibration period. A second audit was performed of the Nesjavellir geothermal system (Steingrimsson et al. 2000 [156686]) because the model underestimated enthalpy decline in some wells. Recalibration led to slight changes in the conceptual model within the producing region of the reservoir. The new model matched well data better, but the larger-scale reservoir performance predictions remained unchanged.

The geothermal industry relies heavily on the use of models, and at many fields several generations of models have been used. Beginning in the early 1980s, UNOCAL developed and maintained 3-D models of U.S., Philippine, and Indonesian geothermal fields (e.g., Williamson 1992 [156613]; Strobel 1993 [156614]; Murray et al. 1995 [156612]). The Wairakei geothermal field (New Zealand) has been modeled since the late 1960s, including many types of models and levels of complexity (O'Sullivan et al. 1998 [154567]). The Kawerau geothermal field (New Zealand) has also been extensively modeled for more than a decade (White et al. 1997 [156340]). These models have been upgraded over time as new information, codes, and techniques became available. The accumulated longevity of the models at a particular field indicates a significant degree of confidence in geothermal reservoir modeling.

Application to Yucca Mountain

There are a number of similarities and differences between modeling geothermal reservoirs and modeling the potential high-level nuclear waste repository at Yucca Mountain. The volume and number of dimensions modeled at Yucca Mountain are similar to those employed for geothermal reservoir modeling. The number of gridblocks in Yucca Mountain models ranges from hundreds to millions. The time scale for Yucca Mountain THC coupled process models is similar to the time scales of natural-state geothermal modeling, but significantly exceeds the time scale of history-matching reservoir models used to predict future reservoir behavior. The temperature and pressure conditions expected at Yucca Mountain are well within the range observed and modeled for geothermal reservoirs.

The aims of modeling geothermal fields and modeling Yucca Mountain are different. Geothermal reservoirs are generally modeled to optimize energy extraction for economic gain. To that end, fluid extraction and injection rates, enthalpy, and the number and location of replacement wells are needed. Modeling for the potential Yucca Mountain repository is performed to describe the environment within the repository drifts and to assess the potential for release of the emplaced radionuclides and their fate. Data collection at Yucca Mountain to constrain these models has been extensive; however, much of it is related to small-scale measurement and requires scaling to be adequately represented in the numerical models. Repository performance depends on: (1) the amount of water that may seep into the repository, (2) the temperature and humidity near the waste packages, and (3) the ability of the natural system to sorb and retain radionuclides possibly escaping the repository (Bodvarsson et al. 1999 [120055], pp. 3, 5). As understanding geothermal systems requires modeling at various scales (i.e., well scale, zone scale, and field scale), so modeling for Yucca Mountain requires modeling at multiple scales (drift scale, mountain scale), but in addition requires an understanding at smaller scales, because flow on smaller scales may impact repository performance.

Prediction time frames for geothermal fields range from 10–50 years. It is generally accepted in the geothermal-modeling community that predictions for a well-studied geothermal field are valid only for a time scale on the order of magnitude of the history-matching data (Bodvarsson et al. 1993 [138618]), because of uncertainties in assigning parameters to the model. It is not realistic to collect history-matching data for a 10,000-year period of model confidence for the thermal system at Yucca Mountain. Tests applying thermal perturbations to Yucca Mountain are planned for as long as eight years. Because of this, the modeling efforts for the potential repository have investigated potential behavior for a large range of possible conditions, including

higher and lower percolation fluxes resulting from climate changes, different heat loads, and different waste package arrangements. Sensitivity analyses have been performed for a variety of model parameters (Bandurraga and Bodvarsson 1999 [103949]).

Modeling for the Yucca Mountain repository has benefited greatly from the foundation produced from the robust modeling techniques developed in geothermal modeling. Wu et al. (1999 ([117161], pp. 186–188) reviewed many of the earlier thermal-hydrologic (TH) modeling efforts. These coupled, multiphase, multicomponent models simulate the flow and distribution of moisture, gas and heat at Yucca Mountain for use in predicting current and future conditions in the UZ. For example, Tsang and Birkholzer (1999 [137577]) used a 3-D coupled TH numerical model to predict the results of the Single Heater Test at Yucca Mountain. They obtained good agreement between measured temperatures and model results, and the simulated dryout and condensation zones were consistent with radar tomography and air-permeability data.

More recent Yucca Mountain modeling efforts (e.g., BSC 2001 [154677]) have utilized the TOUGHREACT code (Xu and Pruess 2001 [156280]), which couples reactive chemistry and transport to the TOUGH2 code used to create many of the TH models. The coupled THC models incorporate heat and fluid flow, chemical transport, kinetic and equilibrium mineral-water reactions, and coupling between mineral dissolution and precipitation, porosity, and permeability for a fracture-matrix system. Three heater tests have been performed (the Large Block Test, the Single Heater Test, and the still-active Drift-Scale Test [DST]) to allow assessment of the numerical models. These tests provide data (for validation of Yucca Mountain numerical models) that are analogous to production data used for history-matching exercises performed on geothermal reservoir models. The duration of these thermal-perturbation tests is short relative to the time scale of the potential repository, with the DST having a four-year heating phase followed by a planned four-year cooling phase. These thermal tests have been used to validate the THC model by comparing measured gas and water chemistry from the DST to the results of simulations obtained using the DST THC model (BSC 2001 [154677]). The THC model captures the observed changes in pH, Ca, Cl, and CO_2 concentrations over time for areas that have different thermal histories, and is consistent with the results of TH modeling (BSC 2001 [154677], Sections 6.2.7 and 6.2.8).

Simulations of the anticipated system at Yucca Mountain have been performed using coupled-process modeling to assess THC effects on seepage and fluid flow within the near-field environment (BSC 2001 [154677]). Fracture porosity reductions in the near-field environment resulting from the precipitation of calcite and silica are predicted to be less than 3% (for the homogeneous model; higher fracture porosity reductions of 5% were obtained for heterogeneous fracture permebility models), and thus only minor changes in permeability and fluid flow caused by THC processes are expected to occur (BSC 2001 [155950], Section 4.3.6.4.2). Similar to postaudit reviews of geothermal reservoir models, Yucca Mountain models should be regularly updated, as new data become available, to maximize their effectiveness as a repository management tool.

11.2.9 Chemical Transport in Geothermal Systems

The transport of chemical species in geothermal systems is intimately linked to advective fluid flow. Chemical constituents of geothermal fluids are commonly used to infer deep reservoir

temperatures, identify sources of fluids (such as magmatic, meteoric, connate, and condensate waters), and monitor important processes such as injectate breakthrough and influx of ground waters into producing portions of geothermal reservoirs. Because fluid velocities are rapid (and often faster than chemical reequilibration rates) within most geothermal systems, the chemistry of reservoir fluids sampled at surface thermal features can be used to estimate reservoir conditions. For example, chloride springs found at many geothermal systems are typically derived in large part from deep reservoir fluids. The chemical compositions of geothermal waters are commonly used to determine reservoir temperatures using a variety of silica and alkali geothermometers (Fournier 1991 [105419]). Natural and introduced chemical tracers are used to monitor fluid velocities, estimate flow paths, examine fracture-matrix interaction, and identify the sources of fluids within geothermal systems. The presence of hydrothermal minerals along veins and fractures in fossil geothermal systems is evidence for chemical transport (and subsequent mineralization) in these systems.

11.2.9.1 Geothermal Tracer Tests

For conservative tracers (such as iodine and chloride), tracer travel time represents the flow rate of advecting fluid within the geothermal reservoir. Tracer tests at Dixie Valley and Wairakei (previously summarized in Section 11.2.8.1) indicate minimum tracer velocities ranging from 0.7 to 38 m/hr. In some Japanese fields, tracer returns have been observed at rates of up to 100 m/hr, indicating high-conductivity fractures. Observed tracer speeds in the Hatchobaru field are as high as 80 m/hr (Horne 1982 [156362], p. 501).

Naturally occurring tracers are commonly used in geothermal fields to evaluate important processes such as heat flow, groundwater influx, and reinjectate breakthrough. Measurements of the total amounts of chloride and boron (nonreactive components that are often magmatic in origin) associated with surface feature discharges have been used to estimate heat flow values of geothermal systems (e.g., Fournier et al. 1976 [156817]; Sorey and Lewis 1976 [156809]). Because reinjected fluids have higher chloride contents than produced fluids (due to the concentration of chloride in the liquid phase resulting from the removal of steam), the arrival of reinjected waters in production zones can be detected and monitored by tracking chloride contents of production well brines. Chloride generally behaves in a conservative fashion (it is nonsorbing and is not involved in mineral precipitation, except in very saline water), and thus generally reflects the effects of mixing and boiling only.

Bulalo, The Philippines

Tracer tests conducted at the Bulalo geothermal field have been used to monitor the dispersal of injected fluids within the reservoir, track the influx of groundwater influx, and identify high-permeability flow paths (Villadolid 1991 [156656]). Changes in chloride contents and fluid enthalpies were used in production wells to identify the contribution of reinjected fluids in production wells. Elevated concentrations of tritium were interpreted to indicate zones where downflux of groundwater along permeable flow paths occurred. Rapid increases in magnesium concentrations following acid stimulation in neighboring wells were used to identify fast flow paths between wells.

11.2.9.2 Application to Yucca Mountain

Gravity-driven fracture flow is predominant through the fractured units with low matrix permeability at Yucca Mountain. Chemical transport accompanying percolation flux and associated seepage into cavities over time is evidenced by the precipitation of calcite and opal along fracture and cavity surfaces. Textural observations and fluid inclusion, isotopic, and geochronologic data on the coatings suggest that these secondary minerals were deposited from infiltrating meteoric water under unsaturated conditions (Whelan et al. 2001 [154773], p. 6). Using an equilibrium evaporation model to predict calcite and opal precipitation associated with seepage into lithophysal cavities, Marshall et al. (2000 [151018], p. 4) calculated that the total seepage volume over the past 10 million years (m.y.) is approximately 5×10^4 times greater than the volume of secondary calcite precipitated over the same time period at Yucca Mountain. This model assumes that all water is calcite-saturated, and no significant dissolution of calcite has occurred. The seepage flux estimated from this model (4×10^{-6} mm/yr (Marshall et al. 2000 [151018], p. 5)) may be used to calibrate predicted rates of seepage into drifts for numerical models (e.g., Birkholzer et al. 1999 [105170]) as well as provide insights relating to chemical transport rates and mechanisms at Yucca Mountain.

A key factor affecting chemical transport at Yucca Mountain involves possible interaction between minerals and dissolved constituents. The effects of ion exchange are demonstrated by the marked difference in strontium concentrations of perched waters in the Topopah Spring and Calico Hills tuffs. The strontium contents of perched waters in the UZ-14 and WT-24 boreholes (that sample the stratigraphically higher Topopah Spring tuff) range from 169–240 ppm (Sonnenthal and Bodvarsson 1999 [117127], Table 3). Much lower strontium concentrations (3–11 ppm) were measured for perched waters from the SD-7, SD-9, and NRG-7A boreholes in the Calico Hills tuff. The lower strontium values from these samples were interpreted by Sonnenthal and Bodvarsson (1999 [117127], pp. 119–120) to result from ion exchange between the perched waters and Ca-rich zeolites, which are abundant in the Calico Hills tuff (see Figure 7-2). These zeolite-rich tuffs form an important part of the geologic barrier inhibiting radionuclide transport from the repository down to the water table at Yucca Mountain.

11.2.10 Geothermal Examples of Boiling and Dryout

Many geothermal systems have localized boiling zones resulting from upward flow of high-enthalpy fluids, or from depressurization induced by geothermal production. Dryout zones (areas where fluids have boiled to dryness) are much less common, and typically are associated with the transition between liquid-dominated to steam-dominated geothermal systems. The effects of boiling on fluid chemistry, mineral precipitation, and reservoir permeability have been documented for a number of natural-state and producing geothermal systems. Dryout zones are more transient features, and thus are more difficult to characterize. However, as discussed in Section 11.2.10.2, detailed study of cores from the Karaha-Telaga Bodas geothermal field provides some insights as to how these zones develop and their significance. Summaries of some relevant geothermal examples of boiling and dryout are presented below.

11.2.10.1 Boiling in Geothermal Systems

Boiling is a common phenomenon in high-enthalpy geothermal systems. Many of these systems have high-temperature (≥100°C) thermal features (boiling hotsprings and superheated fumaroles) resulting from the depressurization of high-enthalpy fluids ascending to the surface. Localized boiling within the reservoir can also occur as a result of production of geothermal fluids, which decreases reservoir pressure. The process of boiling results in increased concentrations of dissolved constituents in the residual liquid phase, as well as the partitioning of volatile species (such as CO_2) into the gas phase. These changes often lead to the precipitation of phases such as amorphous silica and calcite. Several examples of the observed effects of boiling in geothermal systems are given below.

Waiotapu, New Zealand

The Waiotapu geothermal system is the largest of the 20 major geothermal systems located in the Taupo Volcanic Zone on the North Island of New Zealand (Hedenquist 1991 [156315]). Surface thermal features include fumaroles and associated acid sulfate springs along the flanks of dacite cones, and numerous chloride, acid-sulfate and mixed composition hot springs located in Waiotapu Valley. The chloride springs represent the liquid component of the hot (≥230°C) reservoir fluid that feeds these surface features.

Champagne Pool, one of the largest of the chloride springs at Waiotapu, has a surface temperature of 75°C (Hedenquist 1991 [156315], Table 1, pp. 2756, 2758–2764). It derives its name from the outgassing of CO_2 near the surface, thus giving it the appearance of champagne. The elevated chloride contents of this feature (1,898 ppm) suggest that it has experienced minimal dilution from meteoric fluids. The effects of boiling and evaporation on the waters from this feature can be seen by the isotopic enrichment in deuterium and ^{18}O resulting from the loss of vapor. The dissolved silica concentration of 445 ppm is much higher than the equilibrium solubility concentrations of both quartz and amorphous silica at the pool temperature, and results from the processes of boiling and cooling of a hot (≥230°C) reservoir fluid as it ascends to the surface. An extensive silica sinter deposit surrounds this thermal feature, and similar deposits are common for many of the other chloride springs at Waiotapu.

Cerro Prieto, Mexico

Localized aquifer boiling occurs in the shallow two-phase reservoir at Cerro Prieto (Truesdell et al. 1984 [156350]). Boiling increases the total dissolved solids (TDS) concentrations in the residual liquid through steam production, but also causes a decrease in fluid temperatures, thus reducing the solubility of most mineral phases. The increase in dissolved silica concentrations and decrease in silica solubility often results in the precipitation of silica polymorphs. Boiling also results in the partitioning of CO_2 into the gas phase, thus causing pH to increase and calcite to precipitate.

Large decreases (up to 70%) in discharge rates from wells located in the boiling zone at Cerro Prieto (Figure 11.2-6) have been interpreted to result from the precipitation of quartz and calcite, which decreased permeability for these zones (Truesdell et al. 1984 [156350], Table 2, p. 226).

This interpretation is supported by the observed decrease in silica and bicarbonate contents of the produced fluids of these wells with time.

Relevance to Yucca Mountain

For the higher-temperature operating mode at Yucca Mountain, a heat pipe may form above the repository when temperatures reach boiling. Water originally stored in the rock matrix, combined with water infiltrating from the surface, would boil near the margins of the heated drifts and migrate (as vapor) to cooler surrounding areas, where condensation would occur. Similar to the cases mentioned above, boiling will lead to increases in the concentration of dissolved species in the residual liquid phase, resulting in supersaturation and subsequent precipitation of phases such as amorphous silica.

The impact of boiling on mineral precipitation at Yucca Mountain should be significantly less than that observed in most geothermal systems because of the restricted area where boiling would occur, the much smaller quantities of fluid involved, and the lower initial concentrations of dissolved silica. A simple calculation using the matrix porosity, saturation, and pore-water silica concentrations and fracture volume can be made to estimate the maximum amount of silica that could potentially precipitate in adjoining fractures (Simmons 2002 [157578], SN-LBNL-SCI-190-V2, p. 79). Assumptions for this model include a matrix porosity of 10%, a matrix fluid saturation of 90%, a silica pore-water concentration of 70 mg/L, and a fracture volume of the rock of 0.5%. Also assumed is that with boiling, the water and associated dissolved silica are completely transferred from the matrix pore space into the fractures, where the water is subsequently boiled to dryness so that all of the dissolved silica precipitates as amorphous silica. For a 1 m^3 block of rock undergoing this process, that would correspond to a matrix water volume of 90 L and a dissolved silica amount of 6.3 g. The fracture volume for this block would be 5 L, and using a density of 2100 g/L for amorphous silica, the volume of amorphous silica available for precipitation is thus equivalent to 0.003 L. This corresponds to 0.06% of the available fracture volume. This very minor reduction in fracture porosity would result in a negligible reduction in fracture permeability.

Another bounding calculation can be made by estimating the amount of silica precipitation resulting from transport of additional dissolved silica to the boiling zone resulting from continued influx of infiltrating water from the surface (Simmons 2002 [157578], SN-LBNL-SCI-190-V2, p. 80). This calculation uses the same 1 m^3 block as a starting point, with a fracture volume of 0.5%, a fluid infiltration rate of 5 mm/yr, a fluid composition of 70 mg SiO_2/L, and assumes that: (1) all infiltrating water is focused into the fractures and (2) all of the water entering this zone from above undergoes complete boiling, resulting in the precipitation of dissolved silica as amorphous silica. For a boiling zone duration of 1,200 years, this translates into an infiltration fluid volume of 6000 L with a corresponding silica amount of 420 g. Using the density and fracture volumes given above, this corresponds to 4% of the available fracture volume. This simplistic bounding calculation is meant to illustrate the potential for fracture sealing at Yucca Mountain. Migration of the boiling front with time at Yucca Mountain would result in a larger area with reduced porosity and permeability, but with smaller average reductions. Variability in fracture apertures could lead to sealing of small aperture fractures and focussing of flow into larger aperture fractures. A fracture sealing experiment conducted in a block of ash flow tuff and accompanying numerical simulations demonstrate that similar

amounts of total fracture sealing could result in large (up to two orders of magnitude) reductions in permeability in the case where mineralization is highly focused (BSC 2001 [155950], Section 4.3.6.7.4).

One factor that could significantly increase the amount of silica precipitation in the fracture zone is the transport of additional dissolved silica to the boiling zone through reflux of fluids associated with a heat pipe. The return of condensed vapor that has dissolved silicate minerals back into the boiling zone could effectively transport significant amounts of silica into the fractures of the boiling zone. However, it is difficult to quantify the impact of this process. THC coupled-process modeling of the near-field environment, using a homogeneous fracture-permeability model, predicts that porosity reduction caused by precipitation of silica and calcite will be less than 3% over the 100,000-year simulation of the higher-temperature operating mode (BSC 2001 [155950], Section 4.3.6.4.2). This fairly small change relative to geothermal systems is in part due to the much lower fluid fluxes and lower temperatures expected at Yucca Mountain.

Boiling would not occur for the lower-temperature operating mode at Yucca Mountain. Moderately elevated temperatures (~80°C) around the drift area for this case would lead to higher amounts of evaporation, and thus result in higher concentrations of dissolved constituents in the remaining fluids in the area around the heated drifts. However, the amount of silica precipitation calculated above for the higher-temperature operating mode would be much reduced for the lower-temperature operating mode. THC simulations performed for the near-field environment for the lower-temperature operating mode predict that less than 1% porosity reduction will occur, because amorphous silica will remain undersaturated except in areas adjacent to the drift wall, where substantial evaporation will take place (BSC 2001 [155950], Section 4.3.6.5).

11.2.10.2 Dryout Zones in Geothermal Systems

Dryout is less common than boiling in geothermal systems, because most systems are liquid-saturated, and thus always contain some water. However, dryout zones do occur in steam-dominated geothermal systems, and evidence of these zones in such a system is presented in the summary below.

Karaha-Telaga Bodas, Indonesia

The Karaha-Telaga Bodas geothermal system, located on the island of Java in Indonesia, consists of a horizontally zoned reservoir with an upper condensate layer, an intermediate vapor-dominated zone, and an underlying deep liquid-dominated zone (Allis et al. 2000 [156317], Figures 4 and 5, pp. 220–221). Mineralogic and fluid inclusion studies of core samples from the T-8 corehole reveal a complex history, with calcite and quartz (after chalcedony) veins present at shallower depths, and veins containing epidote, actinolite, albite and quartz (after chalcedony) present in deeper samples (Moore et al. 2000 [156319], pp. 260–262). The precipitation of chalcedony (revealed by botryoidal textures) at elevated temperatures is unusual (Figure 11.2-7) and is interpreted to result from extreme silica supersaturation resulting from decompressional boiling (Moore et al. 2000 [156319]). The abundance of vapor-rich inclusions in the vein

minerals is consistent with this model. Many of the hydrothermal minerals are coated with scale (consisting of Ti- and K-bearing phases along with iron chloride, and halite) with desiccation

cracks (Figure 11.2-8). These minerals are thought to have formed as a result of dryout (Moore et al. 2000 [156319], pp. 260-261). The youngest fluid inclusions, associated with scale-coated anhydrite, have extremely high salinities (31% NaCl equivalent), and Moore et al. (2000 [156319], pp. 262–263) interpreted that the inclusions and scale formed as a result of condensate boiling to dryness. The high solubility of the chloride minerals suggests that the rocks containing the scale have not been subjected to rewetting after they were formed.

Relevance to Yucca Mountain

Dryout is predicted to occur in the rock mass around the potential repository drifts at Yucca Mountain (for the higher-temperature operating mode) as the waste packages transfer their heat to the surrounding environment. The size of the dryout zone will vary with time and may extend up to 13 m away from the drift walls (as previously mentioned in Section 11.2.5), depending on the waste package configuration (BSC 2001 [154677], Section 6.4.5.1). During the dryout phase, liquid water will be converted to water vapor, which will effectively displace air from this zone. This is important because the oxygen necessary for many corrosion reactions will only be present in low concentrations. As the heat output from the waste package diminishes with time, dryout zones will gradually undergo rewetting from influx of condensate and precipitation infiltration as temperatures drop below the local boiling point. The rewetting process will be accompanied by an influx of air (BSC 2001 [154677], Section 6.6.5).

In the dryout zone near repository drifts, water will be driven from the pore space in the rocks. The rock in the potential repository has a porosity of about 10%, which is about 90% filled with water in the natural condition (90% water saturation). This water is expected to be an important source of circulating water near the repository. Heating of the matrix rock, even to temperatures below boiling, may cause dryout in fractures. As the rock mass heats following waste emplacement, the volume of the dryout zone may increase to include regions formerly altered in the heat pipe. Mineralogic changes expected in this region will include precipitation of minerals in fractures (see discussion above), dehydration of naturally present sorbing clay minerals, carbonate mineral decomposition, and deposition of minerals on fracture faces from liquid driven from the rock.

With rewetting of the dryout zone, some of the more soluble mineral salts are likely to be redissolved. This could initially result in the formation of fairly saline fluids that could cause corrosion problems with the waste package in the drift. However, with continued seepage into the former dryout area, the resulting fluids will become increasingly more dilute. Dryout will be much less pronounced for the lower-temperature (sub-boiling) operating mode.

11.2.11 Geothermal Examples of Condensation and Mineral Dissolution

The processes of condensation and mineral dissolution and their effects can also be detected in many geothermal systems. Condensation of upflowing steam, when it comes into contact with cooler meteoric waters in the shallow portions of geothermal systems, results in the production of steam-heated waters (e.g., Hedenquist 1991 [156315], pp. 2756–2757). These dilute fluids often have fairly distinct chemical compositions and often reflect the effects of the gas phase accompanying the steam. Waters that receive an influx of CO_2 are typically bicarbonate fluids,

whereas those interacting with H_2S become acid-sulfate waters. The acid-sulfate waters are often associated with acid-sulfate alteration, where feldspars readily alter to kaolinite.

Mineral dissolution is not as readily evident in geothermal systems, but can be detected in core samples. At The Geysers geothermal field, corroded faces of quartz crystals found in hydrothermal veins indicate that these crystals underwent partial dissolution prior to being coated in later chalcedony (Moore et al. 2000 [156318], Figure 9, pp. 1722–1723). Similar dissolution features are also observed for calcite. These textural features (Figure 11.2-9) are interpreted to represent dissolution resulting from the downward percolation of condensate near the site of condensation in the upper portion of a vapor-dominated heat pipe (Moore et al. 2000 [156318], Figure 11, pp. 1731–1732).

11.2.11.1 Relevance to Yucca Mountain

Condensation and dissolution are processes that are likely to occur at Yucca Mountain. A tuff dissolution experiment was conducted to simulate mineral dissolution by condensate water in fractured tuff (Kneafsey et al. 2001 [154460]). Deionized water containing dissolved CO_2 was flowed through a column containing crushed Topopah Spring tuff at a temperature of 94°C. The reacted water exiting the column was regularly collected and analyzed. The experiment achieved a pseudo-steady-state flow composition after 11 days. Silica (92 ppm) was the dominant dissolved consituent. A similar plug-flow reactor experiment (using higher temperature conditions) was conducted by Johnson et al. (1998 [101630]), and a series of unsaturated nonisothermal vertical column tests were conducted by Lowry (2001 [157900]). These experiments demonstrate the ability of condensate waters to dissolve (and subsequently transport) significant quantities of dissolved constituents. As mentioned in the discussion on boiling, reflux of condensate fluids containing dissolved silica could serve as an important source for the generation of fracture-plugging minerals precipitated at the boiling front.

11.2.12 Geothermal Examples of Mineral Alteration and Precipitation

Mineral alteration and precipitation are ubiquitous in geothermal fields. The nature and extent of alteration depends on a variety of factors, including temperature, initial rock mineralogy, initial water and gas chemistry, fluid/rock ratios, and the rock surface area exposed to fluids. Many geothermal systems show a series of mineral assemblages that corresponds to different temperature and fluid chemistry regimes (e.g., Muffler and White 1969 [156650]; Arnórsson 1995 [156321]). Mineral alteration and precipitation can significantly affect porosity, permeability and sorptive properties (at least locally) of both matrix and fractures, resulting in the sealing of former fluid flow pathways.

Precipitation of new minerals in vugs, pore spaces, and fractures can occur when fluids reach supersaturation with respect to dissolved constituents. The rate of precipitation is often controlled by kinetic processes, and thus is highly dependent on factors such as nucleation sites and temperature. Supersaturation can be caused by processes such as boiling, cooling, heating (in the case of minerals with retrograde solubility, such as anhydrite and calcite), degassing, and mixing of two distinct fluids. The effects of boiling have previously been discussed, so this section will focus on the other processes mentioned.

11.2.12.1 Hydrothermal Alteration and Seal Formation in Geothermal Systems

Imperial Valley

The effects of water-rock interaction have been studied at a number of geothermal fields (Salton Sea, East Mesa, Heber, Brawley, Cerro Prieto, and the Dunes) within the Imperial Valley (e.g., Muffler and White 1969 [156650]; Schiffman et al. 1985 [154644]; Cho et al. 1988 [154599]). Elders (1987 [154632]) examined the Salton Sea geothermal field as a potential natural analogue for evaluating processes related to radioactive waste storage. One of the features examined was the impact of water-rock interaction and mineralization on fluid flow and solute transport. While primary lithology plays a major role in the distribution of permeability and porosity within the field, processes such as compaction and hydrothermal alteration have significantly modified these rock properties. Carbonate-cemented sandstones form the primary caprock for the Salton Sea geothermal system, and represent the first of four distinct mineralogic zones related to hydrothermal alteration. Within this sealed zone, calcite cement fills up to 50% of the pore space, resulting in very low matrix permeabilities for this interval (Elders and Cohen 1983 [157502], p. 100). Matrix permeability appears to favor horizontal fluid flow, as low permeability shale interbeds serve as barriers to vertical fluid flow. Fractures provide fluid flow pathways that can cut across these lithologic barriers. Complex sequences of fracture mineralization observed at the Salton Sea indicate that fractures have been episodically opened and sealed throughout the life of the geothermal system (Elders 1982 [154602] pp. 63–64).

Silica sealing has been documented at the Dunes geothermal system (Bird and Elders 1976 [154601], Figure 3, p. 289). An exploration well drilled at this prospect (DWR No. 1) has a depth of 612 m, with a maximum temperature of 104°C. Fluids sampled from this well are NaCl brines with up to 4,000 ppm TDS. Seven distinct zones of sandstones and conglomerates have undergone intensive silicification, which significantly reduced porosity and permeability. These silicified zones (Figure 11.2-10) are located in what originally were the most permeable strata within the sedimentary section. Silicification appears to be most intense near the upper portions of these units, immediately below low-permeability shale interbeds. The silicified zones have mineral assemblages of quartz + adularia + hematite and quartz + adularia + pyrite, reflecting enrichments of silica and potassium to these zones caused by mass transfer accompanying hydrothermal alteration. Brittle fractures developed in the silicified zones. The precipitation of silica is thought to be caused by the lateral migration of hot brine to a cooler environment. Smectite and kaolinite have reacted with potassium-rich brines to form adularia.

Wairakei Geothermal Field, New Zealand

Fluid chemistry and mineralogy data from the Wairakei field were used to test the EQ3/6 geochemical modeling codes and the GEMBOCHS thermodynamic databases (Bruton 1995 [100105]). Water and gas compositions obtained from well samples were used to reconstruct reservoir fluid compositions, and these fluid compositions were used as input for the EQ3/6 code to calculate equilibrium mineral assemblages. These calculated assemblages were then compared to the observed downhole mineralogy for these wells to help identify which thermodynamic datasets produced the best match between the observed and calculated mineralogy. Lower temperature portions of the reservoir exhibit similar mineralogy (including zeolites such as mordenite, clinoptilolite, stilbite, and dachiardite) to that observed in the Yucca Mountain tuffs.

Vein mineral assemblages contain fewer phases than those found associated with the matrix. Bruton (1995 [100105], p. 18) inferred that the fracture, vein, and vug minerals are the product of a fluid-dominated system, whereas the more complex matrix alteration mineralogy results from high rock-water ratios.

Medicine Lake Geothermal Field, California

The Quaternary Medicine Lake volcano in northern California is host to a high-temperature geothermal system. Exploratory drilling has revealed that the geothermal reservoir is capped by hydrothermally altered rock rich in smectite-group swelling clays that form a barrier to fluid flow (Hulen and Lutz 1999 [154600], pp. 217, 219). Glassy dacitic to rhyolitic tuffs and pumiceous lavas have been strongly altered to smectites, calcite, zeolites, quartz, potassium feldspar, hematite, and pyrite. This argillic alteration mineral assemblage also fills fractures and vugs, and forms a hydrologic barrier between a shallow, cool groundwater zone and a deeper, hot geothermal reservoir.

Fossil Systems

Fossil hydrothermal systems also demonstrate the impact that water-rock interaction has on permeability. Figures 11.2-11 and 11.2-12 illustrate variations in permeability for interbedded siliceous diatomite and pumiceous tuff from northern Japan (Chigira and Nakata 1996 [156349], Figure 2, Table 1; Chigira et al. 1995 [156364], pp. 75–76). An andesite dike intruded these bedded rocks, inducing a hydrothermal system that resulted in the alteration of the tuffs and diatomite, thereby reducing permeability up to four orders of magnitude. While the initial temperatures immediately adjacent to the dike probably approached those of the andesite magma (~1000°C), conductive and convective heat transfer resulted in a significantly lower temperature (<150°C) alteration assemblage (opal-CT, quartz, and several zeolite minerals) near the heat source (Nakata et al. 1998 [156365], p. 334).

11.2.12.2 Scale Formation in Geothermal Reinjection

Reinjection of geothermal water is necessary in many fields because of the need to dispose of produced water and maintain reservoir pressure. The precipitation of minerals can pose a serious problem in the reinjection of geothermal fluids. Reinjection occurs following energy extraction, thus the resulting geothermal fluid has been cooled and concentrated (owing to steam extraction) from its original, in-reservoir condition. This often results in silica concentrations exceeding saturation values, causing scale formation in reinjection pipelines, wells, and the receiving formation (Corsi 1986 [156344], pp. 839–840).

Silica behavior in geothermal environments has been studied in great detail (Bohlmann et al. 1980 [156363]; Weres and Apps 1982 [156644]; Rimstidt and Barnes 1980 [101708]), but the scaling behavior of a particular geothermal fluid is still difficult to predict. This is because traces of contaminants can significantly affect the rate of silica polymerization and deposition (Mroczek and McDowell 1990 [156342], p. 1619). Additionally, quantitative data on other factors such as pH, temperature, and supersaturation may not be known for the conditions for which one desires to predict. Reduction in the ability to inject these fluids has been noticed at several geothermal fields (for example, Hatchobaru and Otake, Japan) (Horne 1982 [156362];

Itoi et al. 1984 [156347]) and is considered a delicate problem with reinjection (Stefánsson 1997 [156343]).

Otake Geothermal Field, Japan

In an effort to understand silica precipitation in the Otake geothermal field, Japan, an extensive research effort was undertaken including field-scale reinjection, laboratory experiments, and numerical modeling. In the field, Itoi and colleagues (Itoi et al. 1987 [156346], pp. 541–542; 1989 [156345], pp. 153–155) injected geothermal waters into two wells over 656 days. The 120–162°C waters were extracted and cooled to temperatures between 50 and 80°C to cause silica supersaturation ratios between 2 to 3.2, and were reinjected. Over the course of the experiments, the permeability of the two wells declined unsteadily to 4% and 0.35% of their initial values, respectively (Figure 11.2-13). Under the conditions of the injection, the volume of silica, if all precipitated, would have been about 170 and 196 m^3 for the two wells. Borehole televiewer and caliper logs indicated that little of the total mass of injected silica was deposited in the well bores; however, the well screens were strongly fouled by silica scale.

Of interest in the Otake geothermal field is the likely occurrence of formation sealing, over both gradual and punctuated temporal intervals, probably resulting from the plugging of narrow fracture and pore apertures. Yet, there are significant differences between this reinjection study and the potential anthropogenic system at Yucca Mountain. First, supersaturation ratios at Yucca Mountain will only be high near the boiling front. In the field experiments at Otake, the supersaturation ratios were controlled by cooling the water, resulting in the entire reinjected volume being supersaturated with respect to silica. Supersaturation in the Yucca Mountain system will be controlled either by boiling off water as water approaches the drifts, or by cooling as water flows away from the repository below the drifts. Second, water flow rates will be much lower at Yucca Mountain. Flow at Otake is hydraulically saturated, and large volumes of water were reinjected into the wells over the test duration. Flow at Yucca Mountain will be hydraulically unsaturated with a flow rate many orders of magnitude less than at Otake, considering the spatial scale of the experiment at Otake. Permeability at Otake was dramatically reduced as a result of silica precipitation from injection of large (5×10^5 m^3) volumes of water into each well over the test duration (Itoi et al. 1989 [156345], pp. 153–155). If we assume that this water affects a spherical shell 50 m in diameter within the reservoir, this provides a fluid flux of several m/yr, which is three orders of magnitude larger than expected fluxes at Yucca Mountain (order of ten mm/yr) (Flint et al. 2001 [156351], pp. 22–23).

Laboratory experiments were run to evaluate permeability changes caused by silica precipitation using water from the Otake geothermal field. In these experiments, geothermal water at about 92°C was run through a column (50 cm × 5 cm diameter) of 2 mm aluminum beads or rock particles (Itoi et al. 1984 [156347] pp. 301–302; 1986 [156352], p. 229). Silica was deposited primarily in the top 10 cm of the column. Specific deposits of silica (defined as the ratio of silica weight to bead weight) of less than 0.02 caused a two-orders-of-magnitude permeability decrease. These results were compared to the drilling of a replacement injection well next to a fouled well at the Hatchobaru Geothermal Field, Japan. The new well had the same injectability as the original old well, indicating that silica precipitation is occurring near the source.

Reinjection at New Zealand Geothermal Fields

A variety of studies of silica precipitation from geothermal waters from the Taupo Volcanic Zone has been performed (Mroczek and Reeves 1994 [156360]; Mroczek and McDowell 1990 [156342]; Mroczek 1994 [154621]; Carroll et al. 1998 [124275]). Field experiments conducted at several of the geothermal fields in this area measured scale deposition rates under different process conditions in pipes, open channels, and gravel beds to determine the conditions under which the scaling could be tolerated in piping, wells, and reinjection aquifers. Data were collected at the Rotokawa well RK4, Ohaaki wells BR20, BR22, BR11, and Wairakei well 61. Geothermal fluid, being pretreated to the proper initial condition by cooling, aeration, and flashing, was then flowed through packed beds or pipes, and the amount of silica deposited was measured, generally by weighing.

The main conclusions drawn from the field studies are: (1) silica deposition occurs prior to the beginning of polymerization when all the silica is present as monomers; (2) only a small fraction of total silica deposits as scale, such that the total silica concentration is relatively unchanged; (3) deposition remains constant or increases with increasing fluid residence time; (4) deposition rates from lower-temperature, low-silica and poorly buffered Wairakei water exposed to the atmosphere were up to more than an order of magnitude higher than unaerated water; however, aeration had little effect on Ohaaki BR22 water; (5) nucleation appears slow in nonhomogeneous nucleation systems, but once started, scale will continue to grow rapidly; (6) scale appeared to be denser and deposition rates lower at higher velocities; (7) deposition onto clean iron pipes decreases after some time, presumed to be after the surface is uniformly coated with silica, and deposits formed at higher temperature were tougher and more adherent than those formed at lower temperatures.

11.2.12.3 Application to Yucca Mountain

The potential effects of fracture mineralization on fluid flow have already been discussed in the section on boiling. Other potential impacts to consider include alteration and precipitation of hydrothermal minerals that would impact the sorptive properties of the Yucca Mountain unsaturated zone and affect transport of fluids below the drift areas.

Below the potential repository, regions containing zeolites are present. Zeolites are hydrous secondary minerals that are well known for having sorptive properties. Heating of the zeolites may cause dehydration or transformation to phases (such as the less-sorptive zeolite analcime) that will reduce the sorptive capacity of the subrepository horizons. The zeolites at Yucca Mountain were formed by diagenetic alteration of vitric tuff in response to a magmatically induced thermal pulse (Broxton et al. 1987 [102004], pp. 107–108). The increase in temperature caused by waste emplacement could result in the formation of additional zeolites in the vitric tuffs below the potential repository horizon. Because of heat conduction, the temperatures will decrease with distance from the repository. Many dissolved components, such as silica, decrease in solubility as the temperature decreases. However, the precipitation of amorphous silica below the potential repository is expected to be limited in extent (BSC 2001 [155950], Section 3.3.6.3.2).

11.2.13 General Observations and Conclusions

Geothermal systems illustrate a variety of THC processes that are relevant to Yucca Mountain. They include advective and conductive heating, fracture-dominated fluid flow, chemical transport, boiling and dryout, condensation, and mineral alteration, dissolution, and precipitation. Some of the more pertinent observations made regarding these processes are listed below:

- Fluid flow in low-permeability rocks (such as the welded ash flow tuffs found at Yucca Mountain) is controlled by interconnected fractures. Alteration in low-permeability rocks is typically focused along fracture flow pathways. Only a small portion of the fracture volume needs to be sealed in order to retard fluid flow effectively. At Yucca Mountain, fluid flow and low-temperature water-rock interaction over the past 10 m.y. have resulted in the precipitation of minor amounts of opal and calcite on fracture and lithophysal cavity surfaces. More extensive water-rock interaction may occur in fractures in the near field if a heat pipe is generated after waste emplacement occurs.

- The main sealing minerals in geothermal systems are silica polymorphs (amorphous silica, chalcedony, cristobalite, and quartz), swelling clays (smectite and saponite), zeolites, anhydrite, and calcite. These minerals typically form an impermeable cap above the high-temperature geothermal reservoir where convective fluid flow occurs. The main minerals predicted to precipitate in the near field of the potential Yucca Mountain repository are amorphous silica and calcite.

- Sealing can occur in geothermal systems over a relatively short time frame (days to years). Precipitation of minerals can be triggered by a variety of processes, including boiling, water-rock interaction, heating and cooling of fluids, and fluid mixing. Mineral solubilities, reaction rate kinetics, and the flux and chemistry of circulating fluids control the rates and volumes of mineralization. The unsaturated conditions, lower temperatures, and much lower fluid flow rates predicted for the Yucca Mountain system in comparison to geothermal systems, should result in less extensive water-rock interaction than is observed in geothermal systems. Current THC models for Yucca Mountain (BSC 2001 [155950], Section 4.3.6.4.2) predict that significant fracture sealing in the near field is unlikely.

- Fracturing and sealing occur episodically in geothermal systems. Different generations of fracture mineralization indicate that there are multiple pulses of fluid flow, recording distinct temperature conditions and fluid compositions, throughout the lifespan of a geothermal system. Most mineralization at Yucca Mountain is predicted to occur soon after waste emplacement (1,000 to 2,000 years), when temperatures would reach boiling (for the higher-temperature operating mode) above the emplacement drifts. The absence of boiling for the lower-temperature operating mode would result in reduced amounts of fracture mineralization.

- The effects of processes such as boiling, condensation, dissolution, and precipitation for the higher-temperature operating mode for Yucca Mountain will be most significant in the near-field environment. Changes in permeability and porosity are expected to be relatively minor at the mountain scale, where thermal perturbations will be reduced; this

also applies to the lower-temperature (sub-boiling) design. Relatively small changes in zeolite concentrations (<1% volume) were predicted within the nonwelded zeolite-bearing Paintbrush and Calico Hills tuffs resulting from precipitation and dissolution reactions (BSC 2001 [155950], Section 3.3.6.3.2), and thus the sorptive properties of the potential repository would not be greatly modified.

- TH reservoir models have been effectively used for many producing geothermal systems to model initial state conditions and to predict changes in field performance resulting from production and injection activities. The successful use of these models provides confidence that they can be applied to predict fluid and heat flow at Yucca Mountain. Incorporation of chemical reactions and transport processes into these models has not been done extensively for geothermal systems.

- THC coupled-process modeling approaches used at Yucca Mountain can be validated by applying the technique to a number of well-constrained geothermal systems. A simplified model of a portion of the Yellowstone geothermal system is currently under construction. The goal of these simulations will be to reproduce the observed variations in alteration mineralogy, porosity, and permeability and to demonstrate the effects of THC processes on fluid flow and chemical transport.

Detailed reviews of selected geothermal systems improve understanding of fluid flow in fractured rocks, the timing and episodicity of alteration, and the effects of alteration on permeability. A number of geothermal systems hosted by rhyolitic ash flow tuffs such as Long Valley, California (Mariner and Willey 1976 [156811]; Flexser 1991 [156815]; Sorey et al. 1991 [156816]), and Baca, New Mexico (Hulen and Nielson 1986 [156813]; White 1986 [156814]; Goff et al. 1992 [156808]; Goff and Gardner (1994 [156812]) have been the subject of earlier studies of core and fluid samples. Further examination of the zonation, distribution, and ages of alteration minerals, and porosity and permeability variations as a function of degree of welding, alteration, and fracture intensity, can serve as additional validation of THC models. To construct an integrated time/temperature/fluid composition/alteration history of these systems, it may be necessary to supplement existing information with new fluid inclusion data, permeability and porosity measurements, and radiometric age determinations. In the next section, a detailed review of the Yellowstone geothermal system is presented, with attention focused on silica mineralization and sealing, geochemical modeling, and their relevance to the Yucca Mountain system.

11.3 YELLOWSTONE AS A NATURAL ANALOGUE FOR THC PROCESSES

11.3.1 Introduction and Objectives

The Yellowstone geothermal system has previously been utilized as a natural analogue for Yucca Mountain (CRWMS M&O 2000 [141407]). During the course of the current review of geothermal natural analogues (Section 11.2), Yellowstone was identified as a particularly useful example of a number of important THC processes of interest. The Yellowstone geothermal system has reservoir rocks very similar in mineralogy and chemistry to rhyolitic tuffs found at Yucca Mountain. Important processes such as boiling, mineral dissolution and precipitation, and changes in permeability caused by self-sealing have been documented at Yellowstone. An added

benefit is the availability of rock and fluid samples collected from surface and subsurface locations (see Section 11.3.5). In addition to reviewing the existing body of literature on Yellowstone, permeability and porosity variations were also studied in two Yellowstone coreholes (Dobson et al. 2001 [154503]; [154547]).

In this section, several aspects of the Yellowstone geothermal system are reviewed in the context of coupled THC processes. These include: (1) observed changes in surface thermal feature chemistry and associated mineralization; (2) a study of the role of lithology and alteration on porosity and permeability in the reservoir rocks of the Yellowstone geothermal system; and (3) the validation of water-rock geochemical modeling through study of fluid chemistry and alteration mineral assemblages. The objective of this review is to illustrate how such processes can affect fluid flow behavior, and ultimately, apply these observations to the potential Yucca Mountain repository.

11.3.2 Introduction to the Yellowstone Geothermal System

Yellowstone National Park is the site of one of the largest active geothermal systems in the world (Figure 11.3-1), with hundreds of thermal features located both within and outside of the 0.6 Ma Yellowstone caldera (Fournier 1989 [156245], p. 16). The Yellowstone volcanic center has had three major caldera-forming ash flow tuff eruptions (at 2.0, 1.3, and 0.6 Ma); these eruptions have been interspersed with lesser eruptions of lavas and tuffs that are predominantly rhyolitic in composition (Hildreth et al. 1984 [156248], pp. 8339–8350; Christiansen 2001 [156739], pp. G11–G68). While the most recent eruptive activity at Yellowstone occurred at about 70 ka, the high heat flow at Yellowstone suggests that magma currently underlies much of the Yellowstone caldera.

Studies of the active hydrothermal features at Yellowstone suggest that the geothermal system consists of two distinct reservoirs: a liquid-dominated reservoir in the western portion of the caldera and a steam-dominated system in the eastern portion (Fournier 1989 [156245], p. 17). The chemistry of chloride-rich waters sampled from the Upper, Midway, Lower, West Thumb, Shoshone, and Norris Geyser Basins indicates that the reservoirs feeding these features have temperatures ranging from 180 to 325°C, with a fairly dilute (<2,000 ppm TDS) neutral chloride brine (Fournier 1989 [156245], pp. 18–20; Fournier et al. 1992 [156247], p. 1289).

The U. S. Geological Survey drilled 13 research core holes in Yellowstone National Park in 1967–1968, with the objectives of determining the temperature and pressure gradients and describing the nature of water-rock interaction at the Yellowstone geothermal system (White et al. 1975 [154530], Table 3, pp. 1–2). These holes range in depth from 66–332 m, with most holes having depths of 150 m. Pressure and temperature measurements were made as the drilling progressed, with additional pressure and temperature surveys conducted in most wells after completion. The highest measured temperature (237.5°C) was obtained at the bottom of the deepest hole; most of the wells have maximum temperatures of 165–200°C. Continuous core samples collected from each well were subsequently subjected to detailed mineralogic study to characterize the primary lithologies and the alteration phases formed by water-rock interaction.

11.3.3 Silica Mineralization at Porkchop Geyser

Numerous studies at Yellowstone have focused on hydrothermal silica sealing and its effect on permeability (Keith et al. 1978 [106316]; Sturchio et al. 1986 [156253]; Fournier et al. 1991 [156246]). Mechanisms for silica precipitation include: (1) cooling of silica-saturated waters; (2) mixing of fluids with different chemistries and temperatures; and (3) boiling. Silica sinter is a commonly observed trait of many of the thermal features at Yellowstone National Park. Porkchop Geyser, located in the Norris Geyser Basin, provides a natural laboratory to evaluate rapid changes in permeability due to amorphous silica sealing caused by boiling (Fournier et al. 1991 [156246] pp. 1118–1119).

Porkchop Geyser has been the subject of chemical monitoring for over 50 years. Early changes in flow characteristics were attributed to the 1959 magnitude 7.5 Hebgen Lake earthquake, which caused many observed changes in thermal activity throughout Yellowstone (Marler 1964 [156249]). Since the earthquake, flow properties of this thermal feature have evolved from a quiescent hot spring (1960–1971) to an infrequently geysering pool (1971–1985) to a perpetually spouting geyser (1985–1989). The geyser eruption height increased significantly (from 6–9 m to 20–30 m) immediately preceding a small hydrothermal eruption that occurred on September 5, 1989. This eruption consisted of a single blast that formed a crater measuring 13.9 by 11.7 m (Figure 11.3-2), surrounded by ejecta blocks of siliceous sinter (Fournier et al. 1991 [156246], p. 1115). Some of the ejected sinter blocks (Figure 11.3-3) had coatings (up to 1 cm thick) of clear to translucent botryoidal masses of silica; a few of these masses were still pliable shortly after the eruption, suggesting that the amorphous silica formed as a colloidal coating on subsurface cavity walls just prior to eruption.

The observed temporal changes in flow properties were accompanied by systematic changes in the chemistry of the Porkchop Geyser fluids (Figure 11.3-4). Sodium-potassium-calcium (NKC) geothermometry temperatures increase with time from 214°C in 1961 up to 273°C a few months prior to the hydrothermal eruption (Fournier et al. 1991 [156246], Figure 4, Table 1, pp. 1116–1118). These increases in calculated reservoir temperatures are accompanied by increasing silica concentrations (from 420 ppm in 1961 to 741 ppm in 1989). No colloidal silica was either detected by observation (via the presence of an opalescent color to the water) or by analysis (comparison of colorimetric and total silica measurements) prior to the time that the thermal feature became a perpetual geyser. While the lack of standing water precluded such measurements during the time when Porkchop Geyser was a perpetually spouting feature (1985 to 1989), the presence of colloidal silica during this time can be inferred from posteruption conditions. The boiling water partially filling the eruption crater has an opalescent color, and 18% of the total silica measured on January, 1990, consisted of colloidal silica.

The above observations were interpreted by Fournier et al. (1991 [156246], p. 1118–1120) to reflect changes in the upflow water chemistry and in the amount of boiling occurring during upflow. The increasing NKC geothermometry temperatures since 1961 suggest that the waters for this feature were derived from an increasingly hotter source with time. The higher silica contents are probably caused by both the higher fluid source temperatures and the increased amounts of boiling occurring during upflow. Deposition of amorphous silica triggered by the increased silica concentrations would result in decreased permeability within the flow channels and contribute to increased pressures below constrictions present in the fluid pathways. Fluid

overpressures probably led to the rupturing of the sinter throttle at the mouth of the geyser, resulting in a rapid depressurization of the shallow part of the geyser plumbing, causing immediate boiling that triggered the hydrothermal explosion.

11.3.3.1 Comparison with Yucca Mountain

While the amounts of heat and fluid flow at Yellowstone are orders of magnitude greater than those expected for Yucca Mountain, the link between boiling, increased silica concentrations, and resulting precipitation of amorphous silica can still be applied to the Yucca Mountain system. Under the higher-temperature operating mode, where boiling temperatures are predicted to persist in the near-drift environment for 1,000 to 2,000 years, dissolved solids will precipitate as dryout occurs (BSC 2001 [154677], pp. 146–171). The amount and composition of minerals precipitated by dryout depends in part on the flux of fluids into the dryout front and the composition of these fluids. Development of a heat pipe above the emplacement drifts at Yucca Mountain could lead to increased fluid flow and chemical transport into the dryout area. Measured concentrations of dissolved silica in heated waters (26.5–51.7°C) collected from hydrology boreholes around the Yucca Mountain Drift-Scale Test (DST) are up to two times those of unheated porewater compositions (BSC 2001 [154677], Table 9). While the DST fluid concentrations (up to 139 ppm SiO_2) are still significantly lower than those observed for Porkchop Geyser (741 ppm), they demonstrate how heating can lead to increased silica concentration that ultimately results in the precipitation of amorphous silica. Sustained reflux of silica-bearing fluids into fractures within the dryout zone at Yucca Mountain could ultimately lead to plugging of high-permeability flow channels, thus changing fluid flow paths in the near-drift area. These changes could persist with time, so that when the near-drift area cools below boiling temperatures, seepage into the drifts is restricted to flow along unsealed fractures with larger apertures. Because of the unsaturated nature of the Yucca Mountain system, fluid overpressures will not develop, and thus hydrothermal explosions such as the one observed at Porkchop Geyser do not need to be considered for Yucca Mountain.

11.3.4 Silica Sealing at Yellowstone

Mineral dissolution and precipitation and associated changes in permeability resulting from water-rock interaction have been observed in a number of geothermal systems (Grindley and Browne 1976 [154531]; Fournier 1985 [154614]). One of the best examples of self-sealing is recorded in the subsurface hydrothermal mineralogy observed in Yellowstone drill cores (White et al. 1975 [154530], pp. 20–22). Keith et al. (1978 [106316], pp. A24–A25) present a summary of hydrothermal alteration studies conducted on cores from two scientific drilling locations in the northern part of the Upper Geyser Basin, located about 3 km northwest of Old Faithful Geyser. These drill holes are separated by only 130 m and have similar stratigraphies, but have significantly different temperature and pressure profiles. Keith et al. (1978 [106316], pp. A24–A25) interpret the contrasts in wellhead pressures at equivalent depths to indicate horizontal self-sealing resulting from hydrothermal alteration. Vertical pressure gradients found in the wells also suggest the presence of low-permeability flow barriers.

To determine the nature and extent of self-sealing at Yellowstone, lithologic and alteration descriptions, matrix permeability measurements, and fracture and vein characterization were conducted on core samples from the Y-5 and Y-8 boreholes (Dobson et al. 2001 [154547], pp.

283–287; [154503]). The Y-5 well, located in the Midway Geyser Basin, penetrates a thick section of Lava Creek rhyolite ash flow tuff that varies in texture from nonwelded to densely welded, with vapor-phase cavities present in some sections (Figure 11.3-5). The Y-8 core hole, located in the Upper Geyser Basin, has a more complex stratigraphy, consisting of volcaniclastic sediments, perlitic rhyolitic lava, and nonwelded pumiceous ash flow tuff (Figure 11.3-6). Both of these wells have an upper conductive gradient that changes into a nearly isothermal (~170°C) section at depths of 55–80 m (Figure 11.3-7). Detailed descriptions of the alteration mineralogy of both of these cores are presented in Keith et al. (1978 [106316], Figure 4, pp. A13–A24) and Keith and Muffler (1978 [152663], Figure 2, pp. 392–398).

Variations in porosity and permeability (Figures 11.3-8 and 11.3-9) correlate with lithology, degree of welding, and alteration (Dobson et al. 2001 [154547], pp. 285–286; [154503]). Perlitic rhyolitic lava samples have low porosities (mean of 10%) and very low matrix permeability values, as most samples were below the 0.1 millidarcy (md) detection limit of the minipermeameter. Volcaniclastic sediments typically have intermediate porosities (mean of 27%) and high permeabilities (>100 md), but silicified sediments have much lower permeabilities and a 50% reduction in porosity. Nonwelded pumiceous tuff samples from the Y-8 well have very high porosities (mean of 53%) and intermediate permeability values that range from 0.54–78.1 md (median value of 5.4 md). Nonwelded to weakly welded ash flow tuffs from the Y-5 well have intermediate porosities (mean of 34%) and permeabilities ranging from 5.57–1190 md (median value of 177 md). Moderately to densely welded tuffs have greatly reduced porosities (mean of 15%) and very low matrix permeabilities (0.002–18.5 md, with a median value of <0.1 md). The large difference in matrix permeability between nonwelded and densely welded tuffs is similar to that reported by Winograd (1971 [156254], Figure 5, p. 999).

Fractures observed in the Yellowstone core samples have a number of different origins, relating to the cooling of volcanic units, regional volcanic and tectonic processes, and hydrothermal activity. The distribution of veins and fractures in the Yellowstone cores (Figures 11.3-10 and 11.3-11) is correlated with texture and lithology (Dobson et al. 2001 [154547], pp. 286–287; [154503]). Veins and fractures are most abundant in the more densely welded tuffs, which have an average of about 5 fracture/vein features per meter of core over the studied interval (17.7–84.7 m for the Y-5 core). These fractures range from planar to irregular to hackly in form and have dips ranging from subhorizontal to near-vertical, and many of the fractures probably originated as joints formed during cooling of the tuff after emplacement (Winograd 1971 [156254], Figure 4, p. 997). The above correlation between fracture frequency and degree of welding is consistent with the observed fracture distribution at Yucca Mountain, where fractures are more abundant in welded Topopah Spring tuff (0.81–4.36 fractures/m) than in the nonwelded Paintbrush tuff (0.46–0.97 fractures/m) (CRWMS M&O 2000 [145771], Table 6).

In the Y-8 core, the perlitic rhyolitic lava has abundant, randomly oriented veinlets and microveinlets that form a stockwork configuration. In contrast, the volcaniclastic sediments and nonwelded to weakly welded tuffs have very few veins and fractures. Fracture and vein apertures range from <0.5 mm up to 20 mm. While most of the fractures observed in the core samples appear to be effectively sealed by mineralization, the presence of euhedral secondary mineral phases such as mordenite, analcime, and bladed calcite indicates that some fractures, veins, and vugs were open to fluid flow and may still serve as open pathways.

Several zones of hydrothermal breccia (Figure 11.3-12) were observed in the cores (Dobson et al. 2001 [154547]; [154503]). The breccia zones typically consist of a discrete, near-vertical vein that broadens upward and contains angular clasts of wall rock up to 5 cm in diameter that form a jigsaw texture in a brownish-red silica, montmorillonite, and Fe-oxide/hydroxide matrix. These breccias, found within the densely welded tuff, represent transient conduits of high fluid flow that are formed by the explosive release of overpressure in the underlying geothermal reservoir, and are subsequently sealed by supersaturated geothermal fluids (Grindley and Browne 1976 [154531], pp. 379–381). Numerous hydrothermal explosion craters have been identified at Yellowstone (Muffler et al. 1971 [156250], pp. 723–724), and a small hydrothermal eruption was observed in 1989 at Porkchop Geyser (Fournier et al. 1991 [156246], pp. 1114–1116). This type of eruption will not occur at Yucca Mountain, because the prevailing unsaturated conditions will preclude the pressure buildup required for this to occur.

Most fluid flow in the Yellowstone geothermal system is associated with high-permeability features, namely the matrix of high-permeability lithologies and open veins and fractures. While the initial permeability distribution is controlled by lithology, subsequent hydrothermal alteration has clearly modified both matrix and fracture permeability (Figure 11.3-13). Hydrothermal alteration resulted in the reduction of matrix permeability and focusing of flow along fractures, where multiple pulses of fluid flow and self-sealing have occurred.

Hydrothermal self-sealing appears to have generated the existing permeability barrier that delineates the top of the convecting geothermal system at Yellowstone. A steep increase in wellhead pressure observed during drilling between 49.7 (0.55 barg [bar gauge]) and 55.2 m (2.0 barg) in the Y-8 well suggests that a major low-permeability zone is located between these depths within the lower part of the volcaniclastic section (White et al. 1975 [154530], Table 5, pp. 18–22). The fluid responsible for this pressure increase probably entered the borehole immediately below the low-permeability silicified interval at 51.7–54.0 m and above the contact with the perlitic rhyolitic lava at 55.2 m. This depth also marks the transition between a steep conductive thermal gradient observed above and a near-isothermal section that extends to the well bottom. The presence of bladed calcite near this interval and elevated $\delta^{18}O$ values of hydrothermal quartz suggest that the silica seal may have formed in response to transient boiling events associated with depressurization (Sturchio et al. 1990 [154524], Table 1, pp. 30–34).

Silicification is not the only type of hydrothermal alteration that has affected fluid flow in the Yellowstone geothermal system. The presence of abundant clay minerals (montmorillonite and celadonite) and zeolites (clinoptilolite, mordenite, and analcime) as replacement minerals and in void spaces also probably reduced the matrix permeability for all of the rock units studied. Dissolution and replacement of obsidian likely led to localized increases in porosity and permeability, especially within the volcaniclastic sediments.

Hydrothermal sealing can occur fairly rapidly. Most of the USGS core holes at Yellowstone were partially or completely plugged by mineral precipitation within 25 years of having been drilled (Fournier et al. 1993 [154527], p. 33). However, the timing and duration of the mineralization observed in the Y-5 and Y-8 cores are not well constrained. Uranium-Thorium disequilibrium dating of Biscuit Basin rhyolite samples from the Y-8 core (Sturchio et al. 1987 [154525], pp. 2029–2030) suggests that uranium was mobilized and added to the rock around 19 ka. Subsequent hydrothermal alteration that decreased permeability (and thus ended uranium

mobility) in this unit is more recent. A radium disequilibrium study of hot spring waters at Yellowstone (Clark and Turekian 1990 [156780], p. 179) suggests that the mean water-rock reaction time (involving congruent rock dissolution and release of radium) in the high-temperature reservoir is 540 years, with a maximum calculated reaction time of 1,150 years.

The presence of multiphase veining in the Yellowstone cores suggests that there have been multiple episodes of fluid flow and self-sealing. A commonly observed vein assemblage for the perlitic rhyolitic lava is an outer band of celadonite, followed by chalcedony, and with most recent precipitation of mordenite. The sequential deposition of these phases indicates that there were progressive changes in fluid chemistry and/or temperature with time that resulted in this paragenetic sequence.

11.3.4.1 Comparison with Yucca Mountain

These observations from the Yellowstone geothermal system can be used to evaluate the coupled THC models developed for Yucca Mountain to predict whether, and in what time scale, permeability changes resulting from water-rock interaction could cause self-sealing at Yucca Mountain. While the Yellowstone system and the potential Yucca Mountain repository share many of the same THC processes, the effects of the processes are expected to differ significantly because of large differences in scale between the two systems, with much less extensive water-rock interaction predicted for the potential Yucca Mountain repository (Table 11.3-1).

Sturchio et al. (1987 [154525], p. 2029) estimate a conservative formational velocity of 1,500 m/yr (4.8×10^{-5} m/s) for the liquid-dominated, convecting Yellowstone geothermal system, about four to five orders of magnitude higher than those predicted for Yucca Mountain. Significantly higher fluid flow velocities occur along fractures, as evidenced by the high fluid discharge rates observed at many of the hot springs and geysers at Yellowstone. The initial heat flux value (67.7 kW/acre or 16.7 W/m^2) estimated for the higher-temperature operating mode at Yucca Mountain (BSC 2001 [155950], Section 3.3.5.4) is about one-third the calculated value (46 W/m^2) for the Firehole River drainage basin, where the Y-5 and Y-8 coreholes are located (Christiansen 2001 [156739], p. G52). However, the heat flux for Yucca Mountain will decline steadily with time as radioactive decay progresses, so that elevated temperatures at Yucca Mountain will not be sustained in the near-field environment beyond several thousand years.

The dissolution, transport, and precipitation of silica are highly dependent on system temperature, mineralogy, and liquid flux rate, as well as on whether boiling occurs. Rates of silica dissolution and equilibrium silica concentrations in geothermal fluids at Yellowstone are significantly higher than those predicted for Yucca Mountain because of the higher temperatures (170° to 240°C) encountered in the Yellowstone system (White et al. 1975 [154530], Table 3). Downhole water samples from the Y-7 and Y-8 wells have silica concentrations of 364 and 290 mg/L, respectively (Sturchio et al. 1989 [154529], p. 1028), more than three times greater than those predicted for the Yucca Mountain system (Kneafsey et al. 2001 [154460], Table 1) and more than twice the maximum measured value (139 ppm) of waters collected from higher-temperature intervals in the Drift-Scale Test (BSC 2001 [154677], Section 6.2.7.3.2). The rate of silica precipitation and concomitant permeability reduction depends not only on the rate of fluid flow, but also on processes such as boiling, cooling, and fluid mixing that result in silica supersaturation and subsequent mineralization. The presence of discrete zones of silicification at

Yellowstone suggests that the processes controlling mineralization are restricted both spatially and temporally.

11.3.5 Geochemical Modeling at Yellowstone

Meijer (1987 [101345]) reviewed four active hydrothermal systems (Newberry, Long Valley, Valles, and Yellowstone) hosted in tuffaceous rocks within the U.S. to select the system that best reflects the predicted geochemical and hydrologic behavior of the Yucca Mountain repository. Meijer (1987 [101345], p. 7) developed the following screening criteria:

- Host rocks are tuffaceous with zeolitic alteration
- Presence of an active hydrothermal system
- Availability of core samples with characterized subsurface alteration mineralogy.
- Availability of chemical analyses of thermal waters
- Availability of geologic and hydrologic data.

Based on these criteria, Meijer (1987 [101345], p. 10) selected the Yellowstone geothermal system as the best analogue case for Yucca Mountain.

Detailed studies of the downhole mineralogy at Yellowstone (e.g., Honda and Muffler 1970 [106045]; Keith et al. 1978 [106316]; Keith and Muffler 1978 [152663]; Bargar et al. 1981 [156244]; Bargar and Beeson 1984 [156241]; 1985 [156243]) show that a variety of secondary minerals are present. The observed hydrothermal mineralization includes the following phases: silica polymorphs (quartz, opal-CT, chalcedony, α-cristobalite), zeolites (clinoptilolite, mordenite, analcime, laumontite, heulandite, dachiardite), sheet silicates (montmorillonite, illite, chlorite, celadonite, kaolinite, lepidolite), carbonates (calcite, siderite, rhodochrosite), Fe-Mn oxides/hydroxides, pyrite, fluorite, adularia, albite, and minor accessory phases. The distribution and abundance of these minerals appears to be controlled by fluid and rock compositions and temperature.

Several thermal water compositions have been identified for the Yellowstone system on the basis of fluid samples collected from surface features and wells (Fournier 1989 [156245], pp. 18–20). Deep thermal waters have low sulfate and high chloride contents, and are near-neutral to slightly alkaline. Steam condensate waters have low chloride and high sulfate contents, and are acidic. Meteoric waters have low TDS contents and are similar to the waters currently found at Yucca Mountain.

Meijer (1987 [101345]) used reported fluid compositions and the EQ3/6 geochemical codes (Wolery 1979 [156741]) to calculate mineral assemblages for a fixed temperature. EQ3 speciates the dissolved constituents and calculates saturation indices for minerals, and EQ6 selects and precipitates phases to bring the fluids back to equilibrium conditions. A number of water samples were used for the geochemical modeling, including a sample with the highest silica content collected from Biscuit Basin that was chosen to represent the deep thermal water composition. Predicted mineral assemblages include silica polymorphs (chalcedony or cristobalite), zeolites (leonhardite or K-clinoptilolite), clays (Ca-nontronite, Ca-saponite) ± calcite and talc. These assemblages are similar to those found in the Yellowstone cores. Meijer attributed discrepancies between the predicted and observed mineralogies to: (1) some of the early-formed mineral

phases not being in equilibrium with the current fluids; and (2) the use of inappropriate thermodynamic data for some of the mineral phases, such as zeolites.

One important observation made from the core samples from Yellowstone is that the effects of hydrothermal alteration on welded devitrified tuffs for temperatures less than 170°C (and where the geothermal fluids are not acidic) appear to be relatively minor. From this observation, Meijer (1987 [101345], p. 48) concluded that the thermal pulse at Yucca Mountain would have only minor effects on the host rocks, limited to transport and redeposition of silica and precipitation of clays and zeolites in fractures, cavities, and the groundmass.

However, the key factor affecting fluid flow through the welded tuff repository horizon at Yucca Mountain is not the degree of alteration, but whether or not fluid flow through fractures is enhanced or restricted by mineral dissolution or precipitation. Meijer's study validates the use of geochemical modeling to predict changes in fluid and rock chemistry resulting from water-rock interaction, but it does not address how alteration of the Yellowstone cores might impact the overall permeability structure of the host rocks.

Comparison with Yucca Mountain

Recent geochemical modeling for the Yucca Mountain system (BSC 2001 [154677]) employs a more dynamic approach that couples heat and fluid flow with geochemical transport and reactions and resulting changes in porosity and permeability. The TOUGHREACT simulators (Versions 2.2 and 2.3) incorporate reactive chemistry and transport into the framework of the TOUGH2 Version 1.4 code, which simulates multiphase flow of gas and fluids together with tracer and heat transport through porous and fractured geologic media (Pruess 1991 [100413]). The TOUGHREACT code allows for the selection of kinetic or equilibrium thermodynamics to be used for mineral dissolution and precipitation, and it has several permeability law options available to relate porosity changes to changes in permeability. Simulations of fluid and heat flow and changes in permeability and porosity resulting from water-rock interaction were conducted for the near-drift region of the potential Yucca Mountain repository (BSC 2001 [154677]). The results of these simulations (conducted for thermal loads where boiling conditions persist for 1,000–2,000 years) suggest that only small changes in permeability and porosity will occur in the near-drift area (resulting from the precipitation of amorphous silica and calcite), and that these changes will not have a significant effect on repository performance.

The approach used for these simulations was validated through the modeling of the Yucca Mountain DST results (BSC 2001 [154677]) and by simulating a series of dissolution and precipitation experiments conducted using Topopah Spring tuff samples (BSC 2001 [155950], Section 4.3.6.7.4). These simulations were able to successfully predict observed changes in fluid and gas chemistry, mineral precipitation, and associated changes in porosity and permeability over the duration of these experiments.

11.3.6 Discussion and Conclusions

The Yellowstone geothermal system serves as a natural laboratory for studying a variety of important THC processes. The presence of abundant thermal features, such as Porkchop Geyser, afford the unique opportunity to track changes in fluid chemistry and temperature over time and

observe associated changes in mineral precipitation and reservoir permeability. Detailed studies of alteration mineralogy using continuous core samples from research holes drilled at Yellowstone reveal a detailed history of water-rock interaction. Observed variations in rock lithology, texture, and degree and nature of hydrothermal alteration can be used to identify correlations with variations in porosity and permeability. Densely welded tuffs have very low matrix permeabilities, but have more abundant fractures than nonwelded tuffs. A permeability seal encountered in the Y-8 core results from the precipitation of abundant secondary silica, which has greatly reduced the porosity and permeability of several intervals of volcaniclastic sandstones. Silica precipitation at Yellowstone results from both cooling and boiling processes, which serve to raise silica concentrations to above saturation levels. Geochemical modeling of fluid compositions has been used to successfully predict observed alteration mineral assemblages at Yellowstone.

THC processes are expected to have a much smaller effect on hydrogeological properties at Yucca Mountain than what is observed at Yellowstone, because of unsaturated conditions, lower temperatures, and much lower fluid fluxes that will result in less extensive water-rock interaction. Development of a heat pipe above emplacement drifts at Yucca Mountain under the higher-temperature operating mode could lead to increased chemical reaction and transport in the near field. Dissolved silica concentrations in waters from boreholes around the Yucca Mountain DST (with water boiling under heat-pipe conditions near 95°C) are up to two times those of ambient pore waters. Reflux and boiling of silica-bearing fluids within the near field at Yucca Mountain could cause fracture plugging, thus changing fluid flow paths. THC simulations conducted to date for the potential Yucca Mountain repository suggest that only small reductions in fracture porosity (1–3%) and permeability (<1 order of magnitude) will occur in the near field as a result of amorphous silica and calcite precipitation (BSC 2001 [155950], Section 4.3.6.4.2). These predicted changes in hydrogeological properties should not significantly affect repository performance.

11.4 PAIUTE RIDGE—A NATURAL ANALOGUE FOR THC COUPLED PROCESSES

11.4.1 Introduction

In addition to active geothermal fields described in Sections 11.2 and 11.3, sites of "fossil" hydrothermal alteration can be useful analogues to illustrate THC processes at Yucca Mountain. An example of this type of natural analogue is the Paiute Ridge intrusive complex, located on the northeastern boundary of the Nevada Test Site (NTS), Nye County, Nevada. The complex consists of late Miocene basaltic dikes and sills intruded into a partially saturated Rainier Mesa tuff and pre-Calico Hills Formation tuffaceous host rocks. The intrusions were emplaced at an estimated paleodepth of about 200 m, similar to the depth of the potential repository. The tuffaceous host rock surrounding the intrusions was hydrothermally altered to varying extent, depending on the distance from the intrusions (Matyskiela 1997 [100058], pp. 1115, 1117; Lichtner et al. 1999 [121006], p. 8).

Natural analogues provide a means of investigating the geologic processes characteristic of the potential repository (which take place over long time spans) and validating coupled-process models used to predict multicomponent flow, transport, and chemical reactions. The Paiute Ridge intrusive complex provides useful physical and chemical data for understanding the

influence of heat released from the repository on the tuff host rock and for THC modeling studies of the repository. Many other such intrusive complexes exist at the NTS and elsewhere that could provide an extensive data set for understanding and predicting the behavior of the potential Yucca Mountain repository.

To model mineral alteration processes properly in the highly fractured tuff host rock, mineral concentrations and associated surface areas in fractures and rock matrix must be distinguished, and kinetic rate constants—including nucleation kinetics associated with the transformation of metastable phases—must be known. In addition, mineral alteration may result in significant changes to hydrologic and transport properties such as permeability, porosity, and tortuosity of the repository host rock. Formation of mineral alteration zones on the scale of millimeters to centimeters could strongly affect the hydrologic properties of the repository host rock. As shown in Sections 11.2.12 and 11.3.4, fractures could become filled with silica minerals, forming a low-permeability zone, or cap rock, above the repository. Alternatively, the rock matrix bordering fractures could become sealed, thus reducing or preventing matrix imbibition and creating fast pathways for infiltrating water to reach the repository. Regardless of whether mineral alteration in the repository host rock is considered beneficial or detrimental to the integrity of the repository, potential changes in physical and chemical properties of the host rock create significant uncertainty in performance assessment models.

11.4.2 THC Coupled Processes Associated with a Yucca Mountain Repository

The tuffaceous host rocks at Yucca Mountain are composed primarily of volcanic glass (absent in the devitrified repository host units), silica polymorphs (cristobalite, tridymite, and opal-CT), feldspars, zeolites, clays, and calcite (Broxton et al. 1987 [102004], Table 2). An important question is to ascertain whether and at what rate this metastable assemblage will revert to a thermodynamically stable configuration as a result of heat introduced by the repository. This transformation can be accelerated with the addition of heat in the presence of liquid water in an otherwise closed system. Uncertainty exists in estimating the impact that heat produced by the decaying nuclear waste will have on the repository's performance over time (Lichtner et al. 1999 [121006], Section 6).

It is important to distinguish between changes in the near-field environment that take place in a closed system and changes resulting from fluid fluxes as a consequence of the heat generated from radioactive decay. For the higher-temperature operating mode, heat pipes may form above the repository drifts. Heat pipes (Section 11.2.4.5) are characterized by counterflow of liquid and vapor, with evaporation taking place at one end of the heat pipe and condensation of water vapor at the other, resulting in degassing of CO_2 and a consequent increase in pH and purging of oxygen (Lichtner and Seth 1996 [100771], pp. 3-140 to 3-141). Liquid water in the condensate zone is relatively dilute with reduced pH and chloride concentrations compared to the ambient groundwater composition. Within the heat-pipe zone, temperature is near boiling at atmospheric pressure. Salts are expected to form in the dryout zone where complete evaporation takes place. High salinities could result during the rewetting phase of the dryout zone, depending on the rate at which liquid water comes in contact with the deposited salts. This thermal period is expected to last for, at most, several thousand years with relatively low liquid fluxes (Lichtner and Seth 1996 [100771]; Hardin 1998 [100350], Figures 5-20 to 5-23; BSC 2001 [154677], Figures 70, 71, pp. 121–131).

Scenarios based on THC simulations range from little or no alteration to extensive alteration with the formation of a silica cap above the repository and alteration of feldspars, silica polymorphs, and glass to zeolites and clay minerals (Hardin 1998 [100350]; Whitbeck and Glassley 1998 [156452]; Nitao 1998 [117880]; BSC 2001 [154677]). The strong-alteration scenario could result in significant changes in porosity and permeability of the repository host rock that would affect its performance. The strong-alteration scenario represents a less probable case, because it assumes extremely small fracture porosity, and must occur over relatively short time spans (1,000–2,000 years) and at relatively low temperatures (~95–100°C). At such low temperatures, nucleation kinetics can inhibit certain reactions, such as precipitation of quartz, zeolites, or clays. As a consequence, there exists significant uncertainty as to which reactions will actually take place, and if so, at what rate. Generally, silicate minerals react relatively slowly at low temperatures, requiring geologic time spans (>10,000 yr) before significant alteration can take place.

Typically, THC calculations are performed using various forms of the dual-continuum model (DCM) to distinguish between fracture and matrix flow systems. The different DCMs are distinguished by the number of matrix nodes and their connectivity (Lichtner 2000 [156428]). Although fracture apertures used in DCMs can be on the order of millimeters or less, matrix block sizes are generally quite large—on the order of a meter to half a meter or larger—governed by the fracture spacing. Employing a DCM with a single matrix node of this size associated with each fracture node, it would be virtually impossible to describe processes taking place in the rock matrix at the millimeter to centimeter scale. DCMs that discretize the rock matrix are computationally intensive, and for this reason have not been used extensively in THC models applied to the Yucca Mountain repository.

11.4.3 Criteria for Selecting an Intrusive Body as a Natural Analogue for THC Processes

Several criteria should be satisfied for an intrusive body to serve as a natural analogue for THC processes at a potential Yucca Mountain repository. These criteria should include the following:

- The intrusive should be of sufficient size to produce enough heat to sustain boiling conditions for time spans of several thousand years. Typically, dikes and sills with widths greater than approximately 30 m (98 ft) will be required.
- The intrusive should be emplaced above the water table.
- Ideally, the host rock in which the intrusive is emplaced should be a volcanic tuff with compositional and physical properties similar to the Topopah Spring tuff at Yucca Mountain.

For the Paiute Ridge intrusive complex to serve as a natural analogue for the Yucca Mountain repository, it is beneficial to demonstrate that the time-temperature-saturation history surrounding an intrusive sill is similar to that predicted for the repository. The amount of heat stored in the intrusion is directly proportional to its width. Typical widths in the Paiute Ridge intrusive complex vary from tens to hundreds of meters. The typical emplacement temperature of a basaltic intrusion is approximately 1,000–1,200°C. This temperature is considerably higher than the maximum temperature of about 120°C estimated for the repository (BSC 2001

[155950], Section 4.3.5.3.3), and thus, the region very near to the intrusion cannot be expected to correspond to repository conditions. However, farther away from the intrusion, the temperature is expected to be buffered at the boiling temperature of water at atmospheric pressure. In this region, evaporation and condensation processes should be very similar to those encountered in a Yucca Mountain repository. Very likely, heat-pipe effects could have occurred with counter flow of liquid and vapor that were similar to those predicted to occur above and below the repository.

The Paiute Ridge intrusive complex satisfies the first two criteria; however, the tuff host rock in which it has intruded corresponds to the Rainier Mesa tuff and not the Topopah Spring tuff (see below). The Rainier Mesa tuff has different chemical and physical properties compared to the Topopah Spring tuff. The Rainier Mesa tuff at Paiute Ridge consists of nonwelded vitric rhyolitic tuff (Simmons 2002 [157578], SN-LANL-SCI-215-V1, pp. 90–94), whereas the Topopah Spring unit proposed for the repository horizon is a densely welded devitrified rhyolitic tuff. Because of this difference in welding, important physical properties, including fracture and matrix porosity and permeability and capillary properties, are different. The mineralogy is also different—the Rainier Mesa tuff contains abundant glass, compared to the devitrified, microcrystalline matrix of the welded Topopah Spring tuff. As a consequence, chemical alteration, as well as wetting and drying characteristics, can be expected to be different. Even so, given the difficulty in finding an exact analogue to the repository host rock, the Paiute Ridge complex can provide answers to many questions associated with THC processes at a potential repository.

11.4.4 Paiute Ridge Intrusive Complex as a Natural Analogue

11.4.4.1 Paiute Ridge Geologic Background

The study site is located about 40 km northeast of Yucca Mountain along the northeastern part of the Nevada Test Site (NTS), Nevada (Figure 11.4-1). The shallow (~200 m depth) Paiute Ridge complex consists of late Miocene (8.7 Ma) alkali basalt that was intruded into massive and bedded middle Miocene Calico Hills Formation, Paintbrush, and Timber Mountain Group tuffs (Byers and Barnes 1967 [101859], p. 2; Perry et al. 1998 [144335], p. 5-42). According to Crowe et al. (1983 [100972], p. 265), the basaltic intrusions are confined to a series of gently tilted fault blocks that are within a north-northwest-trending graben system of 15–20 km length (9.3–12.4 mi) and 4–8 km (2.5–5 mi) wide. Most of the faulting predates the basaltic intrusion in this area. For further details, the reader is referred to Lichtner et al. (1999 [121006]).

Fieldwork was conducted at Paiute Ridge for this study to characterize changes in tuff mineralogy, texture, and chemistry resulting from emplacement of the basaltic intrusions. While some variability in these properties may be attributed to pre-existing compositional, mineralogic, and textural zonation of the tuff (Broxton et al. 1989 [100024]; Mills et al. 1997 [157570]) and to low-temperature alteration associated with cooling of the ash-flow sheet and water-rock interaction since the tuff was deposited at 11.6 Ma, many of the changes in texture, degree of alteration, and whole-rock chemistry observed in the Rainier Mesa tuff samples described in Section 11.4 can be directly related to the proximity of these samples to the basaltic sill contact (Lichtner et al. 1999 [121006]; Matyskiela 1997 [100058]). Similar types of field relations were also observed at the Grants Ridge basalt intrusion (WoldeGabriel et al. 1999 [110071]). The goal of the studies described in Section 11.4 was to identify and characterize the changes in rhyolitic

tuff host rock caused by a thermal pulse analogous to the emplacement of waste packages within the potential repository at Yucca Mountain. The field observations were then used to constrain numerical simulations of the Paiute Ridge system (Section 11.4.7).

11.4.4.2 Field Studies

A reconnaissance field study focused on examining contact relations between basaltic sills, dikes, and plugs, as well as the volcanic tuff country rock. The field area consists of shallow-level intrusions exposed at Slanted Buttes and the valley to the east toward Carbonate Ridge (Lichtner et al. 1999 [121006], Section 3.1, pp. 4–7). Seventeen individual contact regions were investigated. Seven of these regions were within and around the Papoose Lake Sill, a region also studied by Matyskiela (1997 [100058]). Two of these regions were sites of detailed sampling.

The field studies focused on evaluating the possible effect of basaltic intrusions on the physical, mineralogical, and chemical characteristics of the volcanic tuff. The volcanic tuff was examined in the field for changes clearly related to contact metamorphic effects. The contact relations were found to vary with the type and thickness of the basaltic intrusion. As a result, the hydrothermal alteration is more extensive adjacent to thicker sills as compared with thinner dikes.

The most significant chemical and mineralogical alteration was associated with basaltic sills. Contact relations above, beneath, and adjacent to sills were observed on the southern flanks of the Slanted Buttes and at the Papoose Lake Sill. In the latter case, it was possible to observe volcanic tuff above the sill. Alteration was less evident adjacent to dikes compared with sills. This result may have been a consequence of the subvertical contact geometry, but was probably also affected by the relatively narrower aspect of the dikes compared with the sills, resulting in shorter-lived thermal events. Dikes were observed in two locations, on the southern and eastern flanks of Slanted Buttes, and at the Papoose Lake Sill (Figure 11.4-1, Locations B and O). A volcanic plug along the southern part of Slanted Buttes, which is probably the source for the dikes and offshoot sills at Paiute Ridge, was also examined (Figure 11.4-1, Location C). This plug showed the most significant physical interaction with the host tuff. The outcrop around the plug allowed direct observations of the contact, demonstrating plastic deformation of the tuff, brecciation along the contact zone, and stoping of the host tuff into the basalt flow. Unfortunately, the determination of the occurrence of alteration at a distance from the plug was not possible because of poor exposure and talus cover.

A variety of alteration features is readily observable adjacent to contacts. These features include the following:

- Fusion of tuff adjacent to contact with basalt. The tuff is transformed to a dense, glassy erosion-resistant mass adjacent to contact with larger intrusions.

- Formation of altered anastomosing opal vein zones (Figure 11.4-2). The tuff engulfed by these veins is altered in color, texture, and degree of induration. The veins are found both as isolated features and as complex structures that completely infiltrate the rock. In places, the center of the veins retains open fractures that may be lined with late-stage opal deposits.

- Development of silica-rich veins that penetrate the tuff with relatively little obvious alteration of the matrix. These veins may be traceable for many meters.

- Development of pipe-like alteration features. Silica-cored pipes (circular features) cross the tuff, producing concentric alteration halos. These features occur on the scale of a meter or two.

- Milky-white opal deposits along fractures. These appear to be late-stage deposits along open surfaces.

- Calcite-filled fractures widespread in the basaltic sill and adjacent altered tuff (Figures 11.4-3 and 11.4-4).

These alteration features are common and are particularly well developed adjacent to the sills observed in the area. In regions lacking outcrop, altered tuff can still be identified in weathered rock fragments scattered as float.

Two sites were selected for detailed sampling and assessment of the alteration geometry of the host tuff and the intrusive body (Table 11.4-1). These were the western limb of the Papoose Lake Sill (Figure 11.4-1 (Location H), Figure 11.4-5, and transect 7 of Matyskiela (1997 [100058])) and an exposure beneath a sill exposed on the southern part of Slanted Buttes (Figure 11.4-1, Location B). Most of the analytical work was conducted on samples collected from the Papoose Lake Sill and the adjacent host tuff. Hydrothermal alteration features are highlighted in the following sections, demonstrating significant changes above, adjacent to, and beneath the intrusive bodies. In all cases, the alteration effects diminish with distance from the contact.

11.4.4.3 Contact Metamorphic and Hydrothermal Features at Paiute Ridge Intrusive Complex

11.4.4.3.1 Alteration Adjacent to Papoose Lake Sill

The Papoose Lake Sill is approximately 27 m (90 ft) wide and trends N17E at the site of detailed investigation (Figure 11.4-5 and Location H in Figure 11.4-1). The exposure represents a vertical contact with the adjacent fused (vitrophyre) Rainier Mesa tuff along the western edge of the sill. The base of the sill is not exposed here and the host rock above the sill is partially eroded. The basalt along the contact is characterized by vertically jointed plates that are about an inch wide and oriented parallel to it. In contrast, the basal contact between the sill and the host rock as observed in other locations is mainly represented by horizontally jointed narrow plates (e.g., the southern part of Slanted Buttes, Figure 11.4-1, Locations B and E). A few feet from the contact, the Papoose Lake Sill is massive. Detailed descriptions of the samples mentioned in Section 11.4.4.3 are found in Table 11.4-1 (Simmons (2002 [157578], SN-LANL-SCI-215-V1, pp. 7–32, 90–94).

The basalt is generally sparsely vesicular with amygdules and veinlets of calcite. A sample (LANL# 3547) collected along the contact is purplish gray, fine grained, and sparsely porphyritic with partially altered pyroxene phenocrysts. The vitrophyre zone (i.e., fused volcanic tuff) adjacent to the contact varies in thickness from 0.5 to 2.1 m (1.5 to 7 ft) along strike of the

contact. It is generally black, glassy, and foliated with rare opal nodules, silica and calcite veins, and veinlets of reddish opaline tuff. Alteration of the tuff was investigated adjacent to the sill. Two vitrophyre samples (LANL# 3548 and 3549) separated by 8.2 m (27 ft) were collected along strike, 0.9 and 1.4 m (3 and 4.5 ft) west of the contact zone. The vitrophyre sharply transitions to a reddish, strongly indurated baked tuff several feet in width. A sample (LANL# 3550) was collected about 0.5 m (1.5 ft) west of the vitrophyre. It is porphyritic with quartz and plagioclase phenocrysts in a partially devitrified glassy matrix. The baked tuff grades to a nonwelded, pinkish, and weathered tuff (LANL# 3551) that crops out about 1.7 m (5.5 ft) west of the vitrophyre. The pink, weathered tuff sample occurs along the eastern edge of a narrow anastomosing opal vein zone. The 8 cm (3 in) wide pinkish orange opal veins (LANL# 3552 and 3554) trend north to south parallel to the sill contact. The host tuff (LANL# 3552 and 3553) engulfed by the opaline vein zone is pinkish and forms resistant knobs protected by the surrounding veins (Figure 11.4-2).

These anastomosing veins are found as close as 2.4 m (8 ft) from the contact. In places, the vein centers are open and contain white opal. The veins pinch and swell and wind around remnant knobs of tuff. They occur singly and as infiltrating masses. The veins are less common with distance from the contact and were not observed beyond about 14 m (45 ft). At 6.7 m (22 ft) west of the vitrophyre, the tuff (LANL# 3555) is altered. In the altered tuff, pumice clasts and the matrix appear to be totally silicified. In contrast, a sample collected about 0.12 m (0.4 ft) from LANL# 3555 is partially altered, and the pumice clasts are glassy. At 14 m (45 ft) from the contact, opal veins and veinlets are sparse. However, the moderately welded host tuff (LANL# 3557) is partially altered and contains glassy pumice clasts. Silica and calcite replacements occur side by side in the matrix (Figure 11.4-4).

Between 15 and 61 m (50 and 200 ft) from the contact, the nonwelded and unaltered tuff is friable and vitric and contains large pumice fragments. Narrow fractures contain calcite in some places, but no other alteration features were evident in cavities and/or vesicles (Figure 11.4-6). These contact relations represent the most complete record of alteration at close proximity to the intrusive bodies in the study area.

11.4.4.3.2 Alteration Patterns above the Papoose Lake Sill

Although well-preserved sections were not found above the sill, abundant evidence of pervasive alteration was observed in the overlying Rainier Mesa tuff. In some places, the alteration appeared more intense in terms of density of veining or discoloration and silicification of the host tuff. Several samples (LANL# 3560–3565) were collected above the sill between the western and eastern limbs, directly east of the detailed sampling section at Papoose Lake (Figure 11.4-1, Locations I, J, K, N, O, and P; Table 11.4-1). Because of poor exposure in the western half of the overlying tuff, most of the samples were collected closer to the eastern limb. More samples (LANL# 3538–3545) were also collected above the Papoose Lake sill at location K, about 490 m (1,600 ft) northeast of the main sampling location (Location H) along the western limb of the sill (Figure 11.4-1). At Location K, the exposed sill is about 15 m (50 ft) wide. The degree of alteration is similar to Location H, represented by dense anastomosing opal veining that is about 7.6 m (25 ft) wide. However, unlike the sill contact with the tuff at Location H, no vitrophyre or fused tuff was noted near the opal veins above the sill at Location K. The Location K area is not completely exposed, and thus a vitrophere zone that is obscured by talus may exist

in this area. Although the thickness of the veined zone is unknown, it is located about 45 m (150 ft) to the east of the exposed sill margin. The opal veins above the sill are generally oriented N20W, slightly different from the N-S trend noted adjacent to the sill at Location H.

11.4.4.3.3 Alteration Patterns beneath a Sill

The contact zone of a sill was examined in a gully located on the SW flanks of Slanted Butte (Figure 11.4-1, Locations A and B). The contact relations below the sill are generally well exposed and alteration patterns can be observed. The basaltic sill dips about 55° to the south. The sill is about 7.6 m (25 ft) thick at the point of investigation. The basalt is purplish gray, coarsely vesicular, and includes trains of fine vesicles. Amygdules filled with calcite and opal are common. Large altered mafic phenocrysts are also present. The basalt along the contact exhibits a thin chilled margin, consisting of horizontally jointed (with respect to the sill) and narrowly spaced plates along the contact with the underlying tuff. In contrast, at the Papoose Lake Sill in the northern part of Paiute Ridge, vertically jointed plates characterize the sill margin. These features clearly delineate the nature of the contact between the basaltic intrusions and the tuff host rocks. The country rock tuff units are pre-Rainier Mesa tuff and belong to the Wahmonie Formation and Crater Flat Group (Table 11.4-2). Two samples (LANL# 3570 and 3571) were collected from the contact and the top part of the sill (Figure 11.4-1, Location B). The pinkish tuff along the contact with the basalt does not form a foliated vitrophyre (as was noted at the Papoose Lake Sill in the northern part of the Paiute Ridge area), but exhibits a dense, coarse-grained granite-like texture, possibly as a result of slow cooling. Incipient mineral layering is noted within the fused tuff directly beneath the sill. About a foot beneath the contact, the tuff (LANL# 3572) grades from coarser to fine-grained crystalline material. This resistant contact zone extends for 1.2–1.5 m (4–5 ft) below the basalt. Unlike the sections sampled in the northern part of the Paiute Ridge area, there are at least five tuff units beneath the sill that are cut by a dike finger that is vertically wedged along a fault into the underlying tuff sequence. The fault zone is extensively altered to clay. Two tuff samples (LANL# 3573 and 3574), collected about 1.3 m (4.4 ft) beneath the contact, are generally nonwelded. A moderately welded, light gray tuff (LANL# 3575–3578) that contains brown and dark lithic fragments occurs about 4.6 m (15 ft) beneath the sill. At 6.4 m (21 ft) beneath the sill, the same unit (LANL# 3576 and 3577) contains multiple layers of white to reddish orange opal veins and veinlets mostly parallel to bedding and to lithologic contacts.

These opal veins are of different character than those observed at the Papoose Lake Sill section. They consist of white siliceous cores surrounded by a discoloration halo in some places and no observable halo in other places. They occur parallel to the sill-tuff contact and are about an inch in thickness.

These fractured veins pinch and swell along strike and mostly occur in a 0.6 m (2 ft) wide zone. About 1 m (3.4 ft) below the vein zone, the tuff (LANL# 3578) is nonwelded and contains no opal veins. A white crystal-rich tuff crops out about 11 m (35 ft) beneath the sill. It is coarse grained with pumice clasts and abundant feldspar, quartz, and biotite phenocrysts. On the south side of the dike that wedges down into the underlying tuff, the crystal-rich tuff is intruded by a 0.12–0.46 m (0.4–1.5 ft) wide opal vein that is 4.9 m (16 ft) beneath the sill. The vein trends obliquely to the tuff-sill contact and is traceable for more than 30 m (100 ft). This vein strikes

N-S and dips 65° to the east. In addition, siliceous pipes occur about 4.6 m (15 ft) below contact. They are well-indurated and characterized by a white core and circular reddish halo.

11.4.5 Original Depth of Intrusions

Paleozoic limestone, quartzite, and shale unconformably underlie middle Miocene tephra of the Timber Mountain and Paintbrush tuffs and older undivided tuff units at the Paiute Ridge study area (Byers and Barnes 1967 [101859]; Perry et al. 1998 [144335]). The Tertiary tuffs at the northern and southern study areas were extensively intruded by shallow late Miocene basaltic dikes, sills, and plugs. Based on reconstructed topography above the sills and dikes, it was suggested that the intrusive bodies were emplaced a few hundreds of meters from the paleosurface (Valentine et al. 1998 [119132], p. 5-29, Figure 5.16; Ratcliff et al. 1994 [106634], p. 413). This assumption is consistent with the presence of abundant vesicles along the edges of the sills and dikes, the localized nature of the contact metamorphic effects adjacent to the sill, and minimal amounts of hydrothermal alteration along the contacts (Valentine et al. 1998 [119132], pp. 5-41 to 5-44, 5-51).

However, based on detailed field observations of contacts between the intrusive bodies and host tuffs throughout the study area, it appears that the sills and dikes started at deeper levels close to the plugs and eroded centers and migrated up section into shallow levels away from the central part of the intrusive complex. For example, the sills generally branch out from major dikes and intruded into pre-Rainier Mesa tuff units in the southern part, whereas the Papoose Lake Sill in the north intruded into the Rainier Mesa tuff. This observation is corroborated by subsurface stratigraphic data from several drill holes (Figure 11.4-1) along the eastern part of Yucca Flats, which provide information about the type and thicknesses of the major tuff units deposited in the basin adjacent to Paiute Ridge during the Miocene (Drellack and Thompson 1990 [156446], pp. 1–11). The thicknesses of the tuff units encountered in these drillholes can be used to estimate the original thicknesses of the corresponding units that crop out in the adjacent Paiute Ridge area (Figure 11.4-1; Table 11.4-2).

According to the subsurface stratigraphic information, the major tuff units intersected in the upper part of the Yucca Flats drill holes consist of the Timber Mountain Group (i.e., Rainier Mesa tuff and Rainier Mesa tuff vitrophyre), the Lower Wahmonie Formation, and the Crater Flat Group in descending stratigraphic order. The Ammonia Tanks tuff at the top of the Timber Mountain Group, the Paintbrush Group, and the Calico Hills Formation units were not defined in the drill holes (Drellack and Thompson 1990 [156446]). Using the thicknesses of the different tuffs in the drill holes (from the surface to the top of the Rainier Mesa vitrophere unit), it is estimated that the late Miocene basaltic magma was intruded into a shallow environment of about 200 m depth.

Information on the degree of alteration of the tuffs encountered in the drill holes can be used to help differentiate between alteration caused by the basaltic sills from more regional alteration events. According to the Yucca Flats drill hole data (Table 11.4-2), pervasive zeolitization (interpreted to predate the intrusion of the basaltic sills) occurs in the lower half of the subsurface sequences, typically below the Rainier Mesa tuff unit. The presence of zeolites (such as clinoptilolite and chabazite; see Table 11.4-3) in Rainier Mesa tuff samples adjacent to the sill

contact (and above the regional zone of pervasive zeolitization) was thus attributed to hydrothermal alteration resulting from the sill intrusion.

11.4.6 Laboratory Methods and Results

Thin sections were prepared of almost all of the samples for petrographic descriptions, using optical and scanning electron microscopic techniques. Selected samples from the host tuff and basaltic sill in the Papoose Lake area were processed for bulk chemical and mineralogical analyses. Additional major-element glass chemistry was obtained for most of the tuffs selected for bulk analysis, using an electron microprobe. Most of the tuff samples selected for analysis were collected adjacent to the sill at Location H.

11.4.6.1 Petrographic Results

The mineralogical and chemical characteristics of the alteration are keys to understanding the conditions of hydrothermal processes. Petrographic observations identify opal and calcite veining associated with some of the alteration features (Simmons 2002 [157578], SN-LANL-SCI-215-V1, pp. 89–94). Calcite appears rather abundant in some sections. The vitrophyre found adjacent to the basalt contact contains significant volcanic glass and is largely free of hydrous mineral alteration. Some interesting observations were made of the anastomosing veins from the Papoose Lake Sill locality.

Preliminary petrographic examination of samples of Rainier Mesa tuff systematically collected at intervals from the contact zone to about 61 m (200 ft) west of the sill indicate variable physical and mineralogical alterations (Figure 11.4-1, Location H). Comparison of two tuff samples from above the sill collected at different distances from the sill outcrop (Figure 11.4-1, Locations K and N) indicated that the intensity of alteration above the sill decreases away from the sill margin. A light pinkish brown tuff (LANL# 3539) collected from a 7.6 m (25 ft) wide, densely veined zone about 46 m (150 ft) from the western edge of a sill northeast of the Papoose Lake Sill is sparsely porphyritic with plagioclase, albitic sanidine, quartz, biotite, and minor amounts of hornblende and clinopyroxene. Secondary minerals of silica, calcite, and minor clay replaced the matrix. These secondary minerals also occur in cavities and along fractures as veinlets, aggregate crystals, and radiating spherules, ranging in width from 25–105 μm. At Papoose Lake Sill (Location H), east of the main outcrop, a number of Rainier Mesa tuff samples collected above the sill are strongly indurated, moderately altered, and contain similar phenocryst assemblages. Secondary minerals of opal, calcite, and zeolite replaced the matrix and also occur in cavities and fractures. Shard fragments and pumice clasts are totally replaced by secondary silica.

Similar physical (e.g., color, hardness, welding, veining) and mineralogical (silica, zeolite, calcite) alteration patterns are noted in the basalt and host tuff samples collected from the main section adjacent to the Papoose Lake Sill. The basalt along the contact is fine grained, vertically jointed with uniformly spaced plates, purplish gray, and sparsely vesicular with minor calcite and/or opal amygdules. The altered basalt is porphyritic with plagioclase and sparse mafic minerals that are altered to reddish brown spots. The matrix is dominated with microlites and microcrystalline aggregates of pyroxene. Secondary calcite, silica, clays, and perhaps zeolites occur as veinlets and crystal aggregates in cavities and along fractures. The veinlets pinch and

swell and range in width from 90 to 135 μm. Some cavities or mineral pseudomorphs are partially filled with abundant microcrystalline aggregates of epidote and calcite (Figure 11.4-3).

Three main alteration zones were identified in the tuff near the basaltic intrusion: (1) a vitrophyre zone immediately adjacent to the sill contact, (2) a baked zone, and (3) an altered zone characterized by opal veining. The host tuff adjacent to the basaltic sill contact was fused and transformed to a foliated, perlitic vitrophyre with opal amygdules and silica veinlets. The phenocryst assemblage in the vitrophyre is similar to the overlying tuff. Secondary silica deposits, represented by overgrowth around phenocrysts up to 27 μm wide and veinlets that are 27 μm to 0.28 mm wide, are commonly noted parallel and transverse to welding fabric. Away from the contact, the intensity of alteration transitions from the 2.1 m (7 ft) wide vitrophyre at the contact to a baked interval and then to a 7.6 m (25 ft) wide zone that is characterized by dense, anastomosing opal veining (Figure 11.4-2). The tuff samples are sparsely porphyritic with variable degrees of welding. In one of the samples (LANL# 3554), the phenocrysts are segregated and form bands of crystals represented by quartz, plagioclase, sanidine, and minor biotite and hornblende. The sample is devoid of matrix, thereby creating a crystal-rich zone due to winnowing. The intensity of alteration and replacement of the matrix, pumice clasts, and phenocrysts by calcite, silica, zeolite, and clays decrease with distance from the vitrophyre interval. Within the altered zone, the secondary minerals generally occur as veinlets, cavity filling, or as aggregates within the matrix. For example, at about 13 m (43 ft) from the contact, the tuff is moderately welded, and the matrix replaced by calcite and silica in separate zones (Figure 11.4-4). In some cases, silica spherules crystallized in fractures, causing these fractures to be widened later by fluid flow and also narrowed by silica and calcite recrystallization along the walls. The sample (LANL# 3558) collected outside the altered zone contains similar phenocryst assemblages, but the amount of secondary silica and calcite significantly diminished. The cavities and vesicle walls are devoid of secondary minerals, suggesting no effect on these outer units furthest from the basaltic intrusion.

Examination of selected samples from the sill and the host tuff using a scanning electron microscope (SEM) shows the size and textural relations of the secondary minerals. For example, calcite occurs in the basalt along the contact in cavities and as 100 μm wide and several-millimeter-long veinlets in the matrix (Figure 11.4-3). Calcite and silica intergrowth is also noted in the matrix. Moreover, potassium-rich euhedral crystals (possibly zeolites) are also present in the altered basalt. Fractures in the vitrophyre adjacent to the sill are filled totally by zeolites that are rich in potassium and calcium. Some of these zeolite crystals are more than 10 μm long. Calcite and silica commonly occur in cavities, and in most cases, calcite postdates silica. Almost all of the tuffs proximal to the contact contain silica, calcite, and abundant zeolites in partially filled cavities and within the matrix (Table 11.4-3). However, two of the samples collected from 23 and 61 m (75 and 200 ft) from the sill show no alteration effects. The cavities and vesicles are clean and the shards show no visible signs of alteration (Figure 11.4-6).

11.4.6.2 Mineralogical Results

The mineralogy of selected basalt and tuff samples was identified using quantitative X-ray diffraction (XRD) analysis (Simmons 2002 [157578], SN-LANL-SCI-215-V1, pp. 56–59). The samples were ground for approximately 10 minutes using acetone in a Brinkmann automated

grinder to reduce the particle size and homogenize the sample and internal standard. The samples were analyzed using calibrated Siemens D-500 powder diffractometers.

Results of the XRD analysis are given in Table 11.4-3. Consistent with the petrographic results, the basalt from the contact and those tuffs collected within 14 m (45 ft) from the sill contain abundant secondary minerals dominated by clinoptilolite (Table 11.4-3). Although petrographic analysis reveals calcite and silica in the basalt, smectite was the only secondary mineral identified by XRD analysis. Despite clay-like alteration noted petrographically in most of the altered tuffs, the XRD results show only variable amounts of opal, tridymite, cristobalite, clinoptilolite, and chabazite in the various tuff samples.

11.4.6.3 Geochemical Results

Aliquots of powdered samples were used for major and trace element analyses using a Rigaku 3064 wavelength dispersive X-ray fluorescence (XRF) (Simmons 2002 [157578], SN-LANL-SCI-215-V1, pp. 63, 69–76). Analysis and statistics of the unknown samples are based on a model that uses intensities for 21 standard rocks. To assess whether the major and trace element variations of the tuff samples are genetic or a result of hydrothermal alteration related to the basaltic intrusion, major and trace element concentrations of bulk-rock samples were plotted against distance from the sill (Figures 11.4-7 and 11.4-8). An average Rainier Mesa rhyolitic tuff composition reported by Broxton et al. (1989 [100024]) is plotted with these data for comparison. A discussion of the major and trace element variability and its origin is presented in Section 11.4.6.4.

11.4.6.4 Discussion

Field and analytical results suggest that the Paiute Ridge basaltic dikes and sills intruded into at least two different tuff units, the Rainier Mesa tuff of the Timber Mountain Group and older bedded tuffs from the Lower Wahmonie Formation and Crater Flat Group that mostly crop out in the southern part of the study area. Generally, the host tuffs in the southern part of the study area are thin, mostly bedded, and crop out along gullies. Those outcrops in the northern part are massive, nonwelded, and occur mostly along ridge tops. Most of the analytical results were obtained on samples collected from the Papoose Lake Sill area at Locations H, N, and K (Figure 11.4-1). These tuffs are pinkish, sparsely porphyritic, variably welded, massive, and generally contain abundant pumice clasts. For example, a light pinkish brown tuff from above a sill at Location K contains plagioclase (30%), quartz (32%), sanidine (38%), and minor amounts of biotite, hornblende, and clinopyroxene. According to Byers et al. (1976 [104639]), mafic phenocrysts such as hornblende, clinopyroxene, biotite, plagioclase, and Fe-Ti oxides are common in the upper part of the Rainier Mesa tuff, and sanidine generally contains cryptoperthite rims. A vitrophyre (fused tuff) and a nonwelded tuff collected at Location H adjacent and at 61 m (200 ft) from the Papoose Lake sill, respectively, also have similar phenocryst assemblages with diagnostic albitic rims on sanidine, which is a characteristic feature of alkali feldspars in the Rainier Mesa tuff (Byers et al. 1976 [104639], p. 42).

Depending on proximity to the sill, variable degrees of alteration related to the intrusion are recorded in the tuff units. For example, the transformation of the nonwelded Rainier Mesa tuff to vitrophyre, hardening and discoloration resulting from baking, and the prevalence of

anastomosing opal veins within 12 m (40 ft) of the sill are macroscopic physical modifications related to the sill. However, such features are not uniformly apparent at all the contacts studied during the field investigation. At Location H of the Papoose Lake Sill area, the 12 m (40 ft) wide alteration aureole adjacent to the sill progressively changes from a 2.1 m (7 ft) wide vitrophyre at the contact to a comparable size of baked interval, and to a 7.6 m (25 ft) wide opal veining zone. However, such systematic alteration is not fully developed at Location K above the sill. There, hardening of the tuff and a 7.6 m (25 ft) wide opal vein zone are developed 46 m (150 ft) east of the western edge of the sill. At Location B in the southern part of the study area, the pre-Rainier Mesa tuff units are exposed beneath the sill and the alteration features are different from those noted at Locations H and K. The tuff directly beneath the sill was transformed into a granitic-like granular-to-fine-grained rock, suggesting slow cooling, following the fusion of the tuff. In contrast, the vitrophyre observed at location H represents a fused Rainier Mesa tuff that chilled rapidly adjacent to the sill. The type of the stratigraphic units and the nature of the fused tuff along the contact (e.g., vitrophyre or granular) suggests that the level of intrusion was deeper in the southern part compared with those sills and dikes along the northern boundary of the basaltic intrusive complex. In the southern part, multiple opal veins, ranging in thickness from a few inches to about a foot thick are present within 6 m (20 ft) below the contact. The opal vein zone (≤7.5 m or 25 ft wide) noted adjacent and beneath the sills at Locations B and H (Figure 11.4-1) represent mass silica mobilization from altered tuff within the hydrothermal aureole. Although other low-temperature secondary minerals are closely associated with opal, no systematic zonation is apparent from the effect of the basaltic intrusion. The anastomosing opal veins engulfed variable sizes of tuff clasts that are partially affected by these veins. Although there was voluminous mobilization of silica along fractures created during the basaltic intrusion, subsequent fluid flow was probably significantly reduced because of the impermeable opal veins. The alteration zone occurred at close proximity and parallel to the basaltic sill (≤14 m or 45 ft), likely creating a barrier between the intrusion and the outer tuff units.

Petrographic examination of samples from hydrothermal alteration zones at Locations H and K revealed other secondary features related to the intrusions. Silica, calcite, zeolite, and clay materials are present as veinlets along fractures, as clusters in cavities and matrix, and as overgrowths around feldspar and quartz phenocrysts. These features appear to contain abundant zeolite (clinoptilolite) and show precipitation layering within the veins (Figures 11.4-6a and 11.4-9b). The figures show a tabular crystal of zeolite overgrowing a second layer of zeolite having a scalloped or rounded morphology.

The presence of zeolite as multiple generations within fractures and cavities of the altered tuffs suggests that zeolites in addition to silica were deposited by hydrothermal alteration associated with the basaltic intrusion. However, older zeolitzed tuffs are present in the southern part of Paiute Ridge and in the lower half of the subsurface units intersected in the drill holes along the eastern part of Yucca Flats (Table 11.4-2; Drellack and Thompson 1990 [156446], pp. 60, 64, 66, 68–69; Valentine et al. 1998 [119132], p. 5-46, 5-55, Table 5.3). The silica and calcite veinlets that range in width from microns to millimeters and in length to several millimeters also formed during this process. The pumice clasts and the glassy matrix of the tuffs from the alteration zone are mostly devitrified and/or totally replaced by calcite and silica. A basalt sample from the contact at Location H is also moderately altered. The rock is purplish gray and contains clay, calcite, epidote, and silica along fractures and in cavities.

Published Rainier Mesa tuff chemical data from the lower part of the unit (Quinlivan and Byers 1977 [156450], Table 6; Broxton et al. 1989 [100024], Table 3) are correlative to the major and trace element concentrations of the tuff samples from Locations H, K, and N in the northern part of Paiute Ridge. This observation is also consistent with the petrographic results. Physical, mineralogical, and chemical variations noted in some of the Paiute Ridge samples collected from the hydrothermal aureole beneath, adjacent, and above the basaltic sills are attributed to the intrusions.

Localized chemical variations are noted in the host tuffs adjacent to the basaltic sills. Variations in major and trace element contents are more pronounced in samples collected near the contact (Figures 11.4-7 to 11.4-8). For less mobile components such as TiO_2, Al_2O_3, total iron, Nb, and Zr, little variation is observed throughout the suite of samples, with most variability occurring within a zone that extends 30–40 feet from the sill contact. While silica appears to be mobile (as observed by the presence of opal veins), the actual range of observed silica concentrations for all of the analyzed tuff samples is fairly small (74–81% SiO_2, normalized to anhydrous compositions). Significantly more variability is observed for the more mobile alkali and alkaline earth elements (Na, K, Rb, Ca, Sr). Most of the variability for Na, K, and Rb occurs within 30 ft of the sill contact, suggesting that the original tuff compositions were modified by hydrothermal alteration resulting from the sill intrusion. However, the distribution of Ca (and Sr to a lesser degree) is much more scattered. The measured CaO concentrations of the tuff samples (ranging from 0.5 to 5.6% CaO, normalized to anhydrous compositions) are generally higher than the average Rainier Mesa rhyolitic tuff composition (0.52 wt.%) of Broxton et al. (1989) [100024] (Table 3). The observed increase in CaO contents is in part caused by the presence of variable amounts of secondary calcite in the tuff samples. The calcite may originate from two separate events, one being the intrusion of the sill, while the other would be low-temperature precipitation of calcite from infiltrating groundwater over millions of years. One of the samples collected about 122 m (400 ft) above the sill at Location O (LANL# 3560) has higher Fe_2O_3, MgO, CaO, Sr, Zr, and Ba concentrations. This may reflect a difference in the bulk rock composition resulting from the presence of lithic fragments within the tuff (Simmons 2002 [157578], SN-LANL-SCI-215-V1, p. 25).

As shown in Table 11.4-3, abundant clinoptilolite with minor chabazite formed from the alteration of glass within the contact aureole of the basaltic sill at Papoose Lake Sill. Hydrolysis of volcanic glass, resulting in higher alkalinity and increased silica and alkali ion to hydrogen activity ratio in pore fluids, provided the necessary environment for the formation of zeolite (Hay 1978 [105967], pp. 135–136; Broxton et al. 1987 [102004], pp. 91, 93). Published field and experimental data suggest that clinoptilolite formation is favored over other zeolites, including chabazite in low alkalinity (pH = 7–9) environments (Mariner and Surdam 1970 [156449], p. 977; Barth-Wirsching and Höller 1989 [156445], Table 5, p. 493; Sheppard 1993 [156451], pp. 10–12). The close spatial association of clinoptilolite and opal within the alteration aureole suggests that the anastomosing opal veins are the result of hydrothermal alteration of glassy matrix and pumice clasts. For example, the most altered tuffs (LANL# 3552, 3554, and 3555) from the contact aureole contain higher silica and lower alkali contents (Simmons 2002 [157578], SN-LANL-SCI-215-V1, pp. 22–23, 71, 92–93). Smectite is absent from the altered tuffs. This may be related to relatively high alkali ion to hydrogen ion activity ratios and relatively high silica activities, which favor the crystallization of clinoptilolite over smectite (Barth-Wirsching and Höller 1989 [156445], Table 5, pp. 496–497; Sheppard 1993 [156451], p.

12). Moreover, the lack of smectite in the altered tuff may be attributed to the low Fe, Mg, and Ca contents in the altered tuff. These cations are important components for smectite formation.

In summary, the field study indicates zones of hydrothermal alteration generally occurred within 10–15 m (30–50 ft) of some of the larger basaltic intrusions, especially sills. In some parts of the contact zone, rather pervasive alteration with a zone of silica veins is observed. In other parts, veining is rather limited or absent. The confinement of these features to areas adjacent to contacts appears to demonstrate that the veining and alteration features were caused by the basaltic intrusions.

11.4.7 Thermal-Hydrologic-Chemical Modeling of Hydrothermal Systems

As mentioned in Section 11.4.3, the Paiute Ridge system meets most of the criteria established for serving as an appropriate analogue for THC processes that are expected to occur at the potential Yucca Mountain repository. The effect of a basaltic intrusion on alteration of the host rock in which it is emplaced and alteration of the intrusion itself was modeled using the computer code FLOTRAN (Lichtner 2001 [156429]). A one-dimensional geometry perpendicular to the intrusion was used for the simulations (Figure 11.4-10). Effects of gravity were not included in the simulations, although gravity could have important effects, depending on the geometrical relation between the intrusion and the host rock. Both equivalent and dual-continuum models were considered.

11.4.7.1 The Computer Code FLOTRAN

To estimate the thermal evolution of host rocks surrounding an intrusion emplaced above the water table, it is essential to take into account the two-phase behavior of the system. Latent heat of solidification of the intrusion is neglected, because this process is relatively fast compared to the time required for the intrusion to reach ambient conditions. Preliminary calculations were performed using the computer code FLOTRAN (Lichtner 2001 [156429]). FEHM (Zyvoloski et al. 1997 [100615]) is limited to temperatures less than approximately 300°C and could not be used. Both FEHM and FLOTRAN are capable of describing two-phase nonisothermal fluid flow in variably saturated media for dual and single continua. A documentation of the mass- and heat-conservation equations in the dual-continuum model used in FLOTRAN, and their relation to the equivalent-continuum formulation, is presented in Simmons 2002 ([157578], SN-LBNL-SCI-108-V2, pp. 17–21).

Equation-of-state properties used in FLOTRAN for pure water were derived from the IFC (International Formulation Committee) (1967 [156448]). Constitutive relations must be provided as functions of pressure and/or temperature for the density, viscosity, saturated vapor pressure curve, internal energy, and enthalpy of pure water. The reported validity of the equation of state properties lies in the range of pressure p and temperature T: $0 < p < 165.4 \times 10^5$ Pa (165.4 Bars), and $0 < T < 800$°C (IFC 1967 [156448], p. 1, Figure 2). Although this is satisfied for pressure, it is not satisfied for the temperature range needed to describe the intrusion. However, as demonstrated in Table 11.4-4, the calculated properties are quite close to the measured values reported by Haar et al. (1984 [105175], Table 3) at the maximum temperature of interest.

In the scoping calculations that follow, a one-dimensional (1-D) model was considered of a semi-infinite medium representing the host rock in contact with the intrusion (Figure 11.4-10). This approach is a simplified model in which the effects of gravity and surface infiltration are neglected. By symmetry, only half of the dike width need be modeled. A 30 m wide completely dry intrusion with an initial temperature of 1,200°C is assumed to be emplaced instantaneously into unsaturated tuff at ambient temperature and pressure.

Rock properties and initial and boundary conditions used in the calculations for the equivalent continuum model are listed in Table 11.4-5. The values used for density, specific heat, and thermal conductivity for basalt are typical for basalts as listed in Drury (1987 [156447], p. 107). Very small values for porosity and permeability of basalt were chosen to simulate an essentially impermeable intrusion. The "tuff" values are representative of the nonwelded Paintbrush tuff (PTn) at Yucca Mountain (approximately analogous to the nonwelded tuffs at Paiute Ridge). (It should be noted that the host rock at Papoose Lake Sill is now believed to be composed of Rainier Mesa tuff, which had not been established at the time these calculations were performed.) Values for van Genuchten parameters (fracture/matrix equivalent continuum) are means for PTn values in Wu et al. (1997 [156453], Table A-1). Thermal properties of tuff are from Francis (1997 [127326], Table B-1). Values for density and porosity are from Peters et al. (1984 [121957], Table A-2). Saturation values ranging from 0.4 to 0.6 are observed for the PTn at Yucca Mountain, and corresponding calibrated model values were taken from Robinson et al. (1997 [100416], Table 5.2). Because of the extreme dryout conditions produced by the high temperature of the intrusion, the results are sensitive to the cutoff used to evaluate the characteristic curves near the residual saturation.

11.4.7.2 Dual-Continuum Model Calculations

Several cases are considered with varying coupling strength between fracture and matrix continua. Values for the fracture-matrix area factor of $\sigma_{fm} = 10^{-6}$, 10^{-4}, 10^{-2}, and 10^{2} are compared and contrasted. Results are shown in Figures 11.4-11 to 11.4-18 for fracture and matrix temperature and saturation as functions of distance for various times indicated in the figures. Boiling and condensation fronts propagate into the country rock as indicated by the 100°C isotherm and changes in saturation. Liquid water is stable only for temperatures below the boiling point, corresponding to approximately 100°C at atmospheric pressure. In the figures, boiling occurs at the leading edge where saturation increases from zero. The boiling front is followed by condensation further away from the intrusion, where both saturation and temperature return to ambient conditions. In the intervening region, the temperature is buffered at the boiling temperature of 100°C. In this region, a heat pipe is present with counterflow of liquid and gas. High flow rates of liquid towards the contact are a consequence of capillary suction, as the country rock is dried out from heat released from the intrusion. At early times, liquid flow rates are on the order of 1,000 m/yr, with gas flow rates several orders of magnitude higher.

As can be seen from the figures, fracture and matrix saturations are very different, even for strong coupling between fracture and matrix, in order to preserve equality of the capillary pressure between the two continua. For $\sigma_{fm} = 100$ (shown in Figures 11.4-11 and 11.4-12), the dual-continuum results agree with the equivalent-continuum model. Fracture and matrix temperatures are identical, and saturations obey Equations II-19 and II-26 in Lichtner (2001

[156429]). With the fracture volume fraction $\varepsilon_f = 0.01$, fracture porosity $\phi_f = 1$, and matrix porosity $\phi_m = 0.47$, it follows that the equivalent continuum porosity $\phi_e \cong \phi_m$ and the equivalent continuum saturation $s_e \cong s_m$, the matrix saturation. The fracture saturation follows from Equation II-26 (Lichtner 2001 [156429]). As can be seen from the figures, fracture and matrix temperatures become significantly different from one another only in the extreme case of very weak coupling strength with $\sigma_{fm} = 10^{-6}$. For weaker coupling, the fracture network cools sufficiently to sustain liquid water at the intrusion-host rock interface for times up to one year, as shown in Figure 11.4-19. As heat is conducted from the matrix to the fracture, the water vaporizes and the fracture network remains dry until the rewetting phase begins. The matrix remains completely dry until rewetting commences.

The effect of fracture-matrix coupling on fracture saturation is shown in Figure 11.4-19, where the fracture saturation at the interface between the basalt intrusion and the tuff host rock is plotted as a function of time. Temporary rewetting of the fracture occurs near the basalt-host rock contact for times up to one year as the intrusion cools. During this time, the matrix remains completely dry and at elevated temperatures well above boiling conditions. The transient rewetting of the fracture, however, does not extend very deep into the intrusion. The fracture becomes dry as more heat is transferred from the matrix. As the intrusion cools, final rewetting requires longer times, ranging from several hundred to over 1,000 years as the coupling strength decreases.

Finally, the role of chemical reactions was investigated briefly by considering the redistribution of silica as the intrusion cools and heats up the surrounding host rock. The incorporation of chemical processes is complicated by the initial high temperature of the intrusion (~1,200°C). This condition leads to phase changes as moisture is redistributed throughout the host rock (initially two-phase) and the intrusion (initially single-phase gas). In the computer code FLOTRAN, all chemical reactions are expressed in terms of a set of primary species that must be chosen from the set of aqueous species linked by homogeneous reactions in local chemical equilibrium. Thus, an aqueous phase must be present at all times to treat chemical processes. Fortunately, it is not necessary to obtain thermodynamic constants at these high temperatures because liquid water is never present, on account of the low pressures involved (on the order of one bar).

To accommodate conditions of phase changes from two-phase to single-phase gas and vice versa, the approach used in FLOTRAN is to freeze the solution composition at some saturation cutoff value, specified by the user, as the system becomes a single-phase gas. For the reverse process, involving the transition from single-phase gas to two-phase, this frozen composition is released back to solution. Solid that precipitates from solution at a boiling front remains as is until that part of the system cools sufficiently for liquid water to once again become stable, after which the solid is allowed to react. It is necessary to make certain that the results obtained are not sensitive to the value of the saturation cutoff used.

For the simplified scoping calculation presented here, the matrix of both the host rock and the intrusion is considered to be composed of pure amorphous silica representing glass, and the fracture continuum is considered to be completely devoid of solid. As the glass matrix dissolves, reprecipitation of amorphous silica takes place in the fracture continuum. It should be noted that a more detailed description of the chemical system is required to distinguish between the

different chemical compositions of the basaltic intrusion and the tuff host rock; however, this level of detail was not attempted in this preliminary study. Fast kinetics were assumed with reaction rates close to local equilibrium. The value for the saturation cutoff used in the calculation was 0.001. Figure 11.4-20 shows the volume fraction of amorphous silica in the fracture at different times for the case of $\sigma_{fm} = 10^{-2}$. As the boiling front propagates into the host rock, silica precipitates from solution in the fractures. The source of silica is derived from the matrix upstream where dissolution of amorphous silica occurs (not shown). This result appears to be consistent with field observations at the Papoose Lake Sill.

11.4.7.3 Discussion

Although the field observations for mineral alteration are not inconsistent with the dual-continuum model predictions, there still remain a number of puzzling features. First, the close confinement of the alteration of the tuff host rock to zones adjacent to the intrusion is difficult to understand. This is the region that would be expected to be dry over the long term until the system cooled and rewetting took place. Whether the alteration could have occurred during the relatively rapid and transient passage of the boiling front as it swept through the host rock is still unresolved. It would appear difficult, however, to explain the extent of alteration of the matrix as caused by such a short-duration, transient event. Unfortunately, alteration of the matrix is not properly described by the dual-continuum connected-matrix model used here. A better approach would appear to be the dual-continuum disconnected-matrix formulation, which was beyond the scope of the present study.

A second puzzling feature is the sporadic appearance of alteration along the contact rather than a more uniform appearance, as modeling would predict. This feature could have several explanations. One is that nucleation kinetics were involved, and in most places, the reactions simply did not take place, although they were thermodynamically favored. This could be a result of low permeability and porosity values present in portions of the tuff (especially those that were fused) which would thus restrict the amount of water that could interact with the rock. Another possibility is that dehydration reactions of the basaltic dike released volatiles that reacted with the tuff host rock. Additionally, the host tuff may have had variable physical and chemical properties prior to the intrusion of the sill that might have resulted in non-uniform alteration.

Sensitivity analyses would help improve future models of the Paiute Ridge system. A number of the model input parameters are uncertain, and a sensitivity analysis would be useful to determine which parameters have the most impact on model results. In this regard, it should be emphasized that, for example, the van Genuchten parameters used for the intrusion and tuff country rock were not based on field measurement but were generic values that are approximate at best. The initial saturation condition of the tuff host rock plays an important role in moisture and heat redistribution, but is difficult, if not impossible, to know saturation values at the time the intrusion was emplaced.

11.4.8 Conclusions of Paiute Ridge Study

Magmatic intrusions in tuffaceous rock above the water table offer a unique opportunity to study conditions analogous to the potential Yucca Mountain high-level nuclear waste repository following emplacement of waste. The Paiute Ridge intrusive complex in partially saturated tuff

appears to offer a possible natural analogue site. A new result of this study is that the Papoose Lake Sill apparently intruded into Rainier Mesa tuff, and the resulting hydrothermal process was characterized by low-temperature alteration of glass to clinoptilolite and opal. The key observations of this study suggest that:

- The intrusion generally occurred at shallow levels and decreased in depth away from the central intrusive complex.
- The basalt along the contact is sheeted into narrow vertically or horizontally jointed plates, depending on whether the host tuff is exposed adjacent to or beneath the sill.
- Variable cooling patterns (e.g., glassy or crystallized fused tuff) occurred as noted along the intrusive contact.
- Alteration of nonwelded tuff to clinoptilolite and opal is similar to that observed in diagenetic processes at Yucca Mountain.
- Fractured zones in the tuff created by the basaltic intrusion were sealed by extensive silica remobilization during hydrothermal processes, resulting in low-porosity, highly indurated tuffs adjacent to the intrusive body.
- Hydrothermal alteration was confined to a narrow zone close to the contact zone, as indicated by major and trace element chemical data.

Field observations at the Paiute Ridge intrusive complex and results from laboratory analysis of altered and unaltered tuffs illustrate the intensity of hydrothermal alteration and extent of THC processes associated with thermal perturbation of rhyolitic ash flow tuffs. The secondary mineral assemblages are similar to those present at Yucca Mountain, and the presence of these minerals in the tuff at Paiute Ridge indicates the extent of the alteration. The pervasive anastomosing opal veins and associated secondary minerals (e.g., clinoptilolite, calcite, cristobalite) appear to have reduced matrix or fracture permeability in the immediate vicinity of the basaltic intrusion. The observed mineral zonations can be used to evaluate coupled process models. The widespread opal veins along fracture-matrix margins provide a means for evaluating porosity/permeability relationships and descriptions of fracture-matrix interaction employed in THC codes.

Preliminary results were presented for a one-dimensional THC dual-continuum model of the interaction of country rock with heat released from an intrusive complex emplaced above the water table. A simplified chemical system was considered involving precipitation and dissolution of amorphous silica. Results demonstrated the possibility of forming opal-filled veins with the source of silica derived from the matrix of the host rock. However, because of the irregularities caused by kinetic barrier effects associated with reaction of glass, it is important to compare and contrast a number of different natural analogue sites to be able to derive general conclusions regarding mineral alteration and, specifically, the effect of heat generated by a potential repository in tuff at Yucca Mountain.

Finally, an unexplained observation of this study is the proximal confinement of alteration of the tuff host rock to the intrusion. Additional modeling studies, and analytical data such as isotopes,

would elucidate the mechanisms responsible for the observed alteration patterns. A more extensive treatment of chemical processes, combined with the dual-continuum disconnected matrix formulation of the dual-continuum model, would allow for discretization of the rock matrix, thus resulting in more representative simulation results.

11.5 ANALOGUES TO THC EFFECTS ON TRANSPORT

The Marysvale hydrothermal uranium-molybdenum ore deposit in Utah has been evaluated as a natural analogue for evaluating the effects of water-rock interaction and radionuclide transport. Depletions in igneous rock $\delta^{18}O$ values were interpreted to result from exchange with circulating meteoric waters (Shea and Foland 1986 [156672], p. 281). The largest ^{18}O depletions were observed along an intrusive contact, where enhanced fluid flow was thought to have occurred. Uranium mineralization related to the hydrothermal event associated with the intrusion appears to be concentrated along faults and fractures (Shea 1984 [156673], p. 327). Uranium is primarily concentrated in uranium-bearing mineral phases, such as uraninite and coffinite, but is also found associated with sericite and chlorite along zones of microfracturing. The observed distribution of uranium was interpreted to be due to both bulk-flow and diffusion-transport processes, with most transport (and subsequent deposition) occurring within the fracture network.

Wollenberg et al. (1995 [157467]) used gamma-ray spectrometry and fission-track radiography to examine the location and abundance of uranium and thorium in tuffaceous rocks encompassing hydrothermal systems at the Long Valley caldera, California, and the Valles caldera, New Mexico. In the lateral flowing hydrothermal system at the Long Valley caldera, where temperatures range from 140–200°C, uranium is concentrated to 50 ppm with Fe-rich mineral phases in brecciated tuff fragments. In the vapor zone of the Valles caldera's hydrothermal system (temperature ~100°C), the concordance of high uranium, low Th/U, and decreasing whole-rock oxygen-isotope ratios suggests that uranium was concentrated in response to hydrothermal circulation when the system was formerly liquid-dominated. In the underlying present-day liquid-dominated zone (temperature to 210°C), up to several tens of parts per million uranium occurs with pyrite and Fe-oxide minerals, and in concentrations to several percent with a Ti-Nb-Y rare-earth mineral.

In the Valles caldera's outflow zone, uranium is also concentrated in Fe-rich zones, as well as in carbonaceous-rich zones in the Paleozoic bedrock that underlies the Quaternary tuff. Thorium, associated with accessory minerals, predominates in breccia zones and in a mineralized fault zone near the base of the Paleozoic sedimentary sequence. Relatively high concentrations of uranium occur in springs representative of water recharging the Valles caldera's hydrothermal system. By contrast, considerably lower uranium concentrations occur in hot waters (>220°C) and in the system's outflow plume, suggesting that uranium is being concentrated in the hotter part of the system. The Long Valley and Valles observations indicate that uranium and radium are locally mobile under hydrothermal conditions, and that the reducing conditions associated with Fe-rich minerals and carbonaceous material are important factors in the adsorption of uranium and its attenuation in water at elevated temperature. The Valles and Long Valley studies provide evidence for at least localized mobility of uranium and its daughters in tuff and underlying sedimentary rocks at temperatures comparable to those expected in a nuclear waste repository environment.

11.6 ANALOGUES TO THM EFFECTS

11.6.1 Insights from Field Tests

Results of heater tests conducted at the NTS in granite and tuff and at the Stripa Swedish underground laboratory in granite showed a decrease in fracture permeability as a result of thermal expansion. The Climax spent fuel test at the NTS was conducted in a 426 m deep shaft in granite. During the three-year test, temperatures in the monitored region of the rock mass reached 80°C (Hardin and Chesnut 1998 [150043], pp. 4-1 to 4-3). No significant changes in mineralogy or microfracturing occurred as a result of heat or irradiation. Monitored permanent displacements were on the order of 0.1–1 mm (Hardin and Chesnut 1998 [150043], p. 4-3). The sense of displacement was consistent with the regional extensional tectonic regime.

Four heater experiments were conducted in G-tunnel, within Rainier Mesa, NTS. In the heated-block test, rock-mass mechanical and thermomechanical properties were measured in tuff under controlled thermal and stress-loading conditions. The block was subjected to maximum temperatures ranging from 76–145°C, and equal biaxial stresses with magnitudes up to 10.6 MPa (Zimmerman et al. 1986 [138273], pp. vii–ix). The permeability of a single, near-vertical fracture was measured. The largest changes in permeability were associated with excavation of the block, when the apparent permeability increased from 76 to 758 microdarcies. Subsequent compressive loading decreased the permeability but did not completely reverse the unloading conditions, and the apparent permeability ranged from 252–332 microdarcies over a stress range of 3.1–10.6 MPa (Hardin and Chesnut 1998 [150043], p. 4-6). Increased temperature under biaxial confinement decreased the fracture aperture, lowering the apparent permeability from 234 to 89 microdarcies during heating.

In addition to full-scale heater tests that investigated short-term near-field effects from thermal loading, a time-scaled heater test was also performed at the Stripa underground laboratory to investigate the long-term thermomechanical response to thermal loading (Robinson 1985 [157445]). In the full-scale and time-scale heater tests, heat flow was not affected by fractures or other discontinuities in the granitic rock mass. Thermoelastic deformation of the rock mass was nonlinear and less than predicted. Fracture closure in response to thermal expansion was confirmed by observation of diminished water inflow to the heater and instrument boreholes (Nelson et al. 1981 [150092], pp. 78–80) and by increased compressional wave velocity during heating (King and Paulsson 1981 [157444], p. 699).

11.6.2 Krasnoyarsk

Krasnoyarsk-26 (K-26) is an underground facility in south-central Siberia where nuclear power has been generated by three underground reactors for approximately four decades, with a byproduct of weapons-grade plutonium. The power generated by these reactors is used to provide heat, electricity, and hot water for the city of Zheleznogorsk. Although K-26 differs from Yucca Mountain in geology and hydrologic regime, with K-26 located in saturated, fractured Archean-Proterozoic gneisses, it is the longest "heater test" on record, with a 40-year record of thermal measurements.

A schematic of the underground workings is shown in Figure 11.6-1. The depth of the underground workings has not been reported precisely, but is estimated to be at ~200–300 m below the surface in saturated bedrock (Gupalo 2001 [157471], p. 9). Large sources of heat are present in the P-2 and P-4 underground workings, where air temperatures reach 60–65°C (Gupalo 2001 [157471] p. 15). Based on temperatures measurements in 125 boreholes around the heat sources over 30 years, the dynamics of the rock-mass heating have been obtained. The maximum temperature of the rock is 63°C. The 30°C isotherm is established at a distance of 30 m from the heat sources (Gupalo 2001 [157471], pp. 52, 83).

Facilities at B-3 and B-4 were constructed for "technological works" in 1960, but they have not been used. This makes it possible to monitor coupled processes in both types of underground facilities, those that have and have not been impacted by heat. The dimensions of the chambers containing the heat source are approximately 20 m wide × 60 m long × 40 m in height (Gupalo 2001 [157471], pp. 24, 83; 1999 [157470], p. 9). All chambers have a 1.6 m thick concrete lining.

The geologic conditions of the P-2, P-4, B-3, and B-4 facilities are quite different. Chamber P-2 is located in the footwall of a steeply dipping zone of cataclasis and is surrounded by schistose zones. Chambers P-4 and B-4 are located in fractured gneiss (Gupalo 2001 [157471], p. 15).

The convergence of underground chamber walls as a result of manmade disturbances has been small over the 40-year lifetime of the facility. The largest values of convergence were measured in chamber P-2, where convergence ranged from 16.9–21.5 mm. In chamber P4, maximum convergence of walls is half that of P-2. In B-4, maximum convergence of walls amounted to 1.55 mm, one order of magnitude less than the heated facilities in P-2 and P-4. Approximately similar heat sources operate in P-2 (T = 45°C) and P-4 (T = 62°C), such that their impact on the host rock is similar. The increased deformation in P-2, as compared to P-4, is attributed to the unfavorable mining and geologic conditions, compared to the rock mass in pillars surrounding chamber P-4 (Gupalo et al. 1999 [157470], p. 45).

According to the velocity of ultrasonic waves measured from logging seven boreholes, three zones of deformation can be distinguished in the rock mass: (1) a zone of concrete lining (0.0–1.6 m) and adjacent rock layer with high disturbance level (1.6–2.0 m); (2) a zone of contour rock layer of intermediate disturbance (1.6–2.0 m); (3) the undisturbed rock mass (over 4.0 m) (Gupalo et al. 1999 [157470], p. 80). The vertical component of convergence was determined to be 2.1 mm (+0.09 mm/yr from 1976 to 1998). (Gupalo 2001 [157471], p. 80).

The effect of thermal loads on rock-mass deformation was found to be significant in the disturbed zone. Within a homogeneous rock mass, convergence of chamber walls over a 40-year observation period was 1.0 mm in the absence of thermal impacts, but dislocations increased 8 to 10 times under increased temperature effects (Gupalo 2001 [157471], p. 81).

There is a clear temperature-related effect of the underground facilities on fracture-vein waters. The area of enhanced temperatures of underground water reaches 38–70 m above the roof of the workings, and maximum recorded temperatures of the underground waters is 36°C. (Gupalo 2001 [157471], p. 83).

Although the K-26 example is more analogous to preclosure conditions rather than postclosure performance at Yucca Mountain, it provides an example of relative thermomechanical stability under sub-boiling conditions in a more heterogeneous rock mass than that found at Yucca Mountain. It also provides a test case that compares a thermomechanically disturbed regime to one that is merely mechanically disturbed in the same rock mass, to determine the thermal component of disturbance.

11.6.3 THM Insights from Geothermal Fields

During the 1970s and 1980s, The Geysers geothermal region was rapidly developed as a site of geothermal power production. The likelihood that this could cause significant strain within the reservoir, with corresponding surface displacements, led to a series of deformation monitoring surveys from 1973 to 1996. For the period 1980-1994, peak volume strains occurred in excess of 5×10^{-4}. Changes in reservoir steam pressures were well correlated with volume strain and contraction of the reservoir (Mossop and Segall 1999 [157466], p. 29,113).

Seismicity has been induced by oil and gas production in areas where pore pressures have decreased, in some cases by several tens of MPa (Segall and Fitzgerald 1998 [157464], p. 117). Induced earthquakes are also common in geothermal fields, such as The Geysers, where strong correlations between earthquake activity and both steam production and condensate injection, have been observed. Stress measurements within hydrocarbon reservoirs show that the least horizontal stress decreases with declining reservoir pressure, as predicted by poroelasticity. Production-induced stressing may promote frictional sliding on pre-existing faults. However, it is not expected that this magnitude of stress would occur at Yucca Mountain.

Studies of hydraulic fracturing experiments in hot dry rock suggest that under thermal conditions, mechanical stresses in the rock at Yucca Mountain will occur along preexisting fracture zones and will develop in the direction of maximum principal stress. The Hijori hot dry rock site in Yamagata, Japan, was the site of hydraulic fracturing experiments in 1988 that were accompanied by microseismic events (Sasaki 1998 [157465], p. 171). The microseismic events were thought to have been caused by shear failures induced by high pore-fluid pressures occurring on planes of weakness in the rock surrounding the main hydraulic fracture. The experiment indicated a migration of the induced microseismic events that eventually distributed along a vertical plane, with the strike of seismicity nearly parallel to the direction of the maximum principal stress. The vertical orientation and east-west strike of the seismic events are essentially coplanar with the caldera ring-fault structure in the southern portion of the Hijiori Caldera. This indicates that a preexisting fracture zone was being reopened and developed in the direction of maximum principal stress.

11.7 SUMMARY AND CONCLUSIONS

Geothermal systems illustrate a variety of THC processes that are relevant to Yucca Mountain. They include advective and conductive heating, fracture-dominated fluid flow, chemical transport, boiling and dryout, condensation, and mineral alteration, dissolution, and precipitation. Yellowstone and other geothermal systems in welded ash flow tuffs or other low-permeability rocks indicate that fluid flow is controlled by interconnected fractures. Alteration in low-permeability rocks is typically focused along fracture-flow pathways. Only a small portion of the

fracture volume needs to be sealed in order to retard fluid flow effectively. At Yucca Mountain, fluid flow and low-temperature water-rock interaction over the past 10 m.y. have resulted in the precipitation of minor amounts of opal and calcite on fracture and lithophysal cavity surfaces.

The main minerals predicted to precipitate in the near field of the potential Yucca Mountain repository are amorphous silica and calcite, which are also commonly found as sealing minerals in geothermal systems.

Sealing in geothermal fields can occur over a relatively short time frame (days to years). Precipitation of minerals can be triggered by a variety of processes, including boiling, water-rock interaction, heating and cooling of fluids, and fluid mixing. The unsaturated conditions, lower temperatures, and much lower fluid-flow rates predicted for the Yucca Mountain system in comparison to geothermal systems, should result in less extensive water-rock interaction than is observed in geothermal systems.

Fracturing and sealing occur episodically in geothermal systems. Different generations of fracture mineralization indicate that there are multiple pulses of fluid flow, recording distinct temperature conditions and fluid compositions, throughout the lifespan of a geothermal system. Most mineralization at Yucca Mountain is predicted to occur soon after waste emplacement (1,000–2,000 yr), when temperatures would reach boiling (for the higher-temperature operating mode) above the emplacement drifts.

The effects of processes such as boiling, condensation, dissolution, and precipitation on the higher-temperature operating mode for Yucca Mountain will be restricted to the near-field environment. Silica precipitation at Yellowstone results from both cooling and boiling processes, which serve to raise silica concentrations to above saturation levels. Geochemical modeling of fluid compositions has been used to successfully predict observed alteration of mineral assemblages at Yellowstone.

As shown in Section 11.3, THC processes are expected to have a much smaller effect on hydrogeological properties at Yucca Mountain than on those observed at Yellowstone. However, development of a heat pipe above emplacement drifts at Yucca Mountain under a higher-temperature operating mode could lead to increased chemical reaction and transport in the near field. Reflux and boiling of silica-bearing fluids within the near field at Yucca Mountain could cause fracture plugging, thus changing fluid-flow paths. THC simulations conducted to date for the potential Yucca Mountain repository suggest that only small reductions in fracture porosity (1–3%) and permeability (<1 order of magnitude) will occur in the near field as a result of amorphous silica and calcite precipitation (BSC 2001 [155950], Section 4.3.6.4.2). Changes in permeability, porosity, and sorptive capacity are expected to be relatively minor at the mountain scale, where thermal perturbations will be minimal; this also applies to the lower-temperature (sub-boiling) design. These predicted changes in hydrogeological properties should not significantly affect repository performance.

Magmatic intrusions in tuffaceous rock above the water table, such as the Paiute Ridge intrusive complex studied in Section 11.4, offer a unique opportunity to study conditions analogous to the predicted postclosure repository conditions at potential Yucca Mountain. The Papoose Lake Sill intruded into Rainier Mesa tuff, and the resulting hydrothermal effects were characterized by

low-temperature alteration of glass to clinoptilolite and opal, similar to those present at Yucca Mountain. Hydrothermal alteration was confined to a narrow zone close to the contact zone. The pervasive anastomosing opal veins and associated secondary minerals (e.g., clinoptilolite, calcite, cristobalite, etc.) appear to have reduced matrix or fracture permeability in the immediate vicinity of the basaltic intrusion.

The widespread opal veins along fracture-matrix margins provide a means for testing and validating porosity/permeability relationships and descriptions of fracture-matrix interaction employed in THC codes. Preliminary results of a one-dimensional THC dual-continuum model of the interaction of country rock with heat released from an intrusive complex emplaced above the water table demonstrated the possibility of forming opal-filled veins with the source of silica derived from the matrix of the host rock. However, because of the irregularities caused by kinetic barrier effects associated with the reaction of glass, it is important to compare and contrast a number of different sites to be able to derive general conclusions regarding mineral alteration and, specifically, the effect of heat generated by a potential repository in tuff at Yucca Mountain.

Examples provided in Section 11.5 indicate that the observed distribution of uranium resulting from hydrothermal conditions at Marysvale was a result of advective transport and diffusion, with most transport-subsequent precipitation of uranium occurring within the fracture network. This observation was also borne out at portions of the Long Valley and Valles calderas. The latter two studies also provided evidence for at least localized mobility of uranium-series radioisotopes at temperatures more comparable to those expected under higher-temperature thermal-loading conditions in a nuclear waste repository environment.

THM effects at Yucca Mountain (Section 11.6) are expected to be less extreme than those operating in geothermal fields where microseismicity is detected. Although rock type, hydrogeology, and design configurations differ from those at Yucca Mountain, the closest analogue identified so far is K-26, which is particularly relevant to lower-temperature design scenarios. Although the 40-year record of experiments should be interpreted cautiously with respect to extrapolation to long time periods, thermomechanical effects, such as drift convergence, might be in the same range of magnitude (on the order of a few mm) as that at Krasnoyarsk for the preclosure period.

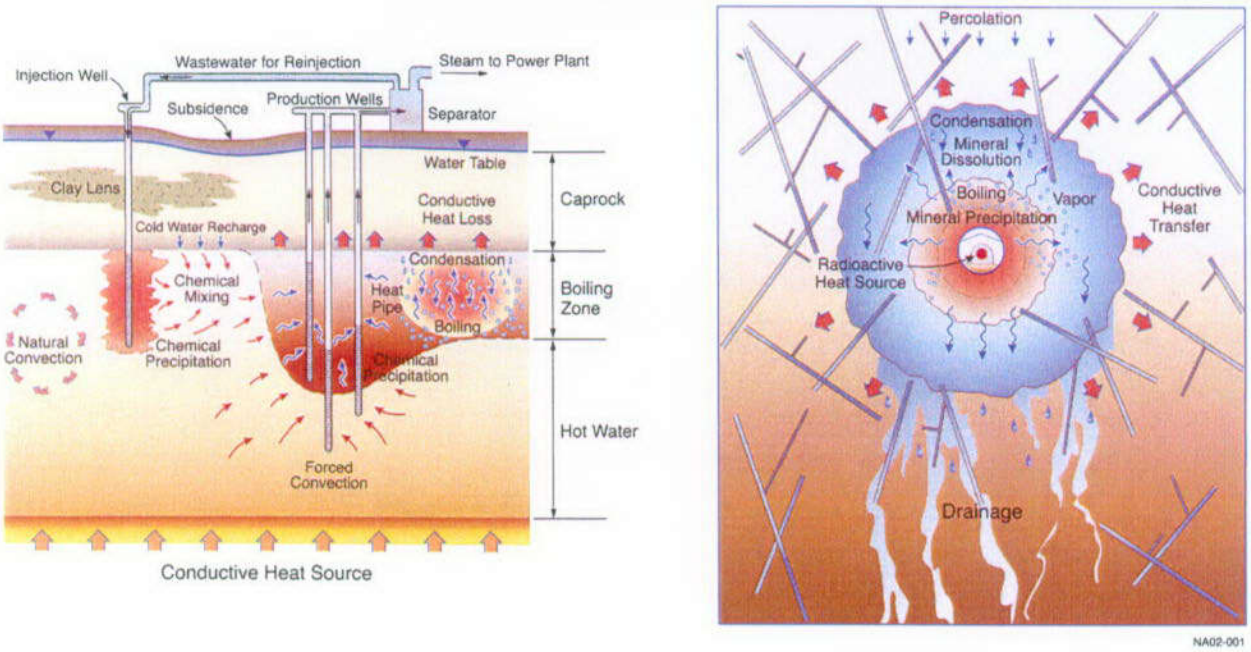

NOTE: Similar processes include boiling and condensation, advective liquid flow, mineral dissolution and precipitation, mixing, recharge (percolation), and heat conduction. A heat pipe is depicted on the right side of the geothermal system, showing countercurrent liquid and vapor flow resulting from boiling and condensation.

Source: Left figure adapted from Bodvarsson and Witherspoon (1989 [156337]), right adapted from CRWMS M&O (2000 [151940]).

Figure 11.2-1. Comparison of Processes in Geothermal (Left) and Anthropogenic (Right) Thermal Systems Created by Emplacing Heat-Generating Nuclear Waste in an Unsaturated Fractured Rock Mass

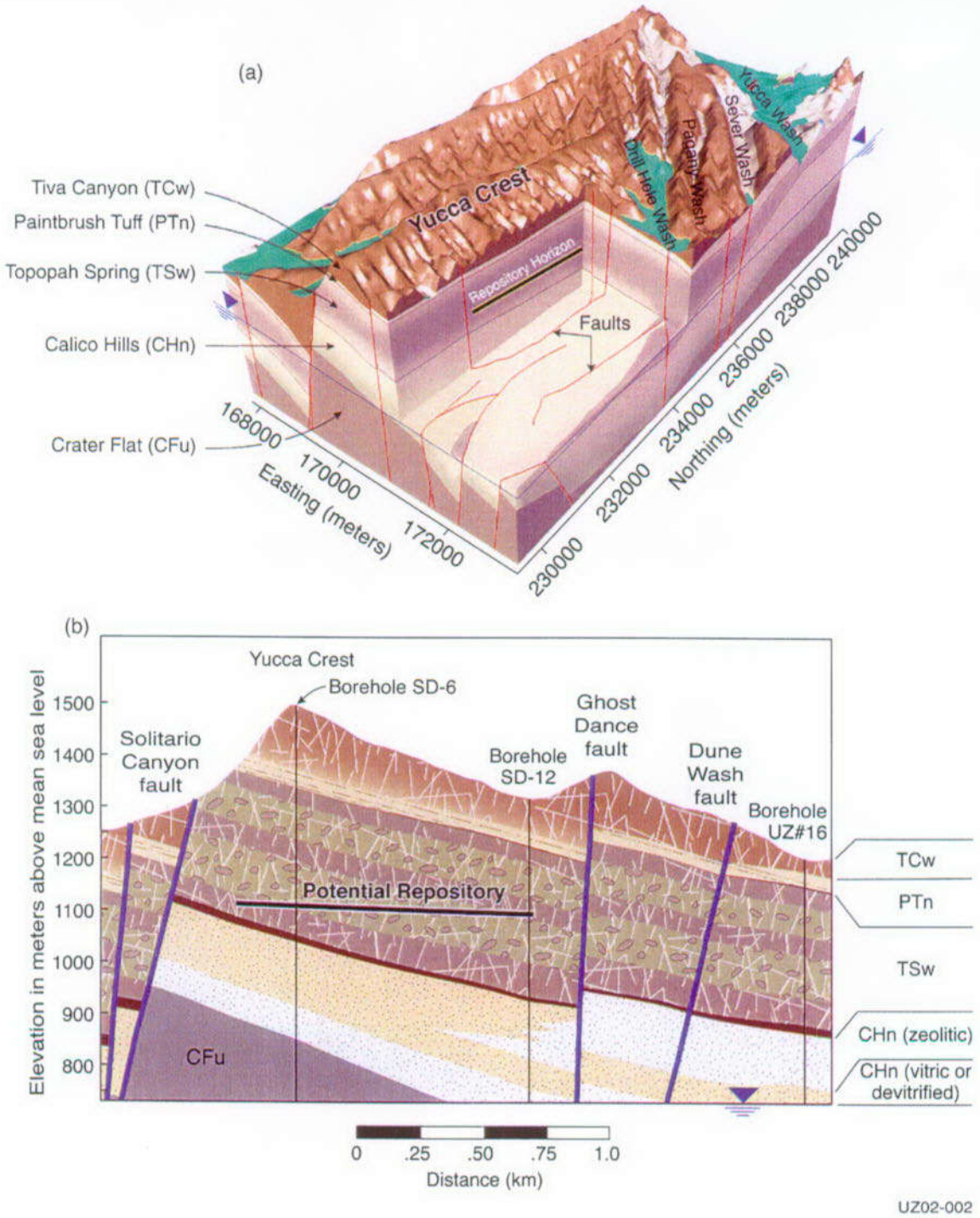

NOTE: In both (a) and (b), the water table is indicated by a blue downward-pointing triangle.

Source: CRWMS M&O 2000 [151940], Figure 3.2-1.

Figure 11.2-2. Schematic Diagram (a) and Cross Section (b) of the Yucca Mountain Lithology and Topography, Including Surface Features and Major Geologic Strata

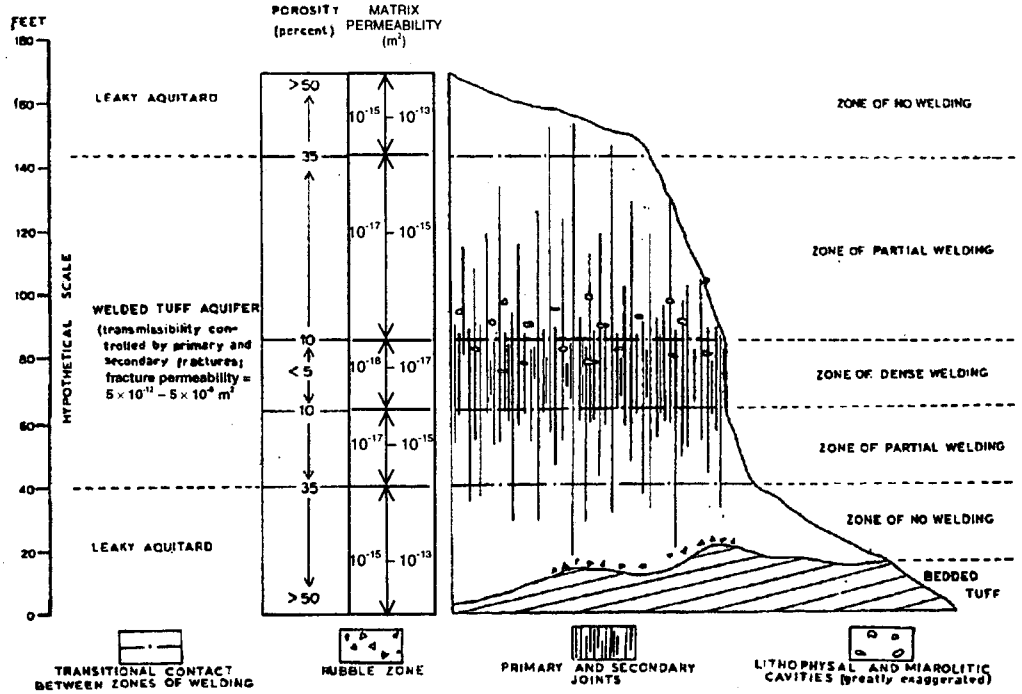

NOTE: While zones of dense welding have intrinsically low matrix permeabilities, these zones also have much more abundant fractures, resulting in higher overall permeability than nonwelded (and unfractured) tuff.

Source: Generic profile modified from Winograd (1971 [156254], Figure 5).

Figure 11.2-3. Typical Variations in Permeability and Porosity in Welded and Unwelded Ash Flow Tuff

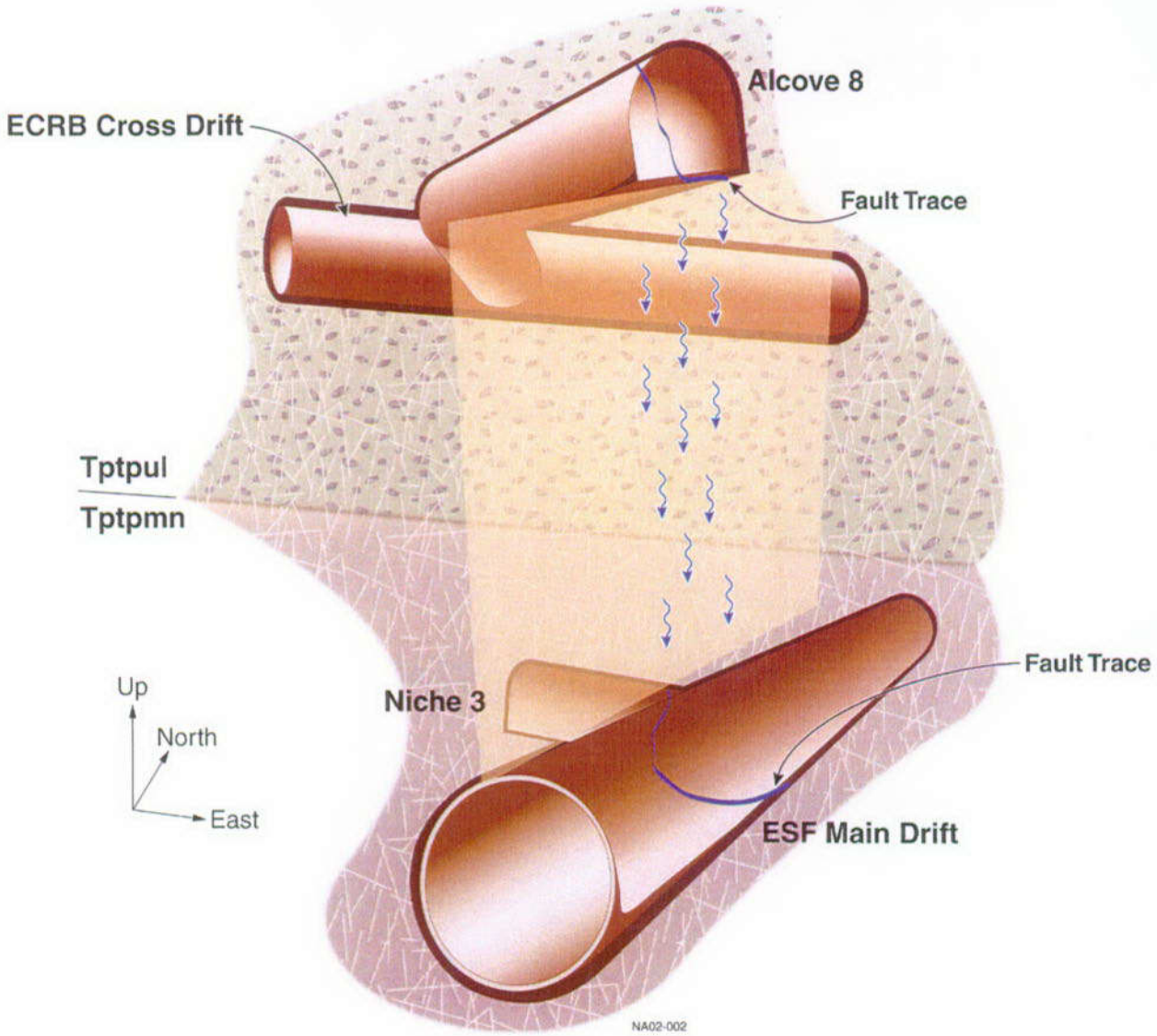

NOTE: Water is introduced into the fault in Alcove 8 and collected in and near Niche 3.

Source: Modified from BSC 2002 [157606], Figure 2.

Figure 11.2-4. Schematic Diagram of Flow Test at Yucca Mountain

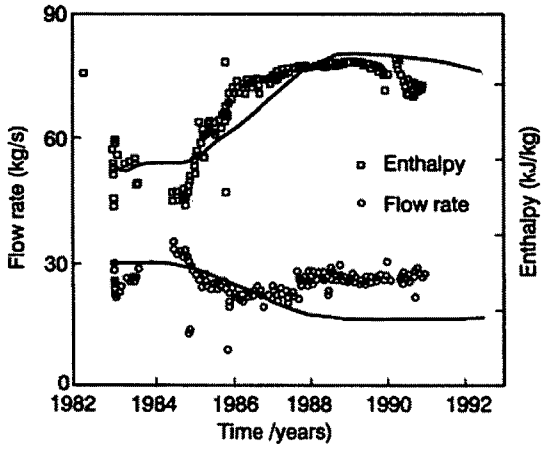

NOTE: Flow rates are slightly greater and enthalpy is slightly less than predicted by the 1986 model from 1988 to 1992.

Source: Steingrimsson et al. 2000 [156686], p. 2904.

Figure 11.2-5. Comparison between Predicted and Observed Flow Rates and Enthalpies for Well 6 of the Nesjavellir Geothermal Field (Iceland)

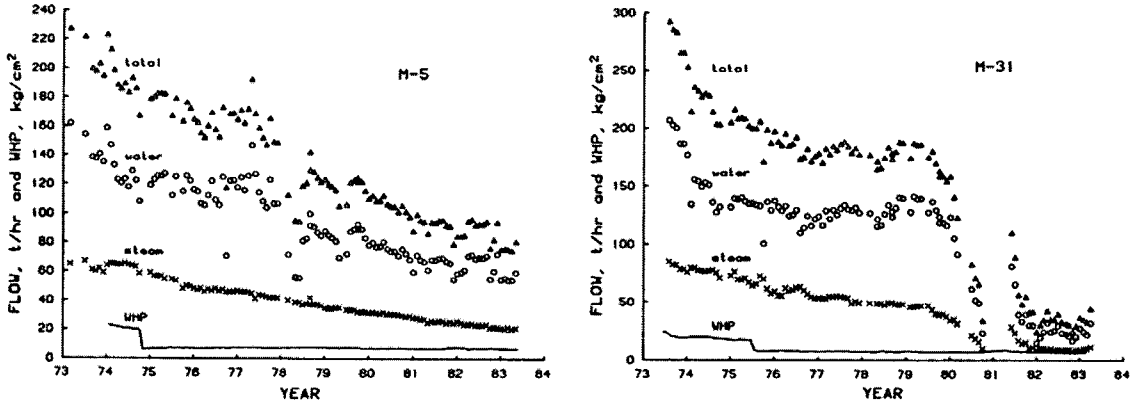

NOTE: Well M-31 experienced near-well boiling with abundant mineral deposition. Cleaning well M-31 in 1981 yielded a short-lived increase in production. WHP = well head pressure.

Source: Truesdell et al. 1984 [156350], p. 227.

Figure 11.2-6. Comparison of Production between Wells M-5 and M-31 at the Cerro Prieto Geothermal Field

NOTE: The botryoidal texture of the quartz indicates that it was deposited as chalcedony or amorphous silica, and that this deposition occurred at >300°C due to rapid decompression. qtz = quartz, qtz(chal) = chalcedony, py = pyrite, act = actinolite, and ep = epidote

Source: Moore et al. 2000 [156319], p. 261.

Figure 11.2-7. Photomicrograph of Fracture Minerals in the Karaha-Telaga Bodas System, Indonesia

NOTE: Titanium-rich scale coats anhydrite and fine needles of actinolite. The scale is peeling off the top of the crystal.

Source: Moore et al. 2000 [156319], p. 260.

Figure 11.2-8. Scanning Electron Microscope Backscattered Image of Fracture Minerals in the Karaha-Telaga Bodas System, Indonesia

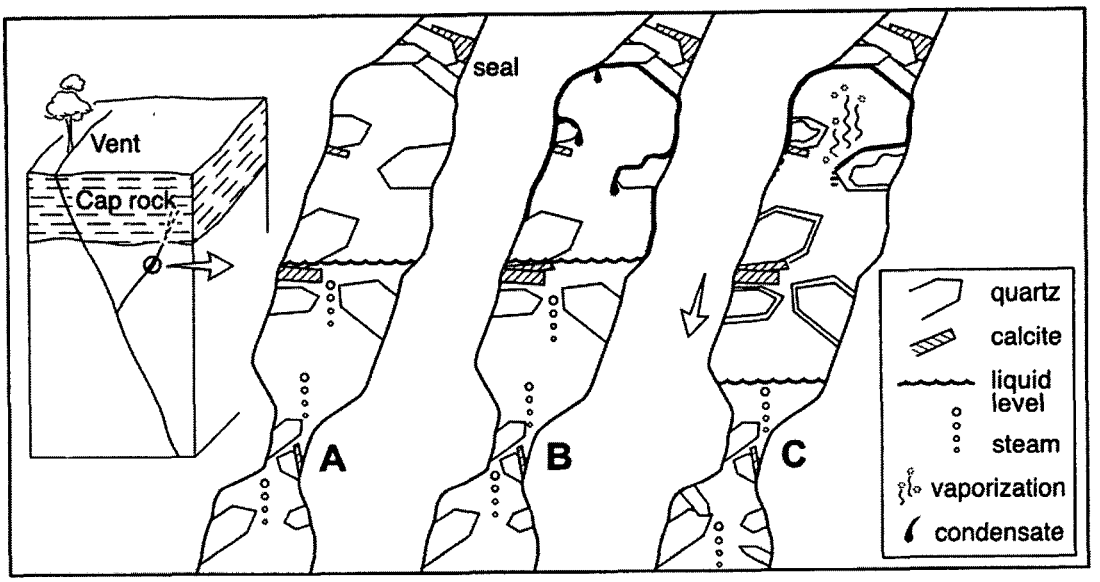

NOTE: In A, quartz and calcite are deposited as the result of boiling possibly due to depressurization in the system. Initially, the rock is too hot for condensation to occur. In B, the top portion of the vein has cooled sufficiently so that condensation occurs. Steam from below migrates through the vein until it reaches the cooler rock where condensation occurs. Corrosion of quartz and calcite occurs near the site of condensation. In C, subsequent lowering of the water table (indicated by the arrow) due to venting results in quartz and calcite deposition due to condensate boiling. Mineral deposition may also occur as condensate reaches the lower, superheated region, and in the liquid-dominated portion of the vein.

Source: Moore et al 2000 [156318], p. 1731.

Figure 11.2-9. Schematic Illustration Showing the Transition from a Liquid Dominated System to a Vapor-Dominated System, Showing only a Portion of the Vein

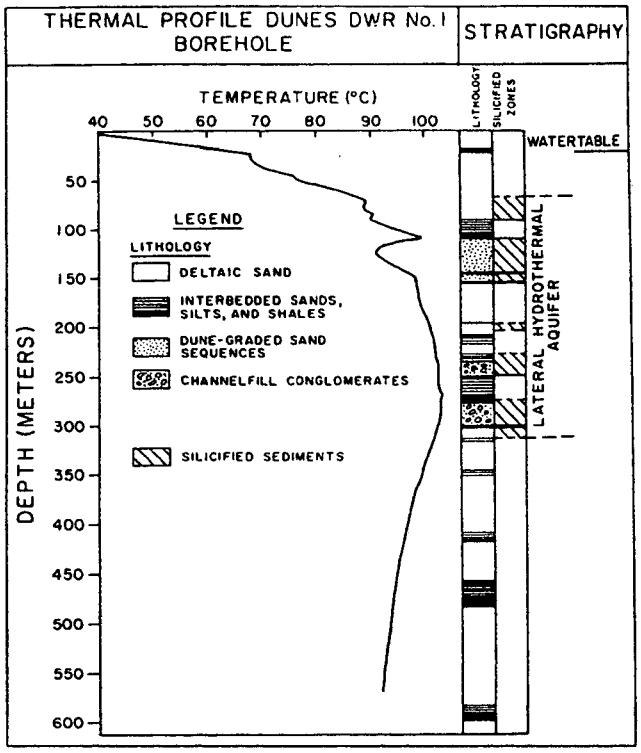

NOTE: The silicified regions are identified in the right column by cross hatching.

Source: Bird and Elders 1976 [154601], p. 286.

Figure 11.2-10. Temperature Profile and Lithology of Borehole DWR No. 1 at the Dunes Geothermal System, California

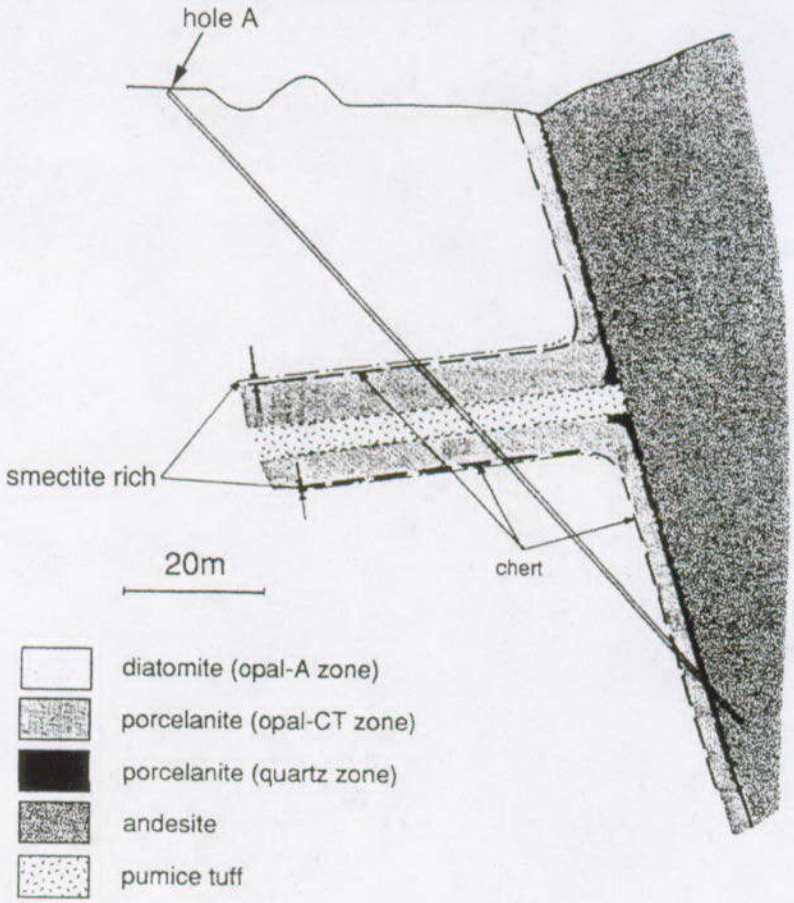

NOTE: The diatomite was altered to porcelanite and chert as a result of a hydrothermal system induced by the intrusion of an andesite dike. The thicknesses of the porcelanite and chert layers range from 20 cm to 20 m (porcelanite) and 5 cm to 20 cm (chert).

Source: Chigira and Nakata 1996 [156349], p. 15.

Figure 11.2-11. Schematic of Lithology near Borehole A in the Miocene Iwaya Formation, Japan

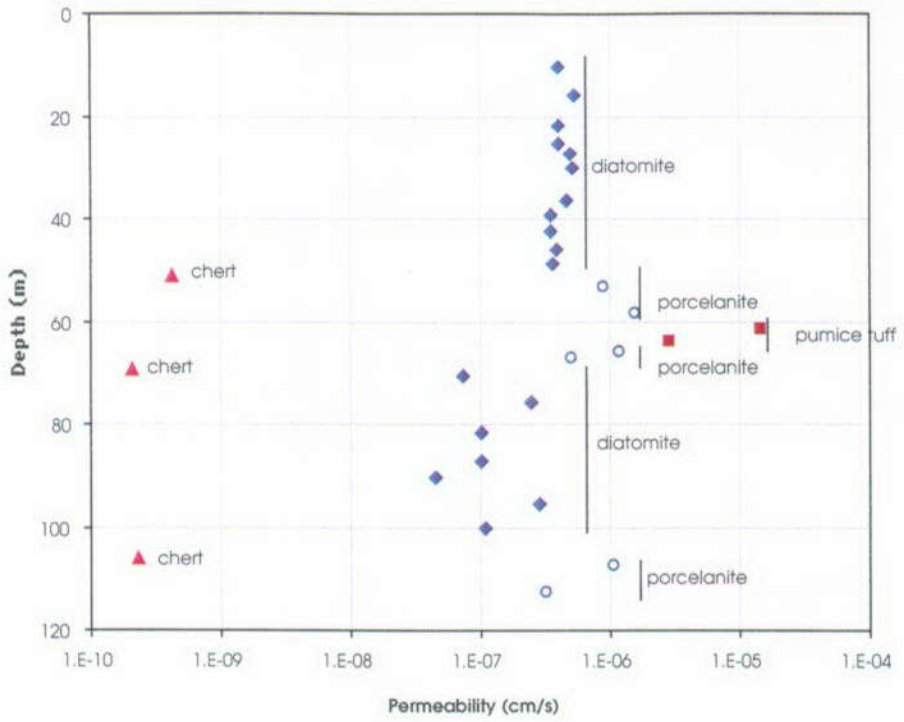

NOTE: Alteration mineral porcelanite has a similar permeability to the original diatomite, but the chert is far less permeable.

Source: Data from Chigira and Nakata 1996 [156349], p. 11.

Figure 11.2-12. Permeability Profile of Samples along Borehole A in the Miocene Iwaya Formation, Japan

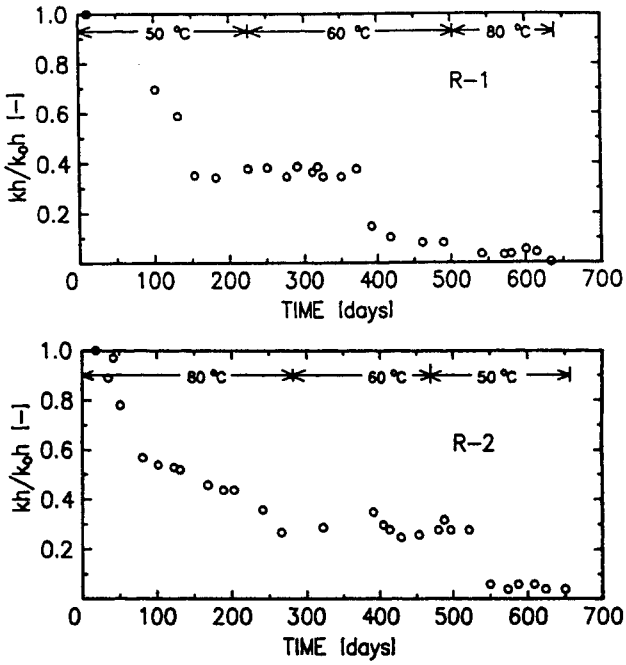

NOTE: The temperatures indicate the temperature of the injected water. The permeability-thickness product (kh) in Well R-1 decreased from 224 darcy-m to 0.79 darcy-m over 624 days. In Well R-2, the permeability-thickness product decreased from 91 darcy-m to 5 darcy-m over 637 days.
kh = permeability-thickness product
k_oh = initial permeability-thickness product

Source: Itoi et al. 1987 [156346], pp. 543–544.

Figure 11.2-13. Reduction in Permeability in Wells R-1 and R-2 over the Duration of a Reinjection Experiment

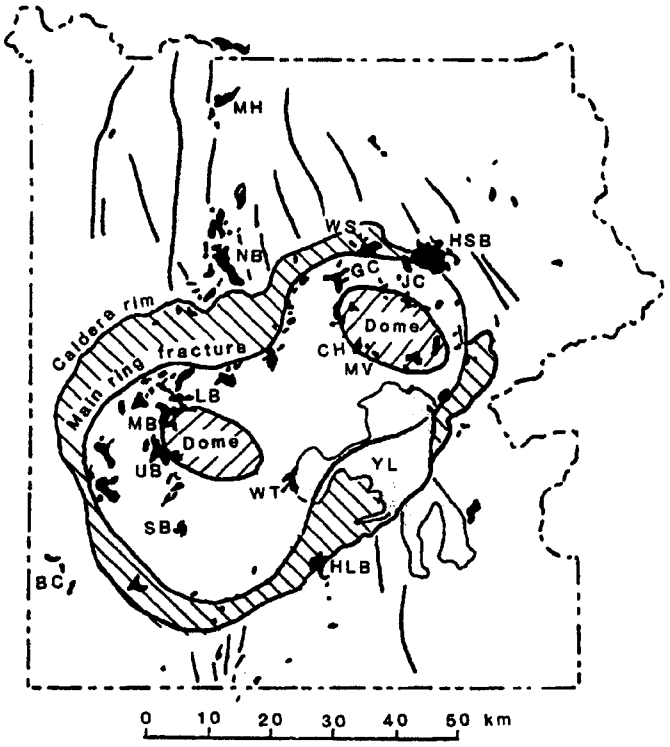

NOTE: Areas abbreviated as follows: BC = Black Creek, CH = Crater Hills, GC = Grand Canyon, HLB = Hart Lake Basin, HSB = Hot Springs Basin, JC = Joseph's Coat Hot Spring, MH = Mammoth Hot Springs, NB = Norris Geyser Basin, LB = Lower Geyser Basin, MB = Midway Geyser Basin, UB = Upper Geyser Basin, SB = Shoshone Geyser Basin, MV = Mud Volcano, WT = West Thumb, WS = Washburn Hot Springs, YL = Yellowstone Lake.

Source: Fournier 1989 [156245], Figure 2.

Figure 11.3-1. Map of Yellowstone National Park, with Outline of 0.6 Ma Caldera Rim

DTN: LB0201YSANALOG.001 [157569]

NOTE: Large sinter blocks had been ejected by 1989 explosion. The pool has an opalescent color, indicating presence of colloidal silica (photo by R. Fournier, USGS).

Source: Simmons 2002 [157578], SN-LBNL-SCI-185-V1, p. 7-1.

Figure 11.3-2. Porkchop Geyser (July 1991)

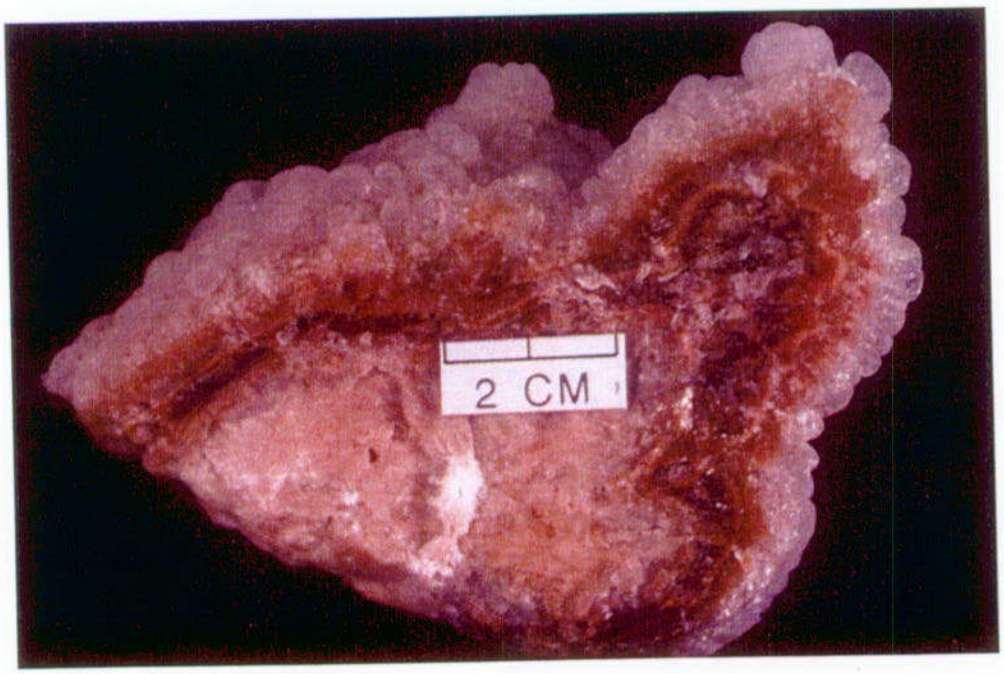

DTN: LB0201YSANALOG.001 [157569]

Source: Simmons 2002 [157578], SN-LBNL-SCI-185-V1, p. 7-1.

Figure 11.3-3. Block from 1989 Porkchop Geyser Eruption, with Gelatinous, Botryoidal Silica Coating Outer Margins and Cavities (photo from T.E.C. Keith, USGS)

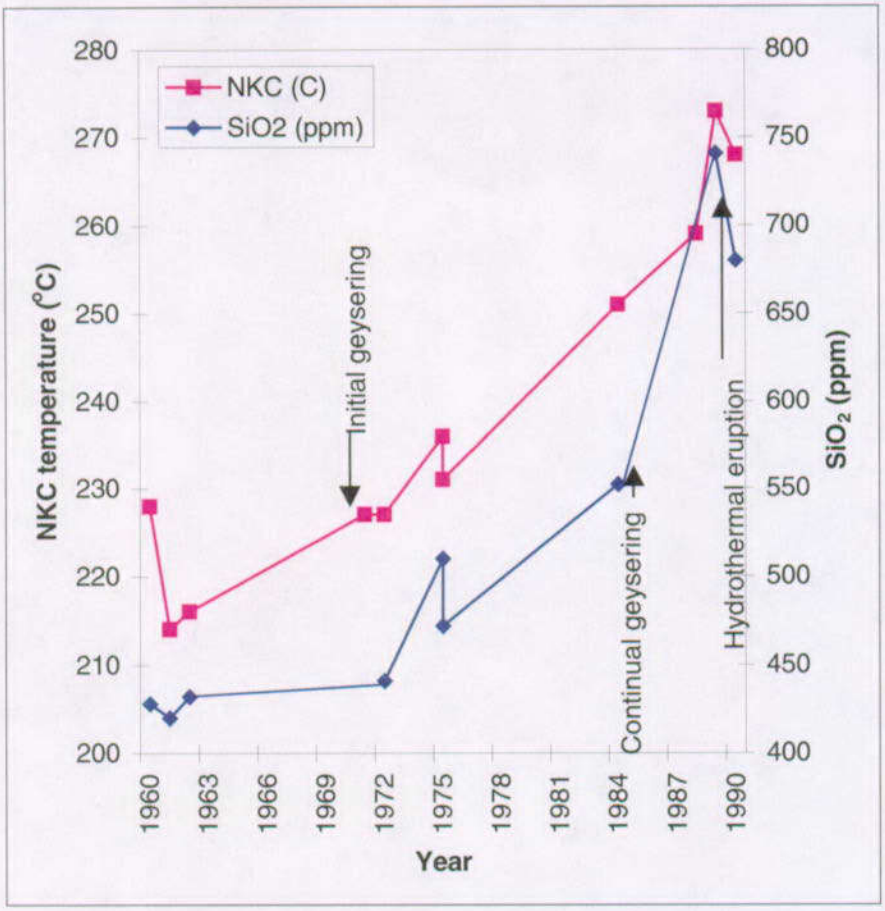

NOTE: Change in flow behavior interpreted to be linked to precipitation of amorphous silica, resulting in the clogging of flow channels.

Source: Fournier et al. 1991 [156246], p. 1116.

Figure 11.3-4. Changes in Calculated Sodium-Potassium-Calcium (NKC) Reservoir Temperatures and Silica Concentrations for Waters Sampled from Porkchop Geyser

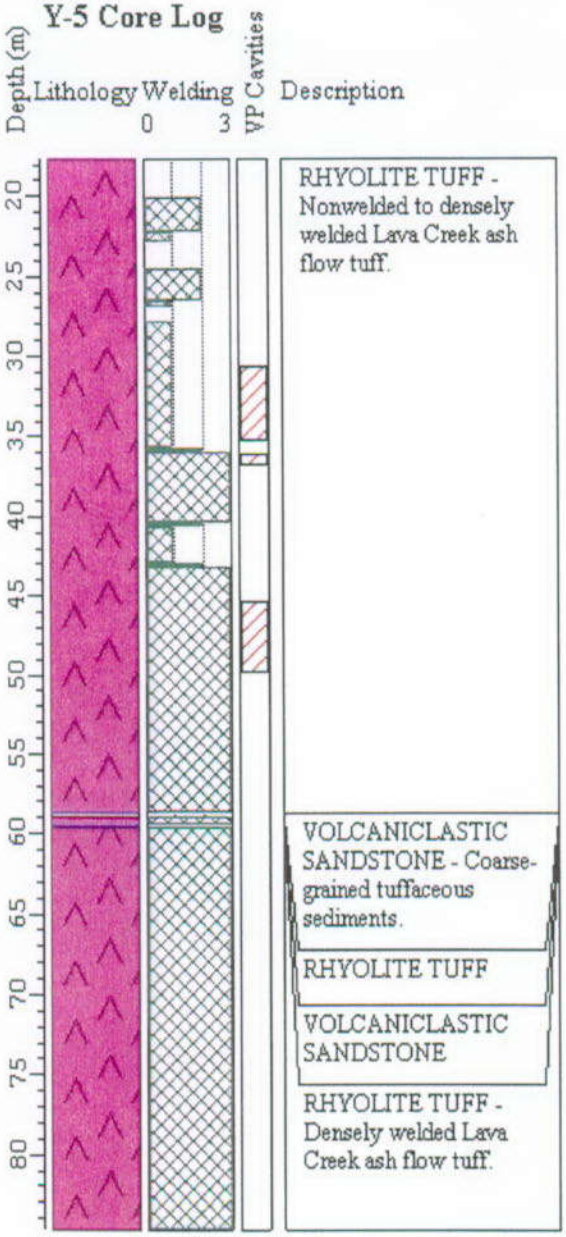

Degree of welding: 0 = nonwelded, 1 = weakly welded, 2 = moderately welded, 3 = densely welded.
VP = vapor-phase

DTN: LB0201YSANALOG.001 [157569]

Source: Dobson et al. 2001 [154547], Figure 2.

Figure 11.3-5. Simplified Geologic Log of the Y-5 Core

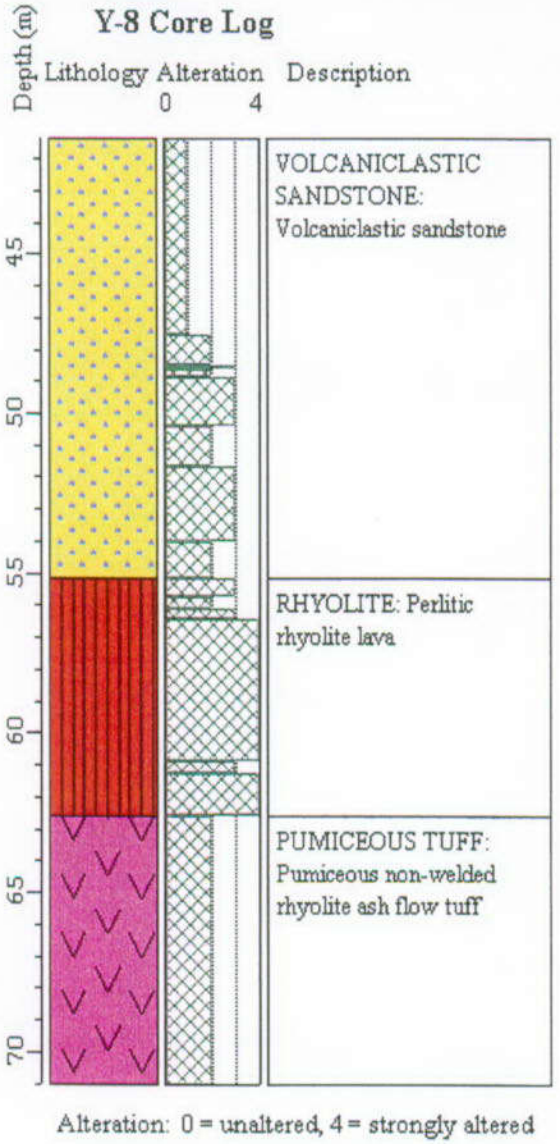

DTN: LB0201YSANALOG.001 [157569]

Source: Dobson et al. 2001 [154547], Figure 3.

Figure 11.3-6. Simplified Geologic Log of the Y-8 Core

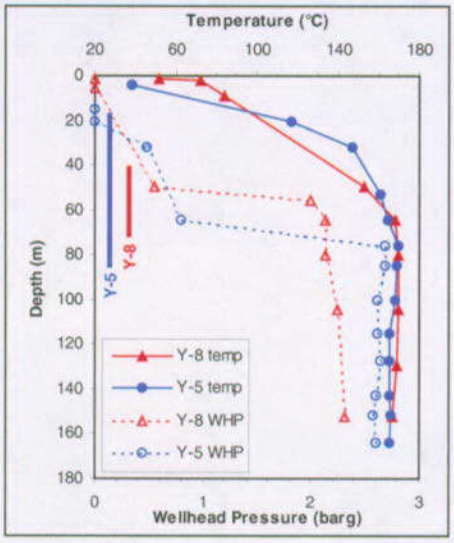

DTN: LB0201YSANALOG.001 [157569]

NOTE: Vertical bars at left indicate studied core-depth intervals. Temperature and pressure data from White et al. 1975 [154530].

Source: Dobson et al. 2001 [154547], Figure 1.

Figure 11.3-7. Downhole Temperature (Solid Lines) and Wellhead Pressure Variations (Dotted Lines) in the Y-5 and Y-8 Wells

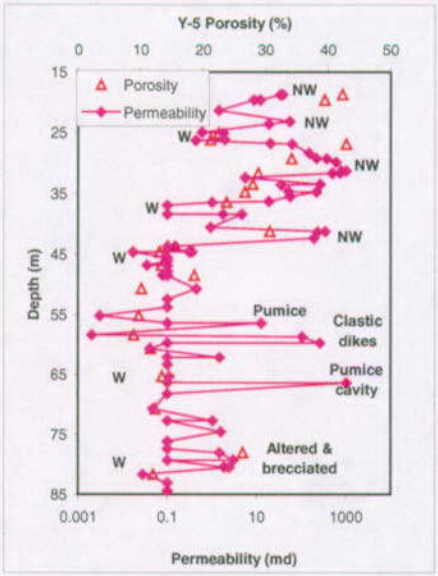

DTN: LB0201YSANALOG.001 [157569]

NOTE: W= moderately to densely welded tuff, NW = nonwelded to weakly welded tuff. The 0.1 md values represent the lower detection limit for minipermeability measurements; actual values are lower.

Source: Dobson et al. 2001 [154547], Figure 4.

Figure 11.3-8. Porosity and Permeability Variations in the Y-5 core

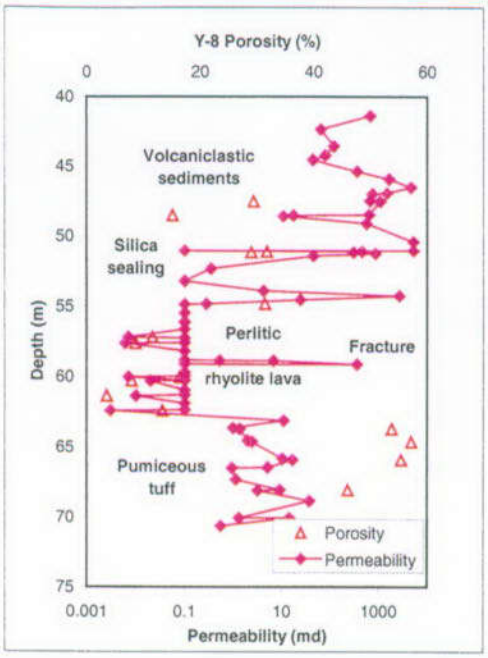

DTN: LB0201YSANALOG.001 [157569]

Source: Dobson et al. 2001 [154547], Figure 5.

Figure 11.3-9. Porosity and Permeability Variations in the Y-8 Core

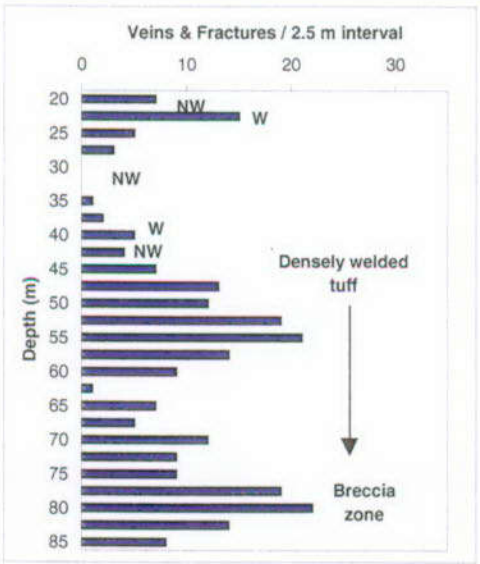

DTN: LB0201YSANALOG.001 [157569]

NOTE: W= moderately to densely welded tuff, NW = nonwelded to weakly welded tuff

Source: Dobson et al. 2001 [154547], Figure 6.

Figure 11.3-10. Veins and Fractures in the Y-5 Core

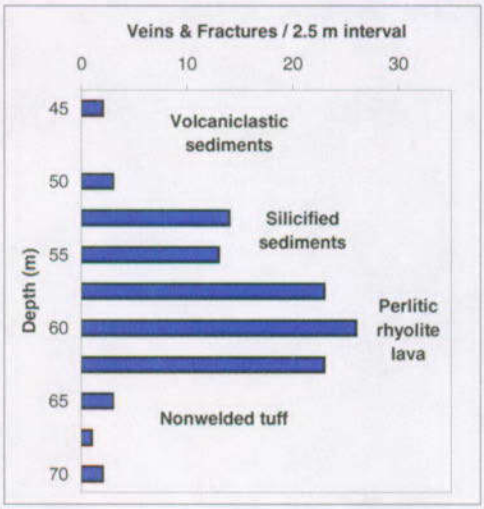

DTN: LB0201YSANALOG.001 [157569]

Source: Dobson et al. 2001 [154547], Figure 8.

Figure 11.3-11. Veins and Fractures in the Y-8 Core

DTN: LB0201YSANALOG.001 [157569]

NOTE: Core width is 4.4 cm. Permeability values of welded tuff clast (A) and matrix (B) are both below the minipermeameter detection limit (0.1 md).

Source: Dobson et al. 2001 [154547], Figure 7.

Figure 11.3-12. Hydrothermal Breccia from the Y-5 Core at 47.7 m (156.5 feet)

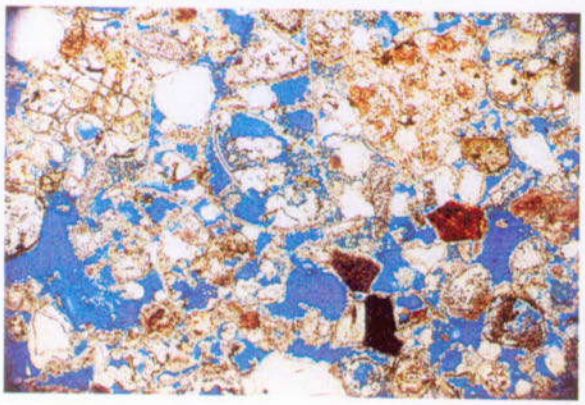

Y-8, 155.9'

Permeability = 1030 md

Porosity = 29.2%

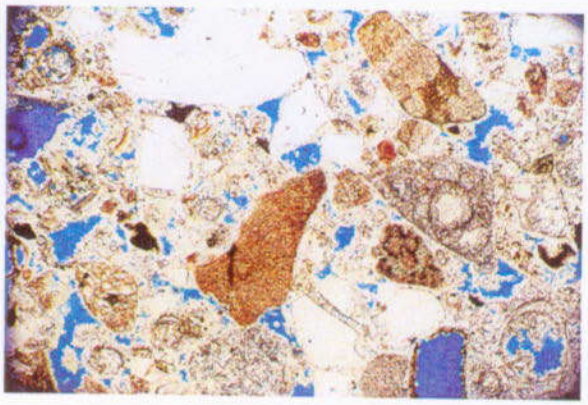

Y-8, 159.2'

Permeability = 16.9 md

Porosity = 15.0%

DTN: LB0201YSANALOG.001 [157569]

NOTE: Silicification of the sample from 159.2' has resulted in a 50% reduction in porosity (change in abundance of blue epoxy denoting porosity) and decrease in permeability of nearly two orders of magnitude.

Source: Simmons 2002 [157578], SN-LBNL-SCI-185-V1, Roll 17, Photos 2 and 4.

Figure 11.3-13. Photomicrographs of Volcaniclastic Sandstone Unit from Y-8 Core

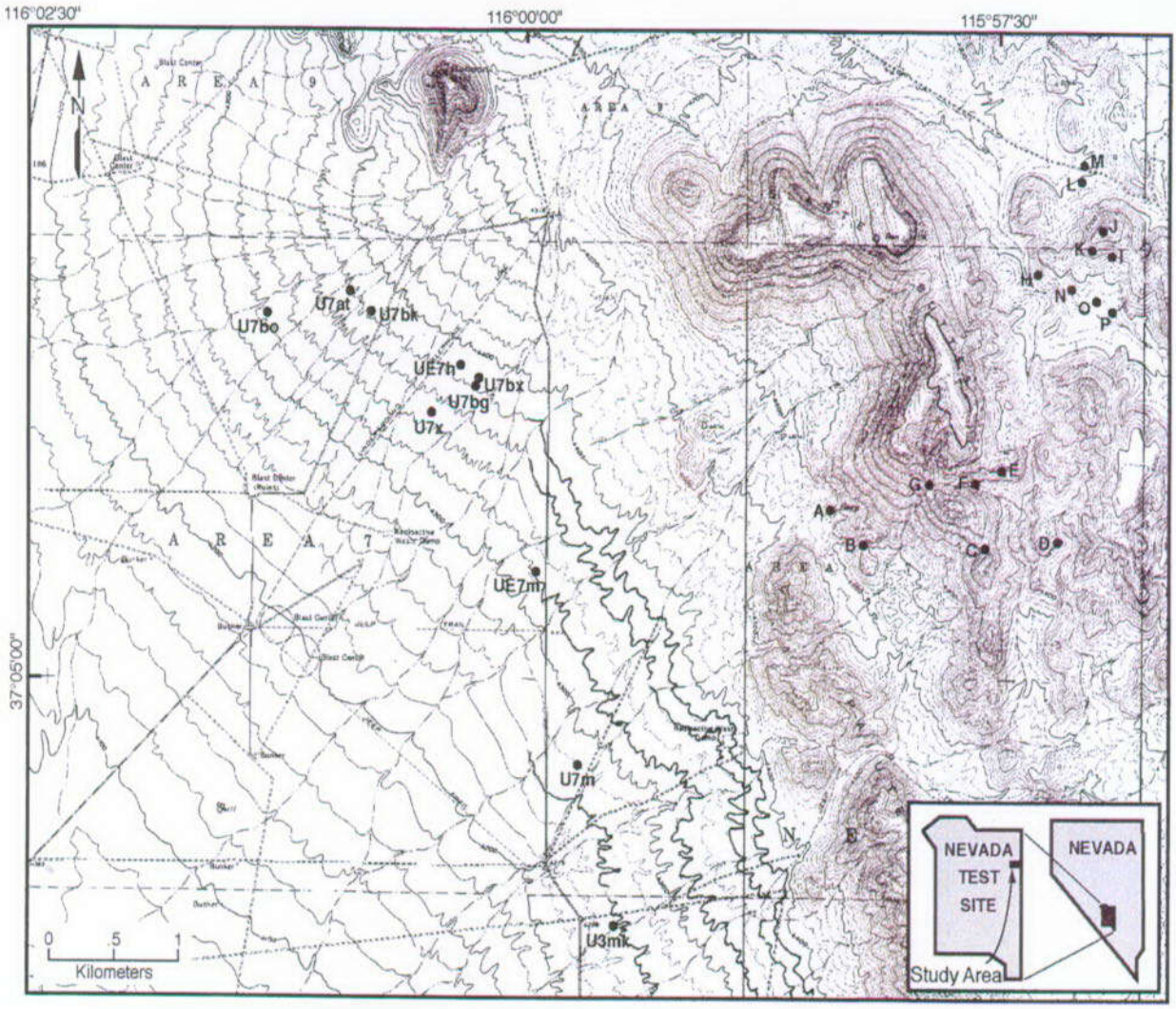

NOTE: Sampling sections, labeled with single letters, and drill holes, which all start with U, are indicated on the right and left sides of the figure, respectively. The stratigraphic units of the drill holes are given in Table 11.4-2.

Source: Simmons 2002 [157578] SN-LANL-SCI-215-V1, p. 6.

Figure 11.4-1. Location Map of the Paiute Ridge Basaltic Intrusion Complex in the Nevada Test Site

NOTE: These veins are within 8 ft (2.4 m) from the basaltic intrusion contact adjacent to the Papoose Lake Sill in the northern part of Paiute Ridge. The vein zone is about 25 ft (7.6 m) wide.

Source: Simmons 2002 [157578]; SN-LANL-SCI-215-V1, p.44, Figure 16B.

Figure 11.4-2. Anastomosing Opal Veins Adjacent to Papoose Lake Sill

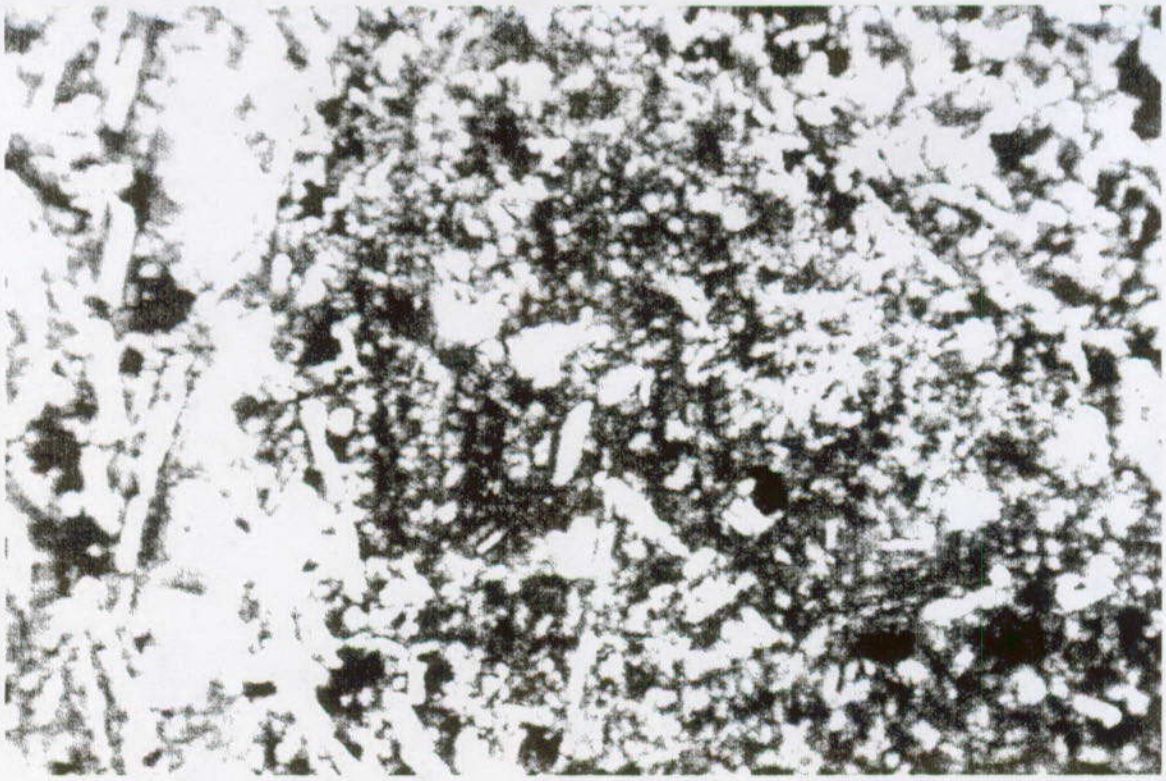

NOTE: Calcite veins along fractures and cavities and epidote grains in cavities are present in the photomicrograph of basalt (LANL# 3547) (view is 170 x 255 μm).

Source: Simmons 2002 [157578], SN-LANL-SCI-215-V1, p. 130.

Figure 11.4-3. Photomicrograph of Basalt from the Contact Zone of the Papoose Lake Sill in the Northern Part of Paiute Ridge

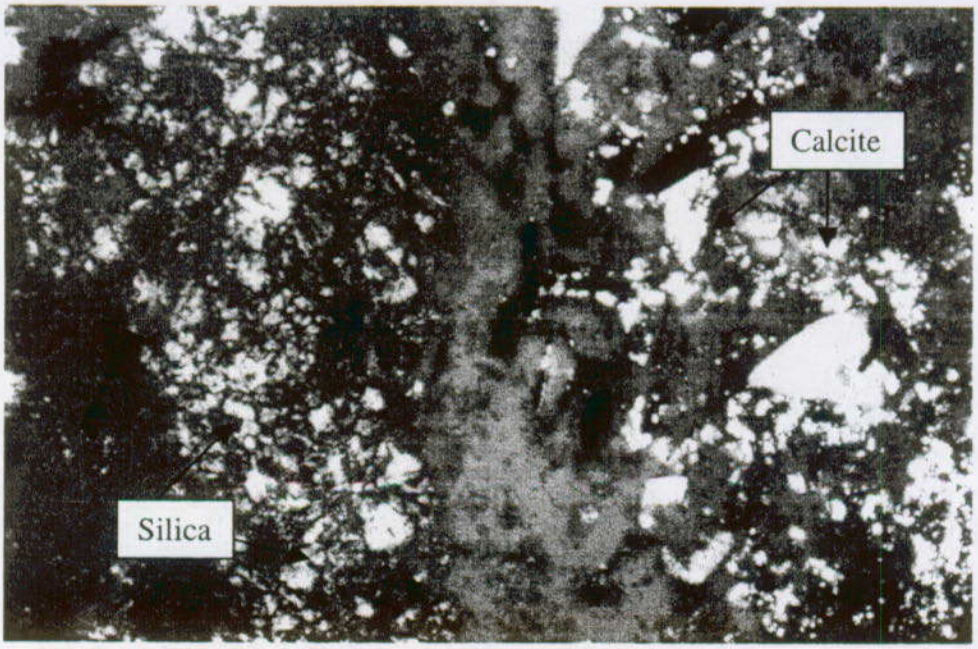

NOTE: This sample (LANL# 3557) was collected 43 ft (13.1 m) from the Papoose Lake Sill contact. Brighter patches of silica (left) and calcite (right) separated by opaque material replace the vitric matrix (view is 70 x 110 μm).

Source: Simmons 2002 [157578]; SN-LANL-SCI-215-V1, p. 131.

Figure 11.4-4. Photomicrograph of Altered Rainier Mesa Tuff

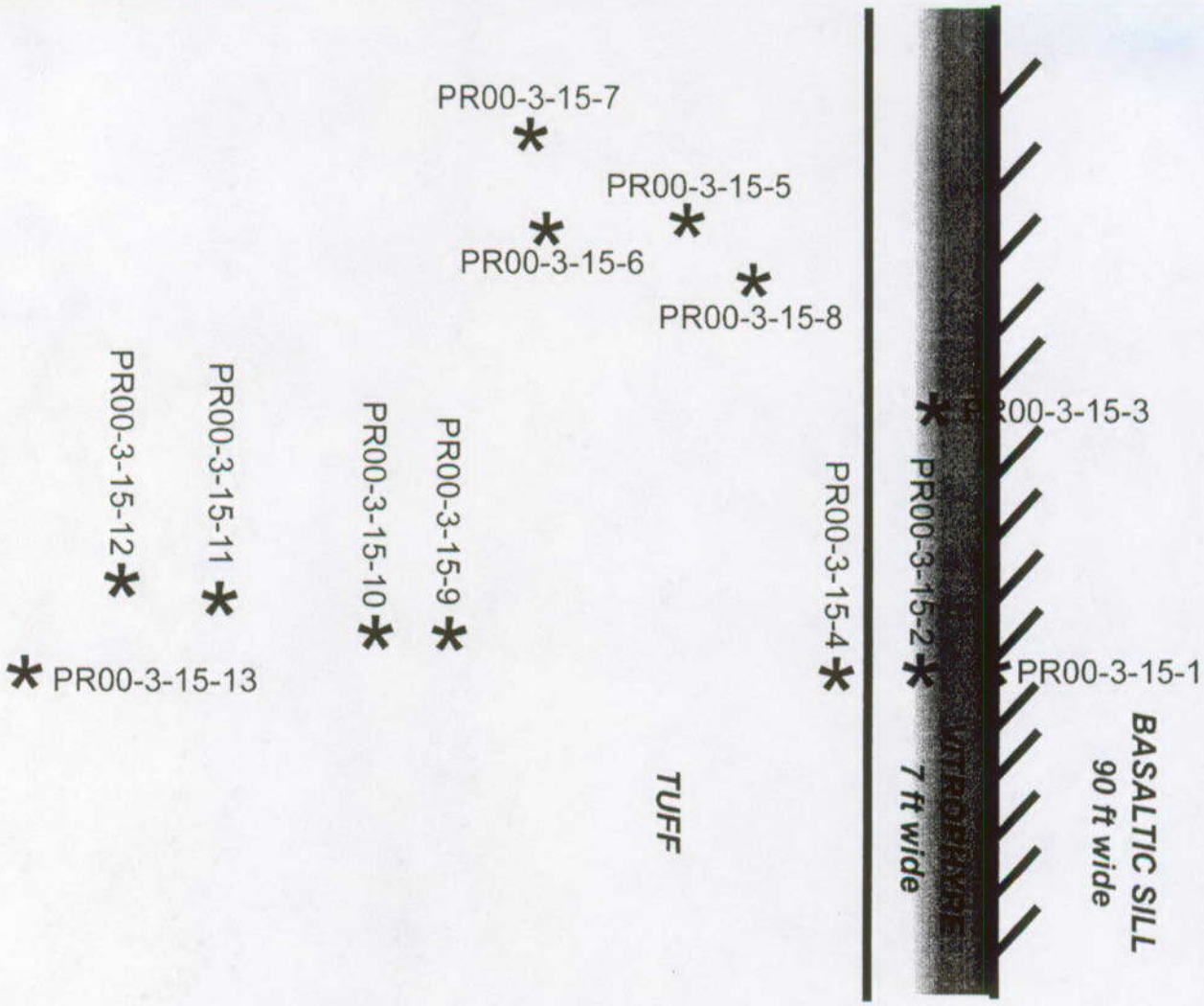

NOTE: Map not to scale; compiled from field notes; see Table 11.4-1 for sample descriptions and measured distances from sill margin.

Source: Simmons 2002 [157578], SN-LBNL-SCI-108-V2, p. 23.

Figure 11.4-5. Schematic Map of Location H, Papoose Lake Basaltic Sill, Paiute Ridge, Nevada Test Site

NOTE: This sample of nonwelded Rainier Mesa Tuff (LANL# 3559) was collected 200 ft (61 m) from the basaltic sill contact. It is apparent that the vesicles are devoid of secondary minerals from devitrification after deposition or from the hydrothermal process related to the basaltic intrusion.

Source: Simmons 2002 [157578]; SN-LANL-SCI-215-V1, p. 101.

Figure 11.4-6. Scanning Electron Microscope Image of Vesicles in Nonwelded Rainier Mesa Tuff

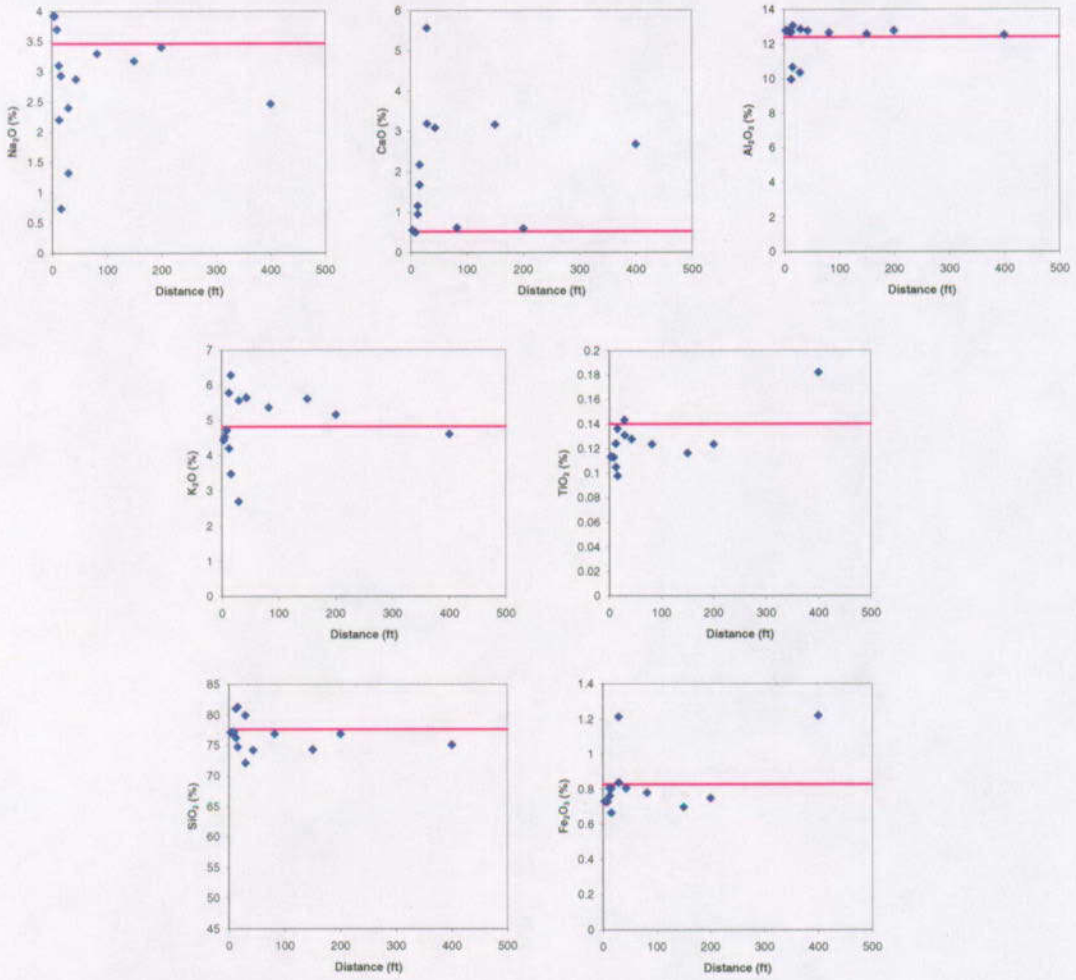

NOTE: These variation diagrams use data in feet for distance and wt% for Na_2O, K_2O, Al_2O_3, CaO, SiO_2, TiO_2, and Fe_2O_3 of tuff samples from the northern part of Paiute Ridge. Major-element contents are calculated to 100% volatile free. Total iron reported as Fe_2O_3. Line indicates average composition of Rainier Mesa rhyolitic tuff reported by Broxton et al. (1989 [100024], Table 3).

Source: Simmons 2002 [157578]; SN-LANL-SCI-215-V1, pp. 63, 69–76.

Figure 11.4-7. Variation Diagrams of Distance Versus Na_2O, K_2O, Al_2O_3, CaO, SiO_2, TiO_2, and Fe_2O_3

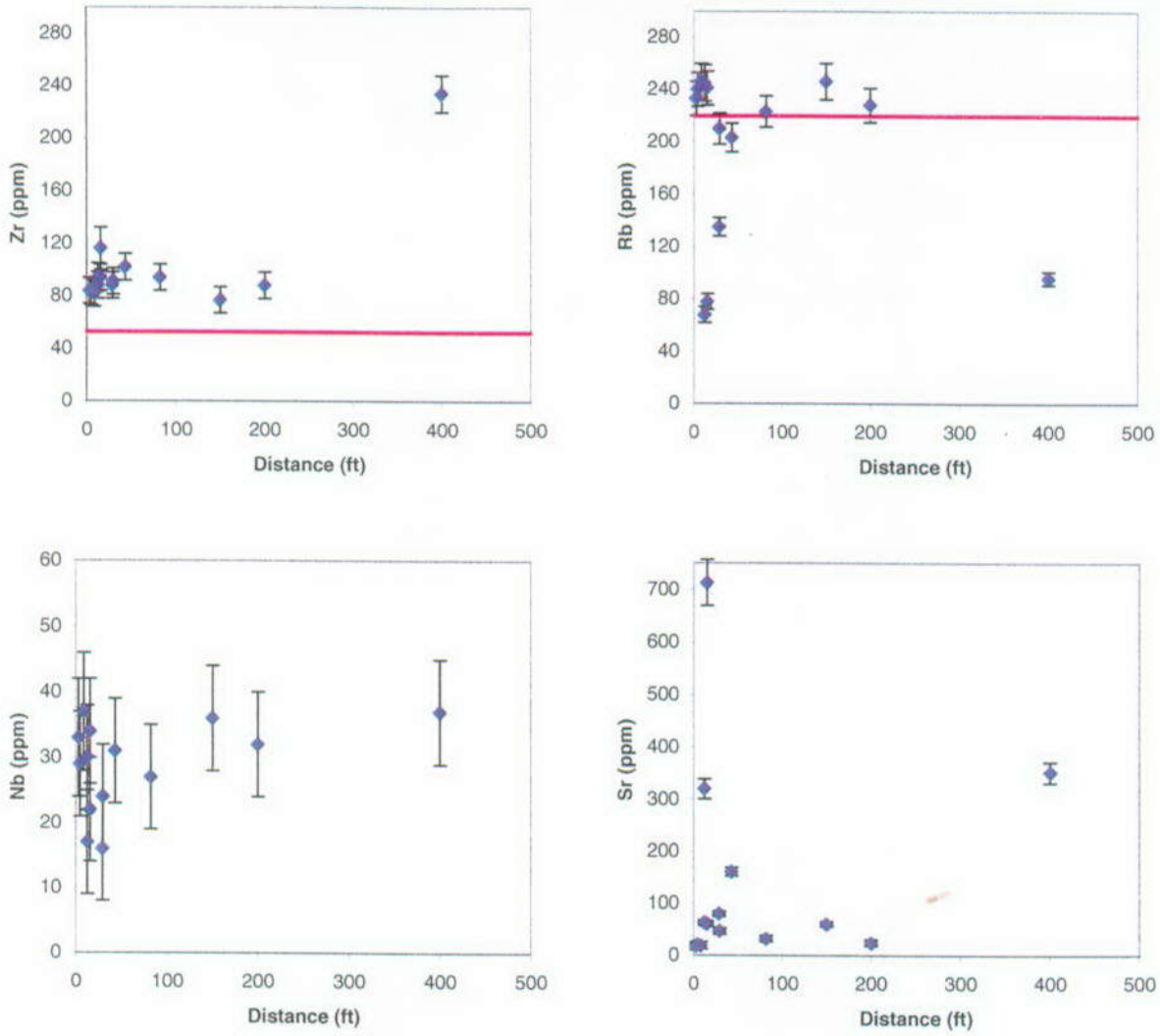

NOTE: These variation diagrams use data in feet for distance versus ppm for Zr, Rb, Nb, and Sr of tuff samples from the northern part of Paiute Ridge. Line indicates average composition of Rainier Mesa rhyolitic tuff reported by Broxton et al. (1989 [100024], Table 3).

Source: Simmons 2002 [157578]; SN-LANL-SCI-215-V1, pp. 63, 69–76.

Figure 11.4-8. Variation Diagrams of Distance Versus Zr, Rb, Nb, and Sr

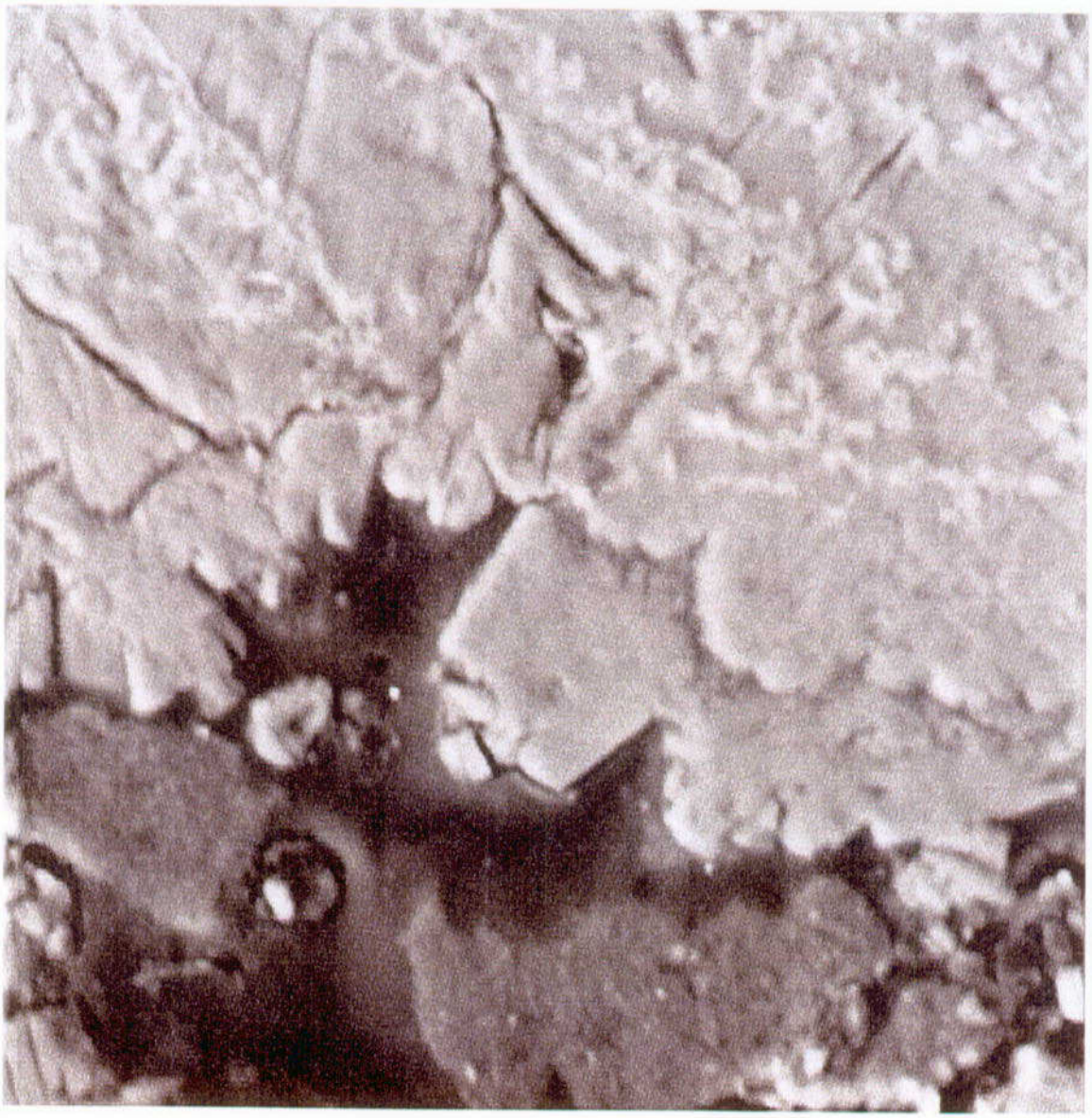

NOTE: 500 µm scale

Source: Simmons 2002 [157578]; SN-LANL-SCI-215-V1, p. 128.

Figure 11.4-9a. Tabular Crystal of Clinoptilolite Overgrowth on a Second Layer of Clinoptilolite with Scalloped or Serrated Edges (LANL# 3552)

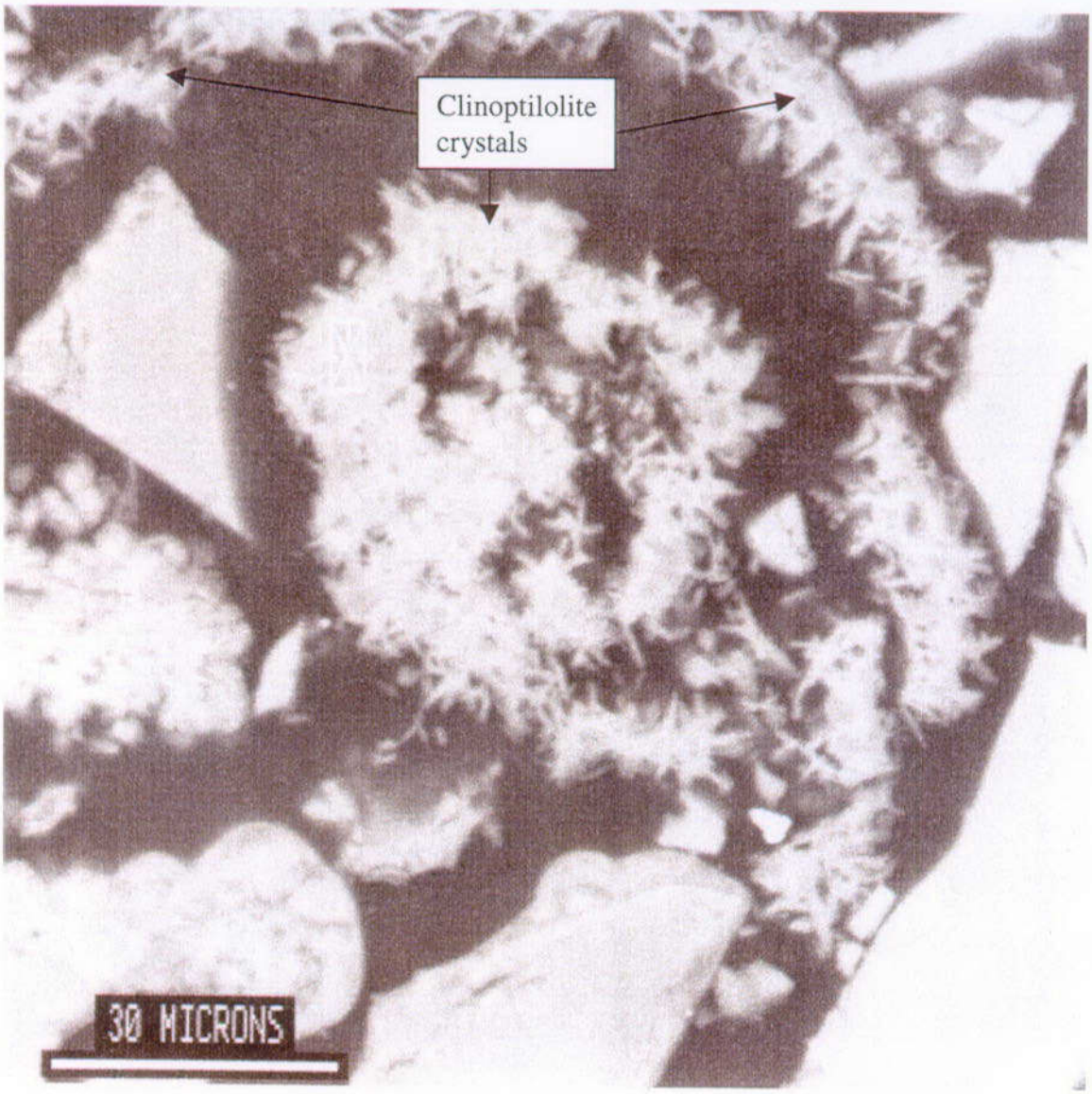

NOTE: This sample of Rainier Mesa Tuff (LANL# 3550) was collected 8.5 ft (2.6 m) from the Papoose Lake Sill contact in the northern part of Paiute Ridge. It is apparent that the cavity is partially filled by clinoptilolite.

Source: Simmons 2002 [157578]; SN-LANL-SCI-215-V1, p. 100.

Figure 11.4-9b. Scanning Electron Microscope Image of Clinoptilolite Crystal Aggregates in a Cavity of Rainier Mesa Tuff

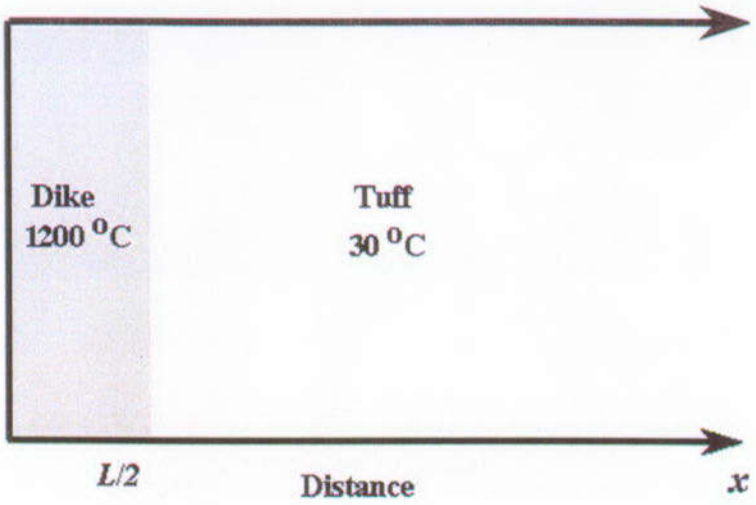

NOTE: This diagram of the half-space computational domain indicates the initial temperature of the intrusion of thickness *L* and tuff country rock for a one-dimensional simulation perpendicular to the intrusion.

Source: Simmons 2002 [157578], SN-LBNL-SCI-108-V2, p. 22.

Figure 11.4-10. Schematic Diagram of the Half-space Computational Domain

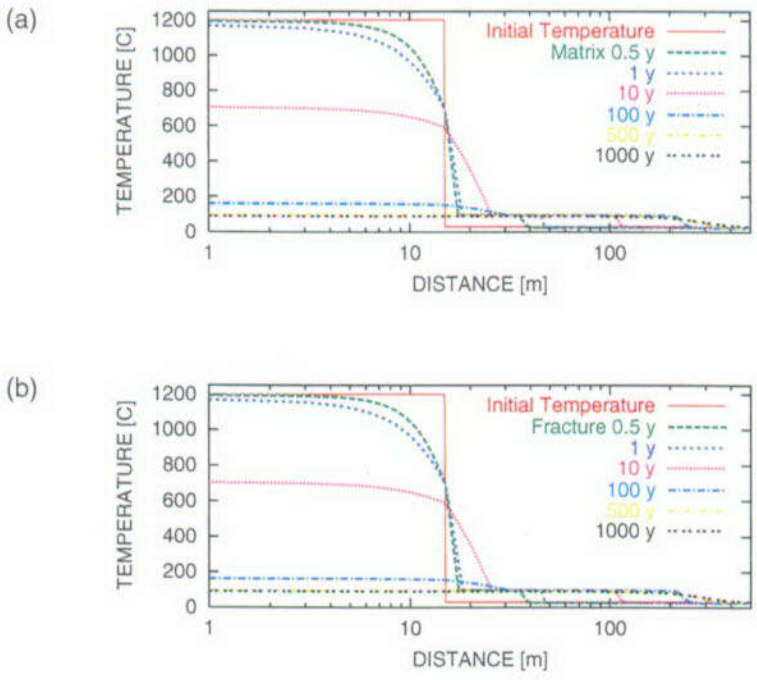

NOTE: $\sigma_{fm} = 10^2$

Source: Simmons 2002 [157578]; SN-LANL-SCI-215-V1, p. 112.

Figure 11.4-11. Matrix (a) and Fracture (b) Temperature Profiles as a Function of Distance at the Indicated Times for the Dual-Continuum Model with Strong Fracture-Matrix Coupling

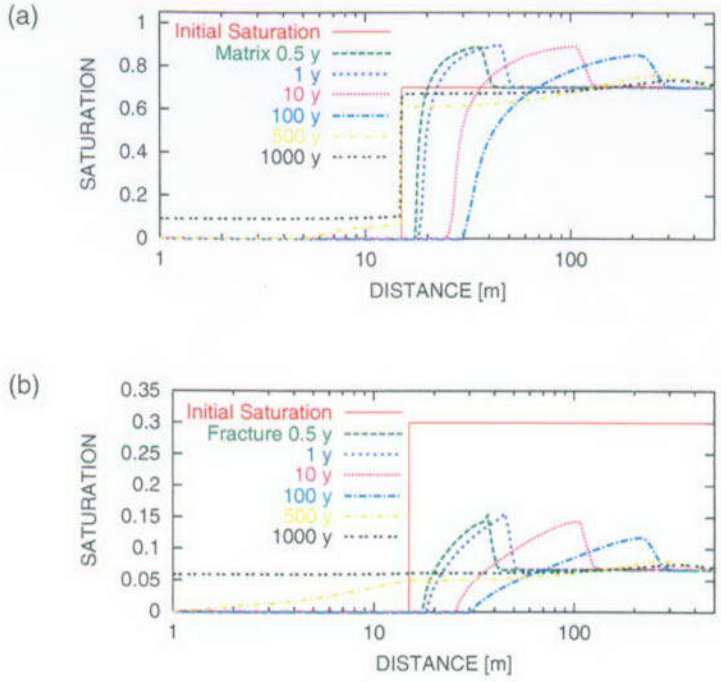

NOTE: $\sigma_{fm} = 10^2$

Source: Simmons 2002 [157578]; SN-LANL-SCI-215-V1, p. 112.

Figure 11.4-12. Matrix (a) and Fracture (b) Saturation Profiles as a Function of Distance at the Indicated Times for the Dual-Continuum Model with Strong Fracture-Matrix Coupling

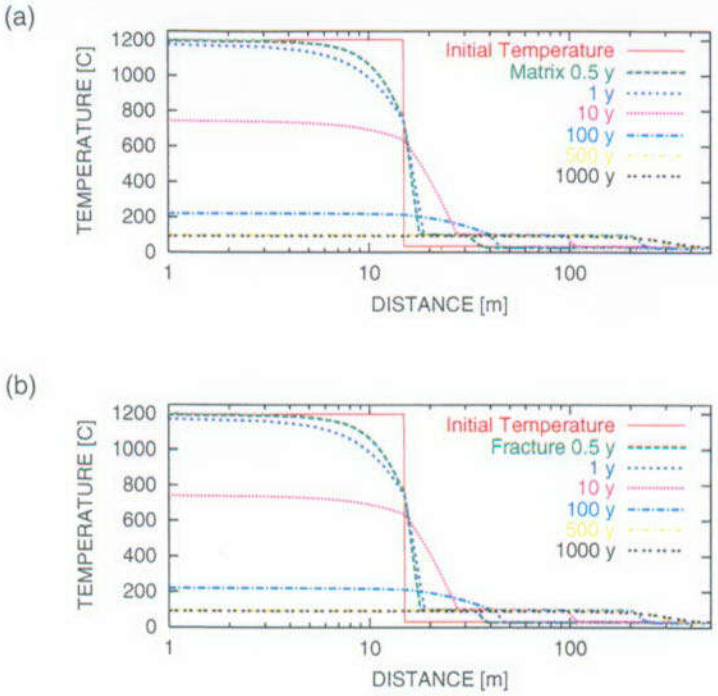

NOTE: $\sigma_{fm} = 10^{-2}$

Source: Simmons 2002 [157578]; SN-LANL-SCI-215-V1, p. 111.

Figure 11.4-13. Matrix (a) and Fracture (b) Temperature Profiles as a Function of Distance at the Indicated Times for the Dual-Continuum Model with Moderate Fracture-Matrix Coupling

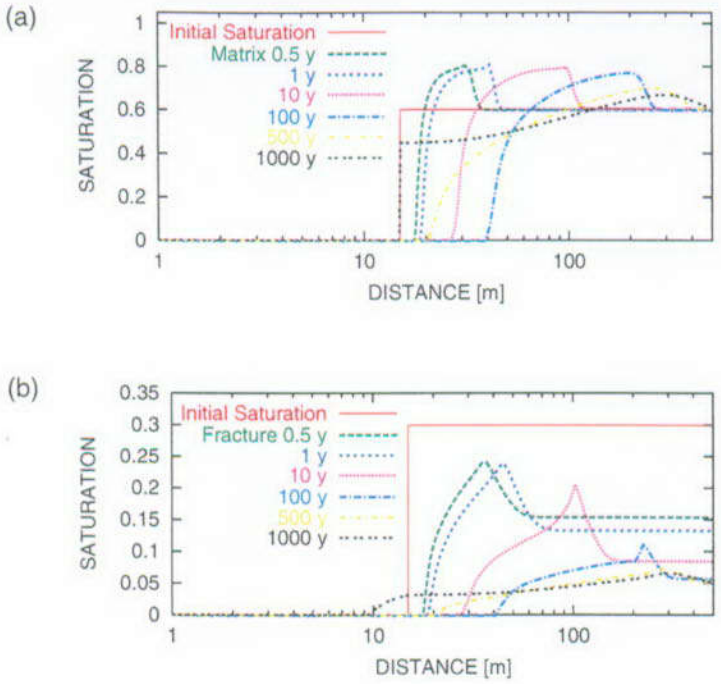

NOTE: $\sigma_{fm} = 10^{-2}$

Source: Simmons 2002 [157578]; SN-LANL-SCI-215-V1, p. 111.

Figure 11.4-14. Matrix (a) and Fracture (b) Saturation Profiles as a Function of Distance at the Indicated Times for the Dual-Continuum Model with Moderate Fracture-Matrix Coupling

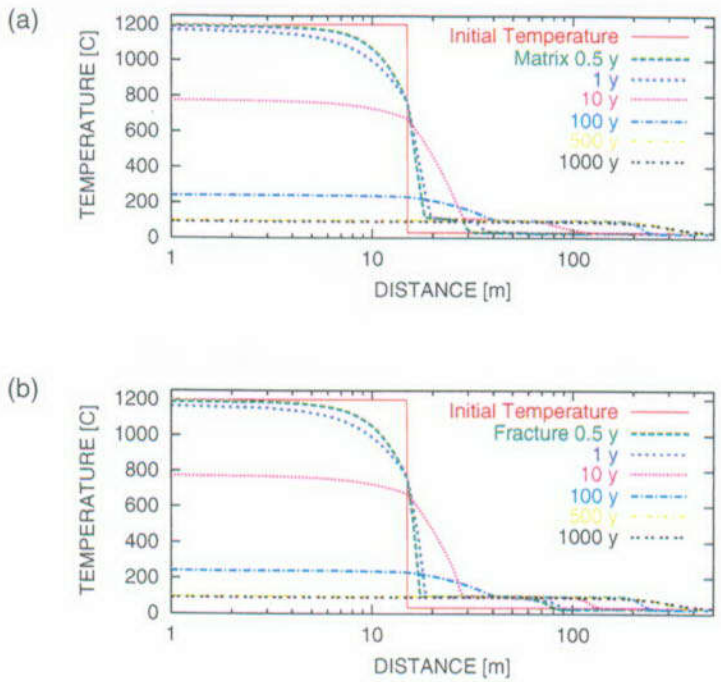

NOTE: $\sigma_{fm} = 10^{-4}$

Source: Simmons 2002 [157578]; SN-LANL-SCI-215-V1, p. 110.

Figure 11.4-15. Matrix (a) and Fracture (b) Temperature Profiles as a Function of Distance at the Indicated Times for the Dual-Continuum Model with Weak Fracture-Matrix Coupling

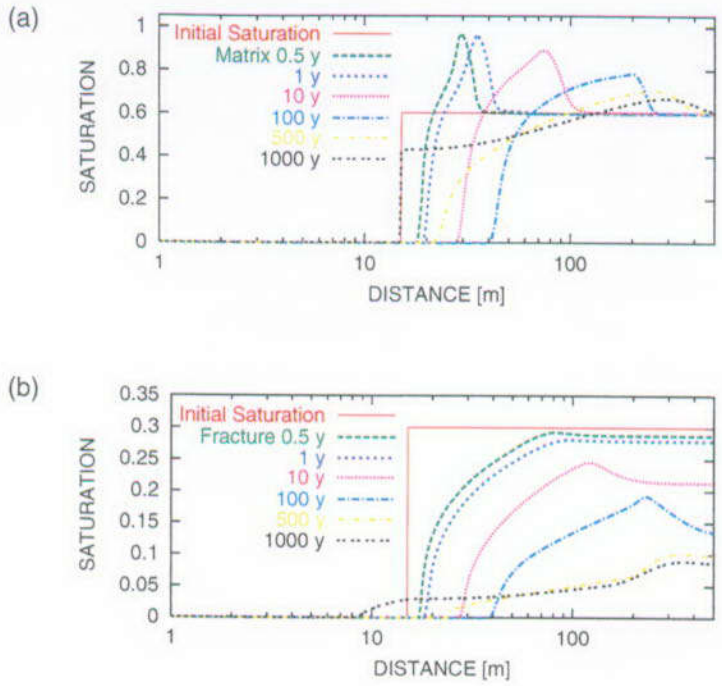

NOTE: $\sigma_{fm} = 10^{-4}$

Source: Simmons 2002 [157578]; SN-LANL-SCI-215-V1, p. 110.

Figure 11.4-16. Matrix (a) and Fracture (b) Saturation Profiles as a Function of Distance at the Indicated Times for the Dual-Continuum Model with Weak Fracture-Matrix Coupling

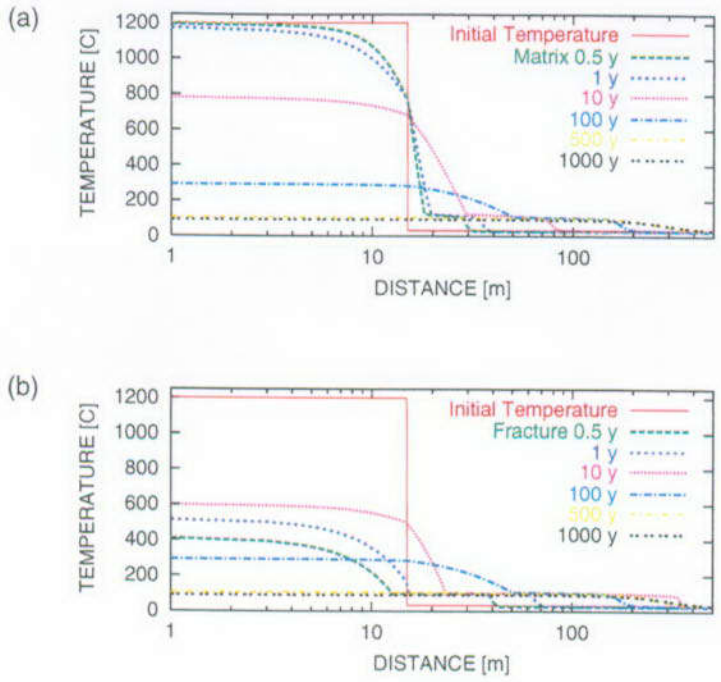

NOTE: $\sigma_{fm} = 10^{-6}$

Source: Simmons 2002 [157578]; SN-LANL-SCI-215-V1, p. 107.

Figure 11.4-17. Matrix (a) and Fracture (b) Temperature Profiles as a Function of Distance at the Indicated Times for the Dual-Continuum Model with Very Weak Fracture-Matrix Coupling

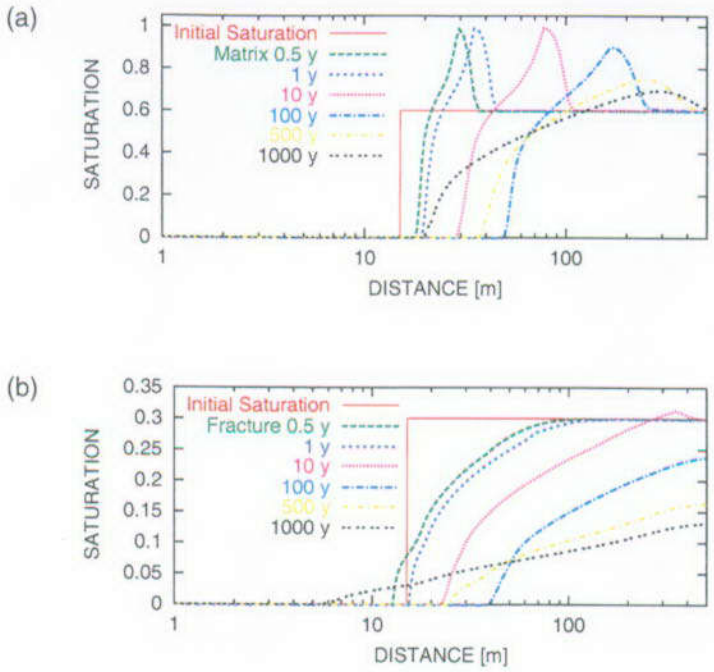

NOTE: $\sigma_{fm} = 10^{-6}$

Source: Simmons 2002 [157578]; SN-LANL-SCI-215-V1, p. 107.

Figure 11.4-18. Matrix (a) and Fracture (b) Saturation Profiles as a Function of Distance at the Indicated Times for the Dual-Continuum Model with Very Weak Fracture-Matrix Coupling

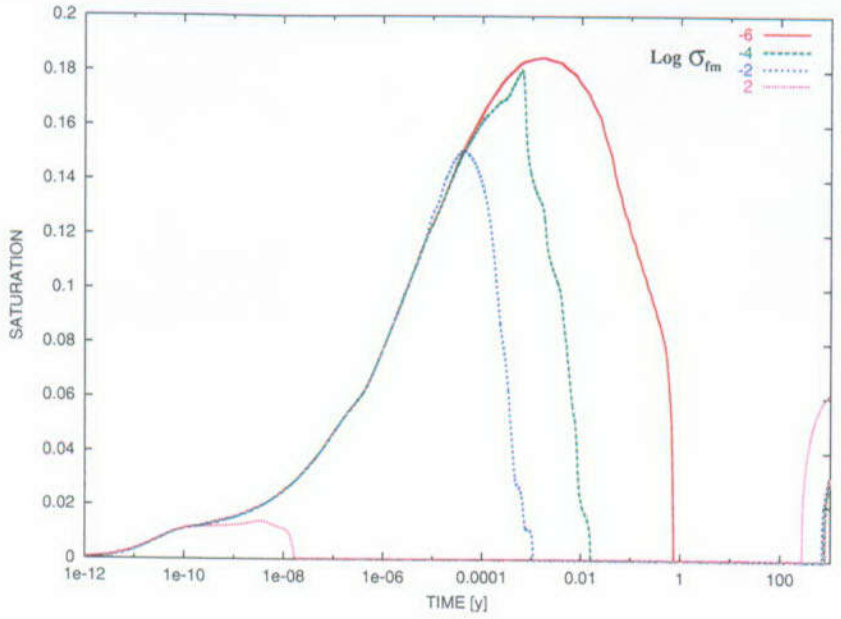

Source: Simmons 2002 [157578]; SN-LANL-SCI-215-V1, p. 118.

Figure 11.4-19. Fracture Saturation as a Function of Time at the Boundary between the Intrusion and Country Rock for Different Fracture-Matrix Coupling Strengths

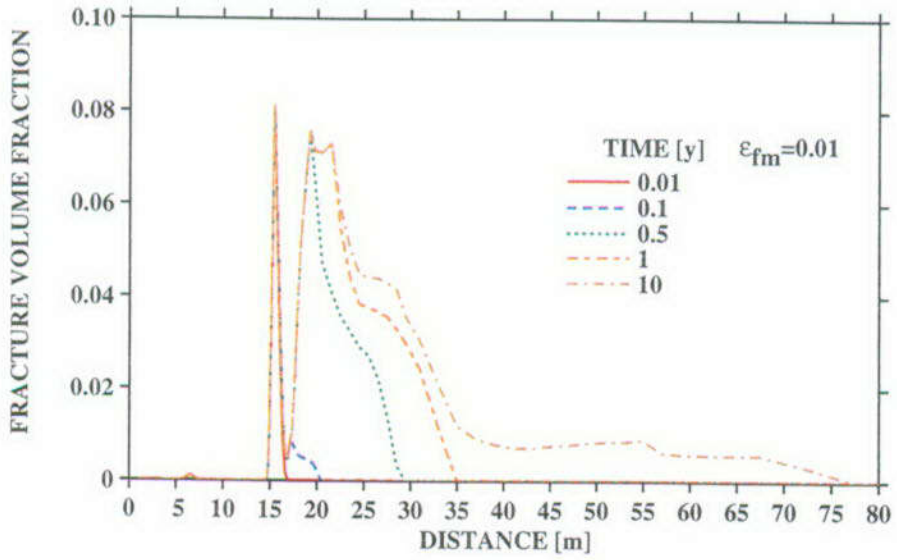

NOTE: $\sigma_{fm} = 10^{-2}$

Source: Simmons 2002 [157578]; SN-LANL-SCI-215-V1, p. 117.

Figure 11.4-20. Fracture Volume Fraction of Amorphous Silica Precipitation as a Function of Distance for Various Times with Moderate Fracture-Matrix Coupling

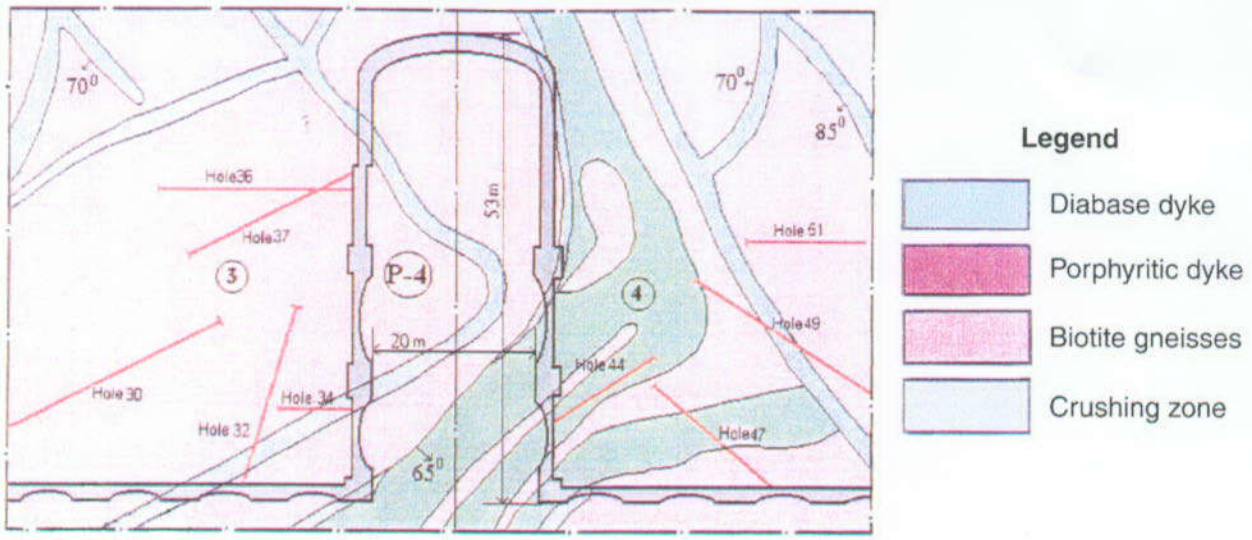

Source: Gupalo et al. 1999 [157470], Figure 2.16.

Figure 11.6-1. Schematic of the Underground Workings at Facility P-4 at K-26, Siberia, in Cross Section

Table 11.2-1. THC Processes in Geothermal Systems and Their Applicability to Yucca Mountain

THC process	Geothermal system component	Geothermal examples	Applicability to Yucca Mountain	Potential impact to repository performance
Advective heating	Heat transfer within convecting geothermal reservoir: develop near-isothermal vertical thermal profiles	Nearly ubiquitous: examples include Yellowstone (Wyoming), Salton Sea (California), Wairakei (New Zealand)	Would only occur very locally in high-temperature (>100°C) design (within heat pipe)	Could result in localized zone of enhanced water-rock interaction and chemical transport
Conductive heating	Heat transfer within low-permeability and unsaturated portions of geothermal systems	Nearly ubiquitous: examples include hot dry rock resources, upper portions of San Vicente (El Salvador), Amatitlan (Guatemala)	Main mechanism of heat transfer at Yucca Mountain (unsaturated conditions)	Heating leads to more rapid chemical reactions. Thermal expansion of rocks could alter fracture permeability
Fracture-dominated fluid flow	Fluid flow in fractured reservoir rocks with low matrix permeability	Silangkitang (Indonesia), Dixie Valley (Nevada), Los Azufres (Mexico)	Main mechanism for fluid flow within welded ash flow tuffs at Yucca Mountain	Could permit rapid movement of fluids along fast flow paths (evidenced by bomb-pulse tritium)
Chemical transport	Advective and diffusive transport of dissolved constituents in fluids. Tracer tests used to determine fluid flow paths and rates.	Ubiquitous. Well-documented tracer tests for many geothermal systems, including The Geysers (California), Dixie Valley (Nevada), Coso (California), Awibengkok (Indonesia)	Advective transport within fractures, and advective and diffusive transport between fractures and matrix	Potential mechanism for movement of radioactive waste materials from repository
Boiling	Development of two-phase and steam zones in geothermal systems due to depressurization and heating	Occurs in most high-temperature liquid-dominated geothermal systems with production, e.g., Awibengkok (Indonesia), Coso (California), and occurs naturally in steam-dominated systems, e.g., The Geysers (California), Karaha-Telaga-Bodas (Indonesia).	Would only occur in high-temperature design near drift walls for limited time	Would create dryout zone around drift for high-temperature design, and could lead to development of heat pipe. Fracture permeability could be modified by precipitation caused by boiling.
Dryout	Occurs during transformation from liquid-dominated to steam-dominated geothermal system	Documented for The Geysers (California), Karaha-Telaga-Bodas (Indonesia)	Would only occur in high-temperature operating mode near drift walls for limited time	Dryout zone would prohibit seepage into drift for early stages of high-temperature operating mode. Would lead to precipitation of dissolved solids in area that could be redissolved as cooling and rewetting occurred.

Table 11.2-1. THC Processes in Geothermal Systems and Their Applicability to Yucca Mountain (Cont.)

THC process	Geothermal system component	Geothermal examples	Applicability to Yucca Mountain	Potential impact to repository performance
Condensation	Occurs during transformation from liquid-dominated to steam-dominated geothermal system, and in upper levels of geothermal systems where rising vapor contacts cooler meteoric waters	Observed in many geothermal systems where rising gas and steam is cooled and mixes with near-surface meteoric fluids, resulting in development of bicarbonate and acid-sulfate springs. Documented for Yellowstone (Wyoming), Wairakei (New Zealand), Waiotapu (New Zealand)	Would mainly occur in high-temperature design above drift areas for limited time; can also occur in low-temperature design, but at a reduced level	Condensation above drift could lead to recycling of fluids, thus resulting in a higher volume of fluids passing through near-field area. This could also result in localized zones of near-saturation conditions and increase water-rock interaction. Condensation could also take place in the drift, resulting in dripping on waste packages.
Mineral dissolution	Occurs typically in condensation zones, or where acid fluids are present	Difficult to document, but observed at The Geysers (California) and Karaha-Telaga-Bodas (Indonesia)	Would occur primarily where condensation occurs	Mineral dissolution associated with condensation zone could lead to local increases in porosity and permeability.
Mineral alteration and precipitation	Occurs in numerous portions of geothermal systems, especially in zones with abundant fluid flow that have undergone heating	Ubiquitous. Degree and type of mineralization depends on rock and fluid compositions, water-rock ratios, and temperature. Boiling can result in significant mineralization. Alteration mineralogy well-characterized at Wairakei (New Zealand), Salton Sea (California), Silangkitang (Indonesia), Krafla (Iceland)	Alteration and precipitation likely to be confined to near-field environment, where boiling and increased fluid flux occur. These effects may be negligible for low-temperature design.	Alteration could lead to changed sorption properties (zeolite and clay formation). Precipitation of silica minerals and calcite in fractures could locally reduce permeability, or lead to focussed flow within a few larger fractures.

Source: Simmons 2002 [157578], SN-LBNL-SCI-108-V2, pp. 14–15.

Table 11.2-2. Estimated Process Time Scales for Potential Repository and Geothermal Reservoirs

Process	Repository Time Scale (yr)	Geothermal Reservoir Time Scale (yr)
Duration of heating (magma or nuclear waste)	1000s	10,000s
Dryout	100s to 2,000	10,000s
Fast-path flow from ground surface to repository or geothermal system	10's	10s
Water recycling in "heat pipe" (cyclic liquid-vapor counterflow)	<<1	1s to 10s
Intermittent flow events	<<<1	<<<1
Physical changes due to dissolution and precipitation	<1 to 1,000s	<1 to 10,000s
Mineralogic changes	<1 to 1,000s	<1 to 10,000s
Climate change	10,000s	10,000s

Source: Simmons 2002 [157578], SN-LBNL-SCI-108-V2, p. 15.

Table 11.3-1. Comparison of Yellowstone and Yucca Mountain Systems

	Potential Yucca Mountain Repository	Yellowstone Geothermal System
Boiling zone temperatures	~95°C	92–270°C
SiO_2 in fluids	<200 ppm	200–700 ppm
Duration of boiling conditions	<1,200 yr (high T) 0 years (low T)	≥15,000 yr
Fluid-flow conditions	Unsaturated	Saturated
Estimated fluid flux	10^{-9} to 10^{-10} m/s	4.8×10^{-5} m/s
Estimated heat flux	16.7 W/m^2 (in near-field area around waste packages)	46 W/m^2 (Firehole River Drainage Basin) 1.7 W/m^2 (Yellowstone Caldera)

Source: Simmons 2002 [157578], SN-LBNL-SCI-108-V2, p. 15.

Table 11.4-1. Samples, Lithologic Types and Descriptions, and Measured and Estimated Distances of Tuff Samples from a Basaltic Intrusion

Sample Number	Distance to Contact (ft) [m]	Lithology	Sample Description
Adjacent and west of Papoose Lake Sill			
PR00-3-15-1 (LANL# 3547)	Contact	Basalt	Purplish gray, fine grained, platy, and altered
PR00-3-15-2 (LANL# 3548)	4.5 [1.4]	Vitrophyre	Fused tuff, glassy, foliated, and 7 ft (2.1 m) wide
PR00-3-15-3 (LANL# 3549)	3.0 [0.9]	Vitrophyre	Fused tuff, glassy, foliated, and contains silica veinlets
PR00-3-15-4 (LANL# 3550)	8.5 [2.6]	Baked tuff	Hardened, pinkish orange, and devitrified
PR00-3-15-5 (LANL# 3551)	12.5 [3.8]	Tuff	Partially welded, cavernous, and pinkish orange
PR00-3-15-6 (LANL# 3552)	15.5 [4.7]	Opal vein	3" wide, NS trend parallel to contact, and reddish
PR00-3-15-7 (LANL# 3553)	15.5 [4.7]	Tuff	Within opal vein zone, pinkish, contains few opal nodules
PR00-3-15-8 (LANL# 3554)	12.5 [3.8]	Opal vein	N20E trend, crystalline, variable thickness, cuts nonwelded tuff
PR00-3-15-9 (LANL# 3555)	29 [8.8]	Tuff	Altered, silicified, pinkish and fine grained
PR00-3-15-10 (LANL# 3556)	29.4 [9.0]	Tuff	Nonwelded, collected within silicified zone, pinkish
PR00-3-15-11 (LANL# 3557)	43 [13.1]	Tuff	Nonwelded, cut by few opal veins, pinkish
PR00-3-15-12 (LANL# 3558)	82 [25]	Tuff	Nonwelded, pinkish, pumice-rich
PR00-3-15-13 (LANL# 3559)	200 [61]	Tuff	Nonwelded, pinkish, friable, pumice-rich, and cavernous
Above and east of Papoose Lake Sill			
PR00-3-14-2 (LANL# 3538)	~150 [46]	Tuff	Pale pink tuff cut by opal veins, dark red halo, pumice clasts
PR00-3-14-3 (LANL# 3539)	~150 [46]	Tuff	Same as LANL# 3538 with thicker veins and alteration
PR00-3-14-4 (LANL# 3540)	~150 [46]	Tuff	Same tuff with pumice clasts and nodule
PR00-3-14-5 (LANL# 3541)	~150 [46]	Tuff	Same tuff with corroded pumice clasts and devitrified
PR00-3-14-6 (LANL# 3542)	~150 [46]	Opal vein	1 cm wide in a similar tuff, contains fresh pumice clasts
PR00-3-14-7 (LANL# 3543)	~150 [46]	Tuff	Same tuff with dense pumice
PR00-3-14-8 (LANL# 3544)	~150 [46]	Tuff	Same tuff with thick opal veins
PR00-3-14-9 (LANL#3545)	>150 [46]	Tuff	Tuff east of opal vein zone, gray, no veins, pumice less distinct
PR00-3-15-14 (LANL# 3560)	~400 [122]	Tuff	Nonwelded, matrix silicified, few opal veins, reddish brown
PR00-3-15-15 (LANL# 3561)	~400 [122]	Tuff	Nonwelded with nodules, pumice-rich, grayish, cavernous
PR00-3-15-16 (LANL# 3562)	~500 [152]	Tuff	Dark reddish orange, nonwelded, friable, massive

Table 11.4-1. Samples, Lithologic Types and Descriptions, and Measured and Estimated Distances of Tuff Samples from a Basaltic Intrusion (Cont.)

Above and east of Papoose Lake Sill (continued)			
PR00-3-15-17 (LANL# 3563)	720 [220], 60.0 [183] west of dike	Tuff	Moderately welded with opal nodules, grayish
PR00-3-15-18 (LANL# 3564)	695 [212], 38.5 [11.7] west of dike	Tuff	Moderately welded with opal nodules, orangish
PR00-3-15-19 (LANL# 3565)	660 [201], 3.0 [0.9] west of dike	Fused tuff	Fused with fiamme and nodules, pinkish brown
Beneath sill (Figure 11.4-1, Section B)			
PR00-3-16-1 (LANL# 3570)	Top part of sill	Basalt	25 ft (7.6 m) thick, sparsely porphyritic, amygdules
PR00-3-16-2 (LANL# 3571)	Contact	Basalt-tuff	Platy basalt, fused granular tuff, no vitrophyre
PR00-3-16-3 (LANL# 3572)	1 [0.3]	Tuff	Pinkish gray, medium grained, partially fused
PR00-3-16-4 (LANL# 3573)	4.4 [1.3]	Tuff	Nonwelded, bedded, coarse, and crystal-rich
PR00-3-16-5 (LANL# 3574)	4.4 [1.3]	Tuff	Fine grained, pinkish gray, tilted 20°S
PR00-3-16-6 (LANL# 3575)	15 [4.6]	Tuff	Moderately welded, light gray, contains lithics
PR00-3-16-7 (LANL# 3576)	21 [6.4]	Opal vein	2 ft (0.6 m) wide, fractured, orange and white veins
PR00-3-16-8 (LANL# 3577)	30.8 [9.4]	Opal vein	Host tuff fractured, same as LANL# 3576
PR00-3-16-9 (LANL# 3578)	34.2 [10.4]	Tuff	Nonwelded, light gray, and contains lithics
PR00-3-16-10 (LANL# 3579)	35 [10.7]	Tuff	Crystal-rich, coarse, pumice-rich, matrix-free
PR00-3-16-11 (LANL# 3580)	16 [4.9]	Opal	0.4-1.5 ft (0.1 to 0.5 m) thick, N-S trend, dips 65°E, (98 ft) (30 m) long
PR00-3-16-12 (LANL#3581)	8 [2.4]	Tuff	Host tuff for the (98 ft) (30 m) long opal vein

Source: Simmons 2002 [157578], SN-LANL-SCI-215-V1, pp. 13–27, 90–94.

Table 11.4-2. Subsurface Stratigraphic Information from Drill Holes along the Eastern Part of Yucca Flats Adjacent to Paiute Ridge

Stratigraphic Units (upper one third of section)		Drill Holes: Interval Thickness, *I* (m), and Depth to the Tops of Formations, *D* (m)																			
		U 3mk		U 7at		U 7bg		U 7bh		U 7bk		U 7bm		U 7bo		UE7h		UE 7m		U 7x	
		I	*D*	*I*	*D*	*I*	*D*	*I*	*D*	*I*	*D*	*I*	*D*	*I*	*D*	*I*	*D*	*I*	*D*	*I*	*D*
Qal (Qta)		65.5		82.3		48.8		54.9		41.1		92.4		138.7		51.8		61		67.1	
Tma	Ammonia Tanks	none	None	none	none	29	48.8	21.3	54.9	none	none	none	none	none	none	18.3	51.8	none	none	none	none
Tmab	Bedded Ammonia Tanks	none	None	none	none		70.1		68.6	none	none	none	none	none	none		62.5	none	none	none	none
Tmr	Rainier Mesa	56.4	65.5	21.3	82.3	67.1	77.7	48.8	76.2	54.9	41.4	95.1	92.4	47.2	138.7	82.3	70.1	94.5	61	73.2	67.1
Tx (Tmrl/Ta)	Rainier Mesa/ Vitrophyre	24.4	**121.9**	35.1	**103.6**	32	**144.8**	39.6	**125**	38.1	**96**	59.4	**187.5**	39.6	**185.9**	4.6	**152.4**	39.6	**155.4**	≥73.1	**140.2**
Tpc	Tiva Canyon	nd	nd	nd	nd	nd	nd	nd	nd	nd	nd	nd	nd	nd	nd	nd	nd	nd	nd	nd	nd
Tpt	Topopah Spring	nd	nd	nd	nd	nd	nd	nd	nd	nd	nd	nd	nd	nd	nd	nd	nd	nd	nd	nd	nd
Tac	Calico Hills	nd	nd	nd	nd	nd	nd	nd	nd	nd	nd	nd	nd	nd	nd	nd	nd	nd	nd	nd	nd
Tw	Lower Wahmonie	24.4	146.3	21.3	138.7	18.3	176.8	19.8	164.6	21.3	134.1	18.3	246.9	15.2	225.6	18.3	157	21.9	195.1	nd	nd
Tc	Crater Flat	56.4	170.7	51.8	160	43.3	195.1	82.3	184.4	44.2	155.4	80.8	265.2	51.8	240.8	59.4	175.3	51.2	217	nd	nd
Tcb	Bull Frog	nd	nd	nd	nd	nd	nd	nd	nd	nd		nd	nd	nd		nd		nd	nd		
	Surface elevation (m)		1297.8		1336.6		1337.5		1338.7		1333.5		1291.7		1319.2		1338.7		1315.2		1328.9
	Drill hole depth (m)		381		460.4		396.2		396.2		376.4		472.4		609.6		780.6		587		533.4
Depth to pervasive zeolitization (m)			281.9		182.9		167.6		157		198.1		243.8		262.1		152.4		240.8		222.5

NOTE: nd means "not defined." Values in bold-type indicate depth to Rainier Mesa Vitrophere Unit.

Source: Drellack and Thompson 1990 [156446], pp. 60, 64, 66, 68–69, 118, 122, 124, 126–127.

Table 11.4-3. Quantitative Mineral Abundances by XRD for Selected Tuff Samples Adjacent to Papoose Lake Sill in the Northern Part of Paiute Ridge

Sample	Smec-tite	Clino-ptilote	Chab-azite	Tridy-mite	Crist-obalite	Opal-CT	2ndary Quartz	K-Spar	Plagio-clase	Glass	Hem-atite	Bio-tite	Horn-blende	Augite	Cal-cite	Total
PR00-3-15-01, LANL# 3547	18.5	—	—	—	—	—	—	8.1	52.8	—	3.0	2.1	—	16.5	—	101.0
PR00-3-15-02, LANL# 3548	—	—	0.8	0.9	0.4	—	5.7	1.0	8.2	79.8	—	0.2	—	—	—	97.1
PR00-3-15-03, LANL# 3549	—	—	1.0	3.4	0.9	—	3.7	3.5	13.9	75.2	—	0.5	—	—	—	102.0
PR00-3-15-04, LANL# 3550	—	—	—	1.4	1.9	—	3.6	3.2	11.4	75.4	—	0.2	—	—	—	97.1
PR00-3-15-05, LANL# 3551	—	—	—	—	—	—	5.3	4.7	7.5	82.8	0.3	1.5	—	—	—	102.2
PR00-3-15-06, LANL# 3552	—	55.9	—	—	1.0	27.7	2.4	7.0	5.6	—	—	0.1	—	—	—	99.6
PR00-3-15-07, LANL# 3553	—	2.8	—	—	—	—	2.9	8.3	8.0	71.8	0.2	2.7	—	—	4.5	101.3
PR00-3-15-08, LANL# 3554	—	26.5	—	—	—	18.7	22.7	13.5	16.9	—	—	0.4	0.1	—	—	98.8
PR00-3-15-09, LANL# 3555	—	64.6	—	—	0.9	23.5	2.3	4.6	8.3	—	—	0.1	—	—	—	104.3
PR00-3-15-10, LANL# 3556	—	6.8	4.6	—	—	—	4.5	6.4	6.4	65.5	0.1	0.9	—	—	2.9	98.2
PR00-3-15-11, LANL# 3557	—	3.8	—	—	—	—	7.3	5.1	8.4	74.5	—	1.5	—	—	1.3	102.0
PR00-3-15-12, LANL# 3558	—	—	—	—	—	—	3.6	2.9	6.5	84.7	0.1	0.4	—	—	—	98.1
PR00-3-15-13, LANL# 3559	0.1	—	—	—	—	—	3.8	3.9	7.1	85.2	0.2	1.4	—	—	—	101.6

NOTES: Mineral abundances are in weight percent — means "not detected"

Source: Simmons 2002 [157578]; SN-LANL-SCI-215-V1, p. 59.

Table 11.4-4. Comparison of Equation of State Properties of Pure Water at 1,200ºC

p (bars)	Density (kg/m^3)		Enthalpy (kJ/kg)		Energy (kJ/kg)		Viscosity (μPa s)	
	FLOTRAN	HGK	FLOTRAN	HGK	FLOTRAN	HGK	FLOTRAN	HGK
1	0.14709	0.14708	5,131.03	5,150.0	4,451.18	4,470.1	40.66	40.38
5	0.7356	0.7354	5,130.4	5,149.2	4,450.7	4,469.4	40.89	40.39
10	1.4714	1.4710	5,129.7	5,148.2	4,450.1	4,468.4	41.18	40.42

NOTES: The comparison is between Haar et al. (1984 [105175]) (the HGK columns) and the equation of state used by FLOTRAN based on the International Formulation Committee of the Sixth International Conference on Properties of Steam (IFC 1967 [156448]) with the reported range of validity of $0 < p < 165.4 \times 10^5$ Pa (165.4 Bars) and $0 < T < 800$°C.

Source: Simmons 2002 [157578]; SN-LANL-SCI-215-V1, pp. 102–103.

Table 11.4-5. Basalt and Tuff Hydrothermal-Model Parameters for Fracture (f) and Matrix (m) and Dual-Continuum Parameters Used in the THC Simulations

Property	Symbol	Units	Mafic Intrusion	Tuff Host Rock
Fracture Permeability	k_f	m^2	2.74×10^{-9}	2.74×10^{-9}
Matrix Permeability	k_m	m^2	1.0×10^{-20}	4.66×10^{-14}
Fracture Porosity	ϕ_f	—	1.0	1.0
Matrix Porosity	ϕ_m	—	0.05	0.47
Rock Density	ρ_r	kg m^{-3}	2,830	2,410
Specific Heat	C_p	J kg^{-1} K^{-1}	1,010	1,100
Thermal Conductivity	C_{wet}	J m^{-1} s^{-1} K^{-1}	1.93	0.61
Thermal Conductivity	C_{dry}	J m^{-1} s^{-1} K^{-1}	1.93	0.61
Gaseous Diffusivity	D	m^2 s^{-1}	2.13×10^{-5}	2.13×10^{-5}
Temperature Exponent	θ	—	1.8	1.8
Tortuosity	τ	—	1.0	1.0
Residual Saturation	s_r	—	0.04	0.04
van Genuchten Parameter	α_f	Pa^{-1}	8.92×10^{-4}	8.92×10^{-4}
van Genuchten Parameter	α_m	Pa^{-1}	4.15×10^{-5}	4.15×10^{-5}
van Genuchten Parameter	λ_f	—	0.449	0.449
van Genuchten Parameter	λ_m	—	0.327	0.327
Initial Temperature	T_0	ºC	1,200	30
Initial Saturation	s_l^0	—	0.0	0.4
Dual Continuum Parameters				
Fracture Volume Fraction	ε_f	—	0.01	0.01
Matrix Block Size	l_m	m	0.5	0.5
Frature-Matrix Area Factor	σ_{fm}	—	100	0.1

Source: Simmons 2002 [157578]; SN-LANL-SCI-215-V1, p. 104.

12. ANALOGUES TO SATURATED ZONE TRANSPORT

12.1 INTRODUCTION

This section discusses analogues to transport in a saturated environment under oxidizing conditions, such as that at Yucca Mountain. Most of the analogue sites studied to date in saturated environments occur in rock types dissimilar to the saturated zone (SZ) at Yucca Mountain, e.g., fractured crystalline granite or gneiss, or sandstone. However, some aspects of these systems have attributes or demonstrate processes that warrant attention with respect to Yucca Mountain and are included in this section. Section 12.1 briefly summarizes the main conclusions of past Yucca Mountain Site Characterization Project (YMP) analogue studies with respect to SZ transport. Section 12.2 provides a background by describing the SZ flow system at Yucca Mountain. Section 12.3 is a study of transport plumes formed from uranium mill tailings at selected sites in the western United States, and the relevance of this information to saturated transport in alluvium at Yucca Mountain. Section 12.4 provides examples from analogues of matrix diffusion and colloid transport in the SZ. The main ideas and conclusions are presented in Section 12.5.

12.1.1 Insights into SZ Transport from Previous Analogue Studies

Some of the processes relevant to radionuclide transport at saturated sites were discussed in *Yucca Mountain Site Description* (CRWMS M&O 2000 [151945], Section 13.4.3). The main points of those discussions are summarized here.

- Filtration of particulate matter is an efficient process at Poços de Caldas (CRWMS M&O 2000 [151945], Section 13.4.3.3). The colloidal material acts as largely irreversible sinks for many immobile elements, such as thorium and rare-earth elements.

- The redox front at Poços de Caldas provided direct evidence of the operation of flow channeling in fractures and solute transport in the rock matrix as the key controls on the shape and movement of the redox front. The very slow, diffusion-dominated movement of the redox front plays a significant role in retarding many trace elements (CRWMS M&O 2000 [151945], Section 13.4.3.3; Romero et al. 1992 [157573], pp. 471–472).

- Poços de Caldas also highlighted the importance of amorphous phases in suspension or as coatings on rock as the principal sorptive surfaces for many trace elements in solution (CRWMS M&O 2000 [151945], Section 13.4.3.3). Some of the fixing processes appeared to be irreversible over long time scales, compared to reversible sorption used in Performance Assessment (PA) models. Sorption onto fracture coatings, particularly calcite, also efficiently retards uranium transport in fractures at Palmottu (CRWMS M&O 2000) [151945], Section 13.4.3.3).

- The Chernobyl study (CRWMS M&O 2000 [151945], Section 13.4.3.3) showed that pathways of rapid groundwater contamination around Chernobyl may not be directly connected to the pathways of near-surface zones of preferential flow.

Other analogues were mentioned as multiple lines of evidence in *FY 01 Supplemental Science and Performance Analyses, Volume 1: Scientific Bases and Analyses* (BSC 2001 [155950], Section 12.4). Using Yucca Mountain as a self-analogue, it was possible to interpret groundwater hydrochemical data to estimate flow paths in the vicinity of Yucca Mountain (BSC 2001 [155950], Section 12.4.1). These estimated flow paths were shown to be consistent with flow paths predicted by the site-scale SZ flow model.

The initial phase of investigation of the Uranium Mill Tailing Remedial Action (UMTRA) sites discovered that some fraction of the total inventory of uranium mill tailings appears to be transported as a nonsorbing to weakly sorbing species under oxidizing conditions (BSC 2001 [155950], Section 12.4.2). This supported the TSPA-SR treatment of uranium as weakly sorbing (BSC 2001 [155950], Section 12.4.2).

12.2 HYDROGEOLOGY AND FRACTURE MINERALOGY OF THE SATURATED ZONE

The water table near the proposed Yucca Mountain repository block is currently at an elevation of approximately 730 m, more than 300 m below the proposed repository horizon (DOE 1998 [100548], Section 2.2.4). Water infiltrating the unsaturated zone (UZ) becomes recharge to the regional flow system. Water moves generally southeast beneath the (UZ) site before flowing south out of the volcanic rocks and into the thick valley fill of the Amargosa Valley. The hydraulic gradient is very low (~0.0001; Fridrich et al. 1994 [100575], p. 138) downgradient from Yucca Mountain, so that travel time of groundwater may be long. Near Yucca Mountain, volcanic rocks up to several thousand meters thick overlie the Paleozoic and older rocks of the region (DOE 1998 [100548], Section 2.2.4.1). Their hydrologic properties change substantially over short distances, which produces a complex hydrogeology. The volcanic-rock section becomes thinner to the south and is a lesser component of the saturated zone flow system in southern Amargosa Valley, where the major aquifer consists of Quaternary-Tertiary heterogeneous valley-fill deposits.

The dominant regional aquifer is the Paleozoic carbonate aquifer, consisting of marine limestones, dolomites, and minor clastic sediments thousands of meters thick. In the vicinity of Yucca Mountain, the carbonate aquifer is not tapped as a source of groundwater because of its great depth (DOE 1998 [100548], Section 2.2.4.1).

Luckey et al. (1996 [100465], pp. 18–20) divided the volcanic rocks below the water table into four hydrogeologic units. From top to bottom, these are the upper volcanic aquifer, the upper volcanic confining unit, the lower volcanic aquifer, and the lower volcanic confining unit. The upper volcanic aquifer is composed of the Topopah Spring Tuff, which occurs in the UZ near the repository, but is present beneath the water table to the east and south of the potential repository and in Crater Flat. The upper volcanic confining unit includes the Calico Hills Formation and the uppermost, unfractured part of the Prow Pass Tuff in areas where they are saturated. The lower volcanic aquifer includes most of the Crater Flat Group (Luckey et al. 1996 [100465] pp. 18–20), and the lower volcanic confining unit includes the lowermost Crater Flat Group and deeper tuffs, lavas, and flow breccias. The upper volcanic aquifer underlying Yucca Mountain is generally productive and provides groundwater for the site. The main distinction between SZ volcanic aquifers and confining units is that the aquifers tend to be more welded and contain more

permeable fractures than the aquitards. However, alteration of the nonwelded tuffs to zeolites and clays, which reduces permeability, is more pronounced at depth. The increase of pressure with depth also reduces fracture permeability, such that the overall tendency is toward decreased permeability with depth, even in aquifers.

The chemistry of SZ waters beneath Yucca Mountain (Oliver and Root 1997 [100069]) reflects processes that affected these waters as they flowed to the Yucca Mountain area from recharge areas to the north (McKinley et al. 1991 [116222]). In general, they are dilute sodium bicarbonate waters that are neutral to mildly alkaline and mildly oxidizing. Similarities between the composition of SZ waters in the recharge areas north of Yucca Mountain and those beneath Yucca Mountain suggest that water compositions primarily reflect water-rock interactions in the recharge areas (DOE 1998 [100548], Section 2.2.4.3).

After reaching the water table, flow continues generally to the southeast away from the potential repository. The majority of saturated flow occurs in zones with enhanced permeabilities caused by fractures. Retardation processes such as sorption, matrix diffusion, and dispersion would also function in the SZ. Water may contact sorbing zeolites in the Calico Hills Formation and Prow Pass Tuff, and, as in the UZ, fracture minerals may have a significant effect on both flow and transport.

Fracture-filling minerals in the SZ include smectite, manganese oxide minerals, hematite, quartz, opal-CT, calcite, and clinoptilolite and mordenite, the same zeolites that characterize the altered rock matrix below the water table (Carlos et al. 1995 [101326], pp. 8–12). Laboratory experiments have shown that fractures containing smectite, manganese oxides, and calcite have particular affinity for plutonium retention (DOE 1998 [100548], Section 2.2.5.2). Thus, analogues related to transport through saturated, oxidizing environments need to consider the role of fracture-filling minerals such as these in retarding the migration of radionuclides.

12.3 URANIUM MILL TAILINGS

12.3.1 Purpose and Approach

This section summarizes pertinent information on the transport of uranium and other constituents of interest in alluvial aquifers at UMTRA sites. The YMP is particularly interested in the dispersion characteristics of the contaminant plumes and in the retardation behavior of constituents, such as uranium, that are found in nuclear waste to be emplaced in a repository.

The scope of Section 12.3 is limited to a review of the subsurface transport behavior of uranium and other constituents of interest at UMTRA sites. All UMTRA sites have been evaluated to identify those sites appropriate for more detailed analysis. The emphasis here is on the transport behavior of uranium and other constituents in alluvial deposits. This is because the potential transport pathways from Yucca Mountain to the accessible environment pass through alluvium and because there are no UMTRA sites with bedrock similar to the volcanic rocks at Yucca Mountain.

The approach is to evaluate the UMTRA sites in terms of aquifer materials, hydrologic characteristics, and groundwater chemistry. Those sites that are closest in hydrologic and

chemical characteristics to the alluvium downgradient from Yucca Mountain and for which sufficient data are available for detailed transport analysis are considered in more detail.

12.3.2 Background

The UMTRA Project was authorized by Congress in 1978 to clean up 24 inactive uranium ore processing sites (DOE 1996 [154693]). Currently, there are 20 UMTRA Project sites in the continental United States, located mostly in the western states (Figure 12-1). Many of the sites are located in the Rocky Mountain states of Colorado (seven sites), Utah (three sites), Wyoming (two sites), New Mexico (two sites), and Idaho (one site). Sites are also located in Arizona (two sites), Oregon (one site), and Texas (one site) (DOE 2000 [157603]).

Most of the sites consisted of a uranium processing mill with associated waste streams and ore and tailings piles. The ore and tailings piles were situated directly on surface soils. Rain and snow melt percolated through the piles, leaching uranium and other constituents, before entering the underlying shallow groundwater systems. The UMTRA Project has monitored the concentrations of radionuclides and other contaminants in shallow groundwaters beneath and downgradient from these sites for 15 to 20 years. The information obtained provides useful insight on the fate and transport of uranium and related ore constituents in shallow aquifers. The information obtained on transport in alluvial aquifers could be particularly useful in the development of models and calculations for radionuclide transport in shallow alluvial aquifers down gradient from Yucca Mountain.

12.3.3 Selection of Analogue Sites

The magnitude of operations at the various UMTRA sites was quite variable. Sites such as Grand Junction, Rifle, and Naturita in Colorado had large operations that resulted in large tailings piles. Operations at Cannonsburg in Pennsylvania and Spook in Wyoming were much smaller, with correspondingly smaller tailings piles. Other sites were in between these two groups in terms of magnitude of operations and size of the tailings piles. The magnitude of the operation is important in this discussion, because the magnitude of the site-characterization activities undertaken by the UMTRA Project was generally proportional to the magnitude of the operation at a given site. To be useful to the Yucca Mountain Project, detailed site-characterization data are required on the flow and transport systems at these sites. Only a limited number of UMTRA sites have been investigated in sufficient detail to be of use as analogues to the transport of uranium and other constituents of interest in the alluvial part of the Yucca Mountain flow system.

The history of operations at the various sites was also quite variable. Operations at the Old Rifle site started as early as 1924. Most of the sites started operation in the mid to late 1950s and ended operations in the early 1960s to early 1970s. During the 1980s and 1990s, the tailings piles located at the 24 sites were either capped in place or removed to another location and encapsulated. Therefore, the tailings piles were sources of contaminants for subsurface transport for, at most, 30 to 70 years.

The ores processed at the various locations contained other chemical elements besides uranium and its daughter products. These elements included vanadium, arsenic, selenium, manganese, molybdenum, barium, and other trace metals. Most of these ore "byproducts" ended up in the

tailings piles. In addition, chemicals used in processing the ore were also dumped on the tailings piles. Important among the latter were sulfuric acid, nitric acid, ammonium hydroxide, and organic complexing agents. While the mills were in operation, rain and melted snow infiltrated into the uncovered tailings piles and leached constituents from the tailings. Liquid spills or leaks from site operations also infiltrated into the subsurface. These spill, leak, and leach solutions have since percolated downward through the subsoils and sediments beneath the sites and reached groundwater, forming plumes of contaminants in shallow aquifers.

Those UMTRA sites where the most extensive subsurface characterization and groundwater monitoring activities were performed are of the most interest to the YMP. The transport of contaminants in groundwater is controlled by numerous site-specific factors. Part of the value of UMTRA sites as analogues, therefore, is the site-specific information they can provide on the factors that control the transport behavior of important constituents such as uranium. Other parameters used to screen sites for more detailed discussion include the hydrogeology and hydrology of the shallow aquifers, and groundwater chemistry. The intent was to select sites with alluvial aquifers and low-ionic-strength groundwaters. The sites chosen for detailed discussion in this report are the Gunnison and New Rifle sites in Colorado.

12.3.3.1 Gunnison, Colorado, UMTRA Site

The following discussion is based primarily on information presented in the *Final Site Observational Work Plan for the UMTRA Project Gunnison Site* (DOE 2001 [156666]) and "Groundwater Hydrology Report" Attachment 3 of *Remedial Action Plan and Site Design for Stabilization of the Inactive Uranium Mill Tailings Site at Gunnison, Colorado, Final* (DOE 1992 [154692]). The Gunnison processing site is located adjacent to the city of Gunnison in Gunnison County, Colorado, on a drainage divide between the Gunnison River and Tomichi Creek in the Gunnison River valley (Figure 12-2). Uranium was processed at the site from 1958 to 1962. Approximately 719,000 yd^3 (550,000 m^3) of contaminated material including tailings were originally present on 68 acres (28 hectares). Between 1992 and 1995, the contaminated material was moved to the Gunnison disposal site, approximately 6 mi (10 km) from the processing site.

The processing site was located on floodplain alluvium between the Gunnison River and Tomichi Creek. The site is about 0.4 mi (0.6 km) east of the Gunnison River and 0.4 mi (0.6 km) west of Tomichi Creek (Figure 12-2). It is bounded on the west by small storm drainage ditches and on the south and west by irrigation ditches. The climate at the site is semi-arid, with an average annual precipitation of 10.5 in. (27 cm), of which approximately half is contributed by snowfall (DOE 2001 [156666], Section 3.1). The average depth to groundwater beneath the site is 5 ft (1.5 m). The uppermost (unconfined) aquifer at the site is in the floodplain alluvium of the Gunnison River and Tomichi Creek. These alluvial deposits extend to at least 110 ft (34 m) beneath the processing site. The aquifer is recharged from rain, snowmelt, the Gunnison River, Tomichi Creek, and seasonal irrigation ditches around the site. The groundwater flows southwest at an average velocity of 270 ft (82 m) per year. Groundwater from beneath the site discharges into the Gunnison River and Tomichi Creek (DOE 1992 [154692], pp. 18-20).

Tailings seepage has contaminated the alluvial groundwater beneath and downgradient from the processing site. Sulfuric acid was used extensively in ore processing at the site (DOE 1992

[154692], p. 23). Because sulfate is a conservative constituent (i.e., is not retarded) in oxidizing groundwaters, it can be used to delineate the maximum extent of movement of site-related contaminants in groundwater. A sulfate plume has been delineated that originates at the site and extends approximately 7,000 ft (2,000 m) in a southwesterly direction (Figure 12-3). Even though the plume intersects, and possibly flows beneath, the Gunnison River, sulfate is conservative relative to uranium at this site. The inferred areal shape of the plume suggests only limited lateral dispersion over most of the length of the plume. A lateral pinching of the plume is also inferred by its shape. Borehole lithology logs show a local variation in unit thicknesses close to the narrowing of the plume. Here, the uppermost sand and gravel unit is about twice its thickness in adjacent boreholes and appears to fill a paleochannel cut into the underlying clayey sand and gravel unit (DOE 1992 [154692], p. 16). The highest concentration contours of both the sulfate and uranium plumes (DOE 1992 [154692], pp. 31, 35, Figures 12-3, 12-4) are tied to a water analysis from this location. Therefore, the widths of the plumes may be locally constrained by geohydrologic variations in the subsurface alluvial deposits. Interpretations of plume shape must be tempered by the fact that the number of sampling points available to construct the plume map was limited. The maximum concentrations of sulfate in groundwaters along the length of the plume show only limited variation (715–378 mg/L). This suggests that downgradient dilution of contaminants originating at the processing site is limited.

A uranium plume has also been delineated in association with the Gunnison site (Figure 12-4). The inferred plume has a shape and lateral extent very similar to the inferred sulfate plume (Figure 12-3). The similar shapes of the two inferred plume maps suggest that the narrow shape of the uranium plume is locally controlled by geohydrologic variations in the alluvium, described above, and not directly related to chemical conditions in the alluvial aquifer. For example, the possibility that lower uranium concentrations outside the inferred plume could simply reflect more reducing conditions that lead to the removal of uranium from groundwater is not supported by the data. The similarity in the lengths of the inferred uranium and sulfate plumes suggests that at least some of the uranium originating from the site may have been transported with little or no retardation. However, the groundwater concentrations of uranium decrease more rapidly with distance from the site than the sulfate concentrations. One possible explanation for the different concentration gradients is that the source terms increased with time. Another possible explanation is that the travel time for uranium was longer than the travel time for sulfate (i.e., that uranium was retarded to some degree). Laboratory data on sorption coefficients for uranium on alluvium from this area support the latter interpretation. The sorption coefficient values obtained for two alluvium samples were 1.70 and 5.24 mL/g (DOE 2000 [156666], Table 4-7). Note that dilution alone is not a likely explanation for the decreasing uranium concentrations downgradient, because sulfate concentrations do not decrease proportionately downgradient.

In summary, the groundwater data for the Gunnison site yield several conclusions that may be significant with regard to radionuclide transport in alluvium at the Yucca Mountain site. To the extent that the hydrology of the alluvial aquifers at the Gunnison site and Yucca Mountain are comparable, the Gunnison data suggest that: (1) lateral dispersion may be very limited downgradient, (2) dilution may not be a significant process over the transport distance in alluvium, and (3) uranium may be only slightly retarded by interaction with aquifer materials.

12.3.3.2 New Rifle Site, Rifle, Colorado

The Rifle UMTRA site is located along the Colorado River approximately 90 miles (144 km) east of Grand Junction, Colorado. The Rifle site actually consists of two separate sites, known as "Old Rifle" and "New Rifle." The Old Rifle site is located approximately 2.3 mi (3.7 km) northeast of the New Rifle site (Figure 12-5). The New Rifle site has been studied in greater detail and is for this reason the subject of this summary. The discussion in this section is based primarily on the *Final Site Observational Work Plan for the UMTRA Project New Rifle Site, Volumes 1 and 2* (DOE 1999 [154687]).

The New Rifle site processed uranium and vanadium ores from 1958 to 1984. The site is located within the broad alluvial floodplain of the Colorado River (Figure 12-6). The New Rifle site occupied much of the width of the Colorado River floodplain in a north-south direction (approximately 3,000 ft) (500 m), with the river located on the southern portion of the floodplain. The ore storage areas were located in the easternmost (upgradient) portion of the site, whereas the tailings pile was located in the western portion of the site. The mill and other buildings were located between the tailings pile and the ore storage areas. Approximately 3.5 million yd^3 (2.7 million m^3) of contaminated material were present on 238 acres (96 hectares) at the site. The transfer of this contaminated material to a disposal cell was completed in 1996.

The climate in the Rifle region is semi-arid, with an average total annual precipitation of 11 in. (28 cm) of which approximately one third is contributed by snowfall (DOE 1999 [154687], Section 3.2). The New Rifle site is underlain by 20–30 ft (6–9 m) of alluvium deposited by the Colorado River (DOE 1999 [154687], Section 5.1.2.2). Unconfined groundwater is present at the base of the alluvium at a depth of 5–10 ft (1.5–3 m) below the ground surface. In general, groundwater flows west-southwest in the alluvium and in the underlying bedrock (DOE 1999 [154687], Section 5.2.2). The alluvial deposits north of the river pinch out approximately 4 mi (6.4 km) to the southwest of the site (Figure 12-5). The alluvium is underlain by the Tertiary Wasatch Formation. The weathered upper few feet of the underlying Wasatch Formation also contain unconfined groundwater. Semiconfined and confined groundwater occurs in interlayered sandstone, siltstone, and claystone beds deeper in the Wasatch Formation. The hydraulic gradient in the deeper Wasatch Formation is upward (DOE 1999 [154687], Section 5.2.3). The major ion composition of waters in the unconfined aquifer is quite variable, largely because of seepage of contaminants from site operations. The downgradient groundwaters in the alluvial aquifer are primarily sodium-calcium sulfate waters. Upgradient (background) groundwaters tend to be of the sodium-calcium bicarbonate-sulfate-chloride type, similar to river waters and of much lower ionic strength than downgradient groundwaters (DOE 1999 [154687], Section 5.3.3).

Processing operations at various locations on the site have resulted in the seepage of contaminants into the alluvial aquifer and the upper Wasatch Formation. The major sources of contaminated seepage were the mill and other processing buildings and vats, vanadium and gypsum ponds, evaporation ponds, and the tailings pile (Figure 12-6). The degree to which contaminants have migrated from various source areas on the site has been investigated with an extensive monitoring program that has been in place since 1985. Monitoring wells have been used to obtain water levels and water samples from the alluvial aquifer and from the Wasatch Formation. Monitoring wells that intersect the Wasatch Formation are located within ~0.25 mi of the operations area. The proximity of the uranium source term to the underlying bedrock aquifer

with the upward hydraulic gradient and the disturbed nature of the UMTRA sites are two conditions that would not be analogous to transport at Yucca Mountain.

The locations of the monitoring wells are shown in Figure 12-7. The site-related inorganic constituents most prevalent in the alluvial aquifer include ammonia, calcium, nitrate, molybdenum, selenium, sulfate, and uranium. Of these constituents, the transport behavior of uranium and selenium are of interest to the Yucca Mountain Project. Nitrate and sulfate are potentially of interest as conservative constituents, to trace the maximum extent of movement of contaminants from the site. However, the existence of reducing conditions in various wells downgradient from the site calls into question the use of nitrate as a conservative constituent. Organic constituents such as kerosene were also released to the alluvial aquifer, particularly in and around the processing buildings and vats.

An estimate of the average extent of movement of contaminants from the site, without accounting for dispersion, can be obtained by calculating the distance groundwater could have traveled from the site since operations were initiated in 1958. The estimate is obtained using the following equation for the average linear groundwater velocity, V_x (Fetter 2001 [156668], p. 125):

$$V_x = - K/n_e(dh/dl), \qquad \text{(Eq. 12-1)}$$

where K is the hydraulic conductivity, n_e is the effective porosity, and dh/dl is the head gradient.

The average hydraulic conductivity for the New Rifle site is reported as 114 ft/day (0.040 cm/s) (DOE 1999 [154687], Section 5.2.2) was derived for the alluvial aquifer based on pump tests. The effective porosity was specified as 0.27. Based on water-level measurements taken in 1998, the average gradient was found to be 0.0030. Substituting these values into the equation yields the following linear groundwater velocity:

$$V_x = (-114 \text{ ft/day})/0.27(0.0030) = 1.27 \text{ ft/day}$$

A linear groundwater velocity of 1.27 ft/day (0.4 m/day) over a period of 40 years (1958–1998) leads to an estimated travel distance of 18,506 ft (5.64 km).

Because the site operations covered most of the alluvial terrace in a north-south direction and because most of the contamination is in the alluvial aquifer, significant lateral dispersion of contaminated groundwater is precluded by the decreasing width of the alluvial deposits in the downgradient direction. However, the magnitude of the source term for different contaminants may have varied over the site. For example, uranium processing facilities were located in the northern portion of the site. Therefore, uranium concentrations might be expected to be highest in groundwater beneath this portion of the site. In fact, well 655, located near the northern end of the site fence shown in Figure 12-7, has the highest uranium concentrations in any of the wells sampled in the 1998 and 1999 sampling rounds (DOE 1999 [154687], p. 5-56). The absence of similarly high concentrations in downgradient wells suggests the operation of some dispersive process. In addition to lateral dispersion, vertical advective dispersion of contaminants in the alluvial aquifer may also occur. However, the saturated thickness of the alluvial deposits is only 10–20 ft (3–6 m) (DOE 1999 [154687], p. 5-19). Furthermore, the hydraulic gradient in the underlying Wasatch Formation is upward. These observations suggest that vertical advective

dispersion of contaminants in the alluvial aquifer would be limited, but dilution may be an active process.

The use of sulfuric acid in processing ores at the site [inferred to be common practice (Merritt 1971 [156670], p. 29)] would have resulted in seepage to the vadose zone with high concentrations of sulfate. The highest measured concentrations were observed in samples taken in the first two years of the monitoring program. The available data suggest that sulfate concentrations in groundwater beneath and downgradient of the site have generally been decreasing since approximately 1986, consistent with the fact that processing operations at the site ended in 1984. Analyses of groundwater samples from (background) wells in the Wasatch Formation located across the Colorado River and upgradient from the site indicate that these waters have lower sulfate concentrations than waters from the alluvial aquifer but substantially higher chloride concentrations. This suggests the SO_4^{2-}/Cl^- ratio may be useful in identifying groundwaters contaminated by site operations. Groundwaters from wells at background locations (DOE 1999 [154687], Appendix C) show that SO_4^{2-}/Cl^- ratios in the Wasatch Formation are less than 2.0, with most less than 0.5. Water samples from the Colorado River have SO_4^{2-}/Cl^- ratios in the range of 0.75 to 0.85. As shown in Figure 12-8, most water samples from wells located on the site have SO_4^{2-}/Cl^- ratios in the range of 10 to 20. This ratio decreases with distance downgradient. The SO_4^{2-}/Cl^- ratio returns to near-background values at wells 220 and 172, the wells farthest downgradient. Thus, the maximum distance contaminants appear to have traveled from the site, based on the SO_4^{2-}/Cl^- ratio of alluvial groundwater samples, is approximately 19,000 ft (5.8 km). This is similar to the maximum travel distance of 18,506 feet (5.64 km) calculated for groundwater based on hydraulic parameters.

The observed decreases in the SO_4^{2-}/Cl^- ratios (Figure 12-8) and SO_4^{2-} concentrations (6,000 to 2,000 mg/L) in alluvial groundwater with increasing distance downgradient suggests that these waters are progressively diluted with waters that have low SO_4^{2-}/Cl^- ratios and low SO_4^{2-} concentrations. Because there is an upward hydraulic gradient in the Wasatch Formation (DOE 1999 [154687], p. 5-27) and because Wasatch Formation groundwaters from upgradient wells have low SO_4^{2-}/Cl^- ratios (< 0.5) and low sulfate concentrations (< 500 mg/L), the diluting waters most likely come from the Wasatch Formation.

Measured uranium concentrations show a pattern similar to that observed in the SO_4^{2-}/Cl^- ratio data. Upgradient alluvial wells located on the eastern portion of the site have uranium concentrations between zero and 0.05 mg/L (Figure 12-9). Wells located near the former uranium processing buildings on site have the highest uranium concentrations of all water samples (0.4–0.5 mg/L). Note that waters with these uranium concentrations are undersaturated with respect to solid uranyl phases, as calculated by Jove Colon et al. (2001 [157472], p. 13, 14), for groundwater compositions typical of the New Rifle site. Uranium concentrations in alluvial groundwaters decrease downgradient and reach the 0.05 mg/L (background) level between 10,000 and 15,000 ft (3–4.6 km) downgradient (Figure 12-9). Thus, it appears uranium has not traveled downgradient as far as sulfate, although the exact travel distance is difficult to quantify because background values show such a large range (0–0.05 mg/L). The uranium "plume length" based on the 1998 sampling data (3–4.6 km) is considerably greater than the 1 km length proposed by Jove Colon et al. (2001 [157472], p. 24) as the "steady-state" length for uranium plumes in groundwater systems (i.e., the length at which uranium concentration in monitoring wells remains fairly constant). In fact, there is no evidence in the New Rifle data that the

uranium migration rate has decreased significantly with time, contrary to the conclusions reached by Jove Colon et al. (2001 [157472], p. 24).

Taking the maximum distance traveled by uranium as 13,000 ft (Figure 12-9) and the maximum distance traveled by sulfate as 18,000 ft (Figure 12-8), an estimated retardation factor (R_t) for uranium of 1.38 (i.e., 18,000/13,000) is obtained. Using the retardation equation (Freeze and Cherry 1979 [101173], Equation 9.14)

$$R_t = (1 + \frac{\rho_b K_d}{\phi}), \qquad \text{(Eq. 12-2)}$$

where ρ_b is the dry bulk density in g/cm^3 and ϕ is the porosity, we can solve for the sorption coefficient (K_d),

$$K_d = \frac{(R_t - 1)\phi}{\rho_b}. \qquad \text{(Eq. 12-3)}$$

Using values for the dry bulk density (ρ_b) and porosity given for the alluvial aquifer in DOE (1999 [154687]), we obtain the following result for the uranium sorption coefficient (K_d):

$$K_d = (1.38 - 1)0.25/1.52 = 0.06 \text{ mL/g}.$$

Batch-sorption coefficient measurements for uranium using alluvial materials from the New Rifle site and a synthetic groundwater show a range of coefficients from -0.3–1.4 mL/g, with an average value of 1.0 mL/g (DOE 1999 [154687], Table 4-6). The K_d calculated here falls within that range, but is lower than the mean average value. This difference may be partly accounted for by the fact that the calculated R_t is based on what may be closer to the maximum, rather than the average, distance traveled by uranium; therefore, the calculation yields a lower K_d.

It is possible also that some uranium could have been transported downgradient as part of a colloidal phase (including microbes). Such colloidal transport could carry the uranium at essentially the velocity of groundwater. As part of the Nye County Early Warning Drilling Program, several monitoring wells have been installed down gradient of the potential repository at Yucca Mountain. Colloid transport is being studied through analyses of groundwater samples collected from these wells (Kung et al. 2001 [157604]).

Selenium has been detected only in groundwaters from wells located within the boundaries of the original New Rifle site. There is no evidence of significant downgradient transport. This is probably a result of the combined effects of a smaller source term and higher sorption coefficients measured for selenium in contact with sediments from the alluvial aquifer (DOE 1999 [154687], pp. 5-41, 5-42).

In summary, the data available on uranium transport at the New Rifle UMTRA site suggest that dilution in the alluvial aquifer is a significant process downgradient from the site and that the sorption of uranium on alluvial sediments also occurs.

12.3.3.3 Summary and Conclusions of UMTRA Study

An evaluation of data available for 24 UMTRA sites determined that only a few of these sites are potentially useful in the evaluation of transport of radionuclides in the alluvial portion of the Yucca Mountain flow system. Most of the sites are of limited use either because they are situated in a hydrogeologic setting different from Yucca Mountain or because there is insufficient information available to perform an adequate evaluation of transport behavior. There are enough data available for the Gunnison and New Rifle sites to perform a useful analysis. The conclusions derived from an analysis of the Gunnison site are (1) that a fraction of the uranium originating at the site is transported in the alluvial aquifer at a rate similar to the rate at which a conservative constituent is transported, and (2) there is little evidence for dispersion of contaminants in the downgradient direction. For the New Rifle site, the main conclusions are (1) that dilution is a significant process in the downgradient direction and (2) that uranium is transported at a slower rate then conservative constituents, although a fraction of the uranium traveled almost as far. The conclusions regarding uranium transport distances relative to conservative constituents must be tempered somewhat by uncertainties regarding the potential presence of unidentified complexing agents, such as organic materials, that could form colloids and enhance uranium transport. An additional note of caution attaches to the use of laboratory batch-derived K_d values for the prediction of large-scale field transport, because the two parameters are conceptually and numerically different.

12.4 OTHER SATURATED ZONE ANALOGUES

12.4.1 Uranium Retardation under Oxidizing Conditions

Studies of the weathered zone overlying the Coles Hill, Virginia, uranium deposit indicate that the natural attenuation of uranium in oxidizing environments may occur in groundwaters with low dissolved carbonate/phosphate ratios (Jerden and Sinha 2001 [157474]). At the Coles Hill site, uranium concentrations are buffered to values <20 ppb due to the precipitation of low-solubility U(VI) phases. The attenuation mechanism involves the transformation of U(IV) coffinite, the primary ore, to U(VI) phosphate minerals. Above the water table in the soil zone, where phosphate minerals are rare, uranium is primarily associated with an aluminum phosphate of the crandallite mineral group and with phosphorous sorbed to ferric hydroxide mineral coatings. Experiments demonstrated that the transformation of U(IV) to U(VI) assemblages could occur in less than two months, given high enough phosphate levels. Model predictions agreed with the field observations: for oxidizing systems with relatively low dissolved carbonate/phosphate ratios, uranium may be immobilized by secondary uranium phosphate precipitation and sorption processes. It is unlikely that low dissolved carbonate/phosphate ratios would occur in bedrock aquifers at Yucca Mountain, but if use of phosphate-containing fertilizer contaminates the alluvial aquifer in Amargosa Valley, the carbonate/phosphate ratio could be lowered, making this a more analogous situation for Yucca Mountain.

12.4.2 Matrix Diffusion

12.4.2.1 El Berrocal

El Berrocal is an area approximately 100 km southwest of Madrid, Spain. The El Berrocal granite forms a large hill and contains a number of small, vein-hosted uranium ore bodies, one of which was the focus of analogue investigations (Figure 12-10). The El Berrocal granite has a uranium content that averages 16 mg/kg, with primary uranium occurring as accessory uraninite dispersed in the granite matrix (De la Cruz et al. 1997 [157473], pp. 82–83). Post-emplacement hydrothermal alteration mobilized some of the uranium, thorium, and rare-earth elements from the granite and redeposited them in a 2-m-wide, steeply dipping quartz vein more than 1 Ma (Rivas et al. 1998 [126287], pp. 15–16). Erosion and weathering exposed the vein-hosted mineralization, causing further elemental mobilization and transport. The groundwaters contain moderate to low concentrations of uranium (4×10^{-9} to 8×10^{-6} M) (De la Cruz et al. 1997 [157473], p. 81; this converts to 9.52×10^{-4} to 1.9 mg/L). Carbonate complexes are the dominant species in oxidized zones and U(IV) hydroxides in reduced zones. The general behavior of uranium can be accounted for by the kinetic control of the dissolution of the source term and solubility controlled by coprecipitation processes.

The multinational El Berrocal project had the objective of investigating these present-day, low-temperature processes, as well as the processes responsible for elemental retardation in the granite. In particular, the study investigated uranium mineral stability, degradation, and dissolution; uranium solubility and speciation; matrix diffusion in the rock adjacent to fractures, and colloidal transport of radionuclides. Study activities included blind predictive testing of geochemical codes and databases. The results of the project indicated that mobilized uranium and thorium tended to be associated by sorption and coprecipitation with certain fracture-coating minerals, notably iron oxyhydroxides and calcite. Enrichment of uranium by a factor of up to 6 was observed, and up to 3 for thorium, relative to the unaltered granite (Miller et al. 2000 [156684], p. 201). Considerable effort was made to understand these coprecipitation processes in order to improve thermodynamic models and databases for performance assessment (Section 15).

12.4.2.2 Matrix Diffusion Comparison Studies

The Palmottu, Finland, site in saturated, fractured gneisses and migmatites was the location of a matrix diffusion study. Radionuclide concentration profiles from a fracture in the rock matrix were examined in several different drillcores (Blomqvuist et al. 1995 [124640]). Alpha-autoradiography showed the distribution of radionuclides decreasing from the fracture surface into the rock matrix. Based on the findings of three drillcore samples, the profile of decreasing radioactive content could be traced >100 mm into the rock (Blomqvist et al. 1995 [124640], pp. 64–65). The radionucides were associated with clay particles and iron oxyhydroxides that had formed from alteration of feldspar and biotite grains. Selective leaching experiments showed that most of the radionuclides that had diffused into the rock matrix were only loosely bound to the iron-rich phases. In some samples, activity correlated to microfractures indicated that fluid flow was channelled even at the microscopic level, whereas in another sample diffusion was predominantly along grain boundaries. This supports the hypothesis that physical disruption around a fracture may enhance transport into the rock matrix (Blomqvist et al. 1995 [124640], pp. 27, 60, 63, 64).

A comprehensive investigation of matrix diffusion processes compared granite samples from a number of locations: the El Berrocal natural analogue site, Spain; the Stripa test mine, Sweden; the Whiteshell Underground Research Laboratory (URL), Canada; and the Grimsel Test Site, Switzerland (Heath 1995 [157478]). Each sample was taken from close to a hydraulically active fracture, cut to provide a series of slices parallel to the fracture, and characterized in detail. For all samples, the region of enhanced uranium mobility correlated with the zone of microstructural alteration in the rock adjacent to the fractures. The actual depth of enhanced uranium mobility varied from site to site; for instance, enhanced uranium mobility extended 35 mm in the shallow El Berrocal granite, but 50 mm in both the altered and unaltered URL granite.

Interpretation of the El Berrocal core sample data indicated the following: not only was matrix diffusion limited to the first few tens of millimeters of rock adjacent to the fracture surface, but also within the rock matrix the mobilized uranium was associated with secondary phases and located in microfissures along grain boundaries (Heath 1995 [157478], p. 51). There was a very good correlation between the distribution of the mobilized uranium, the redox conditions, and the isotopic disequilibrium. Heath (1995 [157478], p. 51) concluded from a combination of all of the data that a complex combination of matrix diffusion and chemical interaction had occurred between the rock and the mobile phases, rather than matrix diffusion alone. From this conclusion, Heath suggested the possibility that retardation processes that rely on matrix diffusion mechanisms may make little overall contribution to performance in a crystalline rock mass. However, the data from El Berrocal provide good evidence that, once radionouclides migrate into the rock matrix from the flowing fracture, they are effectively immobilized irrespective of the process involved.

12.4.3 Colloidal Transport in the SZ

Colloids are ubiquitous in all groundwaters (McCarthy 1996 [157479], p. 197). However, in deep crystalline rocks with a stable geochemical system, the colloid populations are low, ~25 μg/L. In contrast, shallow aquifer systems generally appear to have the largest colloid populations, even in the absence of geochemical stability. Enhanced colloidal populations occur in all rock types where there is some hydrogeochemical perturbation to the system. For example, in fractured granitic systems, colloid populations are 20 to 1,000 times higher in groundwaters affected by inputs of surface water or in hydrothermal zones with large temperature and pressure gradients, compared to stable hydrogeochemical systems (Degueldre 1994 [101128]).

The uptake and transport of radionuclides by colloids has been investigated in several analogue studies of natural systems with enhanced radionuclide content: Cigar Lake, Canada (Vilks et al. 1993 [108261]); Alligator Rivers, Australia (Seo et al. 1994 [157480], p. 75); El Berrocal, Spain (Rivas et al. 1998 [126287]); and Poços de Caldas, Brazil (Miekeley et al. 1992 [106762]). In most of these studies, it was found that some proportion of the total uranium, thorium, and rare-earth elements in the groundwater was associated with the colloids. This proportion was higher for thorium than for uranium because of thorium's lower solubility in most groundwaters. The rare earths generally show an affinity for colloids intermediate between uranium and thorium (Miekeley et al. 1992 [106762], pp. 429, 434).

Unambiguous evidence from natural systems indicating colloidal transport over long distances is rare. The only known example suggesting transport on the kilometer scale is at Menzenschwand,

Germany, where the Ti:Mg ratio and rare-earth-element composition of the natural colloids differed from that of the host granite but were similar to that of a neighboring gneiss several kilometers away and upgradient (Hofmann 1989 [125081], pp. 925–926). However, the flow system at Menzenschwand is not representative of a natural system, because it is perturbed by the presence of a uranium mine with associated fast flow.

Many analogue studies suggest that colloid transport in natural systems is significantly restricted. For instance, at Cigar Lake, the uranium and radium contents of colloids in the ore and the surrounding clay zones are significantly higher than in colloids from the sandstone host rock, indicating that the clay is an effective barrier to colloid migration (Vilks et al. 1993 [108261]). Similar results at Alligator Rivers and Morro de Ferro also suggest that colloids have a limited capacity for migration, because the concentrations of colloid-bound radionuclides outside the orebodies are relatively low (Miekeley et al. 1992 [106762], pp. 420, 432–433).

Colloid concentrations of 0.8–6.9 mg/L for particles greater than 30 nm were observed in two wells on Pahute Mesa at the Nevada Test Site (NTS) (Buddemeier and Hunt 1988 [100712], p. 537). One well was inside the Cheshire experimental site, and the second, a water well, was 300 m away. Tritium, krypton, strontium, cesium, antimony, cobalt, cerium, and europium were detected in pumped water from the water well. All of the cobalt, cesium, and europium were associated with colloids in samples from both locations. Buddemeier and Hunt (1988 [100712], p. 537) maintained that the presence of colloidal radionuclides outside the cavity indicates radionuclide transport as colloids.

In another study at the NTS (Kersting et al. 1999 [103282], p. 56), isotopic ratios of plutonium were used to fingerprint the source of plutonium detected in monitoring wells with a specific underground nuclear test, suggesting that the plutonium migrated a distance of 1.3 km. Plutonium has a tendency to strongly sorb to tuff minerals, which would retard its transport. Thus the observed presence of colloids in waters at the NTS and the observed association of plutonium with colloids were interpreted to indicate that radionuclide transport was expedited by colloids.

A similar conclusion was reported by Triay et al. (1997 [100422], p. 172) to explain the transport of plutonium and americium away from a low-level waste site in alluvial sediments at Mortandad Canyon at Los Alamos, New Mexico. These radionuclides were detected at depths of 30 m in monitoring wells in unsaturated tuff up to 3.4 km downgradient from the waste disposal site (Buddemeier and Hunt 1988 [100712], p. 536). The migration reportedly took place over a period of 30 years (Buddemeier and Hunt 1988 [100712], p. 536). Because sorption studies involving the alluvial sediments suggested that plutonium and americium should be relatively immobile, the observed movement of radionuclides was reported by Triay et al. (1997 [100422], p. 172) to suggest that the transport of plutonium and americium through alluvium resulted from association with highly mobile colloids.

These observations lend support to the concept that radionuclide transport in the far field can be facilitated by colloids, but so far no natural analogue studies have been able to quantify the importance of this process.

12.5 CONCLUSIONS

UMTRA Study: Only a few of the UMTRA sites are potentially useful in the evaluation of radionuclide transport in the alluvial portion of the Yucca Mountain flow system. Most of the sites are of limited use either because they are situated in a hydrogeologic setting different from Yucca Mountain or because there is insufficient information available to perform an adequate evaluation of transport behavior. Enough data were available for the Gunnison and New Rifle sites to perform a useful analysis. The conclusions derived from an analysis of the Gunnison site are: (1) a fraction of the uranium originating at the site is transported in the alluvial aquifer at a rate similar to the rate at which a conservative constituent is transported, and (2) there is little evidence for lateral dispersion of contaminants in the downgradient direction. For the New Rifle site, the main conclusions are: (1) dilution is a significant process in the downgradient direction, and (2) uranium is transported more slowly than conservative constituents. The conclusions regarding uranium transport rates relative to conservative constituents must be tempered by uncertainties regarding the potential presence of unidentified complexing agents.

Diffusion: Matrix diffusion in crystalline rock is generally limited to only a small volume of rock close to fractures, but even a small volume can make a significant difference in radionuclide retardation.

Sorption onto fractures: Comparison of the results from a number of analogue study sites shows that similar sorption behavior is seen at many locations in crystalline rocks. For example, uranium and rare earth elements are frequently associated with calcite and iron oxyhydroxides. However, because it is often impossible to define in detail the paleohydrological history of a site, it is difficult to identify the unique effects of recent low-temperature retardation events. This is possibly the reason for the anomalous observations at El Berrocal related to limited observed uranium sorption on iron oxyhydroxides.

Although several natural analogue studies have demonstrated the effect of sorption and precipitation processes on fracture surfaces, none has been able to distinguish clearly between these processes or to provide quantitative data on retardation with respect to transport of trace elements in natural waters. However, these studies do highlight which phases are most active, and they provide useful information on the effect of interaction between solutes and the rock surface.

Colloid transport: In most studies of natural systems, it was found that some portion of the total uranium, thorium, and rare-earth elements in the groundwater was associated with colloids. Unambiguous evidence from natural systems indicating colloidal transport over kilometer-scale distances is limited to a few reports. Observations from such places as Los Alamos and the NTS lend support to the concept that radionuclide transport in the SZ can be facilitated by colloids, but so far no natural analogue studies have been able to quantify the importance of this process.

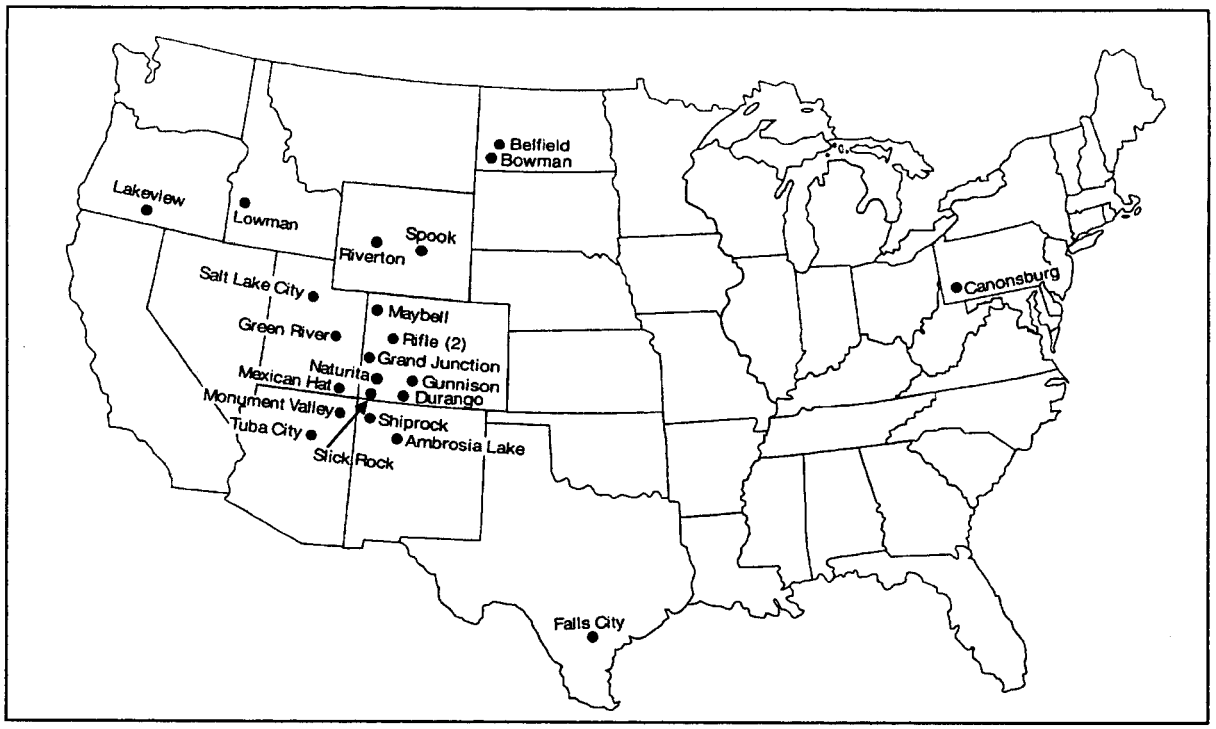

Source: Modified from DOE 2000 [157603].

Figure 12-1. Locations of UMTRA Ground Water Project Sites

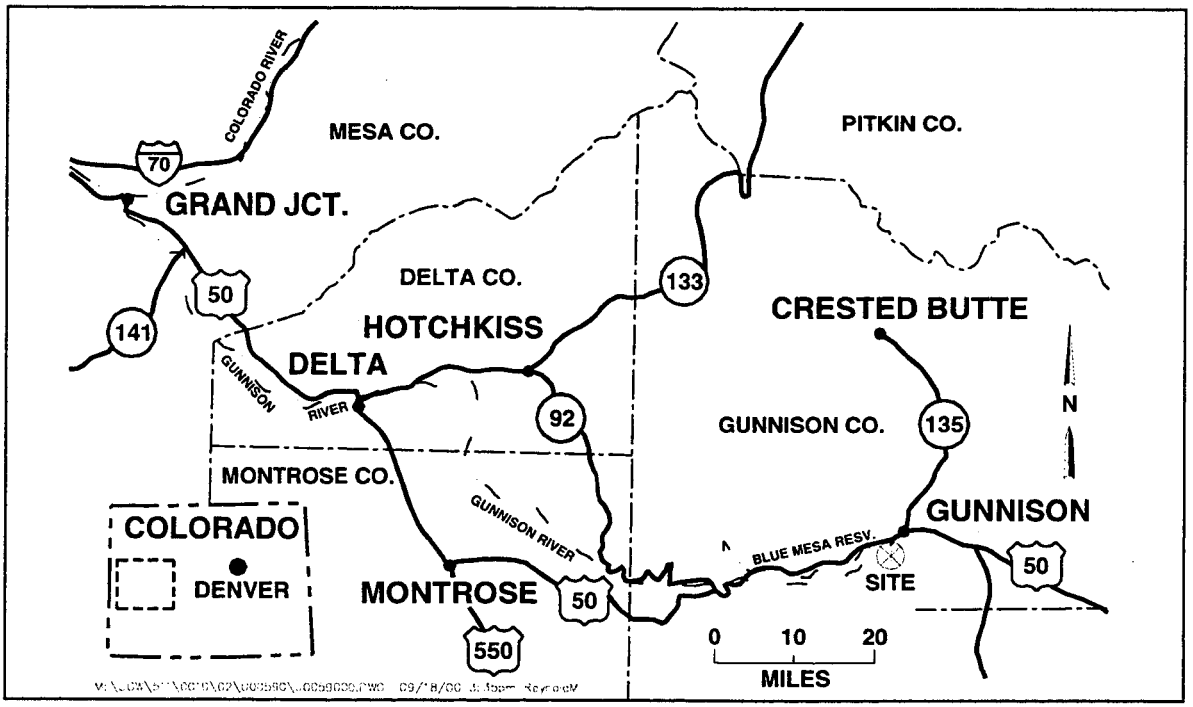

Source: DOE 2001 [156666], Figure 1-1.

Figure 12-2. Location Map for Gunnison UMTRA Site

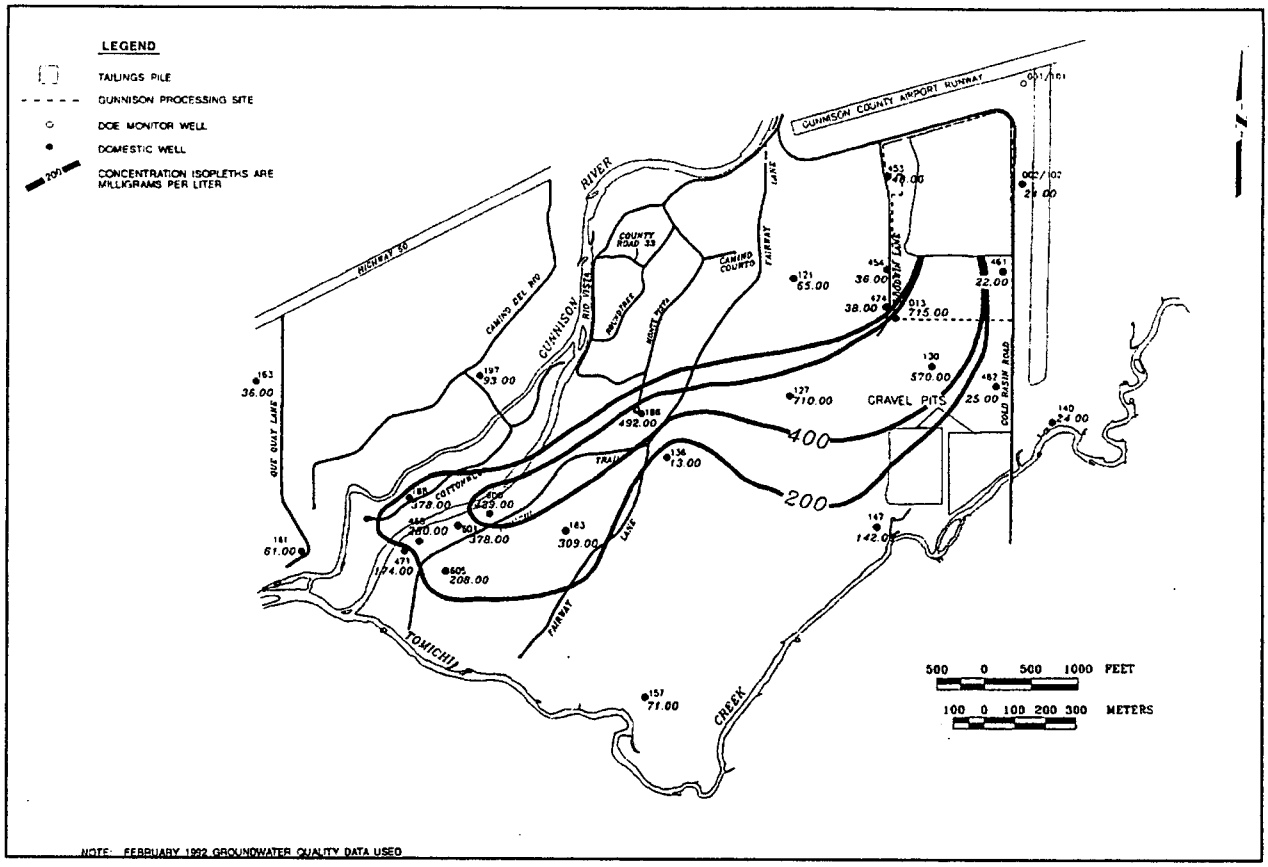

Source: DOE 1992 [154692], Figure 3.10.

Figure 12-3. Plume Map of Sulfate Concentrations (mg/L) in Alluvial Groundwater at Gunnison UMTRA Site

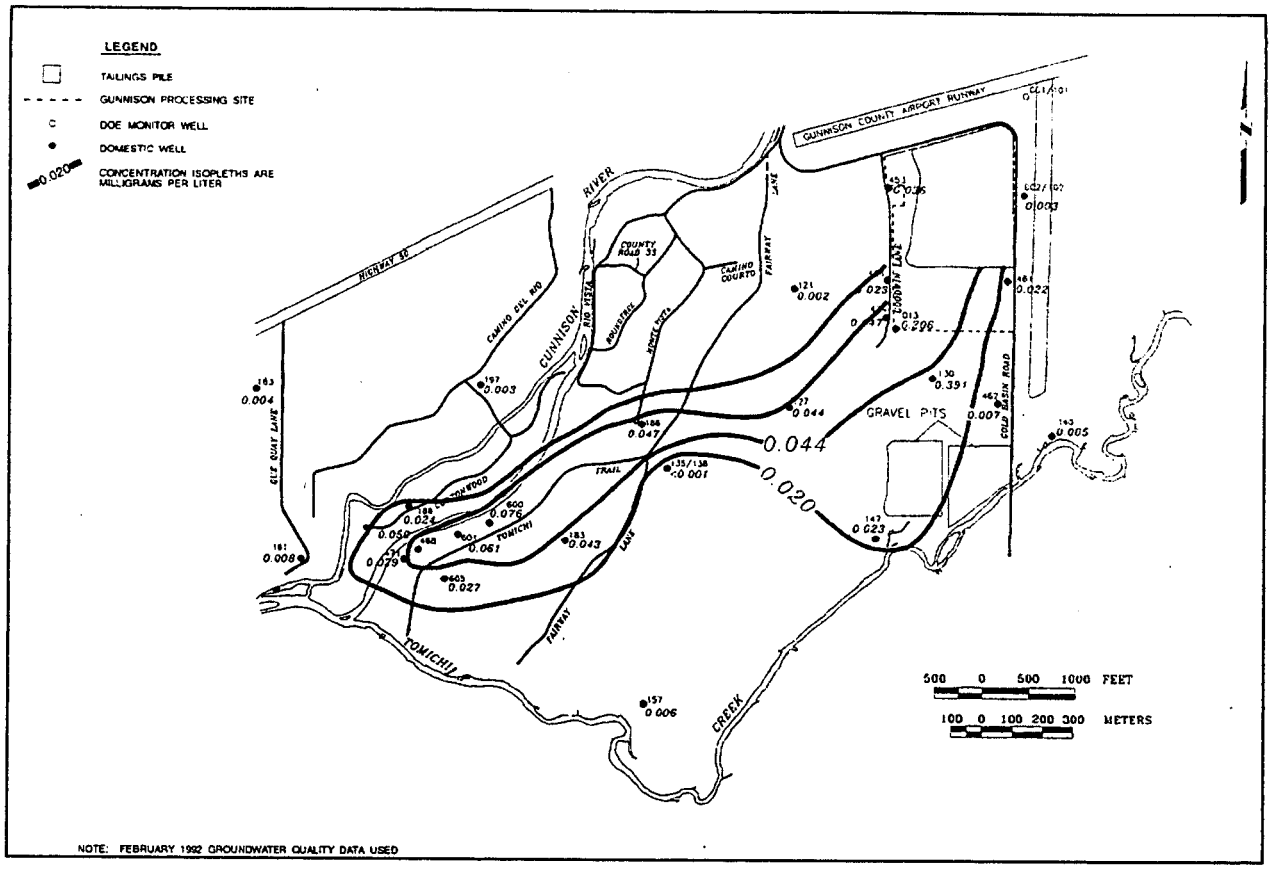

Source: DOE 1992 [154692], Figure 3.12.

Figure 12-4. Plume Map of Uranium Concentrations (mg/L) in Alluvial Groundwater at Gunnison UMTRA Site

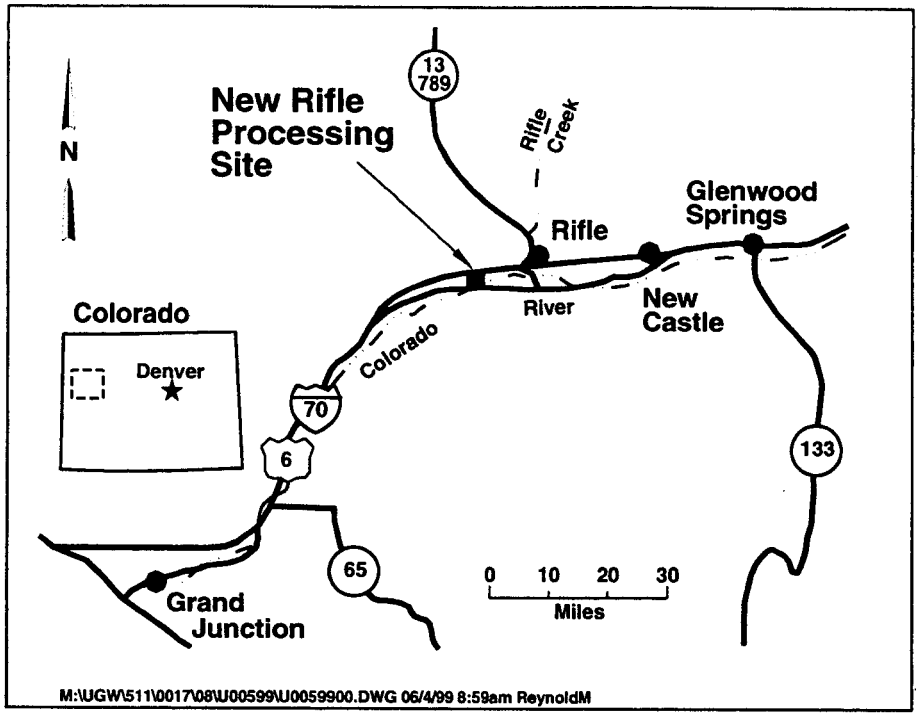

Source: DOE 1999 [154687], Figure 1-1.

Figure 12-5. Location Map for New Rifle UMTRA Site

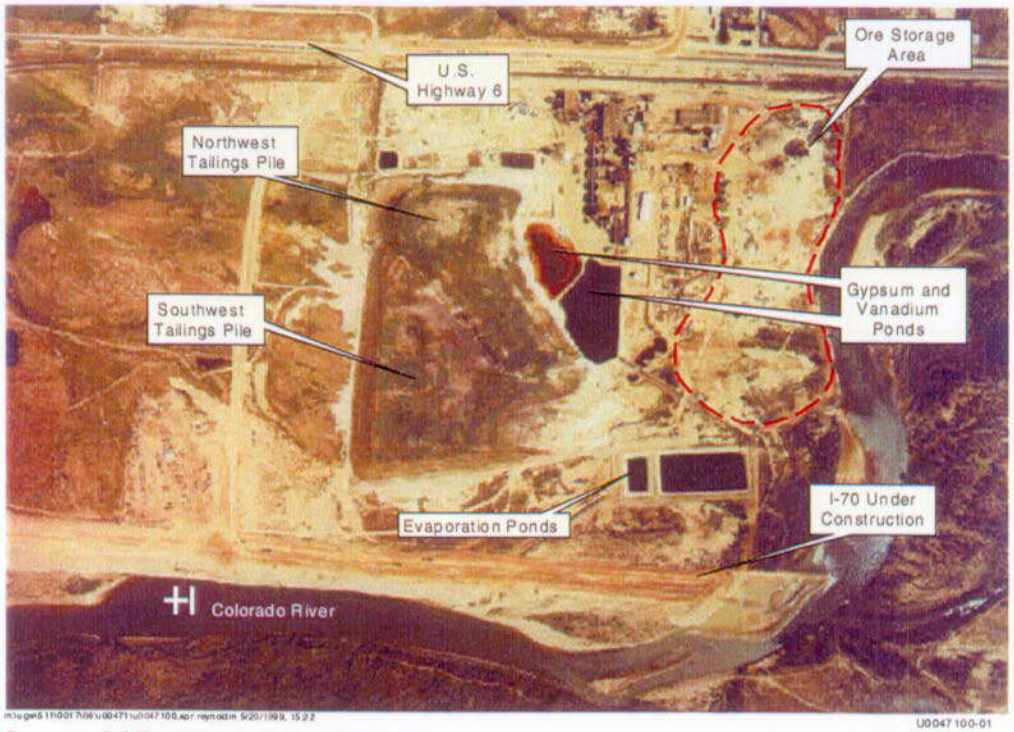

Source: DOE 1999 [154687], Figure 3-1.

Figure 12-6. Aerial Photo of New Rifle UMTRA Site, Showing Location of Tailings Piles (August 1974)

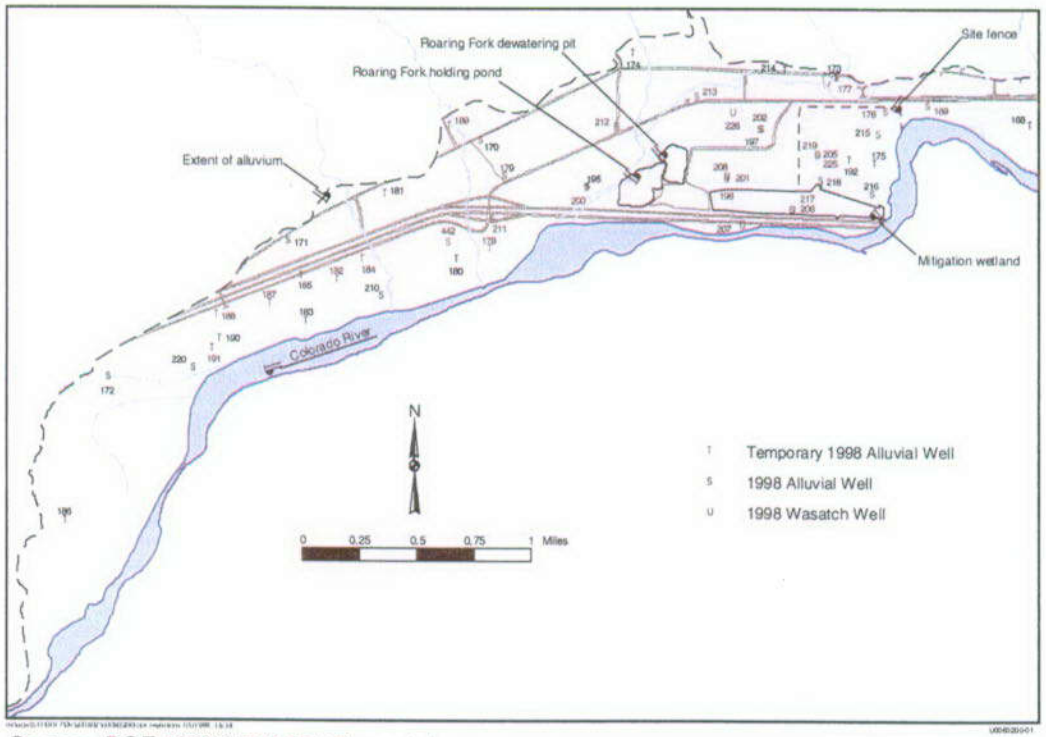

Source: DOE 1999 [154687], Figure 4-1.

Figure 12-7. Map Showing Locations of Wells Screened in Alluvial Aquifer at the New Rifle UMTRA Site

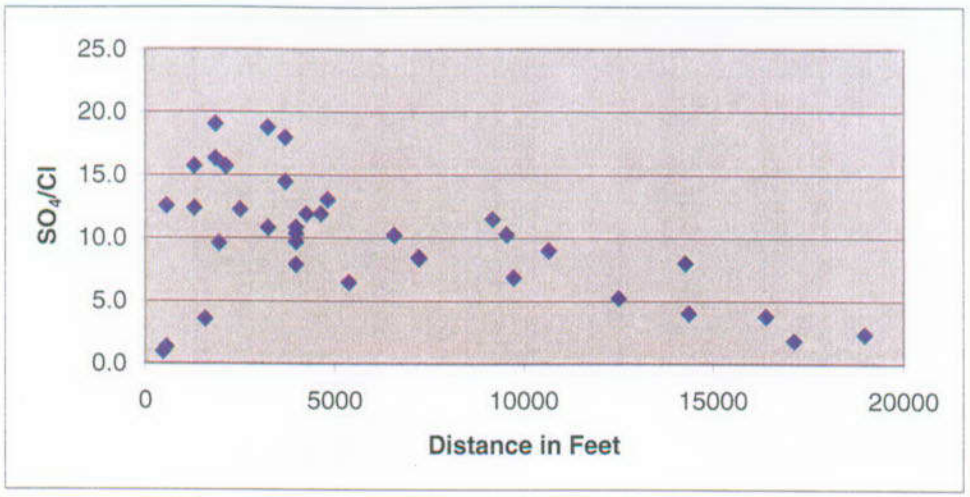

Source: DOE 1999 [154687], Appendix C.

Figure 12-8. Sulfate/Chloride Ratios in Downgradient Alluvial Groundwater versus Distance in Feet from Colorado River Bank on Eastern Edge of New Rifle UMTRA Site

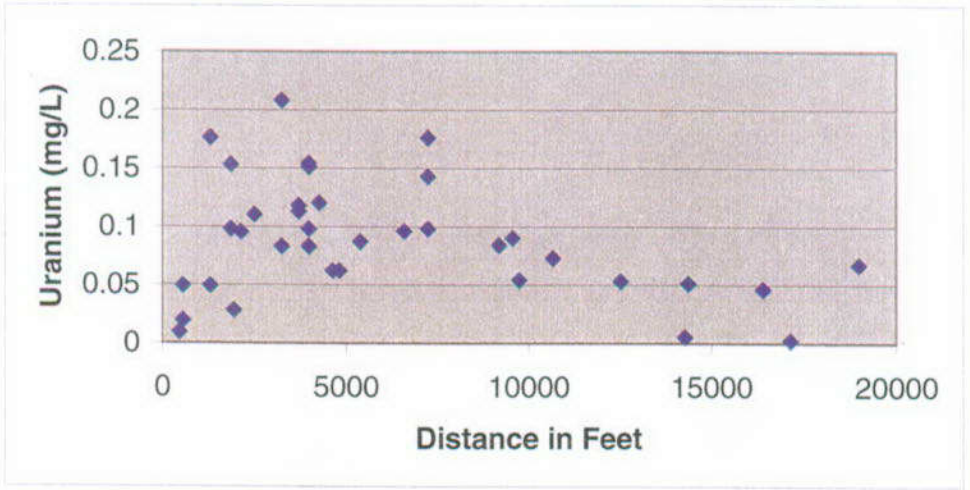

Source: DOE 1999 [154687], Appendix C.

Figure 12-9. Uranium Concentration in Downgradient Alluvial Groundwater versus Distance in Feet from Colorado River Bank on Eastern Edge of New Rifle UMTRA Site

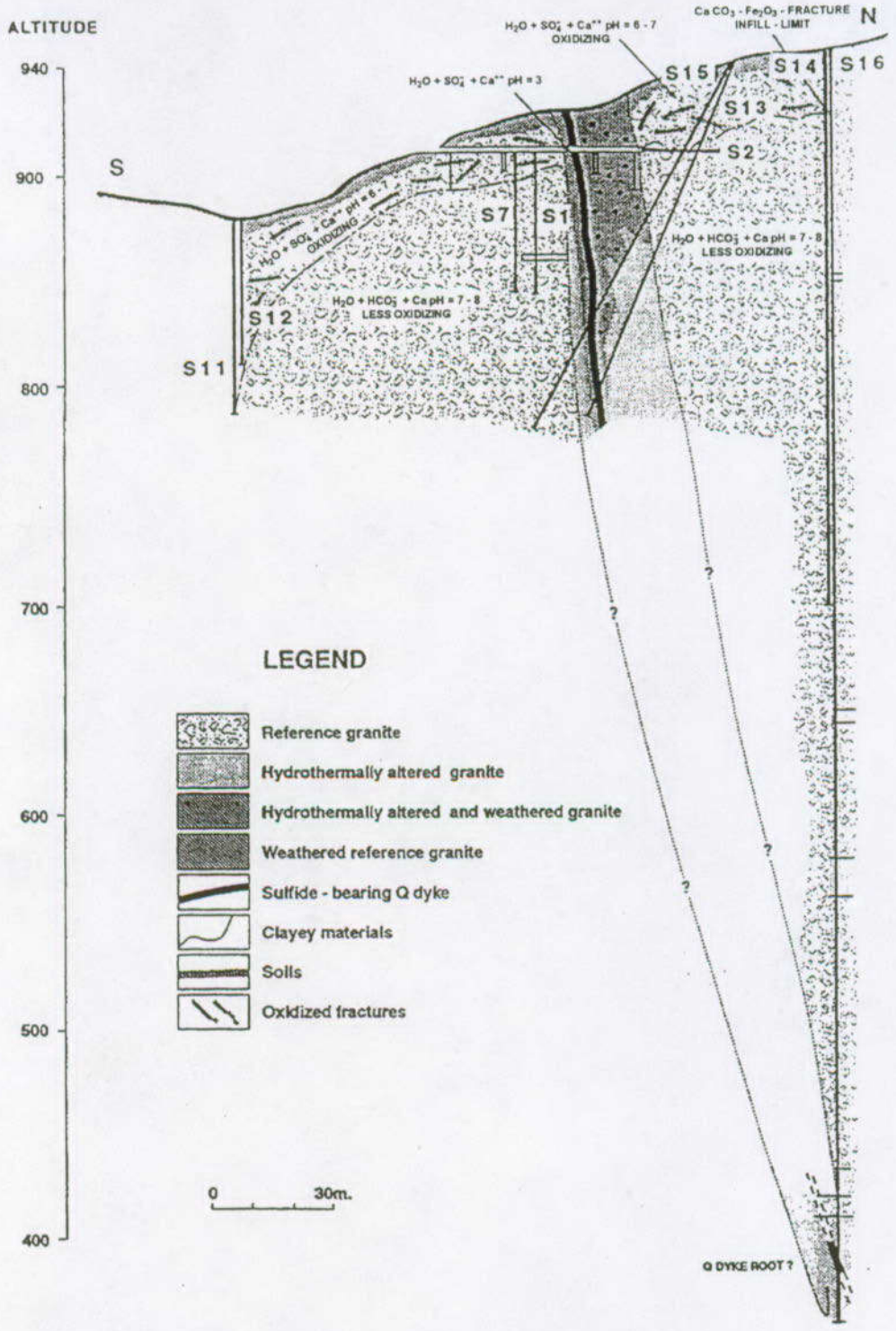

Source: Rivas et al. 1998 [126287], Figure 2-1.

Figure 12-10. N-S Cross Section of the El Berrocal Granite-Uranium-Quartz-Vein System and Location of Selected Boreholes

13. ANALOGUE INFORMATION FOR BIOSPHERE PROCESS MODELS

13.1 INTRODUCTION

Section 13 presents information from the Chernobyl Nuclear Power Plant (ChNPP) accident in Ukraine that relates to parameters of interest in the Yucca Mountain Biosphere Process Model. Unlike the analogues presented in previous sections that dealt primarily with demonstrating confidence in processes and conceptual models, analogues relevant to biosphere models tend to focus on parameter input values. In Section 13.2, the Biosphere Process Model is briefly described to provide background against which to assess its information needs. Section 13.3 focuses on studies of the Chernobyl nuclear accident and its consequences to the biosphere, and their pertinence to the Yucca Mountain Biosphere Process Model.

Although there are many contaminated sites that might have been suitable candidates for providing analogue information for the Biosphere Process Model, Chernobyl was selected for an in-depth survey. Chernobyl provides several advantages over other contaminated sites. First, the Chernobyl site was studied extensively after the 1986 accident, and a wealth of data has been published. Second, because the Chernobyl accident involved an explosion, data regarding the settling of contaminants following atmospheric transport resulting from the explosion provide a rather unique opportunity for use in adding confidence to the disruptive-event-pathway component of the Yucca Mountain Biosphere Process Model.

13.2 BACKGROUND

13.2.1 Reference Environmental Conditions for the Yucca Mountain Biosphere Process Model

The Yucca Mountain reference biosphere conceptual model is based on the biosphere environmental setting, including geography, climate, hydrogeology, geology, and soil conditions, as well as ecosystems (including human communities) (CRWMS M&O 2000 [151615], Section 3.1.1). Yucca Mountain is located in a sparsely populated, semi-arid region in the transition zone between the Great Basin and the Mojave deserts. Yucca Mountain and surrounding areas are in the southern part of the Great Basin, the northern-most subprovince of the Basin and Range Physiographic Province. The topography, which is typical for the Great Basin, is characterized by relatively regularly spaced mountain ranges and intervening alluvial basins, trending from the north to the south. The mountain ranges are formed by fault blocks that are tilted eastward, so that the fault-bounded west-facing slopes are generally high, steep, and straight, in contrast to the gentler and deeply dissected east-facing slopes.

Yucca Mountain has low annual precipitation (from 100 to 200 mm) that decreases from the higher to lower elevations. About 50% of the annual precipitation falls from November through April, caused by large frontal storms. Summers are hot and winters are cool. The Sierra Nevada Mountains that lie to the west create a major barrier to moist air masses moving from the Pacific Ocean. Some thunderstorms in summer are able to create localized land surface flooding and runoff. The average maximum daytime temperature varies from 11°C (52°F) in January to 35°C (95°F) in July. Average nighttime temperatures are above freezing in January (2°C

[36°F]), but winter freezing may occur. Average annual atmospheric humidity is less than 20%. Such conditions cause high evapotranspiration. Vegetation covers 20 to 30% of the ground, with shrubs dominating the native vegetation.

The nearest settlement to Yucca Mountain is situated in the direction of groundwater flow in Amargosa Valley (Nye County). Amargosa Valley is an area of approximately 1,300 km^2. The closest inhabitants to Yucca Mountain are approximately 20 km south at the intersection of U.S. 95 and Nevada State Route 373. The Amargosa Valley population is about 1,270, in approximately 450 households. The Amargosa Valley region is primarily rural agrarian in nature, with agriculture mainly directed toward growing livestock feed (e.g., alfalfa), gardening, and animal husbandry. Both the agriculture and the population are concentrated in the Amargosa Farms area, approximately 30 km south of Yucca Mountain. Agricultural crops and gardens depend entirely on irrigation. Because there is no natural discharge of groundwater into the Amargosa Valley, the source of water for household uses, agriculture, horticulture, and animal husbandry is from local wells. Thus, the pathway for introduction into the biosphere is the use of wells for residential and agricultural purposes.

The direction of groundwater flow is from north to south, with a discharge into the Amargosa Valley region located immediately to the south of Yucca Mountain. If radionuclides were to be released into groundwater or air at Yucca Mountain, groundwater flow and wind patterns could spread some contaminants into this region over time.

Sandy-textured soils are found in Amargosa Valley. The active soil depth is 15 cm, in which deposition from the atmosphere, irrigation, and resuspension may occur. The soil bulk densities in farming areas of Amargosa Valley range from 1.35–1.70 g/cm^3, with a mean value of 1.5 g/cm^3 used in the Yucca Mountain Biosphere Process Model (CRWMS M&O 2000 [151615], Section 3.2.4.1.3).

13.2.2 Biosphere Process Model Pathways

The Biosphere Process Model describes exposure pathways in the biosphere by which radionuclides released from a potential Yucca Mountain repository could reach a human receptor (Figure 13.2-1). The Yucca Mountain biosphere conceptual model considers two scenarios of possible radionuclide releases (CRWMS M&O 2000 [151615], Section 3.1.5). The first scenario assumes pumping of contaminated groundwater and use of this water in a hypothetical farming community (a) under undisturbed repository performance and (b) for some disruptive processes and events, such as volcanic activity, or through human activities such as drilling a borehole through a degraded waste container. Under the contaminated-groundwater scenario, infiltration through the unsaturated zone (UZ) or along a borehole would enable radionuclides to reach the saturated zone (SZ), followed by lateral spreading of radionuclides and pumping of contaminated groundwater. In this case, radionuclide-contaminated groundwater is used as the source of drinking water, irrigation, animal watering, and domestic uses (including gardening), thus increasing the likelihood of uptake by humans. The second scenario assumes that the release is caused by a volcanic discharge through the repository, leading to atmospheric dispersal of the contaminants into the accessible environment through ash fall, which accumulates on the land surface. These contaminants may then be absorbed by plants and digested by animals, thus

entering the food chain and being made available for human consumption. Groundwater is assumed to be uncontaminated in the disruptive volcanic-event scenario.

The Yucca Mountain Biosphere Process Model develops biosphere dose conversion factors (BDCFs), which are multipliers used in Total System Performance Assessment (TSPA) to convert the radionuclide concentration at the source of contamination into an annual dose, as defined by the regulator. For the groundwater-contamination scenario, annual doses are estimated by multiplying radionuclide concentrations in groundwater by the corresponding BDCFs. For the disruptive event scenario that results in a surface-contaminated source term, the doses are obtained by multiplying surface-activity concentration of a radionuclide by the corresponding BDCF (CRWMS 2000 [151615], Section 3.1.4).

13.3 USING CHERNOBYL DATA FOR EVALUATING BIOSPHERE PATHWAYS OF RADIONUCLIDES

13.3.1 Relevance of Chernobyl Information

Information about the distribution of radionuclides in the biosphere following the Chernobyl Nuclear Power Plant (ChNPP) reactor explosion in April 1986 is a valuable source of data for testing environmental transport models (Hoffman et al. 1996 [156616]; Konoplev et al. 1999 [156624]). The 1986 Chernobyl accident resulted from an explosion of the Fourth Reactor Unit of the ChNPP. Figure 13.3-1 shows the location of the ChNPP in the territory of Ukraine. The ChNPP accident resulted in contamination by a variety of radionuclides (^{89}Sr, ^{90}Sr, ^{95}Zr, ^{99}Mo, ^{103}Ru, ^{106}Ru, ^{134}Cs, ^{137}Cs, ^{141}Ce, ^{144}Ce, ^{154}Eu, ^{155}Eu, ^{238}Pu, ^{239} Pu, ^{240}Pu, ^{241}Pu, etc.) of large areas of the former USSR and the globe (Bar'yakhtar 1997 [156953], p. 35; Kashparov 2001 [156819], p. 11). Research into many environmental and health effects of the Chernobyl accident has become a major international enterprise aimed at understanding long-term transport processes and effects of exposure to radioactivity. A significant amount of data has been collected for the past 16 years about the distribution and accumulation of radioactive materials in different parts of the biosphere after the Chernobyl accident, including the main exposure pathways and mechanisms of radioactive contamination of the environment and the population. These data represent a valuable source of information to improve confidence in conceptual models of exposure pathways and processes.

13.3.2 Objective and Approach

Because direct observation of the actual outcome of the Biosphere Process Model scenarios will not be possible for many years, if ever (CRWMS M&O 2000 [151615], Section 3.2.3), one of the approaches to building confidence in biosphere models is to use information obtained from natural and anthropogenic analogue sites. As part of the model validation activities to improve biosphere models for both the groundwater-release and the volcanic-release scenarios, the Yucca Mountain Project is interested in measurements at specific locations to aid in selection of input data for models of specific environmental processes.

The objective of Section 13.3 is to review information from the Chernobyl accident regarding the exposure pathways, inputs to risk assessment, and distribution of radioactive contaminants in the biosphere, to determine its potential relevance for the Yucca Mountain Biosphere Process Model.

In particular, information was collected on the specific environmental processes of radionuclide transfer and resuspension, which could be used to improve confidence in the modeling of Yucca Mountain environmental processes. Major monographs and numerous articles were reviewed in English, Russian, and Ukrainian scientific and professional journals, magazines, and proceedings of international conferences and symposia.

Taking into account the difference in climatologic and environmental conditions of Chernobyl and Yucca Mountain, this survey presents a broad picture of the environmental pathways of radionuclides in the biosphere. Radiation doses resulting from Chernobyl are presented as a means of illustrating the types of data available related to stated needs of the Yucca Mountain Biosphere Department, including the following:

- Radionuclide transfer from soil to plants via root uptake, soil to plants via atmospheric resuspension, and animal fodder to animal food products
- Removal of contaminants via erosion and leaching
- Inhalation of resuspended contaminants deposited on the ground
- Radionuclide accumulation in soils and plants under irrigation using contaminated water
- The ecological half-life of radionuclides in soils and plants.

13.3.3 Chernobyl Accident and Main Exposure Pathways

This section provides background for later discussion by describing the Chernobyl location, climate, and soil conditions; and the accident in terms of its explosion characteristics, radiation release, principal pathways, and types of particles released.

13.3.3.1 Location, Climate, and Soil Conditions

The ChNPP exclusion zone is located in the central part of the Ukrainian Polessye physiographic province. The term "exclusion zone" refers to an area surrounding the site that was sealed off as an institutional control to prevent further access after the accident. Immediately after the accident, the exclusion zone was established within the radius of 30 km from the ChNNP. However, as more measurements of the level of contamination over a larger territory were made, the boundary of the exclusion zone was adjusted to prevent access to highly contaminated areas. Its total area within the Ukrainian borders, except for part of the Kiev reservoir, is 2,044 km^2 (Shestopalov 1996 [107844], p. 3).

The Chernobyl region has a humid climate, with mild, short winters and a warm summer. Average annual precipitation ranges from 550 to 750 mm/yr. The relief consists of slightly undulating plains and ridges, and irregularly located bogs. The relatively dense network of Pripyat and Dnieper River tributaries forms boggy valleys of moderate relief. Approximately 50% of the land in the exclusion zone is covered by forest, 30% by arable farm land, and the remaining 20% by urban areas, marshlands, and water bodies (Shestopalov 1996 [107844], p. 22). The soils are relatively homogeneous, with mostly podsols and peaty podsols (soils of forested, temperate climates) as the topsoil layer in the exclusion zone.

13.3.3.2 Type of Explosion and Amount of the Radionuclide Release

The initial explosion at Chernobyl was a steam explosion (Bar'yakhtar et al. 2000 [157504], pp. 12–13; Tarapon 2001 [156920], p. 95). The total amount of radionuclides released by the accident into the environment expressed in becquerels (Bq) was approximately 11×10^{18} Bq (expressed in curies [Ci] this would equal 3×10^{8} Ci), while approximately 6×10^{17} Bq (1.6×10^{7} Ci) of long-lived radionuclides remained in the destroyed reactor. (Note that 1 Ci = 3.7×10^{10} Bq). The kinetic energy released from the accident has been estimated to be equivalent to 30–40 tons of trinitrotoluene (TNT) (Bar'yakhtar et al. 2000 [157504], p. 13). This was the highest single release of radionuclides into the global environment, with contamination calculated to be equivalent to that of a 12 Mt (megaton) nuclear explosion (Bar'yakhtar et al. 1997 [156953], p. 224). No other nuclear accident approaches the dimensions of the Chernobyl disaster in terms of radiological release, acute radiation health effects, and socioeconomic and psychological impact (Bar'yakhtar et al. 2000 [157504], p. 9).

The Chernobyl accident released approximately 2,000 Ci of isotopes of $^{239, 240}$Pu into the atmosphere (Bar'yakhtar et al. 2000 [157504], Table 2.5.1; Bondarenko 1998 [156952], p. 13, 15). This amount of radiation is comparable to about 0.5% of the total global fallout of these isotopes from nuclear weapons testing from 1945 to 1963 (Bondarenko 1998 [156952], p. 13; Bondarenko et al. 2000 [156593], p. 473). The activity of plutonium isotopes, distributed outside the 30 km exclusion zone, was 1,344 Ci, or 5×10^{13} Bq. The specific activity of α-emitting isotopes of plutonium was calculated to be 1.5×10^{13} Bq/t (Bondarenko 1998 [156952], p. 23).

13.3.3.3 Principal Pathways

The initial explosion and heat plume at Chernobyl carried volatile radioactive materials up to 1.5 km (0.93 miles) in height, from where these materials were transported over large distances by prevailing winds (Figure 13.3-2). About a quarter of the total released radioactivity entered the atmosphere during the first day after the accident. By the fifth day, the release had decreased approximately sixfold, because of mitigation efforts at the ChNPP. The radionuclides that escaped into the atmosphere then migrated and settled in different areas, causing radioactive contamination of living things. Crops, vegetables, grasses, fruits, milk, dairy products, meat, and eggs were contaminated with radionuclides. The most severe radioactive contamination of fields, rivers, tributaries, canals, drainage ditches, and agricultural lands occurred in the Pripyat and Dnieper river basins that surround the ChNNP.

As part of the cleanup effort after the Chernobyl accident, approximately 8×10^{15} Bq of high-, medium-, and low-level radioactive waste (in mostly solid form, such as construction parts, concrete, and soils) were accumulated and stored at more than 800 interim storage and disposal places in the region (Poyarkov 2000 [157503], pp. 1–2; Kukhar' et al. 2000 [157506]). Infiltration through unlined waste storage and disposal sites has caused leaching of contaminants, so these sites provide the current localized source term for soil and groundwater contamination (Shestopalov and Poyarkov 2000 [157507], pp. 146–147).

Figure 13.3-3 illustrates the principal pathways for radionuclides entering the biosphere through terrestrial and aquatic ecosystems after the Chernobyl accident.

13.3.3.4 Types of Particles Released

Two main types of radioactive particles were released from the damaged reactor: (1) a fuel component of finely dispersed fuel particles, containing elements of low volatility, such as cerium, zirconium, barium, lanthanum, strontium, and the actinides; and (2) a condensed component that formed when gases of nuclides (such as iodine, tellurium, cesium, and a lesser amount of strontium and ruthenium) that were ejected during the nuclear fuel fire, condensed on different surfaces (e.g., ground, buildings, and trees–Kashparov 2001 [156819], pp. 11–12). Fuel particles settled primarily on the land surface near the ChNNP zone (Kashparov 2001 [156819], pp. 24, 26).

Hot particles formed from both fuel and condensed components, including particles of uranium dioxide (a few tens of μm in diameter or smaller) made of fuel fused with the metal cladding of the fuel rods and fuel mixed with sand or concrete (Loshchilov et al. 1991 [125894]; NEA 1995 [156632], p. 53). Hot particles have an activity concentration exceeding 10^5 Bq/g (Bar'yakhtar 1997 [156953], p. 235). Chernobyl hot particles behaved differently from nuclear bomb particles and Chernobyl gaseous and aerosol forms (Zheltonozhsky et al. 2001 [156630], p. 151). For example, Chernobyl hot particles (1) did not contain activation products such as ^{60}Co; (2) contained ^{125}Sb and ^{144}Ce, which are absent in atomic bomb hot particles; (3) contained a larger fraction of ^{137}Cs than that in nuclear bombs; (4) had a ratio of ^{154}Eu/^{155}Eu about 10 times greater than that in atomic bomb particles and about 200 times than that in fusion bomb particles; (5) have a lower radiation of uranium and neptinium than that from fusion bombs; and (6) had a lower plutonium content than that in the fusion bombs (Zheltonozhsky et al. 2001 [156630], pp. 156–159). After nuclear weapons testing, over 90% of the activity of ^{90}Sr and ^{137}Cs was present in water-soluble and exchangeable forms in global fallout, but after the Chernobyl accident, the fraction of exchangeable forms of ^{90}Sr and ^{137}Cs in the near-ChNNP zone in 1986 was less than 25% of their activity in a fallout, and the remaining activity was caused by nonexchangeable forms of these radionuclides associated with fuel particles (Kashparov 2001 [156819], p. 27). ^{90}Sr, ^{106}Ru, ^{134}Cs, ^{137}Cs, ^{144}Ce, and ^{147}Pm contributed to the total β-activity of hot particles (Papp et al. 1997 [124806], p. 951). Isotopes of actinide elements ^{238}Pu, ^{239}Pu, ^{240}Pu, and ^{242}Cm contributed mostly to the total α-activity of hot particles. The surface density of hot particles was about 1,600 per m^2 in downtown Kiev (Papp et al. 1997 [124806], p. 951). Hot particles were detected not only on the surface, but they also migrated in soils to depths of about 0.5 m (Gudzenko 1992 [107835], p. 2), as detected in the fall of 1987 (Gudzenko et al. 1990 [125020], p. 122).

The released fuel particles that entered the atmosphere are categorized by relative size into large (tens to several hundred μm) and small particles (median radius of 1.5–3.5 μm). The large fuel particles were formed from the fragmentation of the fuel at high temperatures during the initial phase of the accident. The large particles were primarily deposited within a 5 km zone around the damaged reactor. Small fuel particles consisted of unoxidized uranium dioxide (Bar'yakhtar et al. 2000 [157504], pp. 21–22). Note that hot particles <10 μm in size can be inhaled into the lungs (Loshchilov et al. 1991 [125894], p. 47).

13.3.4 Soil Contamination

This section provides an overview of the distribution of soil contamination resulting from the Chernobyl accident and characteristics of actinide element migration in soils.

13.3.4.1 Lateral Distribution of Soil Contamination

The prevailing wind directions and velocities that occurred immediately after the Chernobyl accident established the contaminant fallout trajectories (see Figure 13.3-2). The surface deposition of contaminants is affected mainly by local wind patterns and rain conditions existing at the time of the accident. Therefore, the surface contamination resulting from the Chernobyl accident is extremely irregular over very large areas. The contaminated spots range in size from a few square meters to more than a thousand square kilometers (Shestopalov 1996 [107844], p. 14). The data on air transport of contaminants demonstrate the important role of the local spatial and temporal patterns in the wind direction and the need for estimating both the source strength and the lateral distribution of contaminants in numerical models (Goldman et al. 1987 [156820]). The area of highest concentration of ^{137}Cs is the "Western finger," which extends almost in a straight line westward from the ChNPP. The plume is 1.5 to 5 km wide; for a distance of <70 km the concentration of ^{137}Cs along its axis decreases from >10,000 Ci/km^2 (3.7×10^5 kBq/m^2) to 10 Ci/km^2 (3.7×10^2 kBq/m^2). Because of the local wind pattern, the "Southern finger" splits into five separate tracks and has the highest concentrations of ^{90}Sr and actinides. The pattern of the widespread "Northern finger" was likely formed by deposition with rain. The "South-West finger" has the most complex, vortex-like shape (Shestopalov 1996 [107844], pp. 13–14).

The results of large-scale soil sampling on a regular grid of about 1 km (radius of 36 km) are shown on two maps of ^{90}Sr and ^{137}Cs contamination in Figure 13.3-4. The difference in distribution patterns for ^{90}Sr and ^{137}Cs is caused by different processes of precipitation for these radionuclides: ^{90}Sr was ejected with fuel particles and precipitated mainly in the near ChNNP zone, while ^{137}Cs was contained in the condensed component, which moved and precipitated further away from the ChNPP (Kashparov 2001 [156819], pp. 24–26). These maps were used to estimate the total contents of radionuclides on the ground surface of the 30 km exclusion zone (without the reactor site and the radioactive waste disposal sites), which showed that initial estimates of the contamination were overestimated. For example, the content of ^{90}Sr is estimated to be approximately 810 TBq (8.1×10^{14} Bq) for the Ukrainian territory, which is 3 to 4 times lower than previous estimates (Kashparov et al. 2001 [157400], p. 295).

13.3.4.2 Vertical Distribution of Radionuclides in Soils

Silant'ev et al. (1989 [126508], p. 224), Isaksson and Erlandsson (1998 [156617], p. 150), and Likar et al. (2001 [156627], Figure 2) determined that, overall, the concentration of radionuclides in the soil profile decreases exponentially with depth to a depth of approximately 3 cm. In the exclusion zone, the downward velocity of migration of ^{137}Cs ranged from 0.4 to 0.7 cm/yr in the first years after the accident, and then dropped to 0.2 cm/yr (Bar'yakhtar 1997 [156953], p. 247).

Vertical migration of uranium and plutonium in soils is limited to the topsoil layer, because these radionuclides were released as hot particles that are more or less stable in the near-surface weathered zone. Table 13.3-1 shows that about 99% of plutonium accumulated within the top 2

cm soil layer. This table also shows that the $^{238}U/^{235}U$ ratio remained unchanged below a depth of 3 cm. Figure 13.3-5 shows measurable quantities of actinides (plutonium, americium and curium) in soil to a depth of 4.5 cm, in spring 1994, in the Kopachi village, located a few kilometers from the ChNNP (Mboulou et al. 1998 [156628]). Figure 13.3-6 shows the actual and predicted distribution of activities with depth for ^{90}Sr, ^{137}Cs, and ^{239}Pu. The total activity of all these radionuclides is mostly in the upper 3 cm layer.

Radionuclide releases from hot particles present an additional source of soil contamination, causing the concentration of mobile ^{137}Cs in soils to reach a maximum 1.5 to 2.5 years after the accident and concentration of ^{90}Sr to reach a maximum 6 to 15 years after the accident (Bar'yakhtar 1997 [156953], p. 243). The decrease in ^{137}Cs concentration in soils in the exclusion zone by about 25%–50%, as observed 10 years after the accident, was caused by several factors (Shestopalov 1996 [107844], p. 14): (1) natural radioactive decay of ^{137}Cs (about 20%); (2) partial washout of the soil surface layer from elevated areas and slopes; (3) soil decontamination; and (4) migration deeper than 20 cm from the soil surface along the zones of preferential flow. A secondary contamination by ^{137}Cs affected many areas, such as local soil depressions, edges of marshes, and reservoir banks, where ^{137}Cs concentration increased by a factor of 2 to 10, and locally up to 50 to 250 times. Concentration of ^{137}Cs in the exclusion zone reached 50,000 to 150,000 Ci/km^2, which is 5 to 15 times greater than that in soils in the so-called "Red Forest" around the ChNPP, where intense radioactivity caused leaves to lose chlorophyll and turn red.

13.3.4.3 Characteristics of Migration of Actinides in Soils

Within the European part of the former Soviet Union, the plutonium content in soils after the Chernobyl accident varies from 10 to 3,700 Bq/m^2 (Lebedev et al. 1992 [125854], p. 516). The typical content of $^{239, 240}Pu$ in Ukraine soils is 70 Bq/m^2 (Bondarenko et al. 2000 [156593], p. 473). The determination of the isotopic composition of plutonium, and especially the ratio $^{238}Pu/^{239, 240}Pu$, is important to assess the source of soil contamination. For example, for the global fallout, this ratio is typically from 0.03 to 0.05. However, in Chernobyl soil samples, this ratio varied from 0.25 to 0.35, which corresponds to the ratio of about 0.3 in spent fuel (Lebedev et al. 1992 [125854], p. 517). In contrast to the radioactive gases and relatively mobile radionuclides such as iodine and cesium, isotopes of plutonium, americium, and other actinides are associated with fuel particles.

Bondarenko (1998 [156952]) and Bondarenko et al. (2000 [156593]) presented the results of an 11-year investigation (1986–98) of the migration of long-lived α-emitting transuranic (TRU) elements in ecologic chains and the human body. The accumulation of TRU elements in plants showed significant variability, depending on the type of soil, vegetation, and presence of microbial activity. The ratio of concentrations of TRU elements in plants varies within several orders of magnitude among the isotopes of each element. The main pathways for the entrance of TRU elements in the human body are ingestion of food and water, and inhalation (Bondarenko 1998 [156952], Section 5; Bondarenko et al. 2000 [156593], pp. 473–474). Migration of TRU elements that accumulated in hot particles begins as hot particles are broken down.

Thus, near-surface soil contamination by ^{90}Sr, ^{137}C, and TRU elements is widespread within a large area around Chernobyl, but vertical distribution of contaminants is mostly limited to depths of several centimeters. This creates favorable conditions for the atmospheric resuspension and

secondary deposition, as described in Section 13.3.5, of hot particles and radionuclides attached to soil particles as a result of wind erosion.

13.3.4.4 Technetium in Soils

At present, there are only limited data on concentration of ^{99}Tc in the environment caused by the ChNPP accident. Uchida et al. (1999 [156945]; 1999 [156925]) presented results of ^{99}Tc measurements in soil samples collected within three forest sites around Chernobyl in 1994 and 1995. Two sites were located 28.5 km and 26 km to the south, and one site is 6 km to the southeast of the ChNPP. The ^{99}Tc concentration was determined by inductively coupled plasma mass spectrometry after its chemical separation from the soil sample. Concentrations of ^{99}Tc in these soil samples ranged from 1.1 to 14.1 Bq/kg at a depth of 6–9 cm, which is one to two orders of magnitude higher than those under background conditions. The regression function describing the change of the ^{99}Tc concentration with distance is ^{99}Tc concentration = $4.88 \times R^{-1.771}$, where ^{99}Tc concentration on the ground is in GBq/km^2 (Note: 1 GBq = 10^9 Bq) and the distance R is in kilometers from the ChNPP (Uchida et al. 1999 [156925], p. 2,764).

The most stable form of technetium under aerobic conditions is Tc(VII), TcO_4^-, which is characterized by high mobility in soils and availability to plants. Under anaerobic conditions and increased soil-water saturation (for example, under irrigation), TcO_4^- could be transformed to a lower oxidation state of Tc(IV), to Tc sulfide forms, or to organic bound forms, which are insoluble and will adsorb and accumulate in soils with time (Tagami and Uchida 1999 [156923], pp. 963-964).

13.3.5 Erosion and Atmospheric Resuspension of Radionuclides

After the Chernobyl release ended, atmospheric resuspension of radionuclides became a secondary source of contamination, which affected people in areas that were not exposed to the original release (Garger et al. 1996 [156602], p. 18). The main cause for the resuspension of radionuclides is wind erosion of soil. The average annual soil erosion in Ukraine from 1987 to 1990 due to spring winds was 1 t/ha (tons/hectare) (Prister et al. 1991 [156824], p. 74), which, for topsoil with a density of 1.3 g/cm^3, corresponds to soil loss of 8×10^{-3} cm/year. Erosion led to the total (spring and fall) annual removal of 0.7×10^5 Bq/ha of ^{137}Cs from soils, with a concentration activity of 1×10^3 Bq/kg (Prister et al. 1991 [156824], Table 7).

Resuspension of radionuclides with dust driven by wind is especially hazardous in agricultural areas. The resuspension of particles with ^{137}Cs increases after the tillage of agricultural lands from background conditions of 0.7 Bq (m^2/day) to 10 Bq (m^2/day) (Loshchilov et al. 1991 [156828], p. 64). For rural areas in Ukraine with different agricultural activities, the concentration of dust in air ranged from 0.3–203 mg/m^3 for a soil moisture content of 3–20% (Loshchilov et al. 1991 [156823], p. 199, Table 1). The maximum concentration of dust in samples collected from air stirred up by agricultural machinery in the Ukraine was 4,000 mg/m^3 during potato planting (Anokhova and Krivtsov 1991 [156829], p. 206).

In the topsoil layer, radionuclides are attached mostly to small soil particles that are less than 1 μm in diameter (Loshchilov et al. 1991 [156823], p. 198). Therefore, the specific activity of small soil particles exceeds that for largest particles (0.1–1 mm; Anokhova and Krivtsov 1991

[156829], p. 206). For example, for ^{134}Cs the specific activity of small particles exceeds that of large particles by a factor of 12.7, for ^{137}Cs by a factor of 9.1, for ^{90}Sr by a factor of 7.4, and for $^{238+239+240}Pu$ by a factor of 19.2 (Anokhova and Krivtsov 1991 [156829], Table 2, p. 208). The specific radioactivity of resuspended dust particles (<10 μm) increases by a factor of 10 compared to that in soils, from which these particles were originated (Loshchilov et al. 1991 [156823], p. 200).

One of the main parameters characterizing the atmospheric resuspension of radionuclides is the resuspension factor. The resuspension factor is defined as the ratio between the airborne (Bq/m^3) and surface (i.e., <1 cm depth) concentration (Bq/m^2) of a radionuclide in question. According to Bondarenko et al. (2000 [156593], pp. 474–475), the resuspension factor in 1998 ranged from 0.34×10^{-10}–17×10^{-10}/m. This value is in agreement with the range of resuspension factors (from 1.4×10^{-10}/m for ^{137}Cs and 1×10^{-11}/m for $^{239,240}Pu$) determined in 1998 by Rosner and Winkler (2001 [156629], pp. 11, 17). The resuspension factor was higher at the earlier stage after the accident. For comparison, in the Yucca Mountain Biosphere Process Model, the resuspension-factor mean value is 8.3×10^{-11}/m (CRWMS M&O 2000 [151615], Section 3.2.4.1.3).

Kashparov et al. (2000 [156622]) investigated the resuspension and redistribution of radionuclides at various distances from fires occurring in areas previously contaminated by the Chernobyl accident and outside the 30 km ChNPP exclusion zone. They determined that the resuspension factor for the active phase of a fire was as high as 10^{-7}–10^{-8}/m (Kashparov et al. 2000 [156622], p. 288). The dose coefficient from the radioactive aerosol inhalation was estimated to be 1.5×10^{-8} Sv (1 Sv = 100 rem), which provides less than 1% of the total dose resulting from inhalation and external radiation (Kashparov et al. 2000 [156622], p. 296). This value for the dose coefficient was obtained for a one-year period following a single intake of radionuclides due to a fire (Kashparov et al. 2000 [156622], p. 297). Equivalent dose is the quantity obtained by multiplying the absorbed dose (the quantity of energy imparted by radiation to a unit mass of matter such as tissue, measured in SI (International System of Units) units in grays, Gy, or rad) in a body organ or tissue by a factor representing the effectiveness of the type of radiation causing harm to the organ or tissue (NEA 1995 [156632], p. 60). Effective dose is the weighted sum of the equivalent doses to the various organs and tissues, multiplied by weighting factors reflecting the differing sensitivities of organs and tissues to radiation (NEA 1995 [156632], p. 59). In SI units, equivalent dose is measured in sieverts (Sv). The whole-body (internal and external) dose (i.e., total effective dose equivalent [TEDE]) limit for a radiological worker is 5 rem/year (DOE 1994 [104736], p. 2-6, Table 2-1). The presence of α-emitting radionuclides (in the 30 km zone) causes a considerable increase in inhalation dose during forest fires, which can exceed external exposure doses (Kashparov et al. 2000 [156622], p. 297).

Thus, measurements and modeling investigations indicated that radionuclide resuspension could become a source of both external and inhalation radiation doses for people, depending on the distance from the release. The size distribution of resuspended particles is important in determining inhalation (i.e., lung) dose.

13.3.6 Groundwater Contamination

This section examines the extent of groundwater contamination resulting from the Chernobyl accident and the type of radionuclides involved.

The largest source of radionuclide contamination of groundwater is from about 800 radioactive waste disposal sites within the Chernobyl exclusion zone. Another large, local source of contamination is the Chernobyl cooling pond (Shestopalov and Poyarkov 2000 [157507], p. 146). Radionuclides dispersed over large areas can migrate to the water table through and around casings of boreholes and in colloidal and dissolved states in percolating water from the vadose zone. Field investigations showed a lack of correlation between ^{137}Cs soil concentration and its travel time to the water table (Gudzenko et al. 1991 [107834], p. 3), indicating that soil contamination is not a major source of groundwater contamination.

Before the Chernobyl accident, the depth to the water table around the ChNPP was approximately 6 to 8 m and was controlled by several drainage systems. Since 1986, some drainage systems have been abandoned, so that the water table has risen, creating a potential instability for the remaining structure of the ChNPP. Subsequently, several countermeasures, such as the construction of a vertical drainage system and an impermeable underground vertical wall, allowed the water table to decline to previous depths.

The highest ^{90}Sr concentrations of groundwaters (10^2–10^4 Bq/L) were measured in water samples taken at interim radioactive storage sites near the ChNPP (Table 13.3-2). By 1995–1996, an increase in the ^{90}Sr and ^{137}Cs concentrations by 2–3 orders of magnitude, in comparison with pre-accident conditions, occurred in the upper section of groundwater within the inner part (5–10 km) of the exclusion zone. At the same time, radionuclide concentration in the groundwater and the artesian aquifer are below the maximum permissible concentration. Despite a low level of current contamination of the artesian aquifer in the Eocene deposits, which is the source of potable water within the exclusion zone, it is predicted that groundwater contamination will increase over the next few decades (Shestopalov and Poyarkov 2000 [157507], p. 141).

The presence of ^{134}Cs in groundwater and the increase of ^{90}Sr concentration by two orders of magnitude (from 4–400 mBq/L) confirm that radionuclides from Chernobyl reached groundwater at 50 to 70 m depths over five years (1987-1992) (Bar'yakhtar 1997 [156953], p. 254). Cs-137 and ^{90}Sr contamination was detected in the Cretaceous aquifer at depths of 80 to 120 m within the 30 km zone 22 months after the accident (Gudzenko 1992 [107835], p. 5). Elevated concentrations of ^{90}Sr and ^{137}Cs occurred at substantial distances from the ChNPP plant in all aquifers down to 200–300 m (Table 13.3-3).

Given these findings, groundwater contamination by ^{90}Sr and ^{137}Cs, caused by leakage from radioactive waste disposal sites within the Chernobyl exclusion zone, cooling pond, and migration through casings of boreholes to depths below 120 m, is expected to influence all nearby aquifers. However, the risk associated with the use of contaminated groundwater water for water supply is marginal, as compared to external radiation and inhalation doses (see Sections 13.3.7 and 13.3.9).

13.3.7 Using Contaminated Water for Irrigation and Water Supply

The Dnieper River water is used for irrigation of more than 1.8 million hectares in Ukraine, involving the territories from Kiev in the north to Crimea in the south (Berkovski et al. 1996 [156592], p. 39). Figure 13.3-8 shows the concentration of radionuclides in water from six reservoirs along the Dnieper River used for irrigation. In the southern Ukraine, which has a semi-arid climate and a depth to the water table of 50–70 m, irrigation water is taken mostly from canals extending from the Dnieper River reservoirs. About 50% of the land is used to plant fodder crops, eventually leading to the contamination of meat and milk products, and about 10% is used to plant vegetables (Berkovski et al. 1996 [156592], p. 39). The water loss into the subsurface on irrigated lands and from irrigation canals accelerates migration of the radioactive elements from crops, soil surface, and surface water sources into the vadose zone and groundwater. The amount of radionuclides migrating into the subsurface depends on the quality (pH and chemical composition) of the irrigation water and soils, soil structure, depth to water table, and evapotranspiration, as well as the type of irrigation.

Table 13.3-4 illustrates that the concentrations of ^{137}Cs in grains, grass, and vegetables grown on lands that were irrigated with contaminated Dnieper River water exceeded by a factor of 2–6 those in crops irrigated using uncontaminated water, while the concentrations in irrigation water increased by a factor of 2–4 (Perepelyatnikov et al. 1991 [156822], p. 112, Table 5). The increase in the concentration observed during irrigation confirms the concept of a buildup factor in soils.

Table 13.3-5 indicates that the accumulation of radionuclides on irrigated lands occurred to depths of at least 10–20 cm. An example is data on the distribution of ^{137}Cs and ^{90}Sr in soils irrigated using contaminated water in the southern Ukraine (Perepelyatnikov et al. 1991 [156822]). After the rice harvest in 1988, irrigation caused an increase in the ^{137}Cs concentration in the 0–0.5 cm topsoil layer by 58% compared to that on unirrigated (bare) lands. In the 0.5–2 cm layer, its concentration increased by 14–19%. For the same time period, the ^{90}Sr contamination increased by a factor of ~2 (from 18–35 mCi/km^2) in comparison with that of bare soil (i.e., without vegetation and irrigation). The accumulation of ^{137}Cs and ^{90}Sr in soils caused the concentration of these radionuclides in rice to increase. For example, in the first harvest after the accident in 1986, the ^{137}Cs concentration increased by a factor of 1.6 compared to 1985 concentrations. The ^{90}Sr concentration began to increase in 1987, and it increased by a factor of 1.3 compared with 1985 values. However, in the southern Ukraine, concentrations had not reached levels detected in 1972, from global fallout generated by nuclear testing (Perepelyatnikov et al. 1991 [156822], pp. 110, 112, Table 4).

Using the average concentrations of ^{137}Cs and ^{90}Sr in the 20 cm soil layer obtained after three years of rice irrigation (last column of Table 13.3-5) and concentrations in bare soils (third column of Table 13.3-5) assuming that the preaccident concentration is equal to that of bare soils, the following buildup factors are obtained: for ^{137}Cs, 0.48/0.37 = 1.3 (for three years), or approximately 10% per year; and for ^{90}Sr, 116/60 = 1.97 (for three years), or approximately 32% per year. It is expected that the radionuclide buildup factor in soils under irrigation will change with time, depending on the processes of leaching and ecological decay of radionuclides.

Thus, irrigation with contaminated water in the southern Ukraine leads to the accumulation of radionuclides in both the topsoil layer and in crops. The data obtained in Ukraine qualitatively confirm the concept of a radionuclide buildup factor in irrigated soils; this concept is employed in the Yucca Mountain Biosphere Process Model.

13.3.8 Leaching and Transfer Coefficients

This section discusses the dissolution rate, leaching parameters, soil-plant transfer of radionuclides, and radionuclide accumulation in fish and livestock.

13.3.8.1 Dissolution Rate and Leaching Parameters

Hot particles exposed at the surface were oxidized, which caused superficial cracking of the particles and increased their surface area, which in turn led to higher dissolution rates. The dissolution rates for nonoxidized and oxidized fuel particles (UO_{2+x}) differ with acidity of the solution (Kashparov et al. 2000 [156623], p. 232). The dissolution rate V for fuel particles depends on the soil pH according to the formula (Bar'yakhtar et al. 2000 [157504], p. 32):

$$V = a \times 10^{b\,pH}\ \mu m/yr \qquad \text{(Eq. 13-1)}$$

where coefficients a = 14.45 and b = –0.431 for weakly oxidized particles, and a = 4.59 and b = -0.234 for strongly oxidized fuel particles. This formula was used to describe radionuclide leaching from fuel particles for pH from 4 to 6. Kashparov et al. (2000 [156623], p. 232, Figure 4), who studied dissolution kinetics of Chernobyl fuel particles over a pH range from 3 to 9, determined that the dissolution rate is minimal in a neutral medium, while it increases in both acidic and alkaline media.

A study of concentrations of Chernobyl radionuclides in Neuherberg, Germany, was carried out by Rosner and Winkler (2001 [156629]). They determined that the annual mean concentrations in air and annual deposition to ground decreased for ^{90}Sr, ^{137}Cs, ^{238}Pu, and $^{239,240}Pu$ from July 1986 to 1998. Figure 13.3-9 shows annual mean values of radionuclide concentrations in air ($\mu Bq/m^3$), specific activities in air dust (Bq/g), and radionuclide ratios in air (Bq/Bq) at Munich-Neuherberg since 1985. The air-dust concentration ($\mu g/m^3$) is shown in this figure for comparison.

The leaching coefficient is defined as a parameter characterizing the downward movement of radionuclides dissolved in percolating waters (CRWMS M&O 2001 [152517], p. 6) and is calculated as part of the total mass of the radionuclide leached from a soil layer per unit of time (CRWMS M&O 2001 [152517], Section 5.1, Equation 1).

The leaching coefficient for ^{90}Sr determined using Chernobyl data varies significantly from 3×10^{-2}–3.1 L/yr (Bar'yakhtar 1997 [156953], p. 240). For comparison, the leaching coefficient for ^{90}Sr used in the Yucca Mountain biosphere process model is 4.47×10^{-2} L/yr (CRWMS M&O 2000 [151615], Table 3-7), which is near the lower limit of the Chernobyl range. The dissolution rate of uranium reached 2.2×10^{-2} L/yr using Chernobyl data (Bar'yakhtar 1997 [156953], p. 241).

The release of radionuclides from solid particles into the soil is governed by the diffusion process (Sobotovich and Dolin 1994 [156821], p. 57). Given the diffusion coefficients for ^{90}Sr ($1.3–2.1 \times 10^{-16}$ cm^2/s) and ^{137}Cs ($2.5–4.8 \times 10^{-17} cm^2/s$), about 65–80% of ^{90}Sr will become mobile in 10 years, and only 20–30% of ^{137}Cs will become mobile over the same time (Sobotovich and Dolin 1994 [156821], p. 59, 60).

Smith et al. (2000 [156906], p. 141) hypothesized that the "fixation" process of radionuclides controls the amount of cesium in soil water and therefore its availability to terrestrial biota. The decline in ^{137}Cs mobility and bioavailability over the first few years after fallout is most likely controlled by slow diffusion of ^{137}Cs into the soil's illitic clay mineral lattice. However, the sorption-desorption process may be reversible for ^{137}Cs, in which case the ecological half-life increases towards its physical half-life decay rate of 30.2 years. Smith et al. (2000 [156906], p. 141) showed a two-component exponential decline model for the ^{137}Cs decline in vegetation, water, and fish.

13.3.8.2 Soil-Plant-Food Transfer of Radionuclides and Food Contamination

Two main mechanisms control radionuclide transfer to plants: (1) direct deposition on plant surfaces from atmospheric resuspension of contaminated soil and from irrigation with contaminated water, and (2) the root uptake of radionuclides. For example, immediately after the Chernobyl accident, when aerosol particles accumulated only on the outer bark of trees, the radioactivity of leaves of some trees in the streets of central Kiev in 1986 varied from 70,000–400,000 Bq/kg (Bar'yakhtar 1997 [156953], pp. 260, 261). At that time, inner tissues of trees and roots did not pick up contamination. Radioactivity of the outer bark of trees decreased in 5–6 years after the accident, while the activity in wood and inner bark increased because contaminants migrated through the root systems. According to Prister et al. (1991 [157548], p. 146) root uptake became significant the second year after the accident. Bulgakov and Konoplev (2000 [156699], p. 776), who reviewed the existing information on root uptake and modeled root uptake by pine trees within the Chernobyl exclusion zone, stated that the radionuclide concentration at the bottom of the root system is the same as in the most contaminated part of the topsoil layer, and the radiocesium transfer from the root's exchangeable complex into the above-surface part of the plant is relatively rapid. For grass, this takes one day. Radionuclide migration from roots into tree trunks is limited by diffusion and convective radionuclide transfer from the soil into the roots.

The soil-to-plant transfer factor (or concentration ratio) is defined as the ratio of radioactivity concentration in the edible part of the plant (Bq/kg) to the radioactivity concentration in soil (Bq/kg). This factor is also termed the accumulation factor by Bar'yakhtar (1997 [156953], p. 270). Table 13.3-6 compares the soil-to-plant-transfer factors for different radionuclides in the Yucca Mountain Biosphere Process Model with those in Chernobyl. The range of these factors for each element depends on many processes affected by the type of elements and soil properties, plant species, concentration of nutrients and carrier elements in soils, moisture content, acidity of soils, and meteorological and climatic conditions.

The soil-plant transfer processes are not important for short-lived radionuclides, such as ^{131}I, because they essentially decay before being taken up by plant roots. The transfer of radionuclides from soils to plants is limited to long-lived radionuclides. However, the soil-plant transfer is a

predominant pathway for cesium and strontium to appear in pasture and/or fodder, and subsequently in meat and milk, thus becoming part of the exposure pathway. Table 13.3-7 summarizes the values of the cesium soil-to-fodder transfer coefficients, depending on the soil pH and types of agricultural products. This table shows that transfer factors for ^{137}Cs vary significantly (several orders of magnitude) depending on types of soils and plants, because of the effects of microbiological activity in soils (metabolism and decay of microorganisms), and in the presence of different complex-forming ligands (Bondarenko 1998 [156952], pp. 28–31).

A plausible explanation for the observation in Table 13.3-7 that transfer coefficients are higher in natural grasses than in other fodder types could be the following. The transfer coefficients depend on the diffusion of radionuclides into the root system. Natural grasses grow on undisturbed soils with better contact between the soils and roots, which increases the diffusion of radionuclides into grasses. In contrast to undisturbed soils, cultivated soils do not have as good contact with the roots, which reduces diffusion of radionuclides into the plants. At the same time, cultivated soils experience more significant weathering and resuspension of radionuclides by wind. Furthermore, application of fertilizers to cultivated soils and soil-plant microbiological activity may immobilize radionuclides.

The effective meadow-vegetation transfer coefficient for ^{90}Sr is of the same order of magnitude as in alfalfa, and is shown in Figure 13.3-10. Accumulation of ^{137}Cs in vegetables (cucumber and tomato) is higher than in wheat and corn (see Table 13.3-4). Accumulation of ^{137}Cs in some meadow grasses depends on the type of soils and increases in wet soils (Shestopalov and Poyarkov 2000 [157507], Table 5.6.3). The data given in this figure can be used to estimate that the transfer coefficient for ^{90}Sr increased from 1×10^{-3}–1×10^{-2} m^2/kg from 1988 to 1994. This increase can be explained by the fact that ^{90}Sr, which settled on soils, is gradually transformed into a soluble form and thus absorbed by plants.

Bruk et al. (1998 [156600], p. 178) determined that during the first five to six years after deposition, the ^{137}Cs concentration in vegetables and animal agricultural products decreased with an environmental half-life period of 0.7–1.5 years (i.e., the length of time required for ½ of the radioacting to decay *in situ*). Thereafter, beginning from 1990–1991, no significant variation of the ^{137}Cs content in food products was found, and the values of the transfer factors for this radionuclide in the main types of food (milk, potatoes) for rural inhabitants were close to those obtained in the pre-accident period (1980–1985), based on the global origin. Reduction of the ^{137}Cs content in produce was most rapid during the early years after the accident, as intensive countermeasures were applied at that time. Half-life periods for ^{137}Cs content in milk (the basic dose-forming product) and other products for the most contaminated areas in Russia amounted to 1.6–4.8 years, depending on the type of countermeasures used. Half-life periods of the decrease in the ^{137}Cs content in other types of agricultural products (grain, potato) were within the range of 2–7 years. Ivanov (2001 [156818], pp. 65–66) approximated the dynamics of the transfer coefficient for ^{137}Cs in the chain soil-plant by a function

$$y = a \exp(-bt) + (1-a) \exp(-ct) \qquad \text{(Eq. 13-2)}$$

where y is the transfer coefficient normalized to the maximum transfer coefficient, t is the time (in years), and a, b, and c are parameters that depend on the type of soil and plants: a = 0.76–0.94, b = 0.44–1.38, and c = 0.038–0.17 (Ivanov 2001 [156818], p. 67, Table 5). According to

Ivanov (2001 [156818], Table 6), the ecological half-life of ^{137}Cs in agricultural plants varied in terms of averaged values from 0.42 (first period) to 22.1 (second period) years, depending on the type of soils. Figure 13.3-11 presents the dynamics of the transfer coefficient for ^{137}Cs in meadow grass.

Zhdanaova et al. (2000 [156951], p. 64) determined that interaction between biota and *micromycetes* fungi destroyed hot particles after the Chernobyl accident. They determined two mechanisms responsible for these processes: (1) microbial metabolic activity; and (2) mechanical destruction by mycelial overgrowth of radioactive particles. From this, it follows that these processes may also decrease the half-life of radionuclides in the environment, compared with physical half-life values. Therefore, the use of physical values of the half-life of radionuclides gives conservative estimates of radionuclide migration in the Yucca Mountain Biosphere Process Model.

Based on an extensive experimental and modeling study of transfer factors for mushrooms, wild animals, berries, meat, and milk in different regions of Ukraine, Belarus, and Russia, Jacob and Prohl (1995 [156864], p. 110) determined that a peroral (oral) dose is higher than that from the external radiation. They applied several models in calculating transfer coefficients in the chain soil→plants→food→human body. The soil-milk transfer coefficient ranges from less than 1 to 20 Bq/L per kBq/m^2.

Table 13.3-8 presents concentrations of ^{137}Cs in the pasture, milk and meat, and their daily uptake (Richards and Hance 1996 [157613]). These concentrations are used to calculate transfer coefficients using the following formula (CRWMS M&O 2000 [152435], Table 1)

$$\text{Transfer coefficient} = \text{Concentration in meat or milk} / \text{Intake}$$

For Chernobyl, the meat and milk transfer coefficients are $1.6–2.0 \times 10^{-2}$ day/kg and $6.4–8.0 \times 10^{-3}$ day/L, respectively. For the Yucca Mountain Biosphere Process Model, the beef and milk transfer coefficients are 5×10^{-2} day/kg and 8×10^{-3} day/L, respectively (CRWMS M&O [151615], Table 3-14). Thus, the Yucca Mountain meat transfer coefficient exceeds that determined for Chernobyl, and the Yucca Mountain milk transfer coefficient is essentially the same as that for Chernobyl.

13.3.8.3 Radionuclide Accumulation in Fish

Smith et al. (2000 [156906]) measured ^{137}Cs activity concentrations in terrestrial vegetation at seven sites, in lake water, and in mature fish in Cumbria, UK. They determined that ^{137}Cs from the 1986 Chernobyl accident has persisted in freshwater fish for much longer than was initially expected because of the so-called "fixation" process of cesium in soil. They concluded that the effective ecological half-life in young fish, water, and terrestrial vegetation has increased from values of 1–4 years measured during the first five years after Chernobyl to 6–30 years determined since 1990. Jonsson et al. (1999 [156620]) measured cesium in nearly 4,000 fish, taking samples 2–4 times every year in a Scandinavian lake contaminated by Chernobyl fallout. The estimated half-life of cesium concentration in fish was 0.3–4.6 years. Jonsson et al. (1999 [156620]) found that the decline in cesium was initially rapid for three to four years and then became much slower. About 10% of the initial peak radioactivity declined with a half-life of 8–

22 years. Smith et al. (2000 [157433]) determined the bioaccumulation factor of different fish in ten lakes of Belarus, Russia, and Ukraine from 1–232 km from Chernobyl from 6–11 years after the accident. They determined that the bioaccumulation factor for ^{137}Cs ranged from 82–14,424 L/kg for different lakes and types of fish (Smith et al. 2000 [157433], Table 2). The bioaccumulation factor used in the Yucca Mountain Biosphere Process Model for freshwater fish for ^{137}Cs is 2,000 L/kg (CRWMS M&O 2000 [151615], Table 3-15), which is within this range. The Yucca Mountain recommendation for the bounding value of the bioaccumulation factor is 15,000 L/kg (CRWMS M&O 2000 [152435], Table 14), which agrees with the maximum value determined by Smith et al. (2000 [157433], Table 2). Smith et al. (2000 [157433], p. 360) used the term *concentration factor*, which is the same as the bioaccumulation factor for the Yucca Mountain Biosphere Process Model.

13.3.8.4 Livestock Uptake

Livestock uptake represents radionuclide transfer to animal food products. The ^{137}Cs transfer coefficients to cattle, milk, and meat in Ukraine from 1987–1993 are different for soils with different soil pH values (Bar'yakhtar 1997 [156953], Table I.5.4). In 1993, radionuclide concentration in beef from collective farms, where fodder was produced on arable soils, ranged from 20–71 Bq/kg. At the same time, the radionuclide concentration in meat from private farms ranged from 75–520 Bq/kg, and in wild animal meat, it ranged from 504–1,540 Bq/kg (Bar'yakhtar 1997 [156953], pp. 370–371). In the Rivne region of Ukraine, the transfer factor for beef ranged from 0.16–0.59 m^2/kg for collective farms, and ranged from 1–1.7 m^2/kg for private farms. The difference between the collective and private farms can be explained by the fact that countermeasures were undertaken on collective farms.

Empirical data from the leaching and transfer coefficients summarized in Section 13.2.8 show that the initial dissolution of hot particles exposed to the atmosphere increases the concentration of radionuclides, which then decreases with time. The ecological half-life of radionuclides in soils, plants, and foodstuff is less than physical values for radionuclides. Diffusion and absorption processes are limiting factors for radionuclide transfer in soils. Radionuclide transfer to a plant depends on two main mechanisms: (1) direct deposition on the plant surfaces from resuspension of contaminated soil particles or from irrigation with contaminated water, and (2) the root uptake of radionuclides, which is limited by diffusion and convective transport from the soil to the root.

13.3.9 Human Receptor Exposure

This section defines the Chernobyl human receptors and critical groups, gives examples of human exposure pathways and BDCF calculations, and presents the radiation doses from plutonium.

13.3.9.1 Chernobyl Human Receptors and Critical Groups

For risk-assessment purposes, the critical group for Chernobyl was selected to be individuals who were born in the year of the accident and who will live in the same contaminated location for 70 years (IAEA 1991 [156750], p. 207). Exposure of the population was from two main pathways: (1) the radiation dose to the thyroid as a result of the concentration of radioiodine and

similar radionuclides in the gland, and (2) the whole-body dose caused largely by external irradiation mainly from radiocesium (NEA 1995 [156632], p. 30). About 80% of the lifetime dose was accumulated in the first ten years after the accident (Los' and Poyarkov 2000 [157508], p. 194). A group of people that can be considered to include the reasonably maximally exposed individual includes pregnant women, fetuses, and school children (Lazjuk et al. 1995 [156626], p. 71). The risk of radiation for these people is correlated with the level of ^{137}Cs contamination, because ^{137}Cs is the most significant contributor to internal and external doses (see Section 13.3.9.2).

Doses received by the public are different for rural populations, including agricultural workers and "come-backers" living within the highly contaminated exclusion zone, and urban populations. Doses have varied with time since the Chernobyl accident.

13.3.9.2 Human Exposure Pathways

Exposure pathways to the populace resulting from the Chernobyl accident occurred through (1) external irradiation from radioactive materials deposited on the ground from the radionuclide fallout or accumulation from irrigation water, and (2) internal irradiation caused by inhalation of airborne materials and ingestion of contaminated foodstuff. Table 13.3-9 presents an example of the typical types of data for the city of Bragin, Belarus, and includes the following categories of data:

- Population (number of children and total inhabitants)
- Deposition density of ^{137}Cs and ^{90}Sr
- Exposure rate
- Concentration in foods
- Consumption rate of foods
- Internal dose.

This table also illustrates changes in the radionuclide concentration with time in different types of foods and actual internal doses in different population groups.

The dose received by the rural population makes up the bulk of the collective dose. Collective dose is the total dose over a population group exposed to a given source and is represented by the product of the average dose to the individuals in the group, multiplied by the number of persons comprising the group—for example, person-sievert (Sv) (NEA 1995 [156632], p. 59). Between 1986 and 1996, the rural population received 77% of the collective total effective dose. From 1986 to 1996, the mean annual collective effective internal dose was 65% versus 35% for the external dose for the rural areas (Los' and Poyarkov 2000 [157508], p. 186). In the urban areas, the main source of the internal dose was inhalation, while in the rural, agricultural areas, the internal dose consisted of both inhalation and ingestion of radionuclide particles.

About 95% of the contribution to external and internal doses to the rural population was by ^{137}Cs (Los' and Poyarkov 2000 [157508], p. 185). Based on Chernobyl investigations, the dose received by the public from TRU elements would be several dozen to several hundred times smaller than that from strontium and cesium over the 70-year period following the accident. Table 13.3-10a shows that the effective dose for the rural population is higher than that for the

urban population, because people in rural areas spent more time outdoors. The effective dose decreased rapidly for the first year after the accident, and then slowly until 1996. Table 13.3-10a presents changes in the effective dose of external radiation from ^{137}Cs with time. These values, if expressed in mrem/yr per pCi/m^2 (Table 13.3-10b), can be compared with BDCFs from external radiation for the Yucca Mountain Disruptive Event Scenario model. The annual value of 1 μSv/(kBq/m^2) corresponds to 3.7×10^{-6} mrem/yr per pCi/m^2.

Table 13.3-10c presents the BDCFs from the Yucca Mountain disruptive event scenario (CRWMS M&O 2001 [152536], Tables 11 and 13). Figure 13.3-12 shows that the calculated Yucca Mountain and observed Chernobyl BDCFs for ^{137}Cs are within the same order of magnitude for both minimum and maximum values. (To relate BDCF values using the method presented above to potential contamination at Yucca Mountain, the BDCF units reported in Table 5-17 of CRWMS M&O (2000 [151615]) have to be converted from mrem/yr per pCi/L to mrem/yr per pCi/m^2. Assuming that the wetted zone due to potential irrigation is 1 cm thick and the volumetric moisture content is 10%, 1 mrem/yr per pCi/L is equivalent to 1 mrem/yr per pCi/m^2.)

Table 13.3-11 shows maximum ^{137}Cs concentrations (kBq/m^2) in soils producing an internal radiation dose of 1 mSv/yr (100 mrem/year). The total radiation dose of 100 mrem/year is the annual permissible limit for the general public (DOE 1994 [104736], p. 2-6). The corresponding BDCFs for the internal radiation were calculated from the formula

BDCF = Internal radiation dose / Radionuclide concentration activity of soil

which is based on the BDCF definition given in CRWMS M&O (2000 [151615], Section 3.1.4.1). Because the Yucca Mountain model uses BDCFs in mrem/year per pCi/m^2, the concentrations in pCi/m^2 (Columns 4 and 5 of Table 13.3-11) were first calculated using the conversion factors 1 kBq = 27,027 pCi, and then the corresponding BDCFs (Columns 6 and 7 of Table 13.3-11) were calculated from the formula

BDCFs = 100 mrem/year / Concentration in soil (pCi/m^2)

Because Table 13.3-11 presents maximum ^{137}Cs concentrations to obtain the annual dose of 1 mSv (1 mSv = 100 mrem), BDCFs calculated are minimal. These can be compared to BDCFs derived for both disruptive and nondisruptive contamination event pathways at Yucca Mountain as shown in Figure 13.3-13. For Chernobyl loamy soils, which have properties closer to Yucca Mountain soils than other types of soils, the BDCF is 1.25×10^{-5} mrem/yr per pCi/m^2 for tilled soils. This value is two to ten times higher than the minimal BDCFs for the Yucca Mountain disruptive contamination scenario. This difference occurs because contaminated groundwater is not taken into account when calculating BDCFs for the disruptive event scenario for Yucca Mountain (CRWMS M&O 2000 [151615], Section 3.3.2), while the use of contaminated groundwater contributed to the internal dose obtained after the Chernobyl accident. (Contaminated groundwater for the Yucca Mountain biosphere is included in dose calculations performed in the TSPA model once the radionuclide concentrations are estimated.) The critical group pathway analyses and sensitivity studies conducted for Yucca Mountain showed that the BDCF values for most radionuclides were dominated by only two consumption rates: water and leafy vegetables (CRWMS M&O 2000 [151615], Section 3.1.2.3). In contrast, Chernobyl data

showed that drinking groundwater was an insignificant contributor to the human dose (Bugai et al. 1996 [156596]). However, milk and milk products contributed significantly to the human dose (Table 13.3-12), more so than would be true for the Yucca Mountain critical population, because the consumption of milk products in Ukraine [the average is 0.18–1.5 L/day in different regions (Bar'yakhtar 1997 [156953], Table I.3.9–I.3.11)] is much higher than that in the United States. (The average used in the Yucca Mountain Biosphere Process Model is 0.011 L/day (CRWMS M&O 2000 [151615], Table 3-16)). More importantly, the short-lived radionuclides associated with the Chernobyl accident are far more significant contributors to human dose.

The IAEA (1991 [156750], Part E, pp. 222–237) estimated external and internal doses based on (1) direct measurements and (2) dose calculations in settlements located within the area with ^{137}Cs concentrations exceeding 550 kBq/m^2 (>15 Ci/km^2). Figures 13.3-13a indicates that a ^{137}Cs body concentration has a log-normal distribution across the population. Different dietary restrictions or habits (such as eating large quantities of forest mushrooms, an example relevant to Yucca Mountain in principle only) could cause variable body concentration distributions between different settlements. Figures 13.3-13b shows a significant scatter of data for the age-dependent distribution of ^{137}Cs.

Commercial fishermen on the Kiev reservoir, who consumed 360 kg/yr of fish in 1986, received 4.7×10^{-4} and 5×10^{-3} Sv from ^{90}Sr and ^{137}Cs, respectively (Berkovski et al. 1996 [156592], p. 41), i.e., the dose ratio of cesium to strontium was 10.6. The predicted contributions to the collective effective dose resulting from irrigation, municipal tap water, and fish for members of the general public for over 70 years following the ChNPP accident are shown in Table 13.3-13.

The predicted contribution of ^{90}Sr to the collective dose resulting from the use of Dnieper water is 80% (Berkovski et al. 1996 [156592], p. 42). Figure 13.3-14 presents the contribution of ^{90}Sr and ^{137}Cs in different components of food-chain pathways to averaged effective internal dose for Kiev in 1993. The contribution of radionuclides through the drinking-water pathway is different in different areas. For example, the drinking-water pathway contribution for the people of Kiev was about 6% of the total radiation dose; for the people of the southern Ukraine, it was 14% to 34% (Voitsekhovich et al. 1996 [156921], Figure 7).

Bugai et al. (1996 [156596]) estimated health risks caused by radionuclide migration to groundwater and compared these risks with risks from exposure to radioactive contamination on the ground surface. They determined that the estimated health risk to hypothetical, self-sufficient residents in the 30 km exclusion zone is dominated by external and internal irradiation from ^{137}Cs, caused mainly by ingestion of agricultural products. The estimated risk caused by drinking contaminated groundwater is approximately an order of magnitude lower. Strontium-90 migration via groundwater to surface water used in downriver population centers shows that groundwater can potentially only marginally contribute to the offsite radiological risk. Bugai et al. (1996 [156596], pp. 13–14) calculated the annual committed effective doses caused by consumption of ^{90}Sr-contaminated water, using an ingestion dose conversion factor of 3.9×10^{-5} mSv/Bq, determined by the Eckerman et al. (1988 [101069], Section II) formula. Committed effective dose equivalent is the resulting dose committed to the whole body from radionuclides absorbed internally over a 50-year period (DOE 1994 [104736], p. 2-3). Berkovski et al. (1996 [156592], p. 42) determined that consumption of drinking water in 1986 by the populace in the

Kiev region led to the maximum individual annual committed effective doses of 1.7×10^{-5} and 2.7×10^{-5} Sv from ^{90}Sr and ^{137}Cs, respectively.

13.3.9.3 Radiation Doses from Plutonium

An effective dose equivalent was used to assess the risk of inhalation of hot particles, accumulated on lungs from the Chernobyl accident, as a function of the distance between particles and α and β-radiation (Loshchilov et al. 1991 [156823], pp. 198, 202). The risk of lung cancer calculated based on the assumption of uniform distribution of radioactivity exceeds that calculated for a point source by a factor of two to three.

The most hazardous particles are those containing plutonium, which can contribute up to 40% of radioactivity in dust (Anokhova and Krivtsov 1991 [156829], p. 206). Calculations showed that the inhalation doses for agricultural laborers working on truck platforms are greater than external doses, and the Pu concentration exceeded the acceptable limit by an order of magnitude (Anokhova and Krivtsov 1991 [156829], pp. 209, 212). In the Yucca Mountain Biosphere Process Model for the disruptive event scenario, the sum of fractions of plutonium-238, -239, and -240 would exceed the contribution of other radionuclides (CRWMS M&O 2000 [151615], Table 3-23), as was observed at Chernobyl. Breathing air containing such high concentrations of plutonium for two months can lead to its accumulation in bones in concentrations exceeding the annual permissible limit (Anokhova and Krivtsov 1991 [156829], p. 209).

The main pathways for plutonium intake resulting from the Chernobyl accident are inhalation (which has been treated as an acute intake since 1986), uniform oral intake from food products, and inhalation of resuspended dust particles. Bondarenko et al. (2000 [156593], p. 475) calculated that the transfer factor of plutonium into grass is 0.3×10^{-3} (Bq/kg)/(Bq/m^2), and it could be as low as 0.15×10^{-6} (Bq/kg)/(Bq/m^2) due to the superficial contamination of grass. They also determined that the "soil-diet" transfer coefficient normalized to unit contamination density is 1.2×10^{-7} (Bq/kg)/(Bq/m^2). In this calculation, Bondarenko et al. (2000 [156593], p. 475), assumed that the "soil-diet" transfer coefficient is 2.4×10^{-5} (Bq/kg)/(Bq/m^2); the soil density is 2 g/cm^3; radioactivity is uniformly distributed within the top 10 cm soil profile; plutonium concentration in soils is 3,700 Bq/m^2, which is typical for the southeastern periphery of the exclusion zone; initial fallout particles of 1 μm in diameter, precipitating on inert soil particles, form agglomerates 5 μm in diameter; rural inhabitants spend one-third of the day outdoors; and the averaged resuspension coefficient is 10^{-9}/m.

Bondarenko et al. (2000 [156593], pp. 476–477) also presented data on the content of α-emitting isotopes of plutonium in the human skeleton. They found that the average plutonium content in 25 samples was 4.9×10^{-2} Bq for regions contaminated at the level of 20 mCi/km^2 (740 Bq/m^2). Table 13.3-14 presents the calculated content of α-emitting plutonium isotopes in the human skeleton in 1998 and compares these data with global fallout. This table indicates that the Chernobyl data exceeded that resulting from global fallout by 2.5–9.2 times.

13.4 SUMMARY AND CONCLUSIONS

Section 13.3 reviewed information from the Chernobyl accident regarding the exposure pathways, distribution of radioactive contaminants in the biosphere, and inputs to risk assessment

that may be relevant to future revisions of the Yucca Mountain Biosphere Process Model. Despite the difference in climatic conditions and the accident/potential-exposure scenarios for Chernobyl and Yucca Mountain, respectively, the Chernobyl data serve as a source of information to improve the confidence in a conceptual model of exposure pathways and process models. As part of the biosphere-model validation for both groundwater release and volcanic release scenarios, the YMP is interested in measurements that could represent input data in validating models for specific environmental processes, as listed in Section 13.2. The main conclusions that can be drawn from Chernobyl with respect to these processes and parameters are described below.

Radionuclide transfer from soil to plant via root uptake (see Section 13.3.8.2). Cesium migration from soils to grasses is relatively rapid. The radionuclide migration from roots into the tree trunks is limited by diffusion and advective radionuclide transfer from the soil (Bulgakov and Konoplev 2000 [156699]). Root uptake became a significant contributor to the food chain in the second year after the accident (Prister et al. 1991 [157548], p. 146).

Radionuclide transfer from soil to plants via atmospheric resuspension, including deposition of resuspended material on plant surfaces (see Section 13.3.5). Resuspension of radionuclides by wind-driven dust is an important factor after the tillage of agricultural lands, increasing the resuspension by more than an order of magnitude. Resuspended material is likely to settle on plant surfaces, thereby increasing their contamination. The Chernobyl data on hot-particle dispersal and dust transport showed that radionuclides attach to dust particles and move as combined particles. Aspects of models of atmospheric contaminant dispersal, radionuclide fallout, radionuclide resuspension, and particle-size distributions developed by Garger et al. (1999 [151483]), Goldman et al. (1987 [156820]), and Kashparov et al. (2000 [156622]) may be relevant to building confidence in a model for radionuclide resuspension resulting from a volcanic eruption through a potential Yucca Mountain repository.

Radionuclide transfer from animal food to animal products (see Sections 13.3.8.2 and 13.3.8.4). These data could be used in assessing the Yucca Mountain models for meat and milk contamination. Environmental half-life periods of decay of ^{137}Cs content in milk and agricultural products were shorter than those initially expected.

Removal of contaminants via erosion and leaching (see Sections 13.3.5 and 13.3.8.1). The average annual topsoil erosion in Ukraine from 1987 to 1990 contributed to the annual removal of 0.7×10^5 Bq/ha of ^{137}Cs from soils (Prister et al. 1991 [156824], Table 7). As a result of biochemical and physical-chemical processes, hot particles have been significantly dissolved by now, and radionuclides have been transferred to soils (Kashparov 2001 [156819], p. 37). The use of physical values of the half-life of radionuclides gives conservative estimates of radionuclide removal from soils in the Yucca Mountain Biosphere Process Model.

Inhalation of resuspended contamination material originally deposited on the ground (see Sections 13.3.5 and 13.3.9.3). The most hazardous particles associated with the Chernobyl accident are those containing plutonium, which can contribute up to 40% of radioactivity in the dust (Anokhova and Krivtsov 1991 [156829], p. 206). The inhalation doses for agricultural laborers are greater than the external doses, with the plutonium concentration exceeding the acceptable limit by an order of magnitude.

Radionuclide accumulation in soils and plants under irrigation using contaminated water (see Section 13.3.7). Irrigation using contaminated water creates radioactive contamination of both irrigated soils and agricultural products (Perepelyatnikov et al. 1991 [156822]; Bondar et al. 1991 [156846]). The increase in the concentration of radionuclides in soils during irrigation in the southern Ukraine, where environmental conditions are more similar to those at Yucca Mountain than are those in the Chernobyl vicinity, confirms the concept of a radionuclide-buildup factor used in the Yucca Mountain Biosphere Process Model.

In summary, results of the Chernobyl literature survey suggest that soil type influences the ecological half-life of radionuclides in the biosphere, both in regard to soil bioaccumulation factors and advective and diffusive transport properties that limit radionuclide transfer to plant roots. With respect to rural populations, agricultural methods—including irrigation and tillage—and crop types play an important role in resuspension of radionuclides. Resuspended material is likely to increase the contamination of plant surfaces. Resuspended radionuclides would increase the inhalation dose for agricultural workers, which would be particularly significant for plutonium associated with the Chernobyl accident.

Chernobyl data include both the relatively short-lived isotopes of iodine, cesium, and strontium, and long-lived transuranic elements such as plutonium and americium. Among the long-lived radionuclides of interest to Yucca Mountain, and not present at Chernobyl, are ^{129}I, ^{227}Ac, ^{232}U, ^{233}U, ^{237}Np, ^{243}Am, ^{210}Pb, ^{231}Pa, ^{226}Ra, ^{230}Th, and ^{242}Pu (CRWMS M&O 2000 [151615], Sections 3.3.1 and 3.3.2).

Numerous data collected for the past 15 years about the distribution and accumulation of radioactive materials in different parts of the biosphere after the Chernobyl accident, including the main exposure pathways and mechanisms of radioactive contamination of the environment and the population, can be used to build confidence in Yucca Mountain conceptual and numerical models. They can also be used to enhance models for long-term transport processes and radiation doses associated with possible exposure to radioactive material in the vicinity of the potential nuclear waste disposal site at Yucca Mountain. For the potential groundwater-contamination scenario at Yucca Mountain, radionuclide-contaminated water, which is to be used as the source of drinking water, irrigation, animal watering, and domestic uses, is expected to increase the likelihood of ingestion uptake of radionuclides by humans. Chernobyl data on the atmospheric distribution of contaminants, their fallout, and redistribution in soils and plants may be considered an anthropogenic analogue for the potential release of radionuclides caused by a volcanic eruption at Yucca Mountain, accompanied by atmospheric dispersal of contaminants into the environment through ash fallout on the land surface. Analogues related to volcanic processes are discussed in Section 14.

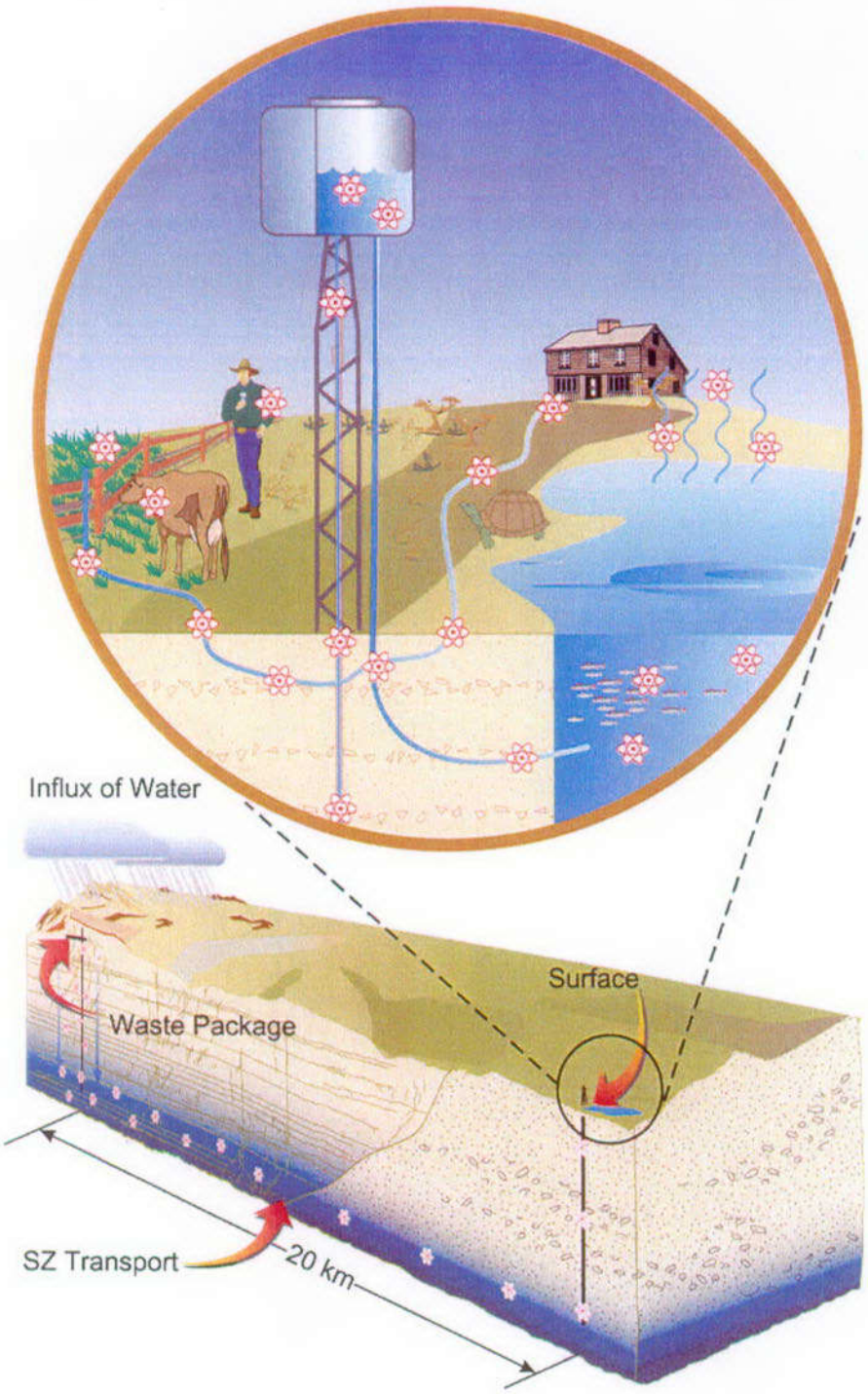

Source: CRWMS M&O 2000 [151615], Figure 3-1.

Figure 13.2-1. Illustration of the Biosphere in Relationship to the Potential Repository System

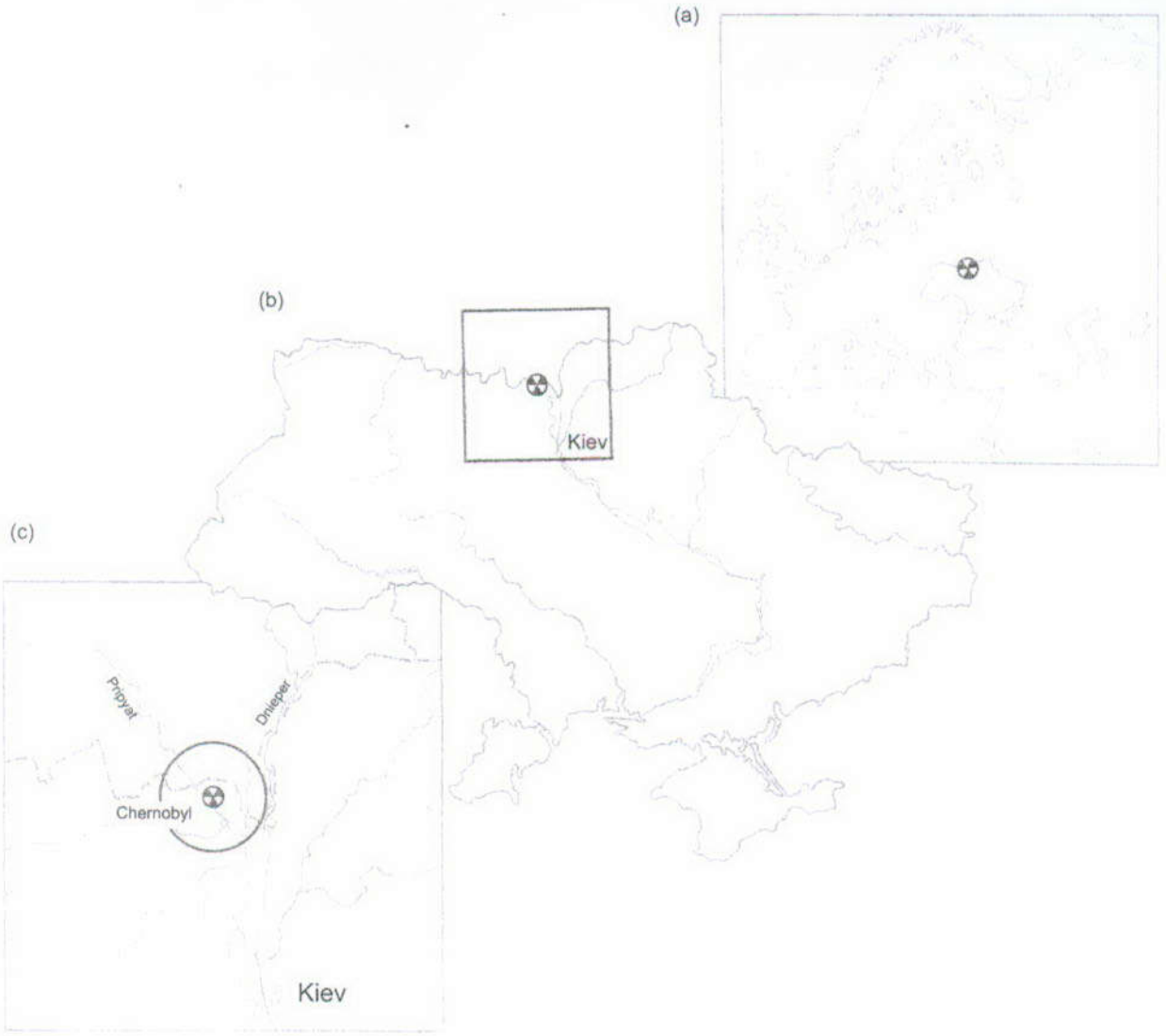

Source: Modified from Shestopalov 1996 [107844], p. 1.

Figure 13.3-1. Location of the ChNPP in (a) Europe, (b) Ukraine, and (c) the Kiev Region

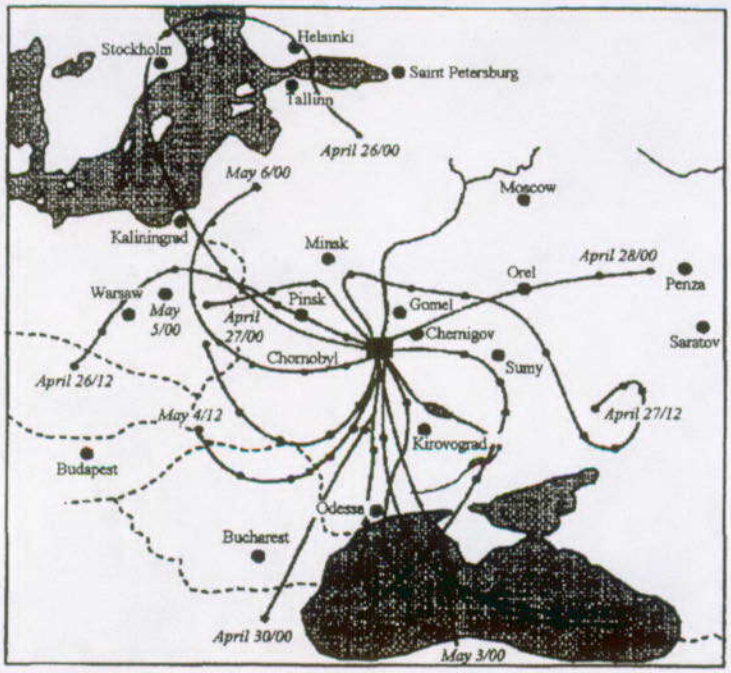

NOTE: Dashed lines indicate country boundaries, and Dates/Times indicate date and time (in hours) in 1986.

Source: Bar'yakhtar et al. 2000 [157504], Figure 2.5.2).

Figure 13.3-2. Fallout Trajectories of the ChNPP Accident

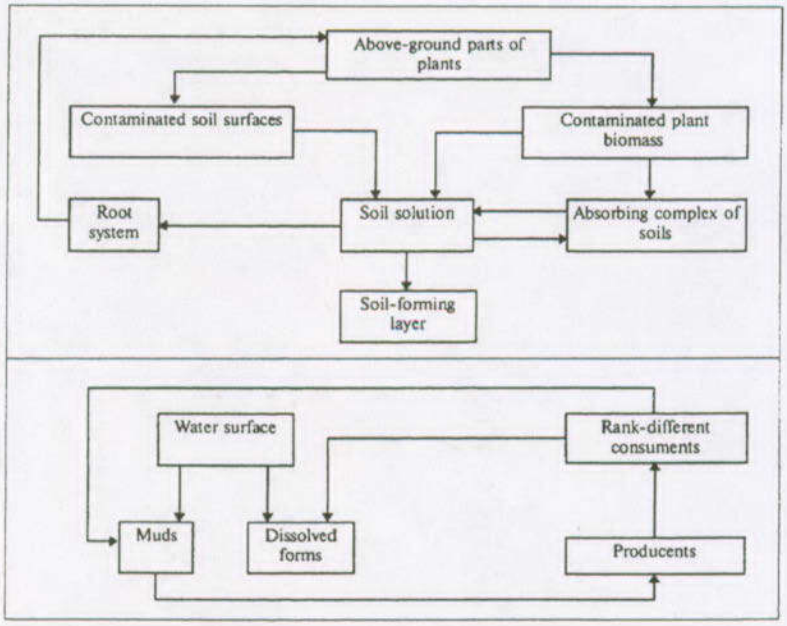

Source: Bar'yakhtar 1997 [156953], Figure I.3.19, p. 263.

Figure 13.3-3. Schematic Illustrating the Principal Pathways for the Radionuclides Entering the Biosphere through Terrestrial and Aquatic Ecosystems That Were Considered in Evaluating the Consequences of the Chernobyl Accident

a)

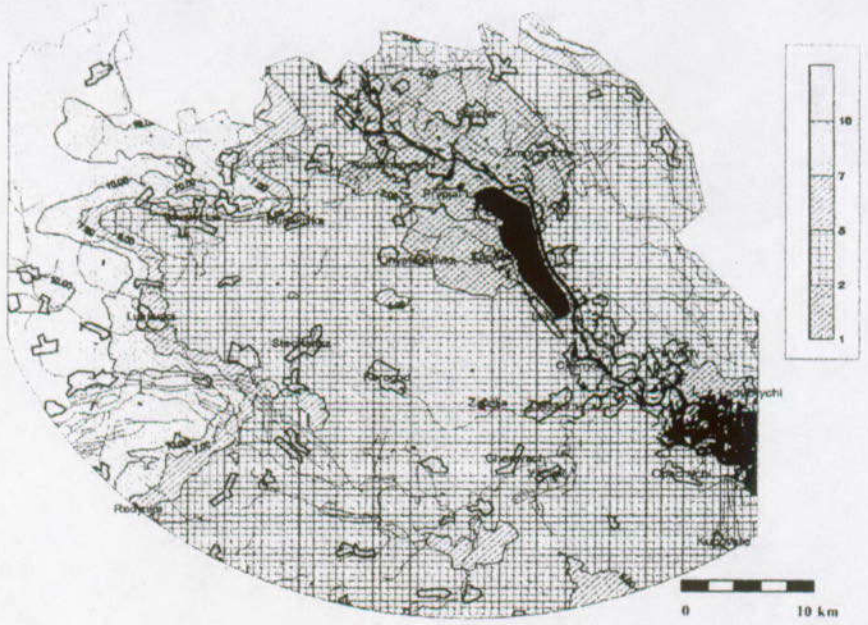

b)

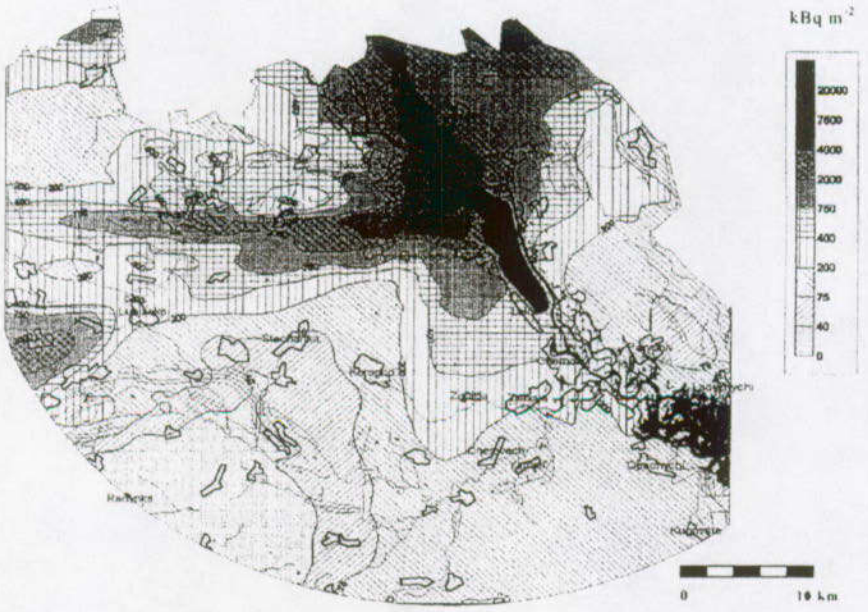

NOTE: Concentrations are kBq/m^2.

Source: Data of the Ukrainian Institute of Agricultural Radioecology (Kashparov et al. 2001 [157400], Figure 3, Figure 2).

Figure 13.3-4. Maps of the Terrestrial Contamination of the 30 km Chernobyl Exclusion Zone in Ukraine: (a) ^{90}Sr; (b) ^{137}Cs

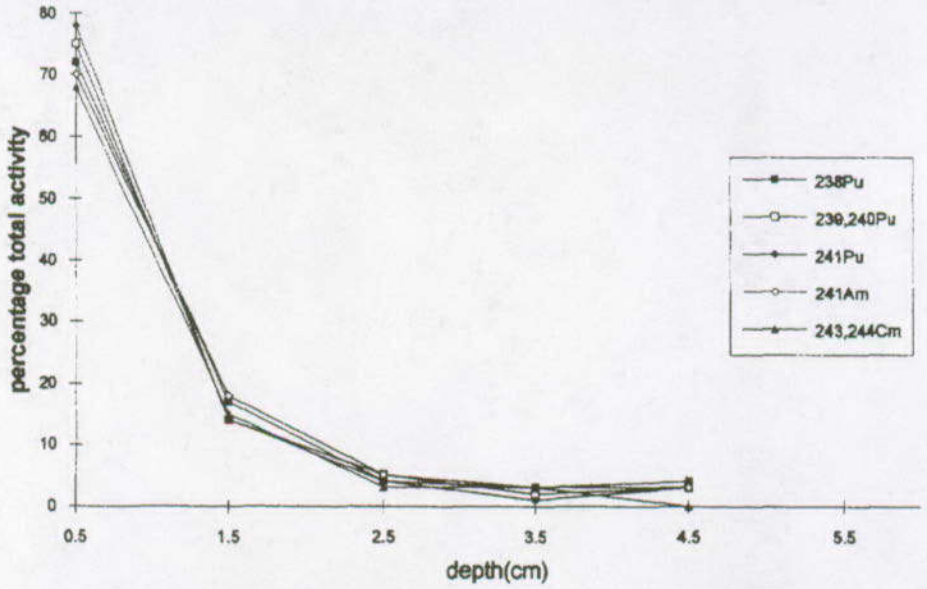

Source: Mboulou et al. 1998 [156628], Figure 1.

Figure 13.3-5. Vertical Distribution of Actinides in Soil to 4.5 cm

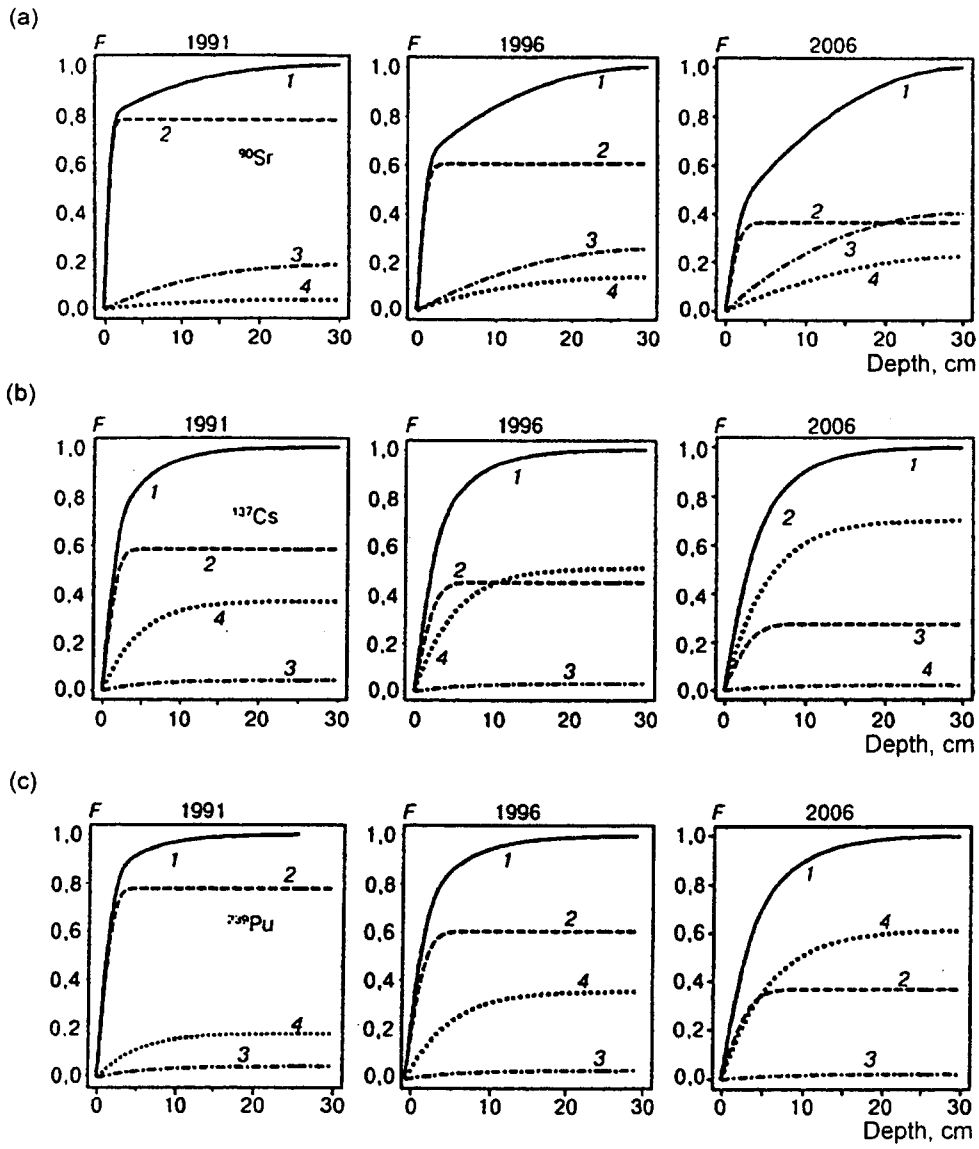

NOTE: 1 - total content, 2 - radionuclides in fuel particles, 3 - mobile forms, and 4 - absorbed forms.

Source: Ivanov 2001 [156818], p. 57.

Figure 13.3-6. Dynamics of Redistribution of ^{90}Sr (a), ^{137}Cs (b), and ^{239}Pu (c) as a Function of Depth and Time in Derno-podzolic Silt Soils

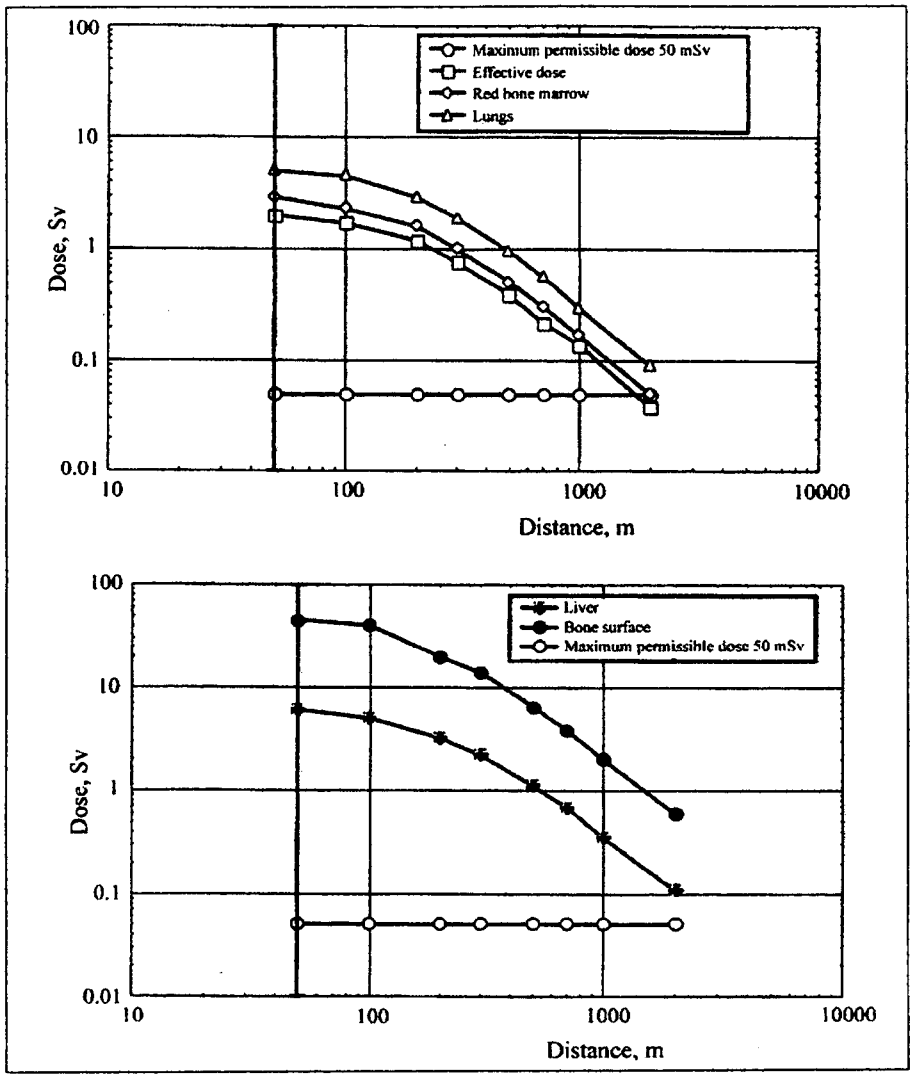

NOTE: For Pasquill weather Category C with no wind and speed of 4.2 m/s at 100 m altitude, which corresponds to a wind speed of 2.53 m/s at the surface.

Source: Bar'yakhtar et al. 2000 [157505], Figure 3.5.2.

Figure 13.3-7. Predicted Inhalation Doses as a Function of the Distance from the Hypothetical Collapsed Shelter

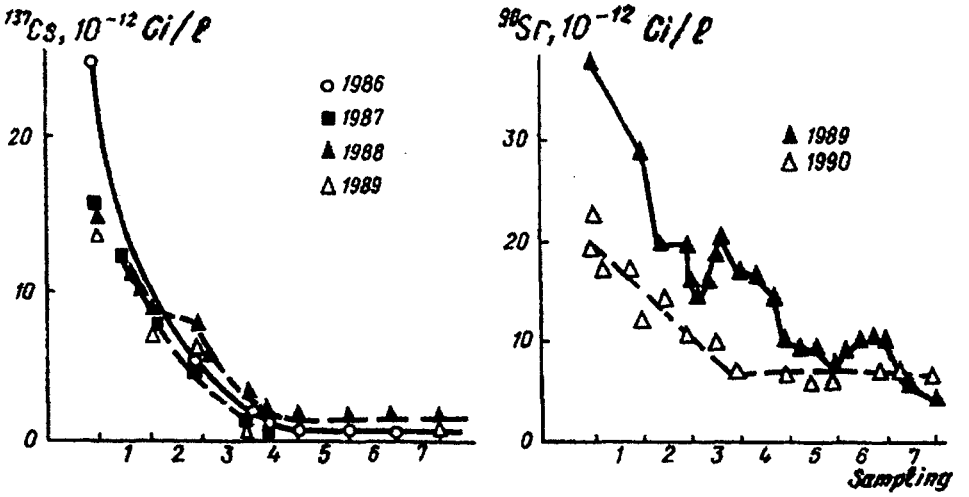

NOTE: 1: mouth of Pripyat; 2: Kiev Reservoir; 3: Kanev Reservoir; 4: Kremenchug Reservoir; 5: Dneprodzerzhinsk Reservoir; 6: Zaporozh'e Reservoir 7: Kakhovka Reservoir.

Source: Modified from Bar'yakhtar 1997 [156953], Figure I.3.16, p. 250.

Figure 13.3-8. Concentration of ^{90}Sr and ^{137}Cs in Water from Seven Sites along the Dnieper River

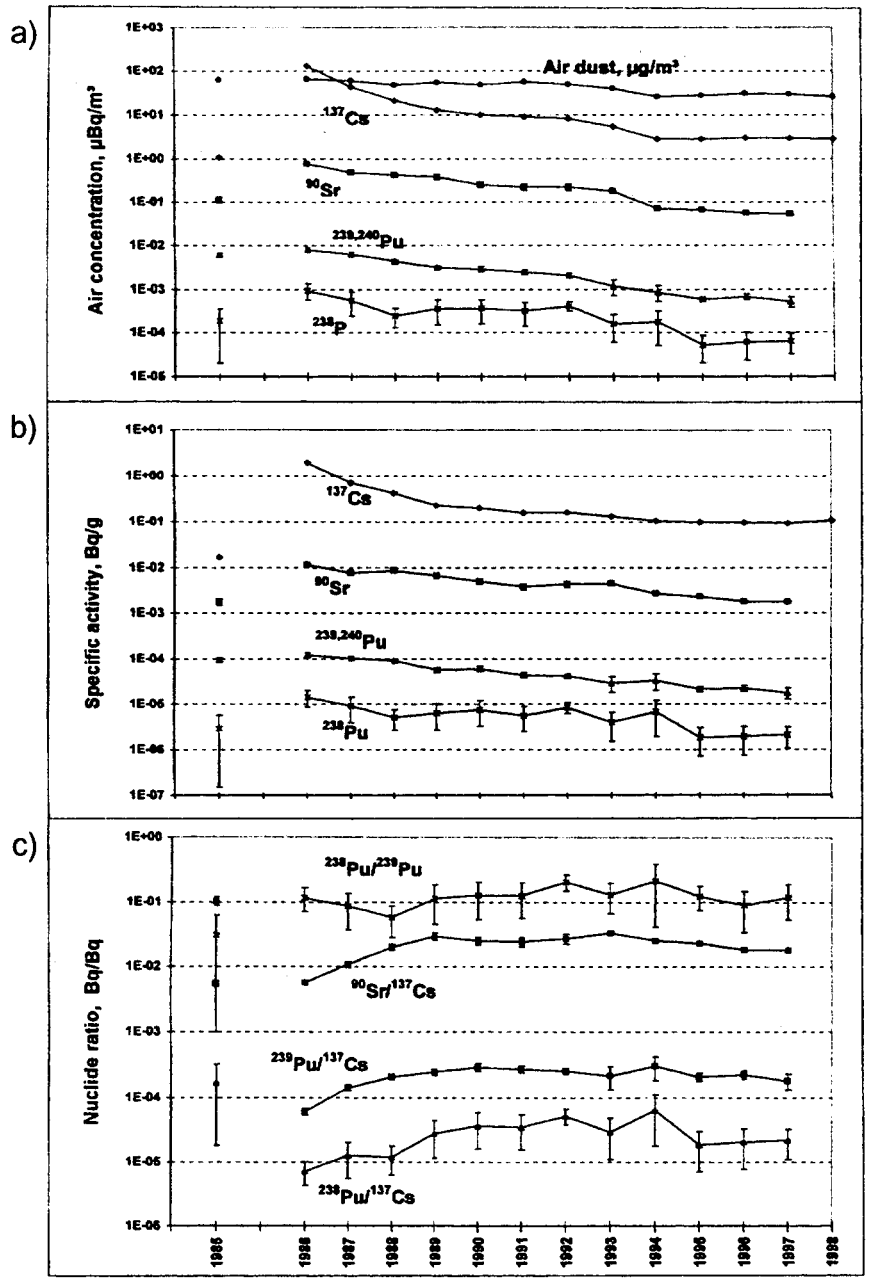

NOTE: All values are corrected for radioactive decay to 1 May 1986. Values for 1986 relate to the second half of the year only, i.e., the Chernobyl deposition phase is not included. The air-dust concentration (µg/m^3) is shown for comparison.

Source: Rosner and Winkler 2001 [156629], Figure 1.

Figure 13.3-9. Mean Values of (a) Radionuclide Concentrations in Air (µBq/m^3), (b) Specific Activities in Air Dust (Bq/g), and (c) Radionuclide Ratios in Air (Bq/Bq) at Munich-Neuherberg Since 1985.

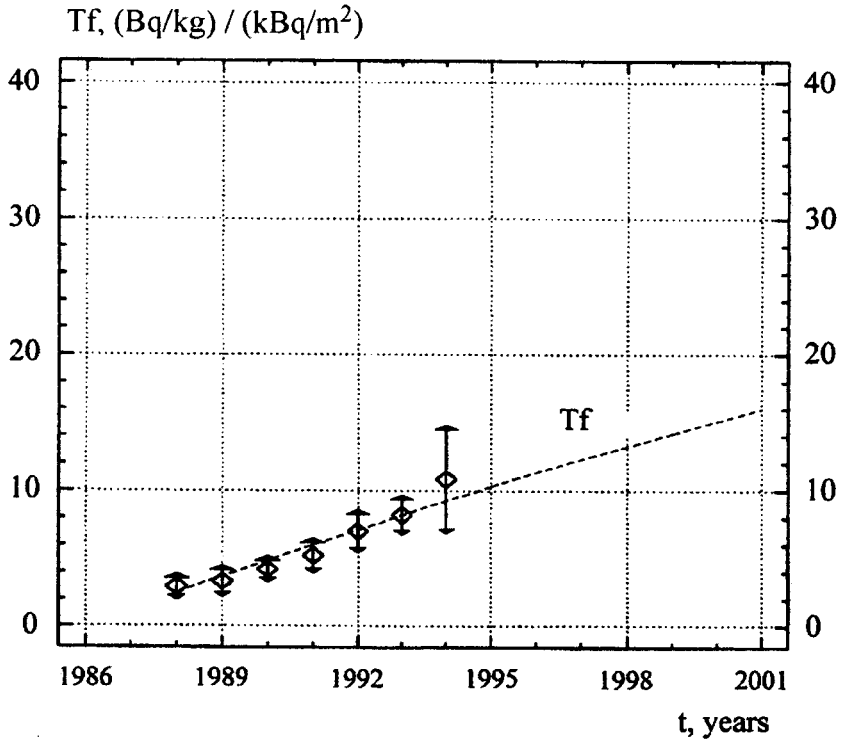

NOTE: Data points are experimental values; the line is the theoretical curve for pH=6.

Source: Bar'yakhtar et al. 2000 [157504], Figure 2-5.9.

Figure 13.3-10. Effective Meadow-Vegetation Transfer Coefficients for ^{90}Sr (T_f), Neglecting Redistribution in the Root Layer

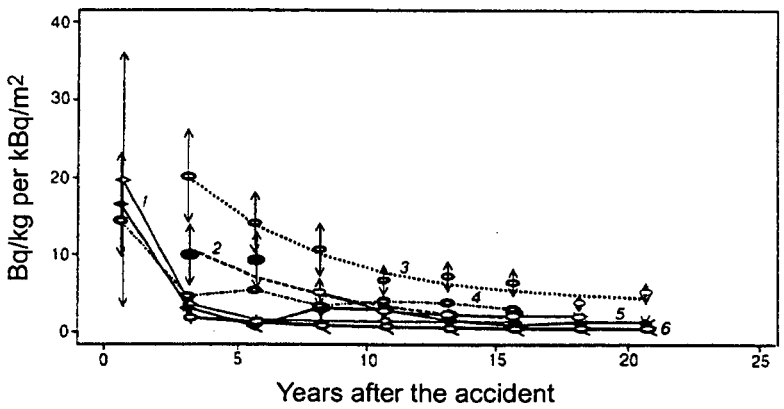

NOTE: 1, 2: derno-podzolic sandy soils; 3: derno-podzolic silty and sandy soils; 4: mineral soils with fuel traces; 5: derno-podzolic sandy soils with fuel traces; 6: loamy and clayey soils.

Source: Ivanov 2001 [156818], Figure 10, p. 63 (summarized the results of several authors).

Figure 13.3-11. Dynamics of the Soil-Plant Transfer Coefficient for ^{137}Cs, Which Is Approximated by a Function $y = a \exp(-bt) + (1-a) \exp(-ct)$, for Meadow Grass Areas

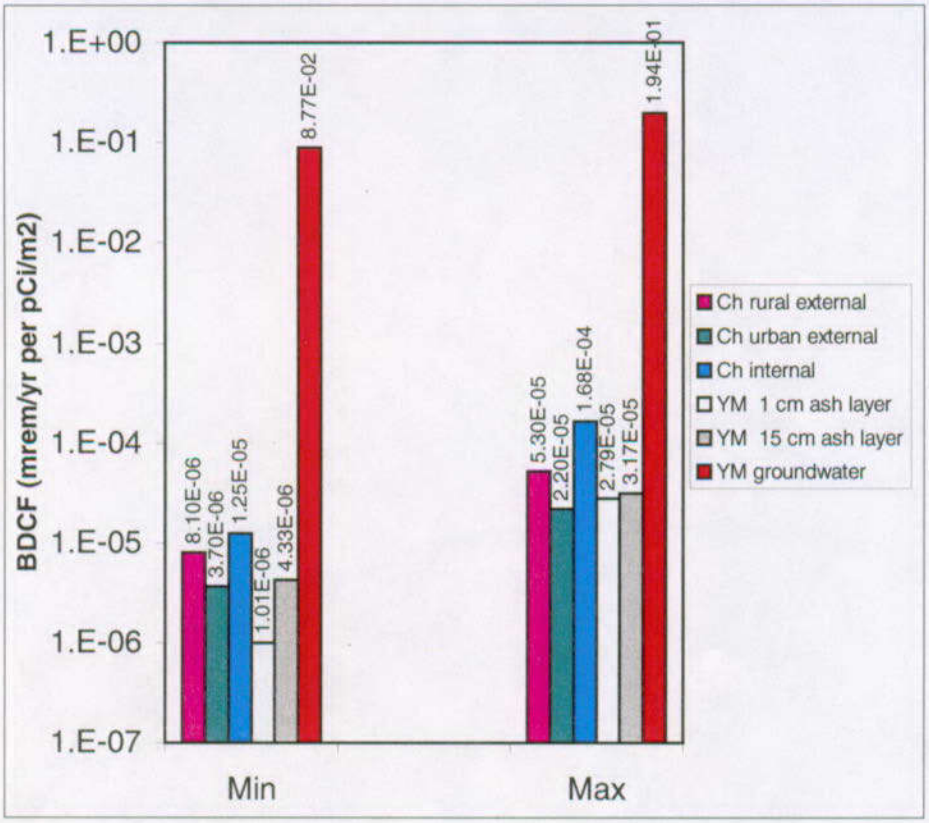

NOTE: For groundwater BDCF, refer to Section 13.3.9.2.

Chernobyl External Dose (Table 13.3-10b); Yucca Mountain (YM) Disruptive Event Contamination Scenario (Table 13.3-10c); and Internal Radiation for Soil Types for Chernobyl (Table 13.3-11).

Source: CRWMS M&O 2000, [151615], Table 3-17 (for Yucca Mountain Groundwater Contamination Scenario).

Figure 13.3-12. Comparison of Minimum and Maximum Values of ^{137}Cs BDCFs for Chernobyl (Ch) and Yucca Mountain

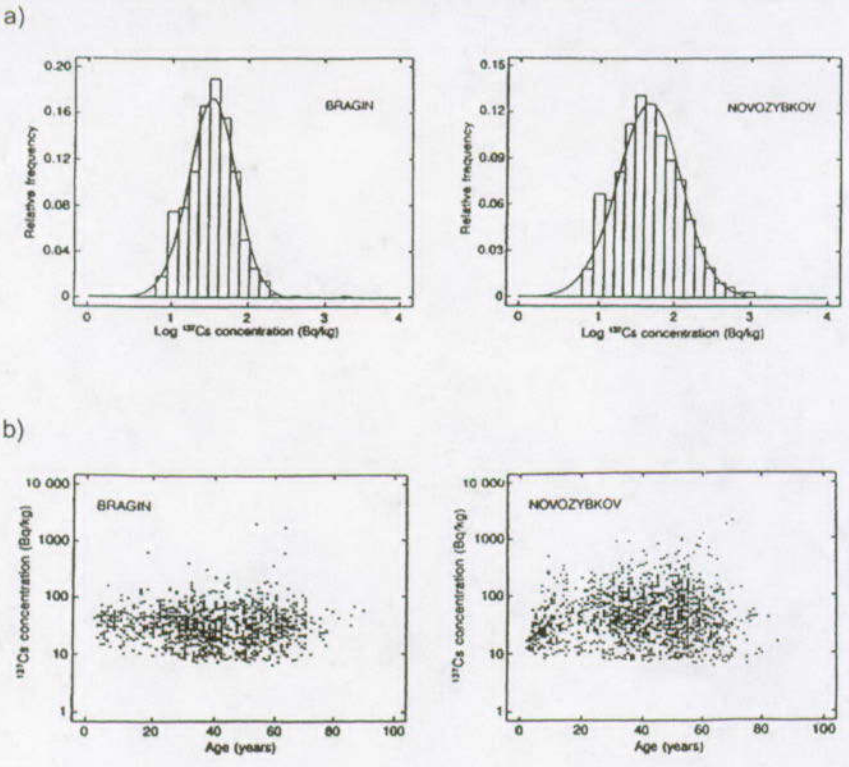

Source: (a) IAEA (International Atomic Energy Agency) 1991 [156750], p. 265;
(b) IAEA 1991 [156750], p. 263.

Figure 13.3-13. (a) Frequency Distributions of the Logarithm of ^{137}Cs Concentration in the Body at Two Selected Settlements (Bragin, Belarus, and Novozybkov, Russia); (b) Scatter Diagram of ^{137}Cs Concentration in the Body as a Function of Age

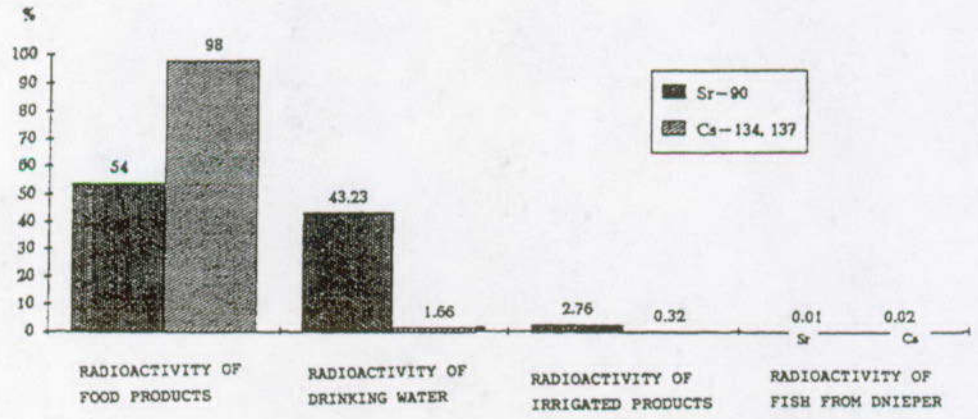

Source: Voitsekhovitch et al. 1996 [156921], Figure 8.

Figure 13.3-14. Contribution of ^{90}Sr and ^{137}Cs in Different Components of Food Chain Pathways to Averaged Effective Internal Dose for the Population of the City of Kiev (1993 scenario)

Table 13.3-1. Vertical Distribution of Plutonium and Uranium in Soils in the Vicinity of the ChNPP

Depth (cm)	$^{239(240)}$Pu (%)	Ratio $^{238}U/^{235}U$
0-1	91-97	79.9-103.5
1-2	2.9-7.9	126.7-135.8
2-3	0.3-0.6	129.6-137.3
3-4	0-0.2	137.1-137.8
4-5	0-0.1	137.6-137.8

Source: Sobotovich 1992 [134218], Table 3.6.

Table 13.3-2. Typical Radioactive Contamination Levels (Bq/L) for Groundwater in the Inner Exclusion Zone

Source of water	^{90}Sr	^{137}Cs	$^{239+240}$Pu	^{241}Am
MPC (maximum permissible concentration)	14.8	555.5	81.5	70.3
Regional groundwater contamination	0.1-10	0.1-1	≤0.01	≤0.01
Shelter	$10\text{-}10^3$	0-100	--	--
Interim radioactive waste storage sites	$10^2\text{-}10^4$	0.1-10	≤0.01-1	≤0.01
Cooling pond	$1\text{-}10^2$	0.1-1	--	--
Artesian aquifer in Eocene deposits	≤0.01	≤0.01	--	--

Source: Shestopalov and Poyarkov 2000 [157507], Table 5.4.1.

Table 13.3-3. Percentages of Measured Concentrations of Radionuclides in Kiev Metropolitan Area Groundwater, 1992–1996

Aquifer	^{137}Cs Concentration, mBq/L				^{90}Sr Concentration, mBq/L		
	<10	10–50	51–150	>150	<10	10–50	>50
Quaternary	24%	56%	14%	6%	53%	40%	7%
Eocene	45%	41%	9%	5%	71%	21%	8%
Late Cretaceous (Cenomanian)–Early Jurassic (Callovian)	46%	31%	13%	10%	80%	20%	--
Middle Jurassic (Bajocian)	47%	28%	15%	10%	62%	35%	3%

NOTE: The depths tested are: Quaternary aquifer: 2–18 m; Eocene aquifer: 45–65 m; Late Cretaceous (Cenomanian)–Early Jurassic (Callovian) aquifer: 80–150 m; Middle Jurassic (Bajocian) aquifer: 200–300 m.

Source: Shestopalov and Poyarkov 2000 [157507], p. 150, Table 5.4.2.

Table 13.3-4. Cesium-137 Concentrations in Agricultural Products Grown on Lands Irrigated Using Water from the Dnieper River Reservoirs, Compared with Lands Irrigated by Water from Other Sources

Type of Plant	Year	Irrigation using Contaminated Water from Dnieper River Reservoirs (see Figure 13.3-8)				Irrigation Using Uncontaminated Water	
		Kanev	Kremenchuh	Dnepro-dzerzhinsk	Kakhovka	Kharkov Region	Donetsk Region
Winter wheat (seeds)	1987	50	50	25	30	8	10
	1988	30	40	10	30	10	10
Corn (seeds)	1987	10	10	5	6	2	2
	1988	10	5	6	3	1	2
Alfalfa	1987	600	600	370	320	80	100
	1988	400	400	300	200	90	90
Cabbage	1987	6	7	3	3	1	1
	1988	6	4	2	3	1	1
Tomato	1987	20	20	10	10	4	5
	1988	20	10	10	20	6	5
Tomato (vegetative mass)	1987	700	800	500	400	160	250
	1988	400	500	200	200	200	200
Cucumber	1987	40	40	20	20	10	10
	1988	30	40	20	10	10	20
Cucumber (vegetative mass)	1987	1,200	1,600	800	600	350	300
	1988	800	1,100	400	300	300	200

NOTE: ^{137}Cs reported as pCi/kg of air-dry mass

Source: Perepelyatnikov et al. 1991 [156822], p. 111, Table 5.

Table 13.3-5. Distribution of (a) ^{137}Cs and (b) ^{90}Sr in the Soil Profile beneath Rice Paddies in 1988 after Three Years of Irrigation, Southern Ukraine

a) ^{137}Cs (in pCi/kg of air-dry soil)

Soil layer (cm)	Year	Type of Agriculture					
	1986 1987 1988	Bare Bare Bare	Rice Alfalfa Fallow	Fallow Rice Alfalfa	Alfalfa Fallow Rice	Rice Fallow Rice	Rice Rice Rice
0–0.5		0.45	0.41	0.52	0.6	0.62	0.71
0.5–2		0.43	0.39	0.39	0.51	0.5	0.49
2–4		0.4	0.4	0.37	0.41	0.38	0.37
4–6		0.38	0.36	0.4	0.38	0.42	0.41
6–8		0.43	0.45	0.42	0.37	0.39	0.42
8–10		0.37	0.37	0.38	0.38	0.37	0.32
10–20		0.19	0.4	0.39	0.41	0.4	0.41
Average in a layer 0–20 cm		0.37	0.4	0.42	0.44	0.45	0.48
Contamination (Ci/km^2)		0.11	0.12	0.12	0.13	0.14	0.14

b) ^{90}Sr (in pCi/kg of air-dry soil)

Soil Layer (cm)	Year	Type of Agriculture					
	1986 1987 1988	Bare Bare Bare	Rice Alfalfa Fallow	Fallow Rice Alfalfa	Alfalfa Fallow Rice	Rice Fallow Rice	Rice Rice Rice
0–0.5		70	--	--	--	110	120
0.5–2		65	--	--	--	110	110
2–4		60	--	--	--	100	122
4–20		58	--	--	--	100	115
Average in a layer 0–20 cm		60	--	--	--	102	116
Contamination (Ci/km^2)		0.018	--	--	--	0.031	0.035

Source: Perepelyatnikov et al. 1991 [156822], pp. 109–110, Tables 2 and 3.

Table 13.3-6. Estimated Soil-to-Plant Transfer Factors for Yucca Mountain Compared with Those Determined from Observations After the Chernobyl Accident

Radionuclide	Soil-to-Plant Transfer Factors (Dimensionless)				
	Yucca Mountain				Chernobyl data
	Leafy	Root	Fruit	Grain	
Strontium	2.0E+00	1.2E+00	2.0E-01	2.0E-01	2.0E-02–1.2E+01
Yttrium	1.5E-02	6.0E-03	6.0E-03	6.0E-03	(3-70) x E-03
Cesium	1.3E-01	4.9E-02	2.2E-01	2.6E-02	2.0E-02–1.1E+00
Radium	8.0E-02	1.3E-02	6.1E-03	1.2E-03	(1-40) x E-03
Thorium	4.0E-03	3.0E-04	2.1E-04	3.4E-05	(1-700) x E-03
Uranium	8.5E-03	1.4E-02	4.0E-03	1.3E-03	1.6E-03–1.0E-01*
Neptunium	3.7E-02	1.7E-02	1.7E-02	2.7E-03	nE-02–nE-01**
Plutonium	3.9E-04	2.0E-04	1.9E-04	2.6E-05	nE-08–1.0E+00
Americium	2.0E-03	4.7E-04	4.1E-04	9.0E-05	nE-06–1.0E-01

NOTE: * Data are for ^{238}U; **n = any number from 1 to 10

Source: Bar'yakhtar 1997 [156953], p. 271 for Chernobyl; CRWMS M&O 2000 [151615], Table 3-10 for Yucca Mountain.

Table 13.3-7. Soil-to-Fodder Transfer Coefficients Determined after the Chernobyl Accident for ^{137}Cs

Crop	Soil Type and pH		
	Derno-podsol pH=4.5-5.5	Gray Forest pH=5.6-6.5	Chernozem pH=6.6-7.2
Hay from natural grass	10	4	1.8
Hay from planted grasses	4	3	1.6
Vetch	2.7	0.45	0.2
Clover	1.8	0.3	0.3
Lupine	1.5	0.4	0.15
Alfalfa	0.8	0.4	0.2
Silage	0.4	0.2	0.08
Fodder beet	0.5	0.35	0.2
Potato	0.25	0.13	0.045
Winter grain	0.5	0.2	0.05
Rye	0.4	0.1	0.04
Barley	0.3	0.1	0.06

NOTE: ^{137}Cs reported as (Bq/kg) / (kBq/m^2) (mean for 1987–1990).

Source: Shestopalov and Poyarkov 2000 [157507], p. 174, Table 5.6.2

Table 13.3-8. Concentrations of ^{137}Cs in Pasture, Meat and Milk, and Calculated Transfer Coefficients

Pasture Contamination (Bq/kg)	Intake* (kBq/day)	Meat (Bq/kg)	Milk (Bq/kg)	Transfer coefficients	
				Meat (day/kg)	Milk (day/L)
250	17.5	280	112	1.6E-02	6.4E-03
500	36	700	280	1.9E-02	7.8E-03
1,000	70	1,400	550	2.0E-02	7.9E-03
1,500	105	2,100	840	2.0E-02	8.0E-03
2,000	140	2,800	1,120	2.0E-02	8.0E-03
3,000	210	4,200	1,680	2.0E-02	8.0E-03
5,000	350	7,000	2,800	2.0E-02	8.0E-03
10,000	700	14,000	5,600	2.0E-02	8.0E-03

NOTE: *Assumes daily intake of 70 kg fresh herbage/animal. For comparison, in the Yucca Mountain biosphere model, the dairy and beef cow feed consumption rates are 55 and 68 kg/day, respectively (CRWMS M&O [151615], Table 3-13).

Source: Richards and Hance 1996 [157613]. Only equilibrium concentrations are included in the table.

Table 13.3-9. Example of the Database to Assess Radiation Dose for the City of Bragin, Belarus

Population					
Population Group	**1986**	**1987**	**1988**	**1989**	**1990**
Children	1,667	--	--	2,065	--
Total inhabitants	5,600	4,900	--	5,888	--
Deposition Density (kBq/m^2)					
Radionuclide	**1986**	**1987**	**1988**	**1989**	**1990**
Cesium-137	1,700	1,000	270 (5–1,000) [1] (n = 8) [2]	1,000 (n = 18) 830 (n = 50)	--
Strontium-90	--	--	--	78 (n = 9)	--
Exposure Rate (μR/h)					
	1986	**1987**	**1988**	**1989**	**1990**
Measurement	8,000 (10 May)	680 (10 May)	--	--	--
Concentration in Foods (Bq/kg) (approximate median values) (Data from Institute of Agricultural Radiology, Gomel)					
	1986	**1987**	**1988**	**1989**	**1990**
Milk	1,600	1,500	220	300	260
Root vegetables	740	630	330	370	370
Green vegetables	3,700	740	370	300	220
Vegetables/fruit	1,100	590	300	220	330
Berries, mushrooms	2,200	1,100	1,300	2,600	1,100
Honey	1,300	1,900	1,500	300	300
Eggs	1,300	190	190	190	300
Meat	1,700	1,100	740	260	300
Fish	--	1,800	740	1,500	220
Consumption Rate (g/day)					
Food Item			**Rural settlement**	**All Belarus**	
Milk			735	690–710	
Bread, white			220	240	
Bread, dark			350	350	
Potatoes			540	680	
Vegetables			190	240	
Fruit, berries			160	150	
Berries			--	1.5	
Mushrooms			6	7	
Meat			150	180	
Fish			46	60	

Internal Dose (mSv) (Data for 1986, 1987: Institute of Biophysics, Moscow; data for 1988, 1989: Institute of Radiation Medicine, Minsk)						
$^{134+137}Cs$		**1986**	**1987**	**1988**	**1989**	**1990**
Average	Children	2 (n = 292)	1 (n = 94)	0.2 (n = 203)	0.1 (n = 3)	--
	Teenagers	5 (n = 87)	3 (n = 131)	0.2 (n = 731)	0.1 (n = 3)	--
	Adults	4 (n = 683)	3 (n = 111)	0.3 (n = 641)	0.2 (n = 131)	--
Maximum	Children	15	7	--	--	--
	Teenagers	22	17	--	--	--
	Adults	12	8	--	--	--
90th percentile	Children	10	5	--	--	--
	Teenagers	13	7	--	--	--
	Adults	8	5	--	--	--

NOTE: [1] Range
[2] Number of measurements

Source: IAEA 1991 [156750], Part E, Table 2-1.

Table 13.3-10a. Dynamics of the Effective Dose of External Radiation to Ukrainians from ^{137}Cs Contamination after the Chernobyl Accident

Population group	Year										
	1986*	1987	1988	1989	1990	1991	1992	1993	1994	1995	1996
Urban	6.0	1.5	1.4	1.4	1.3	1.3	1.2	1.2	1.1	1.0	1.0
Rural	14.3	3.5	3.4	3.3	3.2	3.1	3.0	2.7	2.5	2.4	2.2

NOTE:* 1986 data were estimated after the accident. ^{137}Cs reported for 1986–1996, $\mu Sv/(kBq/m^2)$

Source: Los' and Poyarkov 2000 [157508], Table 6.2.1, p. 187.

Table 13.3-10b. Calculated BDCFs for ^{137}Cs after the Chernobyl Accident

Population group	Year										
	1986	1987	1988	1989	1990	1991	1992	1993	1994	1995	1996
Urban	2.2E-05	5.6E-06	5.2E-06	5.2E-06	4.8E-06	4.8E-06	4.4E-06	4.4E-06	4.1E-06	3.7E-06	3.7E-06
Rural	5.3E-05	1.3E-05	1.3E-05	1.2E-05	1.2E-05	1.1E-05	1.1E-05	1.0E-05	9.3E-06	8.9E-06	8.1E-06

NOTE: See Section 13.3.9.2. Units in mrem/yr per pCi/m^2

Source: Table 13.3-10a.

Table 13.3-10c. Yucca Mountain BDCFs for ^{137}Cs for the Disruptive Event Scenario for the Transition Phase, 1 cm and 15 cm Ash Layers and Annual Average Mass Loading

	1–cm ash layer	15–cm ash layer
BDCFs	mrem/yr per pCi/m^2	mrem/yr per pCi/m^2
Mean	1.86E-06	5.81E-06
Min	1.01E-06	4.33E-06
Max	2.79E-05	3.17E-05

Source: Modified from CRWMS M&O 2001 [152536], Tables 11 and 13.

Table 13.3-11. Maximum ^{137}Cs Concentrations in Soils Producing Internal Dose of 1 mSv/yr and Calculated BDCFs

1	2	3	4	5	6	7
Soil Type	**Concentration kBq/m^2**		**Concentration pCi/m^2**		**BDCF mrem/yr per pCi/m^2**	
	Meadow	**Tilled**	**Meadow**	**Tilled**	**Meadow**	**Tilled**
Peat-bog	22	93	594,594	2,513,511	1.68E-04	3.98E-05
Sandy podzolic	74	130	1,999,998	3,513,510	5.00E-05	2.85E-05
Light-gray podzolic	148	185	3,999,996	4,999,995	2.50E-05	2.00E-05
Loamy chernozem	222	295	5,999,994	7,972,965	1.67E-05	1.25E-05

Source: Shestopalov and Poyarkov 2000 [157507], Table 5.6.4.

Table 13.3-12. Comparison of the Pathway Contribution (%) of Radionuclides Determined from Observations after the Chernobyl Accident in 1993

	^{90}Sr			^{137}Cs		
	Meat	**Leafy vegetables**	**Milk and milk products**	**Meat**	**Leafy vegetables**	**Milk and milk products**
Yucca Mountain	5 (10)	34 (42)	0 (2)	12 (4)	16 (3)	2 (0)
Chernobyl	4	19	54	8	2	74

Source: Yucca Mountain—CRWMS M&O 2000 [151615], Table 3-21; CRWMS M&O 2000 [151615], Table 3-24 (in parentheses)
Chernobyl— Berkovski et al. 1996 [156592], p. 41.

Table 13.3-13. Relative Contributions to the Collective Effective Dose from ^{137}Cs and ^{90}Sr, Resulting from the Chernobyl Accident

Region/Source (%)	Irrigation	Municipal Tap Water	Fish
Kiev Region	18	43	39
Poltava Region	8	25	67
Crimean Republic *	50	50	0

NOTE: * No Dnieper River fish consumed in Crimean Republic

Source: Berkovski et al. 1996 [156592], p. 42.

Table 13.3-14. Calculated Content (Bq) of α-emitting Pu Isotopes in the Human Skeleton in 1998 for the Ukraine-Belarus Territory with Contamination Density of 20 mCi/km^2 (740 Bq/m^2) and Comparison of These Data with Global Fallout

Type of Intake	From Global Fallout	From Chernobyl Fallout
Primary inhalation	1.3×10^{-3}	1.2×10^{-2}
Peroral due to superficial contamination	1.6×10^{-3}	0.56×10^{-2}
Peroral, biologically accessible forms	3.2×10^{-5}	1.1×10^{-4}
Inhalation due to resuspension	1.42×10^{-6}	3.6×10^{-6}
Total	2.9×10^{-3}	1.8×10^{-2}

Source: Bondarenko et al. 2000 [156593], Table 2.

14. ANALOGUES FOR DISRUPTIVE EVENT SCENARIOS

14.1 INTRODUCTION

This section addresses disruptive event scenarios and the ways analogues have been used to define realistic scenarios, to bound parameters in models, and to build confidence that the right processes are included in models and represented by appropriate bounding conditions. Specifically, this section addresses the disruptive event categories for volcanism and seismicity, which are considered in total system performance assessment (TSPA). The scenario for nuclear criticality has been screened out from further consideration in TSPA (DOE 2001 [153849], Section 4.3.3). However, aspects of criticality pertinent to the discussion on waste form degradation are presented in Section 4. The screened-in human-intrusion disruptive event scenario (e.g., drillhole penetrating a waste package) is not conducive to evaluation using natural analogues. Information found in Section 14.3 may help to support arguments associated with Key Technical Issue (KTI) KIA0204 listed in Table 1-1.

14.2 BACKGROUND

14.2.1 Volcanism

The Yucca Mountain stratigraphy is composed of ashfall and ash flow tuffs that were deposited approximately 13 million years ago (Ma) as a result of eruption of the Timber Mountain caldera. This large-volume, explosive, silicic volcanism ended about 7.5 Ma. Basaltic volcanism began during the latter part of the caldera-forming phase and continued into the Quaternary (the last 2 m.y.). Approximately 99% of the southwestern Nevada volcanic field, of which Yucca Mountain is a part, erupted between 15 and 7.5 Ma, with only 0.1% occurring during the basaltic phase of the last 7.5 m.y. In the Yucca Mountain region there are more than 30 basaltic volcanoes that formed between 9 Ma and 80,000 Ma. These volcanoes can be temporally and spatially separated into two distinct periods of volcanism, with the location of eruption of the younger, post-5 Ma volcanism shifted to the southwest (DOE 2001 [153849], Section 4.3.2.1.3).

To assess the probability of volcanic activity disrupting a repository, a panel of experts was assembled to conduct a volcanic hazard assessment (CRWMS M&O 1996 [100116]). The hazard analysis models are based on data from Yucca Mountain studies, along with observations from analogue studies of modern and ancient volcanic eruptions. The results of the hazard analysis estimate that 1.6×10^{-8} igneous events per year could be expected to disrupt the potential repository (CRWMS M&O 2000 [151551], Section 6.5.3 and Section 7, Tables 13 and 13a). This is the probability of a future basaltic dike intersecting the subsurface area of the potential repository. Furthermore, if a dike does intersect the repository, there is a 77% chance that one or more volcanoes would form along the dike within the repository footprint, with magma erupting through the repository. Both the intrusive and volcanic eruptive scenarios are considered in performance assessment because of the potential consequences of radionuclide release that could affect the critical group. The role of analogues in assessing the eruptive style of potential future volcanoes and their expected consequences is addressed in Section 14.3.

14.2.2 Seismicity

Yucca Mountain is located in the Basin and Range tectonic province, where earthquakes occur with some frequency. Geologic features of the site provide information on the region's past seismic activity, which is important in estimating the characteristics of future earthquakes. Based on these studies, the Yucca Mountain region has been rated as having low to moderate seismicity (CRWMS M&O 2000 [142321], Section 6.3.1). Seismic hazards are important to quantify as they could potentially affect the performance of a repository at Yucca Mountain. The seismic hazard at the site was assessed by a probabilistic seismic hazard analysis which produced results that allow assessment of the potential for ground shaking and fault rupture related to earthquakes (Wong and Stepp 1998 [103731].

Extensive design experience gained through operating critical facilities, such as nuclear power plants, will be relied upon to ensure performance of the potential repository and its supporting facilities during and after an earthquake. During the postclosure period, the risks related to seismic activity will decrease because the waste will be deep underground where seismic waves are more attenuated. A surface seismometer and another seismometer at 245 m depth in the Exploratory Studies Facility (ESF) measured seismic waves from a 4.7 magnitude earthquake at Frenchman Flat, about 45 km (28 mi) east of Yucca Mountain (DOE 2001 [153849], Section 4.3.2.2). Recordings from this earthquake, shown in Figure 14-1, clearly indicate the decrease in amplitude of ground motions deep within the mountain. However, a strong earthquake could cause rockfalls in the emplacement drifts or alter the pathways followed by groundwater. Investigations of these potential consequences have concluded that it is highly unlikely that the consequences would be significant to repository performance (DOE 2001 [153849], Section 4.3.2.2). The role of analogues in building confidence in this conclusion is addressed in Section 14.4.

14.3 USE OF ANALOGUES IN VOLCANISM INVESTIGATIONS

Reasoning by analogy was used to debate the conceptual model for the probability of an igneous dike or dike system reaching the near surface without any portion of the system erupting. This is an important issue for volcanic hazard assessment of a potential repository at Yucca Mountain. The San Rafael volcanic field has been used as an analogue to argue that the probability of a separate intrusive event that does not erupt is 2 to 5 times higher than the probability of an eruptive event (NRC 1999 [151592]). However, the Analysis Model Report (AMR) *Characterize Framework for Igneous Activity at Yucca Mountain, Nevada* (CRWMS M&O 2000 [151551], Section 6.3.2.1) uses the Paiute Ridge igneous complex at the northeastern edge of the Nevada Test Site as an appropriate analogue to argue for a significantly lower rate for intrusions that do not result in eruption. Field observations at Paiute Ridge show that while some portions of individual dikes stagnated within approximately 100 m of the surface, other portions of the same dike did erupt. During the time period considered most significant by the panel of experts assembled for evaluating the volcanic hazard (the past 5 m.y., CRWMS M&O 1996, Figure 3-62), there is no known episode of dike intrusion to within a few hundred meters of the surface in the Yucca Mountain region that has not been accompanied by an extrusive event. Thus there is no evidence in the Yucca Mountain regional geologic record to suggest that dike intrusions without accompanying eruptions occur 2 to 5 times more frequently than eruptions (CRWMS M&O 2000 [151551], Section 6.3.2.1). An alternative interpretation of the San Rafael volcanic

field is also presented in the AMR *Characterize Framework for Igneous Activity at Yucca Mountain, Nevada* (CRWMS M&O 2000 [151551], Section 6.3.2.1), which supports an intrusion/extrusion ratio as being closer to 1. This interpretation assumes that it is likely that many individual intrusive/extrusive events are represented at San Rafael, where some portion of a dike system erupted during an event while other portions of the same dike did not erupt. This interpretation is more consistent with the geologic record of the Yucca Mountain region, as demonstrated at the Paiute Ridge analogue complex.

Analyses in the AMR *Characterize Eruptive Processes at Yucca Mountain, Nevada* (CRWMS M&O 2000 [142657]) assume that a plausible eruption during the postclosure performance period would be of the same character as Quaternary basaltic eruptions in the Yucca Mountain region. Eruptive styles and magmatic composition of the Lathrop Wells volcano, the most recent in the region, are emphasized as being the most characteristic. A new volcano would therefore contain some combination of scoria cones, spatter cones, and lava cones on the surface, and one or more dikes in the subsurface. Additional assumptions regarding the character of a future eruption focus on the use of data from a variety of analogue volcanoes and simplifications for a stylized plausible eruption. These include conduit diameter, dike width, the number of dikes associated with formation of a new volcano, magma chemistry, water content of magmas, gas composition, magma physical properties, ascent rate, fragmentation depth, mean particle size, and eruption duration, among others. This is an example of analogue information being used as direct parameter input into models, where the input consists of assumptions based on analogues.

The ASHPLUME computer code (Versions 1.4LV and 2.0) is used in estimation of the aerial density of an ash deposit. Ash-thickness data collected after the 1995 eruption of Cerro Negro, in Nicaragua, provided an opportunity to utilize the ASHPLUME code in simulating the eruption (CRWMS M&O 2000 [152998]). The application of this analogue information is discussed further in Section 15.

14.4 USE OF ANALOGUES IN BOUNDING EFFECTS OF SEISMICITY ON A GEOLOGIC REPOSITORY

Damage from ground shaking caused by an earthquake results largely from shear waves. Density contrasts along the path the shear waves follow from the earthquake source to the surface affect the amplitude of the waves. As the wave moves from dense rock at depth to less dense, more porous, and unconsolidated compressible material near the surface, the speed of the wave is reduced. With decreasing speed the kinetic energy of the wave is maintained by increasing amplitude, thus giving rise to increased shaking and intensity of damage. At the surface the amplitude of a shear wave will be about twice as large as at depth (Stevens 1977 [154501], p. 20). It follows that if the dimensions of an underground opening are considerably less than the wavelength of a shear wave, the shaking effects generated by the amplitude of motion will likewise be considerably less. The decrease in the effects of shear waves with increasing depth is comparable to the similar effect observed in ocean waves, which decrease in intensity and amplitude with the depth of water. A consequence of this is that the damage reported in shallow, near-surface tunnels is greater than that reported in deep mines (Pratt et al. 1978 [151817], p. 26).

There are numerous examples in the literature of underground structures withstanding damage from earthquakes that caused relatively greater damage at the ground surface (Eckel 1970 [157493]; Stevens 1977 [154501]; Sharma and Judd 1991 [154505]; Pratt et al. 1978 [151817]; Power et al. 1998 [157523]). Three earthquakes of recent decades, the Alaskan earthquake of March 28, 1964, the Tang-Shan, China, earthquake of July 28, 1976, and the Kobe, Japan, earthquake of January 16, 1995, clearly demonstrate the ability of underground structures to withstand the ground vibrations associated with severe seismic activity.

In the Alaskan earthquake, no significant damage was reported to underground facilities, including mines and tunnels, as a result of the earthquake, although some rocks were shaken loose in places (Eckel 1970 [157493], p. 27). Coal mines in the Matanuska Valley were undamaged, as was the railroad tunnel near Whittier, and the tunnel and penstocks at the Eklutna hydroelectric project. A small longitudinal crack in the concrete floor of the Chugach Electric Association tunnel between Cooper Lake and Kenai Lake is believed to have been caused by the earthquake. These reports of little or no damage to underground structures from the Alaskan earthquake are significant, because this earthquake was one of the largest (magnitude 8.5) to occur in this country, and the associated surface damage was extreme (Pratt et al. 1978 [151817], p. 32).

The July 28, 1976, earthquake in the heavily industrial city of Tang-Shan, China, had a magnitude of 7.8. Surface intensities at Tang-Shan were such that in the area where the strongest shaking occurred, 80% to 90% of the surface structures collapsed. However, for important engineered structures immediately below the surface, there was generally no serious damage regardless of the depth or size of the structure (Wang 1985 [151821], p. 741). The third example is the more recent Kobe, Japan, earthquake of January 16, 1995. Tunnels in the epicentral region of the Kobe earthquake (magnitude 6.9) experienced no major damage or even partial collapse for peak ground accelerations (PGAs) measured at the surface of ~0.6 g (Savino et al. 1999 [148612]).

A more site-specific, although smaller-magnitude, example was the Little Skull Mountain earthquake of June 29, 1992. This earthquake had a magnitude of 5.6 and occurred about 20 km from Yucca Mountain. Examination shortly after the earthquake of the interior of X-tunnel (125 m deep) in the epicentral region indicated no evidence of damage in the tunnel that could be associated with the earthquake (Savino et al. 1999 [148612]).

The understanding of the response of underground openings to seismic events has advanced greatly in the last 15 years. Sharma and Judd (1991 [154505], pp. 272–275) examined damage trends of underground facilities to seismic effects in an effort to aid future design of such facilities. They created a database consisting of 192 reported underground observations from 85 earthquakes throughout the world (Sharma and Judd 1991 [154505], p. 275). To examine the influence of seismic effects on underground openings, they used the measure of PGA that may be expected to occur at the surface directly above the underground location. The possibility of damage was examined as a function of (1) thickness of overburden, (2) predominant rock type, (3) type of ground support, (4) earthquake magnitude, and (5) epicentral distance of the earthquake.

On the basis of observations from this collection of data, Sharma and Judd (1991 [154505], p. 275) concluded that (1) damage incidence decreases with increasing overburden depth; (2) damage incidence is higher for unconsolidated colluvium than for more competent rocks; (3) internal tunnel support and lining systems appeared not to affect damage incidence; (4) damage increases with increasing earthquake magnitude and decreasing epicentral distance (increasing PGA); (5) no or minor damage can be expected for peak accelerations at the ground surface less than about 0.15 g. Data presented by Sharma and Judd (1991 [154505], Figure 7) indicate that damage to underground facilities at the depth for the potential repository is rare, even at accelerations of 0.4 g. These findings confirmed those of Stevens (1977 [154501], p. 36) and Pratt et al. (1978 [151817], p. 26), who suggested that the host material for an underground facility may be important in predicting the amount of damage caused by the shaking associated with earthquakes.

Although their observations contained 98 cases with no damage, Sharma and Judd (1991 [154505], p. 275) also acknowledge that their data set is biased towards occurrence of damage because "there must be literally hundreds of other instances where no damage occurred but observations were not documented" (Sharma and Judd (1991 [154505], p. 275). Two cases of moderate and heavy damage were reported in tunnels located at a depth of about 210 m near Santa Cruz, California, following the 1906 San Francisco earthquake. Based on the epicentral distance of 110 km, a PGA of 0.09 g was estimated. Generally, this PGA would be correlated with a "No damage" case; however, the epicentral distance on which the PGA estimate was based did not take into account the close proximity to the ruptured San Andreas Fault. Two other cases of damage also required further explanation. Damage reported for a mine in Idaho and the ERP Mine in the Witwatersrand, South Africa, at depths of 1,350 m and 3,000 m, respectively, was probably caused by rock-burst activity rather than a seismic event. This activity is usually pronounced in deep mines and generally can be recognized from the relatively high frequency content of the recorded accelerograms (Sharma and Judd 1991 [154505], p. 274). Stevens (1977 [154501], p. 33) quotes N.G.W. Cook of the South Africa Chamber of Mines as stating, "All the evidence indicates that earth tremors, rock bursts, and bumps arose in the Witwatersrand as a result of mining and have followed the pattern of mining in terms of frequency of incidents and epicentral position and focal depth".

Power et al. (1998 [157523]) collected extensive data on seismic ground-shaking–induced damage to bored tunnels, using more recent data from better instrumented earthquakes than was possible for Sharma and Judd (1991 [154505]). Power et al. (1998 [157523]) found that for ground motion with PGAs less than 0.2 g, there was little or no damage in tunnels, and for PGAs of 0.2–0.6 g, damage varied from slight to heavy (Power et al. 1998 [157523], Section 1.2). At even greater accelerations the damage only ranged from slight to moderate. For example, well-constructed tunnels near Kobe, Japan, experienced PGAs of about 0.6 g but suffered no major damage.

In addition to damage caused by ground vibration, underground tunnels can be damaged by fault displacement and by earthquake-induced ground failure, such as liquefaction or landslides at tunnel portals, which are not considered an issue at Yucca Mountain. In three instances of heavy damage from the 1923 Kanto, Japan, earthquake, observation of damage (with PGA equal to 0.25 g) may have resulted from landsliding. In the other two observed occurrences of heavy damage surveyed by Power et al. (1998 [157523]), tunnel collapse occurred in the shallow

portions of the tunnels. Damage to underground openings is inevitable only when the underground facility is displaced by a fault (Stevens 1977 [154501], p. 35). Carpenter and Chung (1986 [154504]) strongly recommend that faults with the potential for movement be avoided, which is consistent with design criteria for the potential repository at Yucca Mountain (BSC 2001 [155664], Section 1.2.2.1.5; McConnell and Lee 1994 [110957]).

The previous summary shows that tunnels withstand ground vibration well. However, tunnels in solid rock are susceptible to changes in hydrogeologic conditions and may be flooded as a consequence of ground shaking. Thus, although there may have been no apparent damage to the structure, there is a probability of increased fracture density in rocks surrounding the tunnels (Mumme 1991 [157494], p. 77). The potential for changes to the hydrogeologic system caused by fault displacement to affect radionuclide transport in the UZ at Yucca Mountain has been examined in the AMR, *Fault Displacement Effects on Transport in the Unsaturated Zone* (CRWMS M&O 2001 [151953]).

Even near the surface, damage from ground shaking may be slight if the rock is competent. For example, Mitchell Caverns, in the Providence Mountains of California, southwest of Las Vegas, sustained only minor damage in the October 16, 1999, Hector Mine earthquake (magnitude 7.1). The earthquake epicenter was only 30 miles (48 km) away. Damage was limited to a few stalactites being shaken from the ceiling at El Pakiva cave. At El Pakiva, the earthquake loosened some rocks from the face around and above its entrance (Figure 14-2), but the partial occlusion of its entrance by boulders was the result of a previous earthquake (Simmons 2002 [157544], p. 124). Another cave at Mitchell Caverns, Tecopa, experienced rockfall. The rockfall may be related to seismic events, but not to recent ones, because in some areas columns have been recemented by dripstone, and dripstone has begun to form on the ceiling from which the blocks fell. However, the area of cave floor covered by fallen blocks is much smaller than the total area of the cave, and fallen blocks have not obliterated the cavity opening.

Two final examples of the application of natural analogues to building confidence in the ability of a geologic repository at Yucca Mountain to withstand damage from ground vibration and faulting are the following. The AMR *Drift Degradation Analysis* (BSC 2001 [156304], Attachment VII) confirmed results of a rockfall model using information from natural analogues. The DRKBA code, used to model rockfall probabilities, involves a quasi-static method of reducing the joint-strength parameters to account for the seismic effect. This method was verified based on the test runs using the dynamic functions of the distinct element code UDEC. The comparisons between the results from the dynamic and quasi-static analyses showed a consistent prediction of block failure at the opening roof. The seismic effect on both the size and number of blocks in the rockfall model is relatively minor. This is consistent with information from natural analogues.

The AMR *Effects of Fault Displacement on Emplacement Drifts* (CRWMS M&O 2000 [151954]) included a literature survey on accommodating fault displacements encountered by underground structures such as buried oil and gas pipelines, which provide analogues for potential emplacement drift responses to fault offset.

The value of examining information on rockfall resulting from underground nuclear explosions (UNEs) was considered for this report. While an investigation on this topic may be fruitful, there

are significant differences between UNEs and earthquakes in terms of frequency content of the ground motion and the duration of shaking. These differences make the use of UNE results less relevant than results from earthquakes, although the effects of UNEs are better instrumented and documented than the effects of earthquakes.

14.5 SUMMARY AND CONCLUSIONS

Use of natural analogues is a major investigative tool in Yucca Mountain volcanism studies. Analogues have been used to assess the probability of dike eruption, plausible eruptive styles, eruptive parameters, and magma compositions, and have also been used to increase confidence in use of the ASHPLUME code for simulation of an eruption. Examples from observations of underground openings demonstrate that such openings are able to withstand ground shaking for even high PGAs. The ability to withstand ground shaking is increased by thickness of overburden, competence of material (rock versus colluvium), decreased earthquake magnitude, and increased distance of the opening from the earthquake epicenter. Underground openings may be damaged by landsliding or liquefaction associated with an earthquake, if the depth of the opening is relatively shallow. Underground openings are inevitably affected by fault displacement when the opening intersects a fault. Collateral damage by ground shaking can also be caused when ground shaking alters hydrogeologic conditions by increasing fracture density and permeability, and thereby increasing fracture flow to an underground opening. The bulk of evidence from analogue examples of underground openings, particularly in settings similar to Yucca Mountain, such as the Little Skull Mountain earthquake, demonstrates that damage to repository drifts by ground shaking during the postclosure period would be minimal or unlikely.

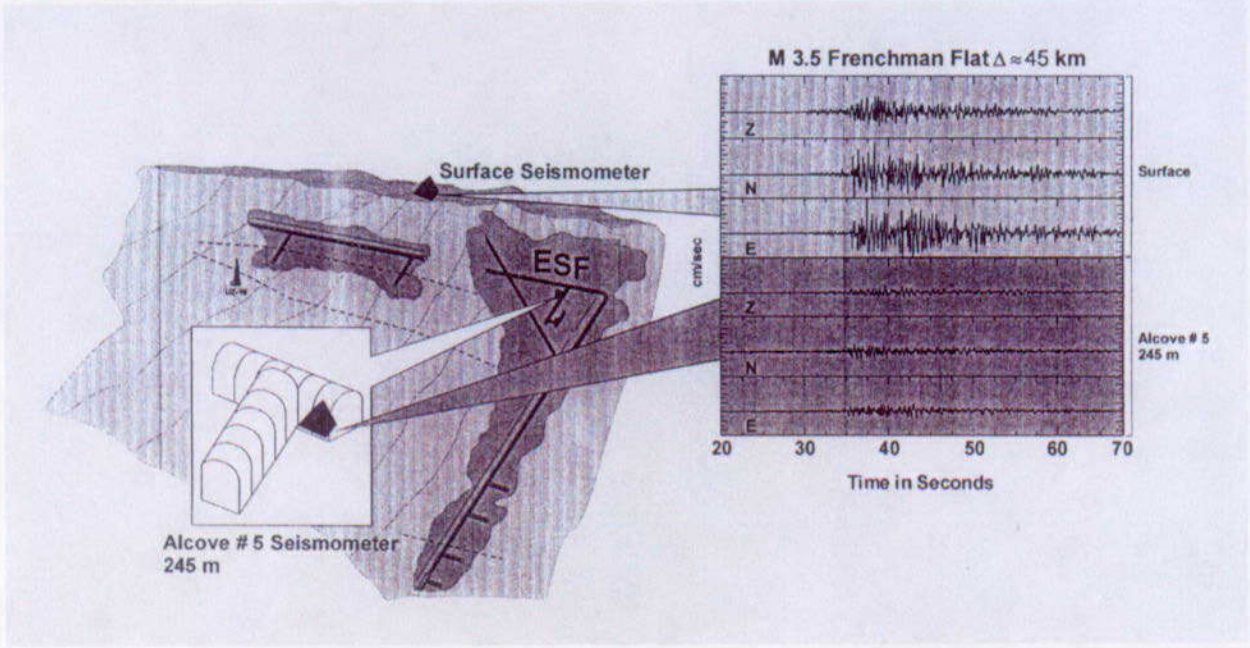

NOTE: The seismograms for the surface and underground are to the same vertical scale. M = magnitude; Δ = distance; Z = amplitude; N = N-S; E = E-W; ESF = Exploratory Studies Facility.

Source: Modified from Savino et al. 1999 [148612].

Figure 14-1. Recordings of Frenchman Flat Earthquake at the Ground Surface and the Thermal Test Alcove of the ESF

Source: Simmons 2002 [157578], SN-LBNL-SCI-108-V2, p. 9.

Figure 14-2. Entrance to Mitchell Caverns, El Pakiva Portal, Showing Fallen Blocks That Partially Occlude the Entrance

15. APPLICATION OF NATURAL ANALOGUES FOR THE YUCCA MOUNTAIN SITE CHARACTERIZATION PROJECT

15.1 INTRODUCTION

This section addresses the application of natural (including anthropogenic) analogues to geologic repository programs. Section 15.2 provides an overview of the applications for which natural analogues are suitable. Section 15.3 tells how natural analogues have been applied in geologic nuclear waste disposal programs worldwide. Section 15.4 reviews the application of natural analogues to past iterations of performance assessment (PA) and the supporting process models for Yucca Mountain. Section 15.5 identifies those model components, as stated by process modelers, that could benefit from confidence built through natural analogues. Section 15.6 categorizes the way natural analogue information has been used in this report. Section 15.7 presents a final summary and conclusions.

15.2 OVERVIEW

Figure 15-1 illustrates the flow of information from natural analogues and other site characterization data into PA models. The figure indicates that natural analogues provide both qualitative and quantitative information, as this report has demonstrated through many examples in the preceding sections. Stated in words, the stages or components in the development of a PA code (shown in Figure 15-1) are the following:

1. Construction of a conceptual model that describes the system and includes all of the important processes and their interactions
2. Translation of conceptual models into mathematical models and encoding those models in the form of a numerical code
3. Acquisition of input data for all the variable and constant parameter values included in the numerical code
4. Verification of the numerical correctness of the computer code
5. Validation of the code's applicability to the repository system in assessing its ability to predict future conditions.

The ways in which analogues can be or have been used to assist in 1, 3, 4, and 5 above are discussed below.

Model construction: In the stage of model construction, natural analogues can be used to tell the PA modeler:

- Which processes and process interactions to include
- Which processes are likely to be dominant and which are of secondary importance

- The spatial and temporal scales over which the model should perform
- Whether the basic premises of the model hold up under extrapolation to long time periods

Some of the analogues discussed in Sections 4, 6, 7, 9,10, 11, and 12 relate to identification of processes that are or may be included in models.

Data acquisition: Information derived from natural analogue studies is often semi-quantitative. For this reason it cannot often directly satisfy the parameter value requirements of a PA code. However, laboratory data have uncertainty related to the lack of similarity between the laboratory and repository systems. Therefore, a role for analogues in data acquisition is to provide a measure of validation for the laboratory data. Even though the analogue data may be imprecise, they can be used to give confidence in the reliability of the laboratory data. An example of this application was given in Section 4, describing the similarity between uraninite alteration phases produced in laboratory dissolution experiments and those uraninite alteration phases identified in rock samples at the Nopal I, Peña Blanca analogue site.

Model validation: Thermodynamic solubility and speciation codes and databases have been extensively applied in a number of natural analogue studies (e.g., Maqarin, Poços de Caldas, Koongarra). Natural analogues can help determine whether the solubility-controlling mineral species and complexes in solution (generally specified by hydrochemical databases or from theoretical or laboratory experiments) are appropriate to the site-specific conditions being modeled, and whether or not mineral phases and/or ionic species in solution indicate chemical equilibrium has been achieved or whether the system is controlled by kinetics.

A subcategory of modeling studies is database evaluation. One application of natural analogues in this category is the evaluation of geochemical models and numerical tools used in describing the predicted migration of radionuclides in a repository system. Blind predictive modeling comparisons are a means of evaluating geochemical databases. For instance, Bruno et al. (2001 [157484]) reviewed and compared the results obtained from the blind prediction modeling exercise carried out for seven natural analogue studies relevant to European repository concepts: Oman; Poços de Caldas, Brazil; Cigar Lake, Canada; Maqarin, Jordan; El Berrocal, Spain; Oklo, Gabon; and Palmottu, Finland. The blind predictive model exercise (Bruno et al. 2001 [157484]) was able to improve conceptual and numerical models to identify relevant radionuclides to major component phases in the rock-water systems of interest. The group achieved a consensus concerning the most appropriate methodology for approaching solubility-limited calculations and identified the main requirements for acquiring improved site characterization data to describe radionuclide mobility.

Tangible illustrations: Natural analogues also have an important role, beyond their application to PA, in providing illustrative information to a broad range of audiences, including the general public. Natural analogues, or comparisons with natural systems, are frequently mentioned as important components of the process of evaluation and acceptance of disposal concepts. In quoting the IAEA (1999 [157485]), Miller et al. (2000 [156684], Section 6.1) stated, "Among all levels of reviewer, from technical peer review panels to nontechnical audiences, there is a clear belief that PAs are only credible if shown to have strong natural parallels." Recognition of the important processes and events that control the repository behavior can be demonstrated from

illustrative geological analogues. Natural analogue assist in the public understanding of the timescales applicable to radioactive decay. These real world examples are important because the extended time periods of interest to disposal are generally longer than those in our normal range of experience.

15.3 PERFORMANCE ASSESSMENT APPLICATIONS OF ANALOGUES IN GEOLOGIC DISPOSAL PROGRAMS WORLDWIDE

Several reviews have examined the level of direct and acknowledged use of natural analogues in published PA documents of geologic repository programs worldwide (e.g., McKinley and Alexander 1996 [157486]; IAEA 1999 [157485]). Results of these reviews indicated that very few total system PA documents provided detailed discussion of how analogues were used to support specific aspects of the assessments, and some PA reports did not discuss how natural analogues support geological disposal in even a general way.

An indirect use of analogues in PA in some programs is in the development of scenarios, where identification of features, events, and processes (FEPs) of importance to repository evolution are required (Chapman et al. 1995 [100970]). The role of analogue information in this case is to provide supplemental evidence to support the inclusion or exclusion of different FEPs in scenarios to be analyzed for PA. An example of this application of analogues is the scenario case for criticality in a waste repository. This scenario was screened out using, in part, understanding of processes that occurred at Oklo (see Section 4).

Miller et al. (2000 [156684], Section 6.1), referring to IAEA 1999 [157845], summarized the use of analogues for model development, data provision, and model validation in ten PAs over the past two decades. These included KBS-3 (Sweden, 1983); Projekt Gewähr (Switzerland, 1985); SKB-91 (Sweden, 1991); TVO (Finland, 1991); AECL EIS (Canada, 1994); Kristallin-I (Switzerland, 1993); NRC IPA (USA, 1995); TILA-99 (Finland, 1999); SR-97 (Sweden, 1999); and SFR (Sweden, 1999). All but one of these PAs used analogues in conceptual model development or scenario development. All of the PAs used data from analogues, either as bounding conditions or as direct parameter values. Seven of the ten PAs used analogues for blind predictive modeling or for the evaluation of models and databases as part of model validation. The NRC, for instance, used natural analogues in the following ways:

- In scenario development for volcanism, as an alternative source-term conceptual model using Peña Blanca data (Murphy and Codell 1999 [149529])
- To establish relative importance of microfractures and matrix transport at Peña Blanca, Mexico
- As backup for vapor-phase transport at the Valles Caldera, New Mexico
- To identify secondary phases for long-term release at Peña Blanca
- For model testing for elemental transport in unsaturated media at Akrotiri, Greece (Murphy 2000 [157487]).

Miller et al. (2000 [156684], Table 6.1.1) noted that few of the analogue applications were explicitly mentioned in the top-level documents associated with these PAs. The lack of acknowledgment of these applications of analogues by PAs is evident from a disconnect between the examples of uses shown in the IAEA (1999 [157485]) report and the applications noted in the report's conclusions. Thus it appears that the role of natural analogues in providing a general conceptual basis for the geological disposal of radioactive waste and for specific waste isolation mechanisms is largely unacknowledged. There are only a few clear examples of parameter values being provided by natural analogues that may be directly input to an assessment model, such as measured matrix diffusion and metal corrosion rates. A semi-quantitative use of natural analogues has been to provide bounding limits to the ranges of parameter values obtained from laboratory studies. The most valuable quantitative role of natural analogues, which cannot be replicated in laboratory systems, is to provide bounding estimates for validation of PA models. So far, this has only been seriously attempted for equilibrium geochemical modeling (e.g., at Poços de Caldas, Oman, Maqarin, and El Berrocal).

15.4 PREVIOUS YMP INCORPORATION OF NATURAL ANALOGUES

Process modelers, as users of analogue information, can and have played an important role in determining how analogues can best be used to support PA and design groups in reducing uncertainties in the long-term behavior of natural and engineered systems.

In the past, the YMP has used analogues for testing and building confidence in conceptual and numerical process models in a number of ways:

- Yucca Mountain as a self analogue: Mineral alteration zones that formed during cooling of Timber Mountain ash flow tuffs are the same as those expected to form under the thermal conditions predicted by numerical codes (Bish and Aronson 1993 [100006]).

- Thermochemical data: Data from the Wairakai, New Zealand, geothermal field were used to build confidence in thermodynamic parameters for silica minerals in databases used in geochemical modeling (Carroll et al. 1995 [109627]).

- Spent fuel alteration parageneses: Mineral phases determined in laboratory experiments were compared to those of Nopal I, at Peña Blanca (Figure 4-1). The results of these studies (summarized in Section 4) have increased the confidence in models describing spent-fuel alteration.

- Saturated zone transport: Scoping calculations were conducted for the Peña Blanca site using the same numerical model that was used to assess total system performance of the potential Yucca Mountain repository. The model attempted to predict the transport of ^{99}Tc, which is expected to be a conservative ion that would be released from the waste inventory. Results of the modeling indicated that both ^{99}Tc and some forms of uranium may be detected in groundwater close to the Nopal I mine at Peña Blanca (CRWMS M&O 2000 [153246], Appendix C, Figure C-12). The scoping predictions were sensitive to the surface area assumed for the inventory of leachable mineral species, because a reduction of mineral surface area led to a reduction in both uranium and ^{99}Tc

concentrations (CRWMS M&O 2000 [153246], Appendix C). The scoping study predictions differ from analyses of groundwater samples collected in the 1980s from a monitoring well 1,300 m downgradient from the Nopal I mine, which detected very low concentrations of uranium. To corroborate the model results for uranium and possibly technetium, the scoping simulations could be rerun using additional data from analyses of water samples collected from wells being drilled at and immediately downgradient from the Nopal I ore deposit (see Section 10.4).

- Verification of models describing volcanism: Immediately after a 1995 volcanic eruption at Cerro Negro, an active basaltic cinder cone in Nicaragua, the thickness of volcanic ash deposited during the eruption was measured. The ash thickness data provided an opportunity to use the ASHPLUME code (CRWMS M&O 1999 [132547]) to simulate the eruption. The goal was to compare calculated ash deposition predicted using the ASHPLUME code to the ash thickness recorded in an actual ashfall event from a small-volume basaltic volcano. Cerro Negro is analogous in size and morphology to a volcanic feature that could form as the result of a volcanic eruption in the vicinity of Yucca Mountain, although the intra-continental arc magmatism that forms the tectonic setting for Cerro Negro is different from the Basin-and-Range style tectonics of the Yucca Mountain area. Two versions of the ASHPLUME code that employ a two-dimensional diffusion model were used. The results of both versions compared well with the observed data for distances from the volcanic event greater than 10 km (CRWMS M&O 2000 [153246], Appendix C, Figure C-1). For distances less than 10 km, ASHPLUME results calculate ash thickness values greater than the observed data, possibly because ASHPLUME assumes a constant wind speed and direction for a given simulation, whereas the actual situation reflected a shift in wind direction, and possibly velocity, during the eruption. Nevertheless, the results in general showed that the ASHPLUME model can reasonably predict the ashfall distribution of a basaltic cinder cone similar to Cerro Negro. This result increases the confidence in ashfall calculations that could be used to simulate possible ash-producing eruptions either near or through a repository at Yucca Mountain.

Analogues were included in discussions of multiple lines of evidence in the *FY 01 Supplemental Science and Performance Analyses, Volume 1: Scientific Bases and Analyses* (BSC 2001 [155950]). To a large degree, these analogues have been referenced in this report in Sections 4, 6, 7, 8, 9, 10, 11, 12, 13, and 14. Analogues have also been used to provide multiple lines of evidence in support of both analysis and model reports (AMRs); in screening arguments for inclusion or exclusion of FEPs in total system PAs (TSPAs); in the quantification of uncertainties (BSC 2001 [155950]); and in expert elicitations such as *Probabilistic Volcanic Hazard Analysis for Yucca Mountain, Nevada* (CRWMS M&O 1996 [100116]); *Probabilistic Seismic Hazard Analyses for Fault Displacement and Vibratory Ground Motion at Yucca Mountain, Nevada* (USGS 1998 [100354]); and *An International Peer Review of the Biosphere Modelling Programme of the US Department of Energy's Yucca Mountain Site Characterization Project, Report of the IAEA International Review Team* (IAEA 2001 [155188]).

15.5 YMP IDENTIFIED NEEDS

Areas identified for the TSPA-VA in which analogue studies might contribute to evaluating of and building confidence in PA models include:

- Seepage threshold and the fraction of waste packages contacted by seeps (including seepage enhanced by thermally induced drift collapse)
- Alteration of hydrologic properties by mineral precipitation or dissolution
- Sorption onto fractures
- The role of colloid filtration in reducing radionuclide migration
- Alloy 22 corrosion
- Np solubility
- Saturated zone (SZ) dilution.

PA requirements for natural analogues were also considered for TSPA-SR and TSPA-LA. A meeting was held in January 2001 to integrate PA needs for building confidence in process models, including areas where natural analogues could contribute. This report includes examples of natural analogue contributions to the stated needs found in performance assessment studies.

15.6 APPLICATIONS FROM THIS REPORT

Table 15.1 is a compilation of the ways in which analogues have been used in this report. The analogues are listed by chapter and are categorized as to their use in building conceptual models or understanding of processes, development of data parameters and their use in TSPA, or use for model validation. It is evident that the majority of uses of analogues for YMP has been in the understanding of which processes to model and how to incorporate them into PA. Less frequent has been their use in model validation, and even less frequent is their use directly in PA. The categorization on this table should not be surprising because it corresponds to the frequency of application of analogues to these steps in TSPA in the international community, as stated in Section 15.3 and in IAEA (1999 [157485], Section 6).

15.7 SUMMARY AND CONCLUSIONS

This section recapitulates the most important points that were summarized at the end of each preceeding section, along with suggestions for areas where analogues could increase needed confidence in process models. Because no new material is introduced in this section, the references to these conclusions are not included. The reader should refer to the section that provides the source of these summary points, or conclusions, or to the Document Input Reference System (DIRS).

15.7.1 Drift Stability (Section 3)

The ability of underground openings to remain open and stable under ambient conditions depends on a number of variables, including: (1) rock strength; (2) the size, shape, and orientation of the opening; (3) orientation, length, and frequency of fracturing; and (4) effectiveness of ground support. Radiometric dating of cave floor minerals at Carlsbad Caverns and Lechuguilla Cave indicates that natural openings larger than those proposed for repository drifts at Yucca Mountain have remained stable and open for millions of years. Collapse of the roof of an opening tends to occur where the fracture density is high and the overburden is thin, as is the case with some lava tubes. Independent factors that contribute to the size of a rockfall block are fracture spacing, rock type, rock texture, and the size and shape of the opening. Paleolithic flint mines (~4,000 to 3,000 BC), Roman mines and aqueducts, and other anthropogenic examples demonstrate that man-made underground openings can also exist for thousands of years.

15.7.2 Waste Form Degradation (Section 4)

The reaction path of alteration of spent nuclear fuel at Yucca Mountain will be similar to that of geologically young, Pb-free uraninite, with schoepite and becquerelite forming as intermediate products, followed by uranyl silicates. The uraninite and its alteration products found at the Nopal I uranium deposit at Peña Blanca have these characteristics. Therefore, the uranium alteration paragenetic sequence at the Nopal I uranium deposit at Peña Blanca is a good analogue for the alteration of uranium oxide spent fuel.

Secondary mineral formation was responsible for incorporating uranium in stable mineral phases at Shinkolobwe, Zaire, where 50 secondary uranium-bearing phases could be identified. Because of its great age (1,800 Ma), radiogenic lead-bearing phases played a role in sequestering uranium. At Okélobondo, Gabon, and Shinkolobwe, other secondary phases, particularly (U,Zr) silicates, formed stable phases.

The concentrations of fission products can be used as tracers in rock and groundwater surrounding uraninite and provide a satisfactory approach to estimating natural dissolution rates. When this approach was evaluated at Cigar Lake, Canada and Koongarra, Australia under reducing and oxidizing conditions, respectively, the dissolution rate at Koongarra was found to be more rapid. Although use of the fission product tracer method has not been reported for Oklo, other lines of evidence indicate that dissolution has been slight at Oklo over the past approximately 2 billion years. Whether or not deep oxidizing waters at Okélobondo have increased the dissolution of uraninite and created an oxidized suite of minerals is a subject that could be evaluated.

Under radiolysis conditions occurring at the time of reactor criticality at Oklo, only several percent of uranium was estimated to have been mobilized for transport from its original site, which experienced far more extreme conditions than those anticipated at Yucca Mountain. Likewise at Okélobondo, radiolysis effects at the time that the natural reactor was active appear confined to rare earth element migration from the core to the rim of minerals containing these elements.

Based on analyses of conditions that occurred at Oklo, it was shown that criticality of spent fuel either within waste packages or by reconcentration of uranium outside of the waste package has a very low likelihood, because the probability of certain processes required to achieve critical conditions occurring simultaneously or sequentially is extremely small and certain required conditions are mutually exclusive.

Although natural glasses are somewhat different in composition from borosilicate nuclear waste glass, studies of natural glass alteration indicate that glass waste forms will be stable in a repository environment at Yucca Mountain. In both natural and borosilicate glass, higher stability is favored by higher silica and alumina content and by lower alkali and water content. However, analogue studies have not considered radiation effects on glass over long time periods and thus cannot be used to confirm experimental results showing that radiation has little effect on waste glass stability.

15.7.3 Waste Package Degradation (Section 6)

The analogues to common metals presented in Section 6 serve mainly to demonstrate that under ambient to slightly elevated temperatures, these metals will be stable for thousands of years, even under oxidizing conditions. The survival of metal archaeological artifacts over prolonged periods of time is related to the corrosion-resistant properties of metals and metal alloys, the development of protective passive film coatings with the onset of corrosion, and the location of artifacts in arid to semi-arid environments. Such features have been used in the selection of materials and design configuration to enhance the durability of waste packages at Yucca Mountain.

The survival of the naturally occurring ordered Ni-Fe alloy in josephinite for millions of years, with only relatively minor amounts of surface oxidation, indicates that this material is highly resistant to oxidation and other forms of corrosion that occur in its geologic environment. While the composition of this metal differs from Alloy 22 (in that it does not contain Cr, Mo, or W), it does provide evidence that a similar alloy can remain passive over prolonged periods of time under similar conditions.

The potential instability of chromium-bearing materials is illustrated by the observed natural release of chromium from chromite in the Sierra de Guanajuato ultramafic rocks under ambient conditions. Corrosion appears to be concentrated along exsolution rims, analagous to structural defects on metal surfaces. However, although the chromite has undergone some alteration, it has survived for over 140 million years.

15.7.4 Engineered Barrier System Components (Section 7)

The highly corrosion-resistant nature of titanium has been demonstrated by long-term experiments conducted on a range of metal alloys in wells at the Salton Sea geothermal field, California. This anthropogenic example supports the selection of titanium alloys for the construction of a corrosion-resistant drip shield for the Engineered Barrier System (EBS).

Although the proposed devitrified welded tuff for the invert ballast does not have high concentrations of zeolite and clay minerals, the high surface area of crushed tuff will retard radionuclide transport through sorption. One example of absorption of actinides in a gravel bed

at Los Alamos, New Mexico provides qualitative evidence of retardation at the contact between an invert-like material and underlying bedrock.

Because the use of cementitious material in the EBS and its environs is restricted to grout for securing rock bolts in the emplacement drifts, hyperalkaline conditions are not expected to develop at Yucca Mountain. However, through reactive-transport modeling of the Maqarin site, it has now been demonstrated that a model can reproduce the same suite of cement minerals, hyperalkaline water compositions, and pH that were found in the field. This result builds confidence in use of such a model for analogous conditions at other sites.

The Poços de Caldas analogue illustrated that iron-bearing colloids may retard the transport of uranium and other spent-fuel components by forming colloids that are then filtrated from suspension at short distances. Degradation of steel structural elements in the EBS could conceivably contribute to this process.

15.7.5 Seepage (Section 8)

An important variable for preservation in underground openings is relative humidity. If relative humidity in the emplacement drift is kept below 100% by ventilation, then seepage of liquid water would be reduced or completely suppressed. Most caves are close to, but below 100% humidity. Thus the amount of seepage in caves found in unsaturated environments would be expected to be low. This would also be true at Yucca Mountain while ventilation is maintained.

The findings in Section 8 support the hypothesis that most of the infiltrating water in the unsaturated zone (UZ) is diverted around underground openings and does not become seepage. The analogues show that this is true even for areas with much greater precipitation rates than that at Yucca Mountain. Although examples exist where large amounts of seepage can be observed (e.g., the Mission Tunnel and Mitchell Caverns), and cave minerals formed by water are common in unsaturated environments, these hydrogeologic settings are significantly different from that at Yucca Mountain, and thus these are not appropriate analogues. However, for all of the analogues that show some seepage, at least some of the seepage that enters underground openings does not drip, but rather flows down the walls. In the few instances where dripping has been noted in settings that are analogous to Yucca Mountain, the drips can be attributed to asperities in the surface of the roof and ceiling of the opening. Whether water flows on walls or drips depends on conditions affecting drop formation and drop detachment (e.g. surface tension, roughness angle, saturation). Thus, although most water would flow around emplacement drifts at Yucca Mountain, the small amount of seepage that does occur would primarily flow down tunnel walls. In the few instances where dripping may occur, it would be expected to occur at asperities also.

15.7.6 UZ Flow and Transport (Sections 9 and 10)

Hydrographs of ponded water and ^{75}Se breakthrough curves measured during the LPIT test conducted at the Idaho National Engineering and Environmental Laboratory (INEEL) were analyzed to determine parameters controlling unsaturated flow and transport. Analysis of these data involved building a numerical model using TOUGH2 in a dual-permeability modeling approach that has been extensively used to simulate flow and transport at Yucca Mountain. The

basalt hydrologic properties showed significantly greater variability than the B-C sediment layer interbed properties. This implies that the field-scale heterogeneity limits the volume to which the spatially averaged basalt parameters could be attributed relative to the B-C sediment layer interbed parameters. This may in part result from the fractured-porous dual-continuum nature of the basalt in comparison to the porous single-continuum nature of the B-C sediment layer interbed.

The transport model calculations predicted retardation factors for neptunium and uranium that are orders of magnitude higher than retardation factors for the other radionuclides at the Radioactive Waste Management Complex (RWMC). This result would indicate that very little movement of neptunium and uranium should be observed. But detection of these radionuclides at depth was inconsistent with their predicted high retardation. Radionuclide transport in the surficial sediment zone at the RWMC could be interpreted in a number of ways. One is that lateral flow occurred, sweeping out part of the radionuclide plume. Another possibility is that a sudden surge of fluid caused by a flooding event released a pulse of radionuclides that propagated downward quickly, such that the peak lies at a greater depth than that at which the data were collected. The UZ Flow and Transport Model at Yucca Mountain considers a range of infiltration rates that are then used to bound the range of percolation flux. Because the Paintbrush nonwelded unit (PTn) at Yucca Mountain has a damping effect on downward flow to the Topopah Spring welded unit (TSw), and a similar damping effect has not been observed in the sedimentary interbeds at the RWMC, it is unlikely that the enhanced transport scenario proposed in the INEEL modeling study would occur at Yucca Mountain.

It is estimated that the transit time for the seep water that infiltrated into the Nopal I Level +00 adit 8 m below surface is about 6–29 days, and for the perched water at 10.7 m depth in an old borehole, the transit time is about 0.4–0.5 years. Although the water transit time in the UZ is quite short, significant dissolution of uranium may have occurred in a low-water flux, high-uranium concentration setting near the Nopal I uranium deposit. The uranium dissolution rates at Nopal I are about three times higher during the dry season than those in the wet season, possibly suggesting a favorable physiochemical condition (e.g., increased oxygenation) for uranium dissolution during dry periods. The low humidity during dry seasons may have also enhanced evaporation, causing higher uranium concentrations in the waters sampled. If analyses from future sampling campaigns confirm that transit time is short in the UZ at Nopal I, then the implications would need to be considered for the similar low-water flux environment at Yucca Mountain.

15.7.7 Coupled Processes (Section 11)

Geothermal systems illustrate a variety of thermal-hydrologic-chemical (THC) processes that are relevant to Yucca Mountain. Yellowstone and other geothermal systems in welded ash flow tuffs or other low-permeability rocks indicate that fluid flow is controlled by interconnected fractures. Alteration in low-permeability rocks is typically focused along fracture flow pathways. Only a small portion of the fracture volume needs to be sealed by precipitated minerals to retard fluid flow effectively. The main minerals predicted to precipitate in the near field of the potential Yucca Mountain repository are amorphous silica and calcite, which are also commonly found as sealing minerals in geothermal systems.

Sealing in geothermal fields can occur over a relatively short time frame (days to years). The unsaturated conditions, lower temperatures, and much lower fluid-flow rates predicted for the Yucca Mountain system, in comparison to geothermal systems, should result in less extensive water-rock interaction than is observed in geothermal systems. Fracturing and sealing occur episodically in geothermal systems. Most mineralization at Yucca Mountain is predicted to occur soon after waste emplacement (1,000 to 2,000 years), when temperatures would reach boiling (for the higher-temperature operating mode) above the emplacement drifts.

As shown in Section 11.3, THC processes are expected to have a much smaller effect on hydrogeological properties at Yucca Mountain than what is observed at Yellowstone. However, development of a heat pipe above emplacement drifts at Yucca Mountain under a higher-temperature operating mode could lead to increased chemical reaction and transport in the near field. Reflux and boiling of silica-bearing fluids within the near field at Yucca Mountain could cause fracture plugging, thus changing fluid flow paths. Geochemical modeling of fluid compositions has been used to successfully predict observed alteration mineral assemblages at Yellowstone. THC simulations conducted to date for the potential Yucca Mountain repository suggest that only small reductions in fracture porosity (1–3%) and permeability (< 1 order of magnitude) will occur in the near field as a result of amorphous silica and calcite precipitation. Changes in permeability, porosity, and sorptive capacity are expected to be relatively minor at the mountain scale, where thermal perturbations will be reduced. This THC result applies to both the higher and lower temperature (sub-boiling) operating modes. These predicted changes in hydrogeological properties should not significantly affect repository performance.

At the Paiute Ridge intrusive complex (Section 11.4), the Papoose Lake Sill intruded into Rainier Mesa Tuff, and the resulting hydrothermal effects were characterized by low-temperature alteration of glass to clinoptilolite and opal, similar to the alteration assemblage present at Yucca Mountain. Hydrothermal alteration was confined to a narrow zone close to the sill-host rock contact. The pervasive opal veins and associated secondary minerals (e.g., clinoptilolite, calcite, cristobalite, etc.) appear to have reduced matrix or fracture permeability in the immediate vicinity of the basaltic intrusion.

Preliminary results of a one-dimensional THC dual-continuum model of the interaction of country rock with heat released from an intrusive complex emplaced above the water table demonstrated the possibility of forming opal-filled veins with the source of silica derived from the matrix of the host rock. However, because of the irregularities caused by kinetic barrier effects associated with reaction of glass, it is important to compare and contrast a number of different sites to be able to derive general conclusions regarding mineral alteration.

Although rock type, hydrogeology, and design configurations differ from those at Yucca Mountain, the closest thermal-hydrologic-mechanical (THM) analogue identified so far is the K-26 site at Krasnoyarsk, which is particularly relevant to lower-temperature design scenarios. Although the 40-year record of experiments should be interpreted cautiously with respect to extrapolation to long time periods, THM effects such as drift convergence might be in the same range of magnitude (on the order of a few mm) as that at Krasnoyarsk for the preclosure period.

15.7.8 Saturated Zone Transport (Section 12)

Only a few of the Uranium Mill Tailing Recovery Act (UMTRA) sites are potentially useful in the evaluation of radionuclide transport in the alluvial portion of the Yucca Mountain flow system. The conclusions derived from an analysis of the Gunnison site are: (1) a fraction of the uranium originating at the site is transported in the alluvial aquifer at a rate similar to the rate at which a conservative constituent is transported; and (2) there is little evidence for lateral dispersion of contaminants in the downgradient direction. For the New Rifle site, the main conclusions are: (1) dilution is a significant process in the downgradient direction; and (2) uranium is transported at almost the same rate as conservative constituents. The conclusions regarding uranium transport distances relative to conservative constituents must be tempered by uncertainties regarding the potential presence of unidentified complexing agents.

Although several natural analogue studies have demonstrated the effect of sorption and precipitation processes on fracture surfaces, none has been able to distinguish clearly between these processes or to provide quantitative data on retardation with respect to transport of trace elements in natural waters. However, these studies do highlight which phases are most active and provide useful information on the effect of interaction between solutes and the rock surface.

In most studies of natural systems, a proportion of the total uranium, thorium, and rare earth elements in the groundwater was associated with colloids. Colloids can serve as sorbers of radionuclides, and may be agents either of retardation (Section 7 and Section 15.7.4) or of fast transport (Section 12). Unambiguous evidence from natural systems indicating colloidal transport over kilometer-scale distances is limited to a few reports. Observations from such places as Los Alamos and the Nevada Test Site lend support to the concept that radionuclide transport in the saturated zone (SZ) can be facilitated by colloids, but so far no natural analogue studies have been able to quantify the importance of this process.

15.7.9 Biosphere (Section 13)

The Chernobyl data on hot-particle dispersal and dust transport showed that radionuclides attach to dust particles and move as combined particles. Aspects of models of atmospheric contaminant dispersal, radionuclide fallout, radionuclide resuspension, and particle size distributions may be relevant to constraining a model for radionuclide resuspension resulting from a volcanic eruption through a potential Yucca Mountain repository.

The use of physical values of the half-life of radionuclides gives conservative estimates of radionuclide removal from soils in the Yucca Mountain biosphere model. The increase in the concentration of radionuclides in soils during irrigation in the southern Ukraine, where environmental conditions are more similar to those at Yucca Mountain than are conditions at Chernobyl, confirms the concept of a radionuclide buildup factor used in the Yucca Mountain biosphere conceptual model.

Results of the Chernobyl literature survey suggest that soil type influences the ecological half-life of radionuclides in the biosphere, both in regard to soil bioaccumulation factors, and advective and diffusive transport properties that limit radionuclide transfer to plant roots. With respect to rural populations, agricultural methods including irrigation, tillage, and types of crops

play an important role in resuspension of radionuclides. Resuspended material is likely to increase the contamination of plant surfaces. Resuspended radionuclides would increase the inhalation dose for agricultural workers, which would be particularly significant for plutonium.

For potential groundwater contamination pathways at Yucca Mountain, radionuclide-contaminated water, which is used as the source of drinking water, irrigation, animal watering, and for domestic applications, is expected to increase the likelihood of ingestion uptake of radionuclides by humans. Chernobyl data showed that the ingestion pathway constitutes a small part of the total radiation dose, as the external pathway is predominant within the Chernobyl Exclusion Zone. Chernobyl data on the atmospheric distribution of contaminants, their fallout, and redistribution in soils and plants may be considered an anthropogenic analogue for the potential release of radionuclides caused by a volcanic eruption at Yucca Mountain, accompanied by atmospheric dispersal of contaminants into the environment through ash fallout on the land surface.

15.7.10 Volcanism and Seismic Effects on Drifts (Section 14)

Use of natural analogues is a major investigative tool in Yucca Mountain volcanism studies. Analogues have been used to assess the probability of dike eruption, plausible eruptive styles, eruptive parameters, and magma compositions, and have also been used to increase confidence in use of the ASHPLUME code for simulation of an eruption. For seismic effects, examples from observations of underground openings demonstrate that such openings are able to withstand ground shaking for a peak ground acceleration as high as 0.4 g. The ability to withstand ground shaking is increased by thickness of overburden, competence of material (i.e., indurated and consolidated rock versus colluvium), decreased earthquake magnitude, and increased distance of the opening from the earthquake epicenter. The bulk of evidence from analogue examples of underground openings, particularly in settings similar to Yucca Mountain (such as the Little Skull Mountain earthquake), demonstrates that damage to repository drifts by ground shaking during the postclosure period would be minimal or unlikely.

15.7.11 Remaining Areas for Increased Process Understanding through Analogue Studies

The analogue examples and studies presented in this report provide varying degrees of confidence in the processes they are intended to support. The investigation of these analogues has helped to indicate the directions along which further analogue studies can best be focused to address processes that are not fully understood. Key areas where analogues may assist in building more confident assessments of processes are the following:

- Irreversible Sorption: PA currently makes the conservative assumption that sorption is reversible because no useful data exist that show it to be irreversible. If analogues could demonstrate convincingly the conditions under which sorption could be irreversible, they would contribute greatly to the realism of models.

- Drift Shadow Zone: The presence of a drift shadow zone is best tested through analogue sites that have remained undisturbed over several decades. Suggested sites are discussed in Section 9.

- Plume Dispersion: Following the UMTRA study, modeling of different types of plumes in alluvium could build confidence in the way plume dispersion is modeled for YMP TSPA. Examples could be found with toxic spills or natural analogues such as Koongarra.

- Geosphere/Biosphere Interface: Radionuclide behavior at the geosphere/biosphere interface could be investigated by natural analogue studies on the migration of radionuclides released from spills, leaks, and underground bomb tests and accidents. Some sites in Russia may yield these types of data.

- Colloids: Analogue studies suggest that colloids provide an inefficient mechanism for transport because of low populations, limited radionuclide uptake, and filtration by the rock. However, to conclude that colloids are an unimportant factor for repository safety would require information from larger-scale natural studies in relevant geological environments, which would allow study of the efficacy of buffering reactions for Eh and pH and evidence for long-distance (km-scale) transport in relevant geologic formations.

- Transport in Unsaturated Ash Flow Tuffs: Peña Blanca is probably the closest overall analogue with conditions similar to Yucca Mountain. Nopal I is a natural environment where groundwater chemistry is somewhat analogous to groundwaters in the Yucca Mountain system, and they contain elevated concentrations of radionuclides and other trace elements from a known source. Nopal I also displays discrete zones in fractured rocks intersected by potentially identifiable preferential groundwater flow paths. Such flow paths would allow definition of a source region and transport pathway, as well as a study of sorption processes on fracture surface minerals.

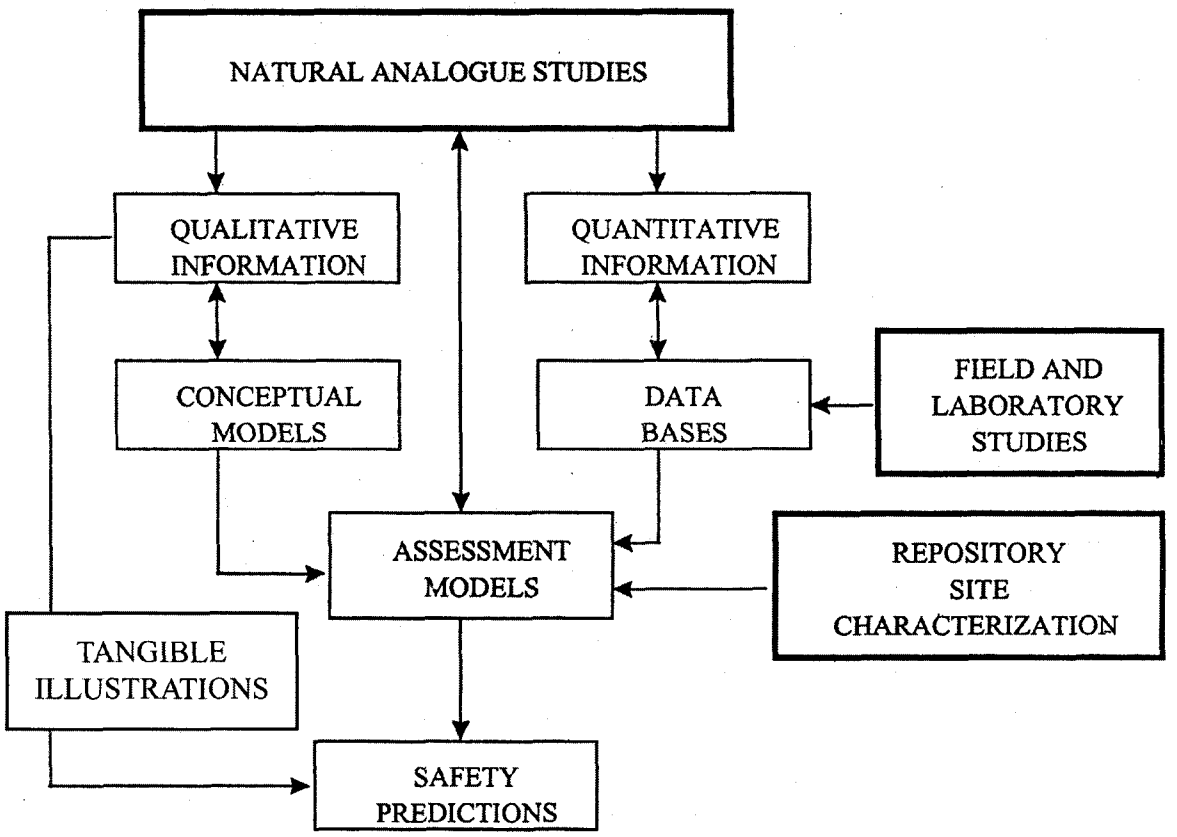

Source: IAEA 1999 [157485], Figure 1.

Figure 15-1. The Role of Natural Analogues and Site Characterization in Performance Assessment

Table 15-1. Natural Analogues in This Report and Their Potential Applications to Performance Assessment

Section in Natural Analogue Report	Conceptual Model Development (Applied Processes from Natural Analogues)	Use of Specific Parameters in Yucca Mountain TSPA Model	Use for Model Validation of Yucca Mountain Characterization
3.2			Dimensions of caves and underground openings that have stood open for thousands of years
3.3			Man-made openings have stood open for thousands of years (oldest 4000 B.C.)
3.5	Variables that determine structural stability of underground openings		
4.2, 4.4			Nopal I validated spent fuel dissolution experiments where U-silicates are long-term solubility-limiting phases
4.3	Retention of fission products at Oklo related to partitioning into uraninite		
4.4	Importance of secondary phases at Shinkolobwe and Okélobondo in retaining U		
4.6			Chemical and physical conditions required to reach criticality at Oklo used to estimate amount of spent fuel needed to create critical conditions at a repository
4.7			Qualitative validation that natural glass alteration studies indicate nuclear waste glass will be stable in repository environment
6.2	Enhanced preservation of objects stored in unsaturated conditions, as observed in Pintwater cave (NV)		
6.2	Vapor condensation resulting in corrosion, as observed in Altamira cave (Spain)		
6.2	Effects of hypersaline fluids on waste package materials, as observed in corrosion behavior of different metal compositions at Salton Sea (CA) geothermal field	Evaporation experiments conducted to determine evolution of Yucca Mountain water compositions and corresponding mineral precipitate	

Table 15-1. Natural Analogues in This Report and Their Potential Applications to Performance Assessment (cont.)

Section in Natural Analogue Report	Conceptual Model Development (Applied Processes from Natural Analogues)	Use of Specific Parameters in Yucca Mountain TSPA Model	Use for Model Validation of Yucca Mountain Characterization
6.2	Formation of protective passive film around metals, as observed in Delhi iron pillar (India)		
6.2	Long-term stability of Ni-Fe metals, as evidenced by occurrence of josephinite in 150 million year old ultramafic rocks (OR)		
7.2	Effects of hypersaline fluids on titanium, as observed in corrosion behavior of titanium alloys at Salton Sea (CA) geothermal field		
7.2	Effects of zeolites and clay minerals on ion exchange and sorption of radionuclides, as observed in tuffs at Yucca Mountain and Los Alamos, NM		
7.3	Development of hyperalkaline plumes from cementitious materials, as observed at Maqarin (Jordan)		Multicomponent reactive transport model used to compare simulated and observed fluid chemistry and rock alteration mineralogy at Maqarin (Jordan)
7.3	Fe-bearing colloids may retard U and other spent fuel components by forming colloids that are filtered from suspension at short distances		
8.2			Analogue studies prediction that most infiltration does not become seepage as observed at Kartchner Caverns, Arizona and Altamira Cave in Spain
8.3	Qualitative evidence of flow diversion around openings in the unsaturated zone independent of climate demonstrated by cave paintings in southern Europe, Egyptian tombs, Buddhist temples		
8.3	Decreases in seepage with decrease in infiltration demonstrated by preservation of fragile human artifacts and organic materials over thousands of years		

Table 15-1. Natural Analogues in This Report and Their Potential Applications to Performance Assessment (cont.)

Section in Natural Analogue Report	Conceptual Model Development (Applied Processes from Natural Analogues)	Use of Specific Parameters in Yucca Mountain TSPA Model	Use for Model Validation of Yucca Mountain Characterization
9.3			Calibration using ITOUGH2 to hydrographs at LPIT yielded parameters consistent with measured data
9.3			Dual-permeability model adequately captured flow but not transport
10.4	Significant dissolution of U may have occurred in groundwaters near Nopal I; also higher dissolution (or more U concentration) during dry season		
10.5	Colloidal transport of U, Th in oxidizing UZ at Steenkampskraal and Koongarra (little at Koongarra)		
11.2	Fluid flow in fractures, as seen in Dixie Valley (USA), Silangkitang (Indonesia) and Wairakei (NZ) geothermal fields		
11.2	Numerical simulation of heat and fluid flow in numerous developed geothermal systems		Confirmation of TOUGH2-based thermal-hydrological reservoir simulations through post-audit history matching of Olkaria (Kenya) and Nesjavellir (Iceland) geothermal fields
11.2	Use of chemical tracers to constrain source of fluids, track movement of fluids, and identify high-permeability flow paths, as conducted at Bulalo (Philippines) geothermal field		
11.2, 11.3	Changes in water chemistry, precipitation of silica and calcite, and reductions in porosity and permeability resulting from boiling, as observed at Waiotapu (NZ), Cerro Prieto (Mexico), and Yellowstone (WY) geothermal fields		
11.2	Precipitation of salts and silica associated with dryout, as observed in Karaha-Telaga Bodas (Indonesia) geothermal field		

Table 15-1. Natural Analogues in This Report and Their Potential Applications to Performance Assessment (cont.)

Section in Natural Analogue Report	Conceptual Model Development (Applied Processes from Natural Analogues)	Use of Specific Parameters in Yucca Mountain TSPA Model	Use for Model Validation of Yucca Mountain Characterization
11.2	Mineral dissolution associated with condensation, as observed at The Geysers (CA) geothermal field		
11.2, 11.3	Reduction in porosity and permeability due to silica precipitation, as observed at the Dunes (CA) and Yellowstone (WY) geothermal fields, and in reinjection wells at Otake (Japan), Rotokawa, Ohaaki, and Wairakei (NZ) geothermal fields		
11.2, 11.3	Use of thermodynamic models to predict fluid-mineral reactions at reservoir conditions		Model validation performed comparing observed and simulated mineral assemblages calculated using EQ3/6 codes, measured geothermal fluid compositions, and observed reservoir conditions at Yellowstone (WY) and Wairakei (NZ) geothermal fields
11.4			Modeled possibility of forming opal-filled veins with source of silica derived from host rock at Paiute Ridge
11.5	Localized U mobility in tuff at temperatures comparable to repository		
11.6			Qualitative- Relative TM stability under sub-boiling conditions in heterogeneous host rock at K-26 (Russia)
12.3			UMTRA plumes – weak to no uranium retardation in examples studied
12.4	Various sites in UZ – some portion of U, Th, and REE transported as colloids		
13.4			Resuspension of radionuclides in dust particles increases by an order of magnitude after soil tillage
13.4		Environmental ½-life of ^{137}Cs in food 0.4–22 yrs (shorter than predicted)	

Table 15-1. Natural Analogues in This Report and Their Potential Applications to Performance Assessment (cont.)

Section in Natural Analogue Report	Conceptual Model Development (Applied Processes from Natural Analogues)	Use of Specific Parameters in Yucca Mountain TSPA Model	Use for Model Validation of Yucca Mountain Characterization
13.4			Neglecting soil erosion as means of radionuclide removal increases model conservatism
13.4			Chernobyl – irrigation with contaminated water causes radionuclide buildup factor
13.4			Chernobyl showed that ingestion pathway constitutes small part of total dose; external pathway predominates, except for agricultural workers
14.3		Intrusion/extrusion ratio near 1 supported by Paiute Ridge field studies and reexamination of dike systems at San Rafael volcanic field	
14.3		Eruptive style and magmatic composition with combination of scoria cone, spatter cones and lava cones on the surface, and one or more dikes in the subsurface based on Lathrop Wells volcano	
14.3			Cerro Negro, in Nicaragua, used to validate the ASHPLUME code's ability to simulate an eruption
14.4	Enhanced ability of underground structures to withstand damage from earthquakes demonstrated by lack of damage in underground facilities during major earthquakes		
14.4			The DRKBA code used to model rockfall probabilities using quasi-static method of reducing the joint strength parameters to account for the seismic effect was verified based on the test runs using the dynamic functions of the distinct element code UDEC.

Source: Simmons 2002 [157578], YMP-LBNL-AMS-NA-2, pp. 11-14.

16. INPUTS AND REFERENCES

The following is a list of the references cited in this document. Column 1 represents the unique six digit numerical identifier, which is placed in the text following the reference callout (e.g., CRWMS M&O 2000 [144054]). The purpose of these numbers is to assist the reader in locating a specific reference. Within the reference list, multiple sources by the same author (e.g., CRWMS M&O 2000) are sorted alphabetically by title.

16.1 CITED DOCUMENTS

156348 Adams, M.C.; Benoit, W.R.; Doughty, C.; Bodvarsson, G.S.; and Moore, J.N. 1989. "The Dixie Valley, Nevada Tracer Test." *Geothermal Resources Council Transactions. 13*, 215-220. Davis, California: Geothermal Resources Council. TIC: 250751.

104751 Ahn, T.M. and Soo, P. 1995. "Corrosion of Low-Carbon Cast Steel in Concentrated Synthetic Groundwater at 80 to 150°C." *Waste Management, 15*, (7), 471-476. New York, New York: Elsevier. TIC: 236890.

156316 Allis, R. and Moore, J.N. 2000. "Evolution of Volcano-Hosted Vapor-Dominated Geothermal Systems." *Geothermal Resources Council Transactions, 24*, 211-216. [Davis, California]: Geothermal Resources Council. TIC: 250762.

156317 Allis, R.; Moore, J.N.; McCulloch, J.; Petty, S.; and DeRocher, T. 2000. "Karaha-Telaga Bodas, Indonesia: A Partially Vapor-Dominated Geothermal System." *Geothermal Resources Council Transactions, 24*, 217-222. [Davis, California]: Geothermal Resources Council. TIC: 250767.

156829 Anokhova, T.P. and Krivtsova, I.L. 1991. "Usloviya truda i mery bezopasnosti rabotayushchikh pri mekhanizirovannykh sposobakh vozdelyvaniya sel'skokhozyaistvennykh kul'tur na territoriyakh, zagryaznennykh radioactivnymi veshzhestvami (Labor conditions and safety measures for people involved in growing agricultural crops on territories contaminated by radioactive materials)." *In: Problemy Sel'skokhozyaistennoi Radiologii (Problems of Agricultural Radiology).* pp. 205-213. Kiev, Ukraine: Ukrainian Research Institute of Agricultural Radioecology. Copyright Requested Library Tracking Number-251866

156425 Appelo, C.A.J. 1996. 'Multicomponent Ion Exchange and Chromatography in Natural Systems." Chapter 4 of *Reactive Transport in Porous Media.* Lichtner, P.C.; Steefel, C.I.; and Oelkers, E.H., eds. Reviews in Mineralogy Volume 34. Washington, D.C.: Mineralogical Society of America. TIC: 236866.

154615 Apps, J.A. 1995. "Natural Geochemical Analogues of the Near Field of High-Level Nuclear Waste Repositories." *Proceedings of the Workshop on the Role of Natural Analogs in Geologic Disposal of High-Level Nuclear Waste, San Antonio, Texas, July 22-25, 1991.* Kovach, L.A. and Murphy, W.M., eds. NUREG/CP-0147. Pages 75-99. Washington, D.C.: U.S. Nuclear Regulatory Commission. TIC: 225202.

123814 Arai, T.; Yusa, Y.; Sasaki, N.; Tsunoda, N.; and Takano, H. 1989. "Natural Analogue Study of Volcanic Glass – A Case Study of Basaltic Glasses in Pyroclastic Fall Deposits of Fuji Volcano, Japan." *Scientific Basis for Nuclear Waste Management XII, Symposium held October 10-13, 1988, Berlin, Germany.* Lutze, W. and Ewing, R.C., eds. *127,* 73-80. Pittsburgh, Pennsylvania: Materials Research Society. TIC: 203660.

156321 Arnórsson, S. 1995. "Geothermal Systems in Iceland: Structure and Conceptual Models—I. High-Temperature Areas." *Geothermics, 24,* (5/6), 561-602. [New York, New York]: Pergamon Press. TIC: 250772.

157383 Balasubramaniam, R. 2000. "On the Corrosion Resistance of the Delhi Iron Pillar." *Corrosion Science, 42,* ([12]), 2103-2129. [New York, New York]: Elsevier. TIC: 251551.

103949 Bandurraga, T.M. and Bodvarsson, G.S. 1999. "Calibrating Hydrogeologic Parameters for the 3-D Site-Scale Unsaturated Zone Model of Yucca Mountain, Nevada." *Journal of Contaminant Hydrology, 38,* (1-3), 25-46. New York, New York: Elsevier. TIC: 244160.

157505 Bar'yakhtar, V.; Poyarkov, V.; Kholosha, V.; and Kuckhar', V. 2000. "The Shelter, Containing the Destroyed Reactor." Chapter 3 of *The Chornobyl Accident, A Comprehensive Risk Assessment.* Vargo, G.J., ed. Columbus, Ohio: Battelle Press. TIC: 251266.

157504 Bar'yakhtar, V.; Poyarkov, V.; Kholosha, V.; and Shteinberg, N. 2000. "The Accident, Chronology, Causes, and Releases." Chapter 2 of *The Chornobyl Accident, A Comprehensive Risk Assessment.* Vargo, G.J., ed. Columbus, Ohio: Battelle Press. TIC: 251266.

157419 Bar-Yosef, O.; Arnold, M.; Mercier, N.; Belfer-Cohen, A.; Goldberg, P.; Housley, R.; Laville, H.; Meignen, L.; Vogel, J.C.; and Vandermeersch, B. 1996. "The Dating of the Upper Paleolithic Layers in Kebara Cave, Mt Carmel." *Journal of Archaeological Science, 23,* 297-306. [New York, New York]: Academic Press Limited. TIC: 251573.

156255 Barenblatt, G.I.; Zheltov, I.P.; and Kochina, I.N. 1960. "Basic Concepts in the Theory of Seepage of Homogeneous Liquids in Fissured Rocks [Strata]." *[Journal of Applied Mathmatics], 24,* (5), 1286-1303. [New York, New York: Pergamon Press]. TIC: 216852.

156241 Bargar, K.E. and Beeson, M.H. 1984. *Hydrothermal Alteration in Research Drill Hole Y–6, Upper Firehole River, Yellowstone National Park, Wyoming.* U.S. Geological Survey Professional Paper 1054-B. Washington, D.C.: U.S. Govenment Printing Office. ACC: HQS.19880517.1948.

156243 Bargar, K.E. and Beeson, M.H. 1985. *Hydrothermal Alteration in Research Drill Hole Y-3, Lower Geyser Basin, Yellowstone National Park, Wyoming.* U.S.

Geological Survey Professional Paper 1054-C. Washington, D.C.: U.S. Government Printing Office. TIC: 230761.

156244 Bargar, K.E.; Beeson, M.H.; and Keith, T.E.C. 1981. "Zeolites in Yellowstone National Park." *The Mineralogical Record, [12]*, 29-38. [Tucson, Arizona: Mineralogical Record]. TIC: 250820.

156426 Barraclough, J.T.; Robertson, J.B.; and Janzer, V.J. 1976. *Hydrology of the Solid Waste Burial Ground as Related to the Potential Migration of Radionuclides, Idaho National Engineering Laboratory, with a section on drilling and sample analyses by L.G. Saindon.* Open-File Report 76-471 (IDO-22056). Denver, Colorado: U.S. Geological Survey. TIC: 251803. Cataloging

156445 Barth-Wirsching, U. and Höller, H. 1989. "Experimental Studies on Zeolite Formation Conditions." *European Journal of Mineralogy, 1*, 489-506. Stuttgart, [Germany]: E. Schweizerbart'sche Verlagsbuchhandlung. TIC: 250916.

156953 Baryakhtar, V.G. 1997. *Chernobyl Catastrophe.* New York, New York: Begell House. TIC: 251556.

157531 Bassett, W.A.; Bird, J.M.; Weathers, M.S.; and Kohlstedt, D.L. 1980. "Josephinite: Crystal Structures and Phase Relations of the Metals." *Physics of the Earth and Planetary Interiors, 23*, 255-261. Amsterdam, The Netherlands: Elsevier. TIC. 251814.

157407 Becker, B.H.; Burgess, J.D.; Holdren, K.J.; Jorgensen, D.K.; Magnuson, S.O.; and Sondrup, A.J. 1998. *Interim risk assessment and contaminant screening for the Waste Area Group 7 remedial investigation.* DOE/ID-10569. Idaho Falls, Idaho: Lockheed Martin Idaho Technologies Company. On Order Library Tracking Number-251834

156213 Behl, B.K. 1998. *The Ajanta Caves, Artistic Wonder of Ancient Buddhist India.* New York, New York: Harry N. Abrams. TIC: 250802.

156592 Berkovski, V.; Ratia, G.; and Nasvit, O. 1996. "Internal Doses to Ukrainian Populations Using Dnieper River Water." *Health Physics, 71*, (1), 37-44. [New York, New York: Pergamon]. TIC: 250875.

154601 Bird, D.K. and Elders, W.A. 1976. "Hydrothermal Alteration and Mass Transfer in the Discharge Portion of the Dunes Geothermal System, Imperial Valley of California, USA." *Proceedings of the Second United Nations Symposium on the Development and Use of Geothermal Resources, San Francisco, California, USA, 20-29 May 1975. 1,* 285-295. Washington, D.C.: U.S. Government Printing Office. TIC: 249829.

157514 Bird, J.M. 2001. "John M. Bird." Ithaca, New York: Cornell University. Accessed January 30, 2002. http://www.geo.cornell.edu/geology/faculty/Bird.html Copyright Requested Library Tracking Number-251749

157397 Bird, J.M. and Ringwood, A.E. 1980. *Container for Radioactive Nuclear Waste Materials*. U.S. Patent Number: 4,192,765. [Washington, D.C.]: U.S. Patent Office. TIC: 251651.

157398 Bird, J.M. and Ringwood, A.E. 1982. *Container for Radioactive Nuclear Waste Materials*. U.S. Patent Number: 4,337,167. [Washington, D.C.]: U.S. Patent Office. TIC: 251653.

157396 Bird, J.M. and Ringwood, A.E. 1984. *Container for Radioactive Nuclear Waste Materials*. U.S. Patent Number: 4,474,689. [Washington, D.C.]: U.S. Patent Office. TIC: 251649.

105170 Birkholzer, J.; Li, G.; Tsang, C-F.; and Tsang, Y. 1999. "Modeling Studies and Analysis of Seepage into Drifts at Yucca Mountain." *Journal of Contaminant Hydrology, 38,* (1-3), 349-384. New York, New York: Elsevier. TIC: 244160.

100006 Bish, D.L. and Aronson, J.L. 1993. "Paleogeothermal and Paleohydrologic Conditions in Silicic Tuff from Yucca Mountain, Nevada." *Clays and Clay Minerals, 41*, (2), 148-161. Long Island City, New York: Pergamon Press. TIC: 224613.

101195 Bish, D.L. and Chipera, S.J. 1989. *Revised Mineralogic Summary of Yucca Mountain, Nevada.* LA-11497-MS. Los Alamos, New Mexico: Los Alamos National Laboratory. ACC: NNA.19891019.0029.

157498 Blanc, P.L. 1996. *Oklo - Natural Analogue for a Radioactive Waste Repository (Phase 1).* EUR 16587. Luxembourg, Luxembourg: Commission of the European Communities. Out of Print/Out of Stock Library Tracking Number-251893

124640 Blomqvist, R.; Suksi, J.; Ruskeeniemi, T.; Ahonen, L.; Niini, H.; Vuorinen, U.; and Jakobsson, K. 1995. *The Palmottu Natural Analogue Project, Summary Report 1992—1994, The Behaviour of Natural Radionuclides in and Around Uranium Deposits; Nr. 8.* YST-88. Espoo, Finland: Geological Survey of Finland. TIC: 247142.

156337 Bodvarsson, G.S. and Witherspoon, P.A. 1989. "Geothermal Reservoir Engineering Part 1." *Geothermal Science and Technology, 2*, (1), 1-68. New York, New York: Gordon and Breach Science Publishers. TIC: 250976.

120055 Bodvarsson, G.S.; Boyle, W.; Patterson, R.; and Williams, D. 1999. "Overview of Scientific Investigations at Yucca Mountain—The Potential Repository for High-Level Nuclear Waste." *Journal of Contaminant Hydrology, 38*, (1-3), 3-24. New York, New York: Elsevier. TIC: 244160.

138618 Bodvarsson, G.S.; Gislason, G.; Gunnlaugsson, E.; Sigurdsson, O.; Stefansson, V.; and Steingrimsson, B. 1993. "Accuracy of Reservoir Predictions for the Nesjavellir Geothermal Field, Iceland." *Proceedings, Eighteenth Workshop, Geothermal Reservoir Engineering, Stanford, California, January 26-28, 1993.* Ramey, H.J., Jr.; Horne, R.N.; Kruger, P.; Miller, F.G.; Brigham, W.E.; and Cook, J.W., eds.

Workshop Report SGP-TR-145. Pages 273-278. Stanford, California: Stanford University. TIC: 246821.

136384 Bodvarsson, G.S.; Pruess, K.; Haukwa, C.; and Ojiambo, S.B. 1990. "Evaluation of Reservoir Model Predictions for Olkaria East Geothermal Field, Kenya." *Geothermics, 19*, (5), 399-414. [New York, New York]: Pergamon Press. TIC: 246739.

156363 Bohlmann, E.G.; Mesmer, R.E.; and Berlinski, P. 1980. "Kinetics of Silica Deposition From Simulated Geothermal Brines." *Society of Petroleum Engineers Journal, 20*, (4), 239-248. Dallas, Texas: Society of Petroleum Engineers. TIC: 250974.

156635 Boles, J.R. 1999. "Calcite Precipitates in the Mission Tunnel: A 90-Year Record of Groundwater Seeps in Fractured Sandstone." *EOS, Transactions (Supplement), 80*, (46), F423. Washington, D.C.: American Geophysical Union. TIC: 251227.

156846 Bondar, P.F.; Loshchilov, N.A.; Dugov, A.I.; Ozornov, A.G.; Svidenyuk, N.L.; Tereshchenko, H.P.; and Maslo, A.V. 1991. "Obshzhie zakonomernosti zagryazneniya produktsii rastienivodstva na teritorii podvergsheisya radioaktivnomu zagryazneniyu v rezultate avarii na ChAES (General characteristics of the contamination of agricultural products on the territory affected by radioactive contamination after the the ChNPP accident)." *In: Problemy Sel'skokhozyaistennoi Radiologii (Problems of Agricultural Radiology).* pp. 88-105. Kiev, Ukraine: Ukrainian Research Institute of Agricultural Radioecology. Copyright Requested Library Tracking Number-251866

156952 Bondarenko, O.A. 1998. *Metody Izucheniya Formirovaniya doz Oblucheniya ot Transuranobykh Elementov (Methods of Investigations of Formation of Radiation Doses of Transuranic Elements).* Kiev, Ukraine: Naukova Dumka. On Order Library Tracking Number-251891

156593 Bondarenko, O.A.; Aryasov, B.B.; and Tsygankov, N.Ya. 2000. "Evaluation of the Plutonium Content in the Human Body Due to Global and Chernobyl Fallout." *Journal of Radioanalytical and Nuclear Chemistry, 243*, (2), 473-478. Dordrecht, The Netherlands: Kluwer Academic Publishers. TIC: 251062.

154716 Botto, R.I. and Morrison, G.H. 1976. "Josephinite: A Unique Nickel-Iron." *American Journal of Science, 276*, (3), 241-274. New Haven, Connecticut: Yale University, Kline Geology Laboratory. TIC: 249797.

156456 Breisch, R.L. 1987. "The Conservation of European Cave Art." *NSS News, [45]*, 285-291. [Huntsville, Alabama: National Speleological Society]. TIC: 251229

133930 Brookins, D.G. 1978. "Retention of Transuranic and Actinide Elements and Bismuth at the Oklo Natural Reactor, Gabon: Application of Eh–pH Diagrams." *Chemical Geology, 23*, 309-323. Amsterdam, The Netherlands: Elsevier. TIC: 247321.

109877 Brookins, D.G. 1986. "Natural Analogues for Radwaste Disposal: Elemental Migration in Igneous Contact Zones." *Chemical Geology, 55*, 337-344. Amsterdam, The Netherlands: Elsevier. TIC: 246170.

102004 Broxton, D.E.; Bish, D.L.; and Warren, R.G. 1987. "Distribution and Chemistry of Diagenetic Minerals at Yucca Mountain, Nye County, Nevada." *Clays and Clay Minerals, 35*, (2), 89-110. Long Island City, New York: Pergamon Press. TIC: 203900.

100024 Broxton, D.E.; Warren, R.G.; Byers, F.M.; and Scott, R.B. 1989. "Chemical and Mineralogic Trends Within the Timber Mountain–Oasis Valley Caldera Complex, Nevada: Evidence for Multiple Cycles of Chemical Evolution in a Long-Lived Silicic Magma System." *Journal of Geophysical Research, 94*, (B5), 5961-5985. Washington, D.C.: American Geophysical Union. TIC: 225928.

156600 Bruk, G.Y.; Shutov, V.N.; Balonov, M.I.; Basalayeva, L.N.; and Kislov, M.V. 1998. "Dynamics of {superscript 137}Cs Content in Agricultural Food Products Produced in Regions of Russia Contaminated after the Chernobyl Accident." *Radiation Protection Dosimetry, 76*, (3), 169-178. [Ashford, Kent, United Kingdom]: Nuclear Technology Publishing. TIC: 251136.

157484 Bruno, J.; Duro, L.; and Grivé, M. 2001. *The Applicability and Limitations of the Geochemical Models and Tools Used in Simulating Radionuclide Behaviour in Natural Waters, Lessons Learned from the Blind Predictive Modelling Exercises Performed in Conjunction with Natural Analogue Studies*. SKB TR-01-20. Stockholm, Sweden: Swedish Nuclear Fuel And Waste Management Company. TIC: 251208.

100105 Bruton, C.J. 1995. *Testing EQ3/6 and GEMBOCHS Using Fluid-Mineral Equilibria in the Wairakei Geothermal System*. Letter Report MOL206. Livermore, California: Lawrence Livermore National Laboratory. ACC: MOL.19960409.0131.

117033 Bruton, C.J.; Glassley, W.E.; and Meike, A. 1995. *Geothermal Areas as Analogues to Chemical Processes in the Near-Field and Altered Zone of the Potential Yucca Mountain, Nevada Repository*. UCRL-ID-119842. Livermore, California: Lawrence Livermore National Laboratory. ACC: MOV.19980504.0002.

156304 BSC (Bechtel SAIC Company) 2001. *Drift Degradation Analysis*. ANL-EBS-MD-000027 REV 01 ICN 01. Las Vegas, Nevada: Bechtel SAIC Company. ACC: MOL.20011029.0311.

154677 BSC (Bechtel SAIC Company) 2001. *Drift-Scale Coupled Processes (DST and THC Seepage) Models*. MDL-NBS-HS-000001 REV 01 ICN 01. Las Vegas, Nevada: Bechtel SAIC Company. ACC: MOL.20010418.0010.

155950 BSC (Bechtel SAIC Company) 2001. *FY 01 Supplemental Science and Performance Analyses, Volume 1: Scientific Bases and Analyses*. TDR-MGR-MD-000007 REV

00 ICN 01. Las Vegas, Nevada: Bechtel SAIC Company. ACC: MOL.20010801.0404; MOL.20010712.0062; MOL.20010815.0001.

154659 BSC (Bechtel SAIC Company) 2001. *FY01 Supplemental Science and Performance Analyses, Volume 2: Performance Analyses.* TDR-MGR-PA-000001 REV 00. Las Vegas, Nevada: Bechtel SAIC Company. ACC: MOL.20010724.0110.

154554 BSC (Bechtel SAIC Company) 2001. *Lower-Temperature Subsurface Layout and Ventilation Concepts.* ANL-WER-MD-000002 REV 00. Las Vegas, Nevada: Bechtel SAIC Company. ACC: MOL.20010718.0225.

155664 BSC (Bechtel SAIC Company) 2001. *Subsurface Facility System Description Document.* SDD-SFS-SE-000001 REV 01 ICN 01. Las Vegas, Nevada: Bechtel SAIC Company. ACC: MOL.20010927.0073.

157151 BSC (Bechtel SAIC Company) 2001. *Technical Update Impact Letter Report.* MIS-MGR-RL-000001 REV 00 ICN 02. Las Vegas, Nevada: Bechtel SAIC Company. ACC: MOL.20011211.0311.

157535 BSC (Bechtel SAIC Company) 2001. *Technical Work Plan for Natural Analogue Studies for License Application.* TWP-NBS-GS-000002 REV 01. Las Vegas, Nevada: Bechtel SAIC Company. ACC: MOL.20020213.0181.

157606 BSC (Bechtel SAIC Company) 2002. *Test Plan for: Alcove 8 Flow and Seepage Testing.* SITP-02-UZ-003 REV00. Las Vegas, Nevada: Bechtel SAIC Company. ACC: MOL.20020204.0144.

157438 Buck, P.E. and DuBarton, A. 1994. "Archaeological Investigations at Pintwater Cave, Nevada, During the 1963-64 Field Season." *Journal of California and Great Basin Anthropology, 16,* (2), 221-242. Riverside, California: Malki Museum Press. Copyright Requested Library Tracking Number-251661

100712 Buddemeier, R.W. and Hunt, J.R. 1988. "Transport of Colloidal Contaminants in Groundwater: Radionuclide Migration at the Nevada Test Site." *Applied Geochemistry, 3,* 535-548. Oxford, England: Pergamon Press. TIC: 224116.

154295 Buecher, R.H. 1999. "Microclimate Study of Kartchner Caverns, Arizona." *Journal of Cave and Karst Studies, 61,* (2), 108-120. Huntsville, Alabama: National Speleological Society. TIC: 249657.

156596 Bugai, D.A.; Waters, R.D.; Dzhepo, S.P.; and Skal'skij, A.S. 1996. "Risks from Radionuclide Migration to Groundwater in the Chernobyl 30-KM Zone." *Health Physics, 71,* (1), 9-18. [New York, New York: Pergamon]. TIC: 251063.

156699 Bulgakov, A.A. and Konoplev, A.V. 2000. "Modeling of Radionuclide Transfer by Tree Root System from Disposal Site to the Soil Surface." *Proceedings, Radioactivity after Nuclear Explosions and Accidents. Volume 1,* 775-780. St.

Petersburg, Russia: Hydrometeoizdat. Copyright Requested Library Tracking Number-251863

144410 Bullivant, D.P. and O'Sullivan, M.J. 1998. "Inverse Modelling of the Wairakei Geothermal Field." *Proceedings of the TOUGH Workshop '98, Berkeley, California, May 4-6, 1998.* Preuss, K., ed. LBNL-41995. Pages 53-58. Berkeley, California: Lawrence Berkeley National Laboratory. TIC: 247159.

156401 Burgess, J.D. 1995. *Results of the Neutron and Natural Gamma Logging, Stratigraphy, and Perched Water Data Collected during a Large-Scale Infiltration Test.* INEL-95/062, EDF-ER-WAG7-60. Idaho Falls, Idaho: Lockheed Martin Idaho Technologies. On Order Library Tracking Number-251836

121857 Byers, C.D.; Jercinovic, M.J.; and Ewing, R.C. 1987. A *Study of Natural Glass Analogues as Applied to Alteration of Nuclear Waste Glass.* NUREG/CR-4842. Washington, D.C.: U.S. Nuclear Regulatory Commission. TIC: 231239.

101859 Byers, F.M., Jr. and Barnes, H. 1967. *Geologic Map of the Paiute Ridge Quadrangle, Nye and Lincoln Counties, Nevada.* Map GQ-577. Washington, D.C.: U.S. Geological Survey. ACC: HQS.19880517.1104.

104639 Byers, F.M., Jr.; Carr, W.J.; Orkild, P.P.; Quinlivan, W.D.; and Sargent, K.A. 1976. *Volcanic Suites and Related Cauldrons of Timber Mountain-Oasis Valley Caldera Complex, Southern Nevada.* Professional Paper 919. Washington, D.C.: U.S. Geological Survey. TIC: 201146.

101326 Carlos, B.A.; Chipera, S.J.; and Bish, D.L. 1995. *Distribution and Chemistry of Fracture-Lining Minerals at Yucca Mountain, Nevada.* LA-12977-MS. Los Alamos, New Mexico: Los Alamos National Laboratory. ACC: MOL.19960306.0564.

154504 Carpenter, D.W. and Chung, D.H. 1986. *Effects of Earthquakes on Underground Facilities: Literature Review and Discussion.* NUREG/CR-4609. Washington, D.C.: U.S. Nuclear Regulatory Commission. TIC: 203428.

124275 Carroll, S.; Mroczek, E.; Alai, M.; and Ebert, M. 1998. "Amorphous Silica Precipitation (60 to 120°C): Comparison of Laboratory and Field Rates." *Geochimica et Cosmochimica Acta, 62,* (8), 1379-1396. New York, New York: Elsevier. TIC: 243029.

109627 Carroll, S.; Mroczek, E.; Bourcier, B.; Alai, M.; and Ebert, M. 1995. *Comparison of Field and Laboratory Precipitation Rates of Amorphous Silica from Geothermal Waters at 100 ° C.* Letter Report MOL207. Livermore, California: Lawrence Livermore National Laboratory. ACC: MOL.19960415.0465.

156256 Cecil, L.D.; Pittman, J.R.; Beasley, T.M.; Michel, R.L; Kubik, P.W.; Sharma, P.; Fen, U.; and Gove, H.E. 1992. "Water Infiltration Rates in the Unsaturated Zone at the Idaho National Engineering Laboratory Estimated from Chlorine-36 and Tritium Profiles, and Neutron Logging." *Water-Rock Interaction, Proceedings of the 7th*

International Symposium on Water-Rock Interaction – WRI-7, Park City, Utah, 13-18 July 1992. Kharaka, Y.K. and Maest, A.S., eds. *1*, 709-718. Brookfield, Vermont: A.A. Balkema. TIC: 208527.

157549 Chambers, A.V.; Haworth, A.; Ilett, D.; Linklater, C.M.; and Tweed, C.J. 1998. "Geochemical Modelling of Hyperalkaline Water/Rock Interactions." Chapter 7 of *MAQARIN Natural Analogue Study: Phase III, Volume I.* Smellie, J.A.T., ed. SKB TR-98-04. Stockholm, Sweden: Swedish Nuclear Fuel and Waste Management Company. TIC: 244013.

124323 Chapman, N.A. and Smellie, J.A.T. 1986. "Introduction and Summary of the Workshop." *Chemical Geology, 55*, 167-173. Amsterdam, The Netherlands: Elsevier. TIC: 246750.

100970 Chapman, N.A.; Andersson, J.; Robinson, P.; Skagius, K.; Wene, C-O.; Wiborgh, M.; and Wingefors, S. 1995. *Systems Analysis, Scenario Construction and Consequence Analysis Definition for SITE-94*. SKI Report 95:26. Stockholm, Sweden: Swedish Nuclear Power Inspectorate. TIC: 238888.

152249 Chauvet, J-M.; Deschamps, E.B.; and Hillaire, C. 1996. *Dawn of Art: The Chauvet Cave*. New York, New York: Harry N. Abrams, Inc. TIC: 248775.

156349 Chigira, M. and Nakata, E. [1996]. "Geological Influence of Andesite Intrusion on Diatomite (Part 2)–Physical Property Ghanges of Diatomite and Self-Sealing Mechanism-." *Energy Technology Data Exchange*, 1-32. [Abiko Japan: Central Research Institute of Electric Power Industry, Abiko Research Laboratory]. TIC: 250950.

156364 Chigira, M.; Nakata, E.; and Watanabe, M. 1995. "Self-Sealing of Rock-Water Systems by Silica Precipitation." *[Proceedings of the 8th International Symposium on Water-Rock Interaction, WRI-8, Vladivostok, Russia, 15-19 August 1995]*. Kharaka, [Y.K.] and Chudeav, [O.V.], eds. Pages 73-77. Rotterdam, [The Netherlands]: A.A. Balkema. TIC: 250782.

154599 Cho, M.; Liou, J.G.; and Bird, D.K. 1988. "Prograde Phase Relations in the State 2-14 Well Metasandstones, Salton Sea Geothermal Field, California." *Journal of Geophysical Research, 93*, (B11), 13,081-13,103. Washington, D.C.: American Geophysical Union. TIC: 249734.

156739 Christiansen, R.L. 2001. *The Quaternary and Pliocene Yellowstone Plateau Volcanic Field of Wyoming, Idaho, and Montana*. Professional Paper 729-G. Menlo Park, California: U.S. Geological Survey. TIC: 251137.

156780 Clark, J.F. and Turekian, K.K. 1990. "Time Scale of Hydrothermal Water-Rock Reactions in Yellowstone National Park Based on Radium Isotopes and Radon." *Journal of Volcanology and Geothermal Research, 40*, 169-180. Amsterdam, The Netherlands: Elsevier. TIC: 251240.

156636 Corchon, M.S.; Valladas, H.; Becares, J.; Arnold, M.; Tisnerat, N.; and Cachier, H. 1996. "Dating of the Paintings and a Review of the Paleolithic Art of the Palomera Cave (Ojo Guareña, Burgos, Spain)." *Zephyrus, 49*, 37-60. [Salamanca, Spain]: Universidad de Salamanca. TIC: 251231.

156344 Corsi, R. 1986. "Scaling and Corrosion in Geothermal Equipment: Problems and Preventive Measures." *Geothermics, 15*, (5/6), 839-856. [New York, New York]: Pergamon. TIC: 250785.

124396 Cowan, R. and Ewing, R.C. 1989. "Freshwater Alteration of Basaltic Glass, Hanauma Bay, Oahu, Hawaii: A Natural Analogue for the Alteration of Borosilicate Glass in Freshwater." *Scientific Basis for Nuclear Waste Management XII, Symposium held October 10-13, 1988, Berlin, Germany.* Lutze, W. and Ewing, R.C., eds. 127, 49-56. Pittsburgh, Pennsylvania: Materials Research Society. TIC: 203660.

157537 Cramer, J.J. 1994. *Natural Analogs in Support of the Canadian Concept for Nuclear Fuel Waste Disposal.* AECL-10291. Pinawa, Manitoba, Canada: Whiteshell Laboratories. TIC: 212296.

157420 Crawford, H. 1979. *Subterranean Britain, Aspects of Underground Archaeology.* New York, New York: St. Martin's Press. TIC: 251575.

100972 Crowe, B.; Self, S.; Vaniman, D.; Amos, R.; and Perry, F. 1983. "Aspects of Potential Magmatic Disruption of a High-Level Radioactive Waste Repository in Southern Nevada." *Journal of Geology, 91*, (3), 259-276. Chicago, Illinois: University of Chicago Press. TIC: 216959.

100116 CRWMS M&O (Civilian Radioactive Waste Management System Management and Operating Contractor) 1996. *Probabilistic Volcanic Hazard Analysis for Yucca Mountain, Nevada.* BA0000000-01717-2200-00082 REV 0. Las Vegas, Nevada: CRWMS M&O. ACC: MOL.19971201.0221.

100223 CRWMS M&O 1997. *Determination of Available Volume for Repository Siting.* BCA000000-01717-0200-00007 REV 00. Las Vegas, Nevada: CRWMS M&O. ACC: MOL.19971009.0699.

132547 CRWMS M&O 1999. *ASHPLUME Version 1.4LV Design Document.* 10022-DD-1.4LV-00, Rev. 00. Las Vegas, Nevada: CRWMS M&O. ACC: MOL.20000424.0415.

107292 CRWMS M&O 1999. *License Application Design Selection Report.* B00000000-01717-4600-00123 REV 01 ICN 01. Las Vegas, Nevada: CRWMS M&O. ACC: MOL.19990908.0319.

145771 CRWMS M&O 2000. *Analysis of Hydrologic Properties Data.* ANL-NBS-HS-000002 REV 00. Las Vegas, Nevada: CRWMS M&O. ACC: MOL.19990721.0519.

151615 CRWMS M&O 2000. *Biosphere Process Model Report.* TDR-MGR-MD-000002 REV 00 ICN 01. Las Vegas, Nevada: CRWMS M&O. ACC: MOL.20000620.0341.

142657 CRWMS M&O 2000. *Characterize Eruptive Processes at Yucca Mountain, Nevada.* ANL-MGR-GS-000002 REV 00. Las Vegas, Nevada: CRWMS M&O. ACC: MOL.20000517.0259.

151551 CRWMS M&O 2000. *Characterize Framework for Igneous Activity at Yucca Mountain, Nevada.* ANL-MGR-GS-000001 REV 00 ICN 01. Las Vegas, Nevada: CRWMS M&O. ACC: MOL.20001221.0001.

142321 CRWMS M&O 2000. *Characterize Framework for Seismicity and Structural Deformation at Yucca Mountain, Nevada.* ANL-CRW-GS-000003 REV 00. Las Vegas, Nevada: CRWMS M&O. ACC: MOL.20000510.0175.

152998 CRWMS M&O 2000. *Comparison of ASHPLUME Model Results to Representative Tephra Fall Deposits.* CAL-WIS-MD-000011 REV 00. Las Vegas, Nevada: CRWMS M&O. ACC: MOL.20001204.0032.

151954 CRWMS M&O 2000. *Effects of Fault Displacement on Emplacement Drifts.* ANL-EBS-GE-000004 REV 00 ICN 01. Las Vegas, Nevada: CRWMS M&O. ACC: MOL.20000504.0297.

151953 CRWMS M&O 2000. *Fault Displacement Effects on Transport in the Unsaturated Zone.* ANL-NBS-HS-000020 REV 01. Las Vegas, Nevada: CRWMS M&O. ACC: MOL.20001002.0154.

141407 CRWMS M&O 2000. *Natural Analogs for the Unsaturated Zone.* ANL-NBS-HS-000007 REV 00. Las Vegas, Nevada: CRWMS M&O. ACC: MOL.19990721.0524.

152269 CRWMS M&O 2000. *Natural Ventilation Study: Demonstration of Concept.* TDR-SVS-SE-000001 REV 00. Las Vegas, Nevada: CRWMS M&O. ACC: MOL.20001201.0103.

152146 CRWMS M&O 2000. *Operating a Below-Boiling Repository: Demonstration of Concept.* TDR-WIS-SE-000001 REV 00. Las Vegas, Nevada: CRWMS M&O. ACC: MOL.20001005.0010.

153246 CRWMS M&O 2000. *Total System Performance Assessment for the Site Recommendation.* TDR-WIS-PA-000001 REV 00 ICN 01. Las Vegas, Nevada: CRWMS M&O. ACC: MOL.20001220.0045.

152435 CRWMS M&O 2000. *Transfer Coefficient Analysis.* ANL-MGR-MD-000008 REV 00 ICN 02. Las Vegas, Nevada: CRWMS M&O. ACC: MOL.20001016.0005.

151940 CRWMS M&O 2000. *Unsaturated Zone Flow and Transport Model Process Model Report.* TDR-NBS-HS-000002 REV 00 ICN 02. Las Vegas, Nevada: CRWMS M&O. ACC: MOL.20000831.0280.

151945 CRWMS M&O 2000. *Yucca Mountain Site Description.* TDR-CRW-GS-000001 REV 01 ICN 01. Las Vegas, Nevada: CRWMS M&O. ACC: MOL.20001003.0111.

152536 CRWMS M&O 2001. *Disruptive Event Biosphere Dose Conversion Factor Analysis.* ANL-MGR-MD-000003 REV 01. Las Vegas, Nevada: CRWMS M&O. ACC: MOL.20010125.0233.

152517 CRWMS M&O 2001. *Evaluate Soil/Radionuclide Removal by Erosion and Leaching.* ANL-NBS-MD-000009 REV 00 ICN 01. Las Vegas, Nevada: CRWMS M&O. ACC: MOL.20010214.0032.

100438 Curtis, D.; Benjamin, T.; Gancarz, A.; Loss, R.; Rosman, K.; DeLaeter, J.; Delmore, J.E.; and Maeck, W.J. 1989. "Fission Product Retention in the Oklo Natural Fission Reactors." *Applied Geochemistry, 4,* 49-62. New York, New York: Pergamon Press. TIC: 237970.

110987 Curtis, D.; Fabryka-Martin, J.; Dixon, P.; and Cramer, J. 1999. "Nature's Uncommon Elements: Plutonium and Technetium." *Geochimica et Cosmochimica Acta, 63,* (2), 275-285. [New York, New York]: Pergamon. TIC: 246120.

157497 Curtis, D.B. 1996. "Radionuclide Release Rates from Spent Fuel for Performance Assessment Modeling." *Sixth EC Natural Analogue Working Group Meeting, Proceedings of an International Workshop Held in Santa Fe, New Mexico, USA on September 12-16, 1994.* von Maravic, H. and Smellie, J., eds. *EUR 16761 EN,* Pages 145-153. Luxembourg, Luxembourg: Commission of the European Communities. TIC: 225227.

124785 Curtis, D.B. and Gancarz, A.J. 1983. *Radiolysis in Nature: Evidence from the Oklo Natural Reactors.* SKB Technical Report 83-10. Stockholm, Sweden: Swedish Nuclear Fuel and Waste Management Company. TIC: 205938.

105270 Curtis, D.B.; Fabryka-Martin, J.; Dixon, P.; Aguilar, R.; and Cramer, J. 1994. "Radionuclide Release Rates from Natural Analogues of Spent Nuclear Fuel." *High Level Radioactive Waste Management, Proceedings of the Fifth Annual International Conference, Las Vegas, Nevada, May 22-26, 1994. 4,* 2228-2236. La Grange Park, Illinois: American Nuclear Society. TIC: 210984.

156374 Dalrymple, G.B.; Grove, M.; Lovera, O.M.; Harrison, T.M.; Hulen, J.B.; and Lanphere, M.A. 1999. "Age and thermal history of the Geysers Plutonic Complex (Felsite Unit), Geysers Geothermal Field, California: A 40Ar/39Ar and U-Pb Study." *Earth and Planetary Science Letters, 173,* 285-298. Amsterdam, The Netherlands: Elsevier. On Order Library Tracking Number-250858

157409 Dames & Moore 1992. *Compilation and summarization of the Subsurface Disposal Area Radionuclide Transport Data at the Radioactive Waste Management Complex.* EGG-ER-10546. Washington, D.C.: U.S. Department of the Interior, Bureau of Mines. On Order Library Tracking Number-251837

157421 Davies, O. 1935. *Roman mines in Europe.* Oxford, [England]: Clarendon Press. TIC: 251576

154436 Davis, J.A.; Coston, J.A.; Kent, D.B.; and Fuller, C.C. 1998. "Application of the Surface Complexation Concept to Complex Mineral Assemblages." *Environmental Science & Technology, 32,* (19), 2820-2828. Washington, D.C.: American Chemical Society. TIC: 249656.

144461 Davis, O.K. 1990. "Caves as Sources of Biotic Remains in Arid Western North America." *Palaeogeography, Palaeoclimatology, Palaeoecology, 76,* (3/4), 331-348. Amsterdam, The Netherlands: Elsevier. TIC: 247413.

101557 Day, W.C.; Potter, C.J.; Sweetkind, D.S.; Dickerson, R.P.; and San Juan, C.A. 1998. *Bedrock Geologic Map of the Central Block Area, Yucca Mountain, Nye County, Nevada.* Miscellaneous Investigations Series Map I-2601. [Washington, D.C.]: U.S. Geological Survey. ACC: MOL.19980611.0339.

157473 De la Cruz, B.; Hernán, P.; and Astudillo, J. 1997. "The El Berrocal Project." *Seventh EC Natural Analogue Working Group Meeting, Proceedings of an International Workshop held in Stein am Rhein, Switzerland from 28 to 30 October 1996.* von Maravic, H. and Smellie, J., eds. *EUR 17851 EN,* Pages 79-103. Luxembourg, Luxembourg: Commission of the European Communities. TIC: 247461.

101128 Degueldre, C.A. 1994. *Colloid Properties in Groundwaters from Crystalline Formations.* PSI Bericht Nr. 94-21. Villigen, Switzerland: Paul Scherrer Institut. TIC: 224100.

154749 Dick, H.J.B. 1974. "Terrestrial Nickel–Iron from the Josephine Peridotite, Its Geologic Occurrence, Associations, and Origin." *Earth and Planetary Science Letters, 24,* (2), 291-298. Amsterdam, The Netherlands: North-Holland. TIC: 249849.

157410 Dicke, C.A. 1997. *Distribution coefficients and contaminant solubilities for the Waste Area Group 7 Baseline Risk Assessment.* INEL/EXT-97-00201. Idaho Falls, Idaho: Lockheed Martin Idaho Technologies Company. On Order Library Tracking Number-251838

154503 Dobson, P.; Hulen, J.; Kneafsey, T.J.; and Simmons, A. 2001. "Permeability at Yellowstone: A Natural Analog for Yucca Mountain Processes." *"Back to the Future - Managing the Back End of the Nuclear Fuel Cycle to Create a More Secure Energy Future," Proceedings of the 9th International High-Level Radioactive Waste*

Management Conference (IHLRWM), Las Vegas, Nevada, April 29-May 3, 2001. La Grange Park, Illinois: American Nuclear Society. TIC: 247873.

154547 Dobson, P.; Hulen, J.; Kneafsey, T.J.; and Simmons, A. 2001. "The Role of Lithology and Alteration on Permeability and Fluid Flow in the Yellowstone Geothermal System, Wyoming." *Proceedings, Twenty-Sixth Workshop on Geothermal Reservoir Engineering, Palo Alto, California, January 29-31, 2001.* Workshop Report SGP-TR-168. Stanford, California: Stanford University. TIC: 249825.

154692 DOE (U.S. Department of Energy) 1992. *"Groundwater Hydrology Report."* Attachment 3 of *Remedial Action Plan and Site Design for Stabilization of the Inactive Uranium Mill Tailings Site at Gunnison, Colorado.* Final. UMTRA-DOE/AL-050508.0000. [Albuquerque, New Mexico: U.S. Department of Energy, UMTRA Project Office]. TIC: 250151.

104736 DOE (U.S. Department of Energy) 1994. *Radiological Control Manual.* MSS/DOE/RP/001, Rev. 1. Washington, D.C.: U.S. Department of Energy. ACC: MOL.19950130.0075.

124789 DOE (U.S. Department of Energy) 1995. *Applications of Natural Analogue Studies to Yucca Mountain as a Potential High Level Radioactive Waste Repository.* DOE/YMSCO-002. Washington, D.C.: U.S. Department of Energy, Office of Civilian Radioactive Waste Management. ACC: MOL.19980928.0280.

154693 DOE (U.S. Department of Energy) 1996. *Final Programmatic Environmental Impact Statement for the Uranium Mill Tailings Remedial Action Ground Water Project.* DOE/EIS-0198. Two volumes. Grand Junction, Colorado: U.S. Department of Energy, Grand Junction Project Office. TIC: 249817.

100548 DOE (U.S. Department of Energy) 1998. *Introduction and Site Characteristics.* Volume 1 of *Viability Assessment of a Repository at Yucca Mountain.* DOE/RW-0508. Washington, D.C.: U.S. Department of Energy, Office of Civilian Radioactive Waste Management. ACC: MOL.19981007.0028.

101779 DOE (U.S. Department of Energy) 1998. *Viability Assessment of a Repository at Yucca Mountain.* DOE/RW-0508. Overview and five volumes. Washington, D.C.: U.S. Department of Energy, Office of Civilian Radioactive Waste Management. ACC: MOL.19981007.0027; MOL.19981007.0028; MOL.19981007.0029; MOL.19981007.0030; MOL.19981007.0031; MOL.19981007.0032.

154687 DOE (U.S. Department of Energy) 1999. *Final Site Observational Work Plan for the UMTRA Project New Rifle Site.* GJO-99-112-TAR, Rev. 1. Grand Junction, Colorado: U.S. Department of Energy, Grand Junction Office. TIC: 249902.

157603 DOE (U.S. Department of Energy) 2000. "UMTRA Ground Water Project Sites." Grand Junction, [Colorado]: U.S. Department of Energy, Grand Junction Office.

Accessed February 13, 2002. TIC: 251850.
http://www.doegjpo.com/ugw/sites/sites.htm

149540 DOE (U.S. Department of Energy) 2000. *Quality Assurance Requirements and Description*. DOE/RW-0333P, Rev. 10. Washington, D.C.: U.S. Department of Energy, Office of Civilian Radioactive Waste Management. ACC: MOL.20000427.0422.

156666 DOE (U.S. Department of Energy) 2001. *Final Site Observational Work Plan for the UMTRA Project Gunnison Site*. Document Number U0058601, Volumes 1 and 2. Grand Junction, Colorado: U.S. Department of Energy, Grand Junction Office. On Order Library Tracking Number-251120

153849 DOE (U.S. Department of Energy) 2001. *Yucca Mountain Science and Engineering Report*. DOE/RW-0539. [Washington, D.C.]: U.S. Department of Energy, Office of Civilian Radioactive Waste Management. ACC: MOL.20010524.0272.

156446 Drellack, S.L., Jr. and Thompson, P.H. 1990. *Selected Stratigraphic Data for Drill Holes in LANL Use Areas of Yucca Flat, NTS*. DOE/NV/10322-39. Las Vegas, Nevada: U.S. Department of Energy, Nevada Operations Office. TIC: 205994.

156447 Drury, M.J. 1987. "Thermal-Diffusivity of Some Crystalline Rocks." *Geothermics, 16*, (2), 105-115. New York, New York: Pergamon Press. TIC: 251764

156402 Dunnivant, F.M.; Newman, M.E.; Bishop, C.W.; Burgess, D.; Giles, J.R.; Higgs, B.D.; Hubbell, J.M.; Neher, E.; Norrell, G.T.; Pfiefer, M.C.; Porro, I.; Starr, R.C.; and Wylie, A.H. 1998. "Water and Radioactive Tracer Flow in a Heterogeneous Field-Scale System." *Ground Water, 36*, (6), 949–958. Westerville, Ohio: Ground Water Publishing Company. TIC: 250984.

157493 Eckel, E.B. 1970. *The Alaska Earthquake, March 27, 1964: Lessons and Conclusions*. Geological Survey Professional Paper 546. Washington, D.C.: U.S. Government Printing Office. TIC: 251802.

101069 Eckerman, K.F.; Wolbarst, A.B.; and Richardson, A.C.B. 1988. *Limiting Values of Radionuclide Intake and Air Concentration and Dose Conversion Factors for Inhalation, Submersion, and Ingestion*. EPA 520/1-88-020. Federal Guidance Report No. 11. Washington, D.C.: U.S. Environmental Protection Agency. ACC: MOL.20010726.0072.

154602 Elders, W.A. 1982. "Determination of Fracture History in Geothermal Reservoirs Through Study of Minerals." *Fractures in Geothermal Reservoirs*. Special Report No. 12. Pages 62-66. Davis, California: Geothermal Resources Council. TIC: 249737.

154632 Elders, W.A. 1987. "A Natural Analogue for Near-Field Behaviour in a High Level Radioactive Waste Repository in Salt: The Salton Sea Geothermal Field, California, USA." *Natural Analogues in Radioactive Waste Disposal, Proceedings, Symposium*

held in Brussels, Belgium, 28-30 April 1987. Côme, B. and Chapman, N.A., eds. EUR 11037 EN. Pages 342-353. Norwell, Massachusetts: Graham & Trotman. TIC: 247254.

157502 Elders, W.A. and Cohen, L.H. 1983. *The Salton Sea Geothermal Field, California, as a Near-Field Natural Analog of a Radioactive Waste Repository in Salt.* BMI/ONWI-513. Columbus, Ohio: Battelle Memorial Institute, Office of Nuclear Waste Isolation. TIC: 251848

100145 Fabryka-Martin, J.T.; Wolfsberg, A.V.; Dixon, P.R.; Levy, S.S.; Musgrave, J.A.; and Turin, H.J. 1997. *Summary Report of Chlorine-36 Studies: Sampling, Analysis, and Simulation of Chlorine-36 in the Exploratory Studies Facility.* LA-13352-MS. Los Alamos, New Mexico: Los Alamos National Laboratory. ACC: MOL.19980812.0254.

156668 Fetter, C.W. 2001. *Applied Hydrogeology.* 4th Edition. Upper Saddle River, New Jersey: Prentice Hall. TIC: 251142.

105591 Finch, R.J. and Ewing, R.C. 1991. "Alteration of Natural UO2 Under Oxidizing Conditions from Shinkolobwe, Katanga, Zaire: A Natural Analogue for the Corrosion of Spent Fuel." *Radiochimica Acta, 52/53*, 395-401. München, Germany: R. Oldenbourg Verlag. TIC: 237035.

127908 Finch, R.J. and Ewing, R.C. 1992. "Alteration of Natural Uranyl Oxide Hydrates in Si-Rich Groundwaters: Implications for Uranium Solubility." *Scientific Basis for Nuclear Waste Management XV, Symposium held November 4-7, 1991, Strasbourg, France.* Sombret, C.G., ed. *257*, 465-472. Pittsburgh, Pennsylvania: Materials Research Society. TIC: 204618.

113030 Finch, R.J. and Ewing, R.C. 1992. "The Corrosion of Uraninite Under Oxidizing Conditions." *Journal of Nuclear Materials, 190*, 133-156. Amsterdam, The Netherlands: Elsevier Science Publishers. TIC: 246369.

104367 Finsterle, S. 1999. *ITOUGH2 User's Guide.* LBNL-40040. Berkeley, California: Lawrence Berkeley National Laboratory. TIC: 243018.

156815 Flexser, S. 1991. "Hydrothermal Alteration and Past and Present Thermal Regimes in the Western Moat of Long Valley Caldera." *Journal of Volcanology and Geothermal Research, 48*, 303-318. Amsterdam, [The Netherlands]: Elsevier. TIC: 251279.

156351 Flint, A.L.; Flint, L.E.; Bodvarsson, G.S.; Kwicklis, E.M.; and Fabryka-Martin, J. 2001. "Evolution of the Conceptual Model of Unsaturated Zone Hydrology at Yucca Mountain, Nevada." *Journal of Hydrology, 247*, (2001), 1-30. [New York, New York]: Elsevier. TIC: 250932.

157411 Flint, A.L.; Flint, L.E.; Kwicklis, E.M.; Fabryka-Martin, J.T.; and Bodvarsson, G.S. 2002. "Estimating Recharge at Yucca Mountain, Nevada, USA: Comparison of

Methods." *Hydrogeology Journal, 10,* (1), 180-240. Berlin, Germany: Springer-Verlag. TIC: 251765.

156355 Forster, C.B.; Caine, J.S.; Schulz, S.; and Nielson, D.L. 1997. "Fault Zone Architecture and Fluid Flow: An Example from Dixie Valley, Nevada." *Proceedings, Twenty-Second Workshop on Geothermal Reservoir Engineering, January 27-29, 1997. Workshop Report SGP-TR-155*, Pages 123-130. Stanford, California: Stanford University. TIC: 249200.

156245 Fournier, R.O. 1989. "Geochemistry and Dynamics of the Yellowstone National Park Hydrothermal System." *Annual Review of Earth and Planetary Sciences, 17,* 13-53. [Palo Alto, California: Annual Reviews]. TIC: 250818.

105419 Fournier, R.O. 1991. "Water Geothermometers Applied to Geothermal Energy." *Application of Geochemistry in Geothermal Reservoir Development.* D'Amore, F., ed. Rome, Italy: UNITAR/UNDP Centre on Small Energy Resources. Copyright Requested Library Tracking Number-251141

154614 Fournier, R.O. [1985]. "Self-Sealing and Brecciation Resulting from Quartz Deposition Within Hydrothermal Systems." *Water-Rock Interaction, [a Collection of Papers Presented at the] Fourth International Symposium on Water-Rock Interaction [(W.R.I.), Organized by the Sub-Group on Water-Rock Interaction, a Part of the Commission on Hydrogeochemistry (I.A.G.C.)], held in Misasa, Japan, on August 29-September 8, 1983.* Pages 137-140. [Amsterdam, The Netherlands: Elsevier]. TIC: 249755.

154527 Fournier, R.O.; Pisto, L.M.; Howell, B.B.; and Hutchinson, R.A. 1993. "Taming a Wild Geothermal Research Well in Yellowstone National Park." *Geothermal Resources Council Transactions, 17,* 33-36. Davis, California: Geothermal Resources Council. TIC: 249701.

156247 Fournier, R.O.; Thompson, J.M.; and Hutchinson, R.A. 1992. "The Geochemistry of Hot Spring Waters at Norris Geyser Basin, Yellowstone National Park, USA." *Water-Rock Interaction, Proceedings of the 7th International Symposium on Water-Rock Interaction – WRI-7, Park City, Utah, 13-18 July 1992.* Kharaka, Y.K. and Maest, A.S., eds. 2, 1289-1292. Brookfield, Vermont: A.A. Balkema. TIC: 208527.

156246 Fournier, R.O.; Thompson, J.M.; Cunningham, C.G.; and Huchinson, R.A. 1991. "Conditions Leading to a Recent Small Hydrothermal Explosion at Yellowstone National Park." *Geological Society of America Bulletin, 103,* (8), 1114-1120. Boulder, Colorado: Geological Society of America. TIC: 250862.

156817 Fournier, R.O.; White, D.E.; and Truesdell, A.H. 1976. "Convective Heat Flow in Yellowstone National Park." *Proceedings of the Second United Nations Symposium on the Development and Use of Geothermal Resources, San Francisco, California, 20-29, May 1975. 1,* 731-739. Washington, D.C.: U.S. Government Printing Office. TIC: 251430.

127326 Francis, N.D. 1997. "The Base-Case Thermal Properties for TSPA-VA Modeling." Memorandum from N.D. Francis (SNL) to Distribution, April 16, 1997. ACC: MOL.19980518.0229.

101173 Freeze, R.A. and Cherry, J.A. 1979. *Groundwater.* Englewood Cliffs, New Jersey: Prentice-Hall. TIC: 217571.

100575 Fridrich, C.J.; Dudley, W.W., Jr.; and Stuckless, J.S. 1994. "Hydrogeologic Analysis of the Saturated-Zone Ground-Water System, Under Yucca Mountain, Nevada." *Journal of Hydrology, 154*, 133-168. Amsterdam, The Netherlands: Elsevier. TIC: 224606.

156602 Garger, E.K.; Hoffman, F.O.; and Miller, C.W. 1996. "Model Testing Using Chernobyl Data: III. Atmospheric Resuspension of Radionuclides in Ukrainian Regions Impacted by Chernobyl Fallout." *Health Physics, 70*, (1), 18-24. [New York, New York: Pergamon]. TIC: 251064.

151483 Garger, E.K.; Hoffman, F.O.; Thiessen, K.M.; Galeriu, D.; Kryshev, A.I.; Lev, T.; Miller, C.W.; Nair, S.K.; Talerko, N.; and Watkins, B. 1999. "Test of Existing Mathematical Models for Atmospheric Resuspension of Radionuclides." *Journal of Environmental Radioactivity, 42*, ([2-3]), 157-175. [London, England]: Elsevier Science. TIC: 248525.

157542 Gauthier-Lafaye, F. 1996. "Introduction to the Oklo problematic." *OKLO Working Group, Proceedings of the Fourth Joint EC-CEA Progress and Final Meeting held in Saclay, France, on 22 and 23 June 1995, pp. 5-16.* Blanc, P.L. and von Maravic, H., eds. *Nuclear Science and Technology Series. EUR 16704 EN*, Brussels, Belgium: Commission of the European Communities. Copyright Requested Library Tracking Number-251757

157499 Gauthier-Lafaye, F.; Ledoux, E.; Smellie, J.; Louvat, D.; Michaud, V.; Pérez del Villar, L.; Oversby, V.; and Bruno, J. 2000. *OKLO Natural Analogue Phase II, Behavior of Nuclear Reaction Products in a Natural Environment.* EUR 19139 EN. Luxembourg, Luxembourg: Commission of the European Communities. TIC: 251886

156338 Giggenbach, W.F. 1997. "The Origin and Evolution of Fluids in Magmatic—Hydrothermal Systems." Chapter 15 of *Geochemistry of Hydrothermal Ore Deposits.* 3rd Edition. Barnes, H.L., ed. New York, New York: John Wiley & Sons. TIC: 250951.

157516 Gill, D. 2001. "The Art and Archaeology of Attica." [Swansea, Wales]: David Gill. Accessed January 30, 2002. TIC: 251750. http://www.davidgill.co.uk/attica/thorikos947.htm

156812 Goff, F. and Gardner, J.N. 1994. "Evolution of a Mineralized Geothermal System, Valles Caldera, New Mexico." *Economic Geology, 89*, 1803-1832. [El Paso, Texas: Economic Geology Publishing Company]. TIC: 251278.

156808 Goff, F.; Gardner, J.N.; Hulen, J.B.; Nielson, D.L.; Charles, R.; WoldeGabriel, G.; Vuataz, F-D.; Musgrave J.A.; Shevenell, L.; and Kennedy B.M. 1992. "The Valles Caldera Hydrothermal System, Past and Present, New Mexico, USA." *Scientific Drilling, 3*, 181-204. [New York, New York]: Springer-Verlag. TIC: 251277.

157422 Golany, G.S. 1983. *Earth-Sheltered Habitat, History, Architecture and Urban Design*. New York, New York: Van Nostrand Reinhold. TIC: 251577.

157423 Golany, G.S. 1989. *Urban Underground Space Design in China, Vernacular and Modern Practice*. Newark, [New Jersey]: University of Delaware Press. TIC: 251579.

156820 Goldman, M.; Catlin, R.J.; and Anspaugh, L. 1987. *Health and Environmental Consequences of the Chernobyl Nuclear Power Plant Accident*. DOE/ER-0332. Washington, D.C.: U.S. Department of Energy. TIC: 251267.

119228 Grambow, B.; Jercinovic, M.J.; Ewing, R.C.; and Byers, C.D. 1986. "Weathered Basalt Glass: A Natural Analogue for the Effects of Reaction Progress on Nuclear Waste Glass Alteration." *Scientific Basis for Nuclear Waste Management IX, Symposium held September 9-11, 1985, Stockholm, Sweden*. Werme, L.O., ed. *50*, 263-272. Pittsburgh, Pennsylvania: Materials Research Society. TIC: 203664.

156218 Grand, P.M. 1967. *Prehistoric Art, Paleolithic Painting and Sculpture*. Greenwich, Connecticut: New York Graphic Society. TIC: 250804.

154663 Grindley, G.W. 1965. *The Geology, Structure, and Exploitation of the Wairakei Geothermal Field, Taupo New Zealand*. Bulletin n.s. 75. Wellington, New Zealand: New Zealand Geological Survey, Department of Scientific and Industrial Research. TIC: 249790.

154531 Grindley, G.W. and Browne, P.R.L. 1976. "Structural and Hydrological Factors Controlling the Permeabilities of Some Hot-Water Geothermal Fields." *Proceedings of the Second United Nations Symposium on the Development and Use of Geothermal Resources, San Francisco, California, USA, 20-29 May 1975. 1.* 377-386. Washington, D.C.: U.S. Government Printing Office. TIC: 249789.

107832 Grossenbacher, K. and Faybishenko, B. 1997. *Spacing of Thermally Induced Columnar Joints in Basalt: Variation with Depth*. Berkeley, California: Lawrence Berkeley National Laboratory, Earth Sciences Division. TIC: 247646.

107835 Gudzenko, V. 1992. "Some Problems of the Radionuclides Migration Research." *Third Research Co-Ordination Meeting on Nuclear Techniques in the Study of Pollutant Transport in the Environment: Interaction of Solutes with Geological Media (Methodological Aspects), Vienna, Austria, 22-25 June 1992*. Vienna, Austria: International Atomic Energy Agency. TIC: 247334.

107834 Gudzenko, V.V.; Klimchuk, A.B.; Yablokova, N.L.; Gudzenko, G.I.; and Golikova, T.A. 1991. *Osushchestvit' Radiogidrogeologicheskie Obsledovanie Tekhnogennykh*

Podzemnykh Polosteig. Kieva s Tsel'yu Otsenki Skorosti Proniknoveniya Radionuklidov v Podzemnuyu Gidrosferu (To Provide Radiohydrogeological Observations in Underground Adits of the City of Kiev for the Purpose of Evaluating the Velocity of Radionuclide Migration in the Groundwater System). Kiev, Ukraine: Institute of Geological Sciences of the Ukrainian National Academy of Sciences. ACC: MOL.20000609.0003.

125020 Gudzenko, V.V.; Shestopalov, V.M.; and Sobotovich, E.V. 1990. "The Isotopic Studies of Subsurface Water Protection from Radioactive Pollution in the Areas of Nuclear Power Plant Siting." *The International Journal of Radiation Applications and Instrumentation. Part E: Nuclear Geophysics, 4,* (1), 119-124. Oxford, England: Pergamon Press. TIC: 247327.

156310 Gunderson, R.; Ganefianto, N.; Riedel, K.; Sirad-Azwar, L.; and Suleiman, S. 2000. "Exploration Results in the Sarulla Block, North Sumatra, Indonesia." *Proceedings of the World Geothermal Congress 2000, Kyushu - Tohoku, Japan, May 28 - June 10, 2000.* Iglesias, E.; Blackwell, D.; Hunt, T.; Lund, J.; and Tamanyu, S.; eds. Pages 1183-1188. Auckland, New Zealand: International Geothermal Association. TIC: 250933.

156361 Gunderson, R.P.; Dobson, P.F.; Sharp, W.D.; Pudjianto, R.; and Hasibuan, A. 1995. "Geology and Thermal Features of the Sarulla Contract Area, North Sumatra, Indonesia." *Proceedings of the World Geothermal Congress 1995, Florence, Italy, May 18-31, 1995.* Barbier, E.; Frye, G.; Iglesias, E.; and Pálmason, G.; eds. *2,* 687-692. Auckland, New Zealand: International Geothermal Association. TIC: 250774.

157470 Gupalo, T.A. 1999. *Development of Quantitative Criteria for Suitability of Rock Mass for Safe Long-Term Storage of Waste from Weapon Plutonium Production, Illustrated by Krasnoyarsk Mining Chemical Combine, Annual Report for the Second Year (01.10.98 -30.09.99).* Project #307B-97. Moscow, Russia: All-Russian Research and Design Institute of Production Engineering (VNIPIPT). Copyright Requested Library Tracking Number-251898

157471 Gupalo, T.A. 2001. *Development of Quantitative Criteria for Suitability of Rock Mass for Safe Long-Term Storage of Waste from Weapons-Grade Plutonium Production, Illustrated by Krasnoyarsk Mining Chemical Combine, Summary Technical Report (01.10.1997 -28.02.2001). Project #307B-97.* Moscow, Russia: All-Russian Research and Design Institute of Production Engineering (VNIPIPT). On Order Library Tracking Number-251899

105175 Haar, L.; Gallagher, J.S.; and Kell, G.S. 1984. *NBS/NRC Steam Tables: Thermodynamic and Transport Properties and Computer Programs for Vapor and Liquid States of Water in SI Units.* New York, New York: Hemisphere Publishing Corporation. TIC: 241793.

100350 Hardin, E.L. 1998. *Near-Field/Altered-Zone Models Report.* UCRL-ID-129179 DR. Livermore, California: Lawrence Livermore National Laboratory. ACC: MOL.19980504.0577.

150043 Hardin, E.L. and Chesnut, D.A. 1997. *Synthesis Report on Thermally Driven Coupled Processes*. UCRL-ID-128495. Livermore, California: Lawrence Livermore National Laboratory. TIC: 234838.

105967 Hay, R.L. 1978. "Geologic Occurrence of Zeolites." *Natural Zeolites, Occurrence, Properties, Use, A Selection of Papers Presented at Zeolite, 76, an International Conference on the Occurrence, Properties, and Utilization of Natural Zeolites, Tucson, Arizona, June 1976*. Sand, L.B. and Mumpton, F.A., eds. Pages 135-143. New York, New York: Pergamon Press. TIC: 206755.

157478 Heath, M.J. 1995. *Rock Matrix Diffusion as a Mechanism for Radionuclide Retardation: Natural Radioelement Migration in Relation to the Microfractography and Petrophysics of Fractured Crystalline Rock, (Report on Phase 1, March 1991 – February 1993)*. EUR 15977 EN. Luxembourg, Luxembourg: Commission of the European Communities. TIC: 251887.

156315 Hedenquist, J.W. 1991. "Boiling and Dilution in the Shallow Portion of the Waiotapu Geothermal System, New Zealand." *Geochimica et Cosmochimica Acta, 55*, (10), 2753-2765. New York, New York: Pergamon Pess. TIC: 250973.

156248 Hildreth, W.; Christiansen, R.L.; and O'Neil, J.R. 1984. "Catastrophic Isotopic Modification of Rhyolitic Magma at Times of Caldera Subsidence, Yellowstone Plateau Volcanic Field." *Journal of Geophysical Research, 89*, (B10), 8339-8369. [Washington, D.C.]: American Geophysical Union. TIC: 250819.

156616 Hoffman, F.O.; Thiessen, K.M.; and Watkins, B. 1996. "Opportunities for the Testing of Environmental Transport Models Using Data Obtained Following the Chernobyl Accident." *Health Physics, 70*, (1), 5-7. [New York, New York: Pergamon]. TIC: 251067.

125081 Hofmann, B.A. 1989. "Geochemical Analogue Study in the Krunkelbach Mine, Menzenschwand, Southern Germany: Geology and Water-Rock Interaction." *Scientific Basis for Nuclear Waste Management XII, Symposium held October 10-13, 1988, Berlin, Germany*. Lutze, W. and Ewing, R.C., eds. *127*, 921-926. Pittsburgh, Pennsylvania: Materials Research Society. TIC: 203660.

106045 Honda, S. and Muffler, L.J.P. 1970. "Hydrothermal Alteration in Core from Research Drill Hole Y-1, Upper Geyser Basin, Yellowstone National Park, Wyoming." *American Mineralogist, 55*, 1714-1737. Washington, D.C.: Mineralogical Society of America. TIC: 219076.

156362 Horne, R.N. 1982. "Geothermal Reinjection Experience in Japan." *Journal of Petroleum Technology, [34]*, 495-503. [Dallas, Texas]: Society of Petroleum Engineers of AIME. TIC: 250934.

157412 Hubbell, J.M. 1993. *Perched Water Monitoring in the Subsurface Disposal Area of the Radioactive Waste Disposal Complex, FY-93*. EDF Serial Number ER&WM-

EDF-002293. Idaho Falls, Idaho: EG&G Idaho. On Order Library Tracking Number-251839

157413 Hubbell, J.M. 1995. *Perched Water Monitoring in the Subsurface Disposal Area of the Radioactive Waste Management Complex, Idaho, FY-94.* EDF Serial Number INEL-95/14. Idaho Falls, Idaho: EG&G Idaho. On Order Library Tracking Number-251840

154600 Hulen, J.B. and Lutz, S.J. 1999. "Altered Volcanic Rocks as Hydrologic Seals on the Geothermal System of Medicine Lake Volcano, California." *Geothermal Resources Council Bulletin, 28,* (7), 217-222. Davis, California: Geothermal Resources Council. TIC: 249735.

156813 Hulen, J.B. and Nielson, D.L. 1986. "Hydrothermal Alteration in the Baca Geothermal System, Redondo Dome, Valles Caldera, New Mexico." *Journal of Geophysical Research, 91,* (B2), 1867-1886. [Washington, D.C.]: American Geophysical Union. TIC: 251351.

157491 Humphrey, T.G. and Tingey, F.H. 1978. *The Subsurface Migration of Radionuclides at the Radioactive Waste Management Complex, 1976-1977.* TREE 1171. [Idaho Falls], Idaho: U.S. Department of Energy, Idaho Operations Office. TIC: 251849.

156750 IAEA (International Atomic Energy Agency) 1991. *The International Chernobyl Project, Assessment of Radiological Consequences and Evaluation of Protective Measures, Summary Brochure.* Vienna, Austria: International Atomic Energy Agency. TIC: 251269.

157485 IAEA (International Atomic Energy Agency) 1999. *Use of Natural Analogs to Support Radionuclide Transport Models for Deep Geological Repositories for Long Lived Radioactive Wastes.* IAEA-TECDOC-1109. Vienna, Austria: International Atomic Energy Agency. On Order Library Tracking Number-251889

155188 IAEA (International Atomic Energy Agency) 2001. *An International Peer Review of the Biosphere Modelling Programme of the US Department of Energy's Yucca Mountain Site Characterization Project, Report of the IAEA International Review Team.* Vienna, Austria: International Atomic Energy Agency. TIC: 250092.

156448 IFC (International Formulation Committee) 1967. *The 1967 IFC Formulation for Industrial Use, A Formulation of the Thermodynamic Properties of Ordinary Water Substance.* Düsseldorf, [Germany]: International Formulation Committee of the Sixth International Conference on the Properties of Steam. TIC: 224838.

156430 INEL (Idaho National Engineering Laboratory) 1995. *A Comprehensive Inventory of Radiological and Nonradiological Contaminants in Waste Buried or Projected to be Buried in the Subsurface Disposal Area of the INEL RWMC During the Years, 1984–2003.* INEL/95-0135, Vol. 1. Idaho Falls, Idaho: Idaho National Engineering Laboratory, Lockheed Idaho Technologies Company. TIC: 251896.

137537 Ingebritsen, S.E. and Sorey, M.L. 1988. "Vapor-Dominated Zones Within Hydrothermal Systems: Evolution and Natural State." *Journal of Geophysical Research, 93*, (B11), 13635-13655. Washington, D.C.: American Geophysical Union. TIC: 247149.

156617 Isaksson, M. and Erlandsson, B. 1998. "Models for the Vertical Migration of {superscript 137}Cs in the Ground — A Field Study." *Journal of Environmental Radioactivity, 41*, (2), 163-182. [New York, New York]: Elsevier. TIC: 251068.

156345 Itoi, R.; Fukuda, M.; Jinno, K.; Hirowatari, K.; Shinohara, N.; and Tomita, T. 1989. "Long-Term, Experiments of Waste Water Injection in the Otake Geothermal Field, Japan." *Geothermics, 18*, (1/2), 153-159. [New York, New York]: Pergamon Press. TIC: 250935.

156346 Itoi, R.; Fukuda, M.; Jinno, K.; Shimizu, S.; and Tomita, T. 1987. "Field Experiments of Injection in the Otake Geothermal Field, Japan." *Geothermal Resources Council Transactions, 11,* 541-545. [Davis, California]: Geothermal Resources Council. TIC: 250936.

156347 Itoi, R.; Maekawa, H.; Fukuda, M.; Jinno, K.; Hatanaka, K.; Yokoyama, T.; and Shimizu, S. 1984. "Experimental Study on the Silica Deposition in a Porous Medium." *Geothermal Resources Council Transactions, 8*, 301-304. [Davis, California]: Geothermal Resources Council. TIC: 250937.

156352 Itoi, R.; Maekawa, H.; Fukuda, M.; Jinno, K.; Hatanaka, K.; Yokoyama, T.; and Shimizu, S. 1986. "Study on Decrease of Reservoir Permeability Due to Deposition of Silica Dissolved in Reinjection Water." *Journal of the Geothermal Research Society of Japan, 8*, (3), 229-241. [Kawasaki, Japan: Do Gakkai]. TIC: 250938.

156818 Ivanov, Y.A. 2001. "Dynamics of Redistribution of Radionuclides in Soils and Plants." *Chornobyl [Chernobyl], The Exclusion Zone, Collected Papers.* Bar'yakhtar, V.G. ed. 47-76. Kyiv, Naukova Dumka: National Academy of Sciences of Ukraine. Cataloging

156864 Jacob, P. and Prohl, G. 1995. *Analysis of Migration Pathways and Dose Distribution.* Final Report for Contracts COSU-CT93-0053 and COSU-CT-94-0091. Brussels, Belgium: European Commission. On Order Library Tracking Number-251878

154296 Jagnow, D.H. 1999. "Geology of Kartchner Caverns State Park, Arizona." *Journal of Cave and Karst Studies, 61*, (2), 49-58. Huntsville, Alabama: National Speleological Society. TIC: 249658.

157489 Jarvis, N.V.; Andreoli, M.A.G.; and Read, D. 1997. "The Steenkampskraal Natural Analogue Study and Nuclear Waste Disposal in South Africa." *Seventh EC Natural Analogue Working Group Meeting, Proceedings of an International Workshop held in Stein am Rhein, Switzerland from 28 to 30 October 1996.* von Maravic, H. and Smellie, J., eds. *EUR 17851 EN*, Pages 9-26. Luxembourg, Luxembourg: Commission of the European Communities. TIC: 247461.

157463 Jen, C-P. and Li, S-H. 2001. "Effects of Hydrodynamic Chromatography on Colloid-Facilitated Migration of Radionuclides in the Fractured Rock." *Waste Management, 21*, ([6]), 499-509. [New York, New York]: Elsevier. TIC: 251645.

156643 Jensen, C.L. and Horne, R.N. 1983. "Matrix Diffusion and its Effect on the Modeling of Tracer Returns from the Fractured Geothermal Reservoir at Wairakei, New Zealand." *Proceedings, Ninth Workshop, Geothermal Reservoir Engineering, December 13-15, 1983, Stanford, California.* Workshop Report SGP-TR-74. Pages 323-329. Stanford, California: Stanford University. TIC: 248733.

157500 Jensen, K.A. and Ewing, R.C. 2001. "The Okélobondo Natural Fission Reactor, Southeast Gabon: Geology, Mineralogy, and Retardation of Nuclear-Reaction products." *Geological Society of America Bulletin, 113*, (1), 32-62. Boulder, Colorado: Geological Society of America. TIC: 251743.

144605 Jercinovic, M.J. and Ewing, R.C. 1987. *Basaltic Glasses from Iceland and the Deep Sea: Natural Analogues to Borosilicate Nuclear Waste-Form Glass.* JSS Project Technical Report 88-01. Stockholm, Sweden: Swedish Nuclear Fuel and Waste Management Company. TIC: 205668.

125289 Jercinovic, M.J.; Ewing, R.C.; and Byers, C.D. 1986. "Alteration Products of Basalt Glass from Frenchman Springs Flow, Wanapum Basalts, Hanford, Washington." *Nuclear Waste Management II, Third Annual Symposium on Ceramics in Nuclear Waste Management, April 28-30, 1986, Chicago, Illinois.* Clark, D.E.; White, W.B.; and Machiels, A.J., eds. Advances in Ceramics Volume 20. Pages 671-679. Westerville, Ohio: American Ceramic Society. TIC: 210019.

157474 Jerden, J.L., Jr. and Sinha, A.K. [2001]. "Natural Attenuation of Uranium in an Oxidizing Rock-Soil-Groundwater System: Coles Hill Uranium Deposit, Virginia." *Abstracts with Programs - Geological Society of America.* Page A364. [Boulder, Colorado]: Geological Society of America. TIC: 251677.

125291 Johnson, A.B., Jr. and Francis, B. 1980. *Durability of Metals from Archaeological Objects, Metal Meteorites, and Native Metals.* PNL-3198. Richland, Washington: Pacific Northwest Laboratory. TIC: 229619.

101630 Johnson, J.W.; Knauss, K.G.; Glassley, W.E.; DeLoach, L.D.; and Tompson, A.F.B 1998. "Reactive Transport Modeling of Plug-Flow Reactor Experiments: Quartz and Tuff Dissolution at 240°C." *Journal of Hydrology, 209*, 81-111. Amsterdam, The Netherlands: Elsevier. TIC: 240986.

156620 Jonsson, B.; Forseth, T.; and Ugedal, O. 1999. "Chernobyl Radioactivity Persists in Fish." *Nature, 400*, ([6743]), 417. [London, England]: Macmillan. TIC: 251069.

157472 Jove Colon, C.F.; Brady, P.V.; Siegel, M.D.; and Lindgren, E.R. 2001. *Historical Case Analysis of Uranium Plume Attenuation.* NUREG/CR-6705. Washington, D.C.: U.S. Nuclear Regulatory Commission. TIC: 251760.

156819 Kashparov, V.A. 2001. "Formuvannya I dinamika radioaktivnogo zabrudnennya navkolishnogo seredovushcha (Formation and dynamics of radioactive contamination of the environment)." *Chornobyl [Chernobyl], The Exclusion Zone, Collected Papers*. Bar'yakhtar, V.G., eds. pp. 11-46. Kyiv, Naukova Dumka: National Academy of Sciences of Ukraine. Cataloging

156622 Kashparov, V.A.; Lundin, S.M.; Kadygrib, A.M.; Protsak, V.P.; Levtchuk, S.E.; Yoschenko, V.I.; Kashpur, V.A.; and Talerko, N.M. 2000. "Forest Fires in the Territory Contaminated as a Result of the Chernobyl Accident: Radioactive Aerosol Resuspension and Exposure of Fire-Fighters." *Journal of Environmental Radioactivity, 51*, 281-298. [New York, New York]: Elsevier. TIC: 251070.

157400 Kashparov, V.A.; Lundin, S.M.; Khomutinin, Yu.V.; Kaminsky, S.P.; Levchuk, S.E.; Protsak, V.P.; Kadygrib, A.M.; Zvarich, S.I.; Yoschenko, V.I.; and Tschiersch, J. 2001. "Soil Contamination with {superscript 90}Sr in the Near Zone of the Chernobyl Accident." *Journal of Environmental Radioactivity, 56*, ([3]), 285-298. [New York, New York]: Elsevier. TIC: 251572.

156623 Kashparov, V.A.; Protsak, V.P.; Ahamdach, N.; Stammose, D.; Peres, J.M.; Yoschenko, V.I.; and Zvarich, S.I. 2000. "Dissolution Kinetics of Particles of Irradiated Chernobyl Nuclear Fuel: Influence of pH and Oxidation State on the Release of Radionuclides in the Contaminated Soil of Chernobyl." *Journal of Nuclear Materials,* 279, ([2-3]), 225-233. [New York, New York]: Elsevier. TIC: 251071.

152663 Keith, T.E.C. and Muffler, L.J.P. 1978. "Minerals Produced During Cooling and Hydrothermal Alteration of Ash Flow Tuff from Yellowstone Drill Hole Y-5." *Journal of Volcanology and Geothermal Research, 3*, 373-402. Amsterdam, The Netherlands: Elsevier. TIC: 219077.

106316 Keith, T.E.C.; White, D.E.; and Beeson, M.H. 1978. *Hydrothermal Alteration and Self-Sealing in Y-7 and Y-8 Drill Holes in Northern Part of Upper Geyser Basin, Yellowstone National Park, Wyoming*. Geological Survey Professional Paper 1054-A. Washington, D.C.: U.S. Government Printing Office. TIC: 219043.

156339 Kennedy, B.M. and Truesdell, A.H. 1996. "The Northwest Geysers High-Temperature Reservoir: Evidence for Active Magmatic Degassing and Implications for the Origin of the Geysers Geothermal Field." *Geothermics, 25*, (3), 365-387. [New York, New York]: Pergamon. TIC: 250939.

103282 Kersting, A.B.; Efurd, D.W.; Finnegan, D.L.; Rokop, D.J.; Smith, D.K.; and Thompson, J.L. 1999. "Migration of Plutonium in Ground Water at the Nevada Test Site." *Nature, 397*, ([6714]), 56-59. [London, England: Macmillan Journals]. TIC: 243597.

125677 Khoury, H.N.; Salameh, E.; Clark, I.D.; Fritz, P.; Milodowski, A.E.; Cave, M.R.; Bajjali, W.; and Alexander, W.R. 1992. "A Natural Analogue of High pH Cement Pore Waters from the Maqarin Area of Northern Jordan. I: Introduction to the Site."

Journal of Geochemical Exploration, 46, (1), 117-132. New York, New York: Elsevier. TIC: 247469.

157444 King, M.S. and Paulsson, B.N.P. 1981. "Acoustic Velocities in a Heated Block of Granite Subjected to Uniaxial Stress." *Geophysical Research Letters, 8*, (7), 669-702. [Washington, D.C.]: American Geophysical Union. TIC: 251659.

113930 Kingston, W.L. and Whitbeck, M. 1991. *Characterization of Colloids Found in Various Groundwater Environments in Central and Southern Nevada.* DOE/NV/10384-36. [Las Vegas, Nevada]: Desert Research Institute, Water Resources Center. ACC: NNA.19930607.0073.

154460 Kneafsey, T.J.; Apps, J.A.; and Sonnenthal, E.L. 2001. "Tuff Dissolution and Precipitation in a Boiling, Unsaturated Fracture." *"Back to the Future – Managing the Back End of the Nuclear Fuel Cycle to Create a More Secure Energy Future," Proceedings of the 9th International High-Level Radioactive Waste Management Conference (IHLRWM), Las Vegas, Nevada, April 29-May 3, 2001.* La Grange Park, Illinois: American Nuclear Society. TIC: 247873.

107839 Knutson, C.F.; McCormick, K.A.; Smith, R.P.; Hackett, W.R.; O'Brien, J.P.; and Crocker, J.C. 1990. *FY 89 Report RWMC Vadose Zone Basalt Characterization.* EGG-WM-8949. Idaho Falls, Idaho: EG&G Idaho. TIC: 245912.

156624 Konoplev, A.V.; Bulgakov, A.A.; Hoffman, F.O.; Kanyar, B.; Lyashenko, G.; Nair, S.K.; Popov, A.; Raskob, W.; Thiessen, K.M.; Watkins, B.; and Zheleznyak, M. 1999. "Validation of Models of Radionuclide Wash-Off from Contaminated Watersheds Using Chernobyl Data." *Journal of Environmental Radioactivity, 42*, 131-141. [New York, New York]: Elsevier. TIC: 251072.

109939 Ku, T.-L.; Luo, S.; Leslie, B.W.; and Hammond, D.E. 1992. "Decay-Series Disequilibria Applied to the Study of Rock-Water Interaction and Geothermal Systems." Chapter 18 of *Uranium-Series Disequilibrium: Applications to Earth, Marine, and Environmental Sciences*. Ivanovich, M. and Harmon, R.S., eds. 2nd Edition. New York, New York: Oxford University Press. TIC: 234680.

157506 Kukhar', V.; Poyarkov, V.; and Kholosha, V. 2000. "Radioactive Waste, Storage and Disposal Sites." Chapter 4 of *The Chornobyl Accident, A Comprehensive Risk Assessment*. Vargo, G.J., ed. Columbus, Ohio: Battelle Press. TIC: 251266.

157604 Kung, S.; Chipera, S.J.; and Reimus, P.W. 2001. "Characteristics of Natural Colloids in the Saturated Alluvium South of Yucca Mountain, Nevada." *Eos, Transactions (Supplement), 82*, (47), F472. Washington, D.C.: American Geophysical Union. TIC: 251883.

100051 Langmuir, D. 1997. *Aqueous Environmental Geochemistry*. Upper Saddle River, New Jersey: Prentice Hall. TIC: 237107.

155885 Larsen, G.; Grönvold, K.; and Thorarinsson, S. 1979. "Volcanic Eruption Through a Geothermal Borehole at Namafjall, Iceland." *Nature, 278*, (5706), 707-710. [London, England]: Macmillan Journals. TIC: 250655.

156626 Lazjuk, G.I.; Kirillova, I.A.; Nikolaev, D.L.; Novikova, I.V.; Formina, Z.N.; and Khmel, R.D. 1995. "Frequency Changes of Inherited Anomalies in the Republic of Belaurs After the Chernobyl Accident." *Radiation Protection Dosimetry, 62*, (1/2), 71-74. [Ashford, Kent, United Kingdom]: Nuclear Technology Publishing. TIC: 251135.

125854 Lebedev, I.A.; Myasoedov, B.F.; Pavlotskaya, F.I.; and Frenkel', V.Ya. 1992. "Plutonium Content in Soils of the European Part of the Country After the Accident at Chernobyl Nuclear Generating Station." *Atomic Energy, A Translation of Atomnaya Energiya, 72*, (6), 515-520. New York, New York: Consultants Bureau. TIC: 247771.

100153 LeCain, G.D. 1997. *Air-Injection Testing in Vertical Boreholes in Welded and Nonwelded Tuff, Yucca Mountain, Nevada.* Water-Resources Investigations Report 96-4262. Denver, Colorado: U.S. Geological Survey. ACC: MOL.19980310.0148.

155241 Lee, J.H. 2001. "Median Lead Concentration in Groundwater Samples Cited in Section 7.3.1.3.4 of the SSPA Report Vol. 1." Memorandum from J.H. Lee (BSC) to P. Pasupathi, June 20, 2001, Proj.06/01.049, with enclosure. ACC: MOL.20010621.0155.

156454 Leroi-Gourhan, A. 1982. "The Archaeology of Lascaux Cave." *Scientific American, 246*, (6), 104-112. New York, New York: Scientific American. TIC: 251232.

101714 Leslie, B.W.; Pearcy, E.C.; and Prikryl, J.D. 1993. "Oxidative Alteration of Uraninite at the Nopal I Deposit, Mexico: Possible Contaminant Transport and Source Term Constraints for the Proposed Repository at Yucca Mountain." *Scientific Basis for Nuclear Waste Management XVI, Symposium held November 30-December 4, 1992, Boston, Massachusetts.* Interrante, C.G. and Pabalan, R.T., eds. *294*, 505-512. Pittsburgh, Pennsylvania: Materials Research Society. TIC: 208880.

101409 Lichtner, P.C. 1996. "Continuum Formulation of Multicomponent-Multiphase Reactive Transport." *Reactive Transport in Porous Media.* Lichtner, P.C.; Steefel, C.I.; and Oelkers, E.H., eds. Reviews in Mineralogy Volume 34. Washington, D.C.: Mineralogical Society of America. TIC: 236866.

156428 Lichtner, P.C. 2000. "Critique of Dual Continuum Formulations of Multicomponent Reactive Transport in Fractured Porous Media." *Dynamics of Fluids in Fractured Rock, [Papers Selected from a Symposium held at Ernest Orlando Lawrence Berkeley National Laboratory on Februrary 10-12, 1999].* Faybishenko, B.; Witherspoon, A.; and Benson, S.M.; eds. Geophysical Monograph 122. 281-298. [Washington, D.C.]: American Geophysical Union. TIC: 250777.

156429 Lichtner, P.C. 2001. *FLOTRAN User's Manual: Two-Phase Nonisothermal Coupled Thermal–Hydrologic–Chemical (THC) Reactive Flow & Transport Code, Version 1.0.* LA-UR-01-2349. Los Alamos, New Mexico: Los Alamos National Laboratory. TIC: 250889.

100771 Lichtner, P.C. and Seth, M. 1996. "Multiphase-Multicomponent Nonisothermal Reactive Transport in Partially Saturated Porous Media." *Proceedings of the 1996 International Conference on Deep Geological Disposal of Radioactive Waste, September 16-19, 1996, Winnipeg, Manitoba, Canada.* Toronto, Ontario, Canada: Canadian Nuclear Society. TIC: 233923.

121006 Lichtner, P.C.; Keating, G.; and Carey, B. 1999. *A Natural Analogue for Thermal-Hydrological-Chemical Coupled Processes at the Proposed Nuclear Waste Repository at Yucca Mountain, Nevada.* LA-13610-MS. Los Alamos, New Mexico: Los Alamos National Laboratory. TIC: 246032.

156627 Likar, A.; Omahen, G.; Lipoglavšek, M.; and Vidmar, T. 2001. "A Theoretical Description of Diffusion and Migration of {superscript 137}Cs in Soil." *Journal of Environmental Radioactivity, 57,* ([3]), 191-201. [New York, New York]:· Elsevier. TIC: 251074.

108896 Linklater, C.M.; Albinsson, Y.; Alexander, W.R.; Casas, I; McKinley, I.G.; and Sellin, P. 1996. "A Natural Analogue of High-pH Cement Pore Waters from the Maqarin Area of Northern Jordan: Comparison of Predicted and Observed Trace-Element Chemistry of Uranium and Selenium." *Journal of Contaminant Hydrology, 21,* (1-4), 59-69. Amsterdam, The Netherlands: Elsevier. TIC: 239819.

154579 Liu, H.H.; Bodvarsson, G.S.; and Pan, L. 2000. "Determination of Particle Transfer in Random Walk Particle Methods for Fractured Porous Media." *Water Resources Research, 36,* (3), 707-713. Washington, D.C.: American Geophysical Union. TIC: 249733.

105729 Liu, H.H.; Doughty, C.; and Bodvarsson, G.S. 1998. "An Active Fracture Model for Unsaturated Flow and Transport in Fractured Rocks." *Water Resources Research, 34,* (10), 2633-2646. Washington, D.C.: American Geophysical Union. TIC: 243012.

157526 Llandudno Museum 1998. "Virtual Tour - Room 3." Llandudno, North Wales: Chardon Trust. Accessed January 31, 2002. http://www.llandudno-tourism.co.uk/museum/english/panel3.htm Copyright Requested Library Tracking Number-251574

157508 Los', I. and Poyarkov, V. 2000. "Individuals, Accident Remediation Personnel and Public Doses." Chapter 6 of *The Chornobyl Accident: A Comprehensive Risk Assessment.* Vargo, G.J., ed. Columbus, Ohio: Battelle Press. TIC: 251266.

125894 Loshchilov, N.A.; Kashparov, V.A.; and Polyakov, V.D. 1991. "Sootnosheniya Transuranovykh Elementov v 'Goryachikh' Chastitsakh, Vypavshikh v Rezultate

Avarii v Blizhnei Zone ChaEs [Relationships of Transuranium Elements in 'Hot' Particles of the Fallout in the Near-Field Zone of the CHNPP]." *Problemy Sel'Skokhozyaistennoi Radiologii [Problems of Agricultural Radiology]*, Pages 45-48. Kiev, Ukraine: Ukrainian Research Institute of Agricultural Radioecology. ACC: MOL.20000609.0007.

156828 Loshchilov, N.A.; Kashparov, V.A.; and Protsak, V.P. 1991. "Vliyanie vtorichnogo pyleperenosa radioaktivnykh veshchestv na zagryasnenie naselennykh punktov v zone Chernobul'skoi avarii (Effect of resuspension of radioactive particles on contamination of settlements within the zone of influence of the Chernobyl accident)." *In: Problemy Sel'skokhozyaistennoi Radiologii (Problems of Agricultural Radiology)*. pp. 61-64. Kiev, Ukraine: Ukrainian Research Institute of Agricultural Radioecology. Copyright Requested Library Tracking Number-251866

156823 Loshchilov, N.A.; Kashparov, V.A.; Yudin, E.B.; Protsak, V.P.; and Ioshchenko, V.I. 1991. "Ingalyatsionnoe postuplenie radionuklidov pri sel'skokhozyaistvennykh rabotakh na territoriyakh, zagryaznennykh v resultate Chernobyl'skoi avarii (Inhalation of radionuclides during agricultural work on territories contaminated by the Chernobyl accident)." *In: Problemy Sel'skokhozyaistennoi Radiologii (Problems of Agricultural Radiology)*. pp. 197-205. Kiev, Ukraine: Ukrainian Research Institute of Agricultural Radioecology. Copyright Requested Library Tracking Number-251866

125914 Louvat, D. and Davies, C., eds. 1998. *Oklo Working Group: Proceedings of the First Joint EC-CEA Workshop on the Oklo-Natural Analogue Phase II Project Held in Sitjes, Spain, from 18 to 20 June 1997*. EUR 18314 EN. Luxembourg, Luxembourg: Office for Official Publications of the European Communities. TIC: 247709.

157900 Lowry, W.E. 2001. *Engineered Barrier Systems Thermal-Hydraulic-Chemical Column Test Report*. TDR-EBS-MD-000018 REV 00. Las Vegas, Nevada: Bechtel SAIC Company. ACC: MOL.20020102.0206.

100465 Luckey, R.R.; Tucci, P.; Faunt, C.C.; Ervin, E.M.; Steinkampf, W.C.; D'Agnese, F.A.; and Patterson, G.L. 1996. *Status of Understanding of the Saturated-Zone Ground-Water Flow System at Yucca Mountain, Nevada, as of 1995*. Water-Resources Investigations Report 96-4077. Denver, Colorado: U.S. Geological Survey. ACC: MOL.19970513.0209.

125923 Lutze, W.; Grambow, B.; Ewing, R.C.; and Jercinovic, M.J. 1987. "The Use of Natural Analogues in the Long-Term Extrapolation of Glass Corrosion Processes." *Natural Analogues in Radioactive Waste Disposal, Symposium held in Brussels on 28-30 April 1987*. Côme, B. and Chapman, N.A., eds. EUR 11037 EN. Pages 142-152. Norwell, Massachusetts: Graham & Trotman. TIC: 247254.

154720 Macdonald, D.D. 1992. "The Point Defect Model for the Passive State." *Journal of the Electrochemical Society, 139*, (12), 3434-3449. Manchester, New Hampshire: Electrochemical Society. TIC: 249804.

156404 Magnuson, S.O. 1995. *Inverse Modeling for Field-Scale Hydrologic and Transport Parameters of Fractured Basalt*. INEL-95/0637. Idaho Falls, Idaho: Idaho National Engineering Laboratory, Lockheed Martin Idaho Technologies. TIC: 250952.

156431 Magnuson, S.O. and Sondrup, A.J. 1998. *Development, Calibration, and Predictive Results of a Simulator for Subsurface Pathway Fate and Transport of Aqueous- and Gaseous-Phase Contaminants in the Subsurface Disposal Area at the Idaho National Engineering and Environmental Laboratory*. INEEL/EXT-97-00609. Idaho Falls, Idaho: Idaho National Engineering Laboratory. TIC: 251678.

126058 Malow, G. and Ewing, R.C. 1981. "Nuclear Waste Glasses and Volcanic Glasses: A Comparison of Their Stabilities." *Scientific Basis for Nuclear Waste Management, Proceedings of the Third International Symposium, Boston, Massachusetts, November 17-20, 1980*. Moore, J.G., ed. *3*, 315-322. New York, New York: Plenum Press. TIC: 204407.

154738 Marcus, P. and Maurice, V. 2000. "Passivity of Metals and Alloys." Chapter 3 of *Corrosion and Environmental Degradation*. Schütze, M., ed. Volume I. Materials Science and Technology Volume 19. New York, New York: Wiley-VCH. TIC: 249831.

156449 Mariner, R.H. and Surdam, R.C. 1970. "Alkalinity and Formation of Zeolites in Saline Alkaline Lakes." *Science, 170*, (3960), 977-980. [Washington, D.C.]: American Association for the Advancement of Science. TIC: 250891.

156811 Mariner, R.H. and Willey, L.M. 1976. "Geochemistry of Thermal Waters in Long Valley, Mono County, California." *Journal of Geophysical Research, 81*, (5), 792-800. [Washington, D.C.]: American Geophysical Union. TIC: 219144.

156249 Marler, G.D. 1964. *Effects of the Hebgen Lake Earthquake of August 17, 1959 on the Hot Springs of the Firehole Geyser Basins, Yellowstone National Park*. Geological Survey Professional Paper 435-Q. Washington, [D.C.]: U.S. Governent Printing Office. TIC: 250923.

151018 Marshall, B.D.; Neymark, L.A.; Paces, J.B.; Peterman, Z.E.; and Whelan, J.F. 2000. "Seepage Flux Conceptualized from Secondary Calcite in Lithophysal Cavities in the Topopah Spring Tuff, Yucca Mountain, Nevada." *SME Annual Meeting, February 28-March 1, 2000, Salt Lake City, Utah*. Preprint 00-12. [Littleton, Colorado]: Society for Mining, Metallurgy, and Exploration. TIC: 248608.

156432 Martian, P. 1995. *UNSAT-H Infiltration Model Calibration at the Subsurface Disposal Area*. INEL-95/0596. Idaho Falls, Idaho: Idaho National Engineering Laboratory, Lockheed Idaho Technologies Company. On Order Library Tracking Number-251842

100058 Matyskiela, W. 1997. "Silica Redistribution and Hydrologic Changes in Heated Fractured Tuff." *Geology, 25*, (12), 1115-1118. Boulder, Colorado: Geological Society of America. TIC: 236809.

156628 Mboulou, M.O.; Hurtgen, C.; Hofkens, K.; and Vandecasteele, C. 1998. "Vertical Distributions in the Kapachi Soil of the Plutonium Isotopes ({superscript 238}Pu, {superscript 239,240}Pu, {superscript 241}Pu), of {superscript 241}Am, and of {superscript 243,244}Cm, Eight Years After the Chernobyl Accident." *Journal of Environmental Radioactivity, 39*, (3), 231-237. [London, England]: Elsevier. TIC: 251075.

157479 McCarthy, J.F. 1996. "Natural Analogue Studies of the Role of Colloids, Natural Organics and Microorganisms on Radionuclide Transport." *Sixth EC Natural Analogue Working Group Meeting, Proceedings of an International Workshop held in Santa Fe, New Mexico, USA on September 12-16, 1994.* von Maravic, H. and Smellie, J., eds. EUR 16761 EN, Pages 195-210. Luxembourg, Luxembourg: Commission of the European Communities. TIC: 225227.

110957 McConnell, K.I. and Lee, M.P. 1994. *Staff Technical Position on Consideration of Fault Displacement Hazards in Geologic Repository Design.* NUREG-1494. Washington, D.C.: U.S. Nuclear Regulatory Commission. TIC: 212360.

157384 McCright, R.D.; Frey, W.F.; and Tardiff, G.E. 1980. "Localized Corrosion of Steels in Geothermal Steam/Brine Mixtures." *Geothermal Resources Council Transactions, 4*, 645-648. [Davis, California]: Geothermal Resources Council. TIC: 251552.

156433 McElroy, D.L. and Hubbell, J.M. 1990. "Vadose Zone Monitoring at the Radioactive Waste Management Complex, Idaho National Engineering Laboratory." *Proceedings of the Topical Meeting on Nuclear Waste Isolation in the Unsaturated Zone, FOCUS '89, September 17-21, 1989, Las Vegas, Nevada.* Pages 359-364. La Grange Park, Illinois: American Nuclear Society. TIC: 212738.

157486 McKinley, I.G. and Alexander, W.R. 1996. "The Uses of Natural Analogue Input in Repository Performance Assessment: An Overview." *Sixth EC Natural Analogue Working Group Meeting, Proceedings of an International Workshop held in Santa Fe, New Mexico, USA on September 12-16, 1994.* von Maravic, H. and Smellie, J., eds. *EUR 16761 EN*, Pages 273-282. Luxembourg, Luxembourg: Commission of the European Communities. TIC: 225227.

126077 McKinley, I.G.; Bath, A.H.; Berner, U.; Cave, M.; and Neal, C. 1988. "Results of the Oman Analogue Study." *Radiochimica Acta, 44/45*, (II), 311-316. München, Germany: R. Oldenbourg Verlag. TIC: 247492.

116222 McKinley, P.W.; Long, M.P.; and Benson, L.V. 1991. *Chemical Analyses of Water from Selected Wells and Springs in the Yucca Mountain Area, Nevada and Southeastern California.* Open-File Report 90-355. Denver, Colorado: U.S. Geological Survey. ACC: NNA.19901031.0004.

101345 Meijer, A. 1987. *Investigations of Natural Geologic and Geochemical Analogs in Relation to a Potential Nuclear Waste Repository at Yucca Mountain, Nevada.* Milestone R398. Draft. Los Alamos, New Mexico: Los Alamos National Laboratory. ACC: NNA.19900112.0350.

156670 Merritt, R.C. 1971. *The Extractive Metallurgy of Uranium.* [Golden, Colorado]: Colorado School of Mines Research Center. TIC: 251119.

106762 Miekeley, N.; Couthinho de Jesus, H.; Porto da Silveira, C.L.; and Degueldre, C. 1992. "Chemical and Physical Characterization of Suspended Particles and Colloids in Waters from the Osamu Utsumi Mine and Morro do Ferro Analogue Study Sites, Poços-de-Caldas, Brazil." *Journal of Geochemical Exploration, 45*, 409-437. Amsterdam, The Netherlands: Elsevier. TIC: 245687.

127199 Miekeley, N.; Coutinho de Jesus, H.; Porto da Silveira, C.L.; and Degueldre, C. 1991. *Chemical and Physical Characterisation of Suspended Particles and Colloids in Waters from the Osamu Utsumi Mine and Morro do Ferro Analogue Study Sites, Pocos de Caldas, Brazil.* SKB Technical Report 90-18. Stockholm, Sweden: Swedish Nuclear Fuel and Waste Management Company. TIC: 206355.

126083 Miekeley, N.; Jesus, H.C.; Silveira, C.L.P.; and Kuechler, I.L. 1989. "Colloid Investigations in the 'Pocos de Caldas' Natural Analogue Project." *Scientific Basis for Nuclear Waste Management XII, Symposium held October 10-13, 1988, Berlin, Germany.* Lutze, W. and Ewing, R.C., eds. *127,* 831-842. Pittsburgh, Pennsylvania: Materials Research Society. TIC: 203660.

156458 Miller, D.M.; Miller, R.J.; Nielson, J.E.; Wilshire, H.G.; Howard, K.A.; and Stone, P. 1991. *Preliminary Geologic Map of the East Mojave National Scenic Area, California.* Open-File Report 91-435. [Menlo Park, California]: U.S. Geological Survey. TIC: 251234.

126089 Miller, W.; Alexander, R.; Chapman, N.; McKinley, I.; and Smellie, J. 1994. *Natural Analogue Studies in the Geological Disposal of Radioactive Wastes.* Studies in Environmental Science 57. New York, New York: Elsevier. TIC: 101822.

156684 Miller, W.; Alexander, R.; Chapman, N.; McKinley, I.; and Smellie, J. 2000. *Geologic Disposal of Radioactive Wastes & Natural Analogues, Lessons from Nature and Archaeology.* Waste Management Series, Volume 2. New York, New York: Pergamon. TIC: 251762

157570 Mills, J.G., Jr.; Saltoun, B.W.; and Vogel, T.A. 1997. "Magma Batches in the Timber Mountain Magmatic System, Southwestern Nevada Volcanic Field, Nevada, USA." *Journal of Volcanology and Geothermal Research, 78,* ([3-4]), 185-208. [Amsterdam, The Netherlands]: Elsevier. TIC: 251831.

156407 Molloy, M.W. [1981]. "Geothermal Reservoir Engineering Code Comparison Project." *Proceedings, Special Panel on Geothermal Model Intercomparison Study, at the Sixth Workshop on Geothermal Reservoir Engineering, December 16-18, 1980.*

Workshop Report SGP-TR-42. Pages 1-26. Stanford, California: Stanford University. TIC: 250930.

100161 Montazer, P. and Wilson, W.E. 1984. *Conceptual Hydrologic Model of Flow in the Unsaturated Zone, Yucca Mountain, Nevada.* Water-Resources Investigations Report 84-4345. Lakewood, Colorado: U.S. Geological Survey. ACC: NNA.19890327.0051.

156320 Moore, D.E.; Hickman, S.; Lockner, D.A.; and Dobson, P.F. 2001. "Hydrothermal Minerals and Microstructures in the Silangkitang Geothermal Field Along the Great Sumatran Fault Zone, Sumatra, Indonesia." *Geological Society of America Bulletin, 113*, (9), 1179-1192. [Boulder, Colorado]: Geological Society of America. TIC: 250940.

156318 Moore, J.N.; Adams, M.C.; and Anderson, A.J. 2000. "The Fluid Inclusion and Mineralogic Record of the Transition from Liquid- to Vapor-Dominated Conditions in the Geysers Geothermal System, California." *Economic Geology, 95*, ([8]), 1719-1737. [Lancaster, Pennsylvania: Economic Geology Publishing]. TIC: 250941.

156319 Moore, J.N.; Lutz, S.J.; Renner, J.L.; McCulloch, J.; and Petty, S. 2000. "Evolution of a Volcanic-Hosted Vapor-Dominated System: Petrologic and Geochemical Data from Corehole T-8, Karaha-Telaga Bodas, Indonesia." *Geothermal Resources Council Transactions, 24*, 259-263. [Davis, California]: Geothermal Resources Council. TIC: 250942.

157466 Mossop, A. and Segall, P. 1999. "Volume Strain Within The Geysers Geothermal Field." *Journal of Geophysical Research, 104*, (B12), Pages 29,113-29,131. [Washington, D.C.]: American Geophysical Union. TIC: 251646.

154621 Mroczek, E.K. 1994. *Review of Silica Deposition Rates at Ohaaki, Rotokawa and Wairakei Geothermal Fields and Comparison of Observed Rates with Predicted Deposition Rates Calculated Using Three Different Kinetic Deposition Models.* Client Report 722305.15. Taupo, New Zealand: Institute of Geological & Nuclear Sciences Limited. TIC: 249770.

156342 Mroczek, E.K. and McDowell, G. 1990. "Silica Scaling Field Experiments." *1990 International Symposium on Geothermal Energy, Transactions, Geothermal Resources Council, 1990 Annual Meeting, 20-24 August, 1990, Kailua-Kona, Hawaii.* Volume 14, Part II. Pages 1619-1625. Davis, California: Geothermal Resources Council. TIC: 246942.

156360 Mroczek, E.K. and Reeves, R.R. 1994. "The Effect of Colloidal Silica on Silica Scaling from Geothermal Fluid." *Proceedings of the 16th New Zealand Geothermal Workshop, 1994.* Soengkono, S. and Lee, K.C., eds. Pages 97-101. Auckland, New Zealand: University of Auckland. TIC: 250972.

156650 Muffler, L.J.P. and White, D.E. 1969. "Active Metamorphism of Upper Cenozoic Sediments in the Salton Sea Geothermal Field and the Salton Trough, Southeastern

California." *Geological Society of America Bulletin, 80,* 157-182. [Boulder, Colorado]: Geological Society of America. TIC: 251080.

156250 Muffler, L.J.P.; White, D.E.; and Truesdell, A.H. 1971. "Hydrothermal Explosion Craters in Yellowstone National Park." *Geological Society of America Bulletin, 82,* (3), 723-740. [Boulder, Colorado]: Geological Society of America. TIC: 250924.

157494 Mumme, I. 1991. "The Effect of Earthquakes on Underground Openings." *Twenty Fifth Newcastle Symposium on "Advances in the Study of the Sydney Basin," 12th to 14th April, 1991, Newcastle, NSW Australia. Publication No. 413,* Pages 75-79. Newcastle, New South Wales, Australia: University of Newcastle, Department of Geology. TIC: 251869.

157487 Murphy, W.M. 2000. "Natural Analogs and Performance Assessment for Geologic Disposal of Nuclear Waste." *Scientific Basis for Nuclear Waste Management XXIII, Symposium held November 29-December 2, 1999, Boston, Massachusetts.* Smith, R.W. and Shoesmith, D.W., eds. *608,* 533-544. Warrendale, Pennsylvania: Materials Research Society. TIC: 249052.

149529 Murphy, W.M. and Codell, R.B. 1999. "Alternate Source Term Models for Yucca Mountain Performance Assessment Based on Natural Analog Data and Secondary Mineral Solubility." *Scientific Basis for Nuclear Waste Management XXII, Symposium held November 30-December 4, 1998, Boston, Massachusetts.* Wronkiewicz, D.J. and Lee, J.H., eds. *556,* 551-558. Warrendale, Pennsylvania: Materials Research Society. TIC: 246426.

156612 Murray, L.E.; Rohrs, D.T.; Rossknecht, T.G.; Aryawijaya, R.; and Pudyastuti, K. 1995. "Resource Evaluation and Development Strategy, Awibengkok Field." *Proceedings of the World Geothermal Congress 1995, Florence, Italy, May 18-31, 1995.* Barbier, E.; Frye, G.; Iglesias, E.; and Pálmason, G.; eds. *[5],* 1525-1529. [Auckland, New Zealand: International Geothermal Association]. TIC: 251065.

156365 Nakata, E.; Chigira, M.; and Watanabe, M. 1998. "Transformation of Diatomite into Porcelanite and Opaline Chert Under the Influence of an Andesite Intrusion in the Miocene Iwaya Formation, Japan." *[Proceedings of the International Symposium on Water-Rock Interaction, WRI-9, Taupo, New Zealand, 30 March-3 April 1998].* Arehart, [G.B.] and Hulston, [J.R.], eds. Pages 333-336. Brookfield, Vermont: A.A. Balkema. TIC: 250944.

100061 National Research Council 1990. *Rethinking High-Level Radioactive Waste Disposal, A Position Statement of the Board on Radioactive Waste Management.* Washington, D.C.: National Academy Press. TIC: 205153.

126123 Naudet, R. 1978. "Etude Parametrique de la Criticite des Reacteurs Naturels." *Les Reacteurs de Fission Naturels, Natural Fission Reactors. Proceedings of a Meeting on the Technical Committee on Natural Fission Reactors, Paris, 19 to 21 December 1977.* Pages 589-599. Vienna, Austria: International Atomic Energy Agency. TIC: 247910.

156632 NEA (Nuclear Energy Agency) 1995. "Chernobyl, Ten Years On, Radiological and Health Impact." Paris, France: Organisation for Economic Co-operation and Development. Accessed December 19, 2001. TIC: 251078. http://www.nea.fr/html/rp/chernobyl/

150092 Nelson, P.H.; Rachiele, R.; Remer, J.S.; and Carlsson, H. 1981. *Water Inflow into Boreholes During the Stripa Heater Experiments.* LBL-12574. Berkeley, California: Lawrence Berkeley Laboratory. TIC: 228851.

156221 Neumayer, E. 1983. *Prehistoric Indian Rock Paintings.* New Dehli, India: Oxford University Press. TIC: 250805.

156434 Newman, M.E. 1996. *Evaluation of the Mobility of Am, Cs, Co, Pu, Sr, and U through INEL Basalts and Interbed Materials: Summary Report of the INEL/Clemson University Laboratory Studies.* WAG7-82, INEL-95/282. Idaho Falls, Idaho: Idaho National Engineering Laboratory, Lockheed Idaho Technologies Company. Copyright Requested Library Tracking Number-251897

154458 Nimmo, J.R.; Perkins, K.S.; Rose, P.E.; Rousseau, J.P.; Orr, B.R.; Twining, B.V.; and Anderson, S.R. 2001. "Kilometer-Scale Rapid Flow in a Fractured-Basalt Unsaturated Zone at the Idaho National Engineering and Environmental Laboratory." *Fractured Rock 2001, An International Conference Addressing Groundwater Flow, Solute Transport, Multiphase Flow, and Remediation in Fractured Rock, March 26-28, 2001, Toronto, Ontario, Canada.* Kueper, B.H.; Novakowski, K.S.; and Reynolds, D.A., eds. Smithville, Ontario, Canada: Smithville Phase IV. TIC: 249909.

117880 Nitao, J.J. 1998. "Thermohydrochemical Alteration of Flow Pathways Above and Below the Repository." Chapter 5.6 of *Near-Field/Altered-Zone Models Report.* Hardin, E.L. UCRL-ID-129179 DR. Livermore, California: Lawrence Livermore National Laboratory. ACC: MOL.19980504.0577.

156637 Norris, R.M. 1999. "Geologic Setting of Mitchell Caverns." *California State Parks Brochure,* (8/99), . xxx, xxx: xxx. Copyright Requested Library Tracking Number-251426

151592 NRC (U.S. Nuclear Regulatory Commission) 1999. "Issue Resolution Status Report Key Technical Issue: Igneous Activity." Rev. 2. [Washington, D.C.]: U.S. Nuclear Regulatory Commission. Accessed September 18, 2000. TIC: 247987. http://www.nrc.gov/NMSS/DWM/ia-rev2.htm

126162 NWTRB (Nuclear Waste Technical Review Board) 1990. *Second Report to the U.S. Congress and the U.S. Secretary of Energy.* Washington, D.C.: Nuclear Waste Technical Review Board. ACC: HQX.19901214.0061.

157447 Nyhan, J.W.; Drennon, B.J.; Abeele, W.V.; Wheeler, M.L.; Purtymun, W.D.; Trujillo, G.; Herrera, W.J.; and Booth, J.W. 1985. "Distribution of Plutonium and Americium Beneath a 33-yr-old Liquid Waste Disposal Site." *Journal of Environmental Quality,*

14, (4), 501-509. Madison, Wisconsin: American Society of Agronomy. TIC: 218692.

154567 O'Sullivan, M.J.; Bullivant, D.P.; Follows, S.E.; and Mannington, W.I. 1998. "Modelling of the Wairakei - Tauhara Geothermal System." *Proceedings of the TOUGH Workshop '98, Berkeley, California, May 4-6, 1998.* Pruess, K., ed. LBNL-41995. Pages 1-6. Berkeley, California: Lawrence Berkeley National Laboratory. TIC: 247159.

156353 O'Sullivan, M.J.; Pruess, K.; and Lippmann, M.J. 2001. "State of the Art of Geothermal Reservoir Simulation." *Geothermics, 30*, ([4]), 395-429. [New York, New York]: Elsevier. TIC: 250945.

100069 Oliver, T. and Root, T. 1997. *Hydrochemical Database for the Yucca Mountain Area, Nye County, Nevada.* Denver, Colorado: U.S. Geological Survey. ACC: MOL.19980302.0367.

100485 Oversby, V.M. 1996. *Criticality in a High Level Waste Repository, A Review of Some Important Factors and an Assessment of the Lessons that can be Learned from the Oklo Reactors.* SKB Technical Report 96-07. Stockholm, Sweden: Swedish Nuclear Fuel and Waste Management Company. TIC: 226156.

155058 Ozment, K. 1999. "Journey to the Copper Age." *National Geographic, 195*, (4), 70-79. Washington, D.C.: National Geographic Society. TIC: 249913.

107408 Paces, J.B.; Neymark, L.A.; Marshall, B.D.; Whelan, J.F.; and Peterman, Z.E. 1998. "Inferences for Yucca Mountain Unsaturated-Zone Hydrology from Secondary Minerals." *High-Level Radioactive Waste Management, Proceedings of the Eighth International Conference, Las Vegas, Nevada, May 11-14, 1998.* Pages 36-39. La Grange Park, Illinois: American Nuclear Society. TIC: 237082.

124806 Papp, Z.; Bolyos, A.; Dezso. Z; and Daroczy, S. 1997. "Direct Determination of 90Sr and 147Pm in Chernobyl Hot Particles Collected in Kiev Using Beta Absorption Method." *Health Physics, 73,* (6), 944-952. Baltimore, Maryland: Williams and Wilkins. TIC: 247152.

126526 Parker, J.C. and van Genuchten, M. Th. 1984. "Determining Transport Parameters from Laboratory and Field Tracer Experiments." *Virginia Agricultural Experiment Station.* Bulletin 84-3. [Blacksburg, Virginia]: Virginia Polytechnic Institute and State University. TIC: 223781.

124812 Payne, T.E.; Edis, R.; and Seo, T. 1992. "Radionuclide Transport by Groundwater Colloids at the Koongarra Uranium Deposit." *Scientific Basis for Nuclear Waste Management XV, Symposium held November 4-7, 1991, Strasbourg, France.* Sombret, C.G., ed. *257,* 481-488. Pittsburgh, Pennsylvania: Materials Research Society. TIC: 204618.

157563 Pearcy, E.C. and Murphy, W.M. 1991. "Geochemical Natural Analogs." Chapter 7 of *Report on Research Activities for Calendar Year 1990.* Patrick, W.C., ed. NUREG/CR-5817. Washington, D.C.: U.S. Nuclear Regulatory Commission. TIC: 208964.

100486 Pearcy, E.C.; Prikryl, J.D.; Murphy, W.M.; and Leslie, B.W. 1994. "Alteration of Uraninite from the Nopal I Deposit, Pena Blanca District, Chihuahua, Mexico, Compared to Degradation of Spent Nuclear Fuel in the Proposed U.S. High-Level Nuclear Waste Repository at Yucca Mountain, Nevada." *Applied Geochemistry, 9,* 713-732. New York, New York: Elsevier Science. TIC: 236934.

156822 Perepelyatnikov, G.P.; Prister, B.S.; and Sobolev, A.S. 1991. "Migratiya radionuklidov v sisteme voda-pochva-rastenie na ugod'yakh oroshaemykh vodoi reki Dnepr posle avarii na ChAES (Migration of radionuclides in the system water-soil-plant on lands irrigated using Dnieper water after the ChNPP accident)." *In: Problemy Sel'skokhozyaistennoi Radiologii (Problems of Agricultural Radiology).* pp. 106-112. Kiev, Ukraine: Ukrainian Research Institute of Agricultural Radioecology. Copyright Requested Library Tracking Number-251866

101053 Perfect, D.L.; Faunt, C.C.; Steinkampf, W.C.; and Turner, A.K. 1995. *Hydrochemical Data Base for the Death Valley Region, California and Nevada.* Open-File Report 94-305. Denver, Colorado: U.S. Geological Survey. ACC: MOL.19940718.0001.

144335 Perry, F.V.; Crowe, B.M.; Valentine, G.A.; and Bowker, L.M., eds. 1998. *Volcanism Studies: Final Report for the Yucca Mountain Project.* LA-13478. Los Alamos, New Mexico: Los Alamos National Laboratory. TIC: 247225.

121957 Peters, R.R.; Klavetter, E.A.; Hall, I.J.; Blair, S.C.; Heller, P.R.; and Gee, G.W. 1984. *Fracture and Matrix Hydrologic Characteristics of Tuffaceous Materials from Yucca Mountain, Nye County, Nevada.* SAND84-1471. Albuquerque, New Mexico: Sandia National Laboratories. ACC: NNA.19900810.0674.

105743 Philip, J.R.; Knight, J.H.; and Waechter, R.T. 1989. "Unsaturated Seepage and Subterranean Holes: Conspectus, and Exclusion Problem for Circular Cylindrical Cavities." *Water Resources Research, 25,* (1), 16-28. Washington, D.C.: American Geophysical Union. TIC: 239117.

110009 Pickett, D.A. and Murphy, W.M. 1999. "Unsaturated Zone Waters from the Nopal I Natural Analog, Chihuahua, Mexico - Implications for Radionuclide Mobility at Yucca Mountain." *Scientific Basis for Nuclear Waste Management XXII, Symposium held November 30-December 4, 1998, Boston, Massachusetts.* Wronkiewicz, D.J. and Lee, J.H., eds. *556,* 809-816. Warrendale, Pennsylvania: Materials Research Society. TIC: 246426.

156638 Pinto, D.G. 1989. *The Archeology of Mitchell Caverns.* California Archeological Reports, No. 25. Sacramento, California: Resource Protection Division, Cultural

Heritage Association, California Dept. of Parks and Recreation. Copyright Requested Library Tracking Number-251647

156159 Polyak, V.J.; McIntosh, W.C.; Güven, N.; and Provencio, P. 1998. "Age and Origin of Carlsbad Cavern and Related Caves from {superscript 40}AR/{superscript 39}AR of Alunite." *Science, 279*, (5358), 1919-1922. Washington, D.C.: American Association for the Advancement of Science. TIC: 250925.

157523 Power, M.S.; Rosidi, D.; and Kaneshiro, J.Y. 1998. "Seismic Vulnerability of Tunnels and Underground Structures Revisited." *North American Tunneling Conference, Newport Beach, California, February 21-28, 1998.* New York, New York: American Institute of Mining, Metallurgical, and Petroleum Engineers. On Order Library Tracking Number-251801

157503 Poyarkov, V. 2000. "Introduction." Chapter 1 of *The Chornobyl Accident, A Comprehensive Risk Assessment.* Vargo, G.J., ed. Columbus, Ohio: Battelle Press. TIC: 251266.

151817 Pratt, H.R.; Hustrulid, W.A.; and Stephenson, D.E. 1978. *Earthquake Damage to Underground Facilities.* DP-1513. Aiken, South Carolina: E.I. du Pont de Nemours and Company, Savannah River Laboratory. TIC: 210276.

156824 Prister, B.S.; Omel'yanenko, N.P.; Perepelyatnikova, L.B.; and Lavrovsky, A.B. 1991. "Vetroerozionnye protsessy i osobennosti sozdaniya optimal'nykh komplekhsnykh reshenii okhrany pochv v zone zagryazneniya radionuklidami (Wind-erosion processes and particularities of the development of optimal, complex measures for soil protection within the zone of radionuclide contamination)." *In: Problemy Sel'skokhozyaistennoi Radiologii (Problems of Agricultural Radiology).* pp. 64-74. Kiev, Ukraine: Ukrainian Research Institute of Agricultural Radioecology. Copyright Requested Library Tracking Number-251866

157548 Prister, B.S.; Perepelyatnikova, L.V.; and Perepelyatnikov, G.P. 1991. "Effectiveness of remediation on the reduction of contamination of agricultural produce in areas contaminated as a result of the ChNPP accident." *In: Problemy Sel'skokhozyaistennoi Radiologii (Problems of Agricultural Radiology).* pp. 141-153. Kiev, Ukraine: Ukrainian Research Institute of Agricultural Radioecology. Copyright Requested Library Tracking Number-251866

100413 Pruess, K. 1991. *TOUGH2—A General-Purpose Numerical Simulator for Multiphase Fluid and Heat Flow.* LBL-29400. Berkeley, California: Lawrence Berkeley Laboratory. ACC: NNA.19940202.0088.

101707 Pruess, K. and Narasimhan, T.N. 1985. "A Practical Method for Modeling Fluid and Heat Flow in Fractured Porous Media." *Society of Petroleum Engineers Journal, 25*, (1), 14-26. Dallas, Texas: Society of Petroleum Engineers. TIC: 221917.

157385 Pye, D.S.; Holligan, D.; Cron, C.J.; and Love, W.W. 1989. "The Use of Beta-C Titanium for Downhole Production Casing in Geothermal Wells." *Geothermics, 18,* (1/2), 259-267. [New York, New York]: Pergamon Press. TIC: 251554.

156640 Quindos, L.S.; Bonet, A.; Diaz-Caneja, N.; Fernandez, P.L.; Gutierrez, I.; Solana, J.R.; Soto, J.; and Villar, E. 1987. "Study of the Environmental Variables Affecting the Natural Preservation of the Altamira Cave Paintings Located at Santillana Del Mar, Spain." *Atmospheric Environment, 21,* (3), 551-560. New York, New York: Pergamon Press. TIC: 251037.

156450 Quinlivan, W.D. and Byers, F.M., Jr. 1977. *Chemical Data and Variation Diagrams of Igneous Rocks from the Timber Mountain-Oasis Valley Caldera Complex, Southern Nevada.* Open File Report 77-724. [Boulder, Colorado]: U.S. Geological Survey. ACC: NNA.19890303.0035.

106634 Ratcliff, C.D.; Geissman, J.W.; Perry, F.V.; Crowe, B.M.; and Zeitler, P.K. 1994. "Paleomagnetic Record of a Geomagnetic Field Reversal from Late Miocene Mafic Intrusions, Southern Nevada." *Science, 266,* 412-416. Washington, D.C.: American Association for the Advancement of Science. TIC: 234818.

156439 Rawson, S.A.; Walton, J.C.; and Baca, R.G. 1991. "Migration of Actinides from a Transuranic Waste Disposal Site in the Vadose Zone." *Radiochimica Acta, 52/53,* 477-486. München, [Germany]: R. Oldenbourg Verlag. TIC: 251669.

157613 Richards, J.I. and Hance, R.J. 1996. "Agricultural Countermeasures." *Chernobyl, IAEA Bulletin, 38,* (3). [Vienna, Austria]: International Atomic Energy Agency. Library Tracking Number-251880

156440 Rightmire, C.T. and Lewis, B.D. 1987. *Geologic Data Collected and Analytical Procedures Used During a Geochemical Investigation of the Unsaturated Zone, Radioactive Waste Management Complex, Idaho National Engineering Laboratory, Idaho.* Open-File Report 87-246. Idaho Falls, Idaho: U.S. Geological Survey. TIC: 251805.

156441 Rightmire, C.T. and Lewis, B.D. 1987. *Hydrogeology and Geochemistry of the Unsaturated Zone, Radioactive Waste Management Complex, Idaho National Engineering Laboratory, Idaho.* U.S. Geological Survey Water-Resources Investigations Report 87-4198. Idaho Falls, Idaho: Radioactive Waste Management Complex, Idaho National Engineering Laboratory. On Order Library Tracking Number-251843

156442 Rightmire, C.T. and Lewis, B.D. 1988. *Influence of the Geochemical Environment on Radionuclide Migration in the Unsaturated Zone, Radioactive Waste Management Complex, Idaho National Engineering Laboratory, Idaho.* U.S. Geological Survey Open-File Report 95-. Idaho Falls, Idaho: Idaho National Engineering Laboratory. On Order Library Tracking Number-251844

101708 Rimstidt, J.D. and Barnes, H.L. 1980. "The Kinetics of Silica–Water Reactions." *Geochimica et Cosmochimica Acta, 44*, 1683-1699. [New York, New York]: Pergamon Press. TIC: 219975.

142190 Rimstidt, J.D.; Newcomb, W.D.; and Shettel, D.L., Jr. 1989. "A Vertical Thermal Gradient Experiment to Simulate Conditions in Vapor Dominated Geothermal Systems, Epithermal Gold Deposits, and High Level Radioactive Repositories in Unsaturated Media." *[Proceedings of the 6th International Symposium on Water-Rock Interaction, WRI-6, Malvern, United Kingdom, 3-8 August 1989].* Miles, D.L., ed. Pages 585-588. Rotterdam, The Netherlands: A.A. Balkema. TIC: 241868.

126287 Rivas, P.; Hernan, P.; Astudillo, J.; Bruno, J.; Carrerra, J.; De la Cruz, B.; Guimera, J.; Gomez, P.; Ivanovich, M.; Marin, C.; Miller, W.; and Perez del Villar, L. 1998. *Nuclear Science and Technology, El Berrocal Project.* EUR 17830 EN. Luxembourg, Luxembourg: Commission of European Communities. TIC: 247318.

100416 Robinson, B.A.; Wolfsberg, A.V.; Viswanathan, H.S.; Bussod, G.Y.; Gable, C.W.; and Meijer, A. 1997. *The Site-Scale Unsaturated Zone Transport Model of Yucca Mountain.* Milestone SP25BM3. Los Alamos, New Mexico: Los Alamos National Laboratory. ACC: MOL.19980203.0570.

157445 Robinson, R.A. 1985. "Summary results and conclusions from the cooperative project at Stripa, between Sweden and the United States during 1977-1980." *Proceedings from the Second NEA/SKB Symposium on the International Stripa Project, Sweden, Stockholm, June 1985.* Washington, D.C.: OECD Nuclear Energy Agency. On Order Library Tracking Number-251879

157386 Robles-Camacho, J. and Armienta, M.A. 2000. "Natural Chromium Contamination of Groundwater at León Valley, México." *Journal of Geochemical Exploration, 68*, ([3]), 167-181. [New York, New York]: Elsevier. TIC: 251555.

154320 Rogers, K.L.; Repenning, C.A.; Luiszer, F.G.; and Benson, R.D. 2000. "Geologic History, Stratigraphy, and Paleontology of SAM Cave, North-Central New Mexico." *New Mexico Geology, 22*, (4), 89-100. Socorro, New Mexico: New Mexico Bureau of Mines and Mineral Resources. TIC: 249818.

157573 Romero, L.; Neretnieks, I.; and Moreno, L. 1992. "Movement of the Redox Front at the Osamu Utsumi Uranium Mine, Pocos de Caldas, Brazil." *Journal of Geochemical Exploration, 45*, (1-3), 471-502. Amsterdam, The Netherlands: Elsevier. TIC: 251833

156341 Rose, P.E.; Benoit, W.R.; and Adams, M.C. 1998. "Tracer Testing at Dixie Valley, Nevada, Using Pyrene Tetrasulfonate, Amino G, and Fluorescein." *Geothermal Resources Council Transactions, 22*, 583-587. Davis, California: Geothermal Resources Council. TIC: 250946.

154862 Rosenberg, N.D.; Gdowski, G.E.; and Knauss, K.G. 2001. "Evaporative Chemical Evolution of Natural Waters at Yucca Mountain, Nevada." *Applied Geochemistry, 16*, ([9-10]), 1231-1240. [New York, New York]: Pergamon. TIC: 249879.

156629 Rosner, G. and Winkler, R. 2001. "Long-Term Variation (1986–1998) of Post-Chernobyl {superscript 90}Sr, {superscript 137}Cs, {superscript 238}Pu and {supercript 239,240}Pu Concentrations in Air, Depositions to Ground, Resuspension Factors and Resuspension Rates in South Germany." *The Science of the Total Environment, 273*, ([1-3]), 11-25. [New York, New York]: Elsevier. TIC: 251076.

102097 Rousseau, J.P.; Kwicklis, E.M.; and Gillies, D.C., eds. 1999. *Hydrogeology of the Unsaturated Zone, North Ramp Area of the Exploratory Studies Facility, Yucca Mountain, Nevada.* Water-Resources Investigations Report 98-4050. Denver, Colorado: U.S. Geological Survey. ACC: MOL.19990419.0335.

156223 Ruspoli, M. 1987. *The Cave of Lascaux, The Final Photographs.* New York, New York: Harry N. Abrams. TIC: 250806.

157316 Salve, R. and Oldenburg, C.M. 2001. "Water Flow Within a Fault in Altered Nonwelded Tuff." *Water Resources Research, 37*, (12), 3043-3056. Washington, D.C.: American Geophysical Union. TIC: 251485.

156848 Salve, R.; Hudson, D.; and Cook, P. 2001. "Investigation of Flow Along a Vertical Fault: Field Techniques." *Eos, Transactions (Supplement), 82*, (47), F382. [Washington, D.C.]: American Geophysical Union. TIC: 251282.

157382 Sánchez-Moral, S.; Soler, V.; Cañaveras, J.C.; Sanz-Rubio, E.; Van Grieken, R.; and Gysels, K. 1999. "Inorganic Deterioration Affecting the Altamira Cave, N Spain: Quantitative Approach to Wall-Corrosion (Solutional Etching) Processes Induced by Visitors." *The Science of the Total Environment, 243/244*, 67-84. [New York, New York]: Elsevier. TIC: 251550.

157465 Sasaki, S. 1998. "Characteristics of Microseismic Events Induced During Hydraulic Fracturing Experiments at the Hijiori Hot Dry Rock Geothermal Energy Site, Yamagata, Japan." *Tectonophysics, 289*, ([1-3]), 171-188. [Amsterdam], The Netherlands: Elsevier. TIC: 251882.

148612 Savino, J.M.; Smith, K.D.; Biasi, G.; Sullivan, T.; and Cline, M. 1999. "Earthquake Ground Motion Effects on Underground Structures/Tunnels." *Eos, Transactions (Supplement), 80*, (17), S10. Washington, D.C.: American Geophysical Union. TIC: 247757.

100075 Sawyer, D.A.; Fleck, R.J.; Lanphere, M.A.; Warren, R.G.; Broxton, D.E.; and Hudson, M.R. 1994. "Episodic Caldera Volcanism in the Miocene Southwestern Nevada Volcanic Field: Revised Stratigraphic Framework, 40Ar/39Ar Geochronology, and Implications for Magmatism and Extension." *Geological Society of America Bulletin, 106*, (10), 1304-1318. Boulder, Colorado: Geological Society of America. TIC: 222523.

156641 Schick, T. 1998. *The Cave of the Warrior, A Fourth Millennium Burial in the Judean Desert*. IAA Reports, No. 5. Jerusalem, Israel: Israel Antiquities Authority. TIC: 251260.

154644 Schiffman, P.; Bird, D.K.; and Elders, W.A. 1985. "Hydrothermal Mineralogy of Calcareous Sandstones from the Colorado River Delta in the Cerro Prieto Geothermal System, Baja California, Mexico." *Mineralogical Magazine, 49*, (Part 3), 435-449. London, England: Mineralogical Society. TIC: 249764.

101156 Scott, R.B.; Spengler, R.W.; Diehl, S.; Lappin, A.R.; and Chornack, M.P. 1983. "Geologic Character of Tuffs in the Unsaturated Zone at Yucca Mountain, Southern Nevada." *Role of the Unsaturated Zone in Radioactive and Hazardous Waste Disposal, May 31-June 4, 1982, Philadelphia, Pennsylvania*. Mercer, J.W.; Rao, P.S.C.; and Marine, I.W., eds. Pages 289-335. Ann Arbor, Michigan: Ann Arbor Science Publishers. TIC: 245124.

157464 Segall, P. and Fitzgerald, S.D. 1998. "A Note on Induced Stress Changes in Hydrocarbon and Geothermal Reservoirs." *Tectonophysics, 289*, ([1-3]), 117-128. [Amsterdam], The Netherlands: Elsevier. TIC: 251894.

157480 Seo, T.; Edis, R.; and Payne, T.E. 1994. "A Study of Colloids in Groundwaters at the Koongarra Uranium Deposit." *Fifth CEC Natural Analogue Working Group Meeting and Alligator Rivers Analogue Project (ARAP) Final Workshop, Proceedings of an International Workshop, held in Toledo, Spain, from 5 to 9 October 1992*. von Maravic, H. and Smellie, J., eds. EUR 15176 EN, Pages 71-76. Luxembourg, Luxembourg: Commission of the European Communities. TIC: 247923.

154505 Sharma, S. and Judd, W.R. 1991. "Underground Opening Damage from Earthquakes." *Engineering Geology, 30*, (3/4), 263-276. Amsterdam, [The Netherlands]: Elsevier. TIC: 226268.

156673 Shea, M. 1984. "Uranium Migration at Some Hydrothermal Veins Near Marysvale, Utah: A Natural Analog for Waste Isolation." *Scientific Basis for Nuclear Waste Management VII, Symposium held November 14-17, 1983, Boston, Massachusetts, U.S.A.* McVay, G.L., ed. *26*, 227-238. New York, New York: Elsevier. TIC: 204393.

156672 Shea, M. and Foland, K.A. 1986. "The Marysvale Natural Analog Study: Preliminary Oxygen Isotope Relations." *Chemical Geology, 55*, 281-295. Amsterdam, The Netherlands: Elsevier. TIC: 251138.

157425 Shepherd, R. 1993. *Ancient mining*. 494 pages. New York, New York: Elsevier. On Order Library Tracking Number-251583

156451 Sheppard, R.A. 1993. "Geology and Diagenetic Mineralogy of the Castle Creek Zeolite Deposit and the Ben-Jel Bentonite Deposit, Chalk Hills Formation, Oreana, Idaho." *Zeo-Trip '93, [An Excursion to Selected Zeolite and Clay Deposits in Southeastern Oregon and Southwestern Idaho], June 26-28, 1993*. [Mumpton, F.A.,

ed]. Pages 1-13. [Brockport, New York: International Committee on Natural Zeolites]. TIC: 251008.

157507 Shestopalov, V. and Poyarkov, V. 2000. "Environmental Contamination." Chapter 5 of *The Chornobyl Accident: A Comprehensive Risk Assessment*. Vargo, G.J., ed. Columbus, Ohio: Battelle Press. TIC: 251266.

107844 Shestopalov, V.M. 1996. *Atlas of Chernobyl Exclusion Zone*. Kiev, Ukraine: [Kartohrafiia]. TIC: 248100.

126508 Silant'ev, A.N.; Shkuratova, I.G.; and Bobovnikova, Ts.I. 1989. "Vertical Soil Migration of Radionuclide Fallout from the Chernobyl' Accident." *Translated from Atomnaya Energiya [Soviet Atomic Energy], 66*, (3), 221-225. New York, New York: Plenum Publishing. TIC: 247772.

157578 Simmons, A.M. 2002. "Scientific Notebooks Referenced in the Natural Analogue Synthesis Report, TDR-NBS-GS-000027 REV00." Interoffice correspondence from A.M. Simmons (BSC) to File, February 14, 2002, with attachments. ACC: MOL.20020311.0230.

157544 Simmons, A.M. 2002. Natural Analogues. Scientific Notebook YMP-LBNL-AMS-NA-1. ACC: MOL.19990927.0459; MOL.20000817.0316; MOL.20010713.0016; MOL.20020204.0265.

157538 Simmons, A.M. 2002. *Scientific Investigation Test Plan for Peña Blanca and Drift Shadow Zone Natural Analog Studies*. SITP-02-NA-001 REV 00. [Berkeley, California]: Lawrence Berkeley National Laboratory. ACC: MOL.20020211.0003.

126511 Simmons, A.M. and Bodvarsson, G.S. 1997. *Building Confidence in Thermohydrologic Models of Yucca Mountain Using Geothermal Analogues*. Milestone SPLE1M4. Berkeley, California: Lawrence Berkeley National Laboratory. ACC: MOL.19970710.0328.

126633 Smellie, J.A.T., ed. 1998. *MAQARIN Natural Analogue Study: Phase III*. SKB Technical Report 98-04. Two volumes. Stockholm, Sweden: Swedish Nuclear Fuel and Waste Management Company. TIC: 244013.

126636 Smellie, J.; Chapman, N.; McKinley, I.; Penna Franca, E.; and Shea, M. 1989. "Testing Safety Assessment Models Using Natural Analogues in High Natural-Series Groundwaters. The Second Year of the Pocos de Caldas Project." *Scientific Basis for Nuclear Waste Management XII, Symposium held October 10-13, 1988, Berlin, Germany*. Lutze, W. and Ewing, R.C., eds. *127*, 863-870. Pittsburgh, Pennsylvania: Materials Research Society. TIC: 203660.

126645 Smellie, J.A.T.; Winberg, A.; and Karlsson, F. 1993. "Swedish Activities in the Oklo Natural Analogue Project." *[2nd Joint CEC-CEA Progress Meeting of the Oklo Working Group, Brussels, Belgium, April 6-7, 1992*. von Maravic, H., ed. EUR

14877 EN]. Pages 131-142. [Luxembourg, Luxembourg: Commission of the European Communities]. TIC: 247581.

156906 Smith, J.T.; Comans, R.N.J.; Beresford, N.A.; Wright, S.M.; Howard, B.J.; and Camplin, W.C. 2000. "Pollution, Chernobyl's Legacy in Food and Water." *Nature, 405*, (6782), 141. [London, England: Macmillan Journals]. TIC: 251283.

157433 Smith, J.T.; Kudelsky, A.V.; Ryabov, I.N.; and Hadderingh, R.H. 2000. "Radiocaesium Concentration Factors of Chernobyl-Contaminated Fish: A Study of the Influence of Potassium, and "Blind" Testing of a Previously Developed Model." *Journal of Environmental Radioactivity, 48*, 359-369. [New York, New York]: Elsevier. TIC: 251582.

134218 Sobotovich, E.V. 1992. *Radiogeokhimiia v Zone Vliianiia Chernobyl'Skoi AES (Radiogeochemistry of the Zone of Influence of Chernobyl NPP).* Kiev, Naukova Dumka, [Ukraine]: Academy of Sciences of Ukraine. ACC: MOL.20000629.0589.

156821 Sobotovich, E.V. and Dolin, V.V. 1994. "Mechanism of Accumulation of Migration Forms of 137Cs and 90Sr in Soils of the Near-Field Zone of CHNPP." *Problems of Chernobyl Exclusion Zone.* Volume 1. pp. 55-60. Chernobyl, Ukraine: Administration of the Chernobyl Exclusion Zone. Cataloging

117127 Sonnenthal, E.L. and Bodvarsson, G.S. 1999. "Constraints on the Hydrology of the Unsaturated Zone at Yucca Mountain, NV from Three-Dimensional Models of Chloride and Strontium Geochemistry." *Journal of Contaminant Hydrology, 38*, (1-3), 107-156. New York, New York: Elsevier. TIC: 244160.

156809 Sorey, M.L. and Lewis, R.E. 1976. "Convective Heat Flow From Hot Springs in the Long Valley Caldera, Mono County, California." *Journal of Geophysical Research, 81*, (5), 785-791. [Washington, D.C.]: American Geophysical Union. TIC: 251349.

156816 Sorey, M.L.; Suemnicht, G.A.; Sturchio, N.C.; and Nordquist, G.A. 1991. "New Evidence on the Hydrothermal System in Long Valley Caldera, California, from Wells, Fluid Sampling, Electrical Geophysics, and Age Determinations of Hot-Spring Deposits." *Journal of Volcanology and Geothermal Research, 48*, 229-263. Amsterdam, [The Netherlands]: Elsevier. TIC: 251348.

156400 Starr, R.C. and Rohe, M.J. 1995. *Large-Scale Aquifer Stress Test and Infiltration Test: Water Management System Operation and Results.* INEL-95/059. [Idaho Falls, Idaho: Idaho National Engineering Laboratory]. TIC: 250953.

156714 Steefel, C.I. and Lichtner, P.C. 1998. "Multicomponent Reactive Transport in Discrete Fractures II: Infiltration of Hyperalkaline Groundwater at Maqarin, Jordan, a Natural Analogue Site." *Journal of Hydrology, 209*, ([1-4]), 200-224. [New York, New York]: Elsevier. TIC: 251162.

156343 Stefánsson, V. 1997. "Geothermal Reinjection Experience." *Geothermics, 26*, (1), 99-139. [New York, New York]: Pergamon Press. TIC: 250947.

156642 Stein, B. and Warrick, S.F. 1979. Granite Mountains Resource Survey. Environmental Field Program, Publication 1. Santa Cruz, California: University of California, Santa Cruz. On Order Library Tracking Number-251328

156686 Steingrimsson, B.; Bodvarsson, G.S.; Gunnlaugsson, E.; Gislason, G.; and Sigurdsson, O. 2000. "Modeling Studies of the Nesjavellir Geothermal Field, Iceland." *Proceedings of the World Geothermal Congress 2000, Kyushu - Tohoku, Japan, May 28 - June 10, 2000.* Iglesias, E.; Blackwell, D.; Hunt, T.; Lund, J.; and Tamanyu, S.; eds. Pages 2899-2904. Auckland, New Zealand: International Geothermal Association. TIC: 251140.

154501 Stevens, P.R. 1977. *A Review of the Effects of Earthquakes on Underground Mines.* Open-File Report 77-313. Reston, Virginia: U.S. Geological Survey. TIC: 211779.

117820 Stockman, H.; Krumhansl, J.; Ho, C.; and McConnell, V. 1994. *The Valles Natural Analogue Project.* NUREG/CR-6221. Washington, D.C.: U.S. Nuclear Regulatory Commission. TIC: 246123.

100419 Stout, R.B. and Leider, H.R., eds. 1997. *Waste Form Characteristics Report Revision 1.* UCRL-ID-108314. Version 1.2. Livermore, California: Lawrence Livermore National Laboratory. ACC: MOL.19980512.0133.

156614 Strobel, C.J. 1993. "Bulalo Field, Philippines: Reservoir Modeling for Prediction of Limits to Sustainable Generation." *Proceedings, Eighteenth Workshop, Geothermal Reservoir Engineering, January 26-28, 1993.* Ramey, H.J., Jr.; Horne, R.N.; Kruger, P.; Miller, F.G.; Brigham, W.E.; and Cook, J.W., eds. Workshop Report SGP-TR-145. Pages 5-10. Stanford, California: Stanford University. TIC: 246821.

151957 Stuckless, J.S. 2000. *Archaeological Analogues for Assessing the Long-Term Performance of a Mined Geologic Repository for High-Level Radioactive Waste.* Open-File Report 00-181. Denver, Colorado: U.S. Geological Survey. ACC: MOL.20000822.0366.

154525 Sturchio, N.C.; Binz, C.M.; and Lewis, C.H., III 1987. "Thorium-Uranium Disequilibrium in a Geothermal Discharge Zone at Yellowstone." *Geochimica et Cosmochimica Acta, 51,* (7), 2025-2034. New York, New York: Pergamon Press. TIC: 249702.

154529 Sturchio, N.C.; Bohlke, J.K.; and Binz, C.M. 1989. "Radium-Thorium Disequilibrium and Zeolite-Water Ion Exchange in a Yellowstone Hydrothermal Environment." *Geochimica et Cosmochimica Acta, 53,* 1025-1034. [New York, New York]: Pergamon Press. TIC: 249703.

154524 Sturchio, N.C.; Keith, T.E.C.; and Muehlenbachs, K. 1990. "Oxygen and Carbon Isotope Ratios of Hydrothermal Minerals from Yellowstone Drill Cores." *Journal of Volcanology and Geothermal Research, 40,* 23-37. Amsterdam, The Netherlands: Elsevier. TIC: 249710.

156253 Sturchio, N.C.; Muehlenbachs, K.; and Seitz, M.G. 1986. "Element Redistribution During Hydrothermal Alteration of Rhyolite in an Active Geothermal System: Yellowstone Drill Cores Y-7 and Y-8." *Geochimica et Cosmochimica Acta, 50,* (8), 1619-1631. New York, New York: Pergamon Journals. TIC: 250863.

156923 Tagami, K. and Uchida, S. 1999. "Chemical Transformation of Technetium in Soil During the Change of Soil Water Conditions." *Chemosphere, 38,* (5), 963-971. [New York, New York]: Elsevier. TIC: 251292.

156920 Tarapon, A.G. 2001. "Reconstruction of the Accident at Chernobyl NPP Using Models of Heat and Mass Transfer." Electronic Modeling, 23, (3), 89-104. Kiev, [Ukraine]: National Academy of Science of Ukraine. TIC: 251290.

157439 Thomassin, J.H. and Rassineux, F. 1992. "Ancient Analogues of Cement-Based Materials: Stability of Calcium Silicate Hydrates." *Applied Geochemistry, Supplemental Issue No. 1,* 137-142. [New York, New York]: Pergamon Press. TIC: 251663.

157429 Toprak, V.; Keller, J.; and Schumacher, R. 1994. "Volcano-tectonic features of the Cappadocian volcanic province." *1994 International Volcanology Congress of the International Association of Volcanology and Chemistry of the Earths Interior.* 58 pages. Amsterdam, The Netherlands: Elsevier. On Order Library Tracking Number-251890

101024 Triay, I.R.; Furlano, A.C.; Weaver, S.C.; Chipera, S.J.; and Bish, D.L. 1996. *Comparison of Neptunium Sorption Results Using Batch and Column Techniques.* LA-12958-MS. Los Alamos, New Mexico: Los Alamos National Laboratory. ACC: MOL.19980924.0049.

100422 Triay, I.R.; Meijer, A.; Conca, J.L.; Kung, K.S.; Rundberg, R.S.; Strietelmeier, B.A.; and Tait, C.D. 1997. *Summary and Synthesis Report on Radionuclide Retardation for the Yucca Mountain Site Characterization Project.* Eckhardt, R.C., ed. LA-13262-MS. Los Alamos, New Mexico: Los Alamos National Laboratory. ACC: MOL.19971210.0177.

156350 Truesdell, A.H.; D'Amore, F.; and Nieva, D. 1984. "The Effects of Localized Aquifer Boiling on Fluid Production at Cerro Prieto." *Geothermal Resources Council Transactions, 8,* 223-229. [Davis, California]: Geothermal Resources Council. TIC: 250948.

137577 Tsang, Y.W. and Birkholzer, J.T. 1999. "Predictions and Observations of the Thermal-Hydrological Conditions in the Single Heater Test." *Journal of Contaminant Hydrology, 38,* (1-3), 385-425. New York, New York: Elsevier. TIC: 244160.

157415 U.S. Geological Survey 2000. *Review of the transport of selected radionuclides in the Interim Risk Assessment for the Radioactive Waste Management Complex, Waste Area Group 7 Operable Unit 7-13/14.* Administrative Report. Idaho Falls, Idaho:

Idaho National Engineering and Environmental Laboratory. On Order Library Tracking Number-251845

156925 Uchida, S.; Tagami, K.; Rühm, W.; and Wirth, E. 1999. "Determination of {superscript 99}Tc Deposited on the Ground Within the 30-km Zone Around the Chernobyl Reactor and Estimation of {superscript 99}Tc Released into Atmosphere by the Accident." *Chemosphere, 39*, (15), 2757-2766. [New York, New York]: Elsevier. TIC: 251293.

156945 Uchida, S.; Tagami, K.; Wirth, E.; and Rühm, W. 1999. "Concentration Levels of Technetium-99 in Forest Soils Collected Within the 30-km Zone Around the Chernobyl Reactor." *Environmental Pollution, 105*, 75-77. [Barking, Essex, England]: Elsevier. TIC: 251333.

157515 Undara Experience 2001. "Undara Experience: Australia's Accessible Outback." Queensland, Australia: Undara Experience. Accessed January 30, 2002. http://www.undara-experience.com.au Copyright Requested Library Tracking Number-251752

156398 Unger, A.J.A.; Faybishenko, B.; Bodvarsson, G.S.; and Simmons, A.M. 2002. *A Three-Dimensional Model for Simulating Ponded Infiltration Tests in the Variably Saturated Fractured Basalt at the Box Canyon Site, Idaho.* LBNL-44633. Berkeley, California: Lawrence Berkeley National Laboratory. ACC: MOL.20020213.0195.

100354 USGS (U.S. Geological Survey) 1998. *Probabilistic Seismic Hazard Analyses for Fault Displacement and Vibratory Ground Motion at Yucca Mountain, Nevada.* Milestone SP32IM3, June 15, 1998. Three volumes. Oakland, California: U.S. Geological Survey. ACC: MOL.19980619.0640.

157517 USGS (U.S. Geological Survey) 2000. "Lava Tube." *Photo Glossary of Volcano Terms.* Menlo Park, California: U.S. Geological Survey. Accessed January 30, 2002. TIC: 251751. http://volcanoes.usgs.gov/Products/Pglossary/LavaTube.html

119132 Valentine, G.A.; WoldeGabriel, G.; Rosenberg, N.D.; Carter Krogh, K.E.; Crowe, B.M.; Stauffer, P.; Auer, L.H.; Gable, C.W.; Goff, F.; Warren, R.; and Perry, F.V. 1998. "Physical Processes of Magmatism and Effects on the Potential Repository: Synthesis of Technical Work Through Fiscal Year 1995." Chapter 5 of *Volcanism Studies: Final Report for the Yucca Mountain Project.* Perry, F.V.; Crowe, B.M.; Valentine, G.A.; and Bowker, L.M., eds. LA-13478. Los Alamos, New Mexico: Los Alamos National Laboratory. TIC: 247225.

100610 van Genuchten, M.T. 1980. "A Closed-Form Equation for Predicting the Hydraulic Conductivity of Unsaturated Soils." *Soil Science Society of America Journal, 44*, (5), 892-898. Madison, Wisconsin: Soil Science Society of America. TIC: 217327.

155042 Vandergraaf, T.T.; Drew, D.J.; Ticknor, K.V.; and Seddon, W.A. 2001. "Radionuclide Migration in Tuff Under Unsaturated Conditions." *"Back to the Future - Managing the Back End of the Nuclear Fuel Cycle to Create a More Secure*

Energy Future," Proceedings of the 9th International High-Level Radioactive Waste Management Conference (IHLRWM), Las Vegas, Nevada, April 29-May 3, 2001. La Grange Park, Illinois: American Nuclear Society. TIC: 247873.

105946 Vaniman, D.T.; Bish, D.L.; Chipera, S.J.; Carlos, B.A.; and Guthrie, G.D., Jr. 1996. *Chemistry and Mineralogy of the Transport Environment at Yucca Mountain.* Volume I *of Summary and Synthesis Report on Mineralogy and Petrology Studies for the Yucca Mountain Site Characterization Project.* Milestone 3665. Los Alamos, New Mexico: Los Alamos National Laboratory. ACC: MOL.19961230.0037.

157427 Vaniman, D.T.; Chipera, S.J.; Bish, D.L.; Carey, J.W.; and Levy, S.S. 2001. "Quantification of Unsaturated-Zone Alteration and Cation Exchange in Zeolitized Tuffs at Yucca Mountain, Nevada, USA." *Geochimica et Cosmochimica Acta, 65,* (20), 3409-3433. [New York, New York]: Elsevier. TIC: 251574.

157416 Vigil, M.J. 1988. *Estimate of Water in Pits During Flooding Events.* Engineering Design File BWP-12. Idaho Falls, Idaho: EG&G Idaho. On Order Library Tracking Number-251846

108261 Vilks, P.; Cramer, J.J.; Bachinski, D.B.; Doern, D.C.; and Miller, H.G. 1993. "Studies of Colloids and Suspended Particles, Cigar Lake Uranium Deposit, Saskatchewan, Canada." *Applied Geochemistry, 8,* (6), 605-616. London, England: Pergamon Press. TIC: 237449.

156656 Villadolid, F.L. 1991. "The Applications of Natural Tracers in Geothermal Development: The Bulalo, Philippines Experience." *Proceedings of the 13th New Zealand Geothermal Workshop, 1991.* Freeston, D.H.; Browne, P.R.L.; and Scott, G.L., eds. Pages 69-74. [Auckland, New Zealand]: Geothermal Institute, The University of Auckland. TIC: 251257.

145806 Villar, E.; Bonet, A.; Diaz-Caneja, B.; Fernandez, P.L.; Gutierrez, I.; Quindos, L.S.; Solana, J.R.; and Soto, J. 1985. "Natural Evolution of Percolation Water in Altamira Cave." *Cave Science, 12,* (1), 21-24. Bridgwater, United Kingdom: British Cave Research Association. TIC: 247713.

156921 Voitsekhovitch, O.; Prister, B.; Nasvit, O.; Los, I.; and Berkovski, V. 1996. "Present Concept on Current Water Protection and Remediation Activities for the Areas Contaminated by the 1986 Chernobyl Accident." *Health Physics, 71,* (1), 19-28. [New York, New York: Pergamon]. TIC: 251291.

127454 Walton, J.C. 1994. "Influence of Evaporation on Waste Package Environment and Radionuclide Release from a Tuff Repository." *Water Resources Research, 30,* (12), 3479-3487. Washington, D.C.: American Geophysical Union. TIC: 246921.

151821 Wang, J-M. 1985. "The Distribution of Earthquake Damage to Underground Facilities During the 1976 Tang-Shan Earthquake." *Earthquake Spectra, 1,* (4), 741-757. [Berkeley, California]: Earthquake Engineering Research Institute. TIC: 226272.

154297 Weeks, K.R. 1998. "Valley of the Kings." *National Geographic, 194*, (3), [5]-33. Washington, D.C.: National Geographic Society. TIC: 249629.

156644 Weres, O. and Apps, J.A. 1982. "Prediction of Chemical Problems in the Reinjection of Geothermal Brines." *Recent Trends in Hydrogeology*. Narasimhan, T.N., ed. Special Paper 189. 407-426. Boulder, Colorado: Geological Society of America. TIC: 251079.

154773 Whelan, J.F.; Roedder, E.; and Paces, J.B. 2001. "Evidence for an Unsaturated-Zone Origin of Secondary Minerals in Yucca Mountain, Nevada." *"Back to the Future - Managing the Back End of the Nuclear Fuel Cycle to Create a More Secure Energy Future," Proceedings of the 9th International High-Level Radioactive Waste Management Conference (IHLRWM), Las Vegas, Nevada, April 29-May 3, 2001*. La Grange Park, Illinois: American Nuclear Society. TIC: 247873.

156452 Whitbeck, M. and Glassley, W.E. 1998. "Reaction Path Model for Water Chemistry and Mineral Evolution in the Altered Zone." Chapter 5.3 of *Near-Field/Altered-Zone Models Report*. UCRL-ID-129179 DR. Livermore, California: Lawrence Livermore National Laboratory. ACC: MOL.19980504.0577.

156814 White, A.F. 1986. "Chemical and Isotopic Characteristics of Fluids Within the Baca Geothermal Reservoir, Valles Caldera, New Mexico." *Journal of Geophysical Research, 91*, (B2), 1855-1866. [Washington, D.C.]: American Geophysical Research Union. TIC: 251350.

154530 White, D.E.; Fournier, R.O.; Muffler, L.J.P.; and Truesdell, A.H. 1975. *Physical Results of Research Drilling in Thermal Areas of Yellowstone National Park, Wyoming*. Geological Survey Professional Paper 892. Washington, D.C.: U.S. Government Printing Office. TIC: 235251.

156340 White, S.P.; Kissling, W.M.; and McGuinness, M.J. 1997. "Models of the Kawareu Geothermal Reservoir." *Geothermal Resources Council Transactions, 21*, 33-39. [Davis, California]: Geothermal Resources Council. TIC: 250949.

157442 Wieland, E. and Spieler, P. 2001. "Colloids in the Mortar Backfill of a Cementitious Repository for Radioactive Waste." *Waste Management, 21*, ([6]), 511-523. [New York, New York]: Elsevier. TIC: 251666.

156613 Williamson, K.H. 1992. "Development of a Reservoir Model for the Geysers Geothermal Field." *Monograph on the Geysers Geothermal Field*. Stone, C., ed. Special Report No. 17. Pages 179-187. Davis, California: Geothermal Resources Council. TIC: 251066.

156254 Winograd, I.J. 1971. "Hydrogeology of Ash Flow Tuff: A Preliminary Statement." *Water Resources Research, 7*, (4), 994-1006. [Washington, D.C.]: American Geophysical Union. TIC: 217736.

127015 Winograd, I.J. 1986. *Archaeology and Public Perception of a Transscientific Problem—Disposal of Toxic Wastes in the Unsaturated Zone.* Circular 990. Denver, Colorado: U.S. Geological Survey. TIC: 237946.

110071 WoldeGabriel, G.; Keating, G.N.; and Valentine, G.A. 1999. "Effects of Shallow Basaltic Intrusion into Pyroclastic Deposits, Grants Ridge, New Mexico, USA." *Journal of Volcanology and Geothermal Research, 92,* ([3]), 389-411. [New York, New York]: Elsevier Science B.V.. TIC: 246037.

156741 Wolery, T.J. 1979. *Calculation of Chemical Equilibrium Between Aqueous Solution and Minerals: The EQ3/6 Software Package.* UCRL-52658. Livermore, California: Lawrence Livermore Laboratory. ACC: HQS.19880517.2586.

157417 Wolfram, S. 1991. *Mathematica, A System for Doing Mathematics by Computer.* 2nd Edition. Redwood City, California: Addison-Wesley. TIC: 251766.

157467 Wollenberg, H.A.; Flexser, S.; and Smith, A.R. 1995. "Mobility and Depositional Controls of Radioelements in Hydrothermal Systems at the Long Valley and Valles Calderas." *Journal of Volcanology and Geothermal Research, 67,* ([1-3]), 171-186. Amsterdam, The Netherlands: Elsevier. TIC: 251861

103731 Wong, I.G. and Stepp, C. 1998. *Probabilistic Seismic Hazard Analyses for Fault Displacement and Vibratory Ground Motion at Yucca Mountain, Nevada.* Milestone SP32IM3, September 23, 1998. Three volumes. Oakland, California: U.S. Geological Survey. ACC: MOL.19981207.0393.

102047 Wronkiewicz, D.J.; Bates, J.K.; Wolf, S.F.; and Buck, E.C. 1996. "Ten-Year Results from Unsaturated Drip Tests with UO2 at 90°C: Implications for the Corrosion of Spent Nuclear Fuel." *Journal of Nuclear Materials, 238,* (1), 78-95. Amsterdam, The Netherlands: North-Holland Publishing Company. TIC: 243361.

117161 Wu, Y-S.; Haukwa, C.; and Bodvarsson, G.S. 1999. "A Site-Scale Model for Fluid and Heat Flow in the Unsaturated Zone of Yucca Mountain, Nevada." *Journal of Contaminant Hydrology, 38,* (1-3), 185-215. New York, New York: Elsevier. TIC: 244160.

156399 Wu, Y.S.; Liu, H.H.; Bodvarsson, G.S.; and Zellmer, K.E. 2001. *A Triple-Continuum Approach for Modeling Flow and Transport Processes in Fractured Rock.* LBNL-48875. Berkeley, California: Lawrence Berkeley National Laboratory. TIC: 251297.

156453 Wu, Y.S.; Ritcey, A.C.; Ahlers, C.F.; Mishra, A.K.; Hinds, J.J.; and Bodvarsson, G.S. 1997. Providing Base-Case Flow Fields for TSPA-VA: *Evaluation of Uncertainty of Present-Day Infiltration Rates Using DKM/Base-Case and DKM/Weeps Parameter Sets.* Milestone SLX01LB2. Berkeley, California: Lawrence Berkeley National Laboratory. ACC: MOL.19980501.0475.

117167 Wu, Y.S.; Ritcey, A.C.; and Bodvarsson, G.S. 1999. "A Modeling Study of Perched Water Phenomena in the Unsaturated Zone at Yucca Mountain." *Journal of Contaminant Hydrology, 38*, (1-3), 157-184. New York, New York: Elsevier. TIC: 244160.

156280 Xu, T. and Pruess, K. 2001. "Modeling Multiphase Non-Isothermal Fluid Flow and Reactive Geochemical Transport in Variably Saturated Fractured Rocks: 1. Methodology." *American Journal of Science, 301*, 16-33. [New Haven, Connecticut: Yale University, Kline Geology Laboratory]. TIC: 251482.

156779 Xu, T. and Pruess, K. 2001. "On Fluid Flow and Mineral Alteration in Fractured Caprock of Magmatic Hydrothermal Systems." *Journal of Geophysical Research, 106*, (B2), 2121-2138. [Washington, D.C.]: American Geophysical Union. TIC: 251239.

100194 Yang, I.C.; Rattray, G.W.; and Yu, P. 1996. *Interpretation of Chemical and Isotopic Data from Boreholes in the Unsaturated Zone at Yucca Mountain, Nevada.* Water-Resources Investigations Report 96-4058. Denver, Colorado: U.S. Geological Survey. ACC: MOL.19980528.0216.

157501 Zetterström, L. 2000. *Oklo, A Review and Critical Evaluation of Literature.* SKB TR 00-17. Stockholm, Sweden: Swedish Nuclear Fuel and Waste Management Company. TIC: 249383.

156951 Zhdanaova, N.; Redchitz, T.; Vasilevskaya, A.I.; Vember, V.; Fomina, M.; Zheltonozhsky, V.A.; Bondarkov, M.D.; Lashko, T.N.; Ukhin, M.A.; Olsson, St.; Mück, K.; Strebl, F.; and Gerzabek, M.H. 2000. *Interaction Between Biota Micromycetes and Hot Particles After the Chernobyl NPP Accident and Atomic Explosions and Investigation of their Influence in Rehabilitating Contaminated Areas, Final Report.* INTAS-UKRAINE 95-0171. Seibersdorf, Austria: Austrian Research Centers. TIC: 251553.

156630 Zheltonozhsky, V.; Mück, K.; and Bondarkov, M. 2001. "Classification of Hot Particles from the Chernobyl Accident and Nuclear Weapons Detonations by Non-Destructive Methods." *Journal of Environmental Radioactivity, 57*, ([2]), 151-166. [New York, New York]: Elsevier. TIC: 251077.

138273 Zimmerman, R.M.; Schuch, R.L.; Mason, D.S.; Wilson, M.L.; Hall, M.E.; Board, M.P.; Bellman, R.P.; and Blanford, M.L. 1986. *Final Report: G-Tunnel Heated Block Experiment.* SAND84-2620. Albuquerque, New Mexico: Sandia National Laboratories. ACC: MOL.19961217.0085.

100615 Zyvoloski, G.A.; Robinson, B.A.; Dash, Z.V.; and Trease, L.L. 1997. *User's Manual for the FEHM Application–A Finite-Element Heat- and Mass-Transfer Code.* LA-13306-M. Los Alamos, New Mexico: Los Alamos National Laboratory. TIC: 235999.

16.2 CODES, STANDARDS, REGULATIONS, AND PROCEDURES

101680 64 FR (Federal Register) 8640. Disposal of High-Level Radioactive Waste in a Proposed Geologic Repository at Yucca Mountain, Nevada. Proposed rule 10 CFR Part 63. Readily available.

156671 66 FR 55732. Disposal of High-Level Radioactive Wastes in a Proposed Geologic Repository at Yucca Mountain, NV. Final Rule 10 CFR Part 63. Readily available.

AP-2.14Q, REV 2, ICN 0. *Review of Technical Products and Data.* Washington, D.C.: U.S. Department of Energy, Office of Civilian Radioactive Waste Management. ACC: MOL.20010801.0316.

AP-3.11Q, Rev. 3, ICN 1. *Technical Reports.* Washington, D.C.: U.S. Department of Energy, Office of Civilian Radioactive Waste Management. ACC: MOL.20020404.0078.

AP-12.1Q, Rev. 0, ICN 2. *Control of Measuring and Test Equipment and Calibration Standards.* Washington, D.C.: U.S. Department of Energy, Office of Civilian Radioactive Waste Management. ACC: MOL.20020207.0111.

AP-SI.1Q, Rev. 3, ICN 3. *Software Management.* Washington, D.C.: U.S. Department of Energy, Office of Civilian Radioactive Waste Management. ACC: MOL.20020102.0200.

AP-SIII.1Q, Rev. 1, ICN 1. *Scientific Notebooks.* Washington, D.C.: U.S. Department of Energy, Office of Civilian Radioactive Waste Management. ACC: MOL.20010905.0138.

AP-SIII.3Q, Rev.1, ICN 1. *Submittal and Incorporation of Data to the Technical Data Management System.* Washington, D.C.: U.S. Department of Energy, Office of Civilian Radioactive Waste Management. ACC: MOL.20020102.0196.

LANL-EES-DP-16, R5. *Siemens X-ray Diffraction Procedure.* Los Alamos, New Mexico: Los Alamos National Laboratory. ACC: NNA.19920430.0206.

LANL-EES-DP-24, R3. *Calibration and Alignment of the Siemens Diffractometers.* Los Alamos, New Mexico: Los Alamos National Laboratory. ACC: NNA.19920430.0207.

LANL-EES-DP-56, R4. *Brinkman Automated Grinder Procedure.* Los Alamos, New Mexico: Los Alamos National Laboratory. ACC: MOL.19980626.0230.

16.3 SOURCE DATA, LISTED BY DATA TRACKING NUMBER

145412 GS980908312322.008. Field, Chemical, and Isotopic Data from Precipitation Sample Collected Behind Service Station in Area 25 and Ground Water Samples Collected at Boreholes UE-25 C #2, UE-25 C #3, USW UZ-14, UE-25 WT #3, UE-25 WT #17, and USW WT-24, 10/06/97 to 07/01/98. Submittal date: 09/15/1998.

157569 LB0201YSANALOG.001. Permeability and Porosity Measurements of Core Samples from Core Samples at Yellowstone National Park. Submittal date: 01/25/2002.

157610 LB0202PBANALOG.001. Stable Isotope Analyses of Pena Blanca Waters. Submittal date: 02/12/2002.

16.4 OUTPUT DATA, LISTED BY DATA TRACKING NUMBER

N/A